NATURAL CONVECTION FLOWS AND ASSOCIATED HEAT TRANSFER PROCESSES IN ROOM FIRES

Thesis by
William Stapf Sargent

In Partial Fulfillment

of the Requirements for the Degree of

Doctor of Philosophy

California Institute of Technology

Pasadena, California

1983
(Submitted November 5, 1982)

To my parents,
whose love and sacrifices
made my education possible

ACKNOWLEDGEMENTS

One of the more difficult tasks in finishing this thesis is to thank adequately the many individuals who have helped me bring this project to fruition.

I would like to start by expressing my deepest appreciation and gratitude to my advisor, Dr. Edward Zukoski, whose guidance, insight, patience, and unflagging enthusiasm were vital to the completion of this project. In addition to sharing his ideas with me, he carefully read and reread the entire manuscript. His comments were of great help to me in revising the text. I would also like to thank Dr. Toshi Kubota who provided many important suggestions throughout the course of this work, and who helped review parts of the manuscript. I am further indebted to many other faculty members who took an interest in this research and offered advice and constructive criticism.

Second, I would like to thank the National Bureau of Standards and the National Science Foundation, whose research grants supported this work. I would also like to thank the California Institute of Technology, and in particular the Aeronautics Department and the Jet Propulsion Center, for providing me with the financial support which made my graduate studies possible.

The experimental phase of this research would not have been possible without the technical assistance of many talented people. I would like to thank Sam Roman, Ty Linton, George Wilson, and Victor Jaramillo

who helped assemble and operate the 1/2 scale fire test room, and Mr. Elton Daly and his associates in the W. M. Keck Laboratory who helped build and modify the 1/4 scale hydraulic simulation facility.

I also owe a great debt of gratitude to the many people who helped me prepare this manuscript. In particular, without the expert and expeditious typing of Jackie Beard, Irene Black, Dorothy Eckerman, Kathy Erikson, Carol Kirsch, Linda Malaby, and Marta Nyiri, this work could not have been completed. They all pitched in and gave me a hand when I really needed it, and I thank them one and all. Finally I would also like to thank Mrs. Pat Lee and Mr. Victor Jaramillo for their help in drafting the figures in this report.

I would also like to acknowledge the many people whose personal contributions helped shape this research. First I would like to thank two of my professors from Princeton, Drs. Jerome Smith and Francis Hama, who sparked my interest in fluid mechanics and encouraged me to attend Caltech. I must also thank many of my fellow graduate students for their friendship and helpful suggestions.

Finally, I thank my wife, Nancy, for her love, support, and understanding while I spent what must have seemed like an endless series of nights and weekends here at the computer terminal.

ABSTRACT

This report presents the results of experimental investigations of natural convection flows and associated heat transfer processes produced by small fires in rooms with a single door or window opening. Calculation procedures have been developed to model the major aspects of these flows.

Two distinct sets of experiments were undertaken. First, in a roughly 1/4 scale facility, a slightly dense solution of brine was allowed to flow into a tank of fresh water. The resulting density difference produced a flow which simulated a very small fire in a room with adiabatic walls. Second, in an approximately 1/2 scale test room, a nearly stoichiometric mixture of air and natural gas was burned at floor level to model moderate strength fires. In this latter facility, we directly measured the heat conducted through the walls, in addition to determining the gas temperature and composition throughout the room.

These two facilities complemented each other. The former offered good flow visualization and allowed us to observe the basic flow phenomena in the absence of heat transfer effects. On the other hand, the latter, which involved relatively larger fires, was a more realistic simulation of an actual room fire, and allowed us to calculate the convective heat transfer to the ceiling and walls. In addition, the stronger sources present in these 1/2 scale tests produced significant

secondary flows. These secondary flows along with heat transfer effects act to modify the gas temperature or density profiles within the room from those observed in the 1/4 scale experiments.

Several calculation procedures have been developed, based on the far field properties of plumes when the density differences are small (the Boussinesq approximation). The simple point source plume solution is used along with hydraulic analysis of flow through an orifice to estimate the temperatures of the hot ceiling layer gas and of the cooler floor zone fluid, as well as the height of the interface between them. A finite source plume model is combined with conservation equations across the interface to compute the evolution of the plume above the interface. This calculation then provides the starting point for an integral analysis of the flow and heat transfer in the turbulent ceiling jet.

The computed results both for the average floor and ceiling zone gas temperatures, and for the convective heat transfer in the ceiling jet agreed reasonably well with our experimental data. This agreement suggests that our computational procedures can be applied to answer practical questions, such as whether the convective heat flux from a given fire in a real room would be sufficient to trigger sprinklers or other detection systems in a given amount of time.

PREFACE

We have been studying the natural convection flow phenomena which are produced by fires in buildings for a number of years. This work has included both small scale experimental simulations under a variety of conditions, and the development of computational procedures to help predict some of the observed phenomena. Because we have attempted to document some of these observed flow phenomena in detail, this thesis necessarily includes some rather lengthy narrative descriptions in Chapters VII and IX. Consequently, we suggest that one first read the introduction (Chapter I) and the conclusions (Chapter X) to gain an overall perspective of this work before becoming immersed in the details.

TABLE OF CONTENTS

LIST OF FIGURES

LIST OF TABLES

LIST OF SYMBOLS

Symbol	Description	Reference
$\hat{A}$	Plume parameter	Eqn. (2.50)
A'	Room model parameter	Eqn. (4.18)
$\bar{A}$	Ceiling jet profile constant	Eqn. (8.48)
A_f	Area of floor	Eqn. (5.12)
A_n	Boundary layer constant	Eqn. (8.47)
A_r	Room model parameter	Eqn. (3.32)
A_z	Plume paramter	Eqn. (2.73)
A_2	Exit area of hot flow	Eqn. (5.4)
b	Plume radius	Eqn. (2.2)
$\bar{b}$	Characteristic plume radius	Eqn. (8.55)
$\bar{b}_t$	Characteristic plume radius at $z = z_{th}$	Eqn. (8.58)
b_c	Effective plume radius at z_c	Eqn. (8.4)
b_t	Effective plume radius at z_{th}	Eqn. (8.16)
B	Room model parameter	Eqn. (3.22)
$\hat{B}$	Plume paramter	Eqn. (2.51)
B_n	Boundary layer constant	Eqn. (8.47)
$\bar{B}$	Ceiling jet profile constant	Eqn. (8.49)
c	Proportionality constant	Eqn. (8.10)
$\tilde{c}$	Tracer concentration	Eqn. (2.15)
$\tilde{c}'$	Tracer concentration fluctuations	Eqn. (2.15)
$\tilde{c}_e$	External tracer concentration	Eqn. (2.16)
c_p	Specific heat of the fluid	Eqn. (2.1)
c_f	Skin friction coefficient	Eqn. (8.32)

c_{fr}	Fraction of Q_{Loss} transferred to lower layer	Eqn. (4.25)
c_q	Heat loss parameter	Eqn. (3.27)
C	Forced plume source parameter	Eqn. (2.41)
C_Y	Numerical plume constant	Eqn. (2.56)
$\bar{C}$	Ceiling jet profile constant	Eqn. (8.51)
C_l	Plume width coefficient	Eqn. (2.60)
C_{l_T}	Plume temperature width coefficient	Eqn. (2.64)
C_{mp}	Plume mass flow coefficient	Eqn. (5.6)
C_T	Plume temperature coefficient	Eqn. (2.58)
C_v	Plume velocity coefficient	Eqn. (2.59)
C_{01}	Inflow orifice coefficient	Eqn. (3.11)
C_{02}	Outflow orifice coefficient	Eqn. (3.8)
C_{021}	Lower outflow orifice coefficient	Eqn. (4.37)
C_{022}	Upper outflow orifice coefficient	Eqn. (4.33)
C_{oo}	Ambient CO_2 concentration	Table (7.2)
C_1	Floor zone CO_2 concentration	Table (7.2)
$\bar{C}_1$	Mean value of floor zone CO_2	Eqn. (7.6)
C_2	Ceiling zone CO_2 concentration	Table (7.2)
$\bar{C}_2$	Mean value of ceiling zone CO_2	Eqn. (7.6)
Cr	Room model mass flow parameter	Eqn. (3.19)
Cr_o	Room model mass flow parameter	Eqn. (4.10)
d_{eff}	Effective plume diameter just above interface	Table(9.2)
d_o	Source diameter = $2r_o$	Eqn. (2.72)
dA_i	Differential emitting element	Eqn. (9.9)
$\bar{D}$	Room model parameter	Eqn. (3.30)
D'	Room model parameter	Eqn. (4.19)

E	Entrainment function in ceiling jet	Eqn. (8.22)
E_o	Non-buoyant entrainment function	Eqn. (8.52)
$\tilde{E}$	Lower layer enthalpy balance parameter	Eqn. (4.28)
f	Fuel to air ratio: $\dot{m}_f/\dot{m}_1$	Eqn. (3.16)
f^*	Iteratively determined value of f	Table (4.2)
$f(Y,y_o)$	Interface height function	Eqn. (3.36)
$f_1(\bar{x})$	First component of interface height function	Eqn. (4.48)
$f_2(\bar{x})$	Second component of interface height function	Eqn. (4.50)
F	Kinematic buoyancy flux of plume	Eqn. (2.1)
$F(a,b,c;x)$	Hypergeometric function	Eqn. (2.41)
$F(Y;y_o)$	General interface height function	Eqn. (4.17)
F_o	Initial plume buoyancy flux	Eqn. (2.3)
F_1	Buoyancy flux below interface	Eqn. (8.3)
F_2	Buoyancy flux above interface	Eqn. (8.3)
$\tilde{F}$	Lower layer enthalpy balance parameter	Eqn. (4.27)
F_i	Geometric view factor	Eqn. (9.11)
Fr	Densimetric Froude number	
Fr_z	Plume Froude number at height z	Eqn. (5.9)
Fr_o	Source densimetric Froude number	Eqn. (2.72)
g	Gravitational acceleration	Eqn. (2.1)
$g(Y)$	Exit plane interface height function	Eqn. (3.35)
$G(Y,y_o)$	General interface height function	Eqn. (4.16)
$G(Re,\tilde{w})$	Turbulence enhancement function	Eqn. (8.9)
h	Characteristic ceiling jet thickness	Eqn. (8.21)
$\bar{h}$	Dimensionless ceiling jet thickness	Eqn. (8.33b)
$\tilde{h}$	Initial thickness of two-dimensional ceiling jet	Eqn. (8.76)

h_c	Heat transfer coefficient	Eqn. (8.9b)
$h_{c_{lam}}$	Heat transfer coefficient at the stagnation point (axisymmetric laminar flow)	Eqn. (8.8b)
$h_{c_{sp}}$	Stagnation point heat transfer coefficient (turbulent flow)	Eqn. (8.16)
h_c'	Dimensionless heat transfer coefficient	Eqn. (8.14)
$h_{c_{ceil}}'$	Dimensionless heat transfer coefficient data measured on ceiling	Eqn. (9.17)
$h_{c_{exp}}$	Experimental value of h_c'	Fig. (8.4)
$h_{c_{s.w.}}'$	Dimensionless heat transfer coefficient data measured on side wall	Eqn. (9.16)
h_e	Initial ceiling jet thickness	Fig. (8.7)
h_p	Mean enthalpy in plume at interface	Eqn. (3.27)
h_2	Mean enthalpy of upper level gas	Eqn. (3.27)
H	Height of the opening	Fig. (3.1)
$\bar{H}$	Dimensionless opening height	Section (3.5)
$\dot{H}$	Enthalpy flux	Section (4.1)
$\tilde{H}$	Kinematic plume enthalpy flux	Eqn. (8.1)
$\dot{H}_{E_o}$	Inflow enthalpy flux mixed with exit stream	Eqn. (4.23)
$\dot{H}_r$	Enthalpy carried into lower layer by mixing	Eqn. (4.23)
$\dot{H}_o$	Enthalpy of entering stream	Eqn. (4.23)
$\dot{H}_1$	Enthalpy flux entrained by lower plume	Eqn. (4.23)
$\dot{H}_{21}$	Enthalpy leaving lower layer through door	Eqn. (4.58)
k_w	Conductivity of the wall or ceiling	Eqn. (9.6)
l	Length scale of ceiling jet profile	Section (8.6.3)
l_e	Initial ceiling jet profile length scale	Eqn. (8.65)

l_W	Plume length scale (mass)	Eqn. (2.70)
l_V	Plume length scale (momentum)	Eqn. (2.71)
L	Width of the room	Eqn. (8.71)
L_1	Effective sill height	Eqn. (3.33)
L_2	Geometric mean of exit area	Eqn. (5.4)
m	Boundary layer profile exponent	Eqn. (8.44)
m	Mass flux in axisymmetric ceiling jet	Eqn. (8.71)
$\tilde{m}$	Mass flux / width in two-dimensional ceiling jet	Eqn. (8.71)
$\dot{m}''$	Mass flow into ceiling jet boundary layer	Eqn. (8.45)
$\dot{m}_{E_o}$	Rate inflow mixed with exit stream	Eqn. (4.8)
$\dot{m}_{Ex}$	Mass flow rate of excess floor layer fluid	Fig. (4.3)
$\dot{m}_f$	Fuel flow rate	Fig. (3.1)
$\dot{m}_p$	Plume mass flow rate at the interface	Fig. (3.1)
$\dot{m}_r$	Mass flow rate of hot gas recirculated	Fig. (3.1)
$\dot{m}_o$	Mass flow rate of fluid entering room	Fig. (3.1)
$\dot{m}_1$	Plume entrainment mass flow rate	Fig. (3.1)
$\dot{m}_2$	Total flow rate of hot gas leaving room	Fig. (3.1)
$\dot{m}_{21}$	Escaping floor zone gas flow rate	Fig. (4.3)
$\dot{m}_{22}$	Escaping ceiling zone gas flow rate	Fig. (4.3)
M	Momentum flux in axisymmetric ceiling jet	Eqn. (8.72)
$\tilde{M}$	Momentum flux / width in two-dimensional ceiling jet	Eqn. (8.72)
n	Dimensionality index: Axi. n=1, Two-D. n=0	Eqn. (8.22)
n_f	Number of equal strength fires	Section (4.2)
N	Friction factor	Eqn. (8.32)
N_o	Constant value of friction factor	Section (9.3)

p	Pressure	Eqn. (8.7)
P_{ext}	External pressure beneath ceiling jet	Eqn. (8.23)
Pr	Prandtl number of the fluid	Eqn. (8.6)
q	Local heat transfer rate	Eqn. (8.9)
q_c	Convective heat transfer rate	Eqn. (8.24)
q_c^*	Dimensionless convective heat transfer rate	Eqn. (8.79)
q_{cond}	Conductive heat transfer rate	Eqn. (9.5)
q_{cond}^*	Dimensionless conductive heat transfer rate	Section (9.6.3)
q_{conv}	Convective heat transfer rate	Eqn. (9.2)
q_{conv}^*	Dimensionless convective heat transfer rate	Eqn. (9.2)
q_{lam}	Heat transfer at the stagnation point for axisymmetric laminar flow	Eqn. (8.6)
$q_{r,emit}$	Emitted radiant flux	Eqn. (9.7)
$q_{r,inc}$	Incident radiant flux	Eqn. (9.7)
$q_{r,net}$	Net radiant flux incident on a surface	Eqn. (9.5)
$q_{r,net}^*$	Dimensionless net radiative flux	Figure (9.56)
Q	Enthalpy flux in axisymmetric ceiling jet	Eqn. (8.73)
$\tilde{Q}$	Enthalpy flux in two-dimensional ceiling jet	Eqn. (8.73)
Q^*	Dimensionless heat input parameter	Eqn. (2.55)
Q_i^*	Dimensionless heat input parameter, evaluated at the interface ($z = z_i$)	Section (3.5)
$Q_{z_c}^*$	Dimensionless heat input paramter, evaluated at the ceiling ($z = z_c$)	Eqn. (3.44)
$Q_{\frac{cooling}{jacket}}$	Enthalpy gain in cooling jacket	Table (9.6)
Q_F	Heat release rate of the fire	Eqn. (2.1)

$\dot{Q}_{ir}$	Total heat loss over the impingement region	Eqn. (8.17)
$Q_{ir_{max}}$	Maximum estimated impingement region loss	Eqn. (8.18)
$Q_{ir_{min}}$	Minimum estimated impingement region loss	Eqn. (8.20)
Q_{Loss}	Total convective losses from upper layer	Section (7.7)
Q_T^*	Calculated total convective flux	Fig. (9.8)
$Q_{T,cond}^*$	Dimensionless total conduction through an area	Table (9.6)
$Q_{T,conv}$	Total convective loss from an area	Eqn. (9.3)
$Q_{T,conv}^*$	Dimensionless total convective loss from an area	Eqn. (9.4)
$\dot{Q}_{floor}$	Heat transfer to lower layer gas	Eqn. (4.23)
r	Radial coordinate	Eqn. (2.12)
$\overline{r}$	Dimensionless radius: $\overline{r} = r/z_c$	Eqn. (8.33)
$\overline{r}'$	Dimensionless distance along ceiling and sidewall	Fig. (9.30)
r_e	Radius at which ceiling jet starts	Eqn. (8.5)
r_o	Source radius	Eqn. (2.70)
Re	Reynolds number	
$\overline{Re}$	Reynolds number ratio	Eqn. (5.8)
Re_d	Reynolds number based on cylinder diameter	Eqn. (8.10)
Re_o	Source Reynolds number based on diameter	Table (5.5)
Re_m	Boundary layer Reynolds number, based on δ	Eqn. (8.42)
Re_r	Ceiling jet Reynolds number based on r	Eqn. (9.13)
Re_{r_e}	Initial ceiling jet Reynolds number at $r = r_e$	Eqn. (9.13)
Re_z	Plume Reynolds number at height z	Eqn. (5.3)
Re_2	Reynolds number of hot exit flow	Eqn. (5.4)
Ri	Richardson number	

Ri_c	Cold inflow Richardson number	Eqn. (3.49)
Ri_H	Opening height Richardson number	Eqn. (3.48)
Ri_w	Richardson number for flow down sidewalls	Eqn. (7.3)
Ri_z	Plume Richardson number at height z	Eqn. (5.9)
Ri_o	Source Richardson number based on diameter	Eqn. (2.72)
s_T	Standard deviation of the temperature data	Section (7.3)
S	Span of the opening	Eqn. (3.8)
$\bar{S}$	Dimensionless span of the opening	Section (3.5)
$\hat{S}$	Ceiling jet profile parameter	Eqn. (8.28)
S^*	Maximum shear velocity ratio	Eqn. (3.47)
t	Time	Eqn. (7.2)
t_{fill}	Time scale to fill closed room	Eqn. (5.12)
t_{res}	Time scale to refill upper layer	Section (5.2)
t_{wall}	Characteristic thermal time scale for ceiling or wall	Section (5.3)
T	Fluid temperature	Eqn. (2.14)
T'	Temperature fluctuations	Eqn. (2.14)
T_e	External temperature	Eqn. (2.16)
T_i	Element surface temperature	Eqn. (9.10)
T_m	Maximum gas temperature	Eqn. (2.28)
T_{m_e}	Initial maximum temperature in ceiling jet	Eqn. (8.37)
T_{mg}	Maximum local gas temperature in ceiling jet	Eqn. (9.2a)
T_{mt}	Maximum plume temperature at z_{th}	Eqn. (8.8)
T_{ref}	Viscosity reference temperature	Eqn. (8.15)
T_{sp}	Stagnation point gas temperature	Eqn. (8.6)
T_w	Surface temperature	Eqn. (8.6)

$T_{w_{out}}$	Outer surface temperature	Eqn. (9.6)
T_o	Reference fluid temperature at plume source	Eqn. (2.1)
T_1	Floor layer gas temperature	Eqn. (4.29)
$\bar{T}_1$	Mean value of floor layer temperature	Fig. (7.3)
T_2	Ceiling layer gas temperature	Figure (3.2)
$\bar{T}_2$	Mean value of ceiling layer temperature	Fig. (7.3)
T_{oo}	Ambient gas temperature in laboratory	Eqn. (7.1)
T_1^*	Dimensionless temperature difference with respect to T_1	Eqn. (9.1)
T_2^*	Dimensionless temperature differece with respect to T_2	Eqn. (9.1)
T_{oo}^*	Dimensionless temperature difference with respect to T_{oo}	Eqn. (7.1)
T^*	Dimensionless ceiling jet temperature difference with respect to T_2	Eqn. (8.78)
u	Radial velocity	Eqn. (2.12)
u'	Radial velocity fluctuations	Eqn. (2.13)
u_e	Radial entrainment velocity	Eqn. (2.10)
u_m	Maximum radial velocity in ceiling jet profile	Eqn. (8.32)
$u_{m,e}$	Initial maximum velocity in ceiling jet	Fig. (8.7)
U	Characteristic radial or axial velocity in ceiling jet	Eqn. (8.21)
$\tilde{U}$	Initial velocity in two-dimensional ceiling jet	Eqn. (8.74)
$\bar{U}$	Dimensionless ceiling jet velocity	Eqn. (8.34)
U_e	Initial ceiling jet velocity	Eqn. (8.34)
U_{ext}	External velocity below ceiling jet	Eqn. (8.22)
U^*	Dimensionless scaled ceiling jet velocity	Eqn. (8.77)
v_o	Inflow velocity of fresh air	Eqn. (3.9)

$\bar{v}_o$	Inflow bulk velocity	Eqn. (3.50)
$v_{o_{max}}$	Maximum inflow velocity	Eqn. (3.46)
v_2	Exit velocity of hot gas	Eqn. (3.7)
$\bar{v}_2$	Exit bulk velocity	Eqn. (5.4)
$v_{2_{max}}$	Maximum exit velocity	Eqn. (3.46)
v_{21}	Exit velocity of warm gas from floor layer	Eqn. (4.36)
v_{22}	Exit velocity of hot gas from upper layer	Eqn. (4.32)
V	Kinematic momentum flux of plume	Eqn. (2.6)
V_o	Initial momentum flux of forced plume or jet	Eqn. (2.8)
V_1	Plume momentum flux just below interface	Section (8.2)
V_2	Plume momentum flux just above interface	Section (8.2)
$\dot{V}_{brine}$	Source flow rate of brine	Table (4.2)
$\dot{V}_p$	Volumetric flow rate of plume at interface	Eqn. (4.28)
$\dot{V}_o$	Inflow rate of ambient air	Eqn. (3.11)
$\dot{V}_2$	Outflow rate of hot gas	Eqn. (3.8)
$\dot{V}_{21}$	Outflow rate of warm gas (floor layer)	Eqn. (4.37)
$\dot{V}_{22}$	Outflow rate of hot gas (ceiling layer)	Eqn. (4.33)
w	Vertical velocity	Eqn. (2.3)
w'	Vertical velocity fluctuations	Eqn. (2.13)
$\bar{w}$	Characteristic plume vertical velocity	Eqn. (8.55)
$\bar{w}_t$	Characteristic plume velocity at $z = z_{th}$	Eqn. (8.58)
w_c	Characteristic vertical velocity	Eqn. (2.26)
w_m	Maximum vertical velocity in plume	Eqn. (2.27)
w_{mt}	Maximum plume velocity at z_{th}	Section (8.3)
$\tilde{w}$	Axial turbulence intensity in the plume	Eqn. (8.10)

W	Kinematic mass flux of plume	Eqn. (2.5)
W_o	Initial kinematic mass flux	Eqn. (2.32)
W_1	Mass flux just below interface	Section (8.2)
W_2	Mass flux just above interface	Section (8.2)
W_{scale}	Characteristic plume mass flux scale	Eqn. (2.74)
x	Axial coordinate for two dimensional ceiling jet flow	Fig. (8.9)
x_e	Starting location of two-dimensional ceiling jet	Section (8.6)
$\overline{x}$	Interface height solution : $\overline{x} = (Y, y_o)^T$	Eqn. (4.48)
y	Vertical coordinate relative to the sill	Eqn. (3.1)
y_o	Height of interface above sill at door	Fig. (3.1)
Y	Height of the interior interface, relative to sill	Fig. (3.1)
z	Vertical coordinate, measured from floor	Eqn. (2.2)
z'	Vertical coordinate, measured from virtual source	Figure (3.1)
z_i'	Height of interface above virtual source	Eqn. (3.25)
$\tilde{z}$	Vertical coordinate, measured from ceiling	Eqn. (8.4)
$\overline{z}$	Dimensionless vertical coordinate: $z = z / z_c$	Eqn. (3.44)
z_c	Height of the ceiling	Fig. (3.1)
z_d^+	Upper edge of interface zone in door-plane	Fig. (7.24)
z_d^-	Lower edge of interface zone in door-plane	Fig. (7.24)
z_f	Height of fire above floor	Fig. (3.1)
z_i, z_{int}	Height of the interface	Fig. (3.1)
z_l	Height of sill above floor	Fig. (3.1)
z_{scale}	Characteristic plume height scale	Eqn. (2.73)
z_{th}	Effective termination height of plume	Section (8.3)
z_u	Height of soffit above floor	Fig. (3.1)

z_{vs}	Height of virtual source	Eqn. (2.73)
z^+	Upper edge of interface zone (interior of room)	Fig. (7.3)
z^-	Lower edge of interface zone (interior of room)	Fig. (7.3)
z^+_{eff}	Local upper edge of interface zone	Section (7.3.1)
z^-_{eff}	Local lower edge of interface zone	Section (7.3.1)
α	Entrainment constant	Eqn. (2.26)
α_{jet}, α_j	Momentum jet entrainment constant	Eqn. (2.69)
α_{plume}, α_p	Buoyant plume entrainment constant	Eqn. (2.69)
β	Entrainment function constant	Eqn. (8.54)
γ	Initial ceiling jet Richarson number	Eqn. (8.37)
∇	Kinematic buoyancy of the fluid per unit volume	Eqn. (2.4)
∇'	Kinematic buoyancy fluctations	Eqn. (2.17)
∇	Characteristic buoyancy of ceiling jet	Eqn. (8.21)
$\overline{\nabla}$	Dimensionless buoyancy of ceiling jet	Eqn. (8.35)
$\tilde{\nabla}$	Initial buoyancy of two-dimensional ceiling jet	Eqn. (8.75)
∇_e	Initial buoyancy of ceiling jet	Eqn. (8.35)
∇_{max}	Maximum kinematic buoyancy	Eqn. (2.32)
δ	Density difference ratio	Eqn. (4.1)
δ^*	Iteratively determined value of δ	Table (4.2)
δ_{crit}	Critical density difference ratio	Section (4.2)
$\vec{\delta}$	Iterative correction vector	Eqn. (4.51)
$\tilde{\delta}$	Boundary layer thickness in ceiling jet	Eqn. (8.42)
$\hat{\delta}$	Approximate ceiling jet thickness	Section (7.3)
$\delta_{1/2}$	Ceiling jet velocity half-width	Eqn. (8.48)
ΔC^*_{21}	Dimensionless CO_2 concentration	Table (7.2)
Δp	Hydrostatic pressure difference across opening	Fig. (3.2)

Δp_i	Pressure difference at interface	Eqn. (3.4)
Δp_{in}	Inflow pressure difference	Eqn. (4.30)
Δp_{out}	Outflow pressure difference	Eqn. (4.32)
Δp_s	Pressure diffrence at stagnation point	Section (8.3)
$\Delta \rho_{brine}$	Initial plume density difference	Section (3.3)
$\Delta \rho_m$	Maximum density difference	Eqn. (2.30)
$<\Delta \rho>$	Mass-averaged density difference	Eqn. (3.24)
ΔT^*	Dimensionless gas temperature difference	Section (7.3.1)
ΔT_{gw}	Measured gas-wall temperature difference	Section (9.6.3)
ΔT^*_{gw}	Dimensionless gas-wall temperature difference	Eqn. (9.2a)
ΔT_m	Maximum temperature difference across profile	Eqn. (2.48)
$\Delta T_{m,e}$	Initial maximum gas temperature difference in ceiling jet	Fig. (8.7)
ΔT_{max}	Maximum temperature difference between ceiling and floor	Table (7.4)
ΔT^*_{max}	Dimensionless maximum temperature difference between ceiling and floor	Table (7.4)
$\overline{\Delta T}_p$	Characteristic plume temperature difference	Eqn. (8.57)
$\overline{\Delta T}_{p_t}$	Characteristic plume temperature difference at $z = z_{th}$	Eqn. (8.62)
ΔT_w	Calculated gas-wall temperature difference	Eqn. (8.17)
$\Delta T_{w_{sp}}$	Stagnation point gas-wall temperature difference	Eqn. (8.17)
ΔT_{21}	Temperature difference across interface	Table (7.4)
ΔT^*_{21}	Dimensionless temperature difference across interface	Table (7.4)
$<\Delta T>$	Mass-averaged temperature difference	Eqn. (3.23)
Δ_w	Thickness of the wall or ceiling	Eqn. (9.6)
ε	Surface emissivity	Eqn. (9.8)

ε_u	Impingement turning efficiency (velocity)	Eqn. (8.60)
ε_T	Impingement turning efficiency (temperature)	Eqn. (8.63)
η	Fraction of $\dot{m}_p$ which exits room	Eqn. (3.15)
η_c	Estimate of η from CO_2 data	Eqn. (7.6)
η_T	Estimate of η from doorway temperature data	Eqn. (7.5)
κ	Stagnation point temperature parameter	Eqn. (8.8a)
κ_o	Inflow recirculation fraction	Eqn. (4.8)
λ	Stagnation point pressure parameter	Eqn. (8.7b)
μ	Dimensionless plume volume flux	Eqn. (2.33)
μ_o	Initial dimensionless plume volume flux	Eqn. (2.38)
ν	Kinematic viscosity of the fluid	
ν_o	Kinematic viscosity at T_o	Eqn. (5.3)
ν_{ref}	Reference viscosity at T_{ref}	Eqn. (8.15)
ν_2	Viscosity of fluid in upper layer at T_2	Eqn. (8.15)
ϕ	Dimensionless plume momentum flux	Eqn. (2.34)
Φ	Interface height difference expression	Eqn. (4.35)
$\hat{\Phi}$	Jacobian derivative matrix	Eqn. (4.52)
Ψ	Weighted interface height expression	Eqn. (4.34)
ρ	Fluid density	Eqn. (2.4)
ρ_{brine}	Density of brine at the source	Table (4.2)
ρ_e	External fluid density	Eqn. (2.4)
ρ_o	Reference fluid density at plume source	Eqn. (2.1)
ρ_1	Lower or floor zone density	Fig. (3.1)
ρ_2	Upper or ceiling layer density	Fig. (3.1)
σ	Profile width parameter	Eqn. (2.28)
$\hat{\sigma}$	Stefan-Boltzmann constant	Eqn. (9.8)

τ	Dimensionless time: $\tau = t/t_{res}$	Eqn. (7.2)
τ_w	Wall shear stress	Eqn. (8.23)
θ_i	Incidence angle of emitting surface	Eqn. (9.9)
θ_t	Incidence angle of receiving surface	Eqn. (9.9)
$\hat{\xi}$	Mixing fraction: $\hat{\xi} = 1 - \eta$	Table (4.2)
$\overline{\hat{\xi}}$	Average value (experimental) of $\hat{\xi}$	Table (7.8)
ξ	Ceiling jet turning fraction	Fig. (8.9)
ζ	Dimensionless plume height	Eqn. (2.35)
ζ_o	Dimensionless plume virtual source location	Eqn. (2.41)

I. INTRODUCTION

1.1 Natural Convection Effects in Building Fires

Each year in the United States, fires in buildings take thousands of lives and cause damage in excess of 6 billion dollars. As these costs in life and property have increased, interest has risen in studying building fires in order to achieve a better understanding of the physical processes involved.

One aspect that is of considerable interest is the fluid dynamics of the combustion products (i.e. the smoke). The flow of smoke is particularly important in modern, multistory buildings. Such buildings are constructed from essentially fire proof materials (i.e. concrete and steel), and fires in them are often contained to a particular room, suite, or floor. However, buoyancy forces lift the hot smoke through vertical shafts and can very effectively fill the upper stories of the building with lethal fumes. The increased use of polyvinyl chlorides and polyurethanes in rugs, furniture, and decorations makes the smoke even more deadly.

The recent disastrous fire in the ground level Casino of the MGM Grand Hotel in Las Vegas provides a grim example of this phenomenon.[1] Of the 84 people who perished, only 12 were actually killed by the flames. Although the fire itself was limited to the first two stories, dense black smoke, rising through elevator shafts and stairwells, quickly

1. For more details, see the extensive coverage in the Los Angeles Times , November 22-24, 1981.

filled the upper stories of the hotel, and caused at least 60 deaths on the upper six floors.

In order to predict the flow of smoke throughout a building, one must know what the "source conditions" are, that is, one must know what the fire itself is doing as a function of time. We therefore chose to investigate the flow phenomena produced by a small fire in a single room, and to concentrate on its early development. During this period the fire is assumed to remain localized. In addition, in most practical cases, a quasi-steady flow pattern is quickly established. The general features of this flow field are shown in Figure (1.1), which depicts a room with an open doorway through which the smoke can escape and fresh air can enter.

Room fires often exhibit two stages of development. Excluding those fires that have been deliberately set, fires in buildings usually remain confined to an area close to the source of ignition for some finite period of time. During this phase, buoyancy forces produce a turbulent plume of combustion products which fill the upper portion of the room and typically spill out into adjoining spaces through doors, or window-like openings, as shown in Figure (1.1). As the upper portions of the room become heated by this natural convection process, they begin to radiate energy to the lower portions of the room, thereby preheating the fuel and air supply of the fire. Depending on the strength of the fire, and the nature of the fuel load, the fuel in the lower portion of the room can become preheated sufficiently close to the ignition point that the fire can suddenly ignite it and engulf the entire room. This

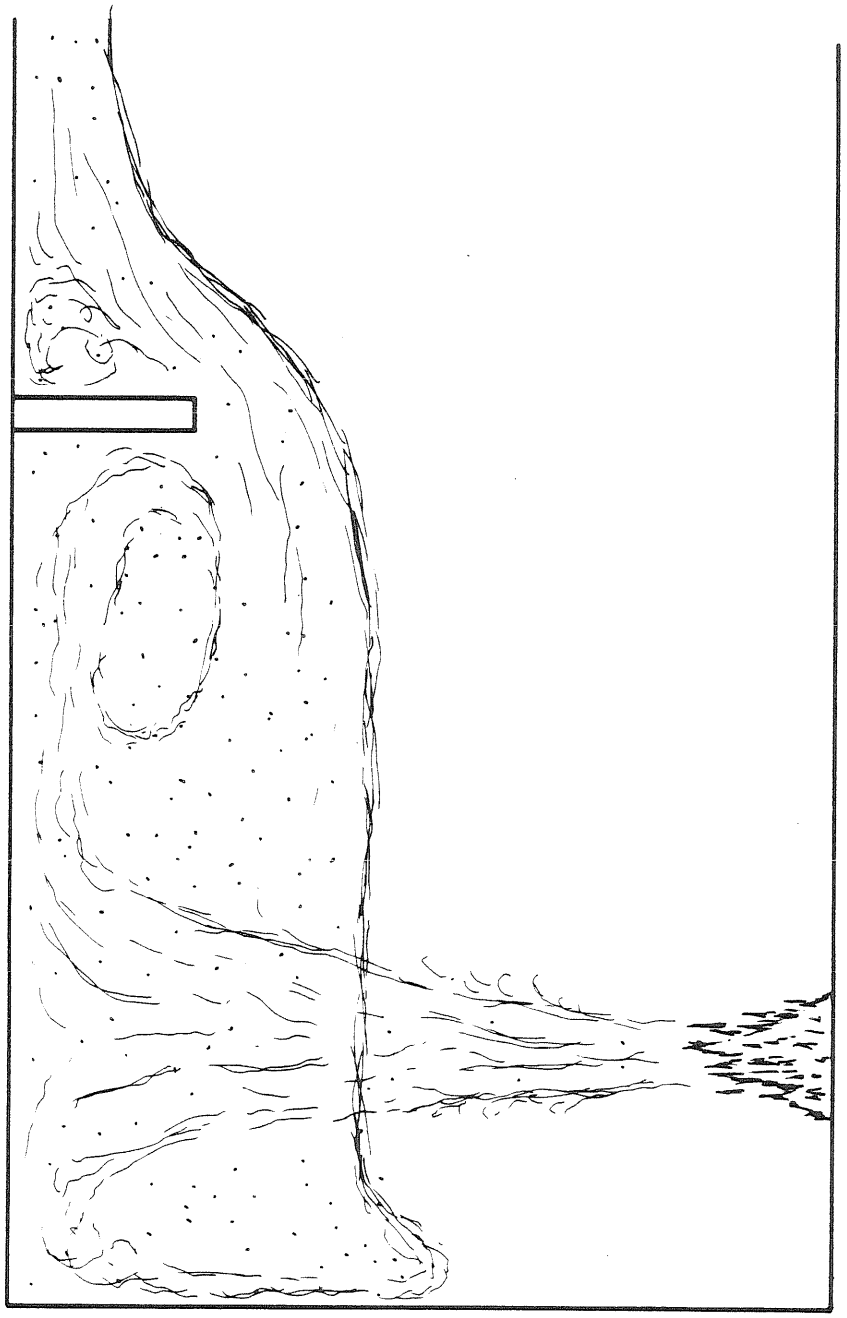

Figure (1.1) General Flow Patterns Induced by a Small Fire in a Room with an Open Doorway

process, referred to as "flash over", obviously has a profound effect on the survivability of those in or near the room, and on the subsequent evolution of the fire, which now has a much larger heat release rate and consequently much greater smoke production.

One of the key features in understanding this flash over phenomenon is a knowledge of the early convective heat transfer processes in which the hot gas from the plume heats the initially cold ceiling and upper walls. Depending on the details of the room geometry and the construction of the ceiling and walls, a very large fraction of the fire's heat release can be transferred to these surfaces. For example, in our 1/2 scale room tests, roughly 26-32% of the heat released by the fire was deposited in the ceiling and upper walls when the room had a fully open doorway. This fraction lost to convection increased to 41% when the lower 55% of the doorway was blocked to form a window. Our calculations have shown that a large fire in a small room may transfer up to 80% of its energy to the ceiling and walls in this manner. This also implies that because of the large convective losses in the very early stages of room fires, there may be relatively little enthalpy left over to spread the fire outside the room. Thus convective heat transfer processes play a central role in determining the evolution of room fires, and this realization motivated our research.

1.2 Scope of this Work

To predict the conditions within the room with the fire, the outflow of smoke from this room to the rest of the structure, and the pos-

sible occurrence of flash over, knowledge is required of the fire induced natural convection flow patterns and the associated convective heat transfer in the early (pre-flash over) stages of the fire. Consequently, our efforts have been focused on studying these flow patterns both theoretically and experimentally. For simplicity, we have chosen to examine the case of a room with a single fire and a single opening to the adjoining space, as shown in Figure (1.1).

The most vigorous element of the natural convection flows which are induced by a fire in a room is the buoyant plume which rises from the fire. Because of the large amount of fluid entrained by this highly turbulent flow, the plume acts as a pump which drives the overall flow pattern sketched in Figure (1.1). Thus numerical models of the plume lie at the heart of our computational procedures. In Chapter II, several related integral models of the plume are presented in a consistent manner for a variety of possible flow conditions.

The transient time scales of the natural convection flow processes are typically short compared to the thermal response times of the solid materials which make up the ceiling and walls of the room. Consequently, a quasi-steady flow pattern will be quickly established, in which the gas temperature profiles will have attained nearly steady state values while the solid surfaces remain relatively cold.

In order to predict the basic temperature profile within the room under these quasi-steady conditions, we extended a simple steady state room model originally developed by Zukoski (1975). This model is based

on the known behavior of turbulent plumes and a hydraulic approximation for counter flow through the opening. Descriptions of the simple and extended forms of this model, along with representative numerical results, may be found in Chapters III and IV, respectively.

Next, to predict the convective heat transfer to the ceiling, we developed a related computational procedure, based again on turbulent plume behavior and the knowledge of wall jets in stratified media. This model, which is described in Chapter VIII, is a generalization of the work of Alpert (1974), who calculated the simpler problem of convective heat transfer to a ceiling in the absence of side walls.

The flow patterns have been studied experimentally in both 1/4 and 1/2 scale facilities. Details concerning the experimental apparatus, data acquisition and processing techniques, and values of the dimensionless scaling parameters for these facilities and for full scale fires are given in Chapter V.

In the 1/4 scale facility, water was used as the working medium and the density differences were produced by injecting a 5-10% denser solution of brine. The density profile within the room was then calculated from the measured salinity profile. We could thus study the effects of buoyancy in the absence of heat transfer. These results have already been documented by Tangren, Sargent, and Zukoski (1978). Therefore, they are only briefly reviewed in Chapter VI in order to highlight the diffrences between them and the 1/2 scale data.

In the 1/2 scale facility, a stochiometric mixture of air and natural gas was burned at floor level. Because the buoyancy was generated by the release of heat, we were able to study both buoyancy and heat transfer effects. Both the gas temperature profiles within the room as well as the surface temperature distributions were measured. In Chapter VII, the gas temperature and carbon dioxide concentration data are presented and analyzed. The heat transfer data were computed from the measured surface temperature distributions. In Chapter IX, these results are presented and compared with the predictions of the ceiling jet calculation, which was described in Chapter VIII.

Finally, a review of our results along with our conclusions is presented in Chapter X.

1.3 Extensions and Generalizations of the Models

The models that have been presented here are of limited scope, but most can easily be generalized. The generally good agreement between our experimental data and our computed results indicates that the assumptions and approximations which we employed are reasonable for modelling the moderately small fires which we have considered.

Since many fires are initially of limited extent, they can be approximated as point sources of heat. Other geometries can be treated by similar analysis. For example, experiments and theoretical models for line sources of heat are presented by Tangren, Sargent, and Zukoski (1978).

The theoretical models described in this work assume that a quasi-steady state flow is quickly established in the early stages of a fire. In addition they also assume that the heat release is small. Consequently, the resulting density or temperature differences will also be small, and the Boussinesq approximation can be used to simplify the calculations. However, these restrictions can be relaxed. Zukoski (1978) developed a model for the transient behavior of the gas within a closed room with a fire. Subsequently, Zukoski and Kubota (1980) incorporated the effects of large density differences, the transient response of the gas, and recent measurements of entrainment in diffusion flames to produce a more general room model.

The room models in this work have been developed for a single opening. However, multiple openings can easily be accomodated as indicated in Chapter IV.

Finally, our hope is that these simple, semi-empirical models for the conditions within the fire room itself can be readily combined with results obtained for the flow of smoke in horizontal hallways and vertical shafts (such as those reported by Cannon and Zukoski (1976)), to simulate fires in buildings with more complicated geometries. Given the initial success of these models in predicting our experimental results, we feel that this approach is quite promising.

II. MODELING THE FIRE PLUME

2.1 Introduction

When a fire starts burning in a room, it is usually confined to a relatively small area initially. Buoyant forces act on the hot gas of the combustion products and produce a turbulent buoyant plume. As the plume rises, it rapidly entrains ambient air, mixing it with the combustion products, and delivers a large volume of heated air and combustion products to some higher elevation (initially the ceiling). The buoyant plume thus acts as a large pump in setting up the flow patterns in a room with a fire. Consequently, modeling the plume's behavior lies at the heart of most room fire models.

The subject of turbulent plumes has been widely studied, starting with Schmidt (1941). One can describe a *pure plume* as the flow resulting from a point source of buoyancy only. A real fire confined to a small area comes close to the idealization of a point source when viewed from heights greater than several fire diameters, because the initial mass and momentum fluxes are small compared to the initial buoyancy. For example, Yokoi (1960) reported that the plume above an array of alcohol burners agreed with the pure plume solution for heights greater than two fire diameters. However, experimental models for buoyant plumes often introduce significant initial mass and momentum fluxes in order to achieve the desired initial buoyancy flux. This gives rise to a buoyant jet or what Morton (1959a) terms a "forced plume." Thus in evaluating experimental data, one must attempt to differentiate mass and momentum induced effects from those due to buoyancy.

2.2 Dimensional Analysis

In order to clarify this distinction, it is useful to examine the two limiting (asymptotic) cases: the pure plume (source of buoyancy only) and the pure jet (source of momentum only). Consider a pure plume with fully developed turbulence, in a uniform environment, and such that the density differences are small compared to the fluid density itself. The last qualification, known as the Boussinesq approximation, arises because small (1%) density differences can produce large natural convection flows, while the inertia of the fluid remains essentially constant. Under the Boussinesq approximation, the fluid density is treated as constant in all the inertia terms of the equations of motion, while the density difference is retained in the buoyancy terms. Unless otherwise specified, this approximation will be used throughout this work. Given this approximation, it becomes very useful to introduce kinematic fluxes for mass, momentum, and buoyancy which are the respective fluxes, divided by the constant reference density. For the case at hand of a pure plume, we have one characteristic quantity describing the plume: the kinematic buoyancy flux $F[L^4/t^3]$. If the buoyancy is produced by adding heat to the fluid, the heat flux can be conveniently related to the buoyancy flux:

$$Q_F = (\rho_0 c_p T_0/g)F \qquad (2.1)$$

where ρ_0, T_0 are the reference density and temperature of the fluid. Thus $\rho_0 F$ is the weight deficit given to a volume of fluid each second. Since we assume fully developed turbulence and consider distances large

compared to any source dimensions there are only two parameters in the problem: z [L], the distance to the source, and F_0. For a pure plume in a uniform environment $F = F_0$, and dimensional analysis then gives:

$$b \propto z \tag{2.2}$$

$$w \propto F_0^{1/3} z^{-1/3} \tag{2.3}$$

$$\tilde{\nabla} \propto F_0^{2/3} z^{-5/3} \tag{2.4}$$

$$W \propto F_0^{1/3} z^{5/3} \tag{2.5}$$

$$V \propto F_0^{2/3} z^{4/3} \tag{2.6}$$

where b is the radial scale of the plume, w is the vertical velocity scale, and $\tilde{\nabla} = g\left(\frac{\rho_e - \rho}{\rho_0}\right)$ is the kinematic buoyancy per unit volume. $W[L^3/t]$ is the kinematic mass flux (or volume flux) and $V[L^4/t^2]$ is the kinematic momentum flux.

Similarly, for a pure jet, where $V = V_0$ there are only two parameters, V_0, and z. Hence:

$$b \propto z \tag{2.7}$$

$$w \propto V_0^{1/2} z^{-1} \tag{2.8}$$

$$W \propto V_0^{1/2} z \tag{2.9}$$

These equations exhibit some interesting features. First, note that in both cases W increases monotonically with z, but that the plume exhibits a faster growth rate. Second, the rate of increase of the kinematic mass flux $\left[\frac{dW}{dz}\right]$ must be equal to the rate fluid is being

entrained into the plume, and that this rate must be proportional to the plume radius b times an entrainment velocity u_e.

Plume	Jet	
$\frac{dW}{dz} \propto F_0^{1/3} z^{2/3} \propto bu_e$	$\frac{dW}{dz} \propto V_0^{1/2} \propto bu_e$	(2.10 a,b)
$u_e \propto F_0^{1/3} z^{-1/3} \propto w$	$u_e \propto V_0^{1/2} z^{-1} \propto w$	(2.11 a,b)

In both cases the entrainment velocity is proportional to the scale of the vertical velocity, as shown by Batchelor (1954). Finally note that in the plume the buoyancy forces continually increase the momentum flux. This feature is of prime importance in understanding the behavior of buoyant jets for it indicates that although a weakly buoyant jet will behave as a jet ($V \sim V_0$ = constant) for moderate z, at large z, $V >> V_0$ and the flow will behave as a plume.

2.3 Equations of Motion

Dimensional analysis gives the asymptotic behavior of plumes and jets, that we would expect to observe far from the source in a semi-infinite, uniform environment. However, in order to calculate plume behavior near a finite source or in a stratified environment, we must solve the equations of motion. For the case of a fully turbulent axisymmetric plume we can neglect the molecular transport terms and can write the Reynolds Equations in a boundary layer form since we expect the radial extent of the motion to be small and hence radial gradients will be large compared to axial (vertical) gradients.

Applying the Boussinesq approximation, the equations of motion are:

Conservation of Mass

$$\frac{\partial w}{\partial z} + \frac{1}{r}\frac{\partial}{\partial r}(ru) = 0 \tag{2.12}$$

Conservation of Momentum

$$w\frac{\partial w}{\partial z} + u\frac{\partial w}{\partial r} = g\left(\frac{\rho_e - \rho}{\rho_0}\right) - \frac{1}{r}\frac{\partial}{\partial r}(r\,\overline{w'u'}) \tag{2.13}$$

Conservation of Energy

$$w\frac{\partial T}{\partial r} + u\frac{\partial T}{\partial z} = -\frac{1}{r}\frac{\partial}{\partial r}(r\,\overline{u'T'}) \tag{2.14}$$

Conservation of Tracer

$$w\frac{\partial \tilde{c}}{\partial z} + u\frac{\partial \tilde{c}}{\partial r} = -\frac{1}{r}\frac{\partial}{\partial r}(r\,\overline{u'\tilde{c}'}) \tag{2.15}$$

Assume the density difference can be linearly related to the tracer concentration and the temperature differences in the fluid:

$$\frac{\rho_e - \rho}{\rho_0} = k_1(\tilde{c} - \tilde{c}_e) + k_2(T - T_e) \tag{2.16}$$

Then the energy and tracer equations can be combined to give an effective "conservation" equation for the kinematic buoyancy:

$$w\frac{\partial}{\partial z}[\tilde{\nabla}] + u\frac{\partial}{\partial r}[\tilde{\nabla}] = -\frac{1}{r}\frac{\partial}{\partial r}[r\,\overline{u'\tilde{\nabla}'}] \tag{2.17}$$

These equations can be simplified (with a resulting loss of information about the profile shapes) by integrating across a horizontal plane subject to the boundary conditions:

r = 0:

$$u = 0 \quad \frac{\partial w}{\partial r} = 0 \quad \frac{\partial \tilde{\nabla}}{\partial r} = 0 \quad \overline{u'w'} = 0 \quad \overline{u'\tilde{\nabla}'} = 0 \tag{2.18}$$

$r \to \infty$:

$$u = 0 \quad w = 0 \quad \tilde{\nabla} = 0 \quad \overline{u'w'} = 0 \quad \overline{u'\tilde{\nabla}'} = 0 \tag{2.19}$$

The equations in integrated form are:

Conservation of Mass

$$\frac{d}{dz}\left[\int_0^\infty wr\, dr\right] = -\lim_{r\to\infty}(ru) \tag{2.20}$$

Conservation of Momentum

$$\frac{d}{dz}\left[\int_0^\infty w^2 r\, dr\right] = \int_0^\infty \tilde{\nabla} r\, dr \tag{2.21}$$

Conservation of Buoyancy (Energy)

$$\frac{d}{dz}\left[\int_0^\infty w\,\tilde{\nabla} r\, dr\right] = -\frac{g}{\rho_0}\frac{d\rho_e}{dz}\int_0^\infty wr\, dr = -\frac{g}{\rho_0}\frac{d\rho_e}{dz}\int_0^\infty (ru)_\infty dz \tag{2.22}$$

The advantage of this set (which has been used by Morton, Taylor, and Turner (1956) and their followers) is that the Reynolds stress terms vanish, but as usual in turbulence calculations, a closure assumption is needed to relate $(ru)_\infty$ to the mean flow properties. In addition the form of the profiles must be assumed. A related alternate set of equations can be constructed by substituting the integrated kinetic energy equation for the continuity equation, as was done by Priestly and Ball (1955), in which case a closure assumption for the behavior of $\overline{u'w'}$ is then needed in the kinetic energy equation. Although List and Imberger (1973) have shown that the latter approach is superior for buoyant jets, Morton (1971) noted that both models give similar results for plumes in a uniform environment and in the lower

region of a stratified environment. Consequently, the conservation equations for mass momentum and buoyancy have been chosen here for convenience.

In order to close the system, we assume first that the profiles of velocity and temperature are similar. Schmidt (1941), Rouse, Yih, and Humphreys (1952), and Yokoi (1960) found that this assumption was satisfied for heights that were large compared to a characteristic source dimension. For the case of a uniform environment (ρ_e = constant) the set of equations reduces to:

$$\frac{dW}{dz} = -2\pi\,(ru)_\infty \qquad W = \int_0^\infty w\,2\pi\,r\,dr \tag{2.23}$$

$$\frac{dV}{dz} = \int_0^\infty 2\pi\,\hat{\nabla}r\,dr \qquad V = \int_0^\infty w^2\,2\pi\,r\,dr \tag{2.24}$$

$$\frac{dF}{dz} = 0 \qquad F = \int_0^\infty w\hat{\nabla}\,2\pi\,r\,dr \tag{2.25}$$

Hence the kinematic buoyancy flux is an invariant of the flow, and we might expect the entrainment velocity to be proportional to w, as we saw in the asymptotic case. G.I. Taylor (1945) appears to have been the first person to use this approach, in order to predict the results of Schmidt (1941). The basic idea is that once the flow is fully developed, the rate of entrainment must be governed by the large scale structure of the turbulence, which in turn is generated by the motion of the plume itself and can be characterized by the scale of the vertical velocity. Following Taylor, we can then write:

$$- 2\pi\ (ru)_{\infty} = 2\pi b\ \alpha w_c \tag{2.26}$$

where α is the entrainment constant and w_c is a characteristic vertical velocity.

Finally, a set of profiles must be chosen. However, as in all integral methods, the choice is not crucial. Profile data reported by Rouse, Yih, and Humphreys (1952) are well fitted by two Gaussian distributions with the temperature profile being broader than the velocity profile. Therefore it is assumed that

$$w = w_m(z)\ e^{-(r/b)^2} \tag{2.27}$$

$$T - T_e = (T_m - T_e)\ e^{-\sigma(r/b)^2} \tag{2.28}$$

where the width of the temperature profile is scaled by $b' = (b/\sqrt{\sigma})$.

With these assumptions the basic equations of motion are

$$\frac{dW}{dz} = \alpha\ 2\pi\ b\ w_m = \alpha\ \sqrt{8\pi}\ V^{1/2} \tag{2.29}$$

$$\frac{dV}{dz} = g\ \frac{\Delta\rho_m}{\rho_0}\ \frac{\pi b^2}{\sigma} = \frac{WF(1+\sigma)}{V\ 2\sigma} \tag{2.30a}$$

$$\underline{\text{or}} \qquad \frac{dV^2}{dz} = \frac{(1+\sigma)}{\sigma}\ WF \tag{2.30b}$$

$$\frac{dF}{dz} = -\frac{gW}{T_0}\ \frac{dT_e}{dz} = \frac{gW}{\rho_0}\ \frac{d\rho_e}{dz} \tag{2.31}$$

$$W = w_m\ \pi b^2 \qquad V = \frac{1}{2}\ w_m{}^2 \pi b^2 \qquad F = \frac{w_m\ \pi b^2\ \hat{\nabla}_m}{(\sigma+1)} \tag{2.32}$$

Given the initial conditions $\{W_0, V_0, F_0\}$ describing the fluxes of mass momentum and energy from a finite source, and a specification of the stratification $\frac{dT_e}{dz}$, equations (2.29-2.31) can be numerically integrated. Note, however, that the similarity assumption is violated in the case $\frac{dT_e}{dz} \neq 0$, for in that case the motion is limited to a finite height, and the plume spreads out radially at the maximum rise height. However, Morton, Taylor, and Turner (1956) and Morton (1959a,b) have shown that over most of the height of the plume, stratification does not appear to significantly affect plume behavior. Note also that equation (2.30a) is singular for $V \to 0$ whereas (2.30b) is not. The computer program to do the numerical integration automatically switched from (2.30b) to (2.30a) when V became greater than one.

2.4 Finite Source Plume in a Uniform Environment

In the uniform environment case, $F = F_0 = \text{constant}$, and significant simplifications are possible. Kubota (1977) has given a parametric solution for this case which will be used. First, define dimensionless volume flux, μ, dimensionless momentum flux, ϕ and height ζ, by

$$W = \frac{(8\pi)^{\frac{1}{4}} V_0^{5/4} \sqrt{\alpha\,\sigma}}{\sqrt{(\sigma + 1)F_0}} \mu \tag{2.33}$$

$$V = V_0 \phi \tag{2.34}$$

$$z = \frac{\sqrt{\sigma}\ V_0^{3/4}}{(8\pi)^{\frac{1}{4}} \sqrt{\alpha}\ \sqrt{(\sigma + 1)F_0}} \zeta \tag{2.35}$$

For the case of positive initial buoyancy considered here, the equations become

$$\frac{d\mu}{d\zeta} = \phi^{\frac{1}{2}} \tag{2.36}$$

$$\frac{d\phi^2}{d\zeta} = \mu \tag{2.37}$$

Eliminating ζ and integrating, the solution is

$$\mu = \sqrt{\mu_0^2 + \frac{8}{5}(\phi^{5/2} - 1)} \tag{2.38}$$

$$\zeta = 2\int_1^{\phi} \frac{\phi_1 \, d\phi_1}{\sqrt{\mu_0^2 + \frac{8}{5}(\phi_1^{5/2} - 1)}} \tag{2.39}$$

The last integral can be evaluated numerically for $\mu_0 > 0$, or it can be written in terms of the hypergeometric function [Kubota (1977)]

$$\zeta = \zeta(\phi) + \zeta_0 \tag{2.40}$$

$$\zeta_0 = -\frac{\sqrt{40}}{3}\left[\sqrt{1 - C} + \frac{2}{7} C \, F\left(\frac{1}{2}, \frac{7}{10}; \frac{17}{10}; C\right)\right] \tag{2.41}$$

$$\zeta(\phi) = \frac{\sqrt{40}}{3}\left[\phi^{3/4}\sqrt{1 - \frac{C}{\phi^{5/2}}} - \frac{2}{7}\frac{C}{\phi^{7/4}} F\left(\frac{1}{2}, \frac{7}{10}; \frac{17}{10}; \frac{C}{\phi^{-5/2}}\right)\right] \tag{2.42}$$

where

$$C = 1 - \frac{5}{8}\mu_0^2 \leq 1 \tag{2.43}$$

and $F(a,b;c;x)$ is the hypergeometric function. The parameter C is

a measure of the balance between the initial mass and momentum flows in a forced plume. $C = 1$ corresponds to the jet-like initial flow from a source of momentum and buoyancy only $(0, V_0, F_0)$, which is equivalent to a pure plume $(0, 0, F_0)$ located at $\zeta_0 = -1.057$ (cf. Morton (1959a)). $C = 0$ is the case of a pure plume $(0, 0, F_0)$ in which

$$\frac{W_0}{V_0} \propto \frac{z_0^{1/3}}{F_0^{1/3}} \tag{2.44}$$

where z_{vs} is the virtual source depth. For $C = 0$, $\zeta_0 = -2.108$. The case $C < 0$ corresponds to a forced plume with too great an initial mass flow. Note that for $\phi >> 1$

$$\mu \approx \sqrt{\frac{8}{5}}\, \phi^{5/4} \tag{2.45}$$

$$\zeta \approx \frac{\sqrt{40}}{3}\, \phi^{3/4} + \zeta_0 \tag{2.46}$$

which is the behavior of a point source pure plume located at $\zeta = \zeta_0$. Thus equation (2.41) gives the virtual source depth of the asymptotic point source plume $(0, 0, F_0)$. This result is quite useful in that for $z > 3.5\,|z_{vs}|$, the asymptotic point source solution agrees with finite source solution within 1%.

The physical variables of interest for the finite source solution are given by:

$$w_m = \left(\frac{2}{\pi V_0}\right)^{\frac{1}{4}} \sqrt{\frac{1+\sigma}{\alpha\sigma}\,|F_0|}\;\frac{\phi}{\mu} \tag{2.47}$$

$$\frac{\Delta T_m}{T_0} = \frac{1}{(8\pi)^{\frac{1}{4}}} \frac{1+\sigma}{g} \frac{F_0}{V_0^{5/4}} \sqrt{\frac{1+\sigma}{\alpha\sigma} |F_0|} \frac{1}{\mu} \qquad (2.48)$$

$$b = \left(\frac{2}{\pi}\right)^{\frac{1}{4}} \frac{V_0^{3/4}}{\sqrt{\frac{1+\sigma}{\alpha\sigma} |F_0|}} \frac{\mu}{\sqrt{\phi}} \qquad (2.49)$$

2.5 Point Source Plume in a Uniform Environment

Finally, for the case of a point source pure-plume in a uniform environment, the equations (2.29-2.31) can be solved as a similarity solution and the results expressed as simple powers of z and F_0. Substituting $W = \hat{A}\, z^{5/3}$ and $V = \hat{B}\, z^{4/3}$ from the asymptotic solution into (2.29, 2.30), one finds the parameters

$$\hat{A} = \frac{3^{4/3}\, \pi^{1/3}\, \alpha^{2/3}}{2\ 5^{2/3}} \left[\left(\frac{1+\sigma}{\sigma}\right) F_0\right]^{2/3} \qquad (2.50)$$

$$\hat{B} = \frac{2\ 3^{5/3}\, \pi^{2/3}\, \alpha^{4/3}}{5^{4/3}} \left[\left(\frac{1+\sigma}{\sigma}\right) F_0\right]^{1/3} \qquad (2.51)$$

The physical variables of interest are

$$w_m = \frac{5^{2/3}}{2\ 3^{1/3}\, \alpha^{2/3}\, \pi^{1/3}} \left[\left(\frac{1+\sigma}{\sigma}\right) F_0\right]^{1/3} z^{-1/3} \qquad (2.52)$$

$$g\frac{\Delta T_m}{T_0} = \frac{5^{4/3}\, [(1+\sigma)F_0]^{2/3}}{2\ 3^{5/3}\, \pi^{2/3}\, \alpha^{4/3}} z^{-5/3} \qquad (2.53)$$

$$b = \left(\frac{6\alpha}{5}\right) z \qquad (2.54)$$

2.6 Typical Results: A 14.75 kW Floor Level Fire

Results from both the finite source solution (2.47-2.49) and point source solution (2.52-2.54) are presented in Figures (2.1) through (2.4). These figures show the behavior of a plume emanating from a 14.75 kW fire, produced by burning an approximately stochiometric mixture of air and natural gas at floor level. The initial mass flux of the fuel-air mixture was measured. The initial momentum flux was estimated as the product of the bulk velocity times the mass flux. The burner radius was 7.62 cm. Three curves are presented in each case. The solid line represents the finite source solution. The squares represent the point source solution, with the plume emanating from a virtual source 14.44 cm below the burner, given by equation (2.41). Finally, the triangles represent the point source solution with no virtual source. In general, we can see that for heights of the order of the virtual source distance, effects of the initial mass and momentum fluxes are important. The Gaussian plume radius starts out at approximately 1/2 the burner radius and quickly necks in as the excess mass is accelerated upward. It then quickly approaches the asymptotic behavior of a pure plume. Similarly, the maximum velocity starts at a finite value, fixed by the mass and momentum flux of the air-fuel mixture, accelerates to a maximum value, and then quickly asymptotes to the pure plume curve. Note that far from the source, the initial conditions become unimportant and the velocity and temperature curves all coalesce. The plume radius, which is a simple linear function of z for large z, shows the expected shift in the origin.

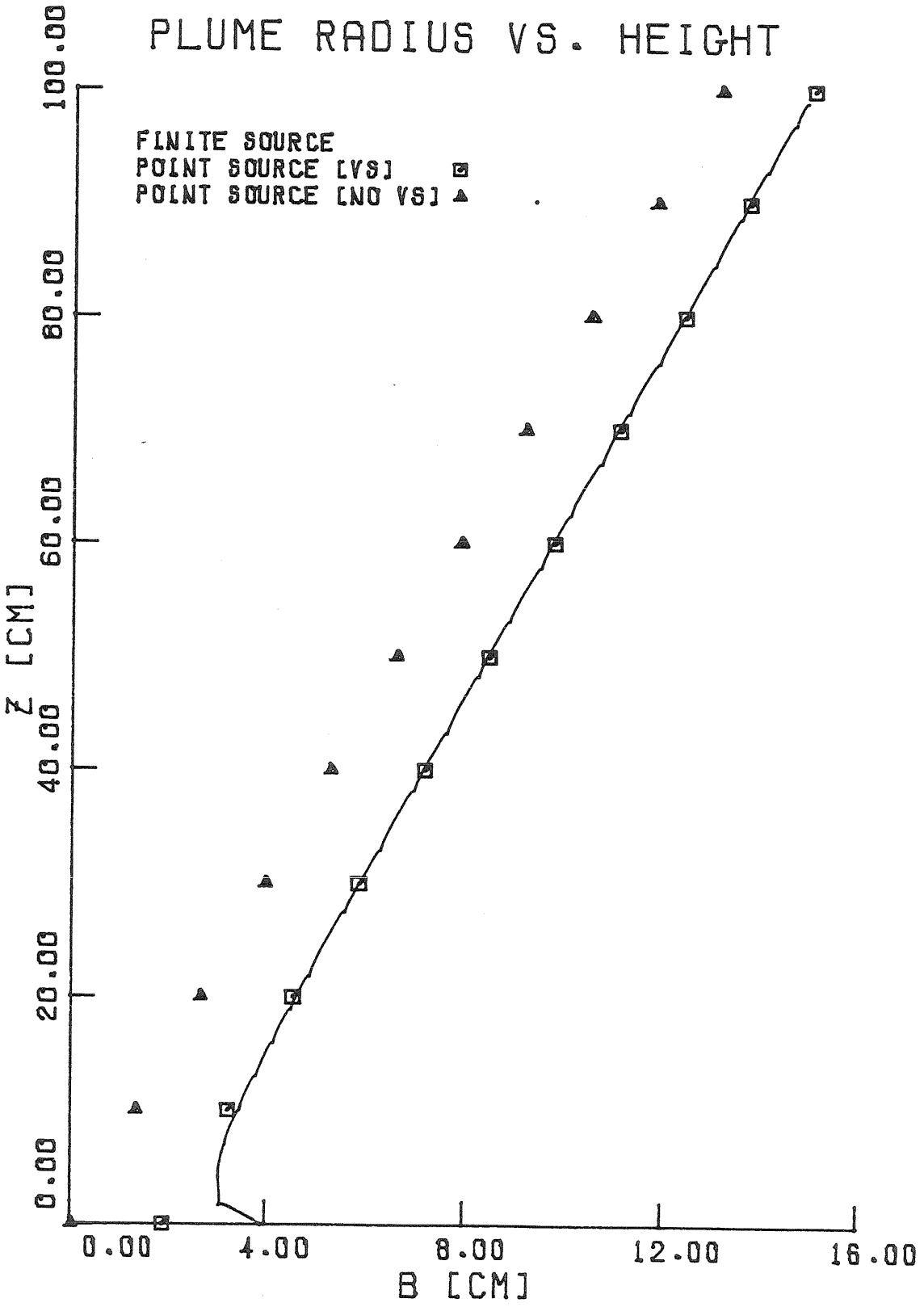

Figure (2.1) Gaussian Plume Radius as a Function of Height above a 14.8 kW Premixed Fire.

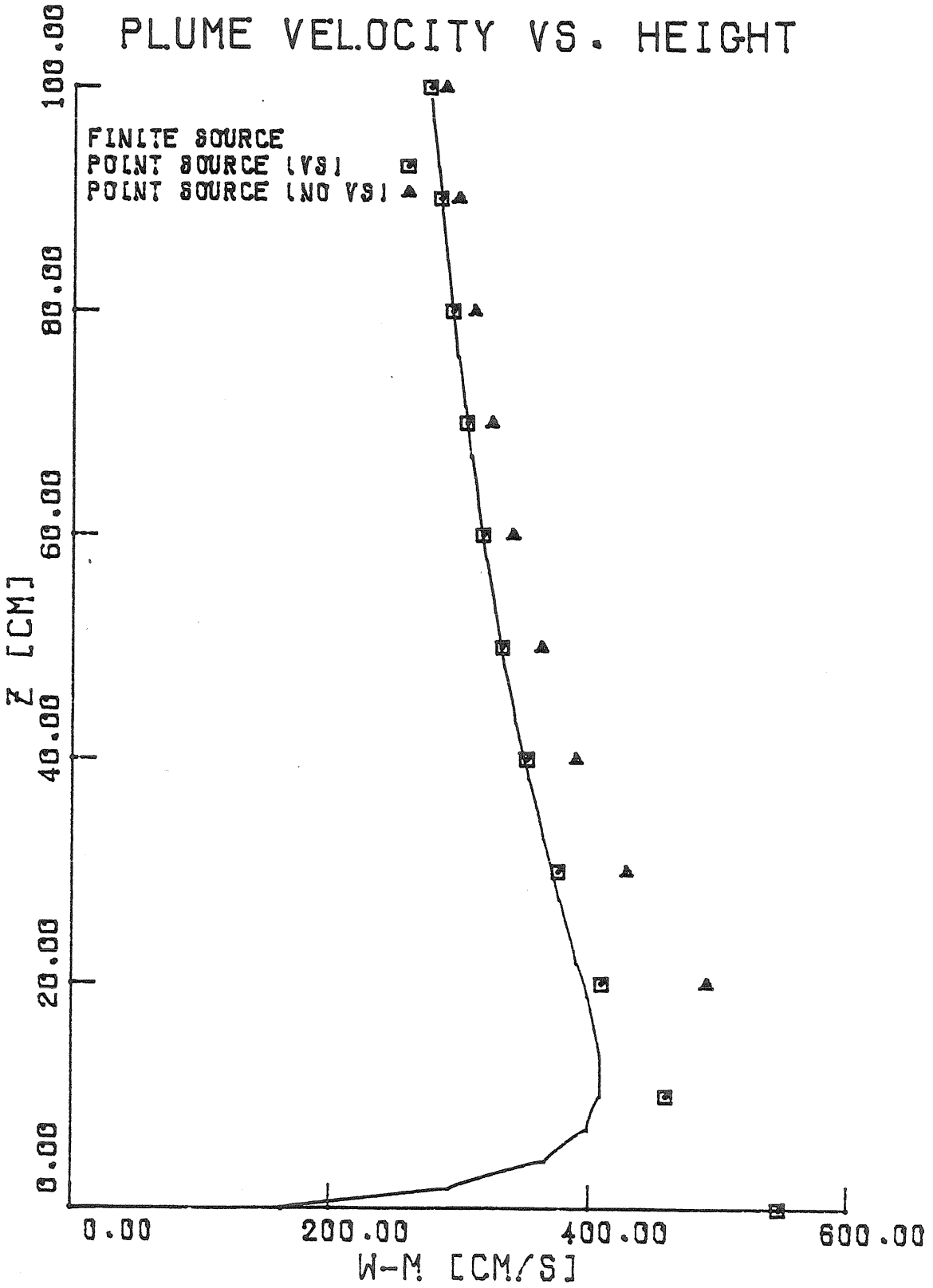

Figure (2.2) Maximum Plume Velocity as a Function of Height above a 14.8 kW Premixed Fire.

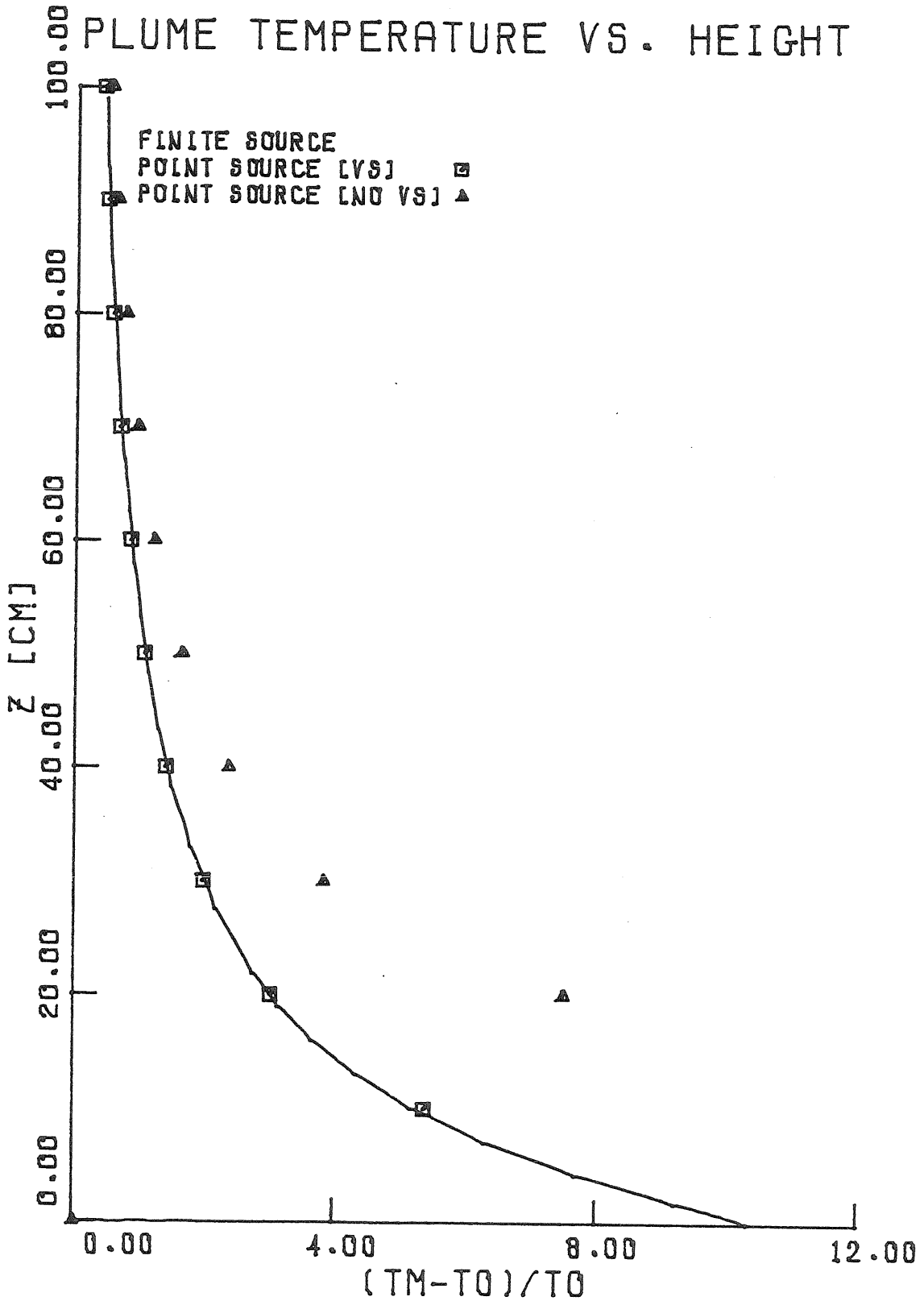

Figure (2.3) Dimensionless Maximum Temperature Difference as a Function of Height above a 14.8 kW Premixed Fire.

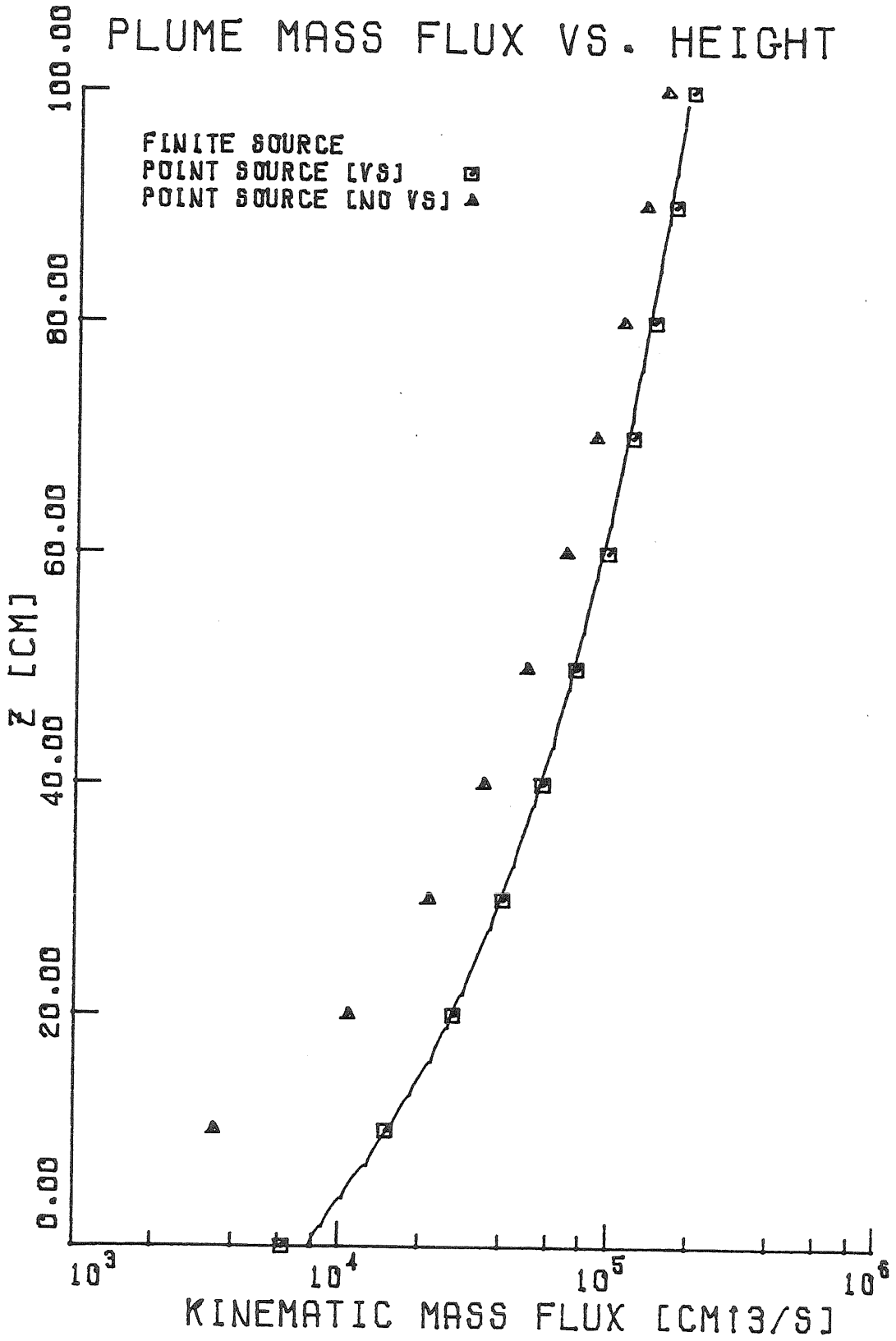

Figure (2.4) Kinematic Plume Mass Flux as a Function of Height above a 14.8 kW Premixed Fire.

In order to demonstrate the effects that the initial mass and momentum fluxes exert on the plume, Figures (2.5) through (2.7) show the companion case of a "prototype" diffusion flame with the same heat release (14.75 kW). In this case the initial mass and momentum fluxes are calculated for a stream of pure natural gas flowing through the same diameter burner. This reduces the initial mass flux, for example, by a factor of nearly 18. As a result the virtual source distance is reduced by a factor of 5.8 to 2.49 cm. It should be noted, however, that in an actual diffusion flame, heat is released over a significant fraction of the flame height, whereas in this model all of the buoyancy (or heat) is added at the origin.

2.7 Point Source Solution in Terms of Q*

For fire modeling, a useful nondimensional heat flux parameter can be formed from the ratio of the heat released to a measure of the energy in the plume at a height z

$$Q^* = \frac{Q_F}{\rho_0 \, c_p \, T_0 \, \sqrt{gz} \, z^2} = \left(\frac{F_0}{g}\right) \frac{1}{\sqrt{gz} \, z^2} \qquad (2.55)$$

Yokoi (1960) did a variety of experiments with alcohol pan fires and with small arrays of fires. He found his data were well fitted by

$$\Delta T_m = \frac{0.423}{C_Y^{8/9}} \left[\frac{T_1 \, Q^2}{c_p^{\,2} \, \rho^2 \, g}\right]^{1/3} z^{-5/3} \qquad (2.56)$$

$$w_m = \frac{0.833}{C_Y^{4/9}} \left[\frac{Q \, g}{T_1 \, c_p}\right]^{1/3} z^{-1/3} \qquad (2.57)$$

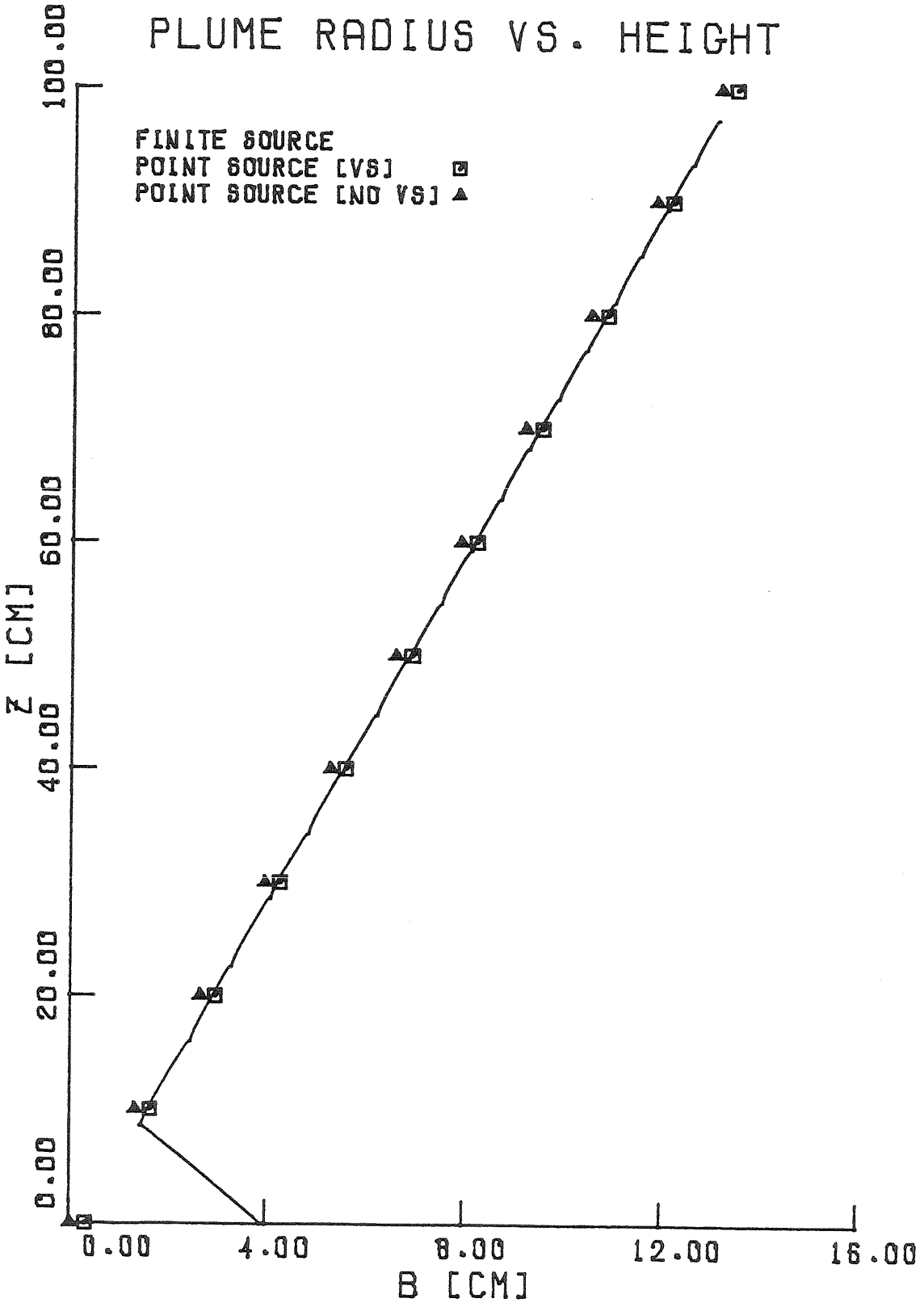

Figure (2.5) Gaussian Plume Radius as a Function of Height above a 14.8 kW Diffusion Flame Fire.

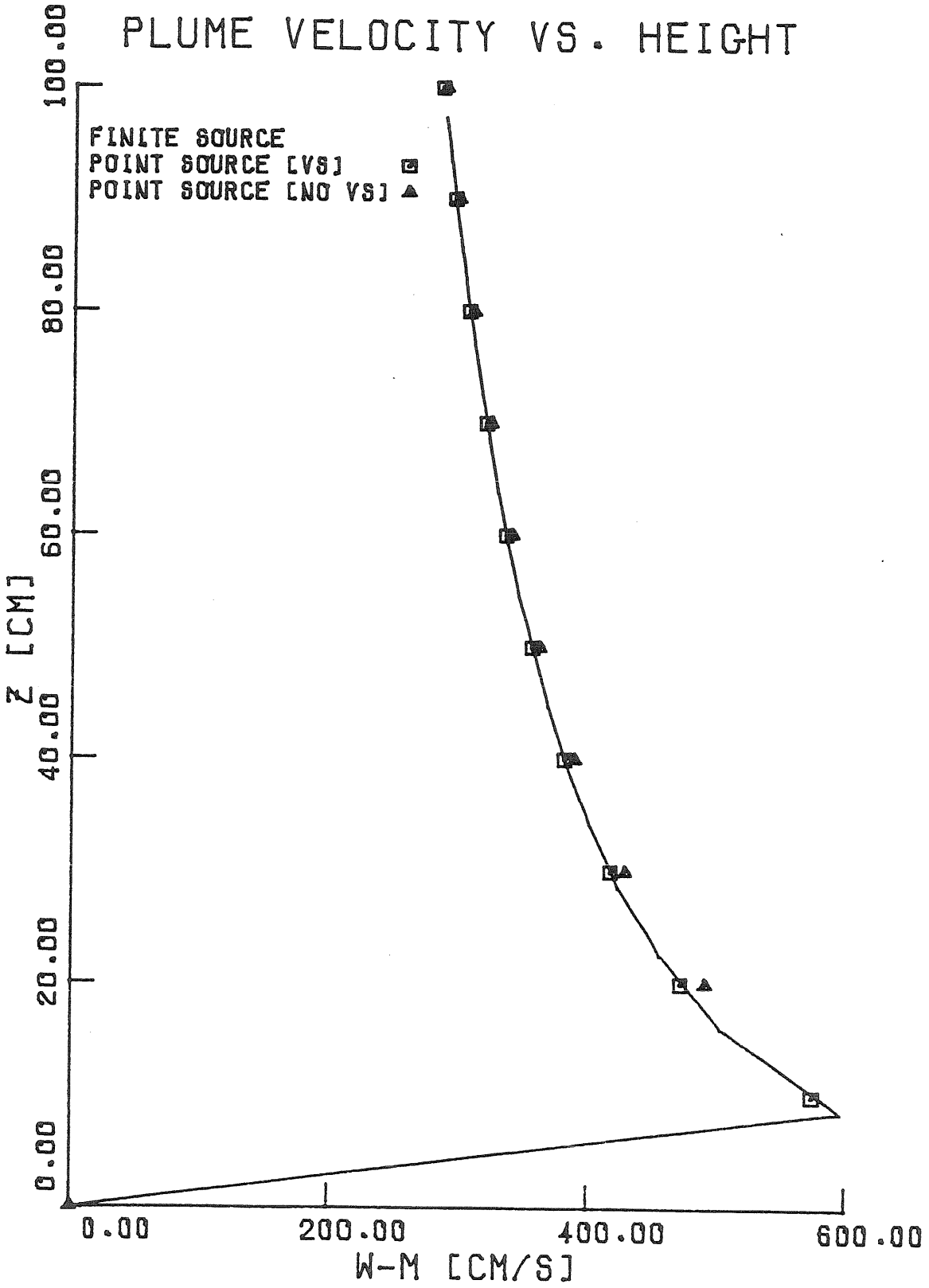

Figure (2.6) Maximum Velocity as a Function of Height above a 14.8 kW Diffusion Flame Fire.

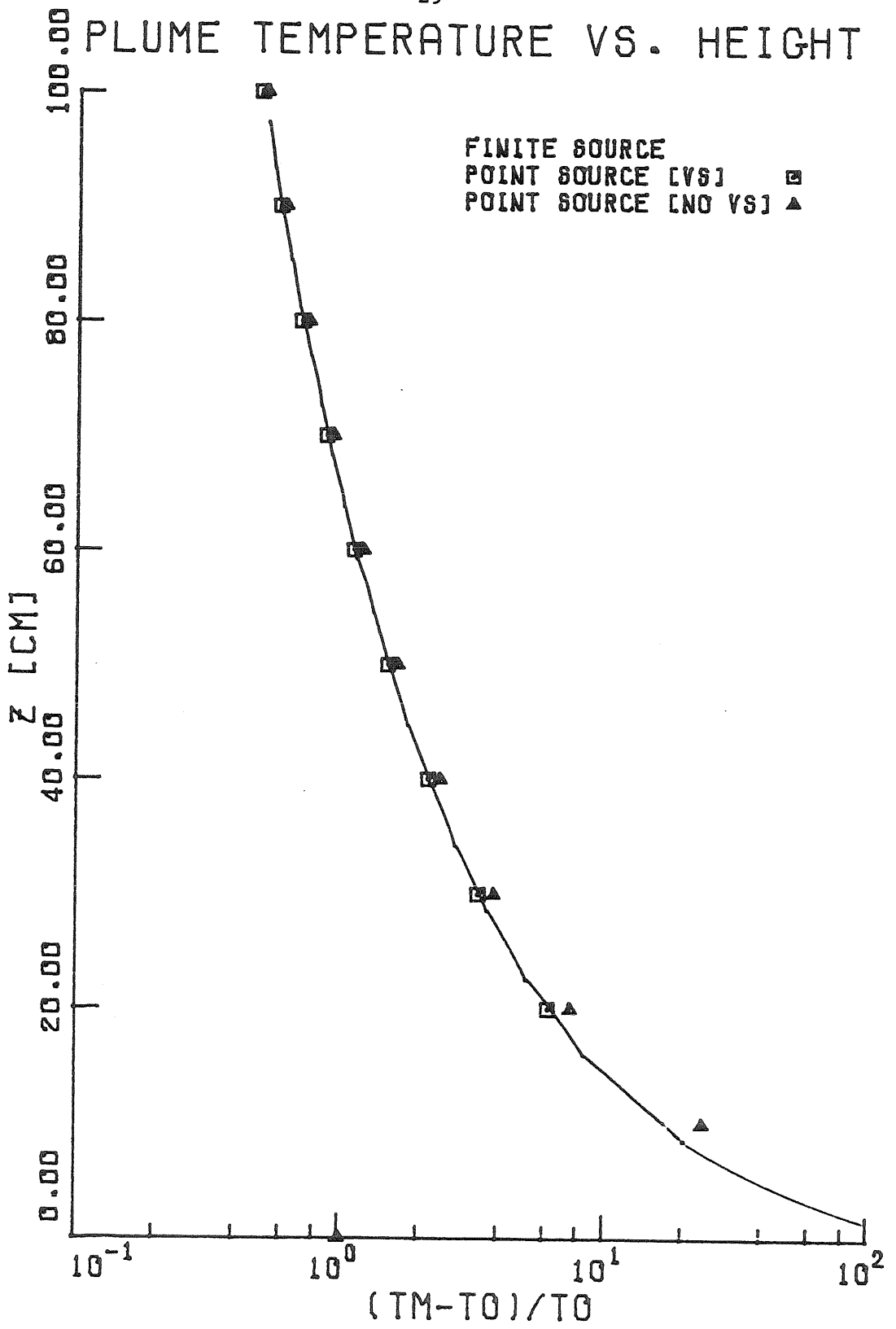

Figure (2.7) Dimensionless Maximum Temperature Difference as a Function of Height above a 14.8 kW Diffusion Flame Fire.

Zukoski (1975) rewrote these relations in terms of Q*:

$$\frac{\Delta T_m}{T_0} = C_T (Q^*)^{2/3} \qquad C_T = \frac{0.423}{C_Y^{8/9}} \tag{2.58}$$

$$\frac{w_m}{\sqrt{gz}} = C_v (Q^*)^{1/3} \qquad C_v = \frac{0.833}{C_Y^{4/9}} \tag{2.59}$$

$$b = C_\ell \, z \tag{2.60}$$

Using Yokoi's value $C_Y^{2/3} = 0.100$, yields $C_T = 9.113$, $C_v = 3.866$.

Expressions (2.52, 2.53) can be rearranged in this form so that

$$C_T = \frac{5^{4/3} \sigma^{1/3} (1+\sigma)^{2/3}}{2 \; 3^{5/3} \pi^{2/3} \alpha^{4/3}} \tag{2.61}$$

$$C_v = \frac{5^{2/3}}{2 \; 3^{1/3} \alpha^{2/3} \pi^{1/3}} \left(\frac{1+\sigma}{\sigma}\right)^{1/3} \tag{2.62}$$

$$C_\ell = \left(\frac{6\alpha}{5}\right) \tag{2.63}$$

$$\frac{C_{\ell_T}}{C_\ell} = \frac{1}{\sqrt{\sigma}} \tag{2.64}$$

Using the values quoted above for $\{C_T, C_v\}$, one can solve for $\{\alpha, \sigma\}$

$$\sigma = \frac{3}{2} \frac{C_T}{C_v^2} = 0.9146 \tag{2.65}$$

$$\alpha = \frac{5}{6} \frac{1}{\sqrt{\pi \, C_v C_T}} \sqrt{1 + \frac{3}{2} \frac{C_T}{C_v^2}} = 0.1096 \tag{2.66}$$

2.8 The Entrainment Constant for Plumes and Jets

While the entrainment hypothesis itself seems like a reasonable closure assumption, the choice for the entrainment constant is not so clear. Table (2.1) lists some values for α and σ that have been reported. There is a significant variation in the values cited, which may be due in part to source effects and to the great sensitivity plumes exhibit to small changes in the surrounding environment.

TABLE 2.1

Experimenter	α	σ
Schmidt (1941)	0.125	
Rouse, Yih, Humphreys (1952)	0.083	0.743
Morton, Taylor, Turner (1956)	0.093	
Morton (1959a,b)	0.082	0.743
Yokoi (1960)	0.110	0.915
Baines, Turner (1969)	0.100	
Zukoski, Kubota, Cetegen (1980)	0.110	
MEAN VALUE	0.100	
Ricou, Spalding (1961) - JET -	0.057	

Zukoski, Kubota, and Cetegen (1980) report good agreement between their measurements of plume mass flow rates produced by large turbulent diffusion flames and the pure plume solution, using Yokoi's value of $\alpha = 0.1096$. The turbulent diffusion flames they and Yokoi studied are a very close approximation to real room fires, and so their value of

α will be used here. However, α does not seem to be a universal constant. While Morton (1959a,b) assumed that the same value of held for both jets and plumes, Ricou and Spalding (1961) and Kotsovinos (1975) have found $\alpha_{jet} < \alpha_{plume}$. Becker and Yamazaki (1978) studied turbulent diffusion flames and found that the flame entrained significantly more volume when the buoyancy was large compared to the initial momentum than when the reverse was true. They further observed that the nature of the turbulence changed with the large structures becoming more pronounced as the buoyancy increased. Zukoski, Kubota and Cetegen (1980) also reported an increase in entrainment associated with the growth of large scale structures in turbulent diffusion flames at larger source Richardson numbers.

Turner (1973) has shown that the spreading rate implied by equations (2.29, 2.30) is

$$\left(\frac{db}{dz}\right)_{jet} = 2\alpha \qquad (F_0 = 0) \tag{2.67}$$

$$\left(\frac{db}{dz}\right)_{plume} = \frac{6}{5}\alpha \qquad (F_0 > 0) \tag{2.68}$$

which would imply jets spread faster than plumes. However, for two dimensional plumes, Kotsovinos (1975) found the spreading rates were approximately equal, which, if this holds for the axisymmetric case would imply

$$\alpha_{jet} = \frac{3}{5}\ \alpha_{plume} \tag{2.69}$$

Using the mean value $\alpha_p = 0.100$, gives $\alpha_j = 0.060$ which is quite close to Ricou and Spalding's $\alpha_j = 0.057$.

List and Imberger (1973) pointed out this discrepancy and argued that there is no unique entrainment "constant" for a forced plume. From dimensional analysis Wright (1977) defines two length scales from a forced plume described by (W_0, V_0, F_0)

$$\ell_W = \frac{W_0}{V_0^{\frac{1}{2}}} = \sqrt{\pi}\ r_0 \tag{2.70}$$

$$\ell_V = \frac{V^{3/4}}{F_0^{1/2}} = \frac{\pi^{1/4} w_0}{\sqrt{\frac{g}{r_0}\frac{\Delta\rho_0}{\rho_0}}} \tag{2.71}$$

where ℓ_W is a measure of the importance of the initial kinematic mass flux to the kinematic momentum, and ℓ_V is a measure of the initial momentum relative to the buoyancy. If $\ell_W < \ell_V$, one would expect three regions of behavior: (1) an initial region extending several source diameters in which the flow becomes established, corresponding to the potential core of a turbulent jet, (2) a jet-like region where the initial momentum flux dominates the plumes behavior, and (3) a plume-like region where the buoyancy generated momentum would be large compared to the initial momentum flux. The ratio of these two gives the source densimetric Froude number (or the inverse square of the source Richardson number)

$$Fr_0 = \frac{\pi^{1/4}}{\sqrt{2}}\frac{\ell_V}{\ell_W} = \frac{w_0}{\sqrt{g\frac{\Delta\rho_0}{\rho_0} d_0}} = \frac{1}{Ri_0^2} \tag{2.72}$$

Yokoi found a nearly constant temperature conical region above his distributed fires extending approximately 3 source radii upwards, and the similarity was established above 4 source radii. Since $\ell_V \approx 0$ in his case, he found $z_s \gtrsim 3\,\ell_W$ was necessary for similarity to be established. This can be considered the lower bound for a plume. On the other hand, the potential core of a turbulent jet extends far approximately 6 source diameters and mean flow similarity is not established until approximately 8 source diameters (Tennekes and Lumley (1972)). Then an upper bound for the initial zone would be $z_s \gtrsim 9\,\ell_w$. Thus for diffusion flames, which represent most real fires, the initial mass and momentum fluxes are very small and source effects appear to be confined to the region in the immediate vicinity of the source, or to the region $z \lesssim \bar{z}_{flame}$ where $\bar{z}_{flame}$ is the mean flame height. However, since in laboratory simulation of plumes nozzles are often used which impart significant initial mass and momentum to the fluid, care must be taken in interpreting the results since z_s may be large, and of comparable order to the other heights of interest.

This effect can also be measured by the virtual source distance;

$$z_{vs} = z_{scale}\,\zeta_0 = (A_z \ell_V)\,\zeta_0 \tag{2.73}$$

where A_z is a parameter depending on (α, σ) from (2.35) and ζ_0 is the dimensionless virtual source depth from (2.41), measuring z in units of the momentum scale, ℓ_V. In addition the dimensionless mass flux is scaled by

$$W_{scale} = \sqrt{8\pi}\,\alpha\, V_0^{1/2}\, z_{scale} \tag{2.74}$$

which is the volume flux a jet (V_0 = constant) would have at a distance $z = z_{scale}$. So that $\mu > 1$ implies greater initial volume flux than in the corresponding jet (with the same V_0). The matched-plume case $C = 0$ implies $\mu_{0\,plume} = \sqrt{\frac{5}{8}}$, so that the matched-plume has less volume flux than the corresponding jet. However, the above analysis is based on the assumption $\alpha_{jet} = \alpha_{plume}$ which does not appear to be valid. Consequently, for the plume solution to be valid we must require $\zeta >> \zeta_0$, or $z >> z_{vs}$.

2.9 Summary

Three related integral models of buoyant plumes have been introduced in this chapter. All of these models are based on the Boussinesq approximation that the density differences are small compared to the density of the fluid itself, and they all incorporate the same entrainment assumption in order to relate the entrainment to the mean velocity in the plume. In the general case of a plume, emanating from a source with finite fluxes of mass and momentum in addition to buoyancy and rising through a non-uniform (i.e., stratified) environment, one can solve the ordinary differential equations (2.29-2.31) numerically with a specified external temperature gradient $\left(\frac{dT_e}{dz}\right)$. However, for most fire situations, the environment will be approximately uniform in temperature. In this case, the buoyancy in the plume remains constant, and some simplifications are possible. If the initial fluxes of mass and momentum are significant, as they may be for a pre-mixed burner, the solution to the reduced set of governing equations may be found in terms of the hypergeometric function as given by equations

(2.38) and (2.40-2.42). Finally, the most likely physical situation turns out to be the simplest of all. Most actual fires can be accurately modeled as diffusion flames, which have very little initial mass and momentum flux. Hence they can be represented as point sources of buoyancy, which is the case of a pure plume. The solution is then given in terms of simple powers of the initial buoyancy flux and the height by equations (2.52-2.54) or alternatively by (2.58-2.60). The accuracy of the point source solution can be significantly improved where there is some initial flux of mass and momentum, by computing the effective virtual source depth, using equation (2.41), and calculating the point source solution from that location, rather than from the physical origin. This last approach will be used in the following two chapters to predict the approximate behavior of the gases in a room with a fire.

III. A SIMPLE STEADY STATE ROOM MODEL

3.1 General Approach

The point source plume model results given by equations (2.58 - 2.60) can be combined with simple hydraulic modeling of stratified flow through an orifice to yield a steady state model for the height of the interface separating the hot smoke layer from the cool air in a room with a fire. The plume model can then be used to find the mean density of the hot layer. This model, whose basic form was given by Zukoski (1975), should be applicable to the early stages of a fire in a room, when the fire is localized and the heat release (Q^*) is small.

Kawagoe (1958) seems to have been the first to apply hydraulic analysis of flow through an orifice to the problem of counter flowing hot and cold streams of air through the opening separating a room with a fire from the environment. Emmons (1973) further developed the model by using the conservation of mass to fix the neutral plane, which Kawagoe had arbitrarily assumed to be at 1/3 the room height, h. Prahl and Emmons (1975), Zukoski (1975), and Rockett (1975) have used these ideas to develop similar models.

The basic features of a small fire in a room are presented in Figure (3.1). A buoyant turbulent plume rises from the fire, located at $z = z_f$ As it rises it entrains air and fills the upper portion of the room with a heated smoke air mixture at mean density ρ_2. For low flow rates, buoyant forces cause this gas to be stably stratified and a sharp interface is formed at height z_i. When this interface falls below the height of the door soffit, z_u, hydrostatic pressure forces

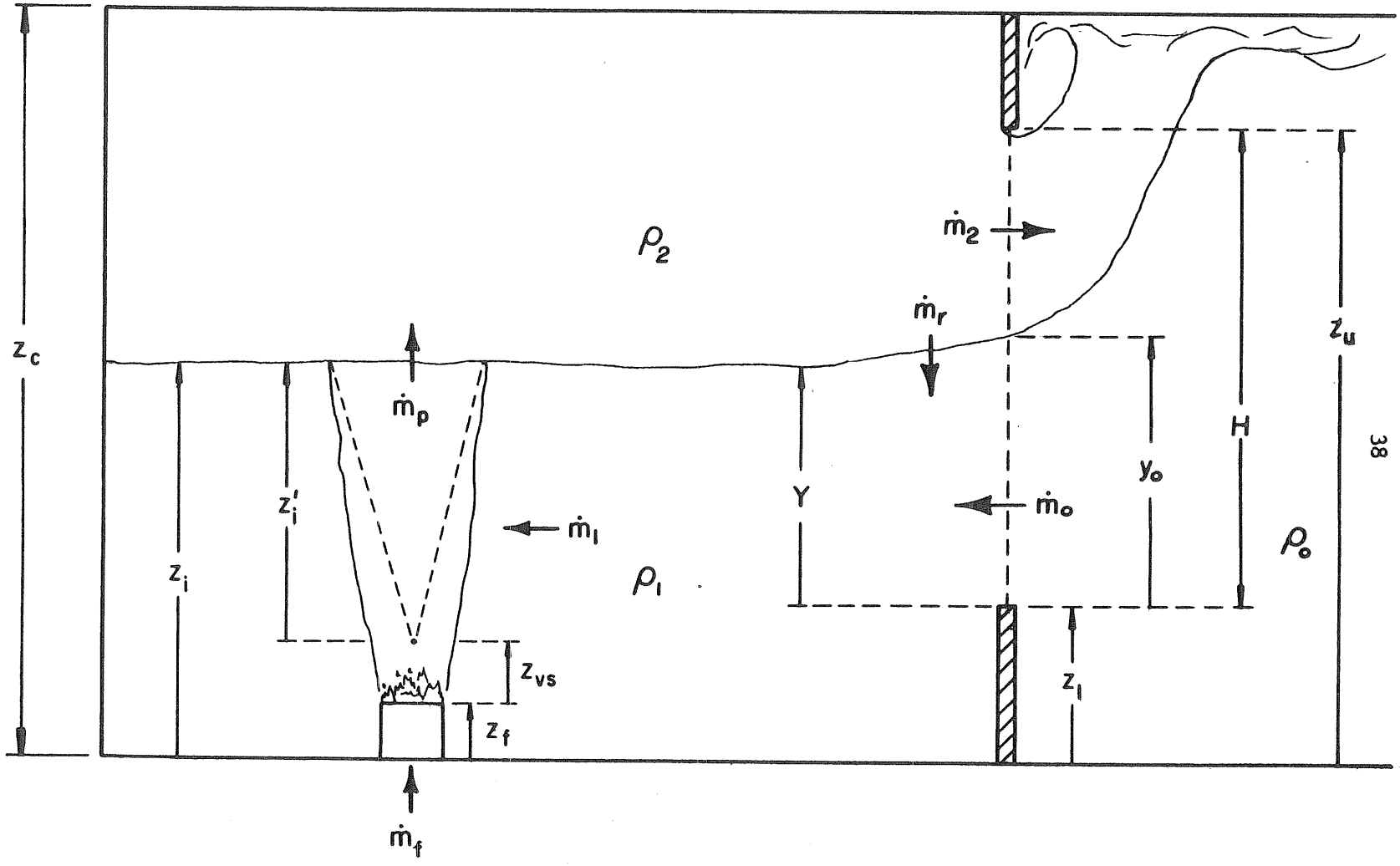

FIGURE 3.1 STEADY STATE ROOM MODEL

will cause an outflow of the hot gas above the neutral plane located at y_o and an inflow of ambient air below y_o. Conservation of mass requires that the plume's entrainment appetite, $\dot{m}_1$, must be met by the inflowing stream $\dot{m}_0$ and any exhaust gas that is recirculated, $\dot{m}_r$ (presumably by mixing at the opening). A similar analysis for the ceiling layer shows that the plume mass flux at the interface, $\dot{m}_p$, must be equal to the flow out the opening, $\dot{m}_2$, less any recirculation losses, $\dot{m}_r$. Furthermore, for the case of adiabatic walls no recirculation losses, and no radiant heat transfer, the mass averaged enthalpy flux in the plume at the interface must be equal to the enthalpy flux out of the opening. The two conservation equations for mass and enthalpy can then be used to solve for the two unknowns in the problem: the interface height z_i, and the mean ceiling layer density ρ_2.

3.2 Hydraulic Modeling of Counterflow Through an Opening

In order to obtain the mass flow rates through the opening, simple hydraulic modeling has been employed. Figure (3.2) shows a schematic view of the flow field. Assume that there is no mixing across the interface, so that $\rho_1 = \rho_0$. If the fluid well away from the opening is essentially at rest, a hydrostatic pressure field will be created by the difference in fluid densities, as shown in the middle of the figure. For this analysis, it is convenient to measure the height from the lower edge of the opening and to denote this variable as y. Then for height greater than the height of the interface in the interior of the room Y, the pressure difference between the interior of the room and the environment must decrease with height; while for heights below Y it will be

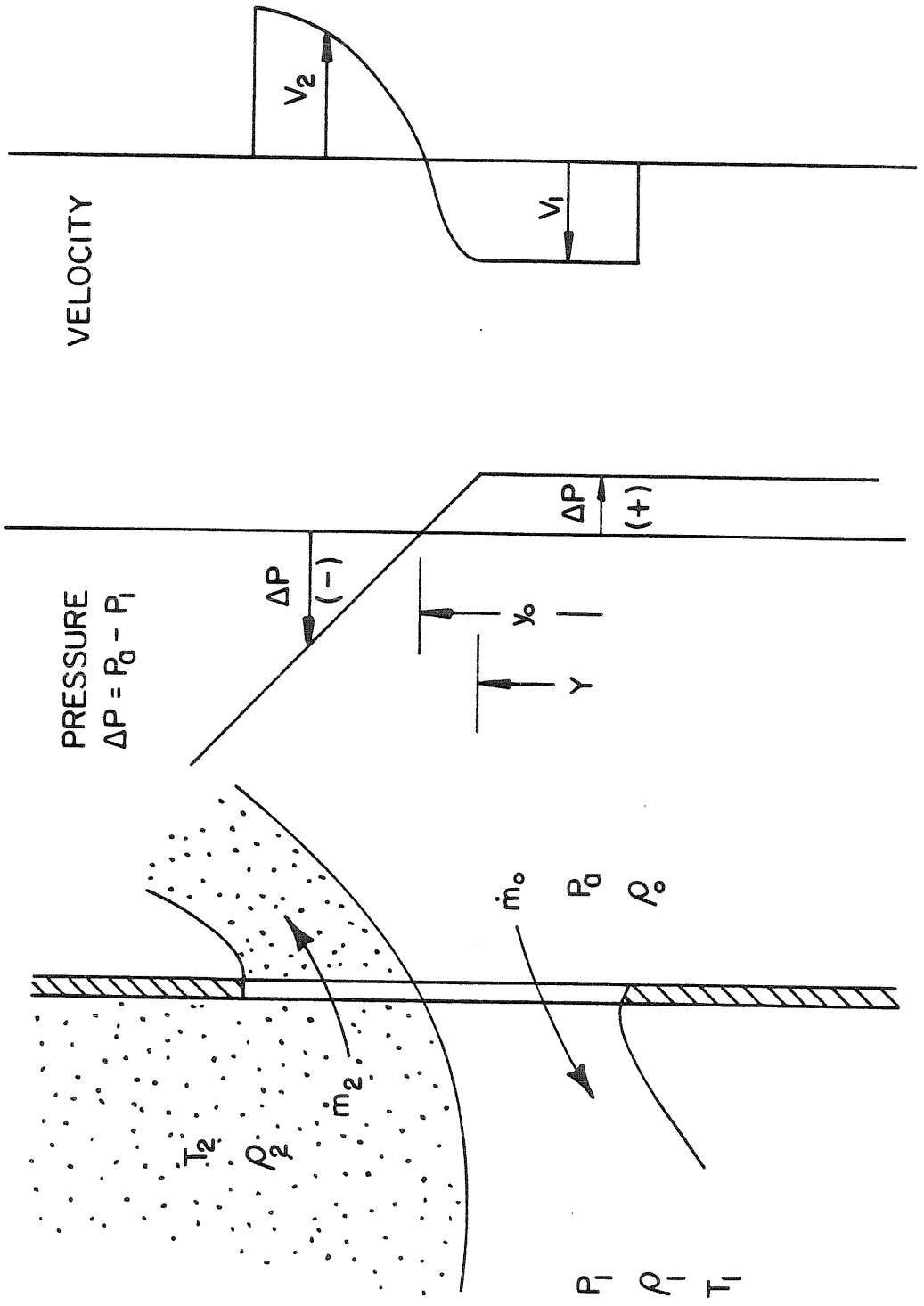

FIGURE 3.2 OPENING COUNTER FLOW MODEL

constant. Thus

$$\frac{d\Delta p}{dy} = -(\rho_0 - \rho_2)\, g \qquad y > Y \qquad (3.1)$$

$$\frac{d\Delta p}{dy} = 0 \qquad y < Y \qquad (3.2)$$

Then

$$\Delta p = -(\rho_0 - \rho_2)\, g\, (y - Y) + \Delta p_i \qquad y \geq Y \qquad (3.3)$$

$$\Delta p = \Delta p_i \qquad y < Y \qquad (3.4)$$

where Δp_i is a constant, whose value can be found from noting that the pressure difference at the neutral plane must be zero : $\Delta p(y_0) = 0$. Then

$$\Delta p_i = (\rho_0 - \rho_2)\, g\, (y - Y) \qquad y < Y \qquad (3.5)$$

$$\Delta p = (\rho_0 - \rho_2)\, g\, (y_o - y) \qquad y \geq Y \qquad (3.6)$$

The outflowing stream will separate from the relatively sharp edged corners of the opening and form a vena contracta along whose edges the pressure is essentially ambient. Bernoulli's equation can then be applied to find (approximately) the velocity distribution. The discharge or volumetric flow rate can then be easily calculated by integration, and can be corrected for viscous effects, and the vena contracta by multiplying by an empirical orifice coefficient. Thus the outflow velocity and discharge become:

$$v_2 = \sqrt{\frac{2}{\rho_2}(\rho_0 - \rho_2)\, g\, (y - y_o)} \quad \text{where} \quad y > Y \qquad (3.7)$$

$$\dot{V}_2 = Co_2\, S \int_{y=y_o}^{H} v_2\, dy = Co_2\, S\, \frac{2}{3}\sqrt{\frac{2(\rho_0-\rho_2)g}{\rho_2}}\, (H - y_o)^{3/2} \qquad (3.8)$$

where S is the width or span of the opening.

The inflowing stream is handled in the same manner, except that now there are two possible configurations: Y > 0 (interface above

window sill) and $Y < 0$ (interface below sill). For the first case, the velocity distribution is integrated in two parts:

$$v_o = \sqrt{\frac{2}{\rho_0} (\rho_0-\rho_2)\ g\ (y_o- y)} \qquad Y \leq y \leq y_o \tag{3.9}$$

$$v_o = \sqrt{\frac{2}{\rho_0} (\rho_0-\rho_2)\ g\ (y_o-Y)} = \text{constant} \qquad y \leq Y \tag{3.10}$$

$$\dot{V}_o = Co_1\ S\ \{\int_o^Y v_1\ dy + \int_Y^{y_o} v_1\ dy\} \tag{3.11}$$

$$\dot{V}_o = Co_1\ S\ \frac{2}{3}\sqrt{\frac{2}{\rho_0} (\rho_0-\rho_2)\ g}\ (y_o-Y)^{1/2}\ (y_o+ \tfrac{1}{2}Y), Y > 0 \tag{3.12}$$

For the second case, $Y < y \leq y_o$, so that for $Y < 0$:

$$\dot{V}_o = Co_1\ S\ \frac{2}{3}\sqrt{\frac{2}{\rho_0} (\rho_0-\rho_2)\ g}\ y_o^{3/2} \tag{3.13}$$

3.3 Conservation of Mass and Energy

Conservation of mass can now be used to obtain a relation between the inflow and outflow, shown schematically in Figure (3.1). Assume that the mass outflow rate $\dot{m}_2$ is a fraction η of the plume mass flow rate at the interface $\dot{m}_p$, where η is some function of the counterflow Richardson number.

The mass flow rate in the plume $\dot{m}_p$ is the sum of the entrained mass flow rate $\dot{m}_1$ and the initial gaseous fuel mass flow rate $\dot{m}_f$. For actual room fires (diffusion flames), $\dot{m}_f$ is very small compared to $\dot{m}_p$ and can be neglected, since the initial buoyancy is produced by a large release of heat per unit mass of fuel. However, for hydraulic modeling studies, the initial density difference was small ($\Delta\rho_{brine} = 5\%$),

and the brine inflow rate was not negligible. Therefore, in order to obtain an approximate solution, the fuel flow rate was assumed to be proportional to the entrained mass flow rate ($\dot{m}_f = f\,\dot{m}_1$), and an iterative procedure was constructed as follows. The solution for the interface heights (and hence the flow rates) was calculated for $f = 0.01$. A new value of f was then calculated based on the known fuel flow rate $\dot{m}_f$, and the calculated entrained fuel flow rate $\dot{m}_1$. Typically the iteration for f converged to $f = f^*$ in 3-4 iterations. For example, for diffusion flames $f \sim 0.002$, while for the brine tests $f \sim 0.1$.

A simple mass balance can now be set up for the various subsections of the room:

Upper Layer:
$$\dot{m}_2 = \dot{m}_p - \dot{m}_r = \eta \dot{m}_p \tag{3.15}$$

Plume:
$$\dot{m}_p = \dot{m}_1 + \dot{m}_f = (1+f)\,\dot{m}_1 \tag{3.16}$$

Lower Layer:
$$\dot{m}_1 = \dot{m}_o + \dot{m}_r = \dot{m}_o + (1-\eta)\,\dot{m}_p \tag{3.17}$$

These equations can be combined to yield

$$\dot{m}_2\, C_r = (1+f)\,\dot{m}_o \tag{3.18}$$

$$C_r = \frac{1}{\eta}\left[1 - (1+f)(1-\eta)\right] \tag{3.19}$$

Substituting expressions (3.8) for $\dot{V}_2$ and (3.12) or (3.13) for $\dot{V}_o$,

and noting that under the Boussinesq approximation $\rho_2 \sim \rho_0 \sim \rho_1$ in the inertia terms, one obtains:

$$\frac{H}{y_o} = 1 + B\ (1 - \frac{Y}{y_o})^{1/3}\ (1 + \tfrac{1}{2}\frac{Y}{y_o})^{2/3} \qquad \text{for } Y > 0 \qquad (3.20)$$

$$y_o = \frac{H}{B+1} \qquad Y < 0 \qquad (3.21)$$

$$B = \left[\frac{(1+f)}{C_r}\ \frac{Co_1}{Co_2}\right]^{2/3} \qquad (3.22)$$

The point source plume equations can be used to evaluate $\dot{m}_p$ as a function of height, and thus to yield a second equation to close the system. From the assumed Gaussian profiles, the mass-averaged temperature can be found to be:

$$\frac{<\Delta T>}{T_o} = \frac{Q_F}{\dot{m}_p c_p T_o} = \frac{1}{(1+\sigma)}\ \frac{\Delta T_m}{T_o} = \frac{C_T}{(1+\sigma)}\ (Q^*)^{2/3} \qquad (3.23)$$

where equation (2.53) has been used to eliminate $\frac{\Delta T_m}{T_o}$. This expression can be inverted to solve for Q^*;

$$Q^* = \left[\frac{(1+\sigma)}{C_T}\ \frac{<\Delta\rho>}{\rho_0}\right]^{3/2} \qquad (3.24)$$

and the results substituted into the plume mass flow expression,

$$\dot{m}_p = \rho_0\ (\pi\ C_v\ C_\ell^2)\ \sqrt{gz'}\ (z')^2 (Q^*)^{1/3} \qquad (3.25)$$

The result is

$$\dot{m}_p\{z_i'\} = \rho_0 \sqrt{g\ \frac{<\Delta\rho>}{\rho_0}}\ (\pi C_v C_\ell^2) \sqrt{\frac{1+\sigma}{C_T}}\ (z_i')^{5/2} \qquad (3.26)$$

where z_i' is the vertical distance from virtual origin of the equivalent point source plume to the interface.

In general, heat transfer will reduce the mean enthalpy per unit mass of the ceiling layer gas, $h = c_p (T - T_\infty)$, below the value of the mean enthalpy per unit mass of the plume at the interface $h_p = c_p \langle \Delta T \rangle$. These losses can be lumped into the parameter, c_q, such that

$$h_2 = c_q h_p \tag{3.27}$$

Then

$$\frac{\langle \Delta\rho \rangle}{\rho_0} = \frac{1}{c_q} \frac{(\rho_0 - \rho_2)}{\rho_0} \tag{3.28}$$

which fixes $\langle \Delta\rho \rangle$ in equation (3.26) in terms of the observed density difference so that:

$$\dot{m}_p = \dot{\rho}_0 \sqrt{g\left(\frac{\rho_0 - \rho_2}{\rho_0}\right)} \mathcal{D} (z_i')^{5/2} \tag{3.29}$$

where

$$\mathcal{D} = \pi C_v C_\ell^{\,2} \sqrt{\frac{1+\sigma}{C_T c_q}} \tag{3.30}$$

One can then solve the upper layer mass balance equation (3.15):

$$\dot{m}_2 = \eta\, m_p\{z_i'\} \tag{3.15}$$

for a second relation for the interface height. The result is:

$$\frac{Y}{H} = A_r \left(1 - \frac{y_o}{H}\right)^{3/5} - \frac{L_1}{H} \tag{3.31}$$

where

$$A_r = \left[\frac{Co_2 \sqrt{c_q}}{\eta \mathcal{D}} \frac{2\sqrt{2}}{3} \frac{S}{H}\right]^{2/5} \tag{3.32}$$

$$L_1 = z_\ell - z_f - z_{vs} \quad \text{or} \quad z_i' = Y + L_1 \tag{3.33}$$

3.4 Solution for the Interface Heights

Equations (3.20) or (3.21) along with equation (3.31) can now be solved for the two interface heights (y_o, Y). For the case of the interior interface below the window sill, (Y < 0), equation (3.21) can be substituted into (3.31) to yield:

$$\frac{y_o}{H} = \frac{1}{B+1} \tag{3.21}$$

$$\frac{Y}{H} = A_r \left(\frac{B}{B+1}\right)^{3/5} - \frac{L_1}{H} \tag{3.34}$$

For the case of the interior interface above the sill, (Y > 0), the pertinent equations are:

$$\frac{H}{y_o} = 1 + B \left(1 - \frac{Y}{y_o}\right)^{1/3} \left(1 + \tfrac{1}{2} \frac{Y}{y_o}\right)^{2/3} \tag{3.20}$$

$$\frac{Y}{H} = A_r \left(1 - \frac{y_o}{H}\right)^{3/5} - \frac{L_1}{H} \tag{3.31}$$

These equations can be solved numerically by inverting (3.31) in the form

$$y_o = g(Y) \tag{3.35}$$

and by rewriting (3.20) as

$$f(Y, y_o) = 0 \tag{3.36}$$

Then equation (3.36) can be solved iteratively by Newton's method

$$Y^{(n+1)} = Y^{(n)} - \frac{f(Y^{(n)}; y_o^{(n)})}{f'(Y^{(n)}; y_o^{(n)})} \tag{3.37}$$

$$y_o^{(n)} = g(Y^{(n)}) \tag{3.38}$$

$$f'(Y^{(n)};\ y_o^{(n)}) = \left.\frac{\partial f}{\partial Y}\right)_{y_o} + \left.\frac{\partial f}{\partial y_o}\right)_{Y} \frac{dg}{dy_o} \tag{3.39}$$

In order to solve these equations, a general steady-state room model program was written in FORTRAN IV, and run on a HP-2100 mini-computer. Double precision arithmetic was used throughout to improve the accuracy of the solution. The program has been documented by Sargent (1982a).

The equations can also be written in dimensionless form. Using the room height z_c as the reference length, and denoting dimensionless variables with a bar, we have:

$$\frac{\bar{H}}{\bar{y}_o} = 1 + B \left(1 - \frac{\bar{Y}}{\bar{y}_o}\right)^{1/3} \left(1 + \tfrac{1}{2}\frac{\bar{Y}}{\bar{y}_o}\right)^{2/3} \qquad (Y>0) \tag{3.40}$$

and

$$\frac{\bar{y}_o}{\bar{H}} = \frac{1}{B+1} \qquad (Y<0) \tag{3.41}$$

$$\frac{\bar{Y}}{\bar{H}} = \bar{A}_r \left(1 - \frac{\bar{y}_o}{\bar{H}}\right)^{3/5} - \frac{L_1}{\bar{H}} \tag{3.42}$$

$$\bar{A}_r = \left[\frac{Co_2}{\eta D}\sqrt{c_q}\,\frac{2\sqrt{2}}{3}\,\frac{\bar{S}}{\bar{H}}\right]^{2/5} \tag{3.43}$$

The numerical solution technique is identical with dimensionless variables. The physical quantities of interest can be found from

$$Q^* = \frac{Q_F}{\rho_0 c_p T_o \sqrt{gz}\ z^2} = \frac{Q^*_{z_c}}{(\bar{z})^{5/2}} \tag{3.44}$$

$$\frac{(\rho_0 - \rho_2)}{\rho_0} = c_q \frac{C_T}{(1+\sigma)} \frac{(Q_{z_c}^*)^{2/3}}{(\bar{z}_i')^{5/3}} \tag{3.45}$$

3.5 Numerical Results and Discussion

This solution has several interesting features. First, since this is a Boussinesq model and densities are assumed to be equal except in the buoyancy terms, the fire heat input drops out of the interface calculation, the latter depending only on opening geometry. Table 3.1 lists results for four heat input rates for a 1/4 scale room with z_c= 50 cm, $\bar{z}_u$ = 0.813, $\bar{z}_\ell$ = 0, and $\bar{S}$ = 0.375. Note that $Q_i^* = Q^*\{z_i'\} = Q_{z_c}^*/(\bar{z}_i')^{5/2} = 3.974\ Q_{z_c}^*$ for these cases. It was assumed that the initial density difference of the plume fluid was 5%, so that clearly the model fails for $Q_{z_c}^* \geq 1 \times 10^{-3}$, since $\frac{<\Delta\rho>}{\rho_0} > \frac{\Delta\rho_{brine}}{\rho_0}$. The last two columns were calculated by Zukoski and Kubota (1980)'s computer program which includes non-Boussinesq orifice flow. Comparing

Table 3.1 Effect of Q^*

$Q_{z_c}^* \times 10^5$	$\bar{z}_i$	$<\Delta\rho>/\rho_0 \times 10^2$	$\tilde{\bar{z}}_i$	$<\tilde{\Delta\rho}>/\rho_0 \times 10^2$
.1	.576	.12	.574	.12
1.0	.576	.55	.574	.55
10.	.576	2.57	.572	2.54
100.	.576	11.95	.563	11.05
1000.	.576	55.45	.522	39.48

these two models, it is evident that z_i becomes an appreciable function of Q^* for $Q_{z_c}^* \geq 1.0 \times 10^3$. However, the error in $\bar{z}_i$ is only 2%, and in $<\Delta\rho>/\rho_0$ is only 7.5% at $Q_{z_c}^* = 1 \times 10^{-3}$. It may be noted this

corresponds to an 11 Kw fire in a 2.5 m room.

The sensitivity of the model to the choice of the entrainment constant is shown in Table 3.2. A factor of 16 increase in the

Table 3.2 Effect of Entrainment Constant

$Q^*_{z_c} = 1.0 \times 10^{-5}$ $\alpha_{STD} = 0.1096$ $\sigma_{STD} = 0.9146$

α/α_{STD}	α	$\bar{z}_i$	$Q^*_i \times 10^5$	$<\Delta\rho>/\rho_0 \times 10^2$
1/4	.0274	.757	2.00	2.23
1/2	.0548	.691	2.52	1.03
1	.1096	.576	3.98	.55
2	.2192	.416	8.98	.38
4	.4384	.262	28.54	.32

entrainment constant causes the interface to drop by a factor of 2.9 and the density deficit ratio to drop by a factor of 6.9.

Table (3.3) lists the model's response to variations in the profile thickness parameter σ. One of the basic assumptions of any

Table 3.3 Effect of Profile Thickness Parameter

$Q^*_{z_c} = 1 \times 10^{-5}$ $\alpha_{STD} = 0.1096$ $\sigma_{STD} = 0.9146$

σ/σ_{STD}	σ	$\bar{z}_i$	$Q^*_i \times 10^5$	$\frac{<\Delta\rho>}{\rho_0} \times 10^3$
1/4	.2287	.525	5.01	4.73
1/2	.4573	.554	4.38	5.14
1	.9146	.576	3.98	5.55
2	1.8292	.591	3.72	5.87
4	3.6584	.600	3.58	6.10

integral method is that one need not know the profile exactly in order to get reasonable answers. Here a 1600% variation in σ caused only a 14% variation in the interface height and a 29% variation in the density deficit ratio.

Prahl and Emmons (1975) and Zukoski (1977) suggest orifice flow coefficients in the range 0.6 - 0.7. Table (3.4) indicates that the model is not particularly sensitive to the coefficients in this range: a 67% increase in $C_{o_1} = C_{o_2}$ produce a 9% increase in (z_i / z_c)

Table 3.4 Effect of Orifice Coefficients

$Q^*_{z_c} = 1 \times 10^{-5}$ $\quad \alpha_{STD} = 0.1096$ $\quad \sigma_{STD} = 0.9146$

C_{o_1}	C_{o_2}	$\bar{z}_i$	$Q_i^* \times 10^5$	$\frac{<\Delta\rho>}{\rho_0} \times 10^3$
.6	.6	0.567	4.12	5.68
.7	.7	0.583	3.85	5.43
.8	.8	0.596	3.64	5.23
1.0	1.0	0.617	3.34	4.94
.6	1.0	.609	3.45	5.04
1.0	.6	.573	4.02	5.58

and a 15% decrease in the density ratio. Note that the interface height is most sensitive to the throttling resistance (C_{o_2}) on the outflowing stream. As this resistance is increased, greater hydrostatic pressure (proportional to (H-Y)) is required, and so the interface must fall.

As discussed previously, this model incorporates the approximation

that $\dot{m}_1 \propto \dot{m}_f$, whereas in fact $\dot{m}_1 \propto (Q \propto \dot{m}_f)^{1/3}$. However, as Table (3.5) shows, the model is almost completely insensitive to this parameter when $\rho_0 = \rho_1$. However, when $\rho_1 \neq \rho_0$ the model does become more sensitive to this parameter, as will be seen in the following chapter.

Table 3.5 Effect of Fuel Mass Flow

f	$\bar{z}_i$	$Q_i^* \times 10^5$	$\frac{<\Delta\rho>}{\rho_0} \times 10^3$
0.00	0.576	3.98	5.55
.01	.576	3.98	5.54
.10	.576	3.95	5.52
.20	.578	3.94	5.51
.40	.580	3.91	5.48

The effects of the height of the fire are tabulated in Table (3.6). As might be expected, raising the fire diminishes the distance over

Table 3.6 Effect of Fire Height

$\bar{p}$	$\bar{z}_i$	$Q_i^* \times 10^5$	$\frac{<\Delta\rho>}{\rho_0} \times 10^3$
0	.576	3.98	5.54
1/4	.676	8.46	9.17
1/2	.755	30.36	21.50

which the plume can entrain cool air, thus producing a significantly hotter ceiling layer, which in turn creates a greater hydrostatic pressure difference per unit depth, and hence requires a shallower

(large z_i) ceiling layer.

The effect of the opening geometry is studied in the next three tables. Notice that Y/H scales with the aspect ratio of doors as $(S/H)^{2/5}$. Table (3.7) shows that the soffit (z_u) height has a dramatic effect on the interface height and the density difference, with the

Table 3.7 Effect of Soffit Height

$\bar{z}_u$	S/H	Y/H	y_o/H	$\bar{z}_i$	$Q_i^* \times 10^5$	$\langle\Delta\rho\rangle/\rho_0 \times 10^3$
1.000	.375	.681	.704	.681	2.61	4.19
.813	.461	.708	.726	.576	3.98	5.55
.600	.625	.745	.756	.447	7.49	8.46
.400	.938	.789	.795	.316	17.86	15.10
.200	1.875	.852	.854	.170	83.53	42.22
.100	3.750	.899	.899	.090	412.3	122.60

interface dropping almost to the floor as the soffit is lowered. Similarly, as the span of the opening is decreased the interface must drop in order to overcome the increased throttling resistance. (Table (3.8))

Table 3.8 Effect of Span

$\bar{S}$	S/H	Y/H	y_o/H	$\bar{z}_i$	$Q_i^* \times 10^5$	$\langle\Delta\rho\rangle/\rho_0 \times 10^3$
1.000	1.230	.816	.819	.663	2.79	4.38
.750	.923	.788	.794	.640	3.05	4.64
.375	.461	.708	.726	.576	3.98	5.54
.188	.231	.614	.657	.499	5.68	7.03

Table (3.9) documents the effect of changing the opening from a door to a window by raising the sill. Note that as the opening height H is diminished, the interface falls below the sill (Y < 0) in order to generate sufficient hydrostatic pressure to produce the required outflow. In these cases the inflowing jet velocity which scales as $\sqrt{y_o - Y}$ and hence is small compared to the maximum outflow velocity ($v_{2_{max}} \propto \sqrt{H - y_o}$) for doors and windows, becomes large compared to the maximum outflow

Table 3.9 Effect of Sill Height

z_ℓ	S/H	Y/H	y_o/H	$\bar{z}_i$	$Q_i^* \times 10^5$	$\frac{<\Delta\rho>}{\rho_0} \times 10^3$
.0	.461	.708	.726	.576	3.98	5.54
.2	.612	.597	.646	.566	4.15	5.70
.4	.908	.314	.523	.530	4.90	6.37
.6	1.761	-1.079	.498	.370	12.00	11.58
.7	3.319	-3.956	.498	.253	31.05	21.82

velocity for small windows. In addition Y < 0, so that the inflowing jet is bent downwards and flows through the ceiling layer gas for a minimum vertical distance Y, during which time it may be expected to entrain ceiling layer gas to produce an effective recirculation flow $\dot{m}_r$.

In order to estimate this effect, one can form the ratio of the maximum velocities:

$$\frac{v_{o_{max}}}{v_{2_{max}}} = \sqrt{\frac{y_o - Y}{H - y_o}} = \sqrt{\frac{\frac{y_o}{H} - \frac{Y}{H}}{1 - \frac{y_o}{H}}} \qquad (3.46)$$

The maximum shear should scale as the relative velocity between the counterflowing streams. One can define a maximum shear velocity ratio

$$S = \frac{v_{o_{max}} + v_{2_{max}}}{v_{2_{max}}} = 1 + \frac{v_{o_{max}}}{v_{2_{max}}} \tag{3.47}$$

and a Richardson number for the opening, which in the Boussinesq

$$Ri_H = \frac{g\frac{(\rho_o - \rho_2)}{\rho_o} H}{S^2 v^2_{max}} = \frac{1}{2S^2} \frac{H}{(H-y_o)} = \frac{\bar{H}}{2\left[\sqrt{\bar{H} - \bar{y}_o} + \sqrt{\bar{y}_o - \bar{Y}}\right]^2} \tag{3.48}$$

approximation becomes a function solely of geometry.

A related Richardson number can be defined for the cold inflowing stream as:

$$Ri_c = \frac{g\left(\frac{\rho_o - \rho_2}{\rho_o}\right) y_o}{(\bar{v}_o)^2} \tag{3.49}$$

where y_o is the vertical distance across the inflowing stream at the opening and $\bar{v}_o$ is the bulk velocity

$$\bar{v}_o = \frac{\dot{V}_o}{S\, y_o} \tag{3.50}$$

Using (2.12, 2.13) for the inflow rate $\dot{V}_o$, we have

$$Ri_c = \frac{9}{8C_{o_1}^2} \frac{1}{\left[1 - \frac{Y}{y_o}\right]\left[1 + \tfrac{1}{2}\frac{Y}{y_o}\right]^2} \qquad Y > 0 \tag{3.51}$$

$$Ri_c = \frac{9}{8C_{o_1}^2} \qquad Y < 0 \tag{3.52}$$

Since Ri_H is based on the maximum relative velocity, while Ri_c depends

only on the cold flow bulk velocity, Ri_H will be considerably smaller than Ri_c. Note that the minimum value for $Ri_c = 2.66$ (for $Co_1 = 0.65$) occurs when Y is less than or equal to zero. Some preliminary measurements by Sene and Zukoski (1980) indicate that mixing in brine flows occurs for $Ri_c < 8.16$. This appears to correspond to $Ri_H \sim 0.51$.

Table (3.10) tabulates maximum velocity ratio, the shear velocity ratio, the opening Richardson number, and the cold flow Richardson number for the flows tabulated in Tables (3.7-3.9). Note that low values of $(v_o/v_2)_{max}$ correspond to large Richardson Numbers. If the span is reduced, or the sill raised, for fixed soffit height, the velocity ratio will increase and the Richardson number will fall, leading to mixing. If the soffit height is reduced, for fixed span, the interface will fall rapidly and since $\dot{V}_o \propto \dot{m}_p \propto z^{5/3}$, the velocity ratio will fall and stratification will increase, leading to greater Richardson numbers.

Table 3.10 Richardson Number Dependence on Opening Geometry

	S/H	Y/H	y_o/H	$(v_o/v_2)_m$	S	H	Ri_H	Ri_c
Soffit	.375	.681	.704	.280	1.28	50.00	1.03	36.83
	.461	.708	.726	.252	1.25	40.65	1.16	50.19
	.625	.745	.756	.213	1.21	30.00	1.39	80.96
	.938	.789	.795	.171	1.17	20.00	1.78	158.8
	1.875	.852	.854	.1140	1.11	10.00	2.75	536.9
	3.750	.899	.899	.063	1.06	5.00	4.38	1920

	S/H	Y/H	y_o/H	$(v_o/v_2)_m$	S	H	Ri_H	Ri_c
Span	1.230	.816	.817	.145	1.15	40.65	2.11	253.8
	.923	.788	.794	.172	1.17	40.65	1.76	154.5
	.461	.708	.726	.252	1.25	40.65	1.16	50.19
	.231	.614	.657	.353	1.35	40.65	0.80	19.01
Sill	.461	.708	.726	.252	1.25	40.65	1.16	50.19
	.612	.597	.646	.371	1.37	30.65	0.75	16.52
	.908	.314	.523	.662	1.66	20.65	0.38	3.89
	1.761	-1.079	.498	1.773	2.77	10.65	0.13	2.66
	3.319	-3.955	.498	2.980	3.98	5.65	0.06	2.66

IV. A GENERALIZED STEADY STATE ROOM MODEL

4.1 Effect of the Floor Layer Density Difference

The simple, two density steady state room model presented in Chapter III can be generalized by assuming the floor layer in the fire room is at intermediate density $\rho_1 (\rho_0 \leq \rho_1 < \rho_2)$. This intermediate density is produced by some combination of turbulent mixing and heat transfer from the hot gas. As the relative velocity of the counter flowing streams increases, the Richardson number at the opening drops and one might expect turbulent mixing to overcome the stable stratification. This phenomenon has been observed in brine flow simulations, where heat transfer effects are absent. In addition, for real fires, the hot ceiling and upper walls will radiate appreciable amounts of energy to the floor, causing its temperature to rise, which in turn will generate heat transfer to floor layer gas.

A useful measure of this intermediate density is the density difference ratio

$$\delta = \frac{\rho_0 - \rho_1}{\rho_0 - \rho_2} \tag{4.1}$$

whose values have been observed in both brine flow simulation and half-scale fire test to lie between 0 and 0.3. Three regimes of behavior can be distinguished for the case $Y > 0$ and they are depicted schematically in Figure (4.1). The simple model discussed in Chapter III represents the case $\delta = 0$. Then $\rho_1 \equiv \rho_0$ and the pressure difference between the outside environment and the fire room remains constant $(\Delta p = \Delta p_i)$ from the level of the interface (Y)

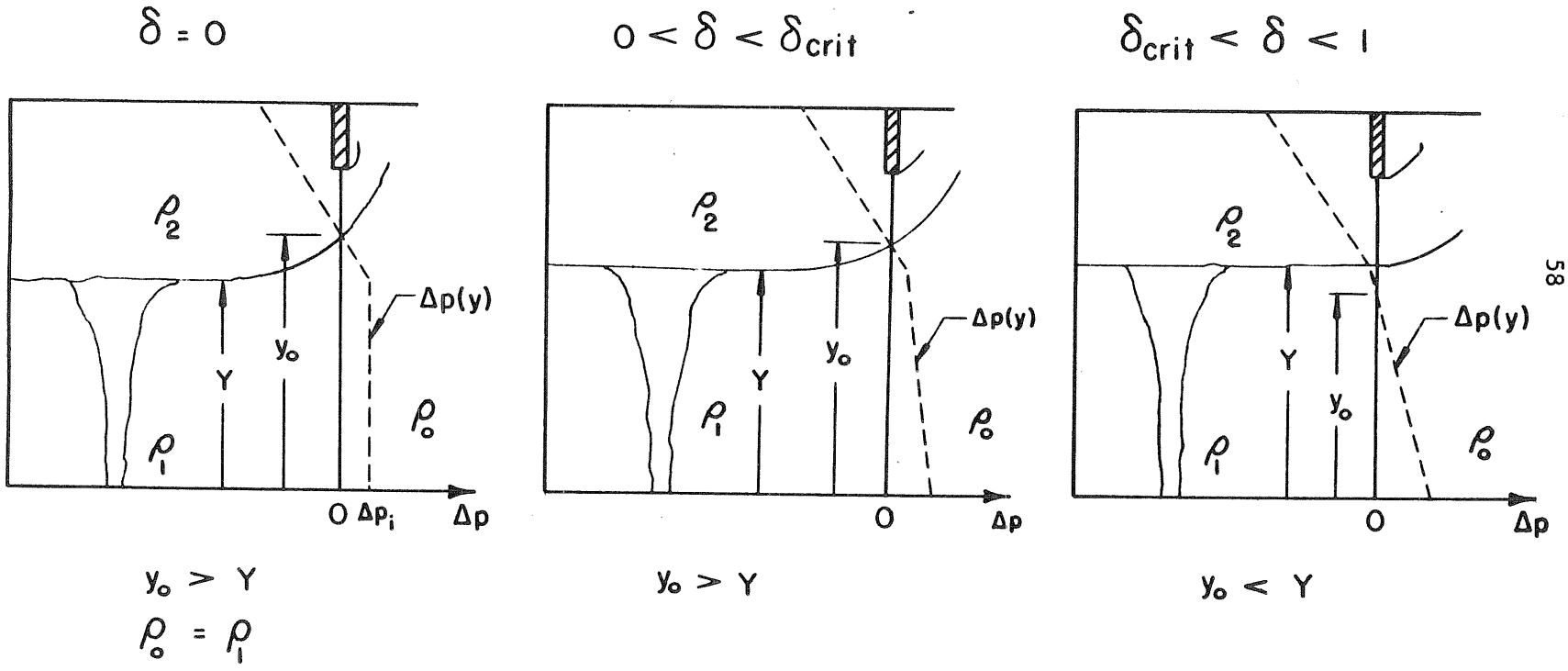

FIGURE 4.1 EFFECT OF LOWER LAYER DENSITY DIFFERENCE

to the floor. If ρ_1 is reduced, or δ increases, the hydrostatic pressure will increase in proportion to δ, such that $\Delta p > \Delta p_i$ for $y < Y$. This increased head will cause a greater inflow, which can be accommodated by allowing the interface, Y, to rise. The increased inflow is then entrained by the plume, whose total entrainment, $\dot{m}_p$, is proportional to $(Y + L_1)^{5/3}$. Finally, since the majority of the plumes output is assumed to flow out under the soffit ($\dot{m}_2 = \eta \dot{m}_p$) the neutral plane, y_0, must descend to accommodate the increased flow ($\dot{m}_2 \propto (H - y_0)^{3/2}$). A critical condition is reached when the neutral plane and the interface height meet: $y_0 = Y$. In this condition, the plume is entraining the maximum amount of lower level air it can, consistent with the requirement that its output flows out under the soffit. This effectively freezes Y for a given η. If δ is further increased, the hydrostatic pressure will increase still further, forcing greater inflow than the plume can accommodate. This excess flow, $\dot{m}_{21}$, will be forced out under the exit stream of the upper layer, $\dot{m}_{22}$, and the neutral plane must then lie some distance below the interface ($y_0 < Y$). Finally, a limiting condition is reached as $\delta \to 1$. Then the entire room is filled with highly buoyant gas (ρ_2) which will flow out through almost all of the opening ($y_0 \to 0$).

4.2 The Case of Small Density Differences

For the case of small lower layer density differences ($\delta < \delta_{crit}$), the relations for the interface pressure difference, equation (3.5),

and the outflow pressure, (3.6) velocity (3.7) and discharge (3.8) remain unchanged, as does the inflow velocity above the interface (3.9). The pressure difference below the interface can be written:

$$\Delta p = \Delta p_i + (\rho_0 - \rho_1)\, g\, (Y - y) \qquad 0 \leq y \leq Y \tag{4.2}$$

$$\Delta p = (\rho_0 - \rho_2)\, g\, \{(y_0 - Y) + \delta(Y - y)\} \tag{4.3}$$

The inflow velocity and discharge are then

$$v_0 = \sqrt{2\left(\frac{\rho_0 - \rho_2}{\rho_0}\right) g\, \{(y_0 - Y) + \delta(Y - y)\}}$$

$$0 \leq y \leq Y \tag{4.4}$$

$$\dot{V}_{0\,\text{lower}} = \frac{S\, C_{01}}{\delta}\, \frac{2}{3} \sqrt{2\left(\frac{\rho_0 - \rho_2}{\rho_0}\right) g} \left[(y_0 - Y + \delta Y)^{3/2} - (y_0 - Y)^{3/2}\right] \tag{4.5}$$

The total inflow is then

$$\dot{V}_0 = S\, C_{01} \frac{2}{3} \sqrt{2\left(\frac{\rho_0 - \rho_2}{\rho_0}\right) g}\; \frac{\left[\{y_0 - (1-\delta)Y\}^{3/2} - (1-\delta)(y_0 - Y)^{3/2}\right]}{\delta} \tag{4.6}$$

Figure (4.2) shows the flow pattern for $0 < \delta < \delta_{crit}$. Conservation of mass can again be applied as in the $\delta = 0$ case to give two equations for Y and y_0. First assume that whatever mixing between the ceiling layer and the lower layer is given by $\dot{m}_r$, and that mixing between the inflowing stream and the exiting stream is given by $\dot{m}_{E_0}$. Assume:

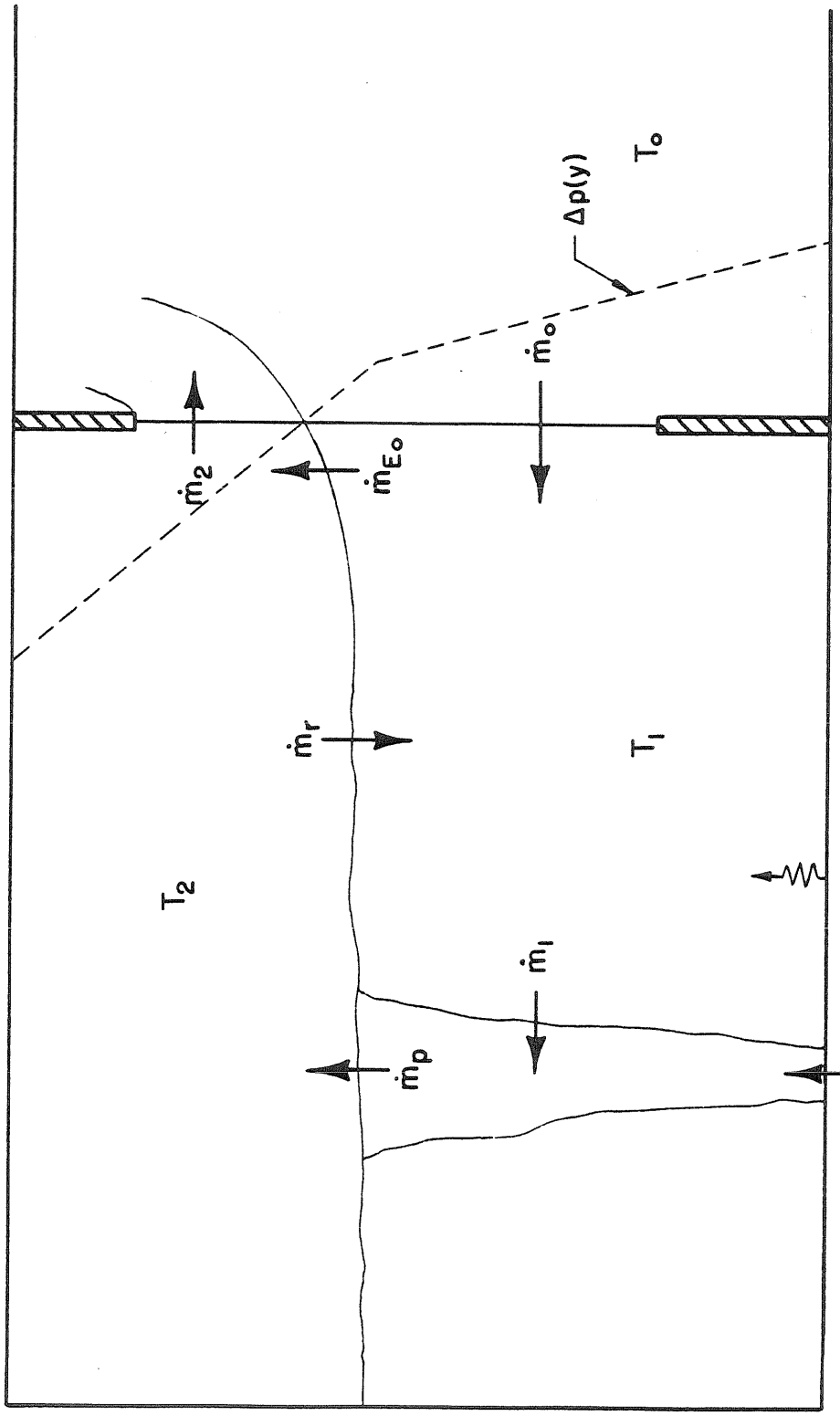

FIGURE 4.2 STEADY STATE ROOM MODEL for $\delta < \delta_{crit}$

$$\dot{m}_r = (1 - \eta)\, \dot{m}_p \tag{4.7}$$

$$\dot{m}_{E_0} = \kappa_0\, \dot{m}_r \tag{4.8}$$

Conservation of mass for the ceiling layer yields:

$$\dot{m}_2 = \eta \dot{m}_p + \kappa_0 (1 - \eta)\, \dot{m}_p = Cr_0\, \dot{m}_p \tag{4.9}$$

where

$$Cr_0 = \eta + \kappa_0 (1 - \eta) \tag{4.10}$$

Conservation of mass for the floor layer yields:

$$\dot{m}_1 = \dot{m}_0 + (1 - \eta)\dot{m}_p - \kappa_0 (1 - \eta)\dot{m}_p$$

$$= \dot{m}_0 + (1 - \kappa_0)(1 - \eta)\dot{m}_p \tag{4.11}$$

Conservation of mass for the plume yields:

$$\dot{m}_p = (1 + f)\dot{m}_1 \tag{4.12}$$

Substituting (4.10) into (4.11) for $\dot{m}_1$, and then using (4.9) to eliminate $\dot{m}_p$, results in an expression involving only the counter flow discharges:

$$Cr\, \dot{m}_2 = (1 + f)\, \dot{m}_0 \tag{4.13}$$

where

$$Cr = \frac{1 - (1 + f)(1 - \kappa_0)(1 - \eta)}{Cr_0} \tag{4.14}$$

Equations (4.9) and (4.13) then form a set of two non-linear algebraic equations for the two unknowns (Y, y_0).

It may be noted that the model can be further generalized at this point to include multiple openings and multiple fires. The simplest case is that of several openings of the same vertical dimensions $\{z_\ell, z_u\}$. These can be immediately modeled as a single opening with an equivalent width equal to the sum of the individual widths. For openings with dissimilar vertical dimensions, such as the case of a room with a door and a ventilation duct opening, terms must be added to the appropriate mass and enthalpy equations. In these cases, direct simultaneous solutions of the two mass balance equations may be needed, as is done for equations (4.48) and (4.50). Similarly, n_f equal strength fires, spaced far enough apart that their plumes do not merge, can be modeled by dividing the coefficient A_r in equation (3.32) by $n_f{}^{2/5}$. For example, comparing a single fire with 2 fires of half the heat release, indicates the interface falls by 13% and the ceiling layer density difference falls by 20% for the standard door. Fires of unequal strength require modifications to the mass and enthalpy equations.

Substituting the discharge relations (4.6, 3.8) into the mass balance equation (4.13) then results in:

$$(H - y_0)^{3/2} = \left[\frac{(1+f)}{Cr} \frac{C_{01}}{C_{02}}\right] \frac{1}{\delta} G(Y, y_0) \qquad (4.15)$$

where

$$G(Y, y_0) = [\{y_0 - (1-\delta)Y\}^{3/2} - (1-\delta)(y_0-Y)^{3/2}] \qquad (4.16)$$

Equation (4.15) can be rewritten in a form suitable for solution using the Newton-Raphson method as:

$$F(Y;\ y_0) \quad = \quad G(Y,\ y_0) \ - \ \delta \left[\frac{H \ - \ y_0}{B} \right]^{3/2} \tag{4.17}$$

where, since the outflow relations remain unchanged, y_0 is given by (3.31).

The solution to the upper layer mass balance equation (4.9) is given as before by (3.31):

$$\frac{(Y \ + \ L_1)}{H} \quad = \quad A' \left[1 \ - \ \frac{y_0}{H} \right]^{3/5} \tag{3.31}$$

where

$$A' \quad = \quad \left[\frac{C_{02} \quad \sqrt{c_q}}{Cr_0 \quad D'} \quad \frac{2\sqrt{2}}{3} \quad \frac{S}{H} \right]^{2/5} \tag{4.18}$$

$$D' \quad = \quad \pi \ C_v \ C_\ell^{\,2} \sqrt{\frac{1 \ + \ \sigma}{C_T} \ \frac{(1 \ - \ \delta)}{c_q}} \tag{4.19}$$

Since the inflow velocity will be increased by the presence of δ, the maximum velocity ratio used in estimating the Richardson number for the opening will change. The maximum inflow velocity is now:

$$v_{0max} \quad = \quad \sqrt{2\left(\frac{\rho_0 \ - \ \rho_2}{\rho_0}\right) g \ \{y \ - \ (1 \ - \ \delta)Y\}} \tag{4.20}$$

and the maximum velocity ratio is:

$$\frac{v_{0max}}{v_{2max}} = \sqrt{\frac{y_0 - (1 - \delta)Y}{H - y_0}} \tag{4.21}$$

Similarly, the cold-flow Richardson number will be affected and is now given by:

$$Ri_c = \frac{9}{8\ C_{01}^2} \frac{\delta^2\ y_0^3}{[G(Y,\ y_0)]^2} \tag{4.22}$$

The temperature (or equivalently, the density) of the lower or floor layer fluid can be estimated from an enthalpy balance for the floor layer, excluding the plume. The enthalpy outflow must be equal to the enthalpy inflow in steady state. Figure (4.2) shows the flow pattern for $0 < \delta < \delta_{crit}$. Thus,

$$\dot{H}_1 = \dot{H}_r + (\dot{H}_0 - \dot{H}_{E_0}) + \dot{Q}_{floor} \tag{4.23}$$

It is convenient to choose T_1 as the reference enthalpy temperature. Then (4.23) becomes:

$$0 = \dot{m}_r\ c_p\ (T_2 - T_1) + (\dot{m}_0 - \dot{m}_{E_0})\ c_p(T_0 - T_1) + \dot{Q}_{floor} \tag{4.24}$$

Assumptions (4.7),(4.8) can now be employed to eliminate $\dot{m}_r$ and $\dot{m}_{E_0}$ in favor of $\dot{m}_p$. We further assume the heat flux from the floor to the gas immediately above it, $\dot{Q}_{floor}$, is proportional to the heat lost from the ceiling layer, some fraction of which heats the ceiling and upper walls, which in turn radiate to the floor. Thus,

$$\dot{Q}_{floor} = c_{fr}\ (1 - c_q)\ \dot{Q}_{plume} \tag{4.25}$$

With these assumptions and the Boussinesq approximation, equation (4.24) becomes

$$\left\{(1-\eta) + c_{fr}\frac{(1-c_q)}{c_q}\right\}(T_2-T_1) = \left[\frac{\mathring{V}_0}{\mathring{V}_p} - \kappa_0(1-\eta)\right](T_1-T_0) \tag{4.26}$$

Let

$$\tilde{F} = (1-\eta) + c_{fr}\frac{(1-c_q)}{c_q} \tag{4.27}$$

$$\tilde{E} = \frac{\mathring{V}_0}{\mathring{V}_p} - \kappa_0(1-\eta) \tag{4.28}$$

Then

$$T_1 = \frac{\tilde{F}\,T_2 + \tilde{E}\,T_0}{\tilde{F} + \tilde{E}} \tag{4.29}$$

4.3 The Case of Large Density Differences

The model must be modified for the case $\delta > \delta_{crit}$ to allow the excess inflow to escape (i.e., $y_0 < Y$). Figure (4.3) shows the flow patterns hydrostatic pressure distribution for this case.

The pressure difference between the environment and the room can be written as:

$$\Delta p_{in} = (\rho_0 - \rho_1)\, g\, (y_0 - y) \qquad y < Y \tag{4.30}$$

$$\Delta p_{in} = -\left[(\rho_0-\rho_2)g(y-Y) + (\rho_0-\rho_1)g(Y-y_0)\right] \quad y > Y \tag{4.31}$$

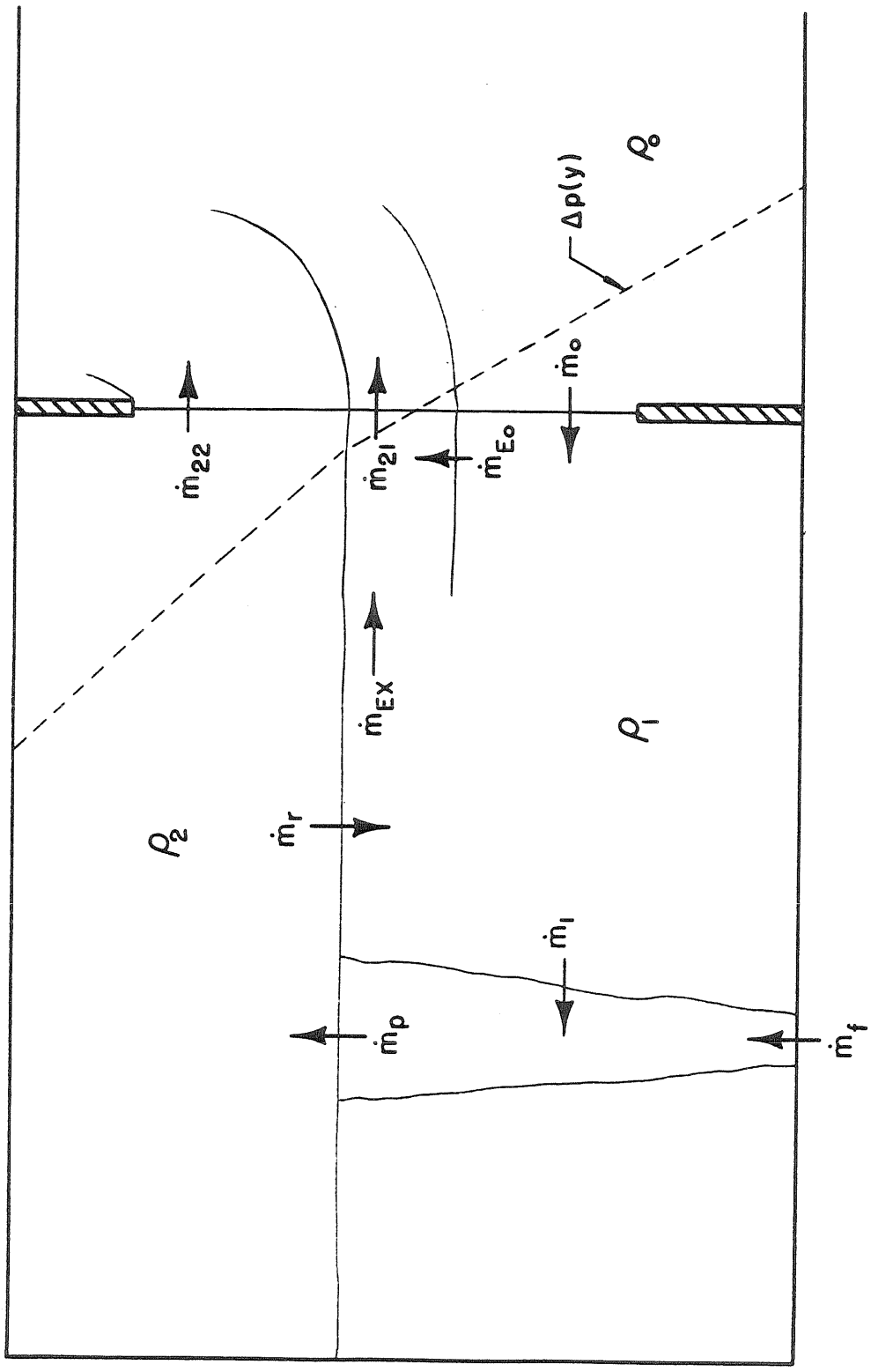

FIGURE 4.3 STEADY STATE ROOM MODEL for $\delta > \delta_{crit}$

The ceiling layer fluid will have an outflow velocity and discharge given by:

$$v_{22} = \sqrt{2\frac{\Delta p_{out}}{\rho_0}} = \sqrt{2\left(\frac{\rho_0-\rho_2}{\rho_0}\right) g \left[y - Y + \delta(Y - y_0)\right]} \quad y > Y \tag{4.32}$$

$$\dot{V}_{22} = C_{022}\, S\, \frac{2}{3} \sqrt{2\left(\frac{\rho_2-\rho_0}{\rho_0}\right) g}\; \Phi^{3/2} - \Psi^{3/2} \tag{4.33}$$

where

$$\Psi = \delta(Y - y_0) \tag{4.34}$$

$$\Phi = H - Y + \Psi \tag{4.35}$$

The increased hydrostatic pressure forces cause more fluid to enter the lower layer than the plume can swallow. The excess fluid, which has been heated by mixing and heat transfer to a uniform temperature T_1 (density ρ_1) must flow out between the ceiling layer and the incoming cold fluid. This fluid has an exit velocity distribution and discharge given by:

$$v_{21} = \sqrt{2\frac{\Delta p_{out}}{\rho_0}} = \sqrt{2\delta\left(\frac{\rho_0-\rho_2}{\rho_0}\right) g\,(y - y_0)} \quad y_0 \leq y \leq Y \tag{4.36}$$

$$\dot{V}_{21} = S\, C_{021}\, \frac{2}{3} \sqrt{2\delta\left(\frac{\rho_0 - \rho_2}{\rho_0}\right) g}\; \Psi^{3/2} \tag{4.37}$$

Note that the velocity will be continuous at the interface: $v_{21}(Y) = v_{22}(Y)$. Since the orifice flow coefficients are not expected to vary greatly from 0.6, assume $C_{021} = C_{022} = C_{02}$.

Ambient fluid from the environment will be drawn into the room by the hydrostatic pressure field with velocity and discharge:

$$v_0 = \sqrt{2\frac{\Delta p_{in}}{\rho_0}} = \sqrt{2\delta\left(\frac{\rho_0 - \rho_2}{\rho_0}\right) g\,(y_0 - y)} \qquad 0 \leq y \leq y_0 \tag{4.38}$$

$$\dot{V}_0 = C_{01}\, S\, \frac{2}{3}\sqrt{2\delta\left(\frac{\rho_0 - \rho_2}{\rho_0}\right) g}\; y_0^{3/2} \tag{4.39}$$

Conservation of mass can now be applied to the room in order to obtain a relation between the outflow, $\dot{m}_{22}$, and the net inflow, $\dot{m}_0 - \dot{m}_{21}$. Referring to Figure (4.3) we have:

Ceiling layer:
$$\dot{m}_p = \dot{m}_{22} + \dot{m}_r \tag{4.40}$$
$$\dot{m}_{22} = \eta \dot{m}_p \tag{4.41}$$

Intermediate Layer:
$$\dot{m}_{21} = \dot{m}_{E_0} + \dot{m}_{Ex} \tag{4.42}$$

Floor layer:
$$\dot{m}_1 = \dot{m}_0 - \dot{m}_{21} + \dot{m}_r \tag{4.43}$$
$$\dot{m}_1 = \dot{m}_0 - \dot{m}_{21} + (1 - \eta)\dot{m}_p \tag{4.44}$$

Plume:
$$\dot{m}_p = \dot{m}_1 + \dot{m}_f = (1 + f)\dot{m}_1 \tag{4.45}$$

The intermediate layer has been modeled as the sum of two flows: $\dot{m}_{Ex}$, the excess inflow which has been circulated through the floor layer and heated to T_1, and $\dot{m}_{E_0}$, the mass entrained from the inflowing fluid at T_0. Note that in this case $\dot{m}_{E_0}$ does not affect the interface or neutral plane heights as was the case for $\delta < \delta_{crit}$. It merely adjusts the enthalpy of the floor level fluid.

Substituting (4.44) into (4.45) for $\dot{m}_1$ and then using (4.41) for $\dot{m}_p$ results in

$$\dot{m}_{22}\ Cr = (1 + f)\ (\dot{m}_0 - \dot{m}_{21}) \tag{4.46}$$

with Cr given by (3.19). Equation (4.46) is thus equivalent to (4.13) with the net inflow $(\dot{m}_0 - \dot{m}_{21})$ replacing $\dot{m}_0$. The second equation for (y_0, Y) is given by (4.41).

Substituting the expressions for the discharge of the outflow (4.33), inflow (4.39), and excess inflow (4.37) into (3.46) results in:

$$\Phi^{3/2} - \Psi^{3/2} = \left[\frac{(1 + f)}{Cr}\frac{C_{01}}{C_{02}}\right]\left\{\delta^{1/2}\ y_0^{3/2} - \frac{C_{02}}{C_{01}}\ \Psi^{3/2}\right\} \tag{4.47}$$

Written in a form suitable for solution via the Newton-Raphson method, with $\vec{x} = (Y, y_0)^T$, (4.47) becomes

$$f_1(\vec{x}) = \Phi^{3/2} - \Psi^{3/2} - (B^{3/2})\left\{\delta^{1/2}\ y_0^{3/2} - \frac{C_{02}}{C_{01}}\ \Psi^{3/2}\right\} \tag{4.48}$$

Substituting the plume mass flow relation (3.29) into (4.41) yields

$$\left[\frac{2}{3}\ \sqrt{2}\ \frac{C_{02}}{\eta D}\ S\right]\ (\Phi^{3/2} - \Psi^{3/2}) = (Y + L_1)^{5/2} \tag{4.49}$$

which can be rewritten as

$$f_2(\vec{x}) = \Phi^{3/2} - \Psi^{3/2} - \frac{(Y + L_1)^{5/2}}{\left[\frac{2}{3}\sqrt{2}\frac{C_{02}}{\eta D}\frac{S}{H}\right] H} \tag{4.50}$$

The solution to the system $\vec{f} = (f_1, f_2)^T = \vec{0}$ can be found iteratively by correcting $\vec{x}^{(k)}$ at the k-th step with $\vec{\delta}^{(k)}$

$$\vec{x}^{(k+1)} = \vec{x}^{(k)} - \vec{\delta}^{(k)} \tag{4.51}$$

where $\vec{\delta}^{(k)}$ is found as the solution to the linear system:

$$\hat{\Phi}(\vec{x})\,\vec{\delta}^{(k)} = \vec{f}(\vec{x}) \tag{4.52}$$

and matrix $\hat{\Phi}$ is given by:

$$\hat{\Phi}(\vec{x}) = \left(\frac{\partial f_i}{\partial x_j}\right) \tag{4.53}$$

Given the solution (Y, y_0) to (4.48) and (4.50), the maximum inflow and outflow velocities are given by

$$v_{0max} = v_0(0) = \sqrt{2\delta\left(\frac{\rho_0 - \rho_2}{\rho_0}\right) g\, y_0} \tag{4.54}$$

$$v_{2max} = v_2(H) = \sqrt{2\left(\frac{\rho_0 - \rho_2}{\rho_0}\right) g\,(H - Y + \delta(Y - y_0))} \tag{4.55}$$

Their ratio

$$\frac{v_{0max}}{v_{2max}} = \sqrt{\frac{\delta\, y_0}{H - Y + \delta(Y - y_0)}} \tag{4.56}$$

can then be used to estimate the Richardson number of the opening via (3.47) and (3.48). The cold-flow Richardson number becomes simply

$$Ri_c = \frac{9}{8\, C_{01}^2 \delta} \tag{4.57}$$

which approaches its minimum value $(9/8C_{01}^2) \approx 2.66$ as $\delta \to 1$.

Conservation of enthalpy can be applied to the lower layer to solve for the temperature. Under steady state conditions, the net enthalpy flow into the lower layer fluid, excluding the plume must be zero. Thus,

$$\dot{H}_1 + \dot{H}_{21} = \dot{H}_0 + \dot{H}_r + \dot{Q}_{floor} \tag{4.58}$$

Choosing T_1 to be the reference enthalpy temperature simplifies (4.58) considerably, since $\dot{H}_1 = \dot{H}_{Ex} = 0$, and we have:

$$\dot{m}_{E_0} c_p(T_0 - T_1) = \dot{m}_0 c_p(T_0 - T_1) + (1 - \eta)\dot{m}_p(T_2 - T_1)$$

$$+ c_{fr} \frac{(1 - c_q)}{c_q} \dot{m}_p c_p(T_2 - T_1) \tag{4.59}$$

This can be written as

$$\left\{ \frac{\dot{V}_0}{\dot{V}_p} - \kappa_0(1 - \eta) \right\} (T_1 - T_0) = \left\{ c_{fr} \frac{(1 - c_q)}{c_q} + (1 - \eta) \right\} (T_2 - T_1) \tag{4.60}$$

which is identical to (4.26). Hence the lower layer temperature is again given by (4.29)

$$T_1 = \frac{\tilde{F} T_2 + \tilde{E} T_0}{\tilde{F} + \tilde{E}} \tag{4.29}$$

4.4 Numerical Results and Discussion

A general program for the steady state room model was written to handle the three cases of interest: $\delta = 0$, $\delta < \delta_{crit}$, and $\delta > \delta_{crit}$.

The following tables have been generated to show the pertinent features of the solution. Program documentation has been given by Sargent (1982a).

Table (4.1) shows the effect of the density difference ratio, δ, on the solution for a door of non-dimensional height 0.813 and width 0.375, where $\eta = 1 - \delta$, $f = 0.01$, and $Q^*_{z_c} = 1.002 \times 10^{-5}$.

TABLE 4.1 Effect of Density Difference Ratio

δ(%)	y_0/H	Y/H	$\left(\frac{\rho_2-\rho_0}{\rho_0}\right) \times 10^3$	Ri_H	Ri_c
.00	.726	.708	5.55	1.163	50.19
.01	.726	.708	5.55	1.162	50.19
.10	.726	.709	5.55	1.158	50.21
1.00	.726	.712	5.55	1.111	50.41
2.00	.726	.716	5.56	1.081	50.67
4.00	.727	.724	5.57	1.013	51.33
5.00	.728	.727	5.58	.982	51.77
5.13	.728	.728	5.58	.978	51.84
5.14	.727	.728	5.58	.977	51.80
6.00	.690	.731	5.59	.952	44.38
8.00	.625	.738	5.61	.902	33.28
10.00	.581	.745	5.63	.861	26.63

With this opening geometry, it may be observed that the critical density difference ratio δ_{crit} lies between 5.13% and 5.14% . For $\delta < \delta_{crit}$, the primary change as δ increases is an increase in the interface height Y, allowing the plume to entrain more fluid. On the other hand, for $\delta > \delta_{crit}$, the interface height remains almost constant, while the neutral plane falls, thereby throttling back the

inflow. The slight increase in Y while this is happening is due to the decrease in the outflow as more of the plume's output is recirculated. Note that the opening Richardson number Ri_H falls from an initial value greater than one (indicating that mixing would be inhibited) to a value less than one (indicating that mixing could occur) when $\delta \approx \delta_{crit}$. On the other hand, the cold-flow Richardson number, Ri_c actually increases with δ, for $\delta < \delta_{crit}$, since y_0 increases. However, for $\delta > \delta_{crit}$, Ri_c falls rapidly as the cube of y_0. This decrease in the Richardson numbers is an interesting result in that the value of δ is dependent both on the mixing and the wall heat transfer. Thus for fires with significant heat transfer, a large enough value of δ may be generated by heat transfer effects to cause the Richardson number to fall sufficiently to allow mixing in an otherwise stable geometry. This would then increase δ even further. Finally, it is interesting to note that while the lower layer temperature changes significantly, the upper layer temperature remains almost constant.

Table (4.2) shows the effect that mixing, modeled as a recirculation $\dot{m}_r$ of the plume's mass flow, has on the solution, where, as in Table (4.1), $Q^*_{z_c} = 1.002 \times 10^{-5}$, $\overline{H} = 0.813$, $\overline{S} = 0.375$. Both calculations are for a 1/4 scale (z_c= 50cm) brine simulation, where $(\rho_{brine} - \rho_0)/\rho_0 = 0.05$ and $\dot{V}_{brine} = 111\ cm^3/S$. As the density difference ratio δ is increased, via increased mixing, the solution becomes more sensitive to the parameter f. For a given value of η,

TABLE 4.2 Effect of Mixing

$\hat{\xi}$	δ^*	f^*	y_0/H	Y/H	$\left(\frac{\rho_2-\rho_1}{\rho_0}\right) \times 10^3$	Ri_H	Ri_c
.0	.000	.124	.724	.710	5.53	1.204	61.05
.1	.109	.121	.530	.749	5.63	.855	24.38
.2	.200	.118	.446	.785	5.76	.725	13.32
.3	.272	.116	.416	.816	5.89	.649	9.78
.5	.382	.113	.395	.872	6.16	.559	6.97
.7	.464	.111	.388	.924	6.39	.505	5.73
.9	.530	.108	.386	.974	6.61	.468	5.02

δ and f must be determined iteratively, and are denoted by δ^* and f^*. Note that for small recirculation, $\hat{\xi} \equiv (1 - \eta)$, δ^* is approximately equal to $\hat{\xi}$. However, for large recirculation, δ^* grows much more slowly than $\hat{\xi}$. As δ^* grows with increased mixing the neutral plane drops from 72% of the door height for no mixing to 39% of the door height for 90% recirculation. As would be expected, less and less of the plume's output flows out under the door soffit as the fraction recirculated is increased, and hence the interface height rises from 71% of the door height with no mixing to 97% of the height with 90% recirculation. This increase in interface height causes $\dot{m}_1$ to increase, and hence f^* to fall. Although $\hat{\xi}$ has a profound effect on the lower layer, the ceiling layer is relatively unaffected and $\left(\frac{\rho_2-\rho_0}{\rho_0}\right)$ rises by only 19.6% as $\hat{\xi}$ is increased from 0 to 90%. Note that both Richardson numbers fall rapidly as $\hat{\xi}$ increases. Also note that Ri_c increases with f, since an increase in f implies a decrease in the inflow for a given interface height.

The critical density difference ratio, δ_{crit}, is a strong function of opening geometry. The smaller the area of inflow, the greater the hydrostatic pressure difference required to deliver the inflow desired. Hence δ_{crit}, which measures when the hydrostatic pressure difference delivers the maximum inflow that the plume can swallow, will increase as the door is narrowed or the window sill raised. These effects can be clearly seen in Table (4.3), where again $Q^*_{z_c} = 1.002 \times 10^{-5}$, $z_c = 50$ cm. The variation of δ_{crit} is greatest for the case of the window since the constriction of the opening is greatest in this case.

TABLE 4.3 Effect of Opening Geometry on δ_{crit}

Door $\bar{H} = .813$			Window $\bar{S} = 0.375$		
$\bar{S}$	$\delta_1 < \delta_{crit} < \delta_2$(%)		$\bar{z}_\ell$	$\delta_1 < \delta_{crit} < \delta_2$(%)	
1.000	.70	1.00	0.00	5.13	5.14
.500	2.00	3.00	.20	13.5	13.6
.375	5.13	5.14	.40	35.4	35.5
.250	9.00	9.50			

Some mixing may occur between the exiting ceiling layer fluid and the inflowing ambient fluid such that the ambient fluid is entrained into the exit stream. This phenomenon is modeled as $\dot{m}_{E_0} = \kappa_0 \dot{m}_r$ where one might expect κ_0 to vary between 0 and 1. Table (4.4) presents two cases, $\delta < \delta_{crit}$ and $\delta > \delta_{crit}$, for a window with $\bar{z}_\ell = 0.2$, $\bar{S} = 0.375$, $z_c = 50$ cm, $Q^*_{z_c} = 1.002 \times 10^{-5}$. For $\delta < \delta_{crit}$, an increase in κ_0 from 0 to 1 causes y_0/H and Y/H to fall

TABLE 4.4 Effect of κ_0

$\delta^{(0)} = 0.303 \quad \hat{\xi} = 0.300 \quad \delta < \delta_{crit}$

κ_0	y_0/H	Y/H	$\left(\frac{\rho_1-\rho_0}{\rho_0}\right) \times 10^3$	$\left(\frac{\rho_2-\rho_0}{\rho_0}\right) \times 10^3$
0.00	.572	.535	2.07	6.83
.50	.550	.464	2.24	7.38
1.00	.535	.401	2.41	7.94

$\delta^{(0)} = 0.06 \quad \hat{\xi} = 0.06 \quad \delta > \delta_{crit}$

κ_0	y_0/H	Y/H	$\left(\frac{\rho_1-\rho_0}{\rho_0}\right) \times 10^3$	$\left(\frac{\rho_2-\rho_0}{\rho_0}\right) \times 10^3$
.00	.548	.621	2.85	7.15
.50	.548	.621	4.19	8.40
1.00	.548	.621	7.90	11.88

by 6 and 25% respectively, as more of the inflowing fluid is diverted into the exit stream. This increases significantly the difference $(y_0 - Y)$, and hence will increase the value of δ_{crit}. Both the lower and upper levels experience a 16% increase in density. As expected, when $\delta > \delta_{crit}$, y_0 and Y are not affected by κ_0, since only $\dot{m}_{21}$ affects y_0 and Y. However, the lower layer enthalpy increases by 177% as inflowing fluid at ambient enthalpy level is diverted into the exit stream. This in turn causes the enthalpy of the upper layer to rise since the plume entrains hotter fluid. Since $\dot{m}_{E_0} = \hat{\xi}\, \dot{m}_r$ and $\dot{m}_r = \hat{\xi}\, \dot{m}_p$, these κ_0 effects will only be important for window flows where the high shear can produce significant values of $\hat{\xi}$.

Heat transfer between the gas and the walls can have two significant effects. First, since the ceiling and upper walls will initially be "cold" compared to the ceiling layer gas, the gas will lose a sizeable fraction of its initial enthalpy to these surfaces. This has been modeled by assuming $(T_2 - T_1) = c_q(\langle T \rangle - T_1)$. If the fire remains confined to a small area, the ceiling and upper walls will be heated by this heat transfer process. They will then begin to transfer some fraction of this heat to the floor and lower walls by radiation. The lower surfaces will then heat the lower level gas. Table (4.5) shows the effect of heat loss $[\propto(1 - c_q)]$ from the ceiling layer for a 1/2 scale fire test room, with $Q^*_{z_c} = 1 \times 10^{-2}$, $z_c = 1.22$m. The room has a door with dimensionless height and width: 0.813 and 0.375, respectively. The obvious effect is the 44% loss in

TABLE 4.5 Effect of Ceiling Layer Heat Loss: $(1 - c_q)$

$(1-c_q)$	y_0/H	Y/H	$\left(\frac{\langle\rho\rangle_1-\rho_1}{\rho_0}\right)\times 10$	$\left(\frac{\rho_2-\rho_1}{\rho_0}\right)\times 10$	$\left(\frac{\rho_2-\rho_0}{\rho_0}\right)\times 10$
0.0	.726	.708	5.54	5.54	5.54
.1	.720	.702	5.63	5.07	5.07
.2	.714	.694	5.74	4.59	4.59
.3	.708	.685	5.86	4.10	4.10
.4	.700	.675	6.01	3.60	3.60
.5	.690	.664	6.19	3.10	3.10

ceiling layer buoyancy and the resulting decrease in the hydrostatic pressure field. This causes y_0 to fall 4.8% to maintain the outflow $[\propto(H - y_0)^{3/2}]$. This effect throttles down the inflow and the interface

adjusts by falling 6.4%, since $\dot{m}_p \propto (z')^{5/3}$. The decrease in mass flow also causes the mass averaged enthalpy in the plume at interface, $(\langle T \rangle - T_1)$ to rise 11% above its adiabatic value.

Once the ceiling and upper walls above the interface become sufficiently hotter than the lower portion of the room, significant radiative heat transfer may occur. Table (4.6) shows the effect this has on the solution for $c_q = 0.6$.

TABLE 4.6 Effect of Heat Transfer to Floor Layer

c_{fr}	δ_{calc}	y_0/H	Y/H	$\left(\frac{\langle\rho\rangle_1-\rho_1}{\rho_0}\right)\times 10$	$\left(\frac{\rho_2-\rho_1}{\rho_0}\right)\times 10$	$\left(\frac{\rho_1-\rho_0}{\rho_0}\right)\times 10$	$\left(\frac{\rho_2-\rho_0}{\rho_0}\right)\times 10$
.0	.000	.700	.675	6.01	3.60	.00	3.60
.1	.063	.700	.675	6.01	3.60	2.42	3.85
.1*	.063	.696	.690	5.80	3.48	2.33	3.71
.2	.118	.700	.675	6.01	3.60	4.83	4.09
.2*	.118	.626	.701	5.64	3.38	4.51	3.84
.3	.167	.700	.675	6.01	3.60	7.25	4.33
.3*	.164	.569	.711	5.51	3.31	6.51	3.96

Each entry for a given non-zero value of c_{fr} has two values: an initial value, calculated with $\delta^{(0)} = 0$, and a value after the iteration for δ has converged ($\delta = \delta^*$). The column labeled "δ_{calc}" lists the corresponding calculated values of δ after the first and last iterations. The initial effect of the floor layer heat transfer is to increase the enthalpy (bouyancy) of the floor layer fluid. This results in greater plume enthalpy and a hotter ceiling layer. However, the

increased bouyancy of the floor layer will generate more inflow, thereby diluting the floor layer somewhat so that $\delta^{(0)} > \delta^*$.

V. LABORATORY MODELS OF ROOM FIRES

5.1 Introduction

In order to observe the flow phenomena involved in room fires, and to test the theoretical models, two series of experiments were conducted using small scale rooms. The first series was conducted in an approximately 1/4 scale facility in which a stream of brine was introduced into a tank of fresh water. Since the initial density difference was only 5-10% of the density of water, this set of laboratory experiments simulated very small fires in rooms without enthalpy losses. The second set of experiments, on the other hand, involved the direct measure of enthalpy losses and other heat transfer effects for moderate fires. The heat transfer measurements were made in a 1/2 scale fire test room in which a lean mixture of natural gas and air was burned at floor level.

5.2 1/4 Scale Saltwater Simulations

Although the initial density differences were quite small, limited by the solubility of salt in water, the 1/4 scale saltwater simulations had several advantageous features. First, these flows clearly satisfy the requirement of the Boussinesq approximation, that the density differences be small compared to the reference density of the fluid. For even a small fire, by comparison, although entrainment will quickly reduce the density difference ratio $\{(\rho_e - \rho) / \rho_o\}$ in the plume, the temperatures will still be large near the flame, and hence in this region the Boussinesq approximation will not strictly hold. This error is aggravated as the flame height becomes larger. Secondly the saltwater-freshwater system allows one to decouple the effects of buoyancy from heat transfer, and thus to study the behavior of the system in limiting case of no losses (c_q=1). Finally, this type of hydraulic modeling has some obvious

practical advantages: it is safe, inexpensive to build, easy to modify, and provides good flow visualization.

The 1/4 scale experiments were conducted in a large glass-walled tank shown schematically in Figure (5.1). The overall tank dimensions were 115 x 235 x 60 cm. The tank was sub-divided into two rooms by a plexiglass partition, with a door cut in it. A plexiglass false floor was inserted in the "fire room" portion of the tank to insure that the "ceiling" in this room was smooth and flat.

Three different tank geometries were used in the course of this work. For the initial 25 experiments, the fire room completely filled the left portion of the tank and measured 130 x 115 x 50 cm. The basic doorway opening measured 38 x 27cm. for these tests. However, blocks of plexiglass could be inserted into the doorway cut out to form door or window openings as desired. Later in order to conduct tests in a room that was geometrically similar to the 1/2 scale fire test room, three portions were glued into place to produce the 1/4 scale fire room 50 x 100 x 50 cm., with its back wall 30 cm. from the tank rear wall. For all 1/4 scale tests, the basic doorway had a span of 19 cm. and a height of 41 cm. Finally, in order to minimize mixing effects in the outer room, the main portion was repositioned as shown in Figure (5.1), so that the back wall of the fire room was flush against the tank wall.

Buoyancy in these experiments was produced by introducing a flow of salt water into the fire room through an inlet assembly. The brine was initially 5 to 10% denser than the surrounding fresh water, and so formed a negatively buoyant plume which settled toward the bottom of the tank. In the following discussion, the vertical coordinate will be taken as positive downward to account for the change in sign of the density

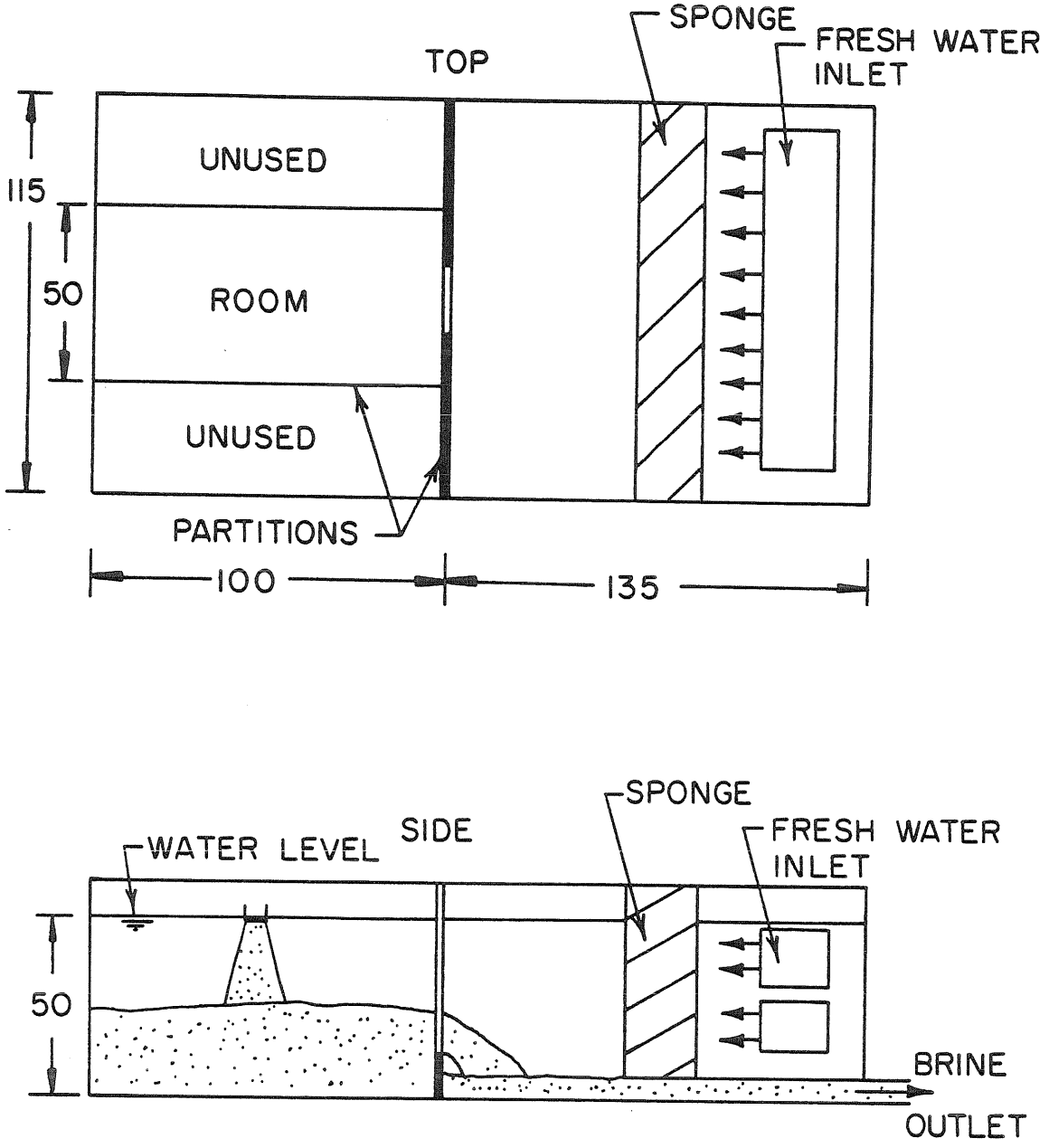

FIG. 5.1 1/4 SCALE HYDRAULIC MODELING FACILITY

difference. This avoids confusion by allowing both the brine experiments and actual fire tests to be described with the same language. Thus, as the plume rises (in the inverted coordinate system), it entrains ambient fluid and the density difference is reduced. When the plume fluid fills up the ceiling region to the depth of the door soffit, ceiling layer fluid begins to flow out under the door soffit and into the adjoining room. In order to model a very large adjoining room, fresh water was continually brought in through two diffusers (perforated PVC pipe mounted in two boxes, as shown in Figure (5.1)), at a rate of approximately 2.4 liters/sec. In order to insure uniform flow we found it necessary to insert a 20 cm thick polyurethane sponge with 4 pores/cm between the inlet boxes and the main partition. A portion of this fresh water entered the fire room through the door or window opening in the main portion to form a door jet as shown in Figure (5.2), most of which was subsequently entrained by the plume. Siphons and pumps mounted under the inlet boxes and sponge removed the salt water/fresh water mixture from the adjoining room. In addition, the water level in the tank was maintained at a constant level by a sharp lipped skimmer placed near the sponge.

The salt water mixture was mixed and stored in a large (500 gallon) holding tank. From there it was pumped to a constant head tank located approximately 2 meters above the main tank. The brine flowed from the constant head tank through calibrated flow meters to the inlet assembly. Initially this consisted of a 2" PVC pipe packed with straws to act as flow straighteners. This produced a 4.8 cm diameter round source. Later tests were also done with a 1" pipe, and with a variable geometry inlet designed and built by Mr. Ernst Tangren. Tests with non-axisymmetric sources were also conducted but will not be described here. [See

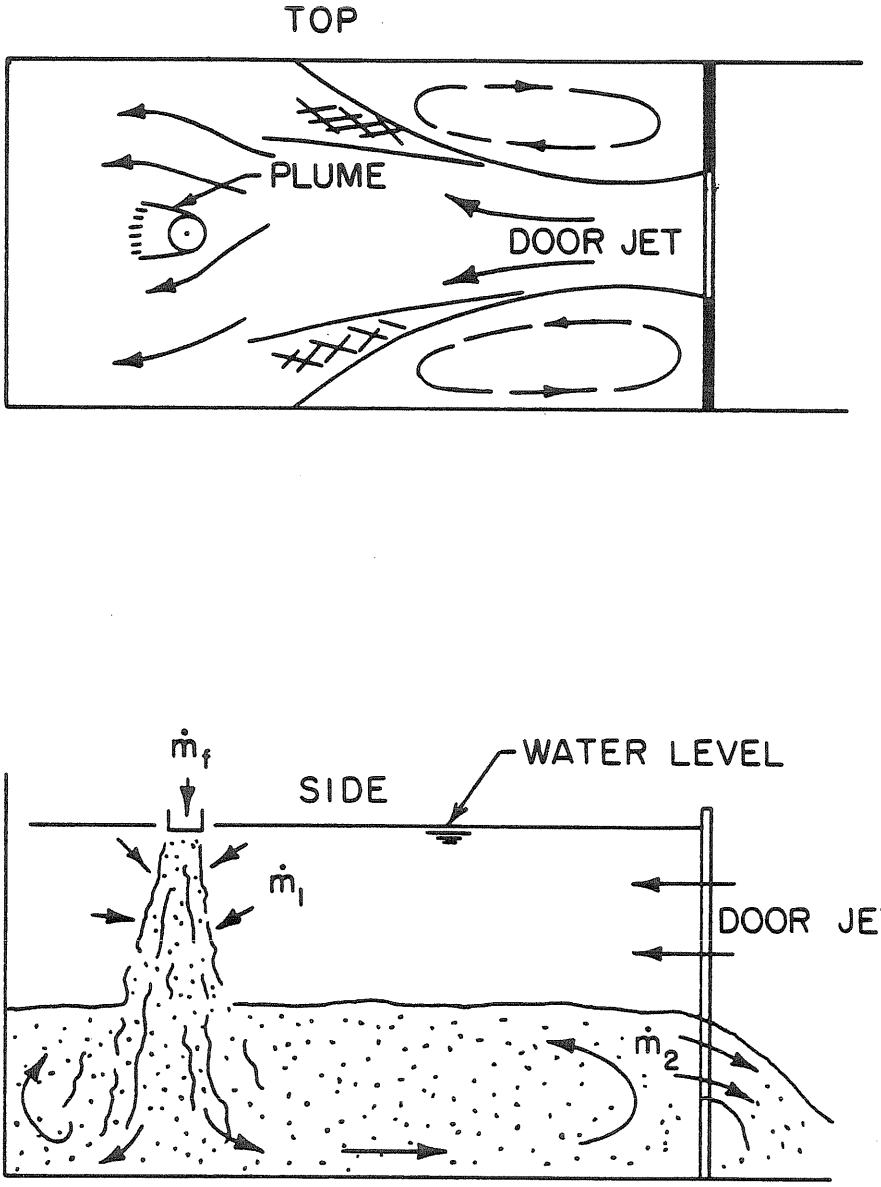

FIGURE 5.2 FLOW FIELD IN OPEN ROOM

Tangren, Sargent, Zukoski (1978).] The inlet assembly could be positioned at any desired location in the fire room. For most of the large room tests (130 x 115 cm floor plan), it was located in the center of the room, while for many of the scale model fire room (100x50 cm floor plan) cases, it was positioned on the longitudinal axis of the room, 3/4 of the way back from the door, in order to accurately model the 1/2 scale fire test room. The flow rate at which the brine was delivered to the inlet assembly was varied between 31 and 245 [cm^3/s]. These flow rates produced plumes which had dimensionless source strength with $Q^*_{z_c}$ values between 2.41×10^{-6} and 1.32×10^{-5} for the standard brine solution, which had a specific gravity of 1.05.

The data gathered from these experiments included flow visualization sketches and photographs, and salinity measurements as a function of height (z).

Flow visualization was accomplished by adding blue dye to brine holding tank. This produced a plume and ceiling layer which were darker then the ambient fluid. In addition, dye injection and $KMnO_4$ crystals were used to study the flow patterns in the ceiling layer and along the ceiling respectively.

The salinity measurements were accomplished by using a conductivity probe as part of a AC driven bridge circuit. The conductivity probe consisted of two short (1.5 mm) platinum wires, supported in an epoxy matrix such that their spacing was approximately 1 mm. The wires and epoxy bead were encased in a stainless steel tube, approximately 2 mm in diameter. For the majority of the tests, the tube was L-shaped, with the horizontal arm, containing the exposed probe, extending approximately 8 cm from the vertical member, the impedance between the two exposed wires

was a function of the salinity of the fluid in which they were immersed, and was measured with a Sanborn 150 Series carrier amplifier and demodulator, with the probe mounted in one leg of a precision resistor full bridge circuit. Before each experiment, the conductivity probe was cleaned and recoated with an oxide of platinum. Calibration was done by measuring the response of the system to a set of solutions of known salt concentration. Reference resistors could be used in place of the probe to recalibrate the system, which tended to drift as a function of time. The tank temperature was measured with an iron constantan thermocouple. The density was then computed from tabular listings of density as a function of salinity and temperature given by Owen (1965). The actual computations and plotting were done by a computer program written in FORTRAN IV and run on a IBM 370/158.

All of the data measured by this author at the lower three brine flow rates were recorded after waiting at least 22 minutes from the start of each experiment, and after waiting at least 10 minutes with the maximum brine flow rate. This delay insured that steady state conditions had been reached. For example with the lowest flow rate and the largest tank, the minimum delay time of 25 minutes was equivalent to 3.0 residence times (t_{res}). Thus the fluid in the upper layer had been effectively replenished 3 times by new fluid from the plume before density measurements were conducted. For the smaller tank and the same flow rate, this delay was equivalent to 8.9 residence times. The minimum delay time of 2.6 residence times occurred at the largest brine flow rate. However, transient response data measured near the ceiling at the two highest brine flow rates indicated that the density difference of the fluid in this region rises to within a few percent of its steady state values in 1.1-1.3

residence times, and thus after only 2.6 residence times the fluid will have attained its steady state density.

5.3 1/2 Scale Fire Test Room

While the 1/4 scale hydraulic modeling facility was ideal for investigating natural convection flows in the absence of heat transfer, the 1/2 scale fire test room was specifically designed to measure heat transfer effects, in addition to effects of geometric scale and greater heat input. The initial buoyancy of the gas could be made quite large because of the high temperatures produced by the combustion of natural gas and air. Consequently, the dimensionless heat input parameter Q^* was 2 to 3 orders of magnitude larger than in the 1/4 scale brine flow simulations. The typical range of the parameter based on the room height ($Q^*_{z_c}$) was $2\text{-}8\text{x}10^{-3}$.

The 1/2 scale fire test facility, sketched in Figure (5.3), consisted of a rectangular room with a natural gas burner mounted in the floor. The room itself was 1.2 m wide, 1.2 m high and 2.4 m long. In the center of the north end wall there was a single doorway 99 cm high, 45.7 cm wide, and 7.6 cm thick. As in the brine experiments, we blocked the lower portion of the doorway to create different window geometries: one with a sill at 27.9 cm, and a smaller one with a sill at 54.6 cm. In order to simulate a room that was part of a larger building the outer face of the north wall was 2.4 m wide, extending 61 cm beyond the sides of the test room, and ran from the floor all the way to the overhead exhaust hood. Similarly, a large ground plane 2.4 m wide extended 1/2 m in front of the room and was mounted flush with the floor of the room in order to prevent separation of the stream of cold air as it flowed into the room. Heated air and combustion products flowing out of the room under the door

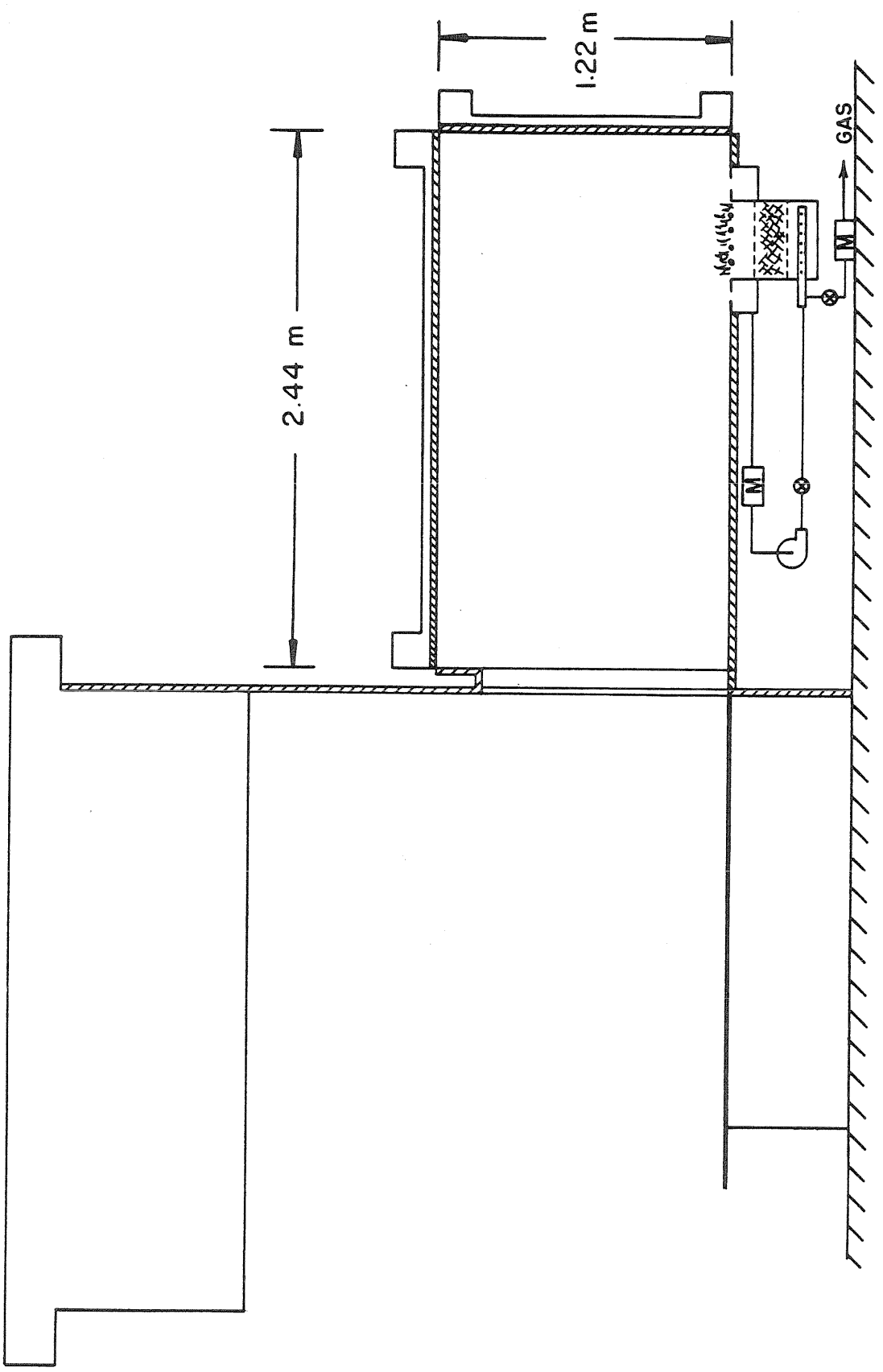

FIGURE 5.3 1/2 SCALE FIRE TEST FACILITY

or window soffit were collected by a large exhaust hood located overhead and discharged outdoors.

The fire room itself was constructed of 1.3 cm thick slabs of asbestos fiber board. This material, Johns-Manville Marinite 65-A, had a density of 1.04×10^3 kg/m^3, a low thermal conductivity of 0.245 W/m-K, and a specific heat of 1.05 kJ/kg-K. Note that in these tests the surface temperatures were nearly always well below 100°C. Therefore we believe that the small moisture content (5%) of the material did not change significantly during these experiments and that the thermal properties remained invariant.

The thermal diffusivity of this material was 2.24×10^{-7} m^2/s, based on the thermal properties quoted above. If one defines a characteristic time for wall heating t_{wall} as the wall thickness squared divided by the thermal diffusivity, its value for this Marinite wall will be 720 seconds. Thus t_{wall} is 39 times as large as the average value of the characteristic transient time scales for the gas t_{res} listed in Table (5.6). We therefore expect, and have observed, that the gas temperature approaches steady state values within a few minutes of ignition, while the solid surfaces require the better part of an hour to reach the same state.

The Marinite sheets were mounted on a 5 cm wide angle iron frame, and all joints were caulked with Dow Corning #732 High Temperature Sealant to prevent air leaks to or from the test room.

To generate a large, easily measurable temperature difference across the walls, and to keep the apparatus from becoming dangerously hot, the ceiling and sidewalls were convectively cooled with air from the laboratory which was blown through a 6.4 mm air space between the outer surface of the Marinite panel and the outer sheet metal cooling jacket.

In an actual room-fire, air must diffuse into the flame zone to supply the fire with oxygen. As a result, such diffusion flames are fuel rich and often extend considerable heights above the fuel source. Depending on the fuel, they may produce considerable soot through incomplete combustion, and may lose a sizable fraction of the initial heat release through radiation. In order to avoid these complications, clean burning natural gas was mixed with air to form an approximately stochiometric mixture which burned with small ($\sim$ 4 cm) blue flames. Zukoski, Kubota, and Veldman (1975) found that thermal radiation was negligible for similar, but smaller, premixed propane and air fires. In order to correctly model the diffusion of air into the flame zone, air from within the room itself was sucked through an annular slot in the floor into a plenum chamber surrounding the burner. The air was withdrawn from this chamber, metered by a standard orifice flow meter, and pumped back into the burner. Natural gas was metered through a Merriam Laminar Flow meter and mixed with the air supply. This mixture then passed through a bed of glass beads in the floor of the burner, and burned above a helical, watercooled flame holder mounted at floor-level. Three burner diameters were used: 7.6, 10.2, and 15.2 cm, resulting in heat releases of 3.6, 7.2, and 14.9 kw, respectively. For these cases, the dimensionless heat input parameter $Q^*_{z_c}$ was $2\text{x}10^{-3}$, $4\text{x}10^{-3}$, and $8\text{x}10^{-3}$, respectively.

Data from the 1/2 scale experiments consisted of inner and outer surface temperatures, gas temperatures, and CO_2 concentrations. The surface temperatures were obtained from 96 sets of 0.13 mm diameter iron constantan thermocouples mounted flush with the inner and outer surfaces of the ceiling and side walls. An additional ten thermocouples were later added to measure the inner surface temperature of the floor. These inner

thermocouples were put in place by cutting a shallow slit approximately 3 cm long in the Marinite panel, and drilling small holes at either end. The thermocouple lines were then pressed into the slit with the junction positioned in the center of this slit and the leads were brought out through the holes. This ensured that the thermocouple leads were parallel to the surface on either side of the bead so as to minimize conduction losses in the leads.

Wall maps showing the inner and outer surface temperatures of the thermocouple locations for a typical experiment (number 15) which involved a 14.9 kW fire and the standard doorway are reproduced in Figures (5.4) - (5.8). In these figures, the thermocouple locations are indicated by the small crosses. The two integers to the left of each cross are indices identifying the inner and outer thermocouples. The three decimal numbers to the right are the inner and outer surface temperatures, and the temperature difference across the surface, respectively.

The data displayed in these figures were taken 3.6 hours after the start of experiment 15 and represent the steady state temperature response of the ceiling, walls, and floor. We will refer to this same set of data in Chapter VII, when we examine the general results deduced from the gas temperature and composition data, and also in Chapter IX, when we will use it to estimate the radiant, conductive, and convective heat transfer rates for experiment 15.

The gas temperatures within the room were measured by six hooded, aspirated iron constantan thermocouples mounted on the horizontal arm of a traversing mechanism. The thermocouples themselves were 0.1 mm in diameter and were centrally located in shielding tubes 3.2 mm in diameter and through which gas was continually aspirated. Smoke flow visualization

TEMPERATURE DISTRIBUTION
CEILING
EXP. 15 SEG. 22 CYCLE 1
DATE 219 1978 19:53:38

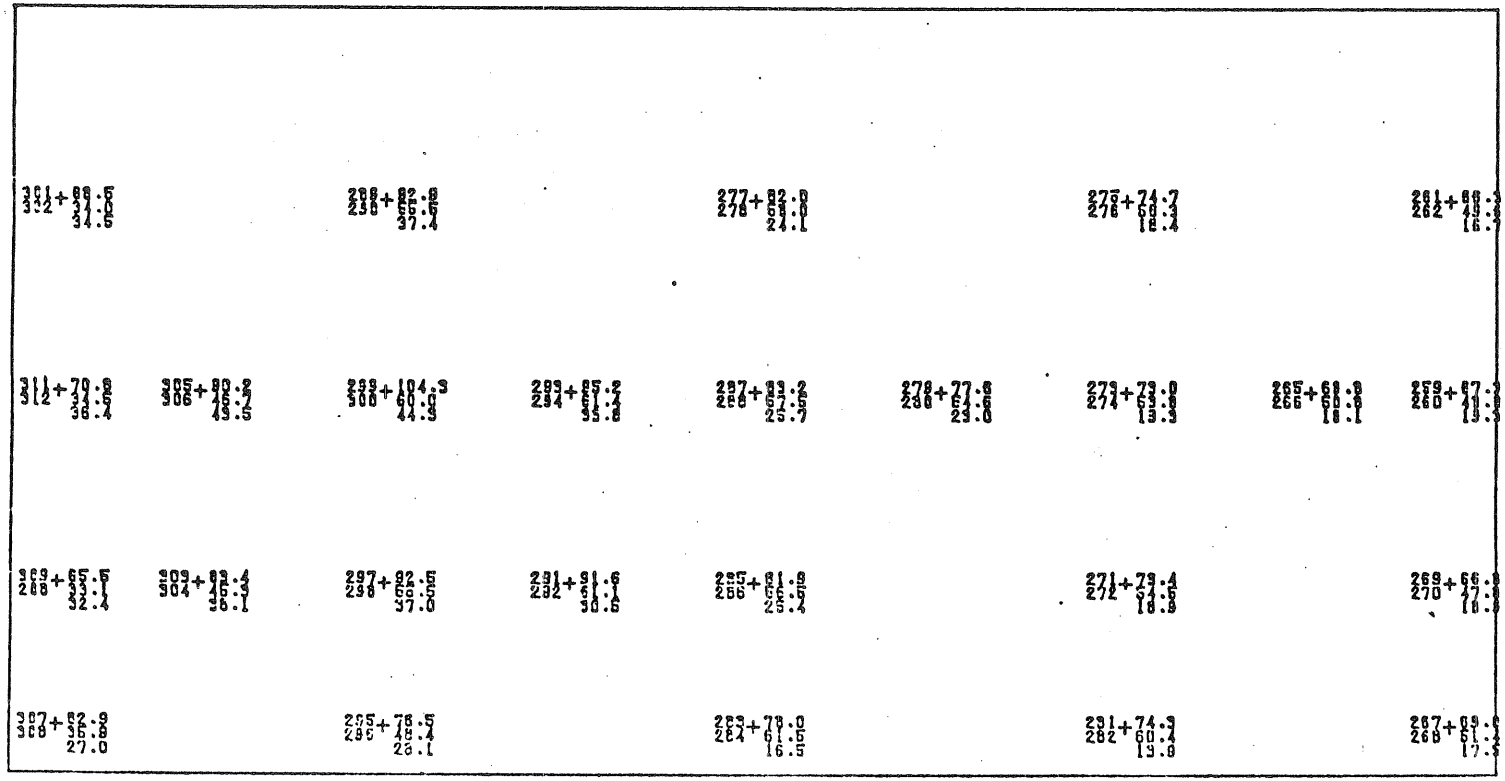

Figure (5.4) Steady State Surface Temperatures on the Ceiling (Exp. 15).

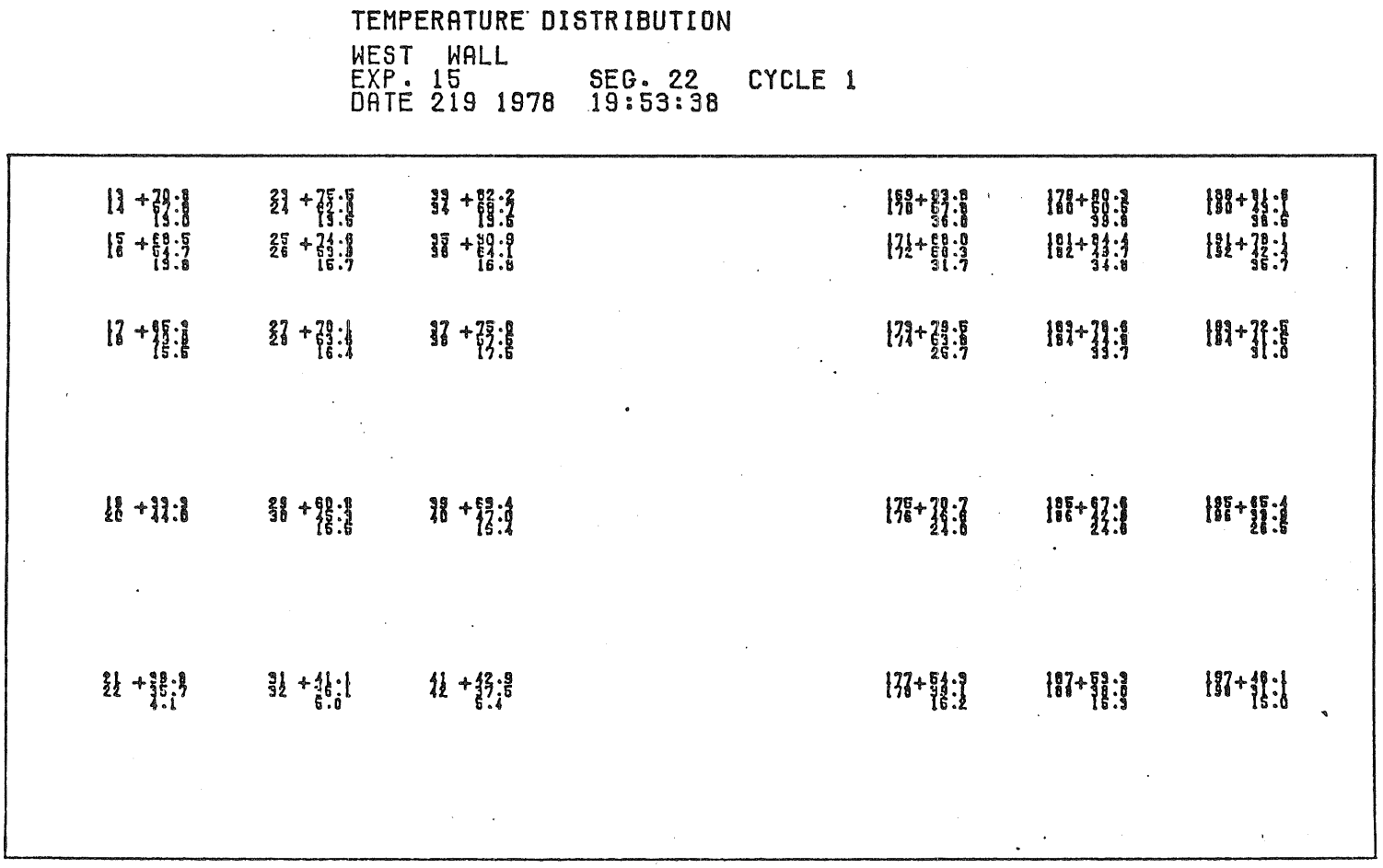

Figure (5.5) Steady State Surface Temperatures on the West Side Wall (Exp. 15).

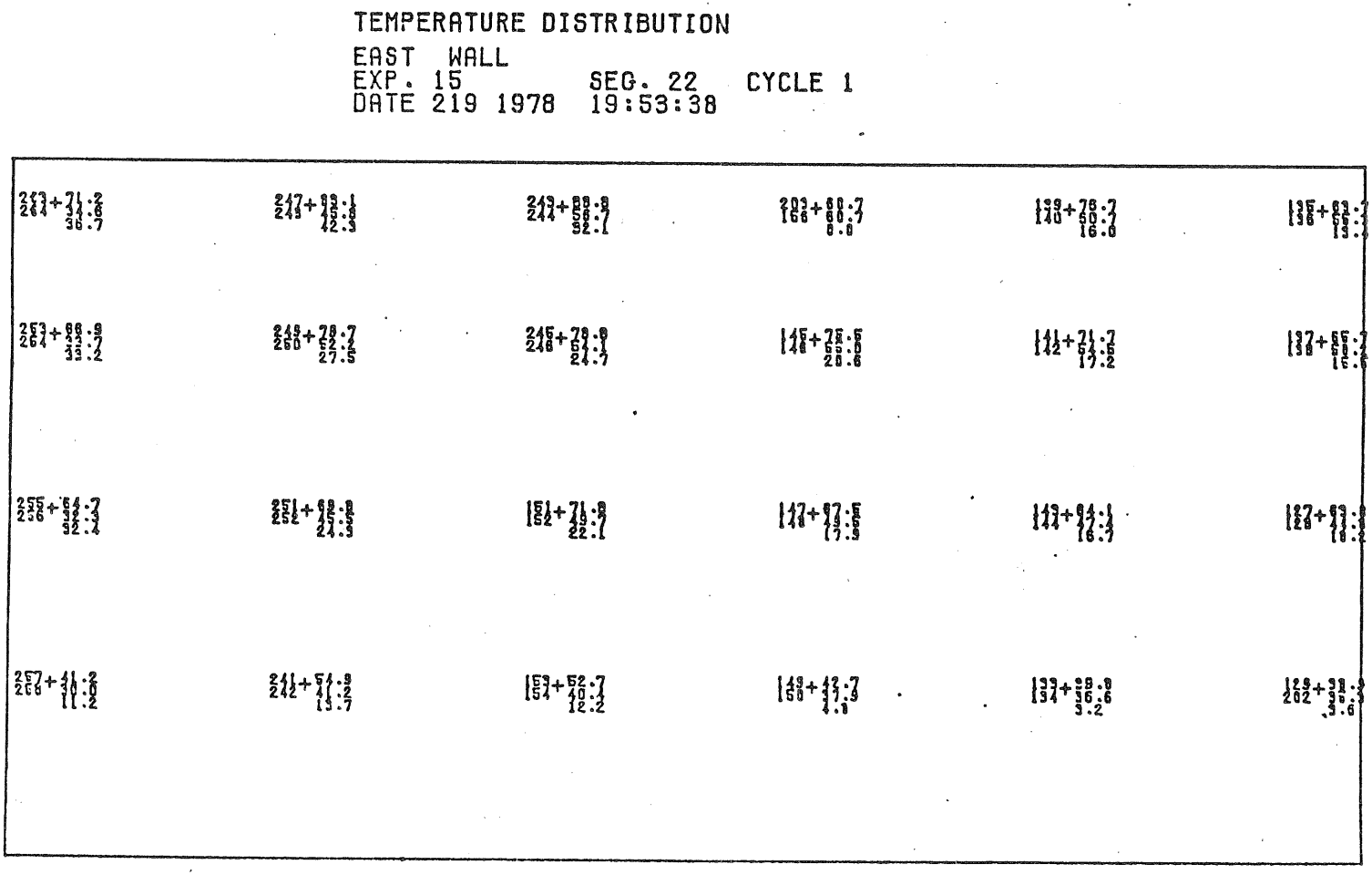

Figure (5.6) Steady State Surface Temperatures on the East Side Wall (Exp. 15).

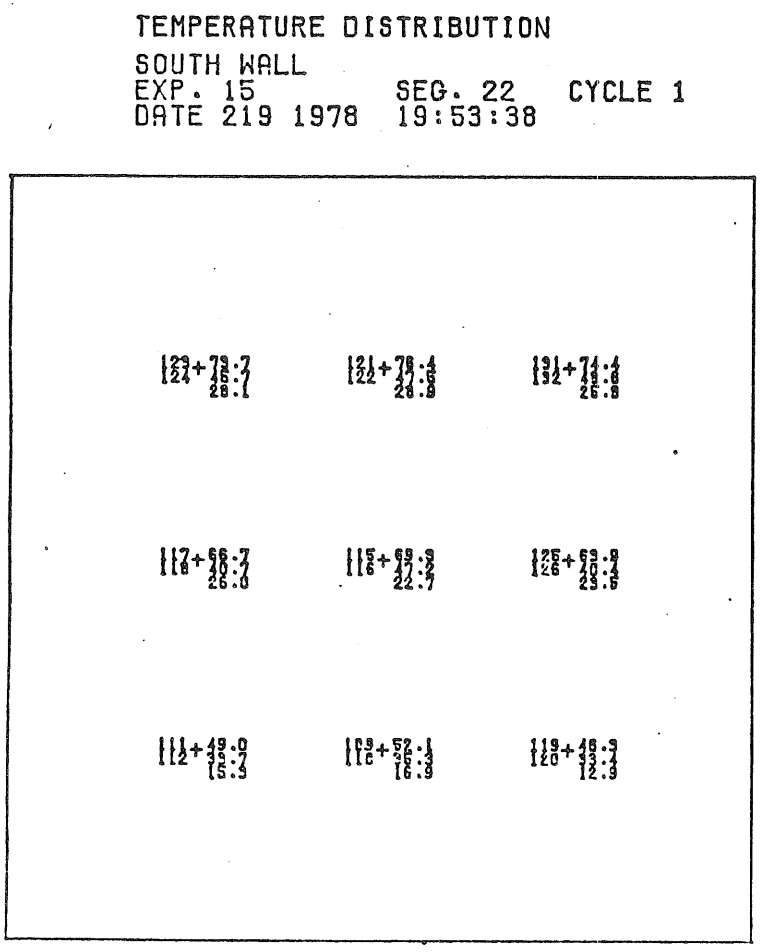

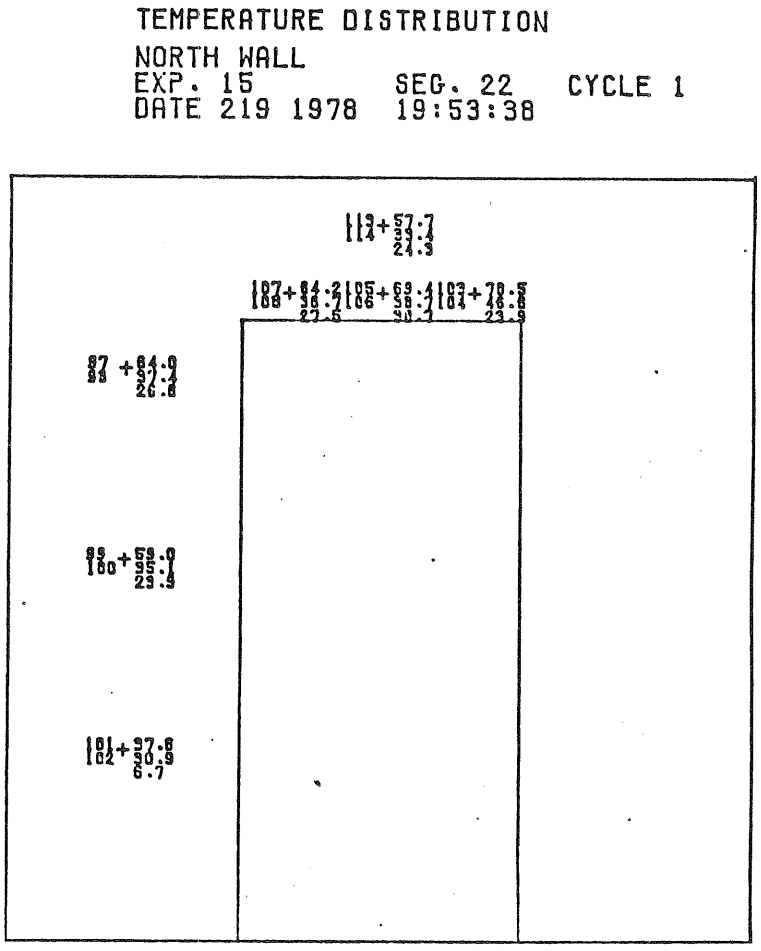

Figure (5.7) Steady State Surface Temperatures on the North and South End Walls (Exp. 15).

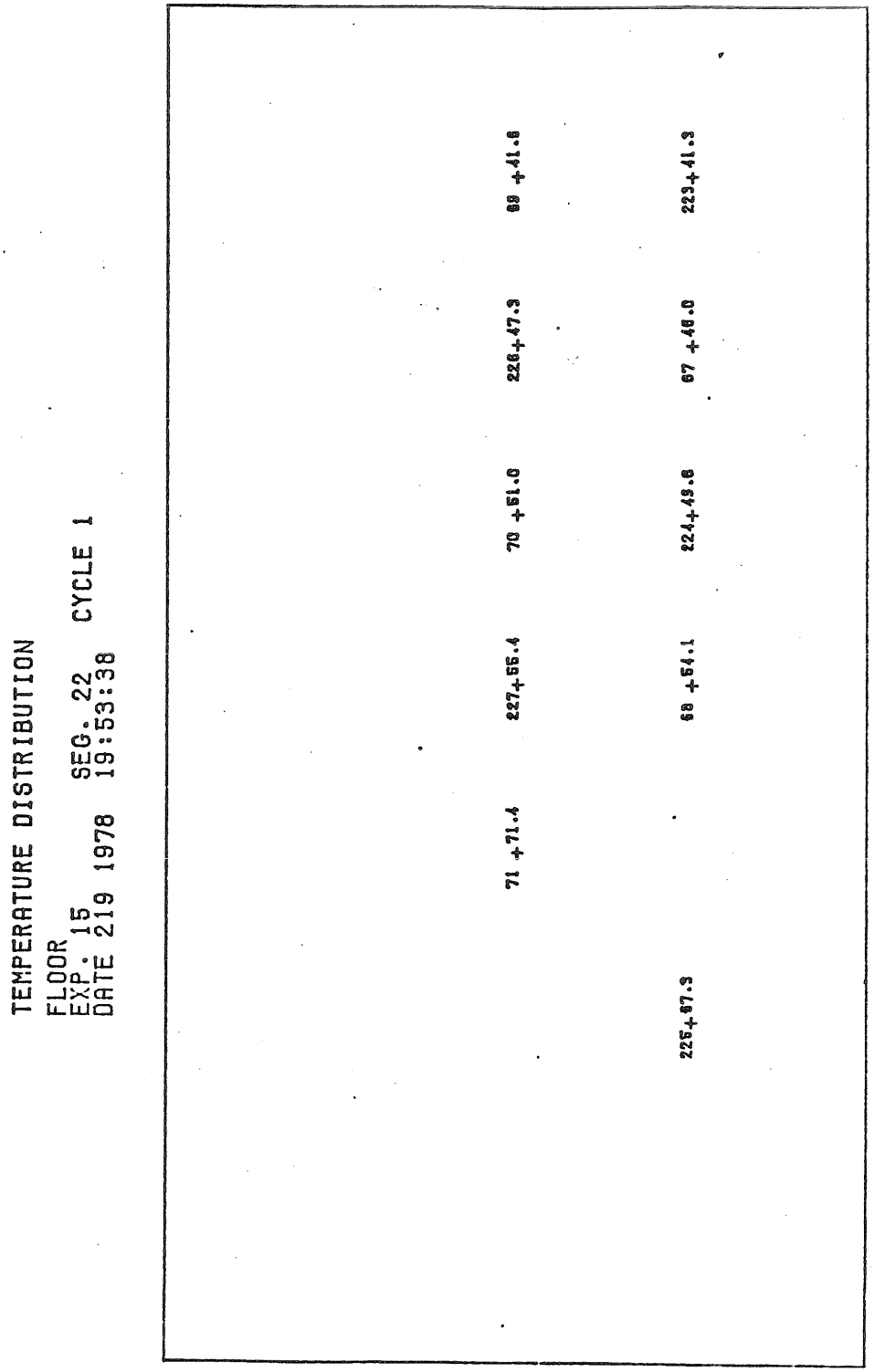

Figure (5.8) Steady State Surface Temperatures on the Floor (Exp. 15).

studies showed that the aspiration only affected the gas in the immediate neighborhood of the mouth of the tube (i.e. - within ∿3 cm). These aspirated probes, which also served to supply gas for the CO_2 measurements, were spaced on average of 14.6 cm apart, starting at a distance of 43.2 cm from the vertical axis of the traversing mechanism. This axis was in turn located 2.5 cm from the west wall in the mid-plane of the room.

The traversing mechanism could be rotated to sweep across the entire room at any given height, as shown in Figure (5.9). The temperatures in this figure were plotted such that the lower left hand edge of the first digit corresponds to the thermocouple location. In addition the traversing mechanism could be raised or lowered to slice through most of the vertical height of the room. Figure (5.10) shows the results of such a vertical traverse. It may be noted that probe 6, which exhibits different behavior from the others, is only 3.0 cm from the east wall in this traverse. This behavior will be further explored in Chapter VII.

The temperature of the gas flowing through the doorway was measured by a series of 13, 0.13 mm diameter thermocouples stretched across the door. The individual thermocouple wires were attached to a wooden frame such that the actual junctions were vertically aligned in the middle of the frame. This assembly could then be horizontally traversed across the doorway to measure gas temperature profiles at various lateral positions. The vertical spacing of the thermocouples was non-uniform, because we were particularly interested in the temperature of the hot gas leaving the room. Results from a typical experiment are shown in Figure (5.11), in which we have displayed data from the upper 12 thermocouples.

The number of thermocouples used in this apparatus made it impractical to monitor each individual thermocouple. Consequently, the 230 sets of

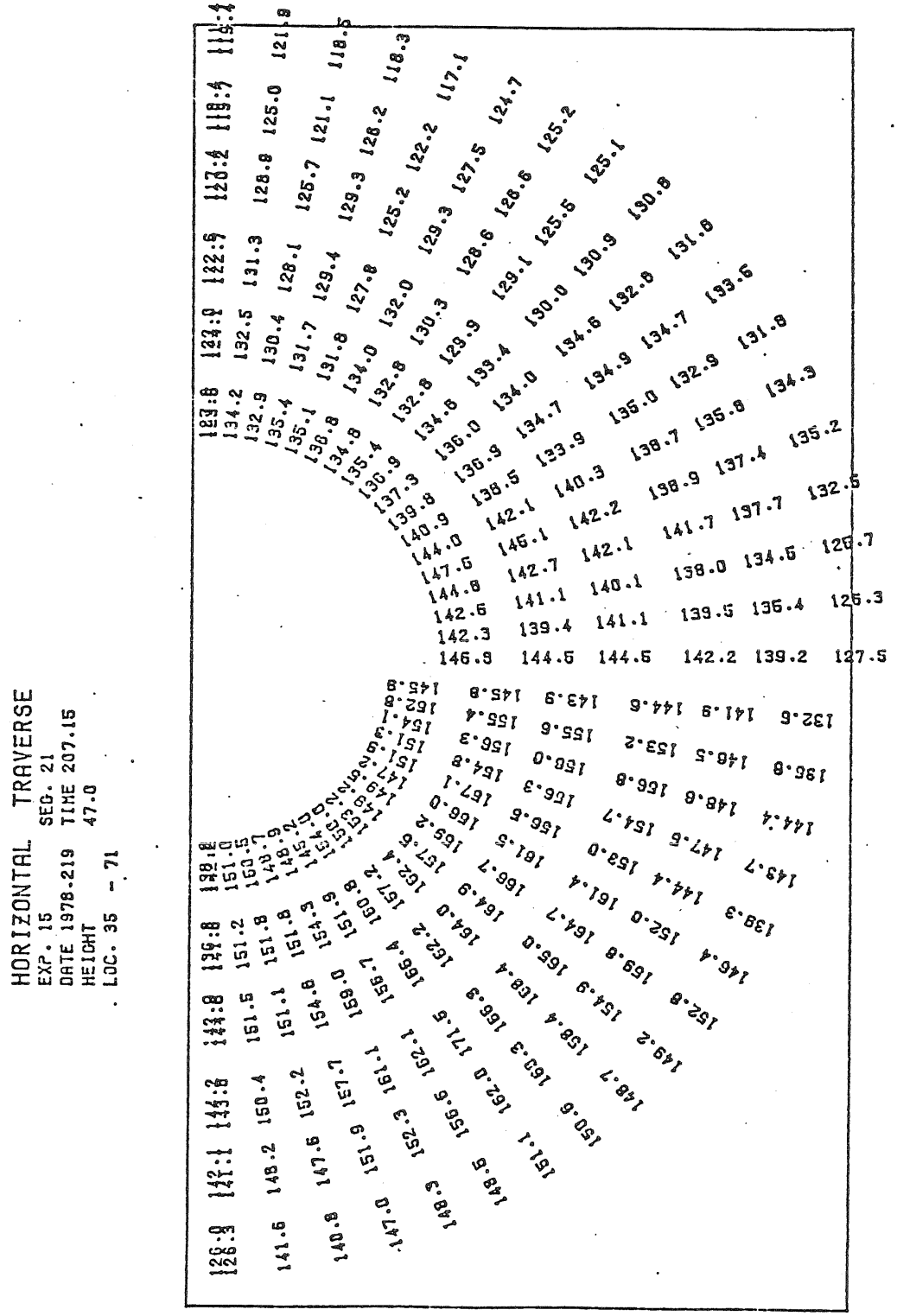

Figure (5.9) Steady State Gas Temperatures Across a Horizontal Plane 2.5 cm Below the Ceiling (Exp. 15).

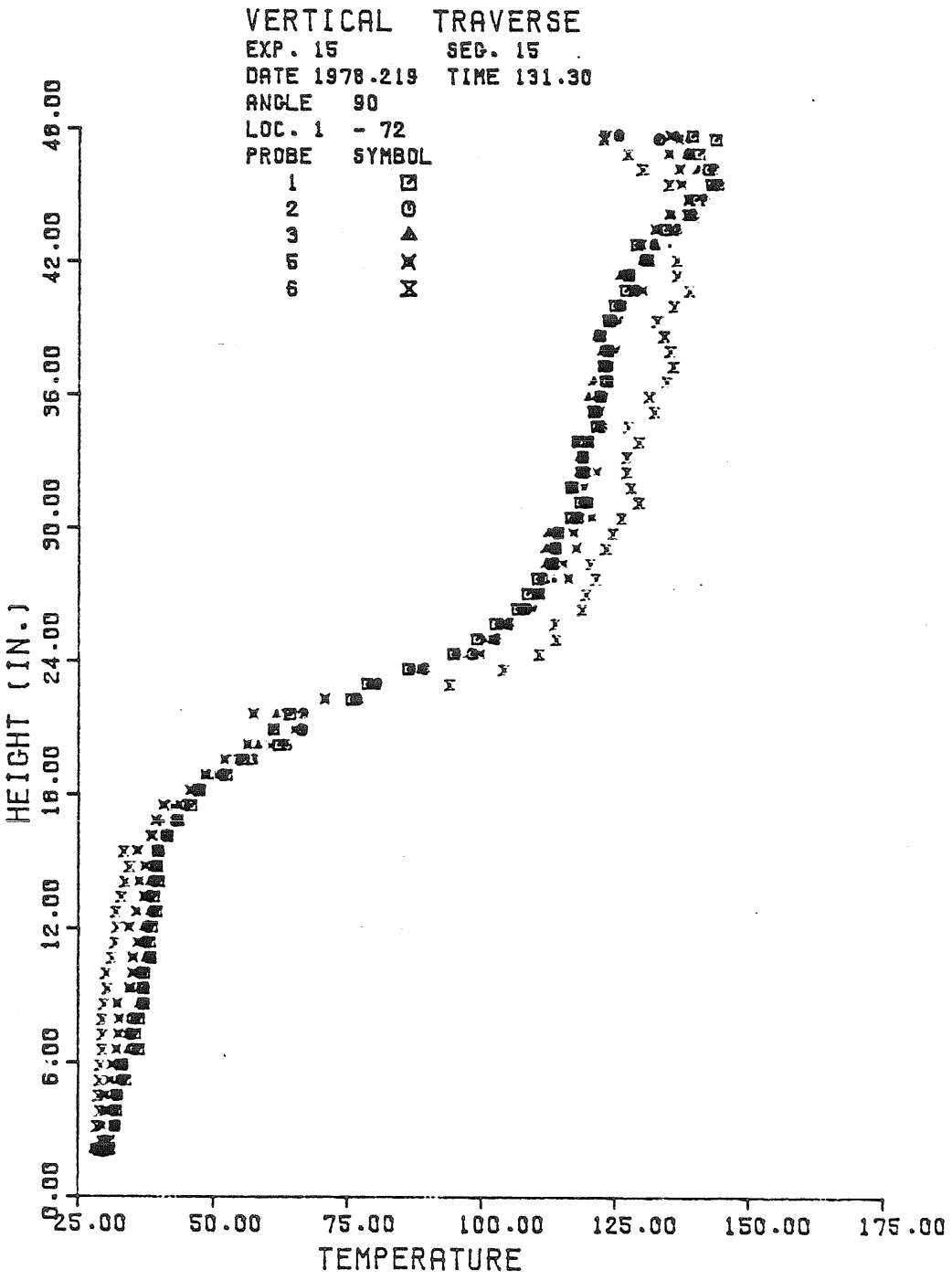

Figure (5.10) Gas Temperatures on a Vertical Plane Through the Middle of the Room (Exp. 15).

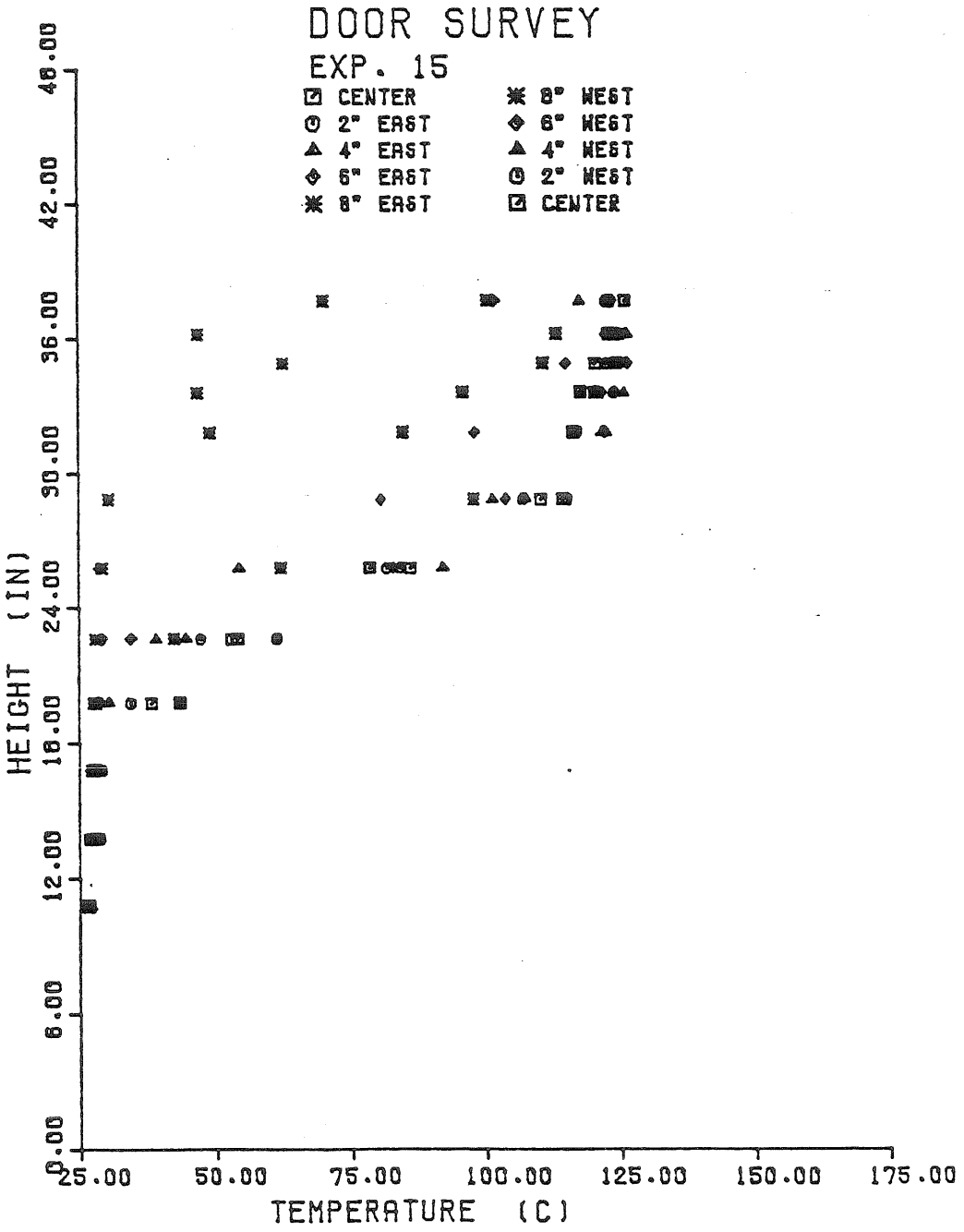

Figure (5.11) Gas Temperatures Measured Across the Outer Edge of the Doorway (Exp. 15).

leads from the hot junctions were distributed among 6 rotary, gold plated thermocouple stepping switches. Each switch, which was driven by a solenoid, could accommodate up to 52 sets of parallel connections. Since there were extra connections on the switch, some key hot junctions were connected twice. The output of switch, as shown schematically in Figure (5.12), was connected to a cold junction immersed in an ice bath. The resulting voltage generated by this circuit was amplified by a Burr-Brown 3660K low drift instrumentation amplifier with a selectable gain setting of either 500 or 1000. The output voltage was then passed to a low-pass active filter with a cutoff set at 30 Hz, to eliminate 60 Hz line noise. The filtered output signal was recorded, either manually or by a mini-computer data acquisition system, and subsequently used to find the temperature of the hot junction.

The concentration of carbon dioxide and oxygen in the gas from one of the six aspirated probes was determined with the aid of a Beckman 864 Infrared Analyzer and a Beckman 741 Oxygen Detector. The gas from the selected probe was first passed through a cold trap to remove water vapor and then warmed to room temperature before entering the detector cells. After leaving the detectors, it passed through a needle valve, used to maintain constant pressure in the cells, and was exhausted by a vacuum pump. Preliminary experiments showed that the oxygen concentration remained nearly constant, indicating that the in flow of air through the door, $\dot{m}_o$, was more than adequate to supply the oxygen consumption of the fire. The large volume of air entrained into the plume then quickly reduced the oxygen deficit produced by combustion. Consequently, the oxygen concentration was not measured in the later experiments. Figure (5.13) shows the CO_2 concentration as a function of height for a typical experiment.

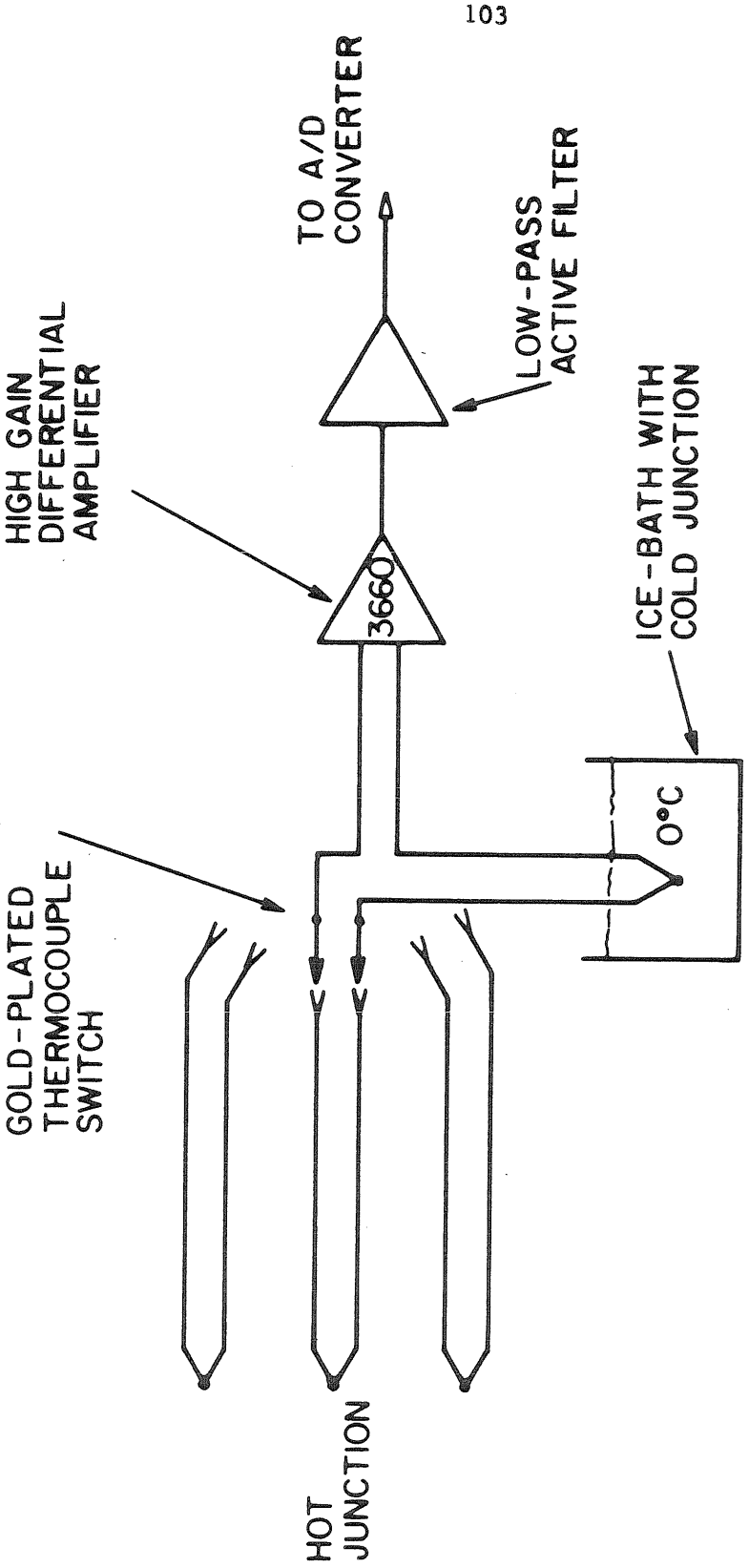

Figure (5.12) Schematic Diagram of Temperature Measurement Circuit.

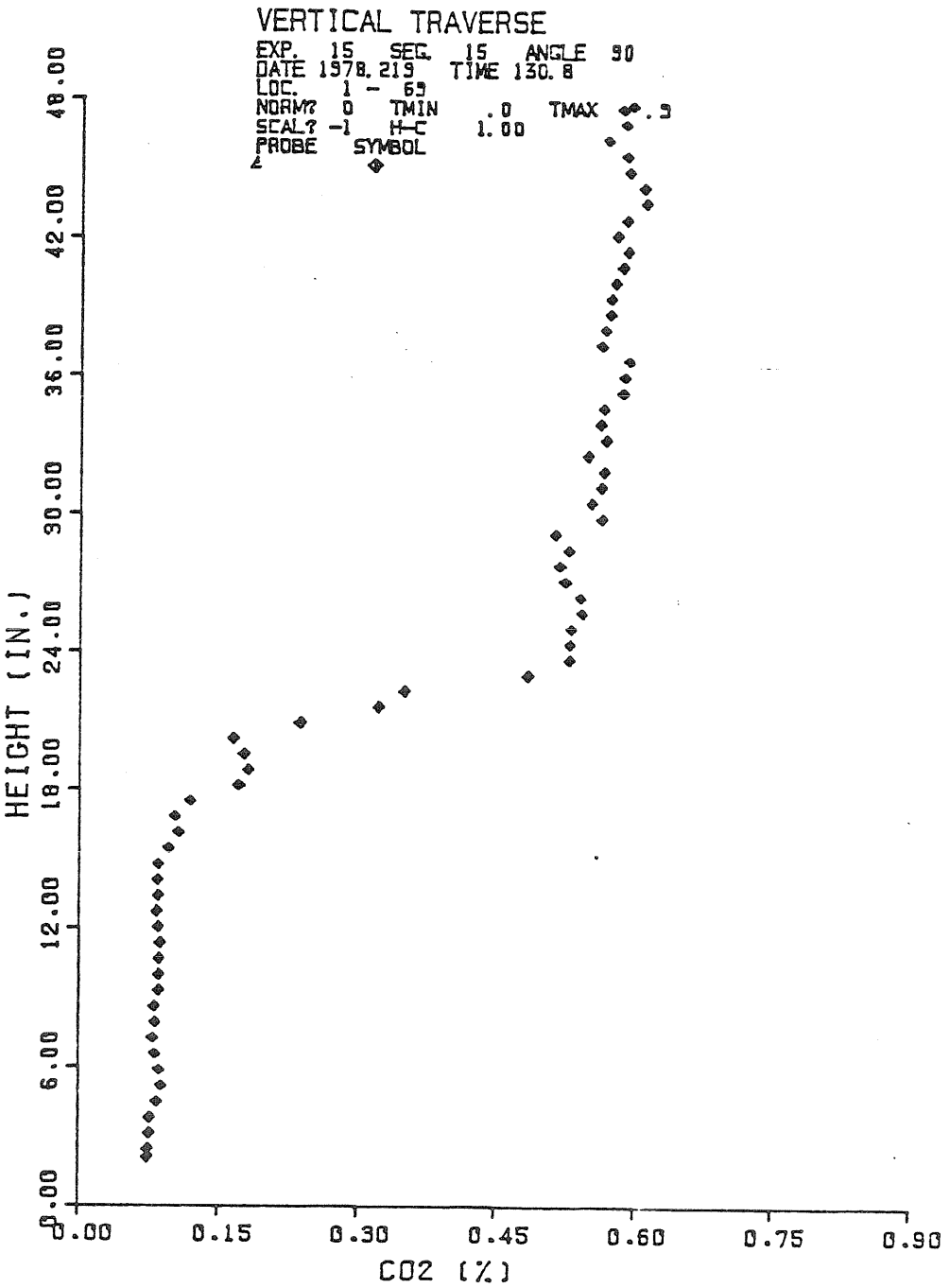

Figure (5.13) CO_2 Concentration Profile in the Middle of the Room (Exp. 15).

The 1/2 scale fire room experiments were made up of three main phases. First the fire was ignited. Then, for approximately 30 minutes, the transient temperature history of the walls and gas was recorded. During this time, every thermocouple's voltage was measured 2 to 4 times a minute. It was observed that the gas temperatures reached an approximate steady state much faster than did the walls. Consequently, after the initial transient period, detailed surveys of the gas composition and temperature were conducted across horizontal and vertical planes within the room. Periodically during this time wall temperatures were also monitored. Finally, after several hours, steady state wall temperature measurements were made.

In the course of these 1/2 scale experiments, three experimental parameters were varied. First, the fire strength ranged from 3.7 to 14.9 kw. Second, the door geometry was changed by inserting plywood blocks to form a large and a medium window. Finally the location of the fire was moved from the longitudinal axis of the room 3/4 of the way back from the door, to the extreme southwest corner. The effects of these variations will be discussed in Chapters VII and IX.

Owing to the large volume of data produced by this apparatus, most of the data acquisition was performed by a Hewlett-Packard HP-2100 mini-computer system. Sixteen channels of analog signals were sent to a Preston model GMAD-1 analog-to-digital (A/D) converter which digitized each channel sequentially. These data were then stored on disk or tape for later processing. The central elements in this data acquisition scheme were the six channels of amplified, filtered thermocouple voltage signals. These could be acquired in two modes, depending on whether the signal represented a gas temperature or a surface temperature.

Signals representing gas temperatures, as measured by the six aspirated probes, or six of the 13 door thermocouple wires, fluctuated significantly, with periods of up to several seconds, due to the turbulence and possible presence of internal waves in the gas. Consequently, to measure these signals, the stepping switches were manually positioned to the six locations desired, and the computer instructed the A/D converter to take samples every τ seconds for t seconds. An average and standard deviation was then computed for each channel. In general we set τ = 0,05 seconds and t = 10 seconds. Thus there were 200 data points used in the computation of the mean and standard deviation of each signal.

On the other hand, the signals from wall thermocouples hardly fluctuated at all, thanks to the relatively high thermal inertia of the wall. This was quite fortunate because in order to estimate the state of the walls at some given time, it was desirable to measure all 192 surface temperatures in as short a time as possible. To do this, an electronic logic circuit was constructed which could be programmed to advance the stepping switch, and which synchronized the A/D converter with the switch. Counters were set in this circuit which determined how many complete revolutions of the switch were to be executed, the total time of each cycle, and the time between each step of the stepping switch. Typical values for the initial 25 minute transient phase of the experiment were: 99 cycles total, 15 seconds per cycle, and 200 ms per step. When acquiring data in this mode, the sequence of events was as follows. The circuit would first cause the stepping switch solenoid to advance the switches one position. Then after an experimentally determined settling time of 45 ms, during which the switch transients were allowed to decay, the circuit allowed the A/D converter to sample all the channels sequentially 10 times,

at a rate of 20 kHz per sample. An average for each channel was then computed and stored on the disk. The stepping switches were actually mounted in pairs, and each of these pairs had a position voltage reference switch whose output specified the switch position. During the "pause" section of each cycle (typically 4.6 seconds), the computer was programmed to convert the temperature signal voltages to temperatures [^{o}C] based on least square fit polynomial calibration curves for each amplifier and for the N.B.S. standard thermocouple tables. The data were then sorted and stored by thermocouple, based on the measured position voltage. Finally this information was then written on magnetic tape for further processing.

In addition to the temperature and stepping switch position signals, the computer also aquired, digitized, and recorded signals representing several other variables of interest. The Beckman 864 Infrared Analyzer and the Datametrics Type 1014A Barocel Electronic Manometer produced outputs proportional to the CO_2 concentration and the selected gas pressure, respectively. This information, along with the Scanivalue pressure switch position voltage signal, was all passed to the A/D converter, as were signals indicating the height and angular orientation of the traversing probe.

Given the convolutions of this data acquisition scheme one may wonder how accurately we can measure the temperatures of the gas and the surfaces. We can partially answer this question by examining data taken during the first few seconds of an experiment when the gas temperatures at the door and the outer surface temperatures should be uniform and equal to ambient values measured in the laboratory. For example, the standard deviation of the door temperature data measured by the 13 door thermocouples was between 0.3 and 0.4^{o}C during the early phases of

experiments 15 and 16, before the thermocouples were positioned in front of the door. Furthermore, the data correlated better with time than with the individual thermocouples. This indicates that some part of this 0.3-0.4^{o}C deviation is caused by motion of the air in the laboratory, probably drafts induced by the air conditioning system. Similarly, the overall average of the standard deviations of the temperatures on the outer side of the ceiling or walls in the early phases of these experiments were 0.10 and 0.12^{o}C, respectively. This value seems to be a reasonable estimate for the precision of our temperature data. Note that this uncertainty is small (0.4%) compared to the average temperature difference across the ceiling of 26.9^{o}C. Furthermore, the average temperature difference between the hot gas and the ceiling is even bigger (61.4^{o}C), so that the determination of the temperatures is not a major source of error.

In using these temperature data to estimate the heat transfer processes, we introduce several potentially more substantial sources of error which are difficult to estimate. First, we need to infer mean gas temperatures at the thermocouple locations, which form a rectangular grid, from temperature data measured along arcs of a circle. This was done manually and probably has an uncertainty proportional to the standard deviations of the gas temperatures near the ceiling which were approximately 5^{o}C in the turbulent ceiling jet. Second, large fluctuations in the gas temperature produce smaller temperature fluctuations at the inner surfaces of the ceiling and walls, as shown in Figure (7.1). The data from experiment 15 which are shown in this figure were measured at the stagnation point, where these fluctuations will be the largest.

Elsewhere on the ceiling and upper walls the turbulent fluctuations will be much smaller and so too will be the surface temperature fluctuations. However, because we do not average the ceiling temperatures over several minutes we ignore these fluctuations. Judging by the data in Figure (7.1), this could add at worst an additional 2.6°C to the uncertainty in determining the ceiling temperature. Finally, as described in Chapter IX, there are a number of simplifying assumptions inherent in our radiant heat transfer computation which increase the uncertainty of the heat transfer calculations. Thus while we can not compute the overall uncertainty in the heat transfer calculations, it is our opinion that it is probably of the order of 10% for most of the results, but it may be larger in a few locations which are most sensitive to the effects described above, such as the stagnation region on the ceiling.

5.4 Scaling Concepts in Fire Modeling

Given the two rather different physical situations involved in our experimental studies of room fires, and the fact that real building fires may have scales more than an order of magnitude greater than those obtainable in our 1/2 scale facility, we should examine how the pertinent dimensionless parameters of the flow may be expected to change with the scale of the system.

First, it seems reasonable to assume that buoyancy will play a predominant role in the early stages of localized fires. This can be conveniently measured by the kinematic buoyancy flux $F[L^4/T^3]$:

$$F = \frac{g Q_F}{\rho_o c_p T_o} \tag{5.1}$$

Assuming the other two physical quantities of importance are the acceleration of gravity g, and the room height z_c, dimensional analysis gives

$$Q^*_{z_c} = \frac{F}{g^{3/2} z_c^{5/2}} = \frac{Q_F}{\rho_o c_p T_o \sqrt{g z_c} z_c^2} \qquad (5.2)$$

as the one independent dimensionless parameter. Table (5.1) shows typical source strengths for given combinations of Q^* and z_c. The room heights chosen represent the 1/4 scale brine facility, the 1/2 scale fire test chamber, and a full scale room. For the 1/4 scale facility, the first column gives the volumetric flow rate $\dot{V}_{brine}$[cm^3/s] of the brine. Because the initial brine density difference is so small (5%), the resulting $Q^*_{z_c}$ values are very small, and correspond to very weak fires. Typical brine runs had $Q^*_{z_c}$ values of $1x10^{-5}$ which scale up to 109 watts, or lightbulb size fires. Typical runs in the 1/2 scale fire test room, on the other hand, had $Q^*_{z_c}$ values of $1\text{-}10x10^{-3}$, which represent actual room fires in the 10 to 100 kw range. While these 1/2 scale tests thus form a reasonable lower bound for actual room fires, they also are at the upper limit of the Boussinesq model's range of validity (see Table 2.1).

We expect viscous effects to depend on an appropriate Reynolds number for the flow. A Reynolds number Re_z based on the asymptotic point source plume relations and the room height can be formed using the maximum velocity in a free plume at height z, given by equation (2.59), as the velocity scale:

$$Re_z = \frac{w_m(z)\, z}{\nu_o} = \frac{\{\sqrt{gz}\, C_v\, (Q^*_z)^{1/3}\}\, z}{\nu_o} \qquad (5.3)$$

Table (5.1) Fire Heat Release as a Function of Room Height

1/4 Scale Brine Tests z_c = 0.5 m		1/2 Scale Fires z_c = 1.2 m	Full Scale Fires z_c = 2.5 m	Dimensionless Heat Input
$\dot{V}_{brine}$ [cm^3/s]	Equivalent† Q_F [kW]	Q_F [kW]	Q_F [kW]	$Q^*_{z_c}$
11	0.0002	0.002	0.011	$1x10^{-6}$
111	0.002	0.018	0.109	$1x10^{-5}$
1107	0.020	0.181	1.09	$1x10^{-4}$
11070	0.195	1.81	10.9	$1x10^{-3}$
110700	1.95	18.1	109	$1x10^{-2}$

† based on $\frac{\Delta\rho_{brine}}{\rho_o}$ = 5 %

Table (5.2) lists this Reynolds number for the three height scales of interest, and shows that the 1/4 scale and 1/2 scale facilities have

Table (5.2) Plume Reynolds Number as a Function of Room Height

$Q^*_{z_c}$	z_c = .5 m	z_c = 1.22 m	z_c = 2.5 m
$1x10^{-6}$	$1.0x10^5$	$2.5x10^4$	$7.2x10^4$
$1x10^{-5}$	$2.2x10^5$	$5.3x10^4$	$1.6x10^5$
$1x10^{-4}$	$4.7x10^5$	$1.1x10^5$	$3.3x10^5$
$1x10^{-3}$	$1.0x10^6$	$2.5x10^5$	$7.2x10^5$
$1x10^{-2}$	$2.2x10^6$	$5.3x10^5$	$1.6x10^6$

roughly comparable Reynolds numbers ($\sim 2.4x10^5$). The equivalent full scale flows however have Reynolds numbers 3 to 7 times as great. However, because the 1/4 and 1/2 scale Reynolds numbers are already large, this increase should not be particularly significant.

A Reynolds number for the exit flow Re_2 can also be estimated as,

$$Re_2 = \frac{\bar{v}_2 L_2}{\nu_o} = \left(\frac{\dot{V}_2}{A_2}\right) \frac{\sqrt{A_2}}{\nu_o} = \frac{\dot{V}_2}{\sqrt{A_2}\nu_o} \qquad (5.4)$$

using the bulk exit velocity as the velocity scale and the geometric mean of the exit area as the length scale. Using z_c to make lengths dimensionless, one finds

$$Q_i^* = \frac{Q_{z_c}^*}{(\bar{z}_i)^{5/2}} \tag{5.5}$$

$$\dot{V}_2 = \eta\, C_{mp}\, \sqrt{g}\; z_c^{5/2}\; (Q_{z_c}^*)^{1/3}\; (\bar{z}_i)^{5/3} \tag{5.6}$$

$$Re_2 = \frac{\eta\, C_{mp}\, \sqrt{g}\; z_c^{3/2}\; (Q_{z_c}^*)^{1/3}\; (\bar{z}_i)^{5/3}}{\sqrt{(\bar{H} - \bar{y}_o)\; \bar{S}}} \tag{5.7}$$

Now for geometrically similar rooms, A and B, the ratio of the exit Reynolds numbers $\overline{Re}$ is:

$$\overline{Re} = \frac{Re_{2,\,A}}{Re_{2,\,B}} = \left(\frac{z_{cA}}{z_{cB}}\right)^{1.5} \left(\frac{Q_{z_{c,A}}^*}{Q_{z_{c,B}}^*}\right)^{1/3} \left(\frac{\nu_B}{\nu_A}\right) \tag{5.8}$$

Table (5.3) Exit Reynolds Numbers as a Function of Room Height

	z_c = 0.5 m		z_c = 1.22 m		z_c = 2.5 m	
$Q_{z_c}^*$	$\overline{Re}$	Re_2	$\overline{Re}$	Re_2	$\overline{Re}$	Re_2
$1x10^{-6}$	$6.47x10^{-2}$	$5.09x10^{3}$	$1.58x10^{-2}$	$1.24x10^{3}$	$4.64x10^{-2}$	$3.65x10^{3}$
$1x10^{-5}$	$1.39x10^{-1}$	$1.10x10^{4}$	$3.41x10^{-2}$	$2.68x10^{3}$	$1.00x10^{-1}$	$7.86x10^{3}$
$1x10^{-4}$	$3.00x10^{-1}$	$2.36x10^{4}$	$7.34x10^{-2}$	$5.77x10^{3}$	$2.15x10^{-1}$	$1.69x10^{4}$
$1x10^{-3}$	$6.47x10^{-1}$	$5.09x10^{4}$	$1.58x10^{-1}$	$1.24x10^{4}$	$4.64x10^{-1}$	$3.65x10^{4}$
$1x10^{-2}$	1.39	$1.10x10^{5}$	$3.41x10^{-1}$	$2.68x10^{4}$	1.000	$7.86x10^{4}$
ν_o	$1.006x10^{-6}$				$15.68x10^{-6}$ m^2/s	

Table (5.3) lists the exit Reynolds numbers and their ratios. The ratios are based on the full scale room with $Q_{z_c}^* = 1x10^{-2}$ as the reference ($Re_{2,B}$). As was the case for the plume Reynolds number, the 1/4 scale and 1/2 scale tests have comparable exit Reynolds numbers ($\sim 1.2x10^{4}$) and are between a fact or of 3 and 7 times smaller than the full scale cases

of interest ($1x10^{-3} \leq Q^*_{z_c} \leq 1x10^{-2}$). However, for the exit flows, the Reynolds numbers are an order of magnitude smaller than the plume Reynolds numbers. This suggests that Reynolds number effects may play a greater role in the counterflow process. For example, the orifice coefficients are known to be functions of the Reynolds number, although they do not vary strongly in the Reynolds number range of interest.

A plume Richardson number or, inverse squared Froude number, can be defined in a manner analogous to the Reynolds number, and can be used to measure the importance of buoyancy relative to the inertia terms.

$$Ri_z = \frac{\frac{\Delta\rho_m}{\rho_o} gz}{w_m^2} = \frac{1}{(Fr_z)^2} \tag{5.9}$$

For the asymptotic case of a point source plume, the Richardson number becomes a constant (see List and Imberger (1973). Thus the buoyancy effects in the plume

$$Ri_z = \frac{C_T (Q^*_z)^{2/3} gz}{C_v^2 gz (Q^*_z)^{2/3}} = \frac{C_T}{C_v^2} = 0.610 \tag{5.10}$$

should be exactly modeled, independent of scale.

The counterflow Richardson Ri_H was introduced in Chapter III, based on the maximum shear velocity ($v_{o_{max}} + v_{2_{max}}$) and the opening height H:

$$Ri_H = \frac{g(\frac{\rho_o - \rho_2}{\rho_o}) H}{(v_{o_{max}} + v_{2_{max}})^2} = \frac{(\frac{\rho_o - \rho_2}{\rho_o}) g H}{S^2 v^2_{2_{max}}} \tag{5.11}$$

If the two layer mode applies ($\delta = 0$), then eqn (3.48) shows that

$$Ri_H = \frac{\bar{H}}{2[\sqrt{\bar{H} - \bar{y}_o} + \sqrt{\bar{y}_o - \bar{Y}}]^2} \tag{3.48}$$

and so for geometrically similar rooms, the counterflow Richardson number will be invariant. If $0 < \delta < \delta_{crit}$, S will be a function of δ, and so geometrically similar rooms will have the same Richardson number, if they have the same δ. The same will be true of $\delta < \delta_{crit}$, but in that case $v_{2_{max}}$ will also be a function of δ, as well as S. As δ increases, one would expect the counterflow velocities to increase, and the Richardson number to fall. Consequently the 1/4 scale brine tests might be expected to have slightly higher counterflow Richardson numbers, since in the brine tests δ can only result from mixing, while in actual fires (1/2 and full scale), δ can also be produced by heat transfer from the floor.

A second related Richardson number Ri_c has also been defined in equation (3.49), based on the properties of the cold inflowing stream:

$$Ri_c = \frac{g(\frac{\rho_o - \rho_2}{\rho_o})y_o}{(\bar{v}_o)^2} \tag{3.49}$$

We have listed typical values for these two parameters in Table (5.4) These results were calculated by our room model, which we described in Chapters III and IV. Note that the magnitudes of both Ri_H and Ri_c are roughly comparable in both the 1/4 scale brine simulations and the 1/2 scale room fire experiments. In particular, the cold inflow Richardson numbers are identical for the small window tests in both sets of experiments. The large Richardson numbers associated with low brine flow rates and low $Q^*_{z_c}$ show that these flows were very stably stratified and, indeed, we visually observed very sharp, quiescent interfaces in these cases. Finally note that Sene and Zukoski (1980) found counterflow mixing to occur near the door or windows for $Ri_c < 8.2$. This indicates that we can

Table (5.4) Door Richardson Numbers for 1/4 and 1/2 Scale Tests

1/4 Scale Brine Experiments

$Q^*_{z_c} \times 10^6$	Opening	Ri_H	Ri_c
2.41	Door	1.36	78.4
4.42	Door	1.26	65.9
8.65	Door	1.16	54.7
13.22	Door	1.02	40.7
8.07	Large Window	0.69	14.0
7.66	Medium Window	0.44	5.1
8.17	Small Window	0.23	2.7

Opening	Sill [cm]	Span [cm]	Soffit [cm]
Door	0	27.0	37.5
Large Window	10.4	27.0	37.5
Medium Window	16.6	27.0	37.5
Small Window	21.7	27.0	37.5

$z_c \sim 50$ cm

1/2 Scale Room Fires

$Q^*_{z_c} \times 10^3$	Opening	Ri_H	Ri_c
1.70	Door	0.79	25.8
1.70	Large Window	0.54	9.7
1.69	Window	0.26	2.7
3.12	Door	0.82	27.0
5.64	Door	0.77	25.4
6.16	Door	0.67	20.7
6.09	Window	0.26	2.7

Opening	Sill [cm]	Span [cm]	Soffit [cm]
Door	0	45.7	99.1
Window	54.6	45.7	99.1

$z_c = 121.9$ cm

expect mixing to occur for the medium and small window geometries in both sets of experiments, and our data confirm that additional mixing of this form does indeed occur in these cases.

The brine flow simulations model small fires with adiabatic walls and no radiant heat transfer. The presence of heat transfer from the gas to the walls produces a variety of effects. By reducing the temperature difference, $(T_2-T_1) = c_q\langle\Delta T_i\rangle$, heat transfer losses throttle down the flow rates. With a smaller hydrostatic pressure difference to drive the flows, the neutral plane y_o, falls, thereby reducing the inflow. The interface then falls to compensate for the loss in $\dot{m}_p$. Secondly, if there is significant radiant heat transfer between the surfaces, the floor will be heated and will in turn heat the lower level gas, increasing δ. If in addition, the smoke contains soot, the hot gas itself may make a sizeable contribution to the radiant heating of the lower room. This would increase δ, and decrease c_q, even farther. Finally, natural convection boundary layers may be set up, as gas near vertical walls is heated or cooled, thereby producing significant secondary flows which may enhance the mixing across the interface between the floor and ceiling layers.

The 1/4 scale brine experiments clearly model the case of a fire in a room with well insulated walls with low emissivity. The 1/2 scale fire room tests on the other hand had forced convection cooled walls and ceiling, whose emissivity was very close to 1 for the temperature range encountered. Actual fire situations probably lie between these two extremes. However, since the heat transfer effects depend on details of room geometry and construction, they are difficult to model in a simple way, and therefore have been lumped into the two parameters c_q and c_{fr}.

Another set of factors affecting the behavior of the plume and hence of the hot upper layer is the size and strength of the fire source. Yokoi (1960) found that plumes from alcohol pan fires obeyed the asymptotic point source relations for heights greater than two source diameters. Zukoski, Kubota, and Cetegen (1980) also reported that the plumes produced by their diffusion flames followed these relations above the flame zone itself. Thus for our models to apply to real fires it seems that we must require that the interface in the room lie above either the flames themselves or a height of two source diameters, whichever is greater.

However, unlike real fires, both of our laboratory sources of buoyancy also imparted significant amounts of mass and momentum to the plume. We have listed several parameters measuring these effects in Table (5.5). Note that in both sets of experiments we never got very far into the far field. Thus the interface height lay between 3.9 and 10.1 source diameters above the fire. More sensitive ways to determine source effects are to measure the height of the interface z_{int} in units of the calculated virtual source depth z_{vs}, or to compute the source Richardson number Ri_o based on the source diameter d_o. These two parameters exhibit the greatest change for the 1/4 scale brine tests because we increased the buoyancy flux by increasing the flow rate of the brine which had only a small density difference ($\Delta\rho/\rho_o \sim 1.05$). This produced a relatively more jet-like flow because the nozzle diameter was constant, and is reflected in the large decrease in the source Richardson number. On the other hand, we increased the fire strength by increasing the burner diameter while holding the initial velocity approximately constant. Thus the 1/2 scale source Richardson numbers are all fairly similar and actually increase with Q^*. Finally note that in both cases, the source Reynolds number

Re_o, based on the source bulk velocity and the source diameter, is of roughly comparable magnitude for both sets of experiments, although the brine experiments generally had smaller initial Reynolds numbers.

A final factor affecting the behavior of the gas within the room is the floor plan of the room itself. This enters in two ways. First, as we shall see in Chapter IX, the aspect ratio of the room affects the initially axisymmetric ceiling jet which is formed by the impingement of the plume upon the ceiling. The higher the aspect ratio of the room, the sooner the presence of the side walls will channel the ceiling jet into a basically two-dimensional flow pattern. This results in a significant change in the convective heat transfer process. Secondly, the volume of the upper layer relative to the mass flux delivered to it by the plume determines how vigorously the upper layer fluid is stirred.

We can quantify this latter effect by computing the mean residence time for fluid in the upper layer. Thus we define t_{res} as the volume of the upper layer divided by the volumetric flow rate in the plume as it crosses the interface. Alternatively, we can compute a related time scale given by Zukoski and Kubota (1980) as:

$$t_{fill} = \frac{A_f}{z_c\sqrt{gz_c}\ (Q^*_{z_c})^{1/3}} \tag{5.12}$$

where A_f is the area of the floor. This time scale is proportional to the time it would take the plume to completely fill the room with combustion products assuming the doorway was basically blocked, except for a small leak at the floor. If we consider two geometrically similar rooms then $A_f \propto z_c^2$, and the ratios of the fill-up time scales is:

Table (5.5) Finite Source Effects: 1/4 Scale Brine and 1/2 Scale Fire Tests

1/4 Scale Brine Tests

EXPT	$Q^*_{z_c} \times 10^6$	d_o[cm]	z_{vs}[cm]	$z_{int}^{\dagger}$[cm]	z_{int}/d_o	$z_{int}/\lvert z_{vs}\rvert$	Ri_o	Re_o
2	2.41	4.8	-3.98	27.7	5.77	6.96	78.52	825
3	4.42	4.8	-5.25	27.3	5.68	5.23	20.60	1632
4	8.65	4.8	-7.05	26.4	5.49	3.74	5.28	3241
5	13.22	4.8	-9.94	25.3	5.27	2.55	1.25	6460

1/2 Scale Fire Tests

EXPT	$Q^*_{z_c} \times 10^3$	d_o[cm]	z_{vs}[cm]	z_{int}[cm]	z_{int}/d_o	$z_{int}/\lvert z_{vs}\rvert$	Ri_o	Re_o
7	2.01	7.62	- 8.66	77.11	10.11	8.90	6.82	3895
10	3.96	10.16	-12.20	73.76	7.26	6.05	8.57	5408
13	7.85	15.24	-17.26	69.80	4.58	4.04	11.89	7878
15	8.14	15.24	-14.40	65.68	4.31	4.56	12.31	7896
16	8.13	15.24	-14.98	59.44	3.90	3.97	10.27	8382

† calculated from room model of Chapters III and IV

$$\frac{t_{fill,A}}{t_{fill,B}} = \left(\frac{z_{c,A}}{z_{c,B}}\right)^{1/2}\left(\frac{Q^*_{z_{c,B}}}{Q^*_{z_{c,A}}}\right)^{1/3} \qquad (5.13)$$

For example the large increase in plume strength, measured by $(Q^*_{z_c})^{1/3}$, dominates the doubling of the room height z_c between the 1/4 scale brine flows and the 1/2 scale room fire experiments. The ratio of the time scales is $\sqrt{2}/10 \sim 1/7$, which indicates that the upper layer fluid is replenished 7 times faster in the 1/2 scale fire tests.

Numerical values of t_{res} and t_{fill}, listed in Table (5.6), clearly indicate that both of these time scales are much shorter in our 1/2 scale room fire experiments than in either of our 1/4 scale brine flow facilities. One manifestation of the reduction of these time scales is that in our 1/2 scale fire tests, the data presented in Chapter VII clearly show that hot gas from the ceiling layer has sufficient initial momentum to flow down the side walls and penetrate into, and in some cases, through the interface. There was no indication of this in our early brine experiments which had time scales roughly 19 times larger. Similarly, the later brine tests, which had time scales roughly 6 times larger than the 1/2 scale fire tests, did not show any vigorous flow of plume fluid down the side walls, although the interface did appear to be more disturbed than in the early brine tests.

Table (5.6) Upper Layer Fluid Time Scales

1/4 Scale Brine Tests

130 cm x 115 cm x 51 cm Tank

$Q^*_{z_c} \times 10^6$	t_{res}[s]	t_{fill}[s]
2.41	498	96.8
4.42	389	79.1
8.65	285	63.2
13.22	231	54.9

100 cm x 50 cm x 51 cm Tank

$Q^*_{z_c} \times 10^6$	t_{res} [s]	t_{fill}[s]
2.41	167	32.4
4.42	123	26.5
8.65	102	21.1
13.22	77	18.4

1/2 Scale Brine Tests

122 cm x 244 cm x 122 cm Room

$Q^*_{z_c} \times 10^3$	t_{res}[s]	t_{fill}[s]
2.01	20.2	5.59
3.96	20.2	4.46
7.85	17.0	3.55
8.14	15.5	3.51
8.13	19.4	3.51

VI. TYPICAL RESULTS OF 1/4 SCALE BRINE FLOW SIMULATIONS

An extensive series of experiments involving the effects of fire strength, fire geometry, fire location, and opening geometry were carried out in our 1/4 scale hydraulic modeling facility. The data confirmed the basic validity of our simple room model for small fires (small $Q^*_{z_c}$) in adiabatic rooms ($c_q = 1$). Because these results have already been discussed in detail by Tangren, Sargent, and Zukoski (1978), we will only highlight the significant features of these experiments in order to examine some of the effects that heat transfer and source strength have in determining the density or temperature profile within the room. Furthermore, in order to compare the results from our 1/4 and 1/2 scale facilities, we will restrict our attention to the case of plumes emanating from axisymmetric sources and rising in rooms with a single door or window opening. It may be noted that this author set up the 1/4 scale facility in this configuration, wrote the data processing routines, and carried out the first 30 experiments listed by Tangren, et al, (1978). Mr. Ernst Tangren then took over the facility, proceeded with further experiments involving both open and closed room geometries, and wrote the report cited above.

The 1/4 scale brine flow simulations modeled the case of very small fires ($Q^*_{z_c} \sim 10^{-6}$) in rooms with adiabatic surfaces. Because the plumes were relatively weak, the flow rates through the doorway were small and consequently the Richardson numbers were large ($Ri_c \sim 60$), indicating that the flow was dominated by the buoyancy of the fluid. In addition, the time that the fluid spent in the upper layer was large

(t_{res} ~ 350 s), which implies that the circulation in this region was rather sluggish. These factors combined to produce a remarkably sharp, flat interface which was clearly visible because of the change in the index of refraction with salinity. Results from a typical experiment involving a room with a doorway are displayed in Figure (6.1). In this figure we have plotted the measured density difference ($\rho_\infty - \rho$) divided by the predicted upper layer density difference ($\rho_\infty - \rho_2$) as a function of the fractional height at the room (z/z_c). The simple room model discussed in Chapter III was used to estimate the upper layer density ρ_2.

The data in Figure (6.1) serve to illustrate several important features of the brine flow simulations which were not seen in our 1/2 scale room fire tests. First, because there is no mechanism by which the fluid in the upper layer can lose its salinity, the density in the upper layer is constant. Consequently it is impossible to detect the ceiling jet, formed by the impingement of the plume upon the ceiling, in a density profile such as Figure (6.1). This situation is equivalent to a constant temperature upper layer in a room with adiabatic walls ($c_q = 1$). Note also that because there is little shear in the large doorway (large Ri_c), and because the ceiling jet is weak and does not penetrate down the side walls to the interface, the floor layer fluid is uncontaminated with plume products from the upper layer ($\Delta\rho$ ~ 0). Furthermore, because the ceiling jet is weak and because there is no way for the floor layer fluid to change its density except by mixing, the fluid in the room is stably stratified

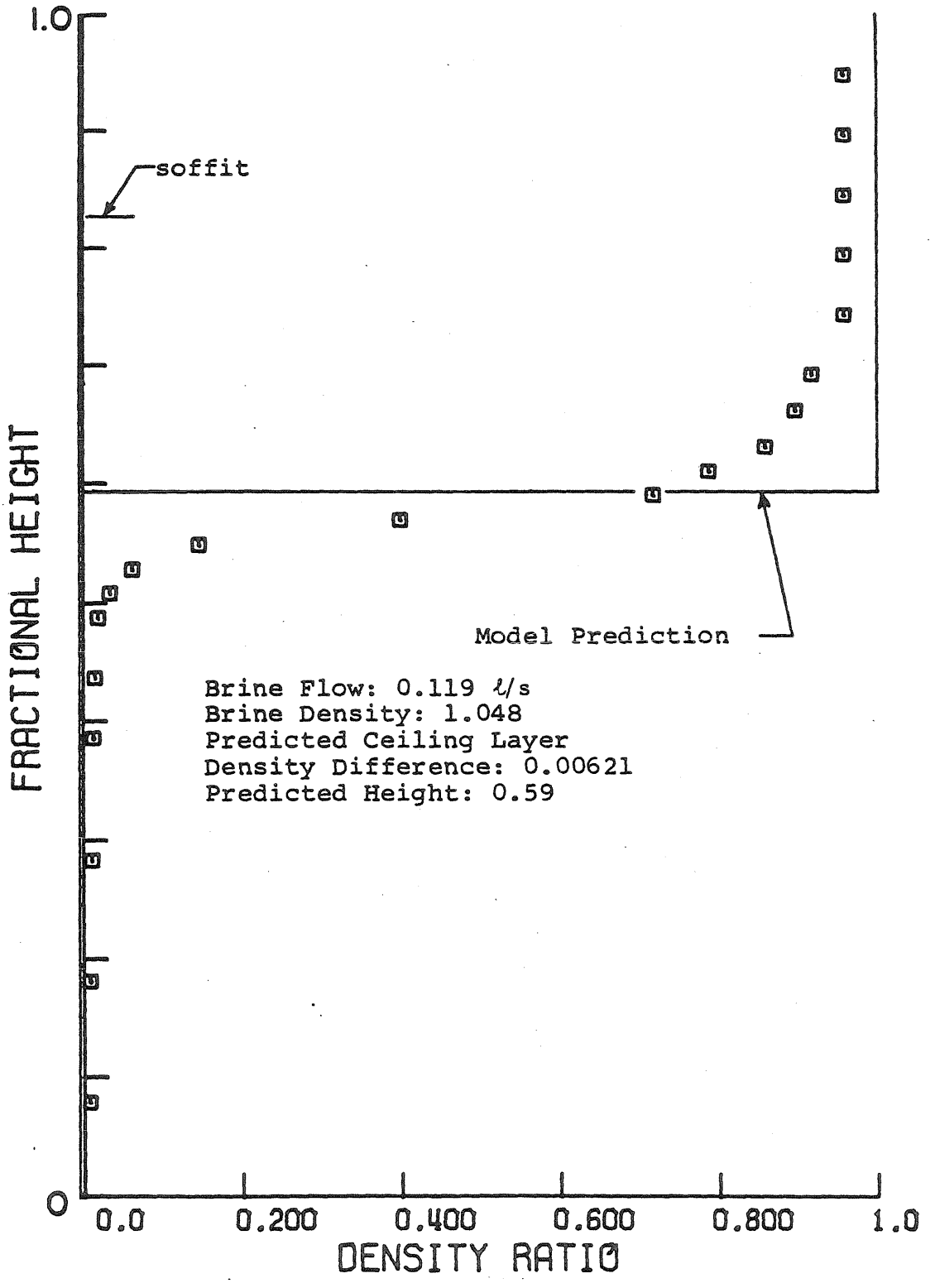

Figure (6.1) Data From Typical Brine Experiment

and the interface is very sharp. Finally note that the simple room model described in Chapter III does a reasonably good job of predicting the interface height and upper layer density.

In real fires and in our 1/2 scale room fire tests, these results are modified in two basic ways. First, because there will almost always be some heat transfer from the gas, the temperature in the upper layer will not be constant and there will be a non-zero gradient of temperature in the upper layer. In relatively small rooms, such as our 1/2 scale test room, the hot gas which comprises the buoyant ceiling jet, formed by the impingement of the plume upon the ceiling, will be hotter than the rest of the upper layer gas beneath it over most of the ceiling. This slightly colder gas which makes up the majority of the upper layer was itself once part of the ceiling jet and thus has already experienced convective and possibly radiative losses as it flowed along the ceiling, and, depending on the room geometry and strength of the plume, possibly down the side walls as well. In addition, radiation from the hot upper surfaces of the room and from the hot gas itself (especially if it contains a significant amount of soot) will heat the lower walls and floor. As these lower surfaces become hotter than the floor layer gas natural convection flows will be created which will produce a non-zero temperature gradient in the floor layer gas, and which will increase the mean floor zone temperature (T_1) above its original ambient value (T_∞). These secondary flows will also tend to perturb the interface

and may cause internal waves which will cause the interface zone to be broader and which will reduce the gradient of the mean temperature in this region.

In addition to heat transfer processes, the strength of the source relative to the room geometry further modifies the shape of the mean density or temperature profiles. We can use t_{res}, the residence time of the upper layer gas as a quantitative estimate of this effect. In our 1/2 scale tests this parameter was roughly 18 times smaller than in the 1/4 scale experiment whose data is shown in Figure (6.1). This indicates that the plume and ceiling jet flows are much more vigorous in our 1/2 scale experiments. Gas temperature data measured near the walls revealed that this vigorous ceiling jet fluid impinged upon the side walls and flowed down them, in some cases penetrating below the interface. This flow pattern, which is discussed in Chapter VII, will further perturb the interface and result in an even thicker interface zone. In addition, this penetration of upper layer gas contributes to the contamination of the floor zone gas with combustion products which we observed in our 1/2 scale experiments even when the Richardson number at the door was large ($Ri_c \sim 25$), which would indicate that mixing at the doorway should be small.

Thus it appears that the small scale hydraulic modeling experiments provided a useful way to study the primary flow phenomena involved in room fires, namely the behavior of the plume and upper layer, and the counter flow of fluid through the door or window openings. However, heat transfer and source strength effects produce significant

secondary flows in real room fires and these flows could not be simulated in our 1/4 scale facility.

VII. TYPICAL RESULTS OF 1/2 SCALE ROOM FIRE TESTS

7.1 Introduction

In this chapter we will present typical gas and surface temperature data from a representative sample of our 1/2 scale room fire tests. The majority of the temperature data were taken under essentially steady-state conditions, because as we shall discuss in the next section, the gas transient is very short, and even the solid surfaces heat up to within a few degrees of their final temperatures within 25 minutes after ingition. In order to present the interesting features of these experiments, while keeping the length of this chapter to a reasonable size, we will discuss a typical experiment (number 15), involving a 15.24 cm diameter fire located on the room's major axis in a room with a door. We will then briefly examine three other experiments (7,10,13), which had fires located in the corner of the room, to see the effect of increasing the dimensionless heat input $Q^*_{z_c}$ from $2\text{x}10^{-3}$ to $8\text{x}10^{-3}$. The last of these (13) will be compared to the previously examined typical case (15) to show the effect that the fire location has on the data. Finally, by comparing the data of experiment 16, in which the opening was a small window, with that of test 15, one can see the role that the opening geometry plays in fixing the flow patterns in the room.

It should be noted that all of these experiments were performed in a rectangular room 1.22 m wide, 2.44 m long, and 1.22 m high. The doorway was 45.7 cm wide and 99.1 cm tall and was located in the center of the north end wall. The lower 54.6 cm of the doorway could be blocked to form a window 45.7 cm wide by 44.5 cm tall. Three different diameter

burners were used to create fires with heat inputs of approximately 3.7, 7.2, and 14 kW, respectively. For a given experiment, the center of the burner was located either on the room's major axis, 61 cm from the rear (south) wall; or in the rear (south west) corner, 18 cm from each wall. A summary of the experimental conditions is presented in Table (7.1).

7.2 Transient Response

The transient response of the upper layer gas in these experiments was very rapid, with the temperature jumping from ambient to nearly steady state values in a matter of seconds. On the other hand, the large thermal "mass" of the walls and ceiling dictated a much slower response, with the solid surfaces approaching quasi-steady state values after a period of 10 to 20 minutes. These trends are clearly portrayed in Figure (7.1) which presents both a characteristic gas temperature data measured 2.5 cm below the ceiling and 2.5 cm from the west side wall, and the ceiling temperatures measured at the stagnation point ($\bar{r} = 0$) on both sides of the ceiling. The temperatures are plotted as the dimensionless temperature difference ratio:

$$T^*_\infty = \frac{(T - T_\infty)}{T_o (Q^*_{z_c})^{2/3}} \qquad (7.1)$$

where $T_\infty = 25^oC$ is the ambient temperature outside the test room at the start of the experiment and $T_o = 28.5^oC$ is the reference temperature of the gas inside the room, measured near the floor. We can define an effective residence time for the gas above the interface t_{res} as the volume of this upper layer divided by the calculated volumetric flow

Table (7.1) 1/2 Scale Room Fire Conditions

Exp. No.	$Q^*_{z_c} \times 10^3$	Opening Geometry	Fire Location	T_∞ [C]	$\overline{T}_1$ [C]	$\overline{T}_2$ [C]	δ	$\frac{z_{int}}{z_c}$	c_q	t_{res} [s]
15	8.14	door	CL	25.3	36.4	112.9	0.104	0.539	0.740	15.5
16	8.13	window	CL	24.9	68.3	154.9	0.324	0.488	0.590	19.4
7	2.01	door	SW	26.0	28.8	64.7	0.072	0.632	0.762*	20.2
10	3.96	door	SW	25.3	30.4	89.1	0.067	0.605	0.680†	20.2
13	7.85	door	SW	23.8	31.5	124.8	0.061	0.573	0.697†	17.0

* Calculated for a plume with α reduced by 10%

† Calculated for a plume with α reduced by 20%

Fire Location: CL = on center-line of room

SW = in southwest corner of room

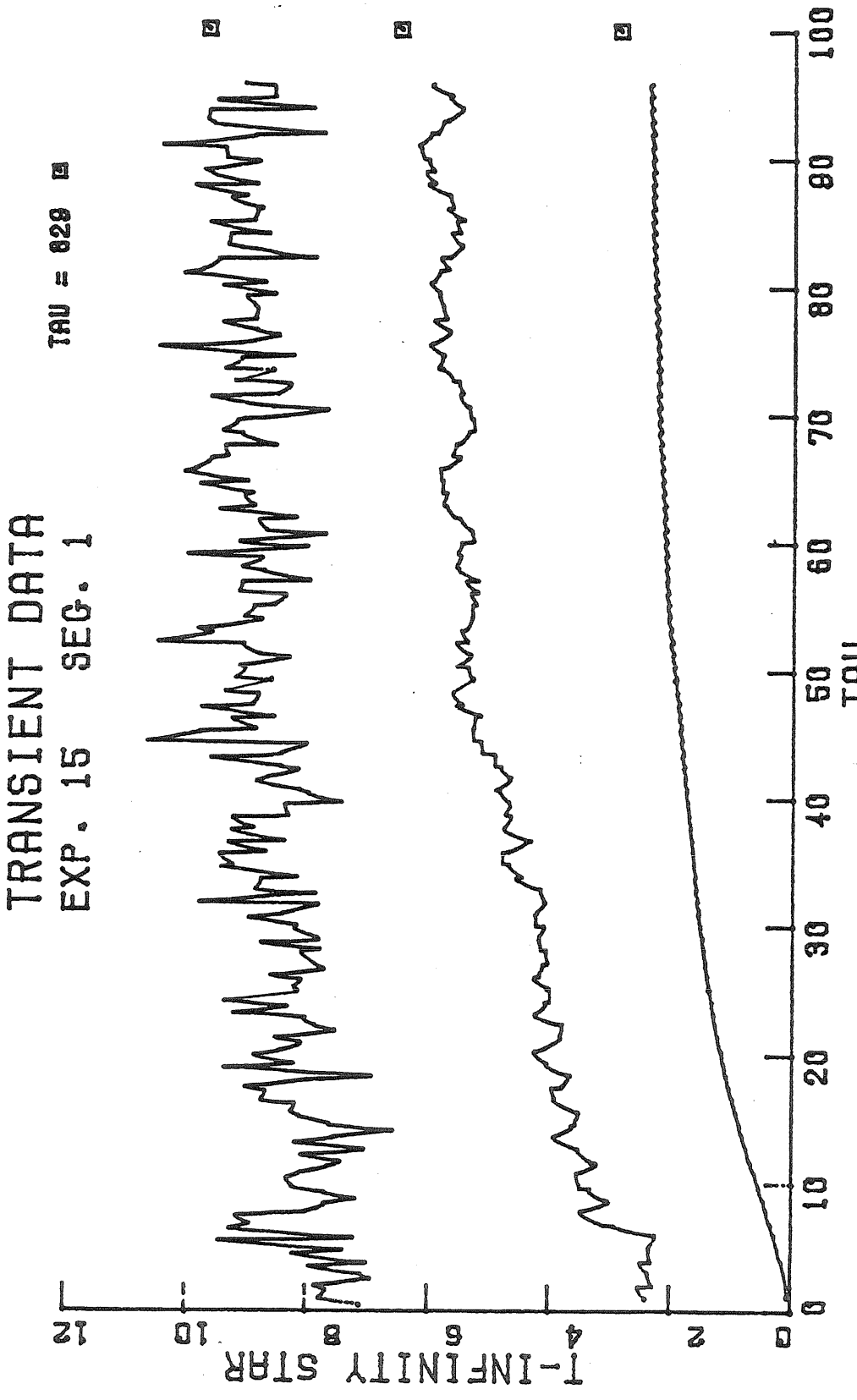

Figure (7.1) Transient Temperature Response of the Gas and Inner and Outer Surface Temperatures on the Ceiling at the Stagnation Point (Exp. 15).

rate of the plume at the interface. Thus t_{res} is a measure of how long it takes the plume to completely replenish the gas in the upper layer. As the values of t_{res} tabulated in the last column of Table (7.1) demonstrate, these times are short and the upper layer of hot gas is refilled 3 to 4 times a minute by the plume. It is thus convenient to measure time in terms of this residence time and to define the dimensionless time τ:

$$\tau = \frac{t}{t_{res}} \tag{7.2}$$

Figure (7.1) presents the dimensionless temperature difference T^*_∞ in terms of the dimensionless time τ for the first 25 minutes of experiment 15. In this experiment, a 15.24 cm diameter fire was located on the center-line of a room with a door. This figure illustrates several points which are typical of the 1/2 scale results. First, the upper layer residence time (t_{res} = 15.5 seconds) is comparable to the cycle time (t_{cycle} = 15 seconds) required to rotate the thermocouple stepping switch through all 52 positions and to process the acquired data. Consequently, we can not observe the transient response of the gas, or the initial response of the ceiling. For example, in only 11.1 seconds after ignition, the gas temperature near the ceiling had already jumped from 25°C to 112°C. Similarly, the inner surface ceiling temperature responded to this sudden increase in gas temperature by rising to 54.4°C after only 16.3 seconds. On the other hand, the outer surface of the ceiling was still close to ambient [25.7°C] at this time. Second, there are obviously large, low frequency fluctuations in the gas temperature. These fluctuations impress themselves somewhat

upon the inner surface of the ceiling and produce low frequency variations in the ceiling temperature. These fluctuations tend to be averaged out by the large thermal mass of the ceiling and result in a smoothly increasing temperature on the convectively cooled outer surface of the ceiling. Finally, note that by $\tau \sim 95$ ($t \sim 25$ minutes), all three temperatures have nearly attained the "steady state" values which were measured more than 8 times later at the end of the experiment ($\tau = 829$). Because of this relatively rapid approach to equilibrium conditions, the wall and gas temperature transient behavior was recorded for approximately the first 25 minutes. Then the quasi-steady state gas temperature and composition within the room were surveyed. Finally, after sufficient time had elapsed for the walls and gas to reach equilibrium temperatures, the wall and gas temperatures were measured to determine the state convective heat transfer distribution, which is discussed in Chapter IX.

7.3 Typical Gas Temperature and Composition Profiles

Experiment number 15, which involved a 14.9 kW fire located on the center-line of our 1/2 scale test room, provided gas temperature and CO_2 concentration data which are typical of our 1/2 scale results.

One useful way to see what is going on is to examine a vertical slice through the gas, normal to the room's major axis. The gas sampling system consisted of a boom with 6 hooded, aspirated thermocouples attached to a vertical shaft which was located near the mid point of the west side wall. We chose to measure the angle of the boom from the north end of the room, which contained the door or window opening. Thus the vertical slice in question will be referred to as a 90^{o} vertical

traverse. The time averaged temperature data from 5 of the 6 probe thermocouples are displayed in Figure (7.2). To obtain these averaged values, the computer sampled each thermocouple 20 times a second for a period of 10 seconds. In addition to computing the average value for each probe thermocouple, the standard deviation s_T was also computed.

Figure (7.2) is highly representative of our gas temperature data in several important respects. First, if one ignores the data from probes 5 and 6, which are 18 and 3 cm respectively from the east side wall, one sees that the gas in the interior of the room is well mixed and homogeneous at a given elevation since all three of the interior probes measure the same mean temperature and standard deviation at any given height. We found that these mean temperature profiles were highly reproducible, and that profiles taken during ascending and descending vertical traverses, separated by 10 minutes, matched very closely. In addition, the magnitude of the standard deviations about the mean also matched, indicating the average fluctuation levels of the gas temperature do not change with time. Finally, it is interesting to note that probe 6, which is only 3 cm from the east wall, sees hotter gas flowing down the wall which penetrates below the level of the hot gas in the interior of the room. Probe 5, which is 18 cm from the wall, encounters the edge of this flow. Its mean temperature data agree with the data from the interior probes, but the fluctuations are larger than in the interior of the room.

Based on the mean temperature profile for the interior gas shown in Figure (7.2), we have defined three regions or zones to characterize the gas temperature and composition. These zones have readily identifiable

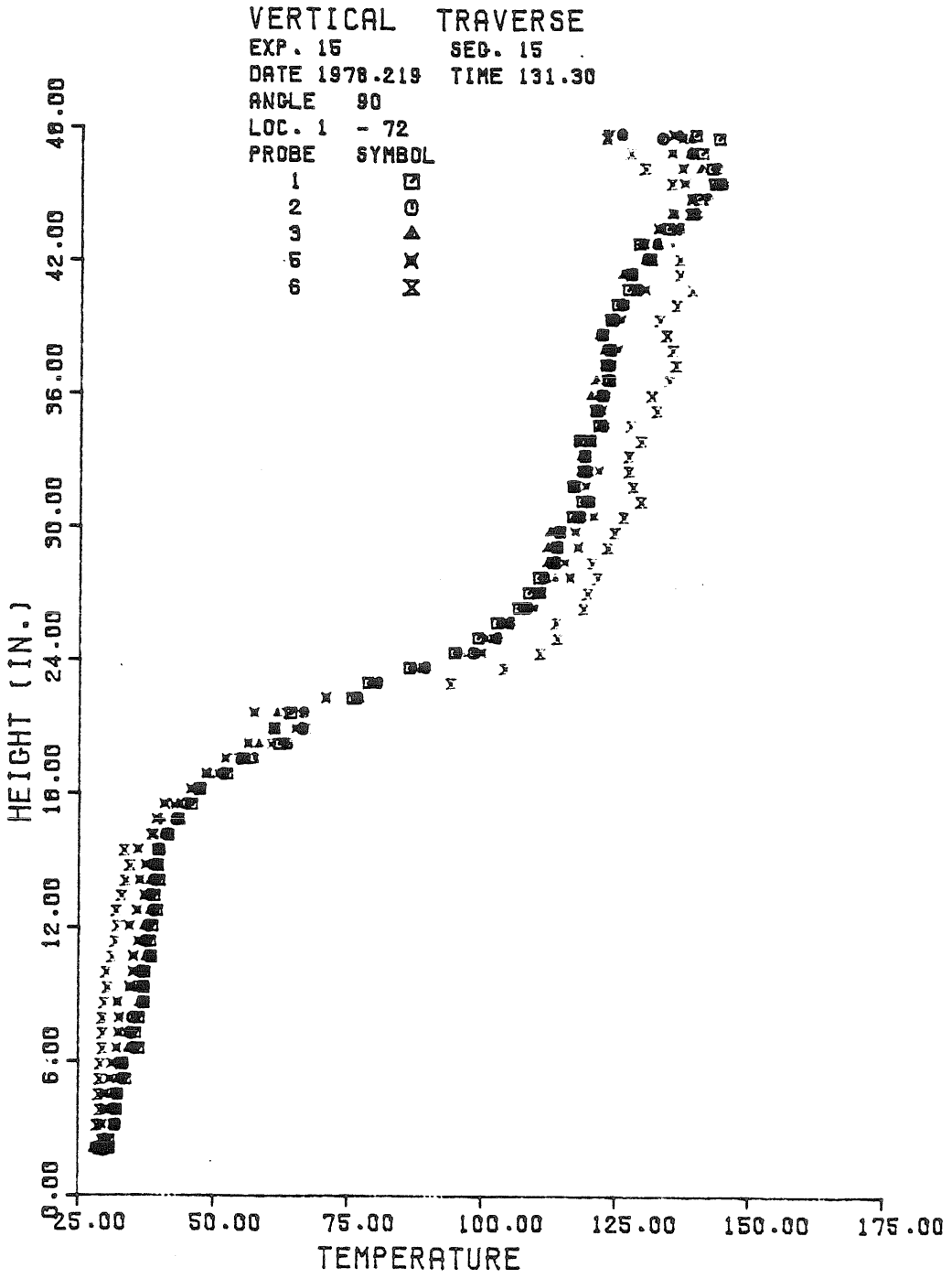

Figure (7.2) Gas Temperatures on Vertical Plane through the Middle of the Room, Exp. 15 (Time-Averaged Values).

characteristics not only in terms of the mean temperatures, but also in terms of the magnitude of the fluctuations about the mean. To emphasize this, in Figure (7.3) we have replotted one probe's mean temperature data and have indicated confidence levels of length $3s_T$ on either side of the mean, where s_T is the standard deviation of the data about the mean. These confidence intervals about the mean indicate the probable range of the temperature fluctuations encountered by the probe. In particular if one assumes that the temperature fluctuations are given by a Gaussian distribution centered at the mean value, then the probability of finding a temperature deviation greater than $3s_T$ is only 0.3%.

Starting at the bottom of Figure (7.3), there is a floor zone of basically cool, quiescent gas (small s_T) which has a relatively small mean temperature gradient $\frac{\partial \overline{T}}{\partial z}$. However, this gas has already been heated slightly above T_∞, the value of the ambient gas in the laboratory. Next in an interface zone, there is a large gradient of the mean temperature, and in which the temperature fluctuations are also large (large s_T). Third, the hot upper layer, which is made up of hot gas from the fire plume, can in turn be subdivided into two parts. Most of the upper layer, which we refer to as the "ceiling layer", contains gas at a nearly uniform temperature with a small constant gradient and with a moderate to small s_T. Finally, just below the ceiling is a sub-layer characterized by a temperature excess or deficit relative to the ceiling layer gradient and by large fluctuation levels (large s_T). This is a manifestation of the ceiling jet of hot plume products which form a buoyant wall-jet and flow away from the plume along the ceiling.

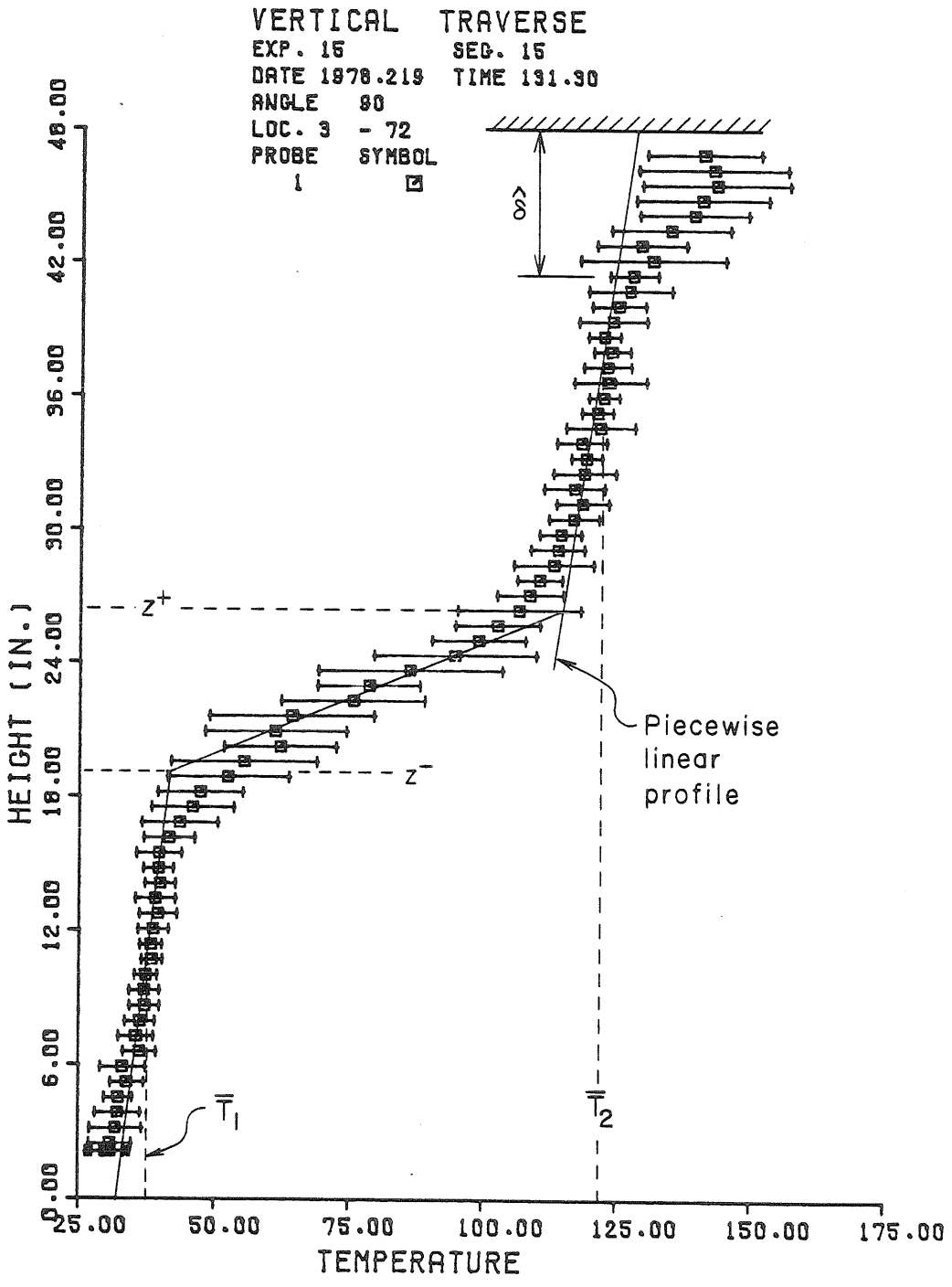

Figure (7.3) Temperature Data from One Probe, Showing Fluctuation Levels of 3 Standard Deviations about the Mean (Exp. 15).

Near the plume this ceiling jet is characterized by a temperature excess as shown in Figure (7.3), while further from the plume impingement point convective losses reduce the temperature excess and eventually result in temperature deficits in this ceiling jet layer.

The mean temperature data in each of the three zones can be approximated rather closely by a constant temperature gradient, resulting in a piecewise linear temperature profile which we have sketched in Figure (7.3). The intersections of these linear profiles can be used to quantify the borders of these zones. Thus we denote the lower edge of the interface zone by z^- and the upper edge by z^+. In addition, we take the arithmetic mean of these linear profiles for the floor and ceiling zones to estimate the average lower layer temperature $\overline{T}_1$ and average upper layer temperature $\overline{T}_2$, respectively. In addition to these average temperatures ($\overline{T}_1$, $\overline{T}_2$), we have also indicated the boundaries of the interface zone (z^+,z^-) and the approximate depth of the ceiling jet ($\hat{\delta}$) in Figure (7.3).

The estimation of the ceiling jet thickness $\hat{\delta}$ from the temperature data is rather subjective. Near the plume the ceiling jet is characterized by a clear temperature excess above the constant ceiling zone gradient and by large temperature fluctuations. However, further from the plume entrainment and convective losses to the ceiling reduce both the temperature excess and the magnitude of the fluctuations, making the determination of $\hat{\delta}$ rather difficult.

In the room models described in Chapters II and III and in the heat transfer calculation procedure of Chapter VIII, we assumed that the gas in the room consists of just two layers: a hot upper layer of combustion

products, and a cool layer of mostly fresh air beneath it. In addition we assumed that each of these two layers has a uniform temperature (T_2 and T_1, respectively) and that these layers are separated by a sharp interface where the temperature jumps from T_1 to T_2. After studying Figure (7.3), the assumption of uniform temperature in the floor and ceiling zones seems plausible, but the location of the sharp interface z_{int} appears to be arbitrary. To resolve this question we compared two basic plume calculations. On one hand we used the complete model for a finite source plume rising through a non-uniform environment ($\frac{dT_e}{dz} \neq 0$) given by equations (2.29)-(2.31). For this calculation we assumed the gradient of the external temperature was constant in each of the three basic zones and equal to the empirical values determined from graphs such as Figure (7.3). We then compared the calculated values for the maximum plume velocity and temperature and Gaussian width at the ceiling with similar quantitites calculated for a finite source plume rising in a uniform environment at $\overline{T}_1$ until it encountered a sharp interface at z_{int} and then rose through a uniformly hot ceiling layer at $\overline{T}_2$. This latter two-stage plume calculation, which is described in Section 8.2, was repeated three times with z_{int} equal to z^-, z^+, and $\frac{1}{2}(z^- + z^+)$ respectively. For all the causes examined in this manner, we found that choosing $z_{int} = z^+$ gave the best agreement with the full, non-uniform environment calculation. Consequently, in the following sections, we will use z^+ as the interface height.

In addition to measuring the temperature with the 6 aspirated probe thermocouples, the aspirated gas from one of the probes could be directed through a carbon dioxide detector, thereby allowing us to produce a gas composition profile such as that shown in Figure (7.4). It

may be noted that because the aspiration rate through the CO_2 analyzer had to be rather low, the gas temperatures from probe 4 were not plotted in Figure (7.2). Comparing Figures (7.4) and (7.3) one can see that the mean CO_2 concentration profile is very similar to the mean temperature profile. Each display 3 distinct zones: a reasonably uniform floor zone which is only slightly contaminated by combustion products, an interface zone with a large but finite gradient of concentration or temperature, and finally a nearly uniform ceiling zone filled with combustion products.

It is interesting to note that the floor and ceiling zone concentration profiles are much more nearly uniform than the corresponding temperature profiles. To be specific, only 14% of the total increase in the CO_2 concentration observed in Figure (7.4) occurs in the ceiling zone, compared to a similar increase of 21% for the temperature data in Figure (7.3). This indicates that the ceiling zone concentration gradient is 31% smaller than the temperature gradient there. This is to be expected since the gas can gain or lose energy to the solid boundaries of the room through convection and radiation, but there is no analogous mass transfer process for CO_2. Consequently, the mass-averaged CO_2 concentration which is delivered by the plume remains nearly constant throughout the entire upper layer, and the ceiling jet, which has a definite temperature excess at this location, is not visible on the concentration profile. These results were consistently observed for all our test conditions and suggest to us that the temperature gradient in the ceiling zone is fixed by radiant and convective heat transfer to the ceiling and walls as well as by a regular pattern of mixing in the ceiling layer.

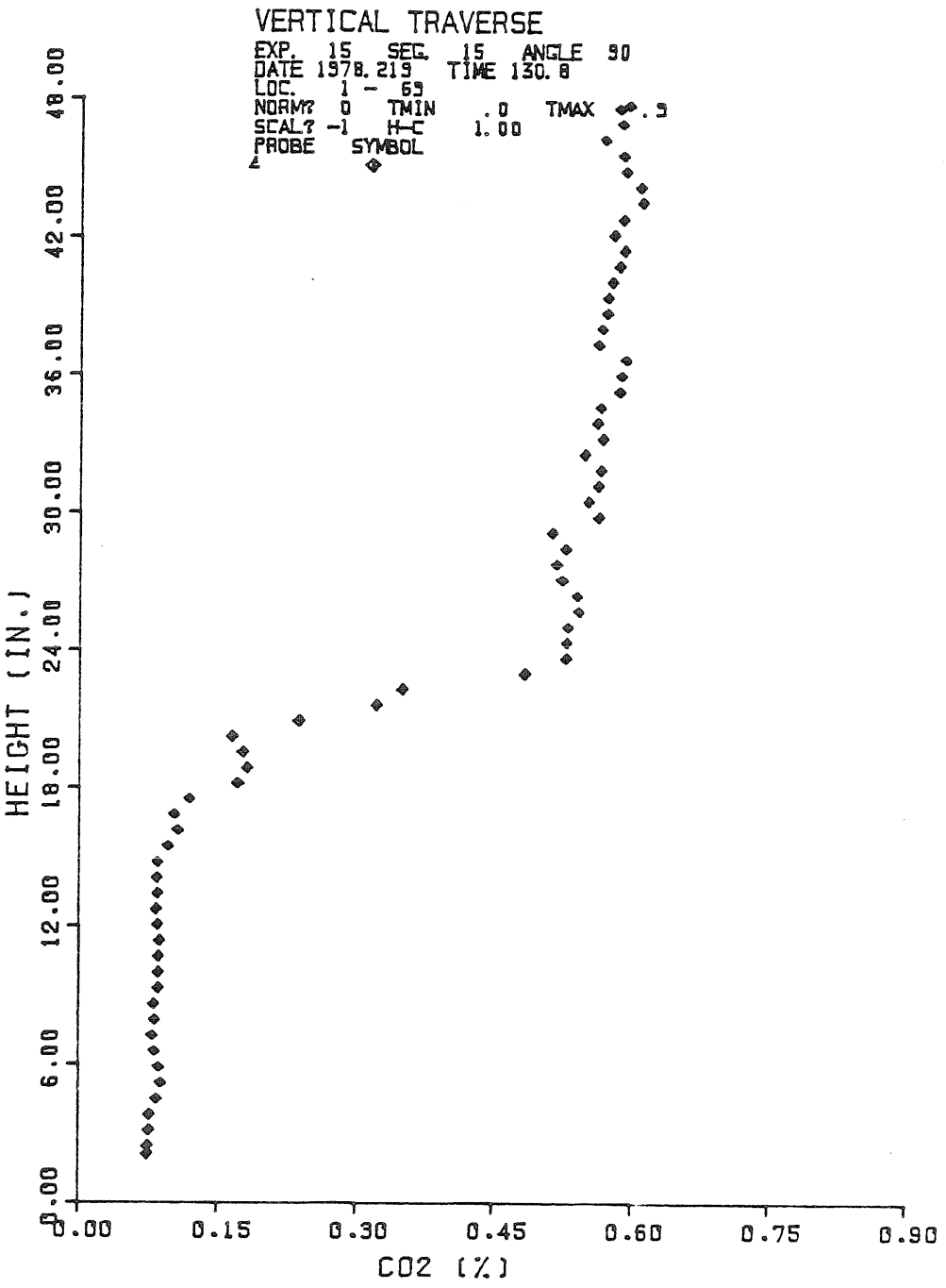

Figure (7.4) CO_2 Concentration Profile in the Middle of the Room (Exp. 15).

We also found that unlike the 1/4 scale brine simulations, the floor zone appears to be slightly contaminated by combustion products. Although natural convection plays a role in heating the floor zone gas (the lower walls and floor are heated by radiation), the fact that the floor zone CO_2 concentration is slightly greater than that measured in ambient air indicates that some combustion products have penetrated below the interface and mixed with the originally ambient gas in this region.

Finally, the measured CO_2 profile allows us to check our two layer plume and interface calculation. To do this we assume the plume entrains air with the uniform floor zone CO_2 concentration between the floor and $\bar{z}$, and that the plume entrains a mixture of gases in the interface zone which can be approximated as the average CO_2 concentration for the interface zone. Then knowing the initial CO_2 concentration in the plume from stoichiometry and the measured fuel and air flow rates, and the increase in mass flow in the finite source plume as a function of height, it is possible to predict the mean CO_2 concentration is delivered to the upper layer. The calculated values agreed well with the measured values listed in Table (7.2). The average deviation is only 2.6%. This agreement confirms that our plume model and choice of interface heights are self-consistent.

7.3.1 General Results: Interior Gas Flow Patterns

During most of the 1/2 scale room fire experiments, vertical traverses through the gas were conducted at eight standard angular positions. These are shown in Figure (7.5), which is a top view of the test room. The larger crosses indicate the two fire locations which were used. The span of the door or window opening has also been added for orientation.

Table (7.2) CO_2 Concentration Data [%/volume]

Expt.	Measured				Calculated		
	Room Air	Floor Zone	Interface Zone	Ceiling Zone	Source	Ceiling Zone	ΔC^*_{21}
7	0.036	0.059	0.167	0.275	6.50	0.270	411
10	0.033	0.064	0.231	0.398	6.64	0.421	404
13	0.032	0.085	0.338	0.591	5.86	0.645	388
15	0.033	0.084	0.328	0.571	6.05	0.583	365
16	0.039	0.408	0.746	1.084	6.33	1.063	507

where $\Delta C^*_{21} = \dfrac{\bar{C}_2 - \bar{C}_1}{C_\infty (Q^*_{z_c})^{2/3}}$

and C_∞ = Room Air CO_2 concentration

$\bar{C}_1$ = Floor Zone CO_2 concentration

$\bar{C}_2$ = Ceiling Zone CO_2 concentration

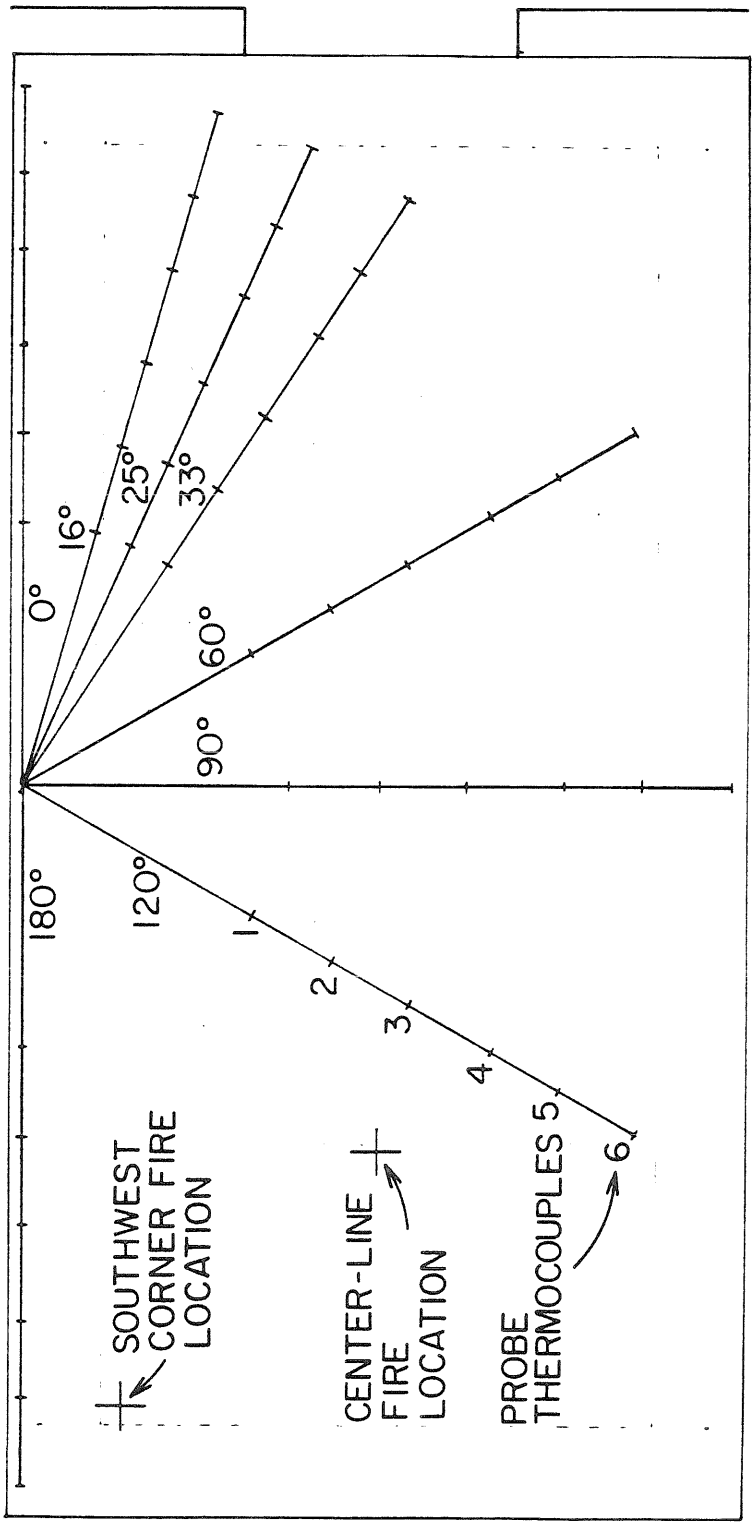

Figure (7.5) Standard Angular Locations at Which Vertical Temperature Profiles Were Measured

Examination of the temperature and CO_2 concentration data yields several general results concerning the behavior of the interior gas. By "interior gas" we mean gas which is at least 15-23 cm from a vertical wall. In this interior section of the room, one very obvious result is that all probes see a mean temperature profile which is very close to the mean profile measured during the 90^o vertical traverse, and which we use to estimate the piecewise linear profile. The CO_2 concentration shows the same results, although the data are somewhat more scattered due to fluctuations which were inherent in the CO_2 analyzer, and the time delay imposed by the gas sampling system. This uniformity in the temperature and concentration profiles indicates that the interior gas is well-mixed. Secondly, because the profiles all match, the interface zone between z^- and z^+ must be of constant depth throughout the interior of the room. It does not grow with distance from the doorway, as one would expect in the case of a mixing layer.

A detailed comparison of the temperature fluctuation data, like that shown in Figure (7.3), confirms the trends just mentioned: uniformity of the mean temperature profile and a constant thickness interface zone. In addition the temperature fluctuation levels appear to be primarily functions of height and depend only weakly on the lateral or longitudinal position within the room. In particular, the fluctuations are small in both the floor and ceiling zones (excluding the ceiling jet). The primary region of large temperature excursions is confined to the interface zone between z^- and z^+. These observations imply that hot gas from the ceiling zone does penetrate into the interface zone some of the time, thereby producing large values of s_T, but that it does not significantly penetrate below z^- or else we would see much larger fluctuations in the floor zone,

Some flow visualization data suggest that in the interior of the room, a substantial fraction of the fluctuations observed in the interface zone is caused by waves on a fairly sharp interface. The waves are of small amplitude (very roughly 10 cm), have wave lengths of roughly 50 cm, and do not break.

The exceptions to these general trends occur close to the door or the fire plume where fluid enters or leaves the system, and close to the floor and ceiling where convective heat transfer processes affect the gas. Near the fire, probes such as 2,3 and 4 on the 120^{o} vertical traverse (for center line fires) encounter intermittent hot regions of gas at the edge of the plume. This produces larger temperature fluctuations in the ceiling zone and ceiling jet than occur elsewhere. On the other hand, very near the door, the inflowing door-jet is at a uniform temperature (T_{∞}) and so s_T is very small.

As indicated by the rather short transient time scale for the upper layer gas ($t_{res} \sim 16$ s), the fluid in the room appears to be agitated and mixing processes are rapid. As a result, the door jet of ambient air at T_{∞} is quickly dispersed, heated, and mixed to form the nearly uniform floor zone gas at $\overline{T}_1$. By the time the gas reaches probe 1 (Figure (7.3)) in the middle of the room, all that is left of the door jet is a shallow tongue, roughly 15 cm thick, of gas which is slightly cooler than the floor zone linear profile ($\Delta T \sim 2.5^{o}C$, $\Delta T^* \sim 0.2$). In addition, as can be seen from Figure (7.3), this gas experiences slightly higher fluctuation levels than the majority of the floor zone gas. Where does this sub-layer of cooler gas originate? In part it is a remnant of the door jet. The hydrostatic pressure difference driving the inflowing door jet will be greatest at the floor resulting in the

largest velocity there. Then because the gas is cooler than the mean floor zone gas, buoyancy will tend to force this fluid to spread out over the floor, and indeed this cooler sub-layer of gas is evident over most of the floor. However, there appears to be some asymmetry in this process. In particular, this cooler sublayer is more pronounced in the eastern half of the room, which may mean that the door jet bends towards the left as it enters the room. Similar swirl patterns were also observed in the 1/4 scale brine simulation.

Given the fact that the floor temperatures (and those of the lower side walls) are consistently larger than the gas temperatures at neighboring locations, natural convection is the chief candidate for driving the mixing process which homogenizes the floor zone. For example, 24 cm from the doorway along the room's major axis the floor is $15^{o}C$ hotter ($\Delta T^* \sim 1.23$) than the inflowing door jet, while in the middle of the room this temperature difference has increased to $26^{o}C$ ($\Delta T^* \sim 2.15$). Finally, in the back half of the room, the difference has further increased to $33.8^{o}C$ ($\Delta T^* \sim 2.77$). Because of these significant temperature differences, we expect the initially cooler gas in contact with the floor to rise and mix with the majority of the floor zone gas. On the other hand since most of the measured floor temperatures are close to the mean gas temperature at $\bar{z}$, we would not expect this convection process to extend very far above the lower boundary of the interface zone. Taking $\bar{z}$ then as the length scale, we can form a Grashof number based on the temperature difference between the floor and the mean lower layer temperature $\bar{T}_1$. This parameter has a numerical value 2.7×10^{8} (or equivalently the Rayleigh number is 1.9×10^{8}), which indicates that the flow will be irregular and turbulent.

In addition to convection effects in the vicinity of the floor (which is heated by radiation), convective heat transfer also significantly affects the ceiling jet behavior. To examine the change in the ceiling jet one can draw an imaginary line 40 cm in from the west wall and ask, "How does the ceiling jet change along this line as a function of distance from the fire?" Figure (7.6) presents the data of probe 1 from the 120^{o} vertical traverse. The probe was 45 cm from the plume axis and shows a ceiling profile with a large temperature excess ($\Delta T \sim 20^{o}C$ above the ceiling zone profile) with the peak located just 1.7 cm below the ceiling. In addition, the temperature fluctuation level is rather high, and is comparable to the deviations in the interface zone. Proceeding outwards, the data in Figure (7.3) show that at a radial distance of 63 cm heat transfer to the ceiling has produced a fuller ceiling jet profile with a smaller temperature excess ($\Delta T \sim 11^{o}C$) with the peak located 6 cm below the ceiling. Furthermore the fluctuation level is much smaller. However, the overall depth of the layer measured by the deviation from the ceiling zone gradient remains nearly constant ($\hat{\delta} \sim 15$ cm). The data in Figure (7.7), measured 84 cm from the fire, show a further erosion of the maximum temperature excess ($\Delta T \sim 10^{o}C$) which occurs approximately 8.8 cm below the ceiling. However, the pattern changes in Figure (7.8), which presents data measured 122 cm from the plume axis by probe 3 during a 33^{o} vertical traverse. Here the mean temperature excess and large temperature excursions which characterized the ceiling jet in the previous figures have all but disappeared, having been eroded by heat transfer to the ceiling and by entrainment of cooler gas from the ceiling zone. Thus it is next to impossible to identify the ceiling jet. On the other hand, the main

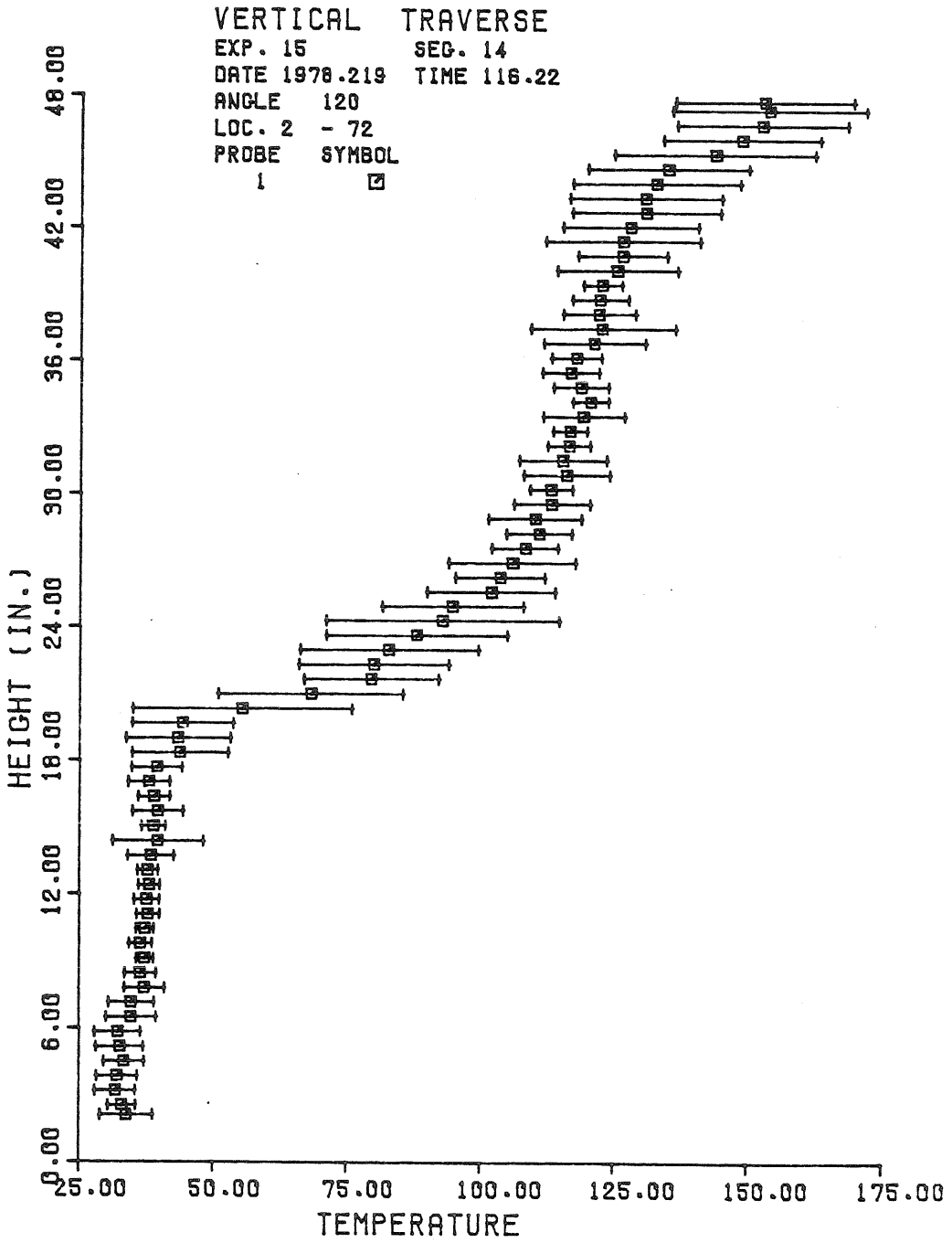

Figure (7.6) Gas Temperature Profile 45 cm from the Plume Axis (Exp. 15).

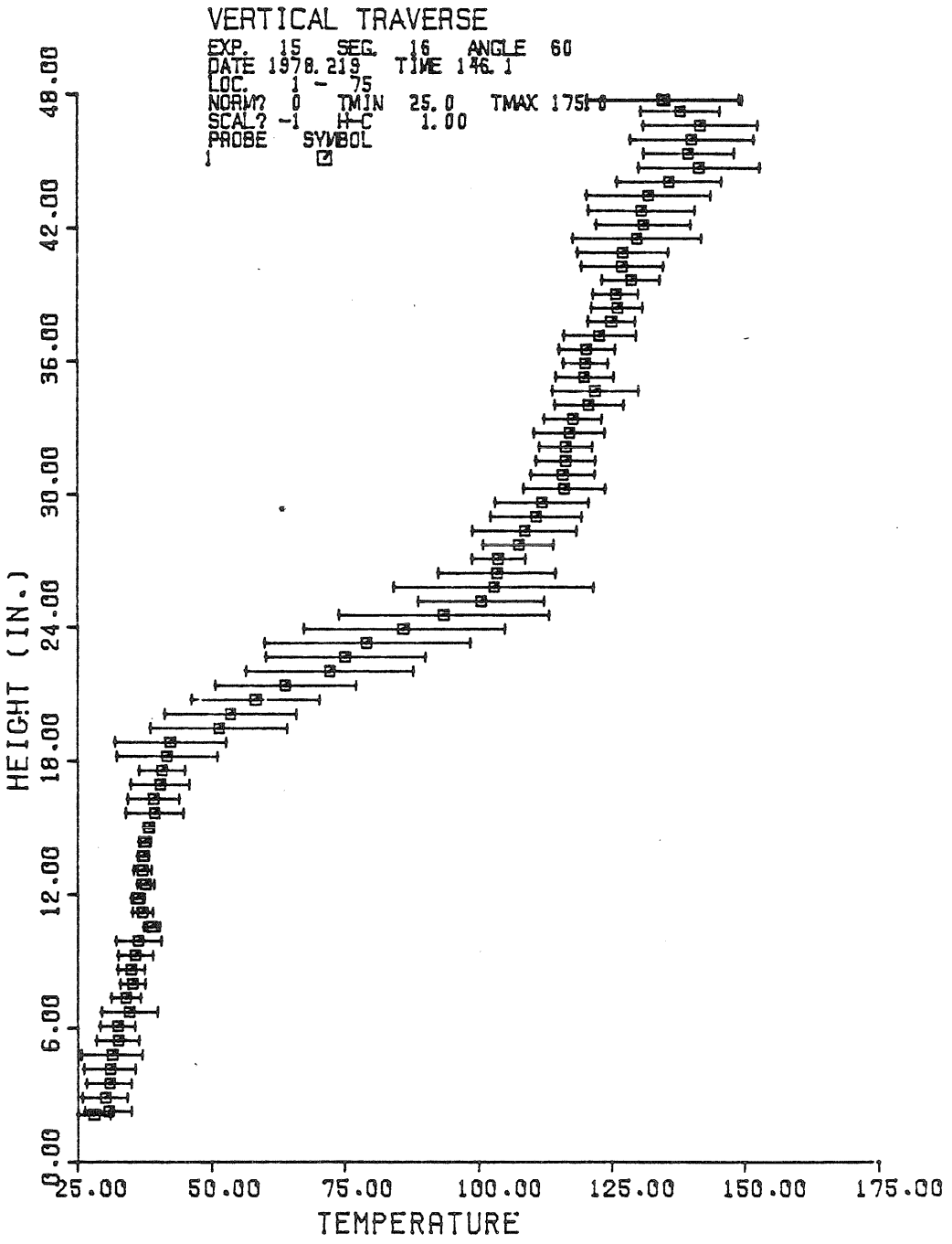

Figure (7.7) Gas Temperature Profile 84 cm from the Plume Axis (Exp. 15).

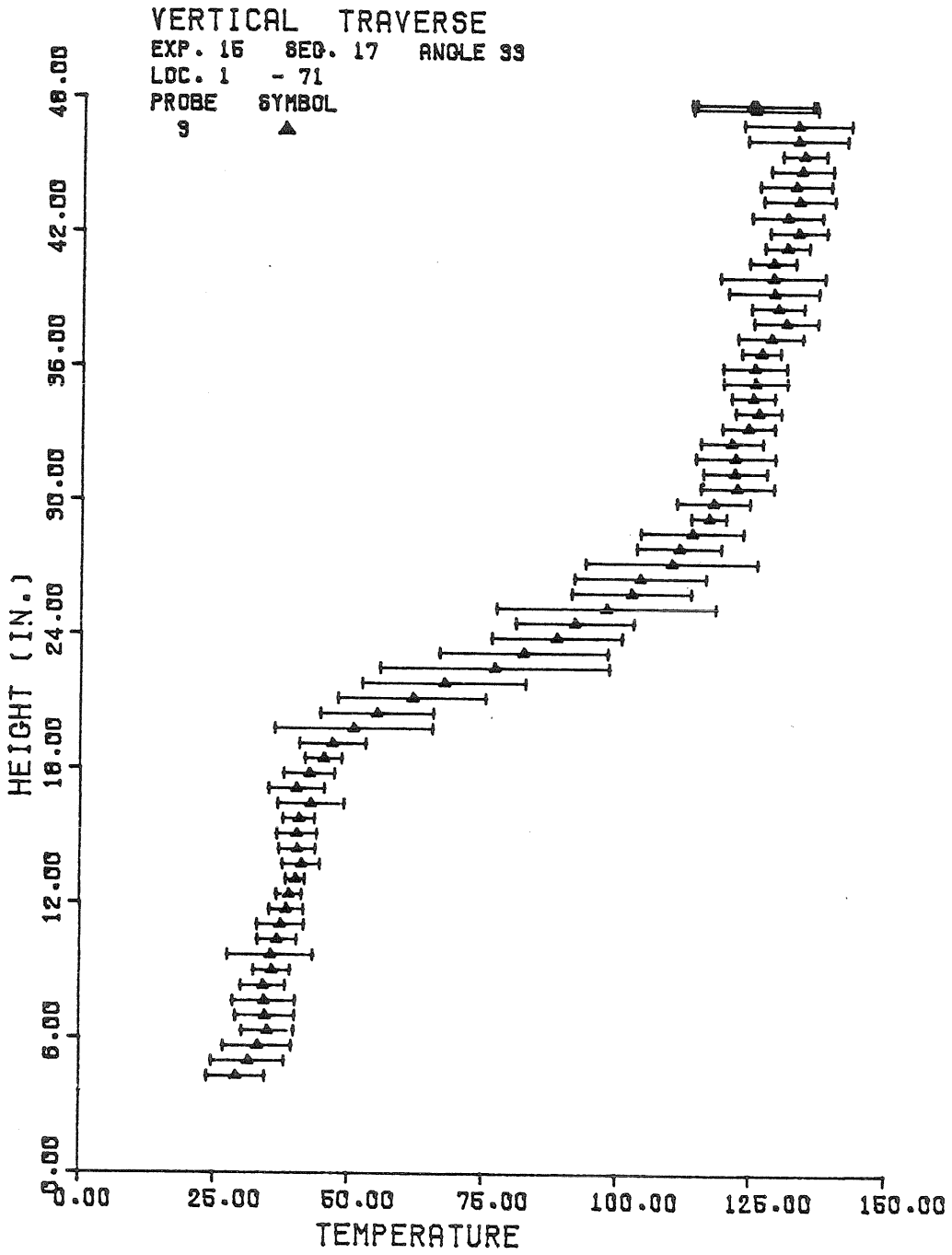

Figure (7.8) Gas Temperature Profile 122 cm from the Plume Axis (Exp. 15).

body of the upper layer gas is now 2-5^{o}C hotter than the linear ceiling zone profile. This deviation from the standard pattern seen in the majority of the interior may be caused by several factors. The pattern observed in Figure (7.8) is typical of that seen near side walls, where we assume hotter gas, originally from the ceiling jet, flows down the side walls until it experiences a large increase in its buoyancy in the interface zone. However, probe 3 in Figure (7.8) is located 61 cm from the nearest (north) wall, while the side wall flow zone is typically comparable in thickness to the ceiling jet ($\sim$ 15 cm). Thus it does not seem likely that we are seeing a similar direct wall flow here. However, the slightly warmer and more uniform ceiling zone profile may be caused by gas from the originally axisymmetric ceiling jet impinging on the side walls near the mid plane of the room and then being reflected back toward the interior of the room. On the other hand, the ceiling jet calculations discussed in Chapter VIII suggest that entrainment in the upper plume and ceiling jet increase the mass flow in the ceiling jet to a value several times the size of the mass flow in the plume crossing the interface. Because the height of the interface is constant, only this latter amount of gas can escape out the doorway. Consequently, there will be considerable recirculation of gas in the upper layer, and this returning ceiling jet gas may be responsible for the slight increase in ceiling zone temperatures. Finally, data measured by probe 5 during a 25^{o} vertical traverse are presented in Figure (7.9). The majority of the ceiling zone data is nearly identical to that shown in Figure (7.8). The only significant difference is that the gas in the upper most 11 cm is now slightly cooler than the gas below it and hence the "ceiling jet"

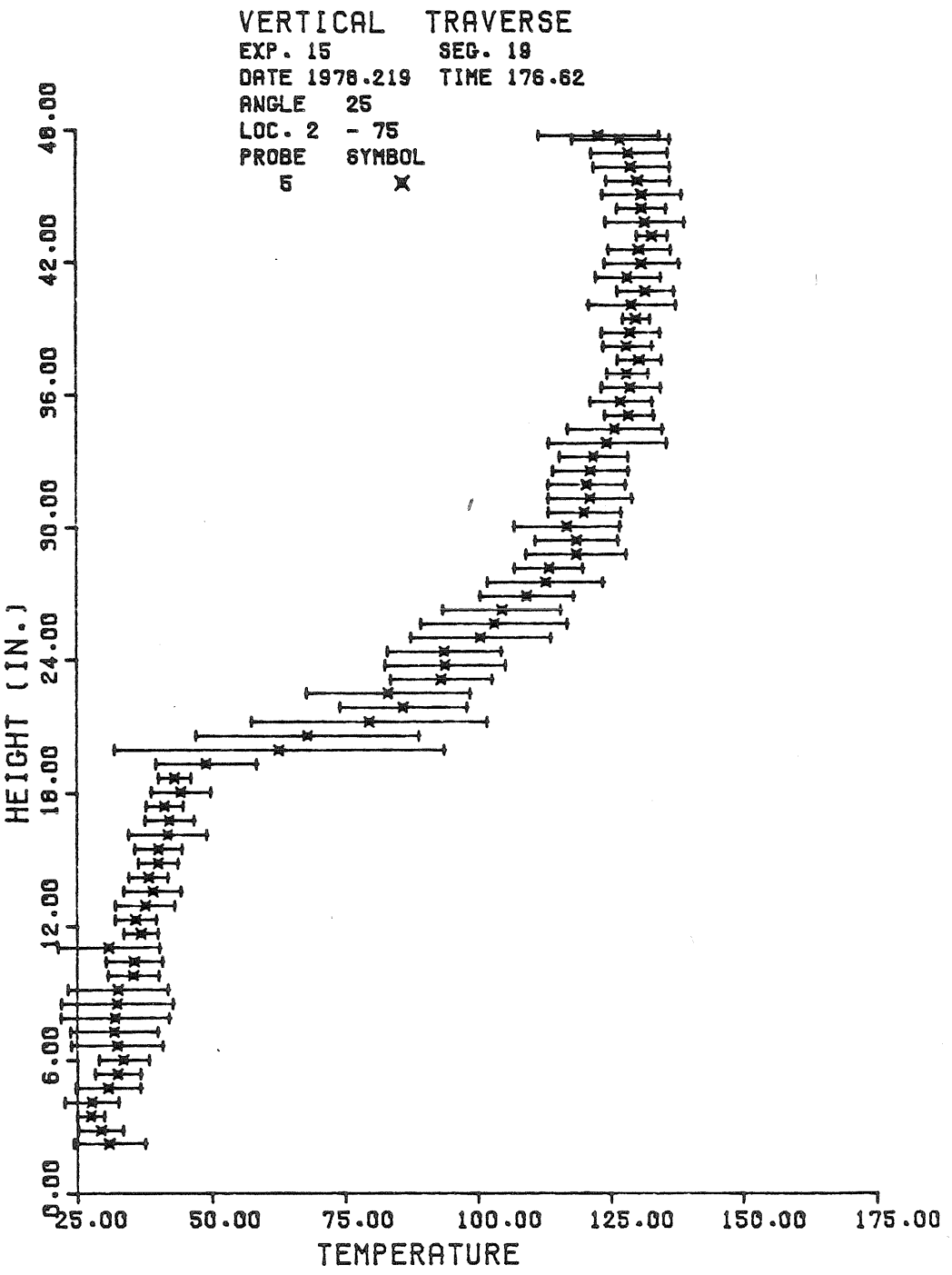

Figure (7.9) Gas Temperature Profile near the North Wall (Exp. 15).

is now negatively buoyant. Since this traverse occurs roughly 29 cm from the north wall, again it does not seem likely that we are seeing a direct wall flow effect. Instead it appears that in the main body of the ceiling zone we are seeing returning gas from the ceiling jet which has interacted with the north end wall and is now flowing toward the plume.

Finally, it may be noted that although it becomes progressively more difficult to identify the boundary of ceiling jet from the temperature data, nevertheless, this flow region appears to be of nearly constant thickness. In addition the temperature decreases gradually with distance. Thus there is no direct evidence for an internal hydraulic jump in the interior of the room. Second, note that the maximum gas temperature, which occurs at progressively greater depths below the ceiling in the ceiling jet as the distance from the fire increases, is nevertheless rather close to the gas temperature 2.5 cm below the ceiling. This is important because in calculating the heat transfer coefficient we use the latter gas temperature as an estimate of the former. The error in this approximation is roughly $5^{o}C$ or less in the interior of the room where we expect our ceiling jet calculation to be valid. This error is less than 7% of the gas-ceiling temperature difference, which is eventually used to find the heat transfer coefficient.

7.3.2 Sidewall Flow Patterns

Within 15-20 cm of the vertical walls, the temperature profile changes from that observed in the majority of the room. This transition is displayed in Figures (7.10), (7.11), and (7.12) which present temperature data measured 47, 18, and 3 cm, respectively, from the east side wall in the middle of the room.

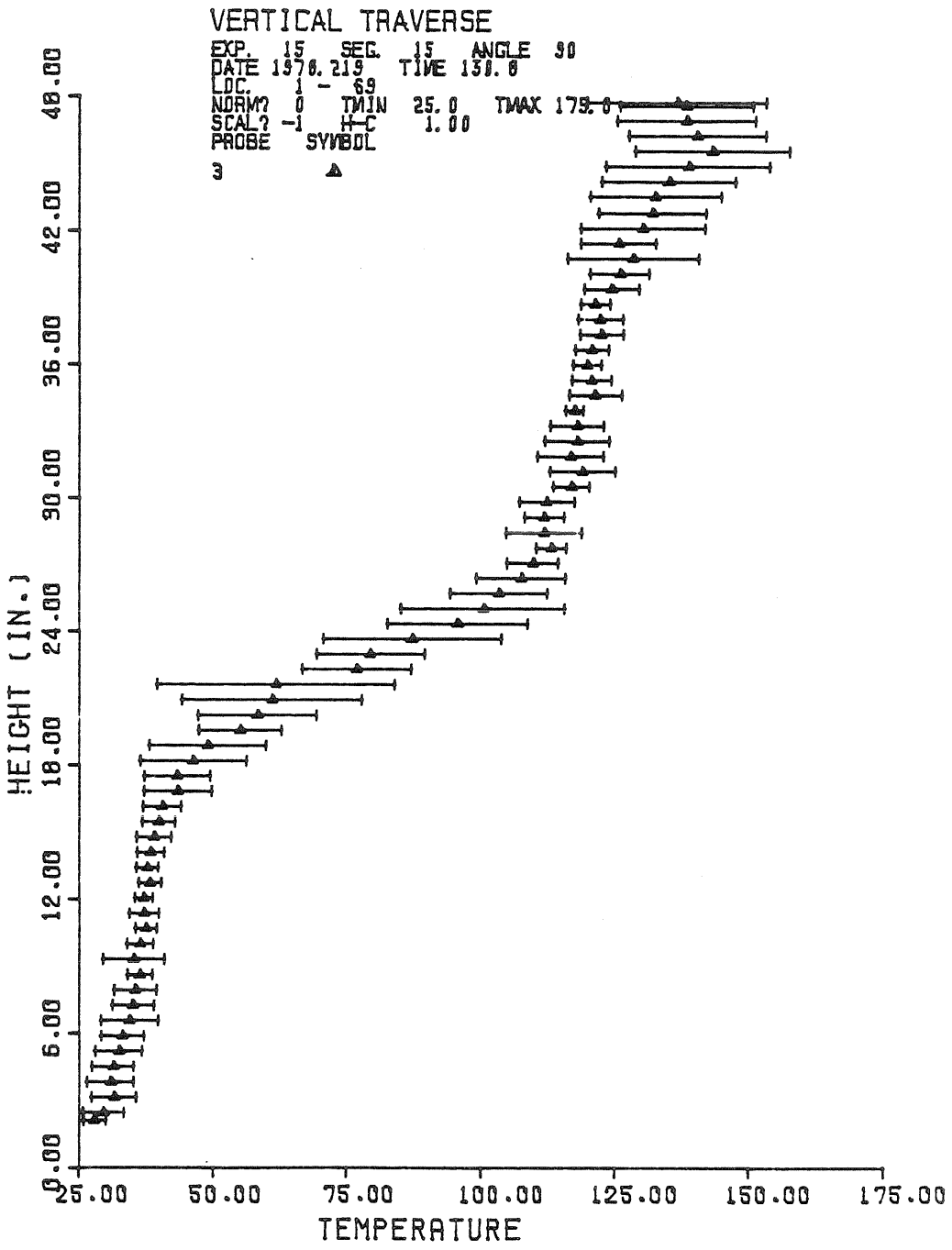

(Figure 7.10) Gas Temperature Profile 47 cm from the East Wall (Exp. 15).

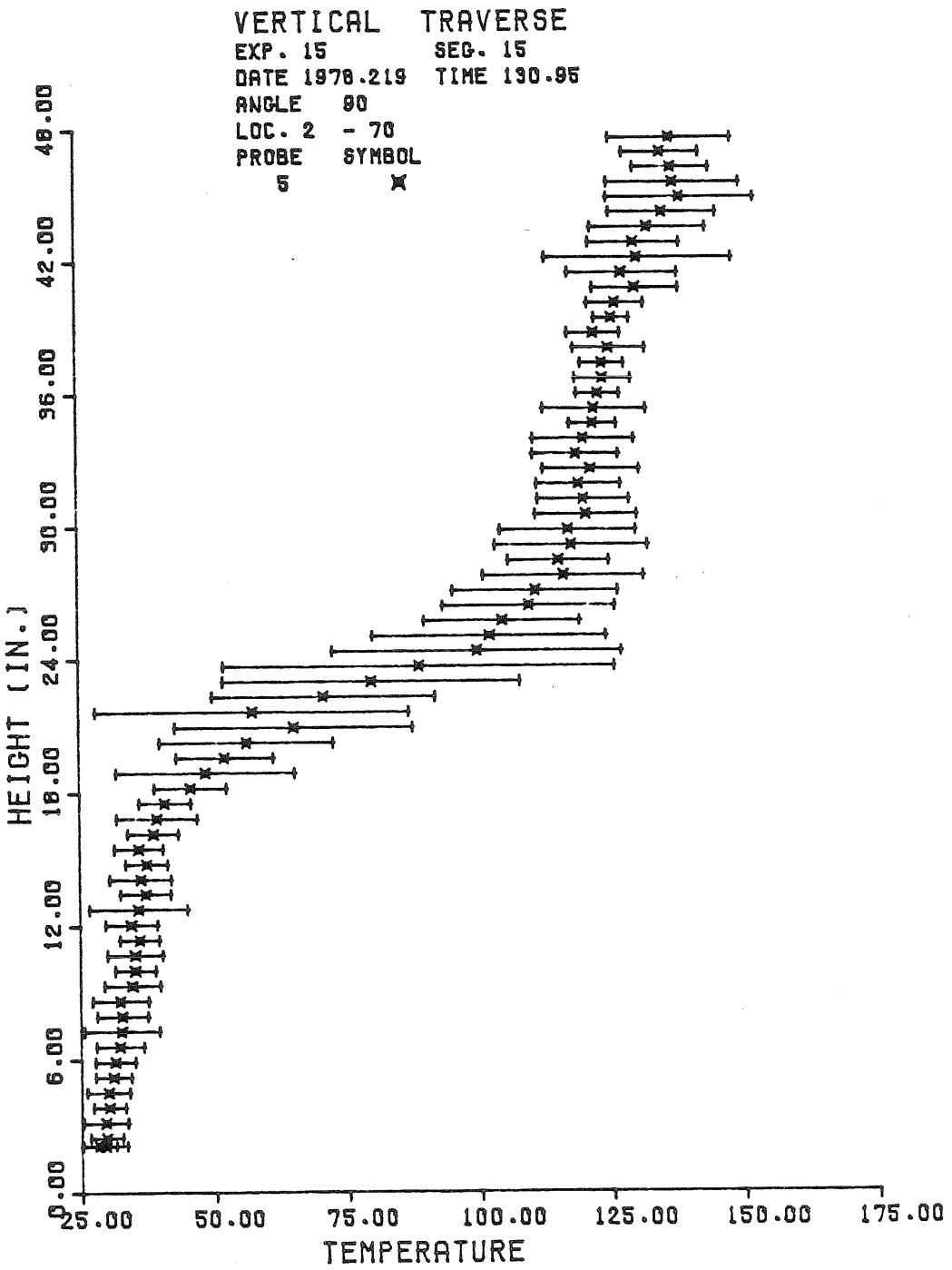

Figure (7.11) Gas Temperature Profile 18 cm from the East Wall (Exp. 15).

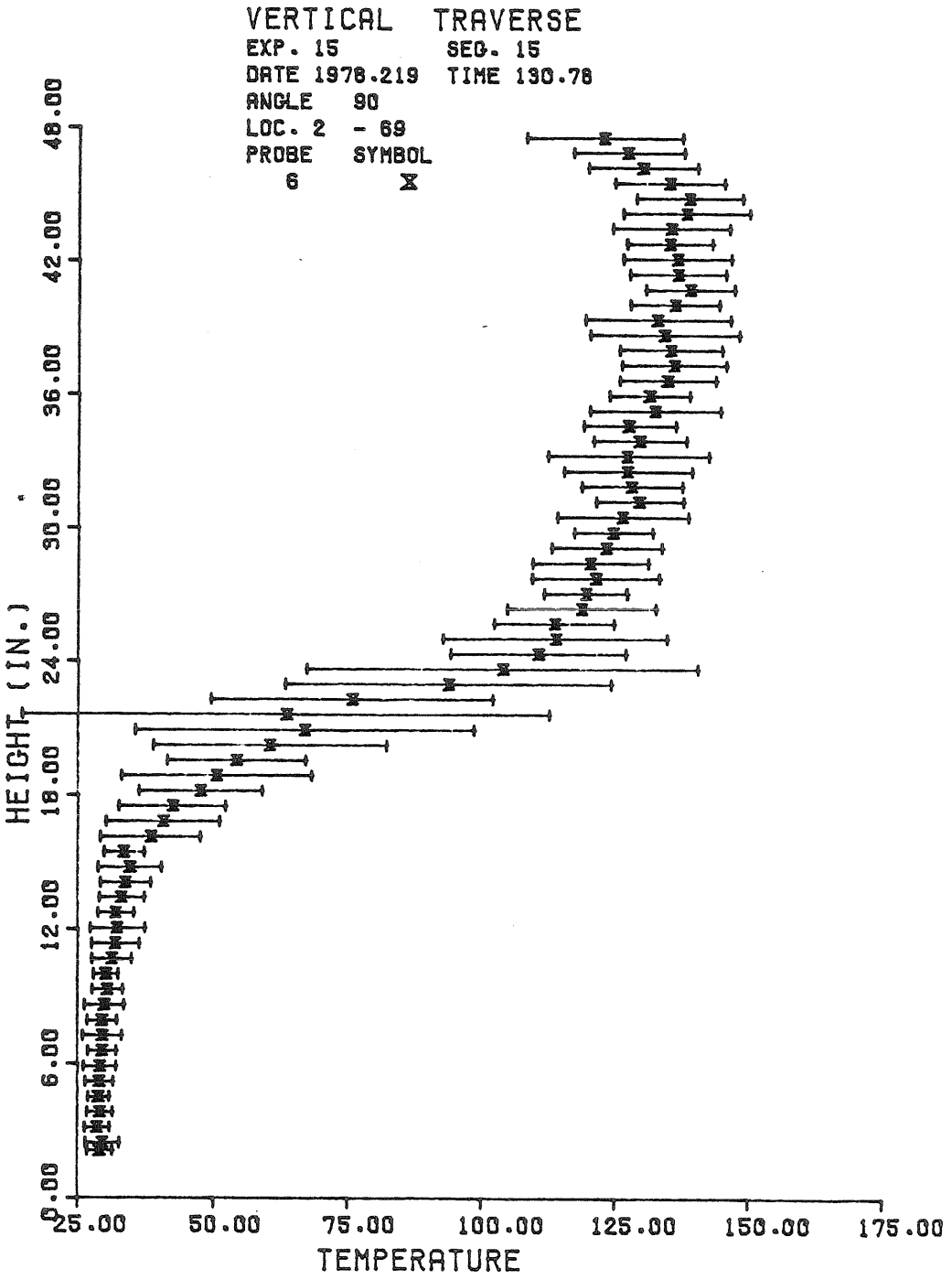

Figure (7.12) Gas Temperature Profile 3 cm from the East Wall (Exp. 15).

The data in Figure (7.10) are almost identical to those in Figure (7.3) which were measured 46 cm from the west wall. The only asymmetry is the greater depth of floor sublayer in Figure (7.10). This slightly cooler sub layer with moderate temperature fluctuations becomes progressively thicker and cooler as one approaches the east wall, until 18 cm from the wall, the bottom 39 cm of the floor zone is filled with this 3-5^{o} cooler gas, as shown by Figure (7.11). Finally, next to the wall, the gas in the floor zone is consistently 6^{o}C cooler than the interior floor zone gas. Near the floor, it also experiences smaller temperature fluctuations because the presence of the two solid surfaces inhibit mixing (Figure (7.10)).

One might think that the presence of this cooler gas near the wall was evidence of a natural convection flow down the wall. However, the wall 30 cm above the floor is 15^{o}C ($\Delta T^* \sim 1.23$) hotter than gas at the same height, so that the gas in contact with the wall will in fact be heated and tend to rise towards the interface. Instead, we think this cooler gas is the remnant of the door jet of fresh air flowing into the room. It appears to enter the room obliquely and impact upon the east wall near the middle of the room. One possible reason for this asymmetric flow pattern is the geometry of the laboratory and its ventilation. Our test chamber was located near the east end of a long rectangular laboratory. During the course of an experiment, fresh air was allowed to enter the laboratory at the far west end and was exhausted by a large hood located over the north end of our 1/2 scale test chamber. We might expect therefore that the gas entering the door of our test room might possess a small amount of momentum in an easterly direction, which could cause the door jet to progress towards the east wall.

Because the lower side walls are consistently hotter than the neighboring gas, natural convection probably does occur, with the heated gas rising towards the interface. As we have just seen, along the east wall this process may be a combination of forced and natural convection. On the other hand along the west wall there is no evidence of fluid which is cooler than the floor zone profile (i.e. the door jet), and so we might expect natural convection to occur at the wall. Based on the mean gas-wall temperature difference of $9.6^{o}C$ along this wall and the height of the lower edge of the interface zone $\bar{z} = 0.50$ m, we find that the Grashof number for flow up the wall is 1.6×10^{8}. Given the disturbances present inside our apparatus, this indicates the flow is probably turbulent.

One can estimate the mass flux which this process delivers to the interface zone by performing an integral analysis as suggested by Eckert and Jackson (1950). The estimated mass flow can then be found from integrating their suggested turbulent velocity profile. Substitution of our data into this expression (kindly provided to me by Dr. Baki Cetegen) indicates that natural convection on all of the lower walls delivers to the lower edge of the interface zone at $\bar{z}$ a flow which is very nearly 1/5 of the calculated mass flux in the plume at the interface. Thus while the plume is still the predominant source of mass delivered to the interface, natural convection, driven by radiation from the ceiling and upper walls, plays a significant role in heating and mixing the floor zone gas.

While local natural convection is probably the dominant heat transfer mechanism along the sidewalls beneath the interface zone, above the lower

edge of the interface the vertical walls appear to be heated primarily by a forced convection flow of hotter than average gas which originates in the ceiling jet and which appears to flow down the sidewalls. This gas penetrates into the interface zone, occasionally reaching the lower edge of the interface z^-.

As one would expect from such a flow pattern, the flow will be more vigorous nearer the source, and near the corners of the room where the presence of the two adjoining vertical walls acts to channel the flow down along this junction. The mean temperature data presented in Figure (7.13) from the six probe theromocouples positioned along the rear half of the west wall tend to confirm these hypotheses. While the floor zone gas is only very slightly warmer than the approximate floor zone linear profile, the ceiling zone gas is roughly 20^oC hotter ($\Delta T^* \sim 1.6$) than the ceiling zone linear profile. At neighboring locations, the upper west wall itself is an average of 61^oC ($\Delta T^*_{gw} \sim 5.0$) colder than this gas, so that the upper side wall experiences considerable convective heat transfer from this hot gas. In addition, the effective lower edge of the ceiling zone z^+_{eff}, as determined by the intersection of the local ceiling and interface zone gradients, falls by at least 4.7 cm which is 32% of standard interface zone thickness ($z^+ - z^-$) for all probes. This increasing depth of the ceiling zone becomes progressively larger as one approaches the southwest corner of the room until probe 6, which is 5.6 cm from this corner, sees the ceiling zone extending down through the entire mean interface zone (i.e. $z^+_{eff} \sim z^-$). In addition, the effective lower edge of the interface zone z^-_{eff} also falls 7.8 cm below the value of z^- for the interior of the room. Very similar trends are also apparent in Figure (7.14) which presents the temperature profiles

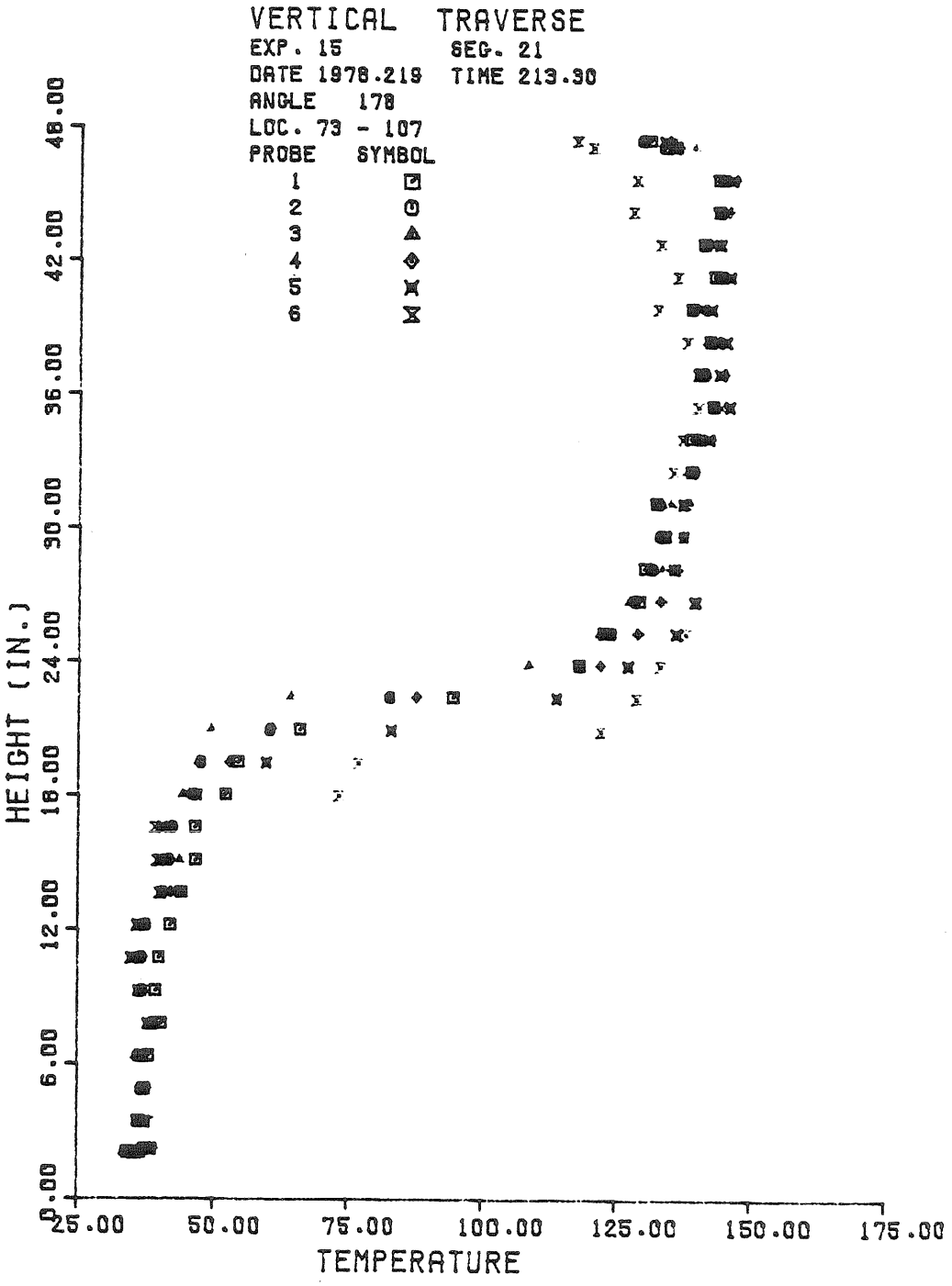

Figure (7.13) Gas Temperature Profiles along the Rear Half of the West Wall (Exp. 15).

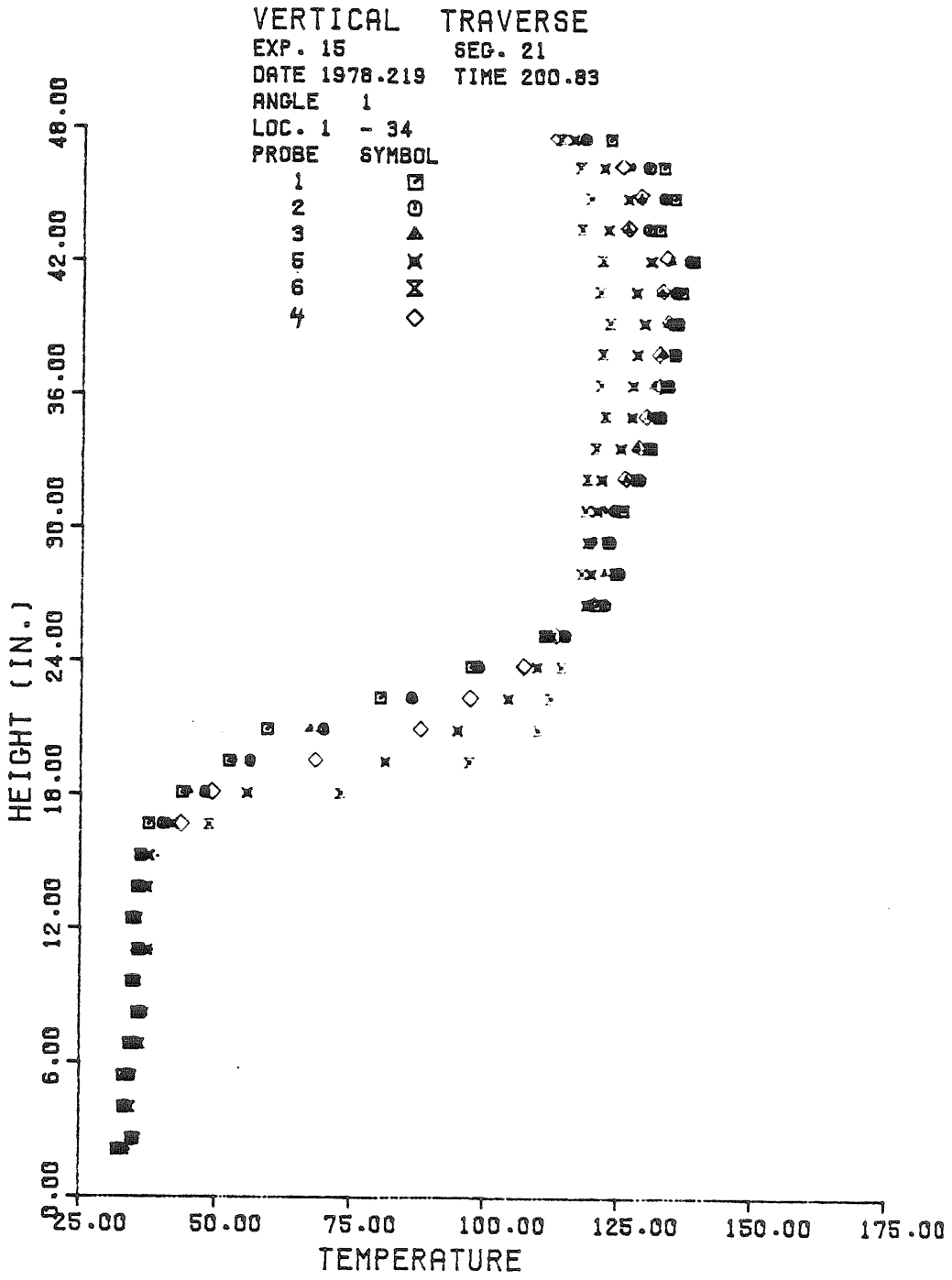

Figure (7.14) Gas Temperature Profiles along the Front Half of the West Wall (Exp. 15).

measured along the north half of the west wall. Here again most of the probes see hotter than average gas in the ceiling zone. Because we are relatively far from the fire, the temperatures decrease progressively as we approach the northwest corner of the room, corresponding to the progressively larger convective losses experienced by the gas in the ceiling jet. Note also that probes 4 and 5, which are 3.4 and 20 cm respectively from the north wall, see progressively lower interface zones until 6 cm from the north wall the interface zone measured by probe 6 is completely beneath the interface zone seen in the interior of the room.

Returning to Figures (7.10) - (7.12) we can examine the development of this flow pattern along a section normal to the wall. Figure (7.10) presents the basic interior gas upper layer behavior: a hot, vigorous ceiling jet, occupying the upper 18 cm of the room, and beneath it, the ceiling zone with mean temperatures close to the ceiling zone linear profile and rather small temperature fluctuations about the mean.

Closer to the wall, the temperature fluctuation data in Figure (7.11) show significant changes from the standard ceiling zone and interface zone profiles, even though the mean temperature data are very close to the mean data in Figure (7.10), except for the uppermost section of the ceiling jet which is 2-5^{o}C cooler. In particular, the data measured by probe 5, which was 18 cm from the east wall, indicate a significant increase in the temperature fluctuations just 14 cm below the lower edge of the ceiling jet. These large temperature excursions are observed down through most of the ceiling zone and are especially pronounced just above and through the interface zone.

Finally, 3 cm from the east wall, the mean temperature data, as well as the fluctuations, show significant deviations from the interior ceiling and interface profiles. The "ceiling jet", if it indeed exists here, is now limited to the top 7.7 cm compared to 18 cm for the majority of the room. It is now a region of sharply falling temperatures ($\Delta T \sim 15^{o}C$) as one approaches the ceiling, and probably indicates a separated flow region in the neighborhood of the junction of the ceiling and the east wall, similar to that seen by Zukoski, Kubota and Veldman (1975) in their curtain wall tests. Beneath this separated flow region, the ceiling zone extends through most of the upper layer and is $10\text{-}12^{o}C$ ($\Delta T^* \sim 0.9$) hotter than the interior ceiling zone profile. At the same time, the east wall is $54^{o}C$ ($\Delta T^*_{gw} \sim 4.4$) colder than this gas, and thus receives a large convective flux from this flow down the wall. Note that if this were a natural, rather than a forced, convection flow, we would expect to find the gas near the wall to be <u>colder</u> than the interior gas. Unfortunately we could not measure gas temperatures closer than 3 cm from the east wall, because in fact there must be a thermal boundary layer close to the wall where the gas temperatures fall and approach the wall temperature.

In order to check whether the ceiling jet fluid has sufficient momentum to penetrate down the wall to the interface at z^+, we can form a Richardson number in the form of the ratio of the hydrostatic head to the dynamic pressure of the ceiling jet fluid:

$$Ri_w = 2\, g \frac{\Delta T}{T_2} \frac{(z_c - z^+)}{U^2} \qquad (7.3)$$

where $\Delta T \sim 10^{o}C$ is the temperature difference between the gas near the wall and the gas in the interior of the room at the same height, and U is the calculated bulk velocity in the axisymmetric ceiling jet described in Chapter VIII. Evaluated at the middle of the east wall, Ri_w is 0.74, which indicates that the ceiling jet fluid has sufficient dynamic pressure to penetrate through the ceiling zone, until it experiences a large increase in its buoyancy within the interface zone. This intermittent penetration of hot gas results in the very large temperature excursions and the $10\text{-}12^{o}C$ hotter mean temperatures seen in the interface in Figure (7.12). Note that if there were just waves on the interface sloshing up and down against the side walls, one would also see large temperature excursions, but the mean temperature would not be consistently hotter. Finally, after this hot gas penetrates, buoyancy will force the hotter sections of gas up through the interface and back into the lower ceiling zone, which gives rise to the larger than normal temperature excursions seen in Figure (7.11) in the upper interface and lower ceiling zone 18 cm from the wall.

We can view this phenomenon of flow down the side walls from another perspective by examining gas temperature data acquired during horizontal traverses of the gas sampling boom. These data are presented in the form of contour plots in Figures (7.15), (7.16), (7.17) and (7.18) which were made at heights of 119, 107, 91, and 61 cm respectively.

The data in Figure (7.15), which were measured just 2.5 cm below the ceiling, show an axisymmetric decrease in temperature near the axis of the plume while in the front half of the room the data appear to follow a more two-dimensional pattern. Note that near the walls, and especially near the southwest corner, there is a sharp decline in temperature, which probably indicates a region of separated flow.

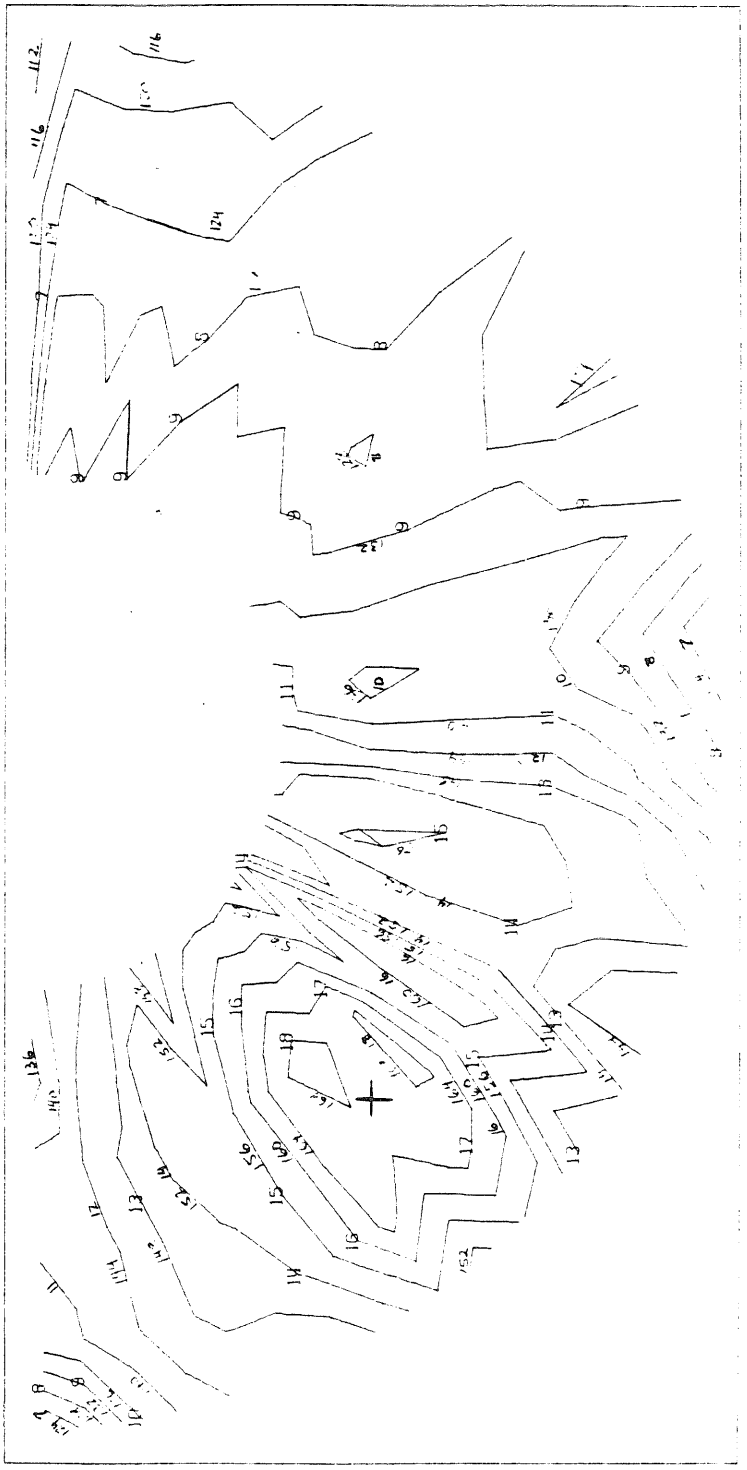

Figure (7.15) Gas Temperature Contours at a Height of 119 cm, 2.5 cm below the Ceiling (Exp. 15)

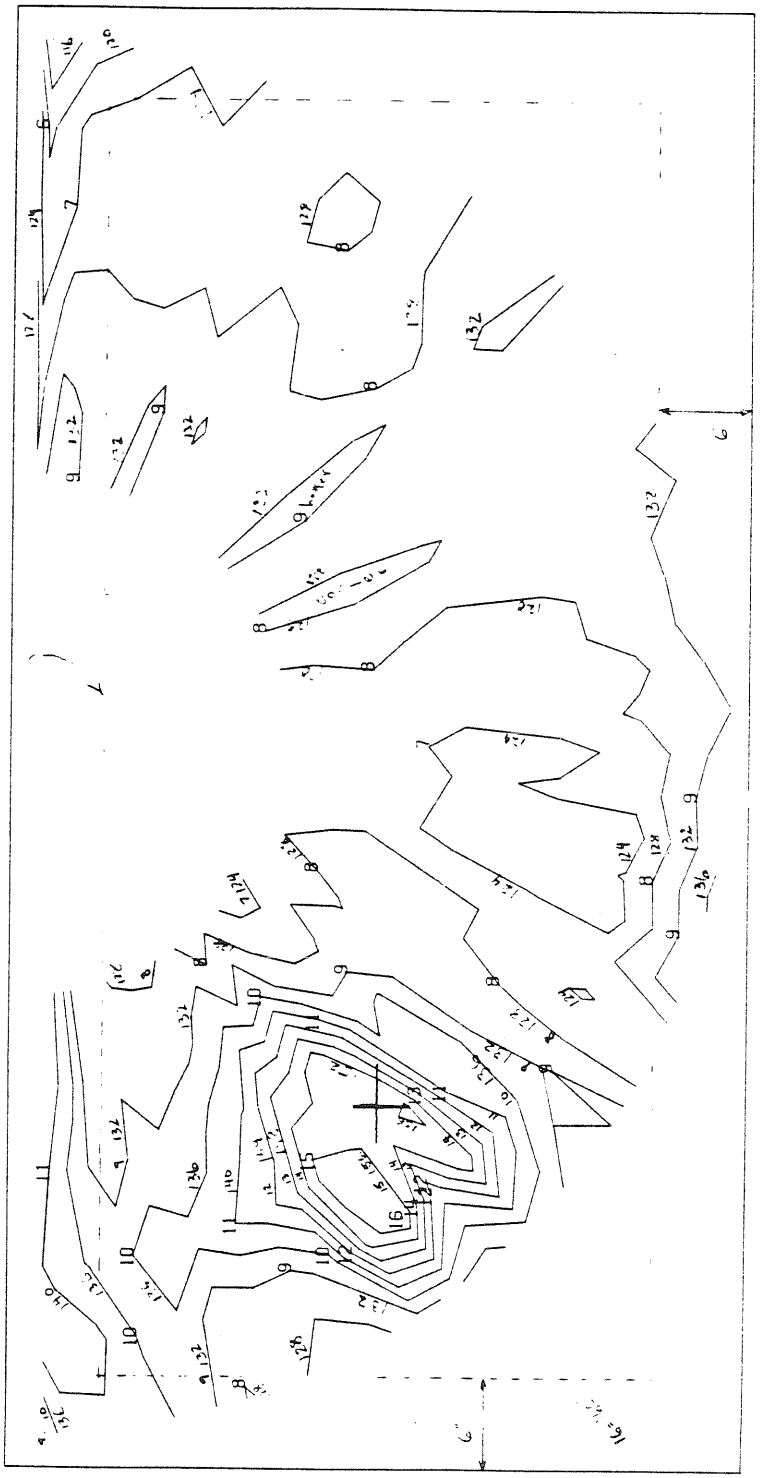

Figure (7.16) Gas Temperature Contours at a Height of 107 cm, 15 cm below the Ceiling (Exp. 15)

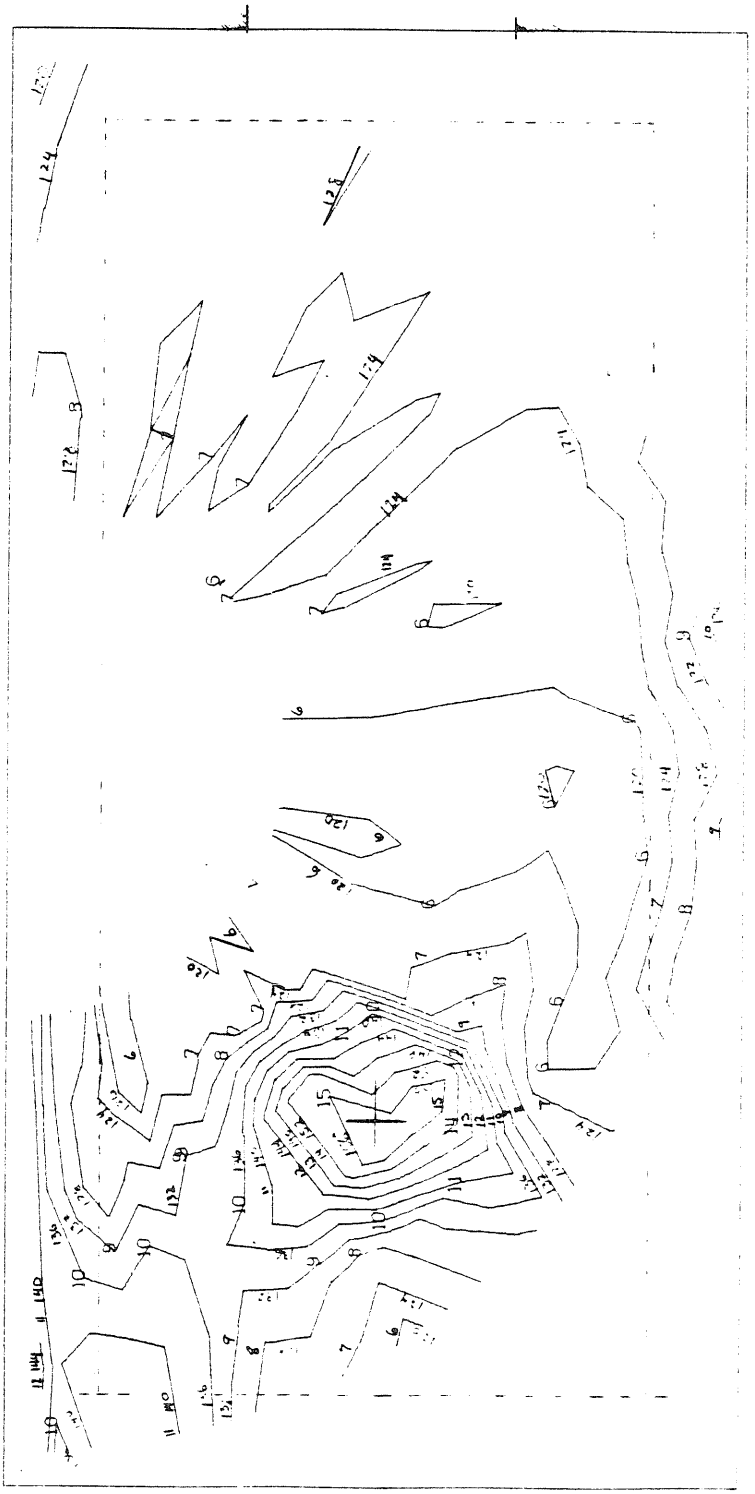

Figure (7.17) Gas Temperature Contours at a Height of 91cm (Exp. 15)

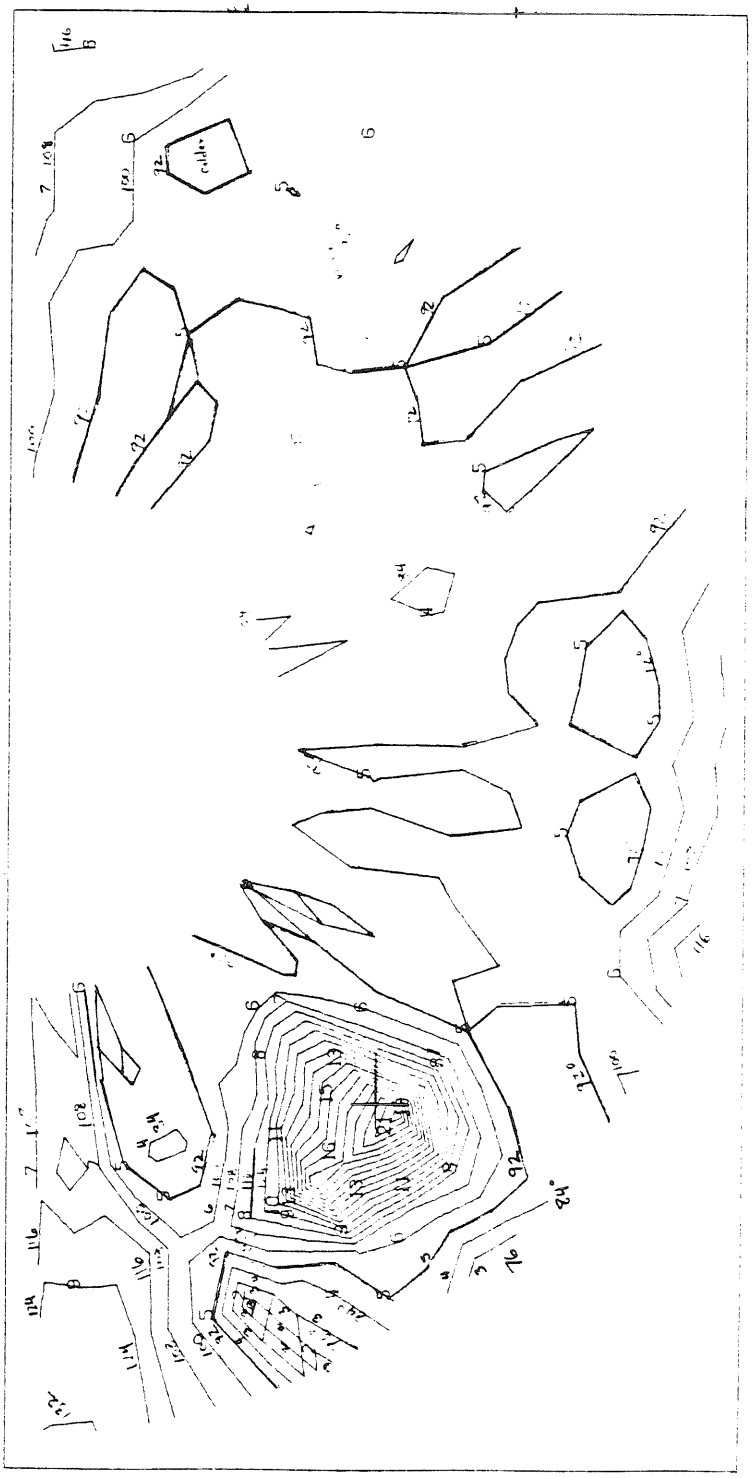

Figure (7.18) Gas Temperature Contours at a Height of 61cm (Exp. 15)

The dominant pattern of hot gas flowing down the side walls has already become established 15 cm below the ceiling, as shown by the data in Figure (7.16). This traverse, which was made at a height just below the lower edge of the ceiling jet, shows that hot gas, at temperatures characteristic of the gas seen near the ceiling in Figure (7.15), flows down the wall in a region some 15-20 cm thick. Across this zone there is a temperature increase of roughly 12-15^{o}C as one approaches the wall.

In the middle of the ceiling zone, 30.5 cm below the ceiling and 7.6 cm below the door soffit, this same pattern is again evident in Figure (7.17). In the center of the room the gas temperature has fallen to 120^{o}C, compared to 126^{o}C in Figure (7.16). However, along the east and rear half of the west side walls, the temperatures are nearly the same as they were in Figure (7.16). Thus the gas in this region along the walls is 16-24^{o}C hotter than it is in the interior of the room.

The data in Figure (7.17) also show that, unlike the data in Figure (7.16), the gas temperatures actually increase roughly 5^{o}C throughout the front third of the room. Note that the temperature range in this region (124-128^{o}C) is the same as in Figure (7.16). Thus this increase is probably symptomatic of the complex interaction between the flow leaving the room and the flow down the walls.

Finally, Figure (7.18) presents the temperature contours measured 4.5 cm below the upper edge of the interior gas interface zone z^{+}. Note that in the southwest corner, where we expect the channeling effect of the two side walls to produce the strongest effect, the gas is 40^{o}C hotter than the gas in the center of the room, whose temperature is roughly 92^{o}C. Note that along the east side wall there is also a strong

temperature gradient, but that the gas is only 24°C hotter here than in the interior. Finally, also note that nearly constant temperature gas flows down the northwest corner of the room as well. This gas, which has a temperature of approximately 116°C can be seen in the northwest corner of all 4 horizontal slices, and represents the ceiling jet gas which has experienced the greatest convective losses since it has flowed the greatest distance along the ceiling from the plume. Because it has lost more of its enthalpy than the surrounding gas, it is negatively buoyant in the ceiling zone, but, as shown in Figure (7.18), it is 24°C hotter and hence positively buoyant in the interface zone.

7.3.3 Flow Patterns near the Door

In addition to traversing probe, 13 bare wire thermocouples were strung across the outer edge of the doorway and attached to a moveable wooden frame. By sliding this frame along the outside face of the north wall, we were able to measure the temperature of the gas passing through the doorway at a number of spanwise locations. These data are presented graphically in Figures (7.19) and (7.20) and partially tabulated in Table (7.3). Figure (7.19), which is a plot of gas temperature versus height at 9 spanwise locations, can be compared directly to the previous vertical traverse plots and shows that the gas flowing through the doorway exhibits the same general trends as the gas in the interior of the room. In particular there are three reasonably distinct zones: a floor zone of ambient air flowing into the fire room, an interface zone characterized by a large gradient in mean temperature and by very large temperature excursions, and finally a ceiling zone of reasonably uniform, hot gas escaping from the room. The door frame was 7.6 cm (3 in.) thick and had sharp edges. Consequently we expect that the hot jet of escaping

Table (7.3) Doorway Temperature Data -- Exp. 15

Height [cm]	$\bar{T}$ [^{0}C]	s_T [^{0}C]	T_{min} [^{0}C]	T_{max} [^{0}C]	$\Delta T_{max-min}$ [^{0}C]
95.7	123.7	4.7	113.0	130.6	17.6
91.9	124.2	4.4	115.7	130.6	14.9
88.6	122.6	3.1	118.2	127.2	9.0
85.3	120.7	2.3	118.6	125.4	6.8
80.8	117.1	4.7	106.8	124.4	17.6
73.3	109.3	4.5	100.5	114.8	14.3
65.5	86.6	9.4	60.0	101.9	41.9
57.5	59.7	8.9	42.0	71.8	29.8
50.2	36.8	7.2	26.9	47.6	20.7
42.7	28.4	2.1	26.7	28.4	1.7
34.9	27.3	0.5	26.6	28.2	1.6
27.4	26.6	0.5	26.0	27.7	1.7
19.8	27.3	0.4	26.7	27.9	1.2

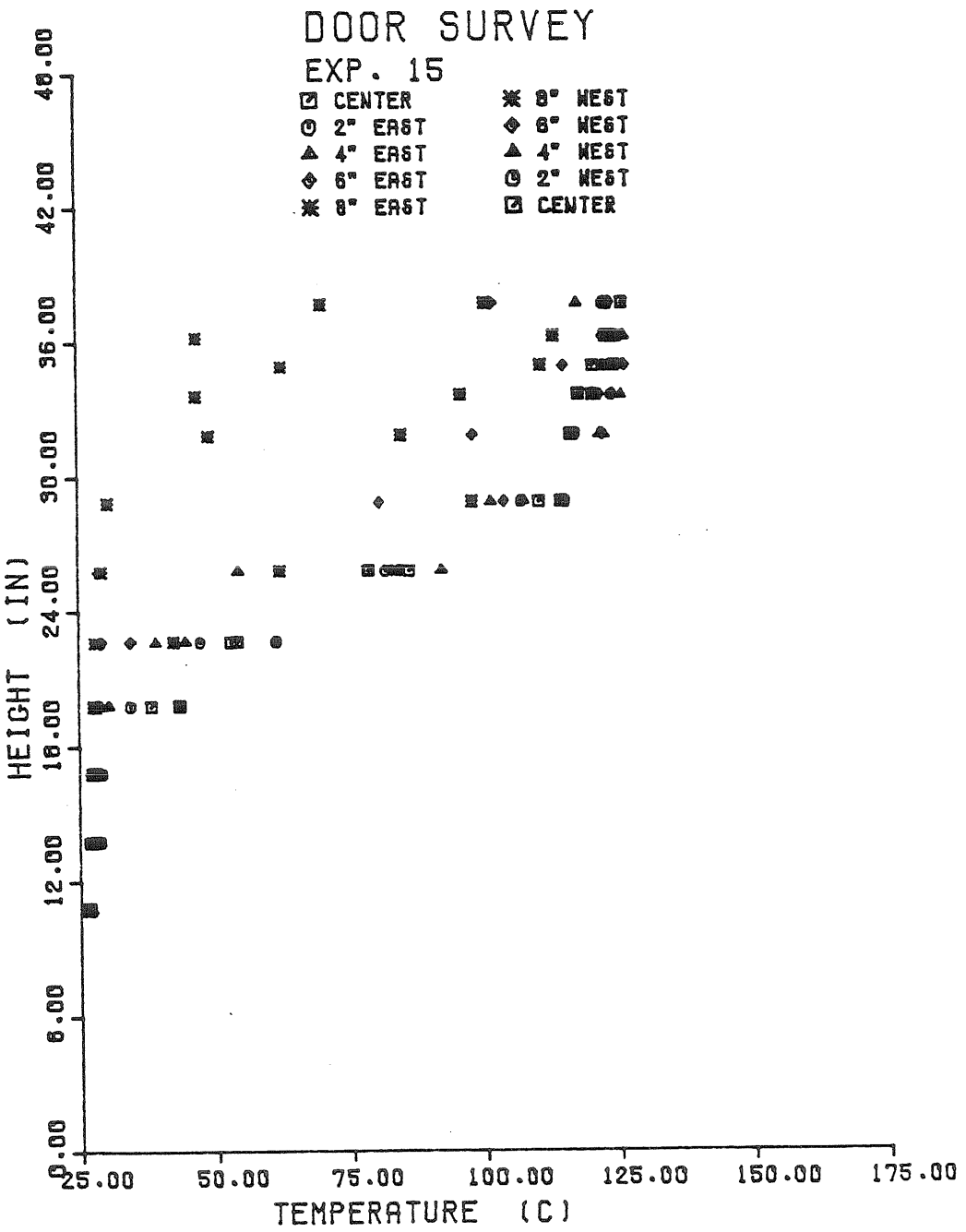

Figure (7.19) Gas Temperature Profiles at 9 Spanwise Locations across the Outer Edge of the Doorway (Exp. 15).

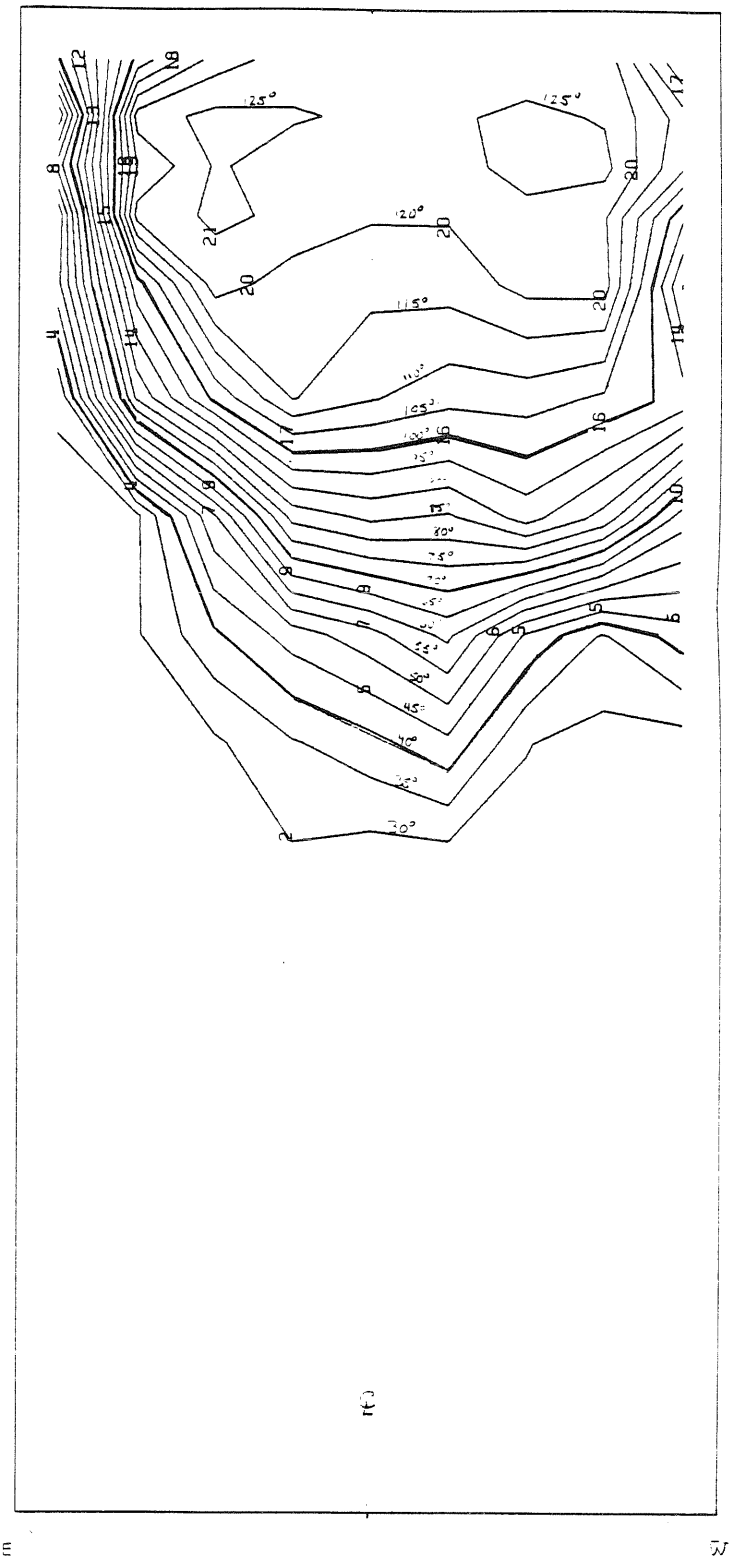

Figure (7.20) Gas Temperature Contours across the Outer Edge of the Doorway (Exp. 15)

gas will separate from the sharp edges and form a vena contracta. The data in Figures (7.19) substantiate this view with the gas temperatures falling rapidly as one approaches to within 2.5 cm of either side of the doorway opening. This can also be seen in Figure (7.20), which is a temperature contour plot of gas in the doorway, viewed from the outside. There is an asymmetry inherent in the data, with hotter flow observed near the west edge of the door. Nevertheless, there is a significant gradient of falling temperatures near each side of the doorway. Note also that the neutral surface is not flat, with more hot gas spilling out at the center than at the edges.

Examination of the temperature data in Figure (7.19) from the central region of the doorway shows that the ceiling zone mean temperature gradient is almost identical to the same gradient measured in the interior room. On the other hand, the interface zone is 85% thicker at the door than inside the room and so has a smaller mean temperature gradient.

As one would expect for flow over a weir, the depth of the interface below the soffit ($z_{soffit} - z^{+}_{eff}$) is 36% greater inside the room than it is at the outer edge of the doorway, where the flow bends sharply upwards as it flows out under the soffit. On the other hand, the lower edge of the interface z^{-}_{eff} is actually 8% lower at the outer edge of the doorway than in the interior of the room. Because the shear will be the largest between the two counter flowing streams in the doorway, we expect that there will be greater mixing across the interface zone here. In addition, we expect hot ceiling jet gas flowing down the north wall to further thicken the interface and indeed the interface zone here is roughly 85% thicker than in the interior of the room.

Smoke flow visualization during a later experiment confirmed that near the doorway, the hot gas within the room bends down sharply and flows out under the soffit. This exiting gas occupies roughly the upper 38 cm of the doorway, which corresponds to the entire ceiling zone and the upper half of the interface zone in Figure (7.19). We also observed that the lower 46 cm was a region of strong inflow, a result that agrees very well with the estimated floor zone in Figure (7.19). We further observed that between 46 and 61 cm the gas, which should experience the minimum hydrostatic pressure difference (see Figure (4.1)), was reasonably stagnant. However, during the smoke flow visualization test we had installed an interior partition with a door which divided our test chamber in half. Therefore, during the smoke flow visualization test, there would not have been as strong a ceiling jet flowing in the north half of the room as there was during experiment 15. Consequently the quantitative smoke flow visualization results may not be directly applicable to the case at hand, but the qualitative behavior should be the same.

We can trace the gas entering and leaving the room by comparing the data from the doorway (see Figure (7.19)), with that measured 25 cm and 38 cm inside the room near the centerline of the room. These data are displayed in Figures(7.21) and (7.22), respectively.

Perhaps the most striking features of these figures is how quickly a combination of buoyancy, heat transfer, and turbulent mixing acts to modify the entering door jet. Figure (7.19) shows that door jet starts out with an initial depth of approximately 46 cm extending across the entire 46 cm span of the doorway. The gas is at a very nearly constant temperature of $27.4^{0}C$, based on the data tabulated in Table (7.3). However, only 25 cm inside the room (33 cm from the outer edge of the

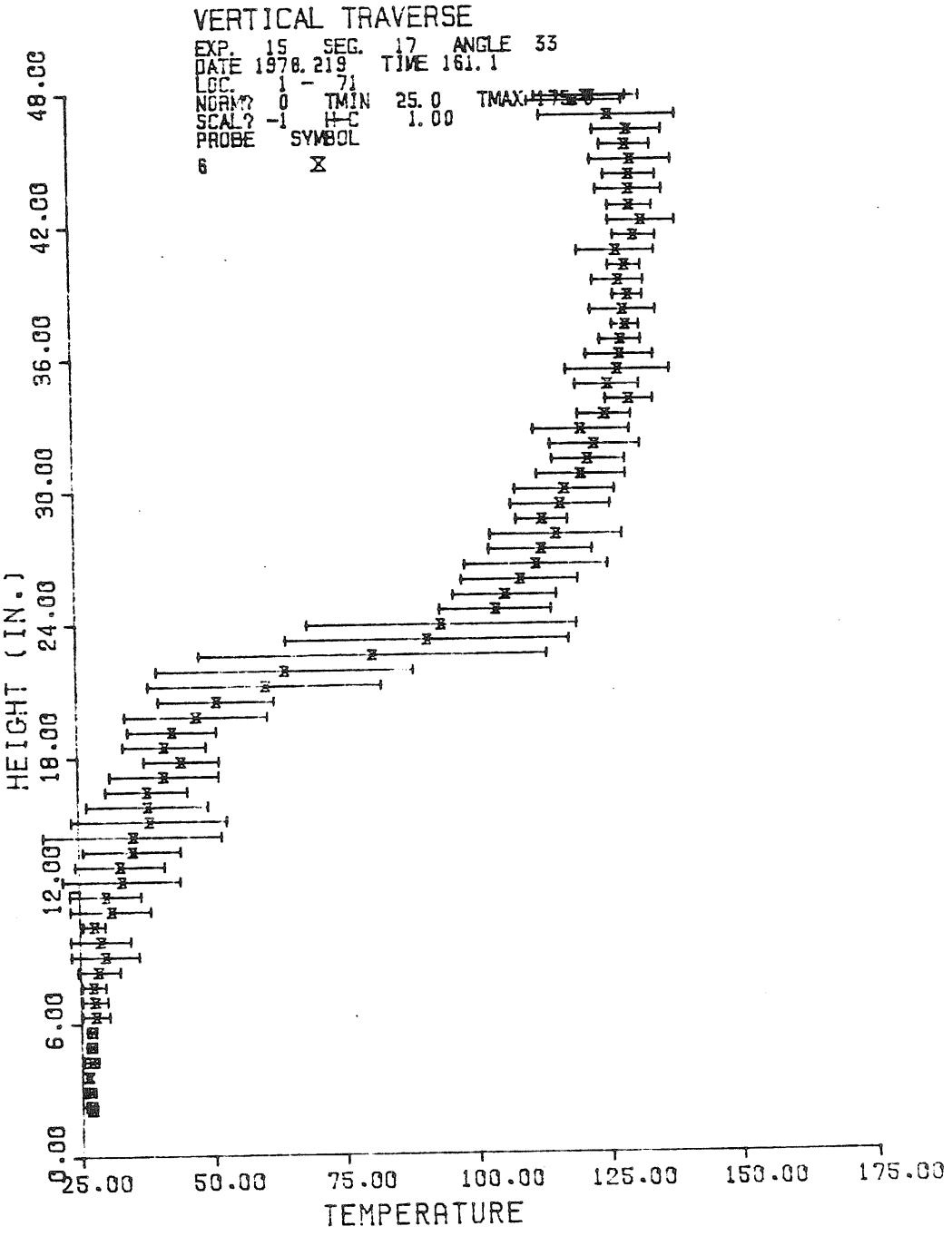

Figure (7.21) Gas Temperature Profile 25 cm from the Doorway (Exp. 15).

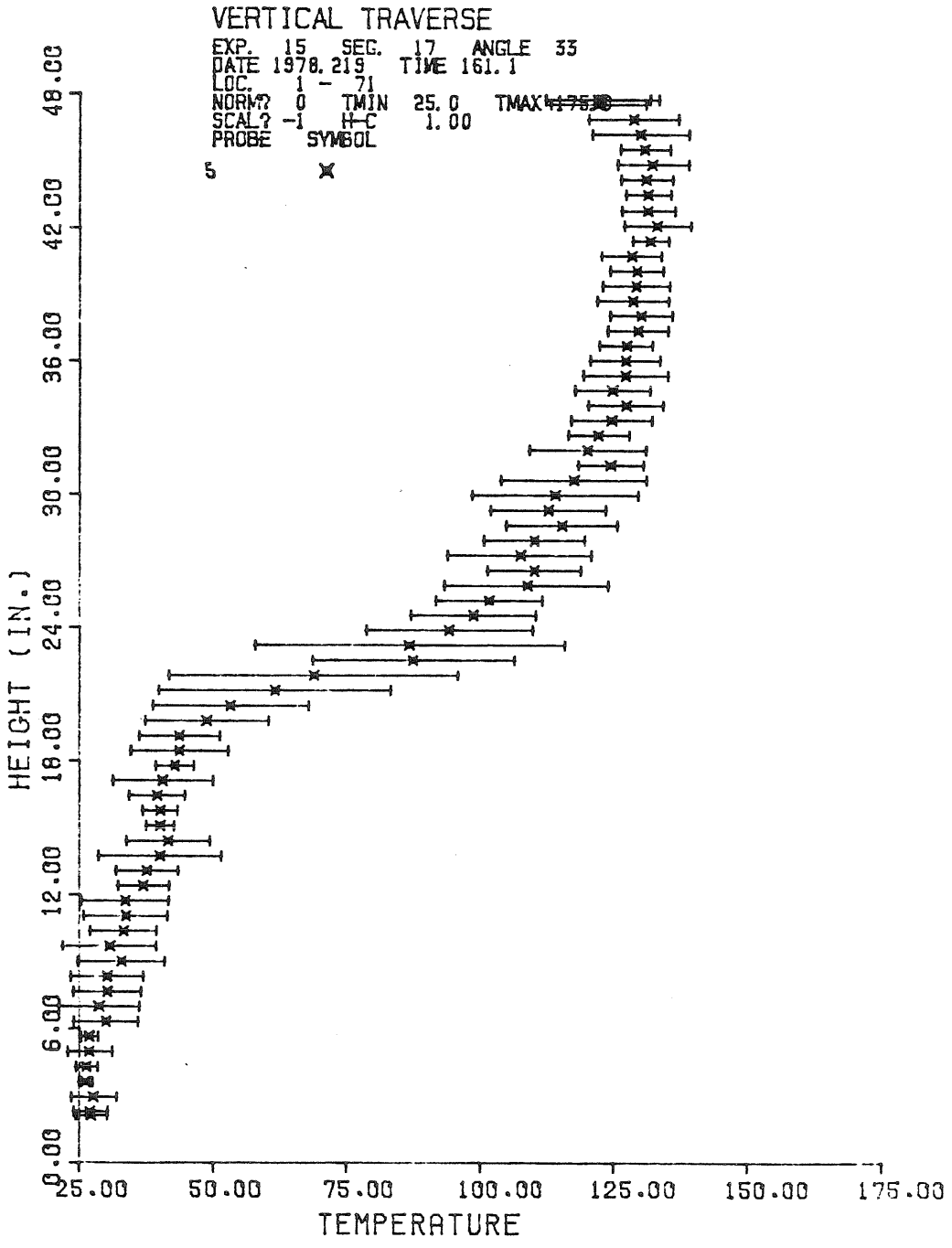

Figure (7.22) Gas Temperature Profile 39 cm from the Doorway (Exp. 15).

door frame), the region of undisturbed fresh air at ambient temperature has been squeezed down to the bottom 15 cm of the floor zone. The gas in the next 11 cm is only slightly warmer than the initial door jet and experiences small to moderate temperature fluctuations. Above this height (26 cm) the temperature fluctuations are very large and the mean temperature is already 5^0C warmer than at the door. As one progresses upward it increases rapidly until by a height of 44 cm it matches the interior floor zone linear profile and is more than 13^0C hotter than initial door jet. Just 13 cm further inside the room, the door jet has been further heated. As shown in Figure (7.22), the bottom 15 cm is still filled with gas that is near ambient temperature, but the gas in the region now experiences moderate temperature fluctuations which were absent in Figure (7.21). Above this cold sublayer, the mean temperature of the gas in the next 16 cm increases rapidly with large temperature fluctuations and approaches the floor zone linear profile by a height of just 31 cm (compared to 44 cm in Figure (7.21)). Note above 31 cm probe 5 sees typical floor zone gas behavior with only moderate temperature fluctuations. The next logical step would be to examine the data of probe 4, but unfortunately, this probe was used to sample the CO_2 concentration and because of the low aspiration rate imposed by the CO_2 analyzer, had poor temperature response. The data from the next probe (number 3), located 61 cm from the inside edge of the doorway, have already been presented in Figure (7.8) and shows that at this location all that remains of the door jet is a slightly cooler region of gas 28 cm thick which experiences larger than normal temperature excursions for the floor zone. This gas is now roughly 8^0C hotter than the original door jet and is within $2-5^0$C of the floor zone linear profile. As we

have noted previouwly, this cooler sublayer of gas is observed over most of the floor and is more pronounced near the east wall.

We can also follow the hot gas escaping from the room in Figures (7.8), (7.19), (7.21), and (7.22) but the changes are much less dramatic than the change in the incident door jet. As we previously noted, the ceiling zone gas measured by probe 3 in Figure (7.8) is uniformly $3-5^{0}C$ warmer than the ceiling zone linear profile throughout nearly all of the upper layer. This trend is carried further as we approach the doorway. The ceiling zone data measured by probe 5, 38 cm from the north wall, and shown in Figure (7.22), are slightly warmer than those seen by probe 3 in Figure (7.8). In addition, the mean temperatures are nearly uniform throughout much of the upper ceiling zone, and below this region the gas experiences large temperature excursions. The interface is also slightly hotter and has a lower upper boundary z^{+}_{eff}. All of these effects are associated with flow of hotter than average ceiling jet gas down a side wall. These trends are even more apparent 13 cm closer to the north wall as displayed in Figure (7.21). The lower ceiling zone gas is now roughly $5^{0}C$ hotter than the same gas in Figure (7.22), and the effective upper edge of interface zone z^{+}_{eff} has dropped down 3 cm or 20% of interior interface zone thickness, indicating that hot gas from above is pushing down the interface. Finally 16 cm from the north wall, the data shown in Figure (7.23) further confirm these trends. Note that the upper edge of the interface has now fallen by more than 40% of the interior zone thickness. In addition the region of large temperature excursions starts at a lower height, indicating that the hot gas from above <u>consistently</u> flows further down the wall and in fact penetrates significantly lower than the door soffit.

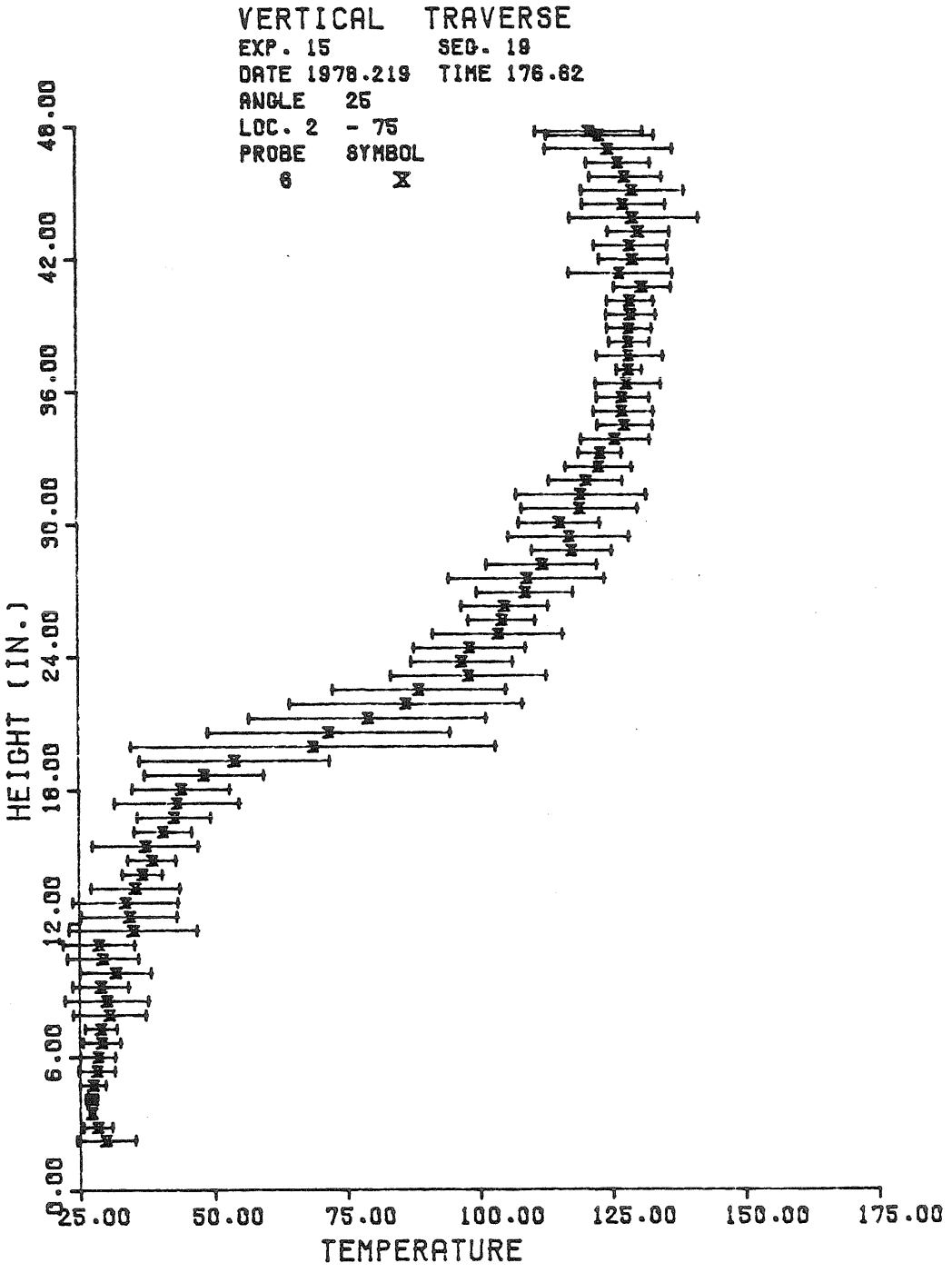

Figure (7.23) Gas Temperature Profile 16 cm from the Doorway (Exp. 15).

The effective lower edge of the interface $\bar{z}_{eff}$ also falls roughly 26% of the interior interface zone thickness. Finally note that the "ceiling jet" here is a region of sharply falling mean temperatures with large temperature excursions which we have already seen in Figure (7.12) and one probably symptomatic of a region of flow separation in the vicinity of the ceiling-north wall junction.

Given the geometry of the traversing mechanism we could not sample gas from the central region of the doorway closer than 13 cm from the north wall or in the 7.6 cm thick doorway itself. Consequently, we can not map the large change of over 16 cm that occurs in the height of the lower edge of the ceiling zone z^{+}_{eff} as this hot gas flows up and out of the doorway. Note however that at and above this effective interface height, the mean temperature data measured at the outer edge of the doorway very nearly matches the ceiling zone mean temperatures at corresponding heights displayed in Figure (7.23), and that these data are 2 - 5°C hotter than the corresponding interior ceiling zone data. It is also interesting to note that effective lower boundaries of the interface zone z^{-}_{eff} in Figures (7.19) and (7.23) coincide, indicating that near the center of the doorway at least, some of the gas from the lower interface zone is also escaping.

We have attempted to sketch the major flow patterns which we have discussed in Figure (7.24), both for flow down the walls and out the doorway. In Figure (7.24a) we show the ceiling jet separating from the ceiling, impinging on a sidewall, and then flowing down the sidewall until buoyancy forces it to rise. As a result, near the walls the boundaries of the interface zone z^{+} and z^{-} are lower than in the interior of the room. Finally, below the interface there will be a thin natural convection flow up the sidewalls and some irregular pattern of natural convection rising from the floor.

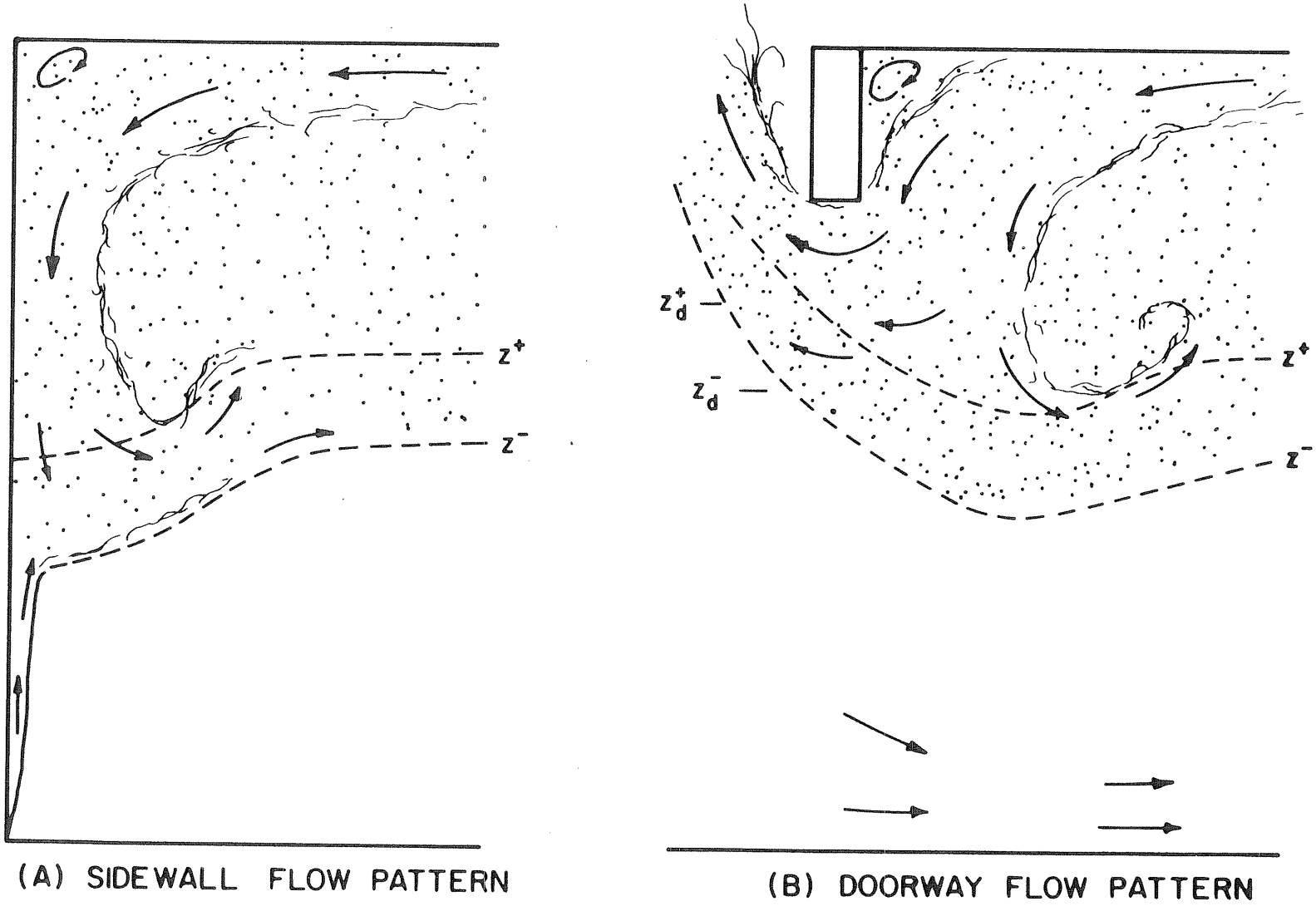

Figure (7.24) Major Flow Patterns Near Walls and Doorway

The flow near the doorway, shown in Figure (7.24b), is a complex blend of two basic phenomena: the flow of hot gas over the weir-like soffit combined with the interaction of the ceiling jet with the north wall. Because the distance between the north wall and the fire is 3 times as large as the distance between the sidewalls and fire, we expect the ceiling jet will be channeled into a basically two-dimensional flow pattern which will separate from the ceiling and flow down the north wall. Its momentum will carry it below the height of the soffit and cause the height of the local interface zone to be depressed. On the other hand, as some of this hot gas escapes, it will bend upwards sharply as it flows out under the soffit, resulting in higher interface zone boundaries z_d^+ and z_d^- along the outer face of the north wall. Finally, near the floor there will be a door jet of fresh air entering the room.

7.4 Effect of Opening Geometry

Changing the size and location of the opening between the room which contains the fire and the external environment can be expected to have a major impact on the gas temperature distribution in the fire room. In particular, by blocking the lower portion of the doorway to create a window-like opening of equal span and soffit height as the original door, we expect to effectively throttle down the flow rates of the gas entering and leaving the room. This will result in a lowering of the interface, which accommodates the reduction of mass flow into the room and hence into the plume. In addition, the greater depth and temperature of the upper layer provide a greater hydrostatic pressure difference which is needed to overcome the effective throttling resistance imposed by the reduction in the exit area. Finally, since the velocity difference between the counter flowing streams in the window

will be larger, while their separation is smaller, we can expect significantly greater turbulent mixing in this high shear zone than occurred with the original doorway.

To test these ideas, we blocked the lower 54.6 cm of the doorway to create a window 44.5 cm high by 45.7 cm wide during experiment 16. This experiment was otherwise identical to experiment 15, which we have just discussed. In particular, both experiments had 14.9 kW fires located on the major axis of the room a distance of ½ the room height from the west, south, and east walls, and 1½ room heights from the door or window in the north wall.

Typical mean temperature data measured across the middle of the room (90^0 vertical traverse) by the 6 aspirated thermocouples are displayed in Figure (7.25). By comparing this figure with Figure (7.2) which shows the corresponding data from experiment 15, one can see all of the effects related to changing the opening geometry which we just mentioned.

These two figures indicate that the same basic phenomena which we observed in experiment 15 are also present in experiment 16. In particular, except for the region very near the side walls, the gas is homogeneous with all probes measuring the same temperature at a given height. In addition, the mean temperature profile can again be reasonably accurately approximated by linear profiles in the floor, interface, and ceiling zones. In the interior of the room, a strong ceiling jet is also present with temperatures roughly 17^0C hotter than the ceiling zone linear profile. Furthermore, 3 cm from the east wall probe 6 again sees significantly hotter gas above the interface than the rest of the probes, while below the interface probes 5 and 6 encounter gas which is slightly

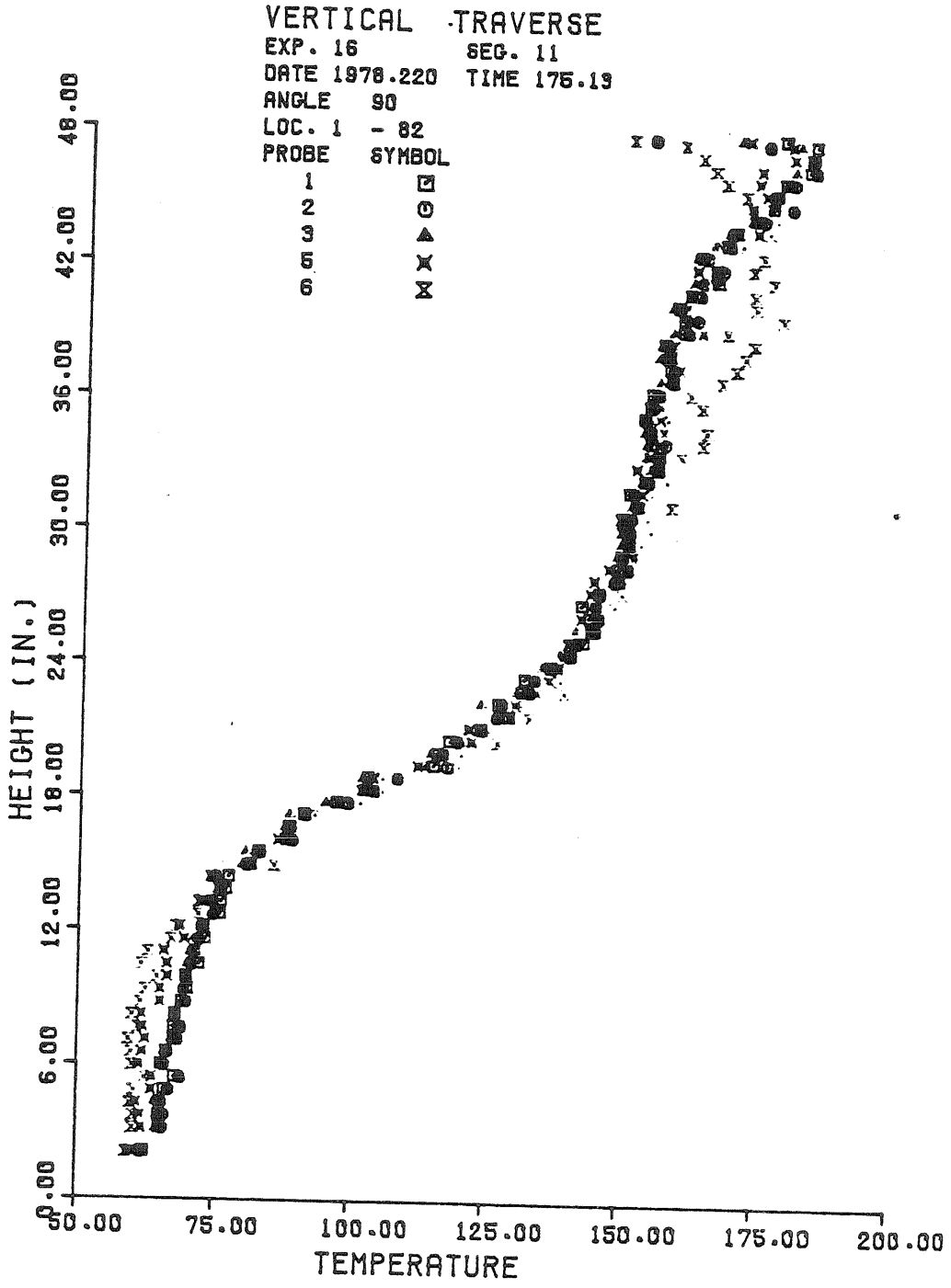

Figure (7.25) Gas Temperature Profiles across the Middle of a Room with a Window (Exp. 16).

cooler (~5^{0}C) than the interior gas at the same height, and which probably is a remnant of the window jet of fresh air entering the room. Finally it is interesting to note that the gradients of the mean temperature in both the floor and ceiling zones, as determined from the approximate linear profiles, are nearly identical to their counterparts from experiment 15.

The significant differences between these two experiments, which result from changing the door into a window, are the reduction in the height of the interface and the relatively large increase in the temperature of the floor zone gas. After comparing Figures (7.25) and (7.2), it is clear that the interface zone is significantly lower and thicker for the window geometry. Both boundaries of this zone in Figure (7.25) are lower than their counterparts in Figure (7.2). The boundary between the ceiling and interface zone drops 6.2 cm or 41% of the interface zone thickness in experiment 15. At the same time, the lower boundary of this zone z^- falls more than twice as much (12.6 cm). This results in an interface zone that is 6.4 cm (42%) thicker for the case of the window than for the door. This implies that the mean temperature gradient is roughly 42% smaller for experiment 16, because the actual temperature difference across the interface ($\Delta T \sim 70.5^0$C) remains remarkably constant.

It is interesting to observe that the upper edge of the interface in the interior of the room is just 4.8 cm above the height of the window sill, while the lower edge is 16.8 cm below the sill. In other words, the hot upper layer nearly fills the room to the height of the window sill. Consequently, the hot gas will bend upwards even more sharply as it escapes from the room than it did when the opening was a door. Even more important, the window jet of fresh air will be forced sharply down-

ward as it enters the room, and plunges through first the lower portion of the hot ceiling layer, and then the intermediate temperature interface zone. As it makes this journey, turbulent mixing significantly heats the gas and increases its CO_2 content. As a result the floor zone is approximately 34^0C ($\Delta T^* \sim 2.78$) hotter when the opening is a window than it was when the opening was a door. Because the plume entrains basically floor zone gas and increases its enthalpy by the amount of heat released by the fire, which remains constant in this case, the ceiling zone gas will also be roughly 34^0C hotter in experiment 16 than it was in experiment 15. Indeed if one shifts the origin by 33.5^0C, Figures (7.2) and (7.25) become virtually identical, except for the change in the interface zone (which we have previously noted) and some details of flow near the walls.

As we reviewed the results from experiment 15, it became apparent that hotter than average gas flowing down the vertical walls contributed to the thick interface zone which we have observed in these experiments, and may have contributed to heating the floor zone gas. We expect these same phenomena to be even stronger in the case when the opening is a window. First, because the interface height z^+ is smaller, the calculated kinematic mass flux delivered to the upper layer by the plume will be 11.4% smaller here than in experiment 15. Consequently the volumetric flux of hot upper layer gas escaping through the window must also be roughly 11.4% less than the amount which escaped throught the door. Because the volume of the upper layer increases, and the volume flux to it decreases as the interface drops, the calculated residence time of the upper layer gas t_{res} for experiment 16 increaes by 25%. However, this does not mean that the upper layer gas is more quiescent in experiment

16. In fact the gas is likely to be more vigorously stirred.

While the kinematic mass flux delivered to the upper level decreases as the interface falls, the volumetric flux delivered by the upper plume to the ceiling jet actually increases 1.4%. Furthermore, we expect the magnitude of the integrated kinematic momentum flux in the ceiling jet to scale with the same flux in the upper plume at the termination height z_{th}. The calculated value of this latter flux actually increases by 6.7% between experiments 16 and 15. Therefore we expect the ceiling jet, and consequently the flow down the side walls, to be slightly more vigorous for experiment 16 compared to experiment 15. This fact, coupled with the reduction in mass flow which escapes, indicates that the return flow, that is the fluid which was in the ceiling jet but which does not exit the room, must be at least 11% greater for the case of the window than it was for the door. This greater circulation within the upper layer may contribute to the thickening of the interface zone. In line with this viewpoint, note that while the boundary between the floor and interface zones is reasonably sharp in both Figure (7.2) and (7.25), the boundary between the interface and ceiling zones is much more gradual in Figure (7.25) than in Figure (7.2).

Gas temperature data measured along the north and south halves of the west side wall and presented in Figures (7.26) and (7.27) confirm that hot gas flows down the sidewalls and penetrates progressively further into the interface zones as one approaches the corners. This is the same pattern visible in Figures (7.13) and (7.14) for experiment 15. The difference here is that although the hot gas does not penetrate much below the lower edge of the interior interface zone $\bar{z}$, it actually travels 20% further down the sidewalls because $\bar{z}$ is much lower in experi-

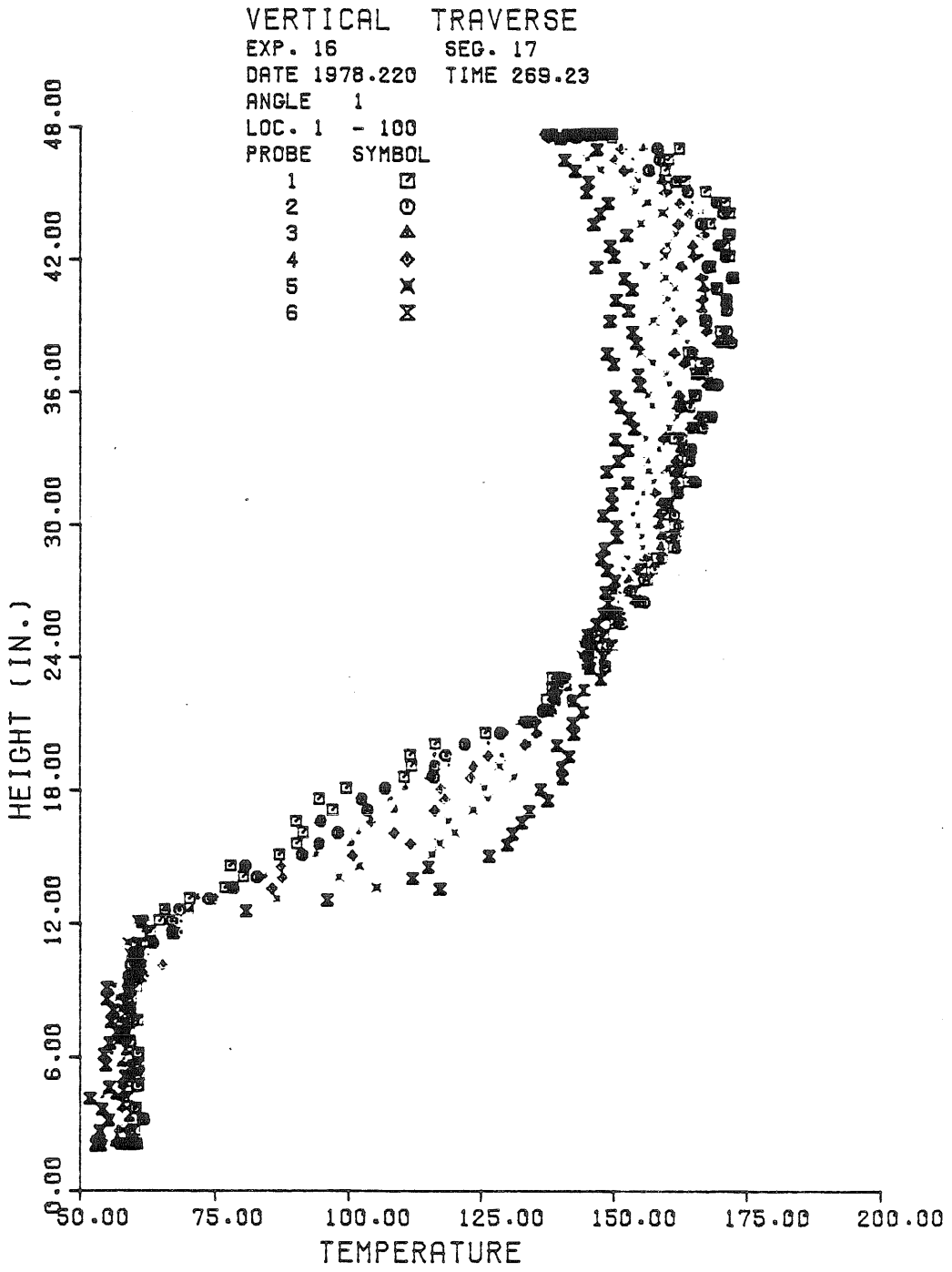

Figure (7.26) Gas Temperature Profiles along Front Half of West Wall (Exp. 16).

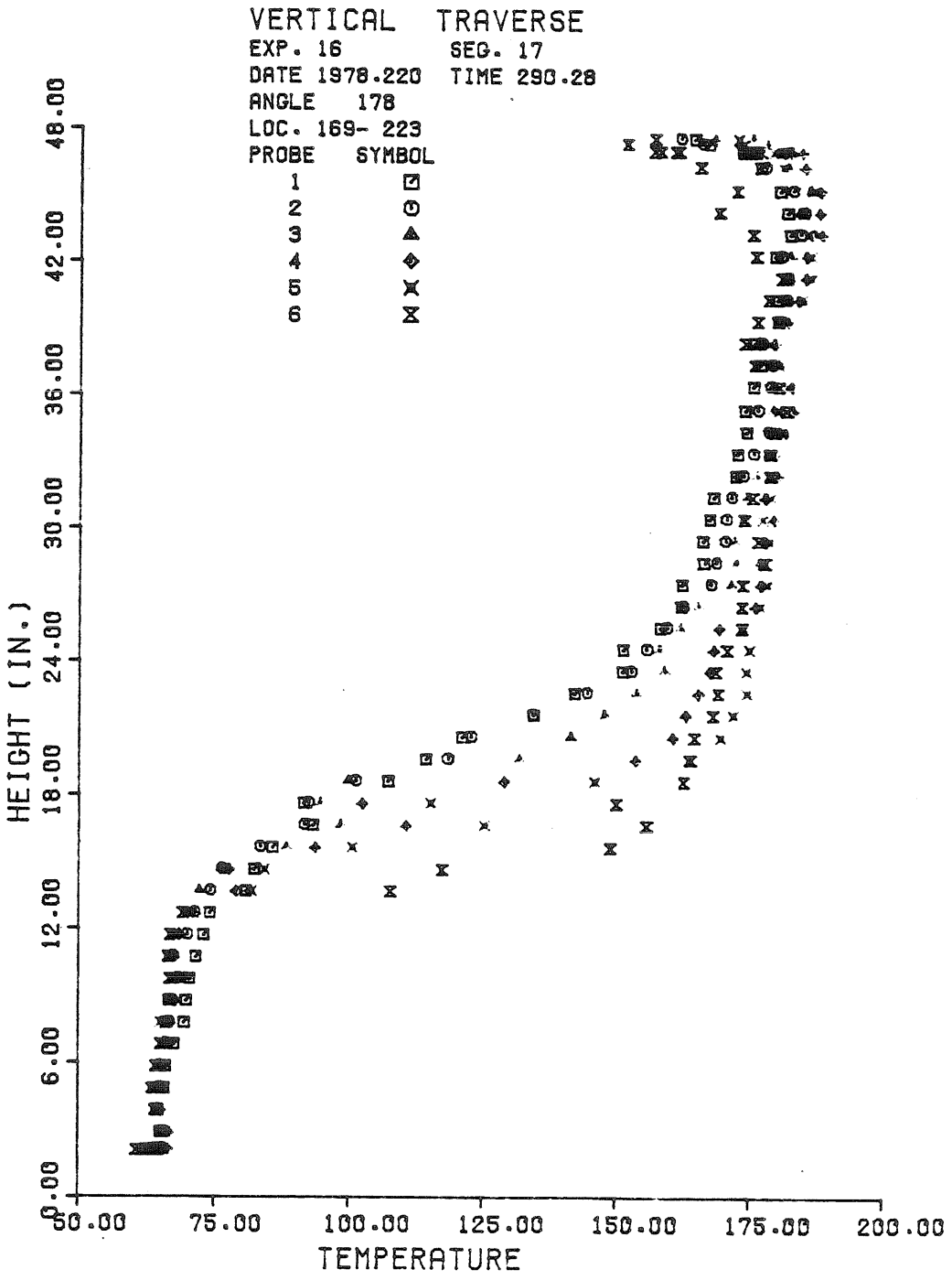

Figure (7.27) Gas Temperature Profiles along Rear Half of West Wall (Exp. 16).

ment 16. Finally note that in both corners hot gas penetrates to within nearly 30 cm of the floor.

As a further check on the similarity of the basic flow phenomena, we can compare the CO_2 concentration measured in the middle of rooms during the 90^0 vertical traverse from these two experiments and displayed in Figures (7.2) and (7.4). The CO_2 concentration profile shown in Figure (7.28) for this experiment confirms the results inferred from the temperature data. There are three distinct zones visible on both the temperature and CO_2 concentration profiles. In addition, the boundaries of these zones (z^+,z^-) are the same for both profiles. Not only is the interface zone lower and thicker for both the temperature and composition profiles when the opening is a window rather than a door, but the floor zone of both profiles also shows evidence of significantly greater mixing between the combustion products and the fresh air which enters the room. For example, in experiment 15, the increase in the floor zone CO_2 content above ambient was only 9% of the increase for the ceiling zone and was only slightly greater than the uncertainty of the measurement. On the other hand, the data in Figure (7.21) show that the floor sone CO_2 concentration is 36% of the ceiling zone CO_2 content and is large compared to the uncertainty of the measurement. Finally note that the average CO_2 concentration in the ceiling zone (ignoring the slow variations inherent in the CO_2 analyzer) is nearly constant for all heights in Figure (7.26). The temperature data however exhibit a definite non-zero ceiling zone gradient, which accounts for 22% of the total temperature rise observed in Figure (7.25). This again indicates that heat transfer and a regular pattern of mixing in the upper layer is responsible for the non-negligible ceiling zone temperature gradient.

As we have noted, except for the change in the height and thickness

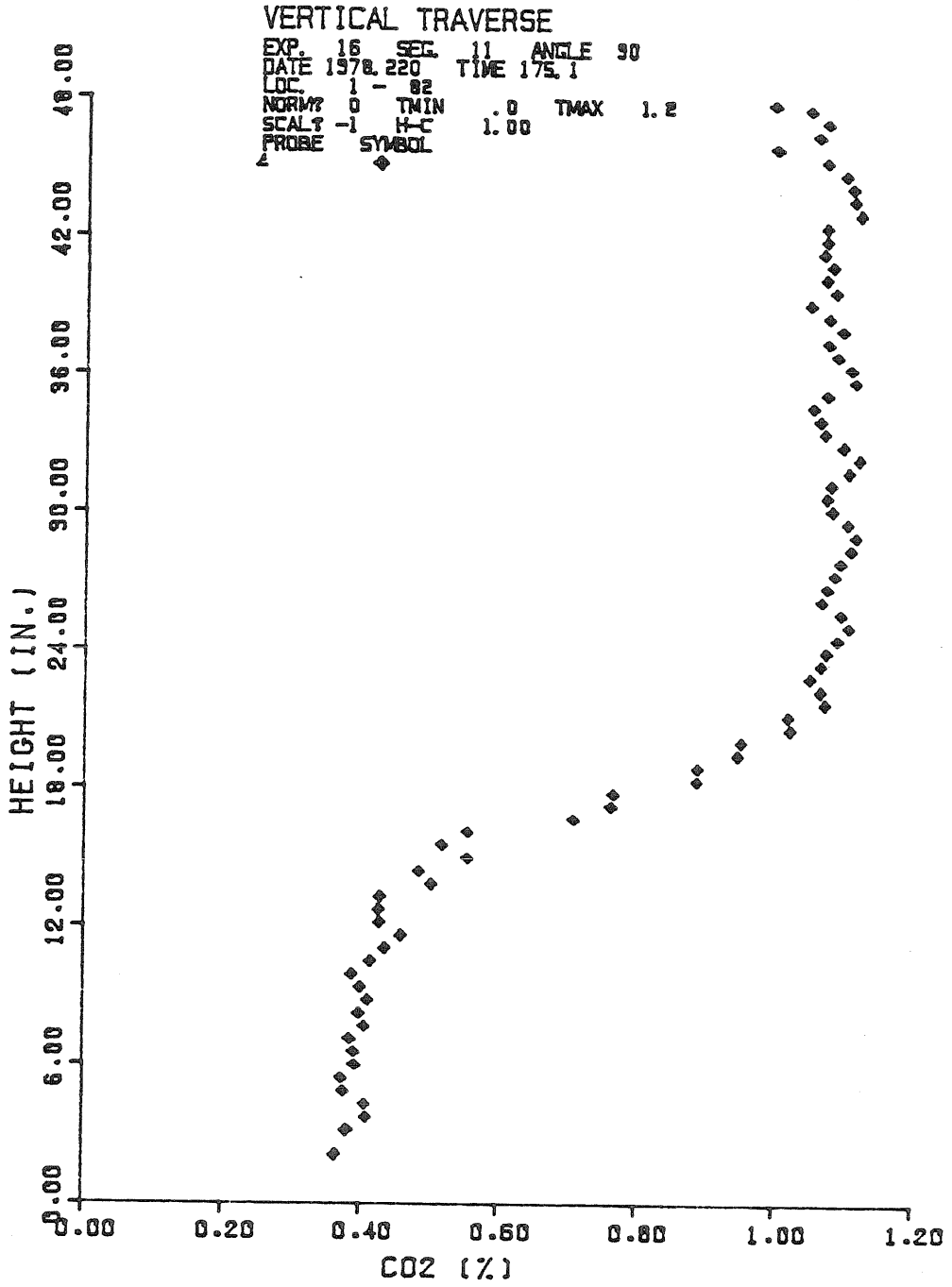

Figure (7.28) CO_2 Concentration Profile for a Room with a Window (Exp. 16).

of the interface zone and the flow patterns near the window itself (which produce a significant increase in the floor zone temperature), the temperature and composition data show that the basic flow patterns within the room, and in particular the interaction of the ceiling jet flow with the side walls, remain the same as the opening geometry is changed.

7.4.1 Flow near the window

Blocking the lower 54.6 cm of the doorways creates a window with a sill that is located at 55% of the height of the original door soffit, and hence reduces the opening area by 55% compared to the original doorway. However, the calculated kinematic mass flux in the plume at the interface, and hence the mass flux leaving the room fall by only 11%. This indicates that the counterflow velocities will be significantly greater in the window than in the original doorway.

The effect that this large reduction in the area of the opening has on the flow through the window is shown in Figure (7.29). In this figure the incident stream of fresh air has been squeezed down to the bottom 39% of the window, compared to the 47% of the doorway which it occupied in Figure (7.19). The stream of hot ceiling zone gas escaping under the soffit in Figure (7.19) is only slightly thinner and so occupies a larger fraction of the opening area (43% of the window compared to 25% of the door). The region that suffers the greatest compression is the interface zone which now fills a mere 17% of the window compared to 28% of the door. These facts indicate that the incident stream of fresh air, which is 62% smaller here than it was in the doorway, will experience a relatively large increase in its velocity compared to the escaping hot gas, which is only 33% thinner here than in the door. In addition to having significantly greater velocity, the incident stream of fresh air is in much closer contact with the exiting hot gas because

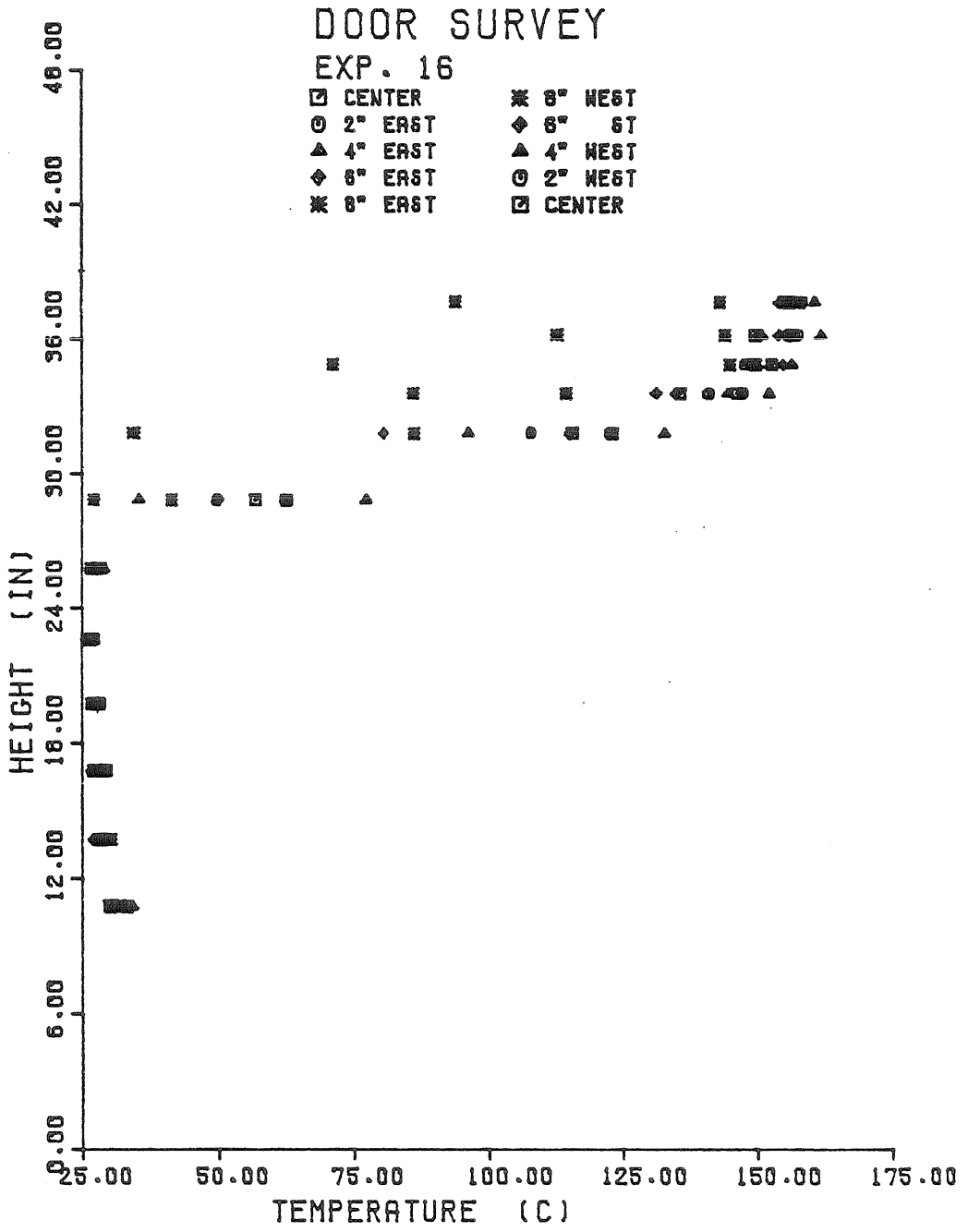

Figure (7.29) Gas Temperature Profiles at 9 Spanwise Locations across the Outer Edge of the Window (Exp. 15).

the interface zone is 73% thinner in the window than it was in the doorway. These facts indicate that there will be significantly greater shear between the two counterflowing streams. Furthermore, the relatively cold fresh air will be negatively buoyant with respect to the gas in both the floor and interface zones. Consequently, the inflowing jet of fresh air, which enters the room above the local interface, will fall through the interface and floor zones and impinge on the floor. In doing so it will act like a negatively buoyant plume and entrain a significant amount of much warmer gas from the lower ceiling zone and the interface zone. The combined action of the increased shear in the window and the descent of the negatively buoyant window jet produce the large increase (34^0C) in the interior floor zone temperatures.

We can chart the progress of this window jet in Figures (7.30) through (7.34) which are completely analogous to Figure (7.8) and Figures (7.21) through (7.23) for experiment 15, which involved a door rather than a window.

The closest data to the inside of window are displayed in Figure (7.30). These data, measured roughly 16 cm from the inner face of the window, clearly show evidence of a jet of cooler fluid entering the room. The minimum average temperature of 40^0C occurs roughly 7 - 8 cm below the edge of the window sill. The very large temperature fluctuations indicate that this is a highly turbulent region. Note that mixing has already increased the gas temperature by 13.5^0C ($\Delta T^* \sim 0.99$). By comparing Figures (7.29) and (7.30), we can see that the local ceiling zone extends down below $\bar{z}_d$, the lower edge of the interface zone at the outer edge of the window. This implies that hot ceiling zone gas flows upwards as it passes under the soffit, similar to the flow through a

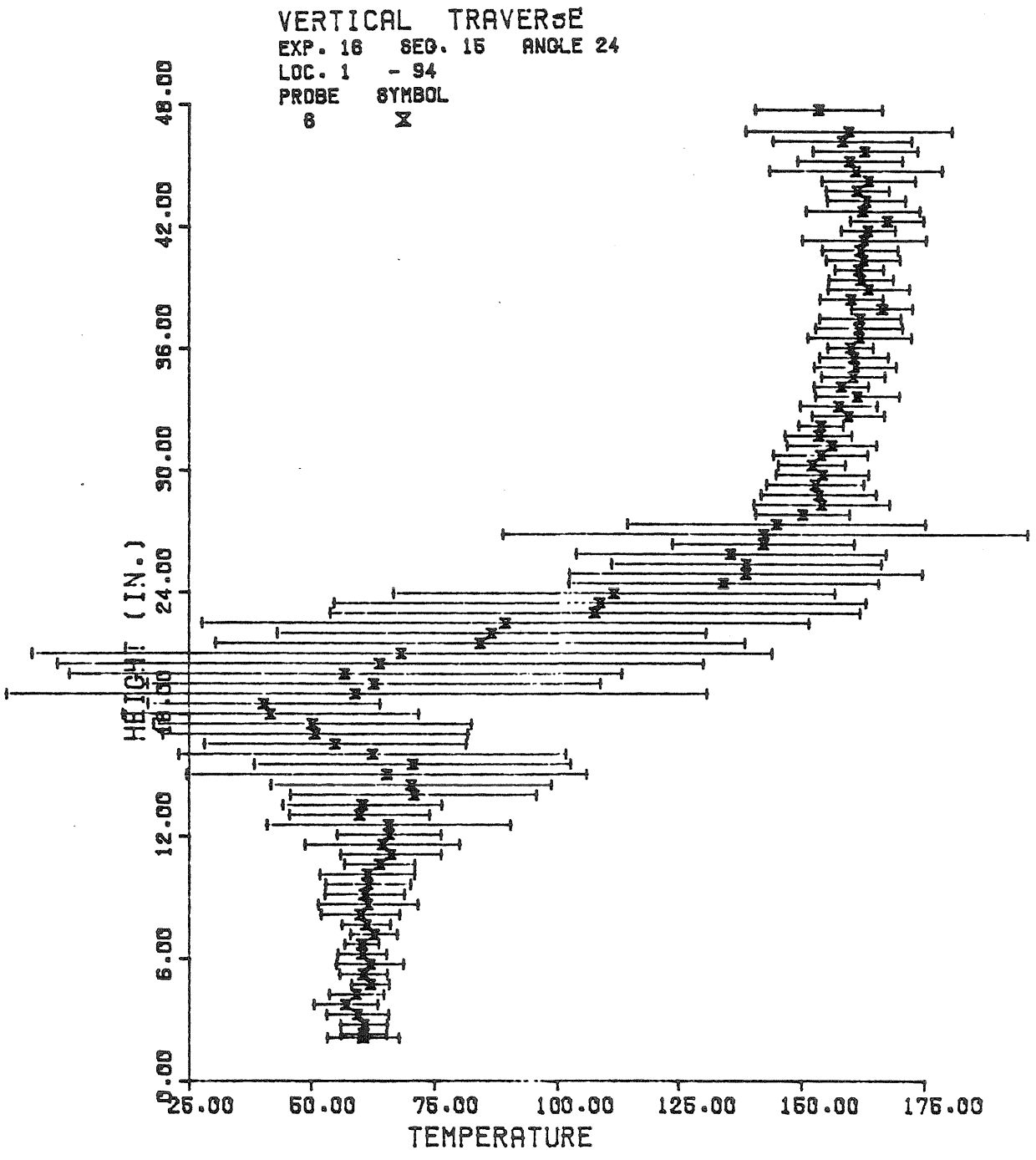

Figure (7.30) Gas Temperature Profile 16 cm from the Window (Exp. 16)

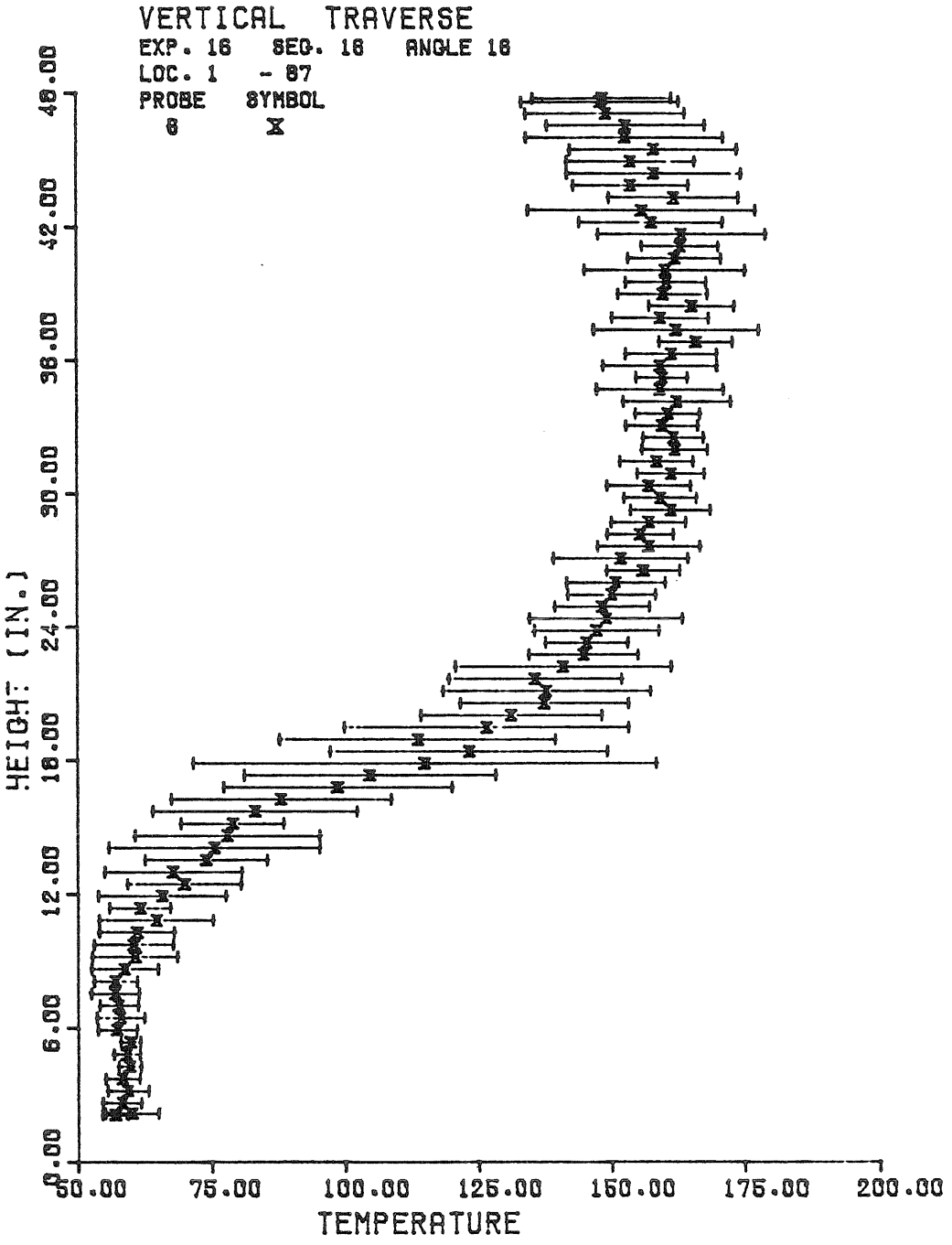

Figure (7.31) Gas Temperature Proifle 3.5 cm West of the Window and 10 cm from the North Wall (Exp. 16).

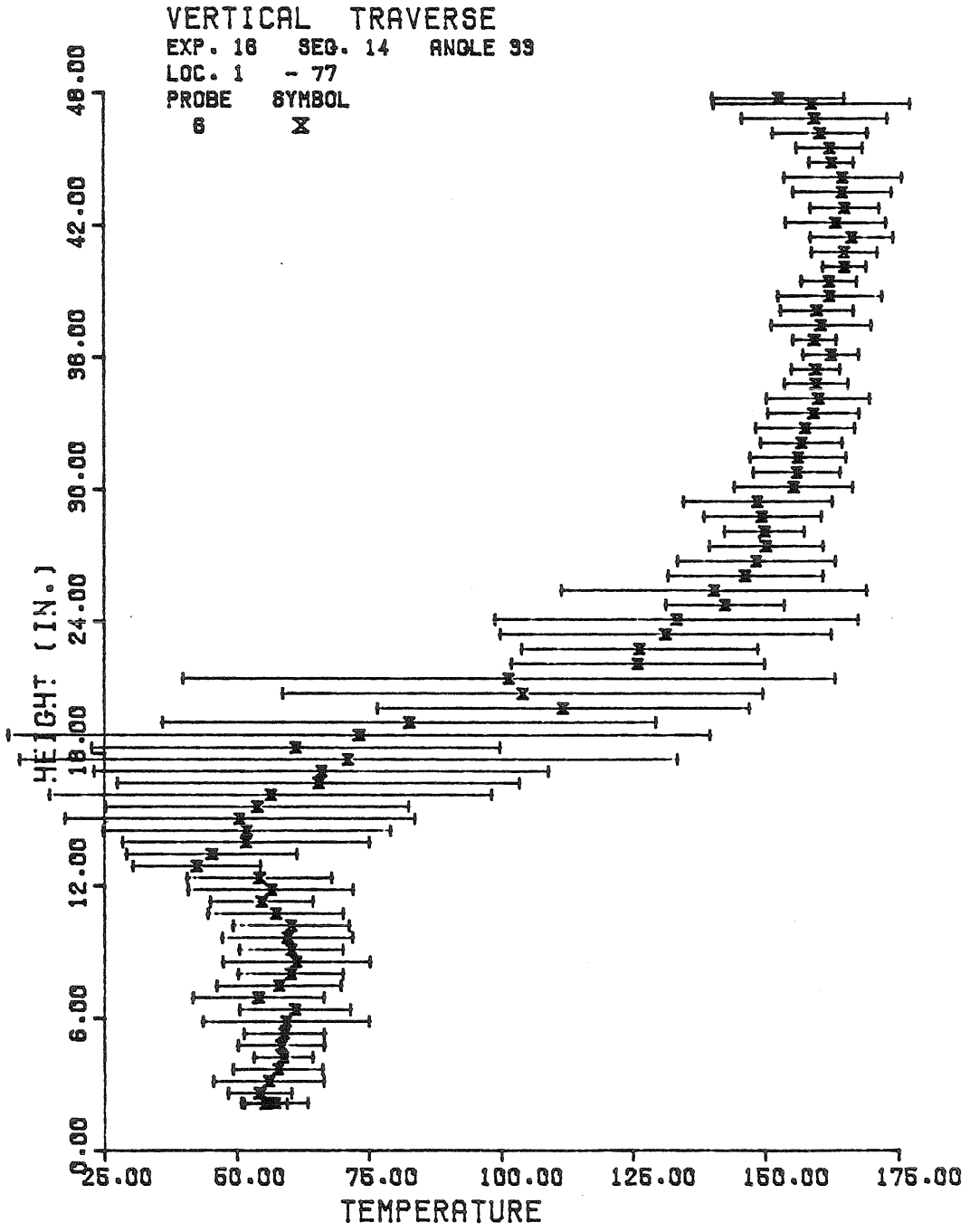

Figure (7.32) Gas Temperature Profile 24 cm from the Window (Exp. 16).

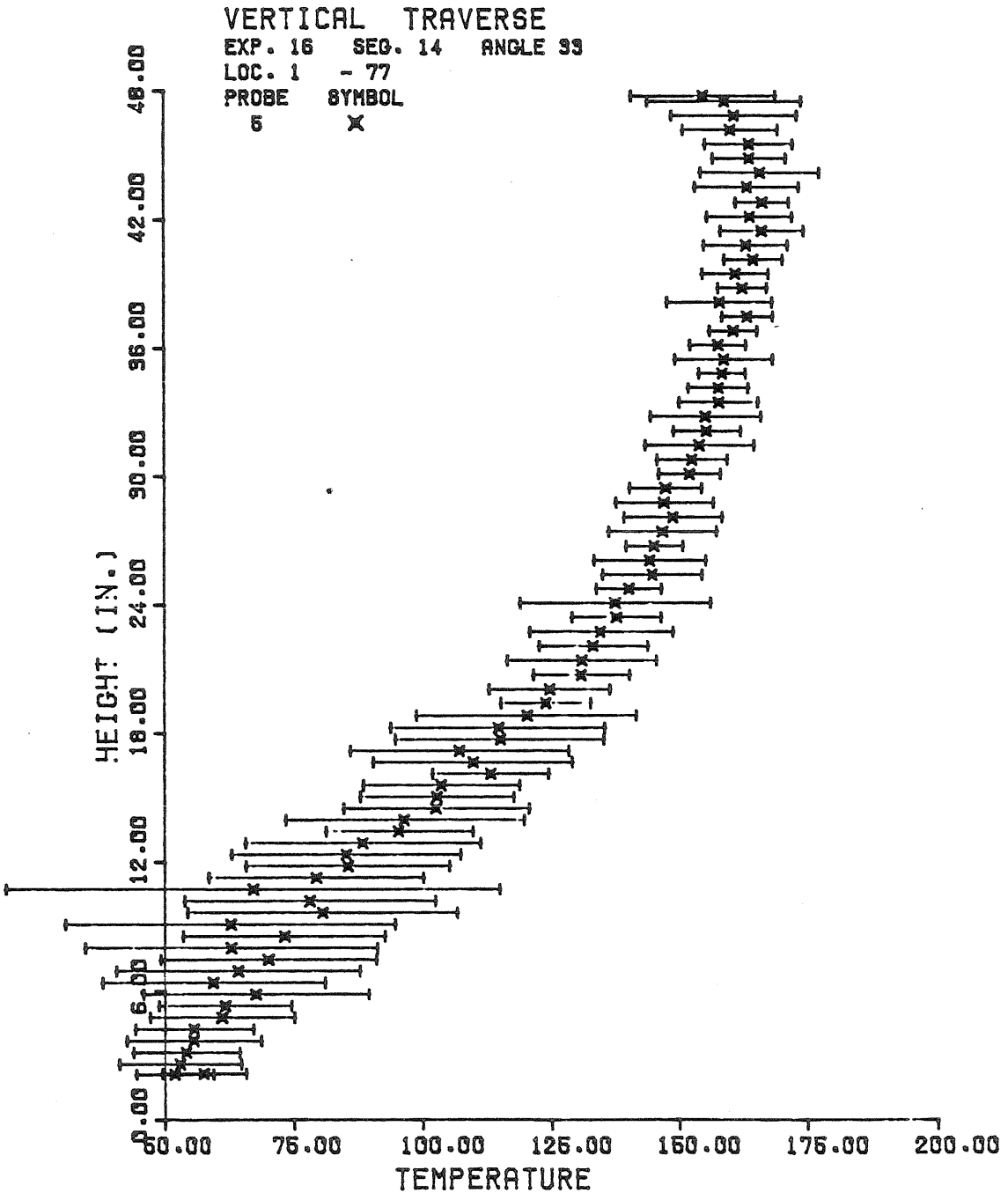

Figure (7.33) Gas Temperature Profile 37 cm from the Window (Exp. 16).

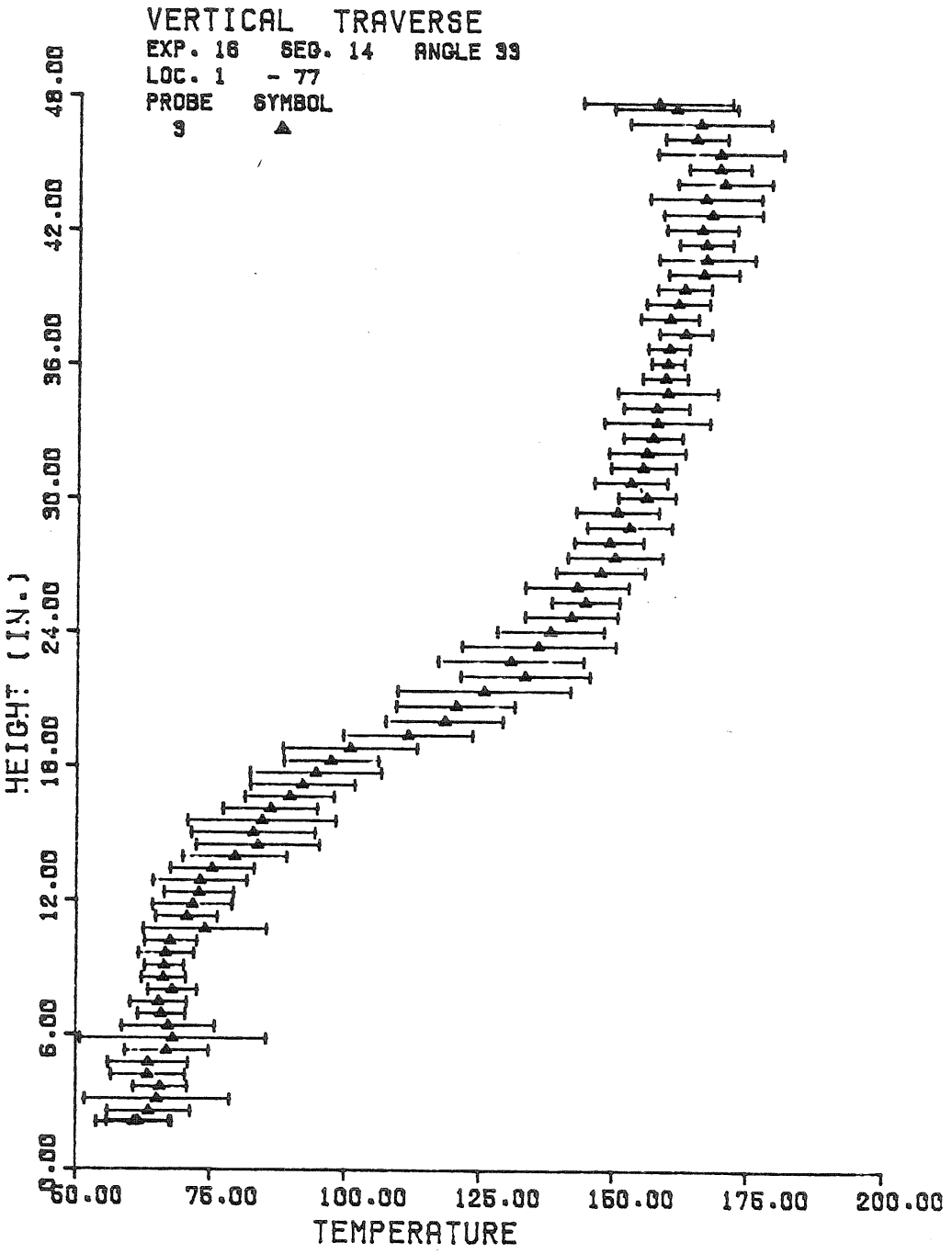

Figure (7.34) Gas Temperature Profile 61 cm from the Window (Exp. 16).

door. However, unlike the latter situation shown in Figure (7.23), where the interface zone is lower and thinner near the door than in the interior of the room, the interface zone in Figure (7.30) is now much thicker and has a much higher upper boundary than in the interior of the room. The upper portion of this zone in Figure (7.30) is not the interface per se, but rather a mixing zone at the edge of the inflowing window jet. In fact Figures (7.30) and (7.23) are very similar in shape except for the window jet which indicates that the local flow of hot gas leaving the room is similar for both doors and windows. The significant difference is the much greater thickness of the interior gas ceiling zone when the opening is a window. Finally it is interesting to notice that the lower edge of the local interface zone is very close to its value in the interior of the room. Below this height, in the floor zone, the gas temperature data are very similar in nature to that seen in the interior of the room. The significant difference is that this gas is $5-7^{0}C$ colder than its counterparts in the interior of the room.

We expect that the mixing process in the window jet will be complicated by the influence of the hot gas which we know flows down the walls. When the opening is a doorway, as in experiment 15, we expect the hydrostatic presence gradient to produce the largest inflow velocities near the floor (see Figure (4.1)), in a region that is undisturbed by the flow of hot gas from the ceiling jet. On the other hand, gas temperature data in Figure (7.31) which were measured just 3.5 cm to the west of the west edge of the window frame and 10 cm from the north wall, show that ceiling zone gas consistently penetrates as far down the west wall as the window sill and that the gas is hotter along the wall than in the interior to within 4 cm of $z_{\bar{}}$, the lower edge of the interior interface

zone. Therefore the window jet is flanked not by cool floor zone gas but by hot combustion products from the ceiling zone. For example, the temperature difference between the minimum temperature in the window jet in Figure (7.30) and the "ambient" gas temperature at the same height, roughly 16 cm away in Figure (7.31), is 82^0C ($\Delta T^* = 6.0$)! Thus the entrainment of this hot gas which flows down the north wall, combined with the mixing which occurs across the counterflow shear layer, produce the initial rapid heating of the window jet as it enters the room.

The mixing zone associated with the negatively buoyant window jet spreads as this jet flows down and into the room. The data in Figure (7.32) measured 24 cm from the inner edge of the window show the center of this window jet has dropped roughly 15 cm and that the minimum temperature at this point has increased to 42.5^0C. Furthermore note that the floor zone gas, which is now roughly 10^0C cooler than the interior gas, experiences much large temperature fluctuations than occurred in Figure (7.30). Finally, also note that the upper edge of the interface or mixing zone has dropped roughly 6 cm from the value seen in Figure (7.30).

This pattern of increased mixing continues as we move in from the window. In Figure (7.33), the data 37 cm in from the window show that this mixing region now fills the entire lower half of the room and the demarcation between the floor and interface zones is lost. Note that the upper edge of this zone now coincides with the upper edge of the interface in the interior of the room.

One very important effect of this mixing process is that the turbulence can overcome the stable stratification, and carry hotter fluid, which has been entrained,down into the floor zone. The result is that

the gas near what would be the lower edge of the interface in the interior of the room is now 30^0C hotter ($\Delta T^* \sim 2.21$) than we would expect. This temperature excess steadily decreases with height until within 15 cm of the floor, the gas is again colder by $5 - 10^0$C than it would be in the interior of the room.

Finally 61 cm from the window, the mixing processes associated with the negatively buoyant window jet have now caused the temperature difference between the window jet and the ambient fluid to disappear. Thus the mean gas temperatures in Figure (7.34) lie very close to the interior gas linear profiles and the only evidence of what was once the window jet is the larger than normal temperature fluctuations seen near the floor.

7.5 Effect of Fire Location

In addition to altering the opening geometry, we also used two different fire locations, shown by the crosses in Figure (7.5), during our ½ scale room tests. In experiments 15 and 16, which we have just examined, the burner was located on the major axis of the room, ½ the room height from the west, south, and east walls. On the other hand, for experiments 7, 10, and 13, which we will examine shortly, the center of the burner was located in the southwest corner, 15% of the room height from the south and west walls. By comparing the data from experiments 13 and 15, which had nearly equal strength fires ($Q^* \sim 8 \times 10^{-3}$), we can see the effect of moving the fire location.

The most significant effect of moving the fire location from the center of the back half of the room to the southwest corner is the reduction of the entrainment into the fire plume. In experiment 13, the south and west walls were 1.2 burner diameters from the center of the

burner. The close proximity of these walls tends to block the flow of ambient gas into the fire plume with the result that at any given height the plume will have a lower kinematic mass or volume flux and higher temperatures than an equivalent strength plume rising in open air.

Tangren, Sargent, and Zukoski (1978) reported a reflective symmetry in their ¼ scale brine flow simulation tests when their plume was located very close to a wall or in a corner. They found that the plume behaved as if it were reflected across the wall or walls and thus acted as though it were ½ or ¼ of a larger plume in a room 2 or 4 times as large as the physical room, depending respectively on whether the plume was located along a wall or in a corner. We can use this result in the simple room model described in Chapter III to show that when this reflective symmetry holds, the plume entrainment constant will be reduced by a factor of $\sqrt{2}$ or 2 depending again on whether the plume is located next to a wall or in a corner.

In our early brine experiments, this author found that plumes placed close to a corner of the room did indeed exhibit reduced entrainment, but that the reduction was less than the factor of 2 predicted by the symmetry argument above. Subsequent work by Mr. Ernst Tangren showed that it was necessary for the plume to be immediately tangent to the walls to achieve the predicted reduction in entrainment. Similar results were also obtained by Zukoski, Kubota, and Cetegen (1980) who found that diffusion flame fire plumes placed next to a vertical wall did not exhibit a large decrease in entrainment until the vertical wall was placed directly over the burner diameter and the back half of the burner was blocked off. These results indicate that, although the close proximity of vertical surfaces certainly impede the entrainment

process, the large reduction in entrainment predicted from symmetry arguments can only be realized when the flow of gas to the back side of the plume is totally blocked.

In these ½ scale experiments, the fire was located a finite distance from the two walls and so we would not expect to see the 50% reduction in α predicted by the symmetry argument. In fact for experiment 13 we found that the plume entrainment constant was reduced by roughly 20% from our standard value of $\alpha = 0.1096$. We arrived at this figure by comparing the measured and predicted stagnation point gas temperatures as we varied α in steps of 10%. (See Chapter IX.) Using this criterion, we found α was reduced by roughly 20% for experiments 10 and 13 which involved medium and large diameter fires, but only by approximately 10% for experiment 7 which had a small diameter fire and hence had the largest gap between the edge of the fire and the walls.

The mean temperature data measured across the center of the room in experiment 13 are presented in Figure (7.35). Note that although the thickness of the interface zone is nearly identical to that measured in experiment 15 and shown in Figure (7.2), the entire zone is roughly 5 cm higher in Figure (7.35). This upward shift constitutes a 30% increase in height compared to the interface zone thickness. In addition note that the temperature difference between the average upper and lower layer temperatures is slightly greater in experiment 13. Although the ceiling zone temperatures, including those of the gas flowing down the east wall, match quite closely, the upper floor zone gas in experiment 13 is roughly 5^0C cooler than the corresponding gas in experiment 15. This brings us to the other noticeable effect of moving the fire location: the reduction in ceiling jet temperatures.

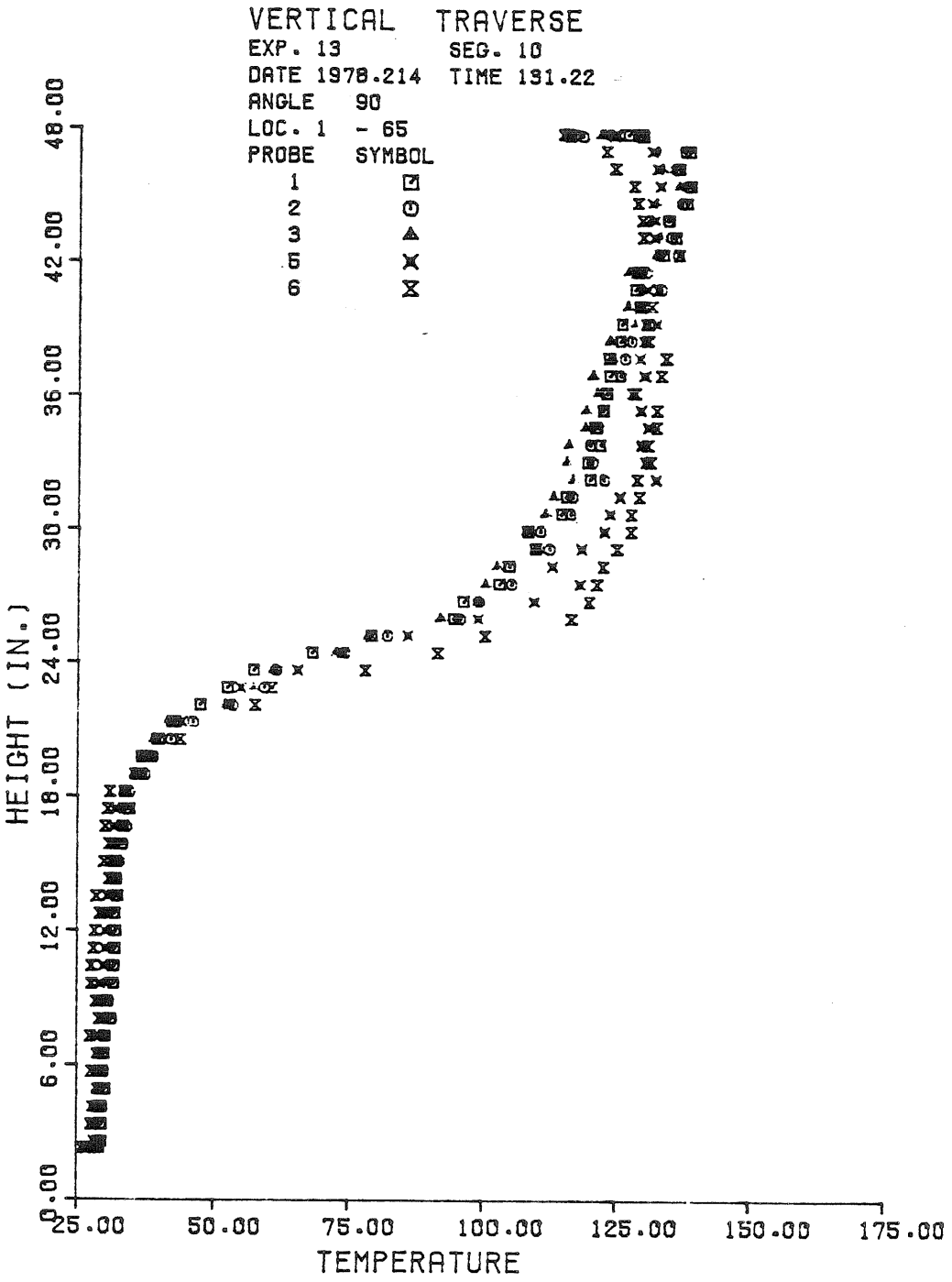

Figure (7.35) Gas Temperature Profiles across the Middle of a Room with a Fire in the Southwest Corner. $Q^* = 7.85 \times 10^{-3}$ (Exp. 13).

When the fire is located in the back corner of the room, not only is the mass flow into the ceiling jet reduced, but the convective heat transfer losses will be greater because the gas must flow a greater distance along the cold ceiling before reaching a given measuring location. Thus the ceiling jet gas is $5 - 7^{0}C$ colder in Figure (7.35) than in Figure (7.2) which is roughly 37% of the room height closer to the source. In addition the temperature profile in Figure (7.35) is much flatter.

As a further example of this effect, consider Figure (7.36) which shows the data from probe 1, 105 cm from the axis of the plume in experiment 13. Compare this figure to Figure (7.7) which presents the data from probe 1 85 cm from the axis of the plume in experiment 15, an increase of 22 cm from Figure (7.2). The mean temperature data throughout the ceiling jet in Figures (7.36) and (7.7) are now very close, although judging by the magnitude of the temperature fluctuations, the ceiling jet in Figure (7.7) is slightly thicker, as we would expect given that the initial mass flux into the ceiling jet is 25% larger in experiment 15.

The increased convective losses thus produce a relatively cooler ceiling jet and this in turn explains why much of the ceiling is roughly $10^{0}C$ cooler in experiment 13. Furthermore, because the ceiling is cooler, the radiant flux to the floor is roughly 4% smaller and hence we expect that the floor zone gas will be cooler in Figure (7.35) than it was in Figure (7.2).

Finally, because the plume impinges in the southwest corner, we expect that the gas will be significantly hotter along the west side wall near the southwest corner, while further from the source it will be colder. These assumptions are confirmed in Figures (7.37) and (7.38).

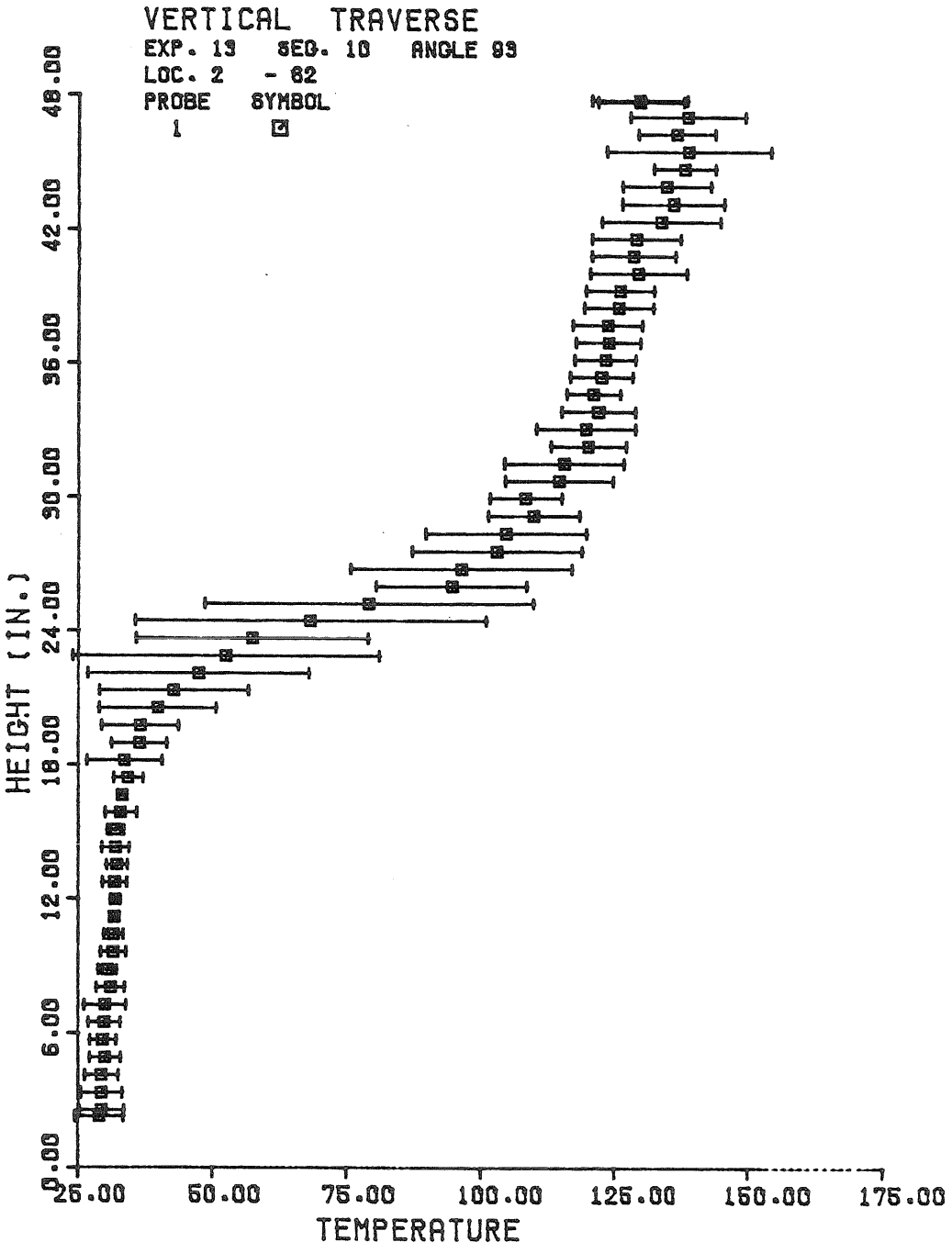

Figure (7.36) Gas Temperature Profile 105 cm from the Plume Axis (Exp. 13).

Along the rear half of the west side wall, probes 5 and 6 detect very hot gas within 40 cm of the floor in Figure (7.37). This appears to be evidence of the plume directly interacting with the wall as it rises. This pattern continues until a height of roughly 100 cm above which all probes see approximately the same hot gas, which is 15^0C hotter than the gas in experiment 15 in the same region of Figure (7.13). On the other hand probes 1 - 3 are farther from the source in experiment 13 than they are in experiment 15 and consequently, they are approximately 25^0C colder throughout much of the ceiling zone in Figure (7.37). Finally, as we would expect, the gas flowing down the north half of the west wall has experienced greater convective losses and so is some $10 - 12^0$C cooler in Figure (7.38) than it was in Figure (7.14).

7.6 Effect of Fire Strength

We have chosen to measure the strength of the fire Q_F in forms of the dimensionless heat input based on the room height z_c:

$$Q^*_{z_c} = \frac{Q_F}{\rho_o c_p T_o \sqrt{g z_c}\, z_c^2} \tag{7.4}$$

As shown in Table (7.1), we varied this parameter by a factor of 3.9 in the sequence of experiments 7, 10, and 13, all of which involved fires located in the southwest corner of the room, and which had the standard doorway.

Mean temperature data measure across the center of the room for these three tests are presented in Figures (7.35), (7.39), and (7.40) for experiments 13, 10, and 7 respectively. Note that the basic flow phenomena which we discussed in connection with experiment 15 are clearly visible in all three figures. There are three basic zones, whose mean temperature data can be reasonable well approximated by linear profiles.

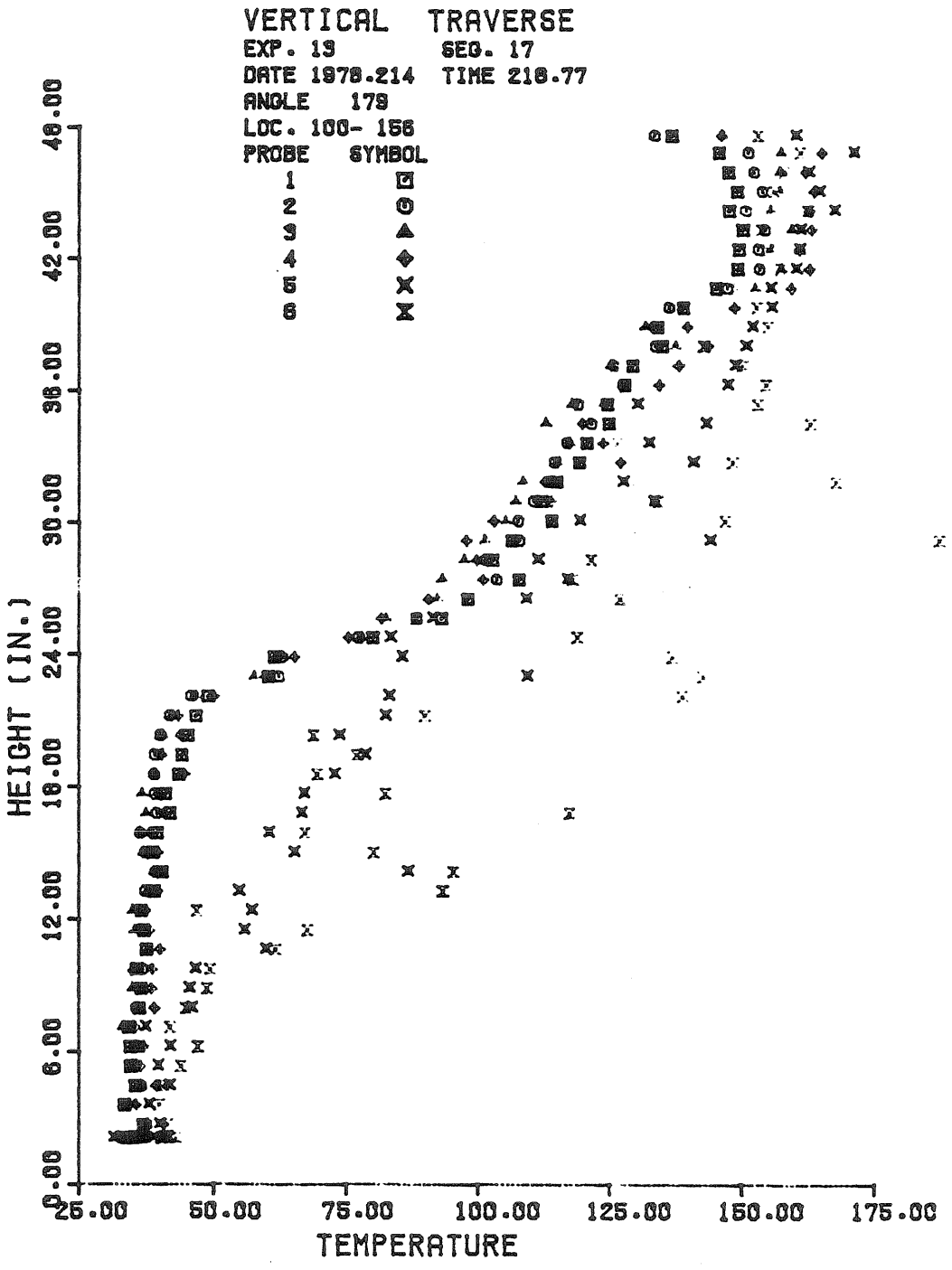

Figure (7.37) Gas Temperature Profiles along the Rear Half of the West Wall (Exp. 13).

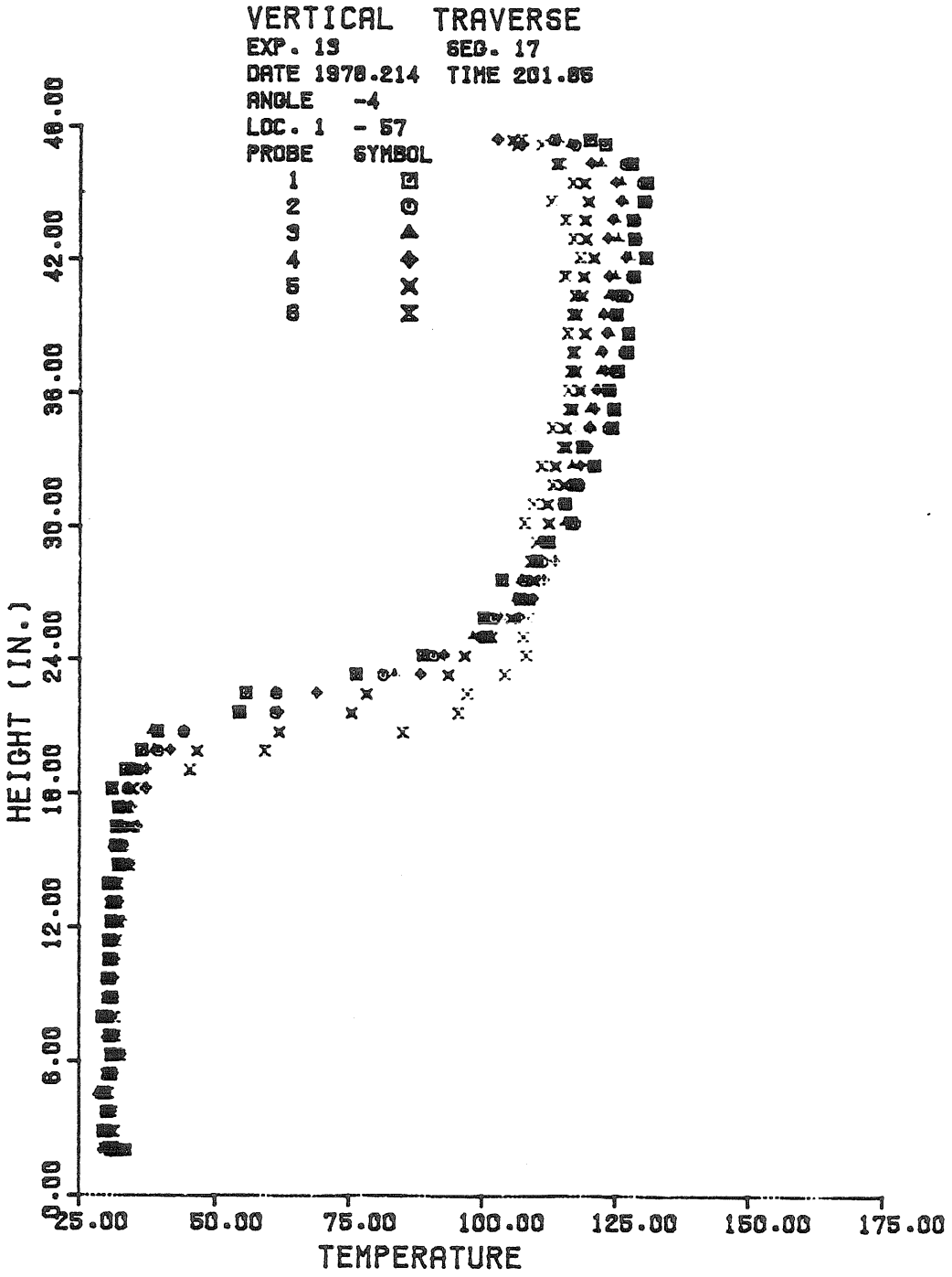

Figure (7.38) Gas Temperature Profiles along the Front Half of the West Wall (Exp. 13).

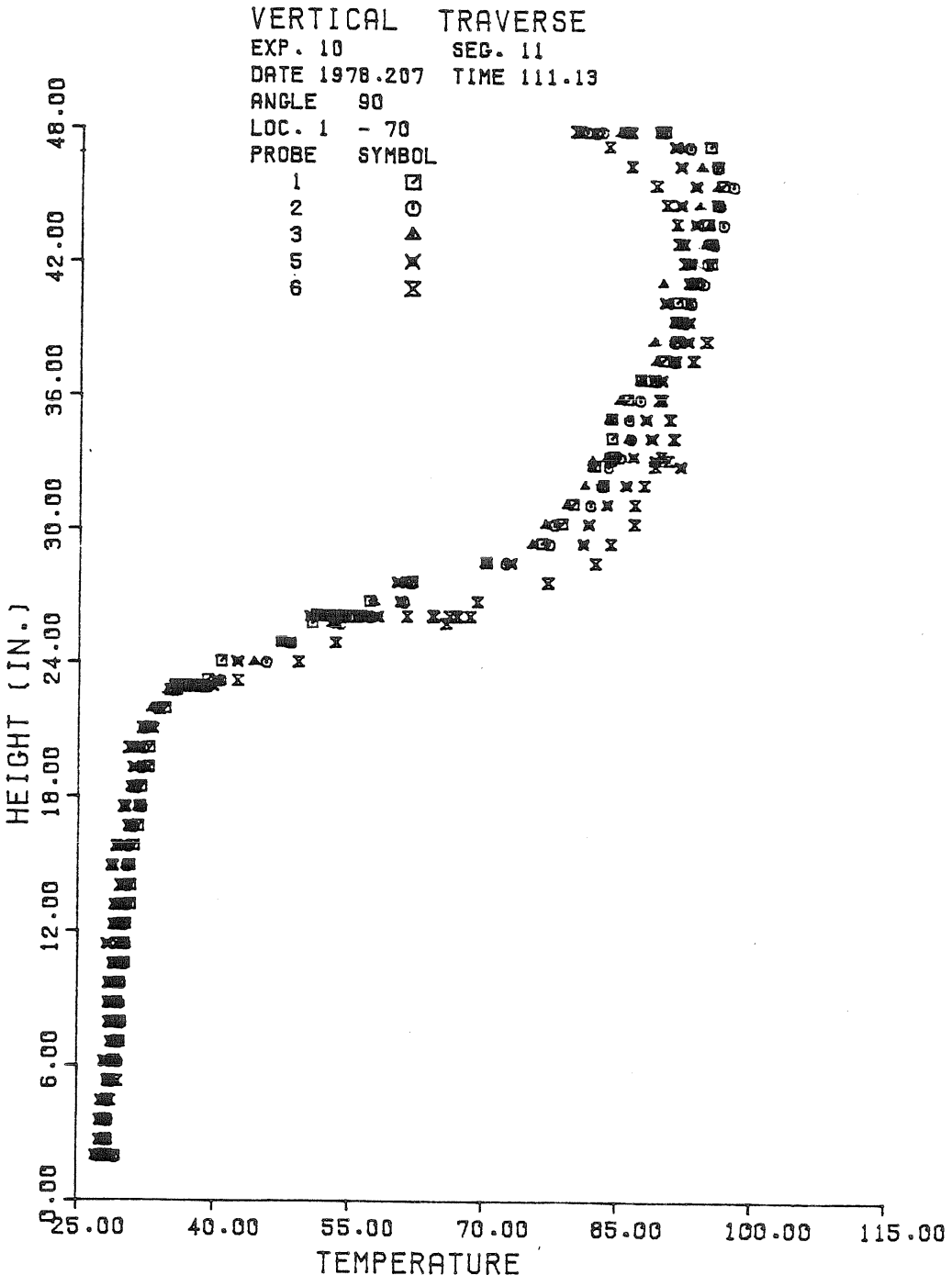

Figure (7.39) Gas Temperature Profiles across the Middle of a Room with a Fire in the Southwest Corner. $Q^* = 3.96 \times 10^{-3}$ (Exp. 10).

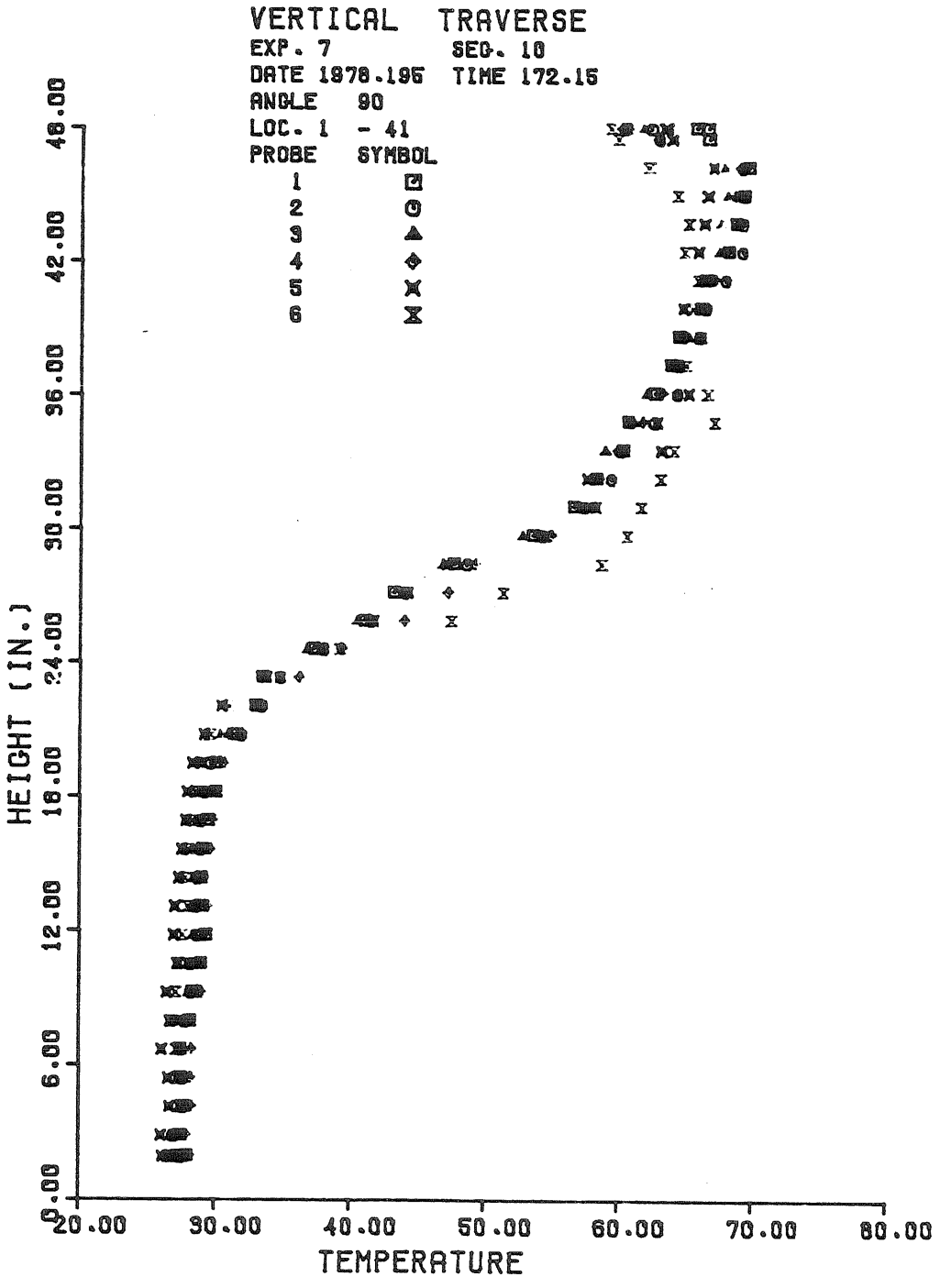

Figure (7.40) Gas Temperature Profiles across the Middle of a Room with a Fire in the Southwest Corner. $Q^* = 2.01 \times 10^{-3}$ (Exp. 7).

In addition there is a ceiling jet of originally hotter than average gas flowing along the ceiling, and there is also a flow of hot gas down the east side wall which penetrates beneath the height of the upper edge of the interface zone. Finally note that the greater interface zone thickness apparent in Figure (7.39) may have been caused by external drafts from the air conditioning system in the laboratory. The vents to this system were closed during the latter experiments and we noted that the fire itself was not blown about as strongly.

The primary effect of increasing the source strength is the expected increase in the upper layer enthalpy. In Table (7.4) we have listed the temperature difference between the average floor and ceiling zone temperatures ΔT_{21} as well as the difference between the minimum and maximum temperatures extrapolated from the floor and ceiling zone linear profiles ΔT_{max}.

Table (7.4) Gas Temperature Differences

Expt.	ΔT_{21} [°C]	ΔT^*_{21}	ΔT_{max} [°C]	ΔT^*_{max}
7	35.8	7.49	45.8	9.57
10	58.7	7.80	72.9	9.69
13	93.3	7.83	111.0	9.31

Note that there is not a unique temperature scale for these experiments. If there were no heat loss from the upper layer, ($c_q = 1$), we would use $T_o(Q^*_{z_i})^{2/3}$ as the temperature scale, as suggested in the in the room model of Chapter III. On the other hand for bare ceiling tests, or equivalently, for complete enthalpy loss ($c_q = 0$), $T_o(Q^*_{z_c})^{2/3}$ is the appropriate choice. We have chosen here to use the latter

normalization for consistency with our heat transfer results, and because there is a significant loss of enthalpy from the upper layer ($c_q < 1$).

The interesting fact presented in Table (7.4) is that although $(Q^*_{z_c})^{2/3}$ changes by a factor of 2.5 the dimensionless temperature differences are roughly constant. This is even more remarkable when we recall that by increasing the fire diameter to increase Q* we effectively changed the plume entrainment constant, by decreasing the distance between the edge of the plume and the wall, and that this effect is not taken into account by the simple power scaling relations. Similarly the dimensionless CO_2 concentration difference also scales with $(Q^*_{z_c})^{2/3}$, as shown by the data in the last column of Table (7.2).

A secondary effect of increasing Q* is the reduction in the height of the interface zone seen in Figures (7.39) and (7.35). Although both experiments 10 and 13 had roughly the same plume entrainment constant, the interface zone in experiment 13 is noticeably lower than in experiment 10. This decrease in the interface height appears to be related to the 50% increase in burner diameter which occurs between experiments 10 and 13. As the source diameter increases, the near field region of the plume becomes increasingly more important. Thus while the interface height measured by z^+ decreases by roughly 4 cm, the virtual source depth, which is a measure of finite source effects in the near field, increases by 5 cm. This is a 40% increase from the virtual source depth in experiment 10 and indicates the height of the interface above the virtual source remains nearly constant. This agrees with the Boussinesq room model which predicts that the interface height is independent of the source strength. Under this approximation,

the greater mass flux in a stronger plume is just balanced by the increased hydrostatic pressure difference which drives the counterflow at the door.

7.7 Modeling the Gas Temperature Data

In Chapters III and IV, we presented a rather simple model for predicting the interface height and upper layer temperature, based on the properties of a point source plume rising through a uniform environment and some assumptions governing the buoyancy driven counter flow of fluid through a single opening to the environment.

Tangren, Sargent, and Zukoski (1978) found that the simple version of the model, described in Chapter III, did a good job of predicting the interface heights and the density differences in their ¼ scale brine flow simulations. The data from these tests, which were conducted at much smaller Q* values than our ½ scale fire experiments, did not exhibit a number of the complicated flow phenomena which we have just discussed in connection with our ½ scale results. In particular, because these were brine flow simulations, there were no heat transfer effects. Consequently the heat loss parameter c_q was unity, and there was no density gradient in the upper layer. Secondly, because the sources were much weaker there was no evidence of flow down the side walls, and the interface was relatively sharp. In addition, when the opening was a door, there was no contamination of the floor zone fluid by fluid from the upper layer.

The success of the simple model in predicting the interface heights and upper layer density in the brine experiments confirmed the validity of the point source plume approximation and the treatment of counter flow through the orifice. In order to extend this approach to the more com-

plicated situation encountered in our ½ scale fire room tests, we added a number of features to the basic model, as described in Chapter IV. In particular we allow for convective losses from the hot upper layer and for an intermediate temperature floor zone, which we assume is heated by a combination of convective heat transfer from the floor and lower walls and turbulent mixing with hot ceiling zone gases. In addition, because our premixed burner supplies the plume with finite initial fluxes of mass and momentum as well as buoyancy, we treat the equivalent point source plume as though it emanated from a virtual source.

To be logically consistent at this point we should present some formulation for calculating the effects of heat transfer and turbulent mixing which we have just mentioned. Unfortunately, we do not have a sufficient understanding of the details of these flow processes to allow us to calculate a priori the parameters which we use to model them. Nevertheless by including these parameters in our formulation, we can study the sensitivity of the solution to their variation, as we did in Chapter IV, and we can use our empirical data to estimate their values in order to check the consistency of the model.

We can estimate the convective heat transfer losses from the hot upper layer in two ways. First, we can use the measured wall temperature data and our radiant heat transfer program which is described in Chapter IX, to calculate the average convective flux to each solid surface which borders on this upper layer. We can then immediately find the total loss from the upper layer which is given as $Q_{Loss} = (1-c_q) Q_F$. On the other hand, using our finite source plume computation and the empirical values for the average upper and lower layer temperatures $\bar{T}_2$ and $\bar{T}_1$, and the interface height $z_{int} = z^+$, we can find a second esti-

mate for the heat loss paramater c_q from equation (8.3). Numerical values for these two estimates are presented in Table (7.5) for the five typical experiments we have been examining. Note that the basic conditions for each of these experiments are listed in Table (7.1). The data in the first column, labelled "constant α", show that if we do not reduce the plume entrainment constant α for experiments 7, 10, and 13, in

Table (7.5) Heat Loss Parameter c_q Estimates

Expt.	Plume Model (constant α)	Plume Model (Reduced α)	Average Convective Flux	$c_{fr_{min}}$
7	0.866	0.762	0.688	0.070
10	0.881	0.680	0.701	0.054
13	0.889	0.697	0.732	0.059
15	0.740	0.740	0.714	0.046
16	0.590	0.590	0.595	0.029

which the fire was located in the corner of the room, we will underestimate the convective losses. On the other hand, the good agreement between the data in the second and third columns confirms that our plume computation and choice of α are consistent with the convective flux data. Note when the opening is a door, the average value of c_q is 0.714. This drops to 0.592 for the window geometry indicating that roughly 12% more of the heat released from the fire is lost to the walls in this situation. This is not surprising because the upper layer temperature is greater and the ceiling zone extends deeper into the room when the opening is a window.

Once we have an estimate for the total convective loss from the upper layer Q_{Loss}, we can use the radiant heat transfer computations to obtain an estimate for c_{fr}, the fraction of Q_{Loss} which is delivered to the lower layer. In our apparatus the front $^5/_8$ of the floor was backed with insulation. We therefore assume that the net radiant flux incident on this area is transferred to the floor zone gas by natural convection. Thus a minimum estimate of c_{fr} is given by this flux divided by Q_{Loss}. We have tabulated these values, which run from 3 - 7% of Q_{Loss}, in the last column of Table (7.5).

Given estimates for the parameters involving heat transfer, we can use the average upper and lower layer temperatures and CO_2 concentrations to find an estimate for the turbulent mixing parameter η, which gives the fraction of the plume mass flux at the interface $\dot{m}_p$ which exits through the door or window. Thus $(1-\eta)\dot{m}_p$ is the mass flux of hot upper layer gas which crosses the interface and is mixed with the floor zone gas. We expect that this flux will consist of two parts. First, as we have seen there appears to be a consistent trend in all the experiments for hot gas to flow down the sidewalls, and, especially in the corners, to penetrate into the floor zone, where some of this hotter fluid will presumably mix with the floor zone gas. On the other hand, when the exit to the room is a window, there will be much greater shear between the counterflowing streams near the window and we expect additional mixing to occur in this region.

To obtain an estimate for η from the temperature data, we perform a simple enthalpy balance on the gas in the floor zone excluding the plume. Assuming that the radiant heating is small and that the mass fluxes of fuel entering the room and of intermediate density air leaving

the room can both be neglected, we obtain the simple expression:

$$\eta_T \approx \frac{\bar{T}_2 - \bar{T}_1}{\bar{T}_2 - T_\infty} \tag{7.5}$$

where T_∞ is the ambient temperature of air in the laboratory. The assumptions inherent in this approach appear to be well founded. Calculations show that both mass fluxes are less than 1.4% $\dot{m}_p$, and that the assumed radiant heating is less than 25% of the enthalpy flux carried by the hot gas which penetrates into the floor zone.

Similarly, to obtain an estimate of η from the CO_2 concentration data we perform a simple mass balance for the air in the lower layer, again excluding the plume itself. If we again ignore the mass flow rates of fuel into, and intermediate density air out of, the room, we are left with the analogous expression to (7.5):

$$\eta_c = \frac{\bar{C}_2 - \bar{C}_1}{\bar{C}_2 - C_\infty} \tag{7.6}$$

where $\bar{C}_1$ and $\bar{C}_2$ are the average floor and ceiling zone CO_2 concentrations, and C_∞ is the concentration in ambient air.

We have tabulated the values of η_T, η_c, and this average value $\bar{\eta}$, which we use in the actual computation, in Table (7.6). Note the values of both η_T and η_c agree very well and indicate that roughly 91% of the plume mass flux escapes through the door, compared to only 66% which can escape through the window. If the contribution of the flow down the wall remains constant, this would indicate that roughly an additional 25% of the plume's mass flux is mixed with the entering window jet in the vicinity of the window. Finally we should note that we have assumed that the mass flux of entering air entrained into the exit

Table (7.6) Mixing Estimates

Expt	η_T	η_c	$\bar{\eta}$
7	0.928	0.904	0.916
10	0.932	0.915	0.924
13	0.931	0.905	0.918
15	0.890	0.905	0.898
16	0.676	0.647	0.662

stream within the room can be neglected, because the hot gas profiles along the outer edge of the door match those within the room. This amounts to setting the parameter κ equal to zero in the room model.

We must also calculate two other parameters before proceeding with the computation. First we need an initial value for the density difference ratio δ defined in equation (4.1). Because this is a Boussinesq model, this becomes:

$$\delta \approx \frac{T_1 - T_\infty}{T_2 - T_\infty} \tag{7.7}$$

We have simply used the empirical values $\bar{T}_1$ and $\bar{T}_2$ in (7.7). Finally, the virtual source of the equivalent point source plume is given by equation (2.41).

The computed results are listed in Table (7.7)along with the experimental data. Typical results for experiment 15 are shown graphically in Figure (7.41). In this figure we have superimposed the calculated temperature profile on top of the three linear profiles measured in the interior of the room.

Given the uncertainty regarding the turbulent mixing processes and the details of the natural convection heating of the floor zone gas, the agreement between the calculations and the experimental data appears to be very good indeed. Basically the model does a good job of predicting

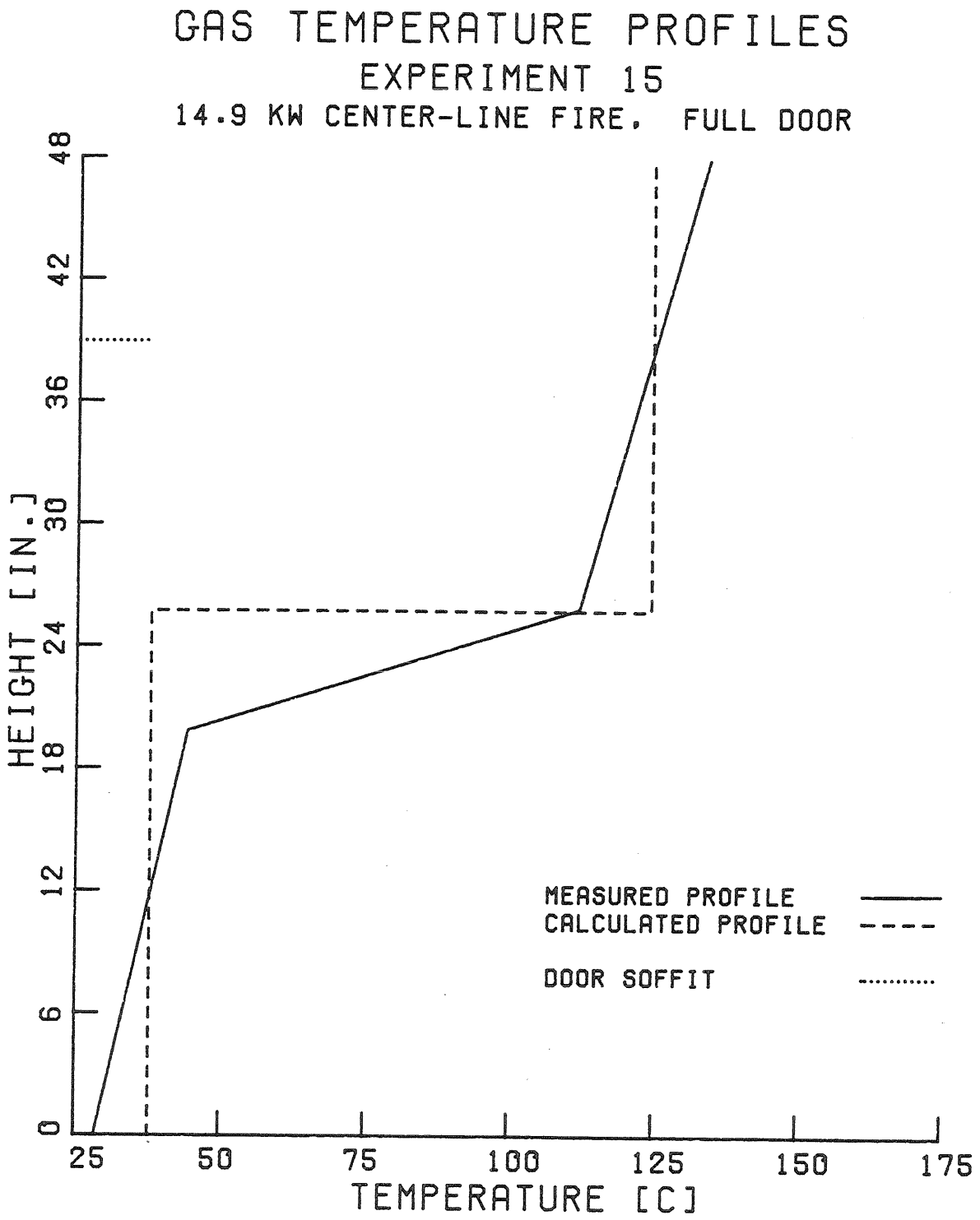

Figure (7.41) Calculated and Measured Gas Temperature Profiles for a Room with an Open Doorway (Exp. 15).

the average upper and lower layer temperatures. It tends to consistently overestimate the temperature of the floor zone gas by an average of $2.7^{0}C$. However, the simple point source plume model, corrected for finite source effects by starting the plume at the virtual rather than the physical source, does a very good job of estimating the enthalpy and mass flow rates in the plume. Consequently the calculated average temperature difference between the floor and ceiling zones is on the average only $0.2^{0}C$ warmer than the experimental value. Similarly, the calculated interface height is an average of only 3.9% less than the experimental data would indicate. Note that because the temperature difference is nearly correct, the average upper layer temperatures are also an average of $2.9^{0}C$ warmer than the experimental values. Finally note that the larger average fractional deviations which occur in estimating the density difference ratio are caused by the fact that the ratio itself is quite small for the southwest corner fires. The actual deviations themselves are nearly constant and have an average value of 0.030.

Because of the uncertainty regarding the mixing and heat transfer processes, and because we have a relatively limited number of experimental conditions, we have not attempted to systematically adjust the parameters to obtain the best possible fit to our data. Nevertheless it seems worthwhile to point out that if we had included the heat transfer from the floor in the lower layer enthalpy balance which we used to estimate η_T, we would have obtained slightly larger values of η_T. If we had then used these larger values of η_T in the computations, the calculated floor zone temperatures would have decreased slightly and we might have improved the agreement with the temperature data and hence with the density

Table (7.7) ½ Scale Room Results: Experimental Data & Model Predictions

Expt.	Lower Layer Temperature [^{0}C]		Upper Layer Temperature [^{0}C]		Interior Interface Height [cm]		Interface Height at doorway [cm]		Density Difference Ratio	
	exptl.	model	exptl.	model	exptl.	model	exptl.	model	exptl.	model
7	28.8	30.7	64.7	71.3	77.0	70.9	74.4	61.9	0.072	0.103
10	30.4	32.9	89.1	93.9	73.8	71.6	73.2	61.5	0.067	0.099
13	31.5	36.2	124.8	128.3	69.9	69.9	65.7	63.1	0.061	0.105
15	36.4	37.8	122.9	124.3	65.7	65.4	65.7	65.8	0.104	0.117
16	68.2	71.4	154.9	153.3	59.5	57.1	76.2	76.8	0.324	0.353
Average Fractional Deviation		7.6%		3.7%		-3.9%		-7.2%		36.9%

difference ratio data as well. However, as η increases, the calculated interface height, which is already slightly low, decreases still further. Thus by improving the temperature fit we would worsen the agreement with interface height data. This indicates some of the inherent limitations of our rather simple model.

We can also use the model predictions to help illuminate the mixing processes which occur near the door or window. In Chapter III we introduced two Richardson numbers for the flow through the door or window opening. The opening Richardson number Ri_H, defined in equation (3.48), is based on the total height H of the opening and on the calculated maximum velocity difference. We also defined an inflow Richardson number Ri_c in equation (3.49) based on the thickness of the inflowing stream and its bulk velocity. In Table (7.8) we have presented the calculated values for these two dimensionless ratios along with $\bar{\xi} = (1 - \bar{\eta})$, the estimated fraction of mass leaving the upper layer which mixes with the lower layer gas.

Table (7.8) Mixing as a Function of Richardson Number

Expt	Ri_H	Ri_c	$\bar{\xi}$
7	0.789	25.8	0.084
10	0.816	27.0	0.076
13	0.767	25.4	0.082
15	0.671	20.7	0.102
16	0.259	2.68	0.338

While we do not have enough data to attempt a statistical correlation, the trends are certainly clear. The first three experiments listed have nearly constant values of both Richardson numbers. The

average values are 0.791 and 26.1 respectively. The amount of mixing is small in all three cases and is close to the average value of 8.1%. Experiment 15 has slightly lower Richardson numbers, indicating greater shear, and has roughly 26% more mixing. Finally when the door is replaced by a window the amount of shear and especially the velocity of the inflowing stream increase dramatically. Thus Ri_H drops by a factor of 3 in experiment 16, while Ri_c falls by a factor of 9.7, compared to the average values of the first three experiments. This reduction results in a 417% increase in the mixing as measured by $\bar{\xi}$.

7.8 Review of General Results

As a summary of the general results we have seen in the gas temperature and composition data, we have presented dimensionless temperature profiles in Figures (7.42) through (7.46) for the five experiments which we have discussed. In these figures the dimensionless temperature difference T^*_∞ gives the increase in the gas temperature above T_∞, the ambient temperature in the laboratory, and is scaled by $T_o(Q^*_{z_c})^{2/3}$. The heights are normalized by the room height z_c. In addition to replotting the three linear profiles inferred from the interior temperature data in these figures, we have also added the predicted upper and lower layer temperatures and the interface height as calculated by our room model.

In all the cases there are three distinct zones. The floor and ceiling zones have relatively small temperature gradients while the interface zone has a large but finite gradient. These gradients, normalized by $\Delta T_{max} = T(z_c) - T(0)$ rather than $T_o(Q^*_{z_c})^{2/3}$ as in Figures (7.42) - (7.46), are listed in Table (7.9). These normalizations are related however because $\Delta T_{max} \approx T_o(Q^*_{z_c})^{2/3}$ as we have seen.

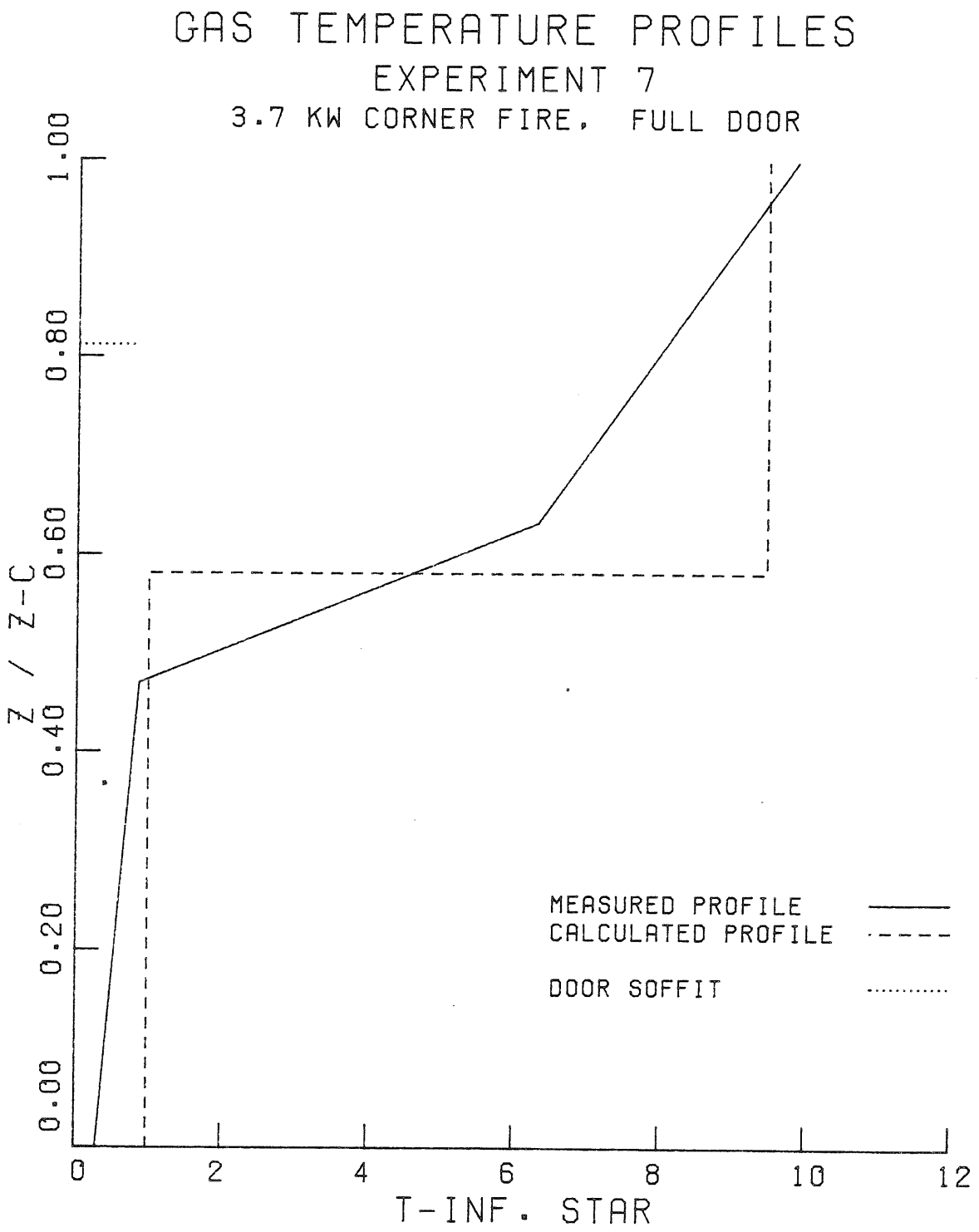

Figure (7.42) Predicted and Measured Dimensionless Temperature Profiles for Exp. 7 ($Q^* = 2 \times 10^{-3}$ Fire in Corner, Doorway)

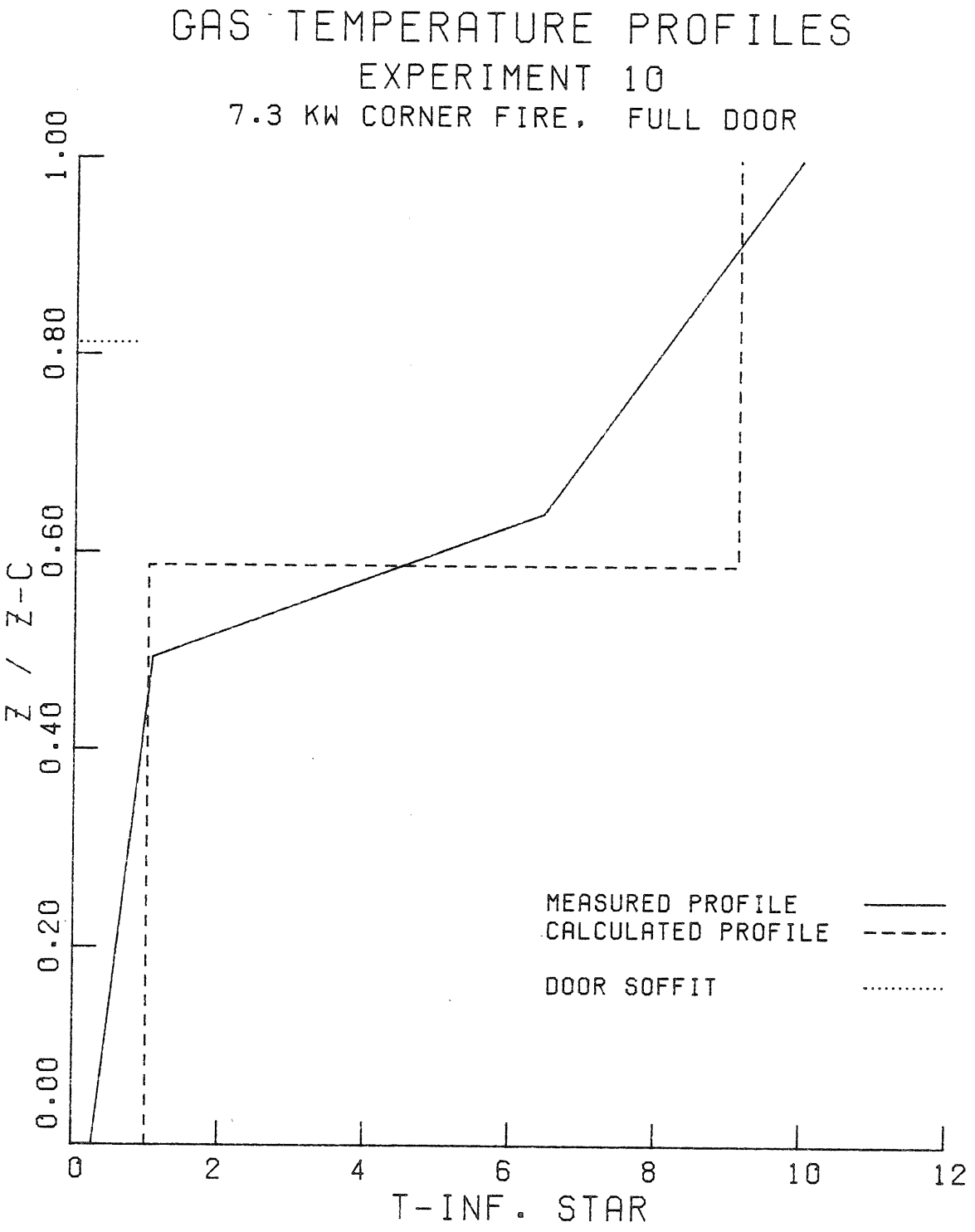

Figure (7.43) Predicted and Measured Dimensionless Temperature Profiles for Exp. 10 ($Q^* = 4 \times 10^{-3}$ Fire in Corner, Doorway).

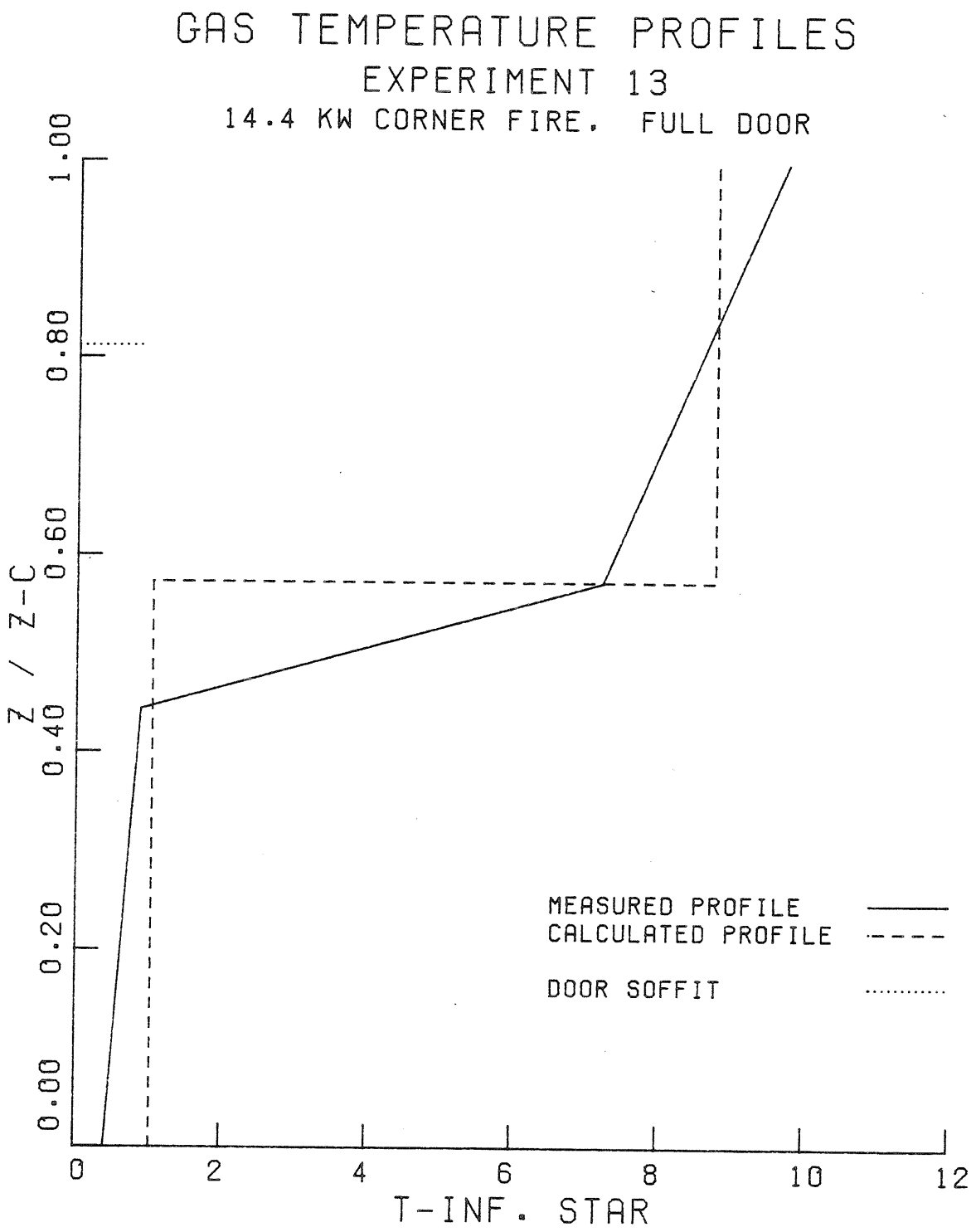

Figure (7.44) Predicted and Measured Dimensionless Temperature Profiles for Exp. 13 ($Q^* = 8 \times 10^{-3}$ Fire in Corner, Doorway).

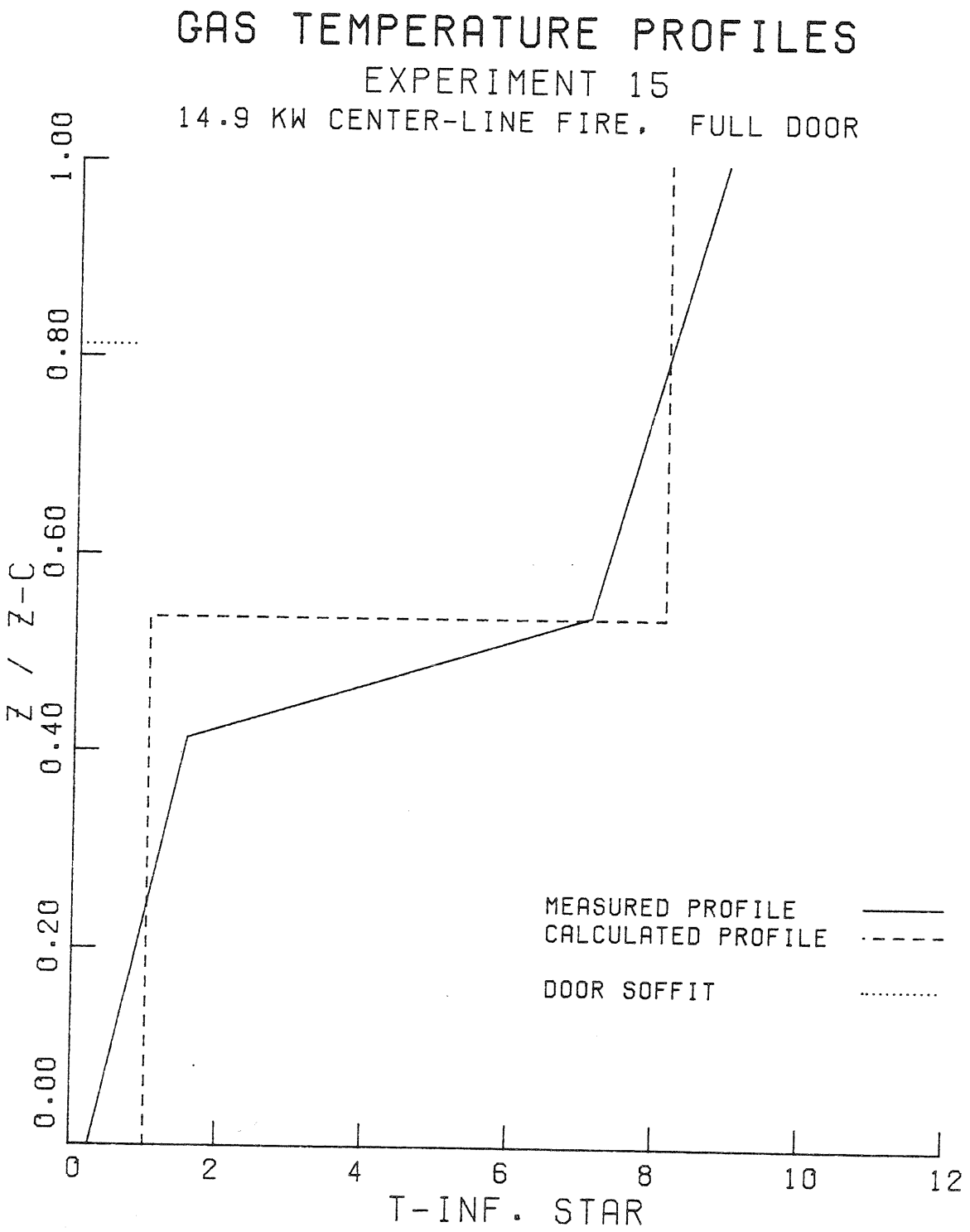

Figure (7.45) Predicted and Measured Dimensionless Temperature Profiles for Exp. 15 ($Q^* = 8 \times 10^{-3}$ Fire on Center-line, Doorway).

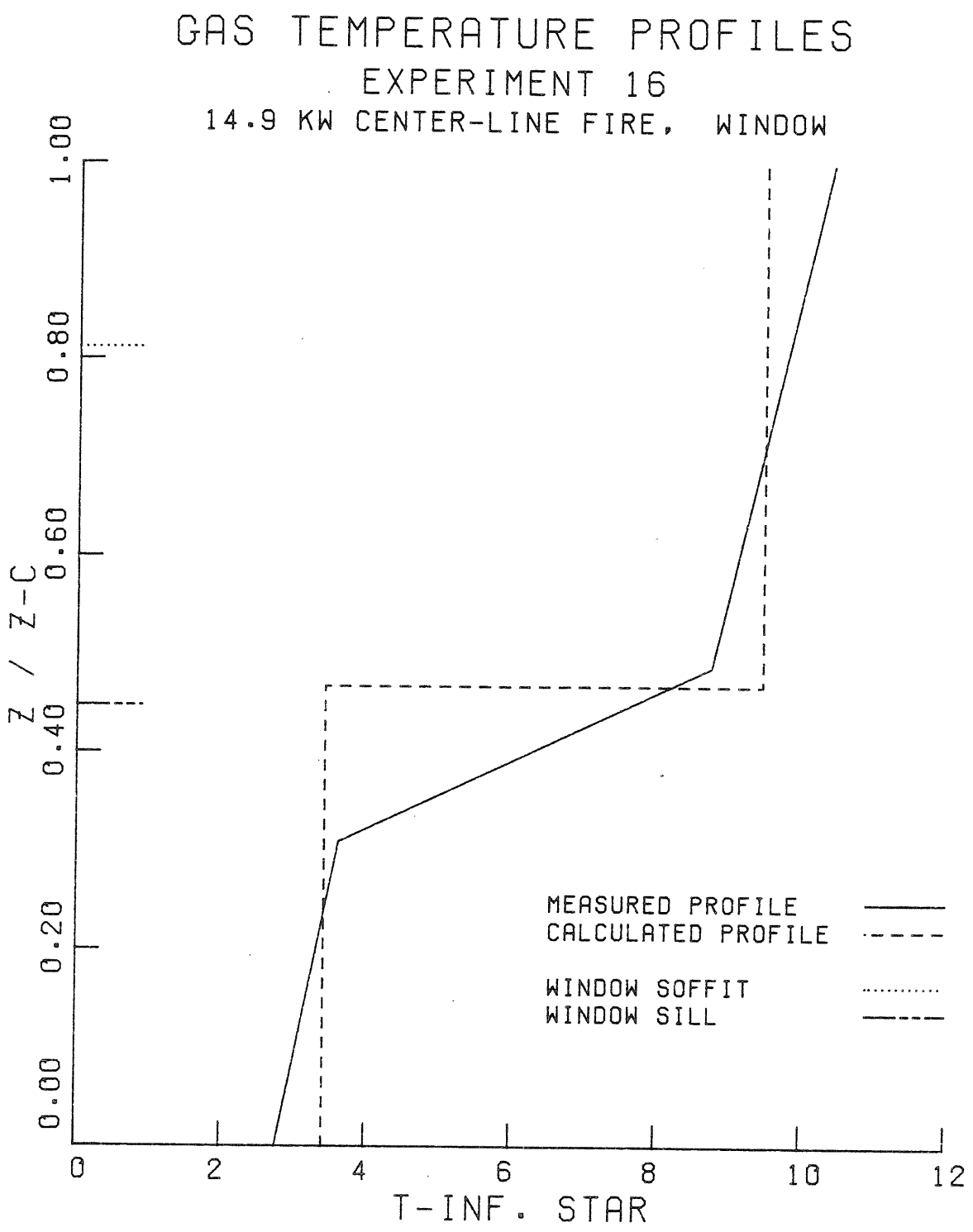

Figure (7.46) Predicted and Measured Dimensionless Temperature Profiles for Exp. 16 ($Q^* = 8 \times 10^{-2}$ Fire on Center-line, Window).

Note that the values of these normalized gradients in each zone are very similar for the experiments involving a door. The somewhat lower interface zone and larger ceiling zone gradients of experiment 7 are probably caused by external drafts in the laboratory. This regularity, coupled with the much smaller ceiling zone CO_2 gradients, suggests to us that the ceiling zone temperature gradient is fixed by a combination of heat transfer and a regular mixing pattern, and that this combination scales roughly with $T_o(Q^*_{z_c})^{2/3}$. Furthermore because the dimensionless curves exhibit roughly the same overall change in T^*_∞, the basic temperature differences must also be proportional to $T_o(Q^*_{z_c})^{2/3}$. This is significant because $(Q^*_{z_c})^{2/3}$ changes by a factor of 2.5 between Figures (7.42) and (7.44). These facts confirm the utility of normalizing the data with qunatities based on the simple point source plume.

The exceptions to the general pattern are caused by changing the opening geometry or fire location. Blocking the lower half of the doorway to create a window causes a significant decrease in the interface height between Figures (7.45) and (7.46). Greater shear near the window results in greater mixing and hence in a hotter floor layer. This in turn results in a hotter ceiling zone because the heat input is constant. Finally, by moving the fire into the rear corner of the room, we effectively reduced the plume's ability to entrain the surrounding air. This causes a reduction in mass flow in the plume and is visible in the form of higher interfaces in Figures (7.42) - (7.44).

Table (7.9) Normalized Interior Gradient Data $\frac{\Delta\Theta}{\Delta\bar{z}}$

Expt.	Floor Zone		Interface Zone		Ceiling Zone	
	Temperature	CO_2	Temperature	CO_2	Temperature	CO_2
7	0.125	0.120 †	3.51	6.49	1.01	0.070
10	0.167	0.099	5.49	8.95	0.776	0.227
13	0.112	0.115	5.28	8.51	0.633	0.238
15	0.091	0.179	5.13	6.68	0.454	0.231
16	0.358	0.466	3.80	4.72	0.419	0.043

where $\frac{\Delta\Theta}{\Delta\bar{z}} = \frac{(\Delta x / \Delta x_{max})}{(z/z_c)}$, $\Delta x_{max} = x(z_c) - x(o)$, and $x = \bar{T}[^0C]$ or $x = \bar{C}[\%CO_2]$

† inferred from data measured along west wall

VIII. CONVECTIVE HEAT TRANSFER MODELS

8.1 Introduction: Flow patterns in the Upper Layer

When a fire breaks out in a room, heat transfer between the hot combustion products and the relatively cold walls can have several important effects. In the very early stages of a fire, convective heat transfer, between the impinging plume and the ceiling, is responsible for the increase in the temperature of the ceiling. If the ceiling is flammable, this heat transfer process may be sufficient to ignite it and cause the fire to spread significantly. In the later stages of the fire, the ceiling may radiate enough energy to the lower portion of the room to cause it to ignite as part of the "flash-over" process, thereby increasing the total heat release and smoke production of the fire tremendously. Even if flash-over does not occur, the radiation of energy from the ceiling to the lower portion of the room can cause significant changes in the flow patterns, as was shown in Chapter IV. Consequently, it is desirable to be able to predict the distribution of convective heat transfer from the hot gas to the ceiling and upper walls.

In order to predict the convective heat transfer in a room fire situation, one must model several features of the typical gas flow path sketched in Figure(8.1). First, since most rooms are of relatively limited height, the fire, viewed from the interface, may appear to be a finite source of mass, momentum and buoyancy, rather than a point source of buoyancy alone. If the flame height is below the interface, the resulting fire plume can be described by the finite source models of Chapter II. On the other hand if the flame extends above

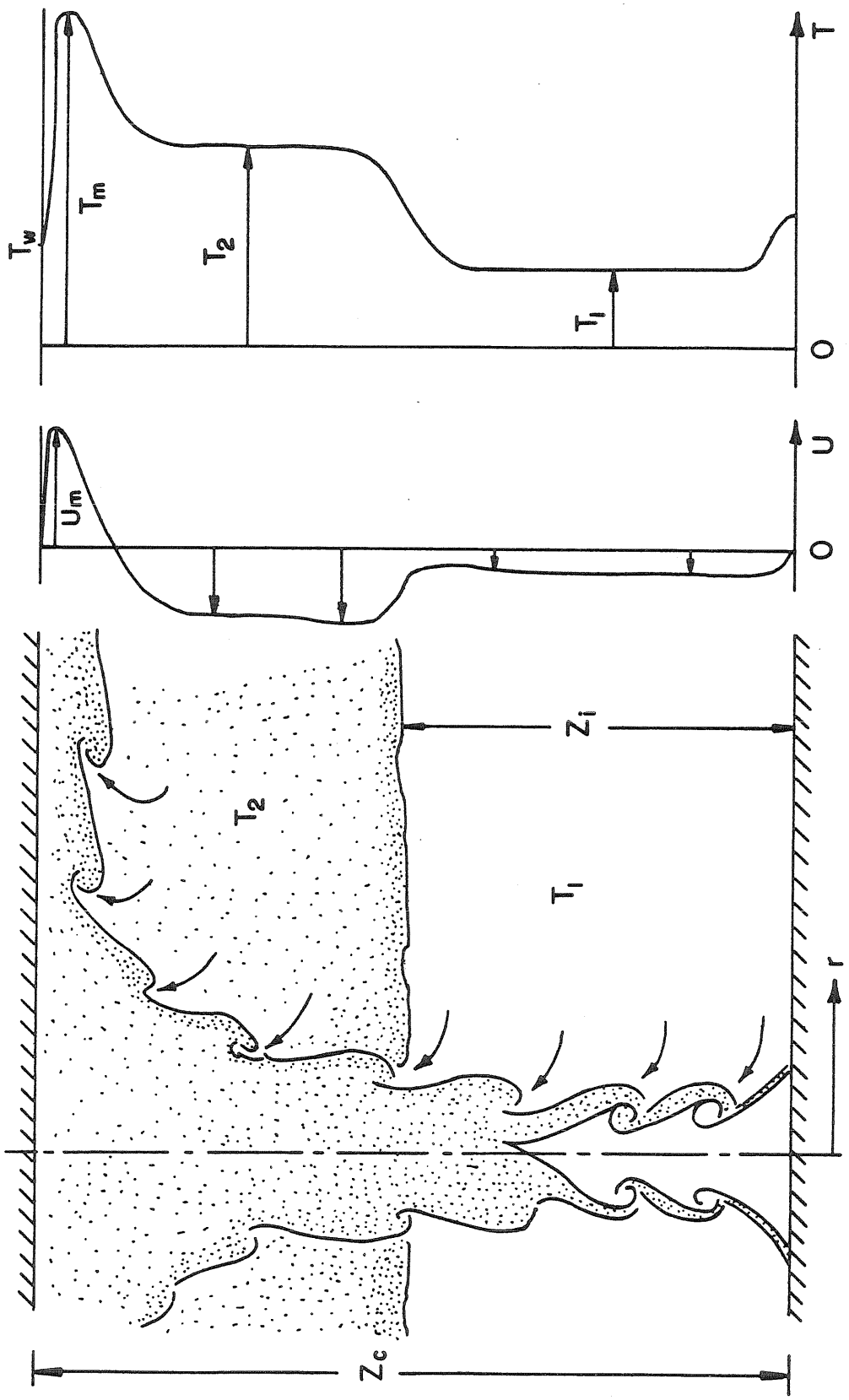

FIGURE 8.1 FLOW PATTERNS IN THE UPPER LAYER

the interface, more complicated entrainment relations are required. We will assume here that the flame does not reach the interface. At the interface another complication arises. Assuming that the ceiling layer is well stirred and approximately at a uniform temperature T_2, the plume will experience a sudden loss of buoyancy on crossing the interface. Directly above the fire, the resulting plume impinges on the ceiling and creates a relatively hot stagnation region. Further away from the stagnation point the hot fluid from the plume spreads out to form a ceiling jet and flows radially or axially away from the impingement region, depending on the plume and room geometries. Finally, since the room is basically a closed structure, a significant return flow must exist which effectively recycles most of the fluid from the ceiling jet, in order to supply the mass flow which is entrained by the upper plume and ceiling jet. For example, if the interface is at half the room height ($\bar{z}_i = 1/2$) and we measure the mass flow in units of $\dot{m}_p$, the mass flow in the plume at the interface, then the mass flow delivered to the ceiling jet will have a value between 2.0 and 3.2 times $\dot{m}_p$, depending on the buoyancy of the upper plume ($c_q = 1$ and $c_q = 0$, respectively). For simplicity, consider a round room with $r = z_c$ ($\bar{r} = 1$), then the calculated mass flow in the ceiling jet increases roughly by a factor of 2.7 to between 5 to 9 $\dot{m}_p$. Since the height of the interface is constant, $\dot{m}_p$ must exit through the door; leaving 4 to 8 times this mass flow to be recirculated. For the case of a two dimensional room and ceiling jet ($\bar{x} = 1$), the recirculating mass flow has a value between 2 and 4 $\dot{m}_p$. It is this recirculation process that

is responsible for keeping the upper layer well stirred and at an approximately uniform temperature T_2, as was assumed in Chapter II. It is also clear from this example that entrainment in the ceiling jet as well as in the plume plays a major role in fixing the properties of these flows.

In the following sections, we will trace the flow path above the interface and introduce relatively simple models, or more accurately, calculation schemes, for the flow phenomena encountered. Starting at the interface, we will first discuss the conditions that the change in external temperature imposes on the plume. Then we will develop estimates for the convective heat transfer as the plume impinges on the ceiling. Finally, we will examine an integral model for the resulting ceiling jet, and the heat transfer associated with it.

8.2 Conditions Across the Interface

In most fires in rooms with one or more openings through which the smoke can escape, a quasi-steady state flow pattern will quickly be established with a stably stratified hot layer of gas in the upper portion of the room, as described in Chapters III and IV. In those chapters, only the lower portion of the plume was of interest. It was modeled simply as a source of mass and enthalpy to the upper layer, and its behavior above the interface was ignored. In addition, all energy losses from the upper layer gas were lumped into the parameter c_q which determined the difference between the mass averaged temperature difference in the plume crossing the interface, $\langle \Delta T \rangle_i$, and the mean upper layer

temperature difference $(T_2 - T_1)$. As a first step in estimating these losses, we must calculate the behavior of the plume crossing the interface. Following Kubota (1977), we assume that mass, momentum and enthalpy are conserved as the flow crosses the interface. Since we have assumed that the Boussinesq approximation is valid, it is convenient to work with the kinematic fluxes of mass, momentum and enthalpy, and to take T_0 as the reference temperature as before. The pressure is constant across the layer and conservation of mass $(W_1 = W_2)$ and momentum $(V_1 = V_2)$ immediately imply that the velocity profile does not change $(b_1 = b_2, w_{m_1} = w_{m_2})$. It is convenient to treat T_1 as the reference enthalpy level so that the kinematic enthalpy flux is:

$$\tilde{\dot{H}} = \int_0^\infty c_p \, w(T - T_1) \, 2\pi r \, dr \tag{8.1}$$

When we apply the conservation of enthalpy across the interface, and recall that the external temperature jumps from T_1 below the interface, to T_2 above it, we can show that:

$$\Delta T_{m_2} = \Delta T_{m_1} - (T_2 - T_1)(1 + \sigma) \tag{8.2}$$

Figure (8.2) shows this process schematically. Since the area under the $w \cdot (T - T_1)$ curve must be constant, the maximum temperature difference relative to the external temperature must fall as the external temperature rises. However, because the buoyancy is proportional to $(T - T_e)$, the kinematic buoyancy must also drop. Kubota (1977) has shown this can be conveniently written as:

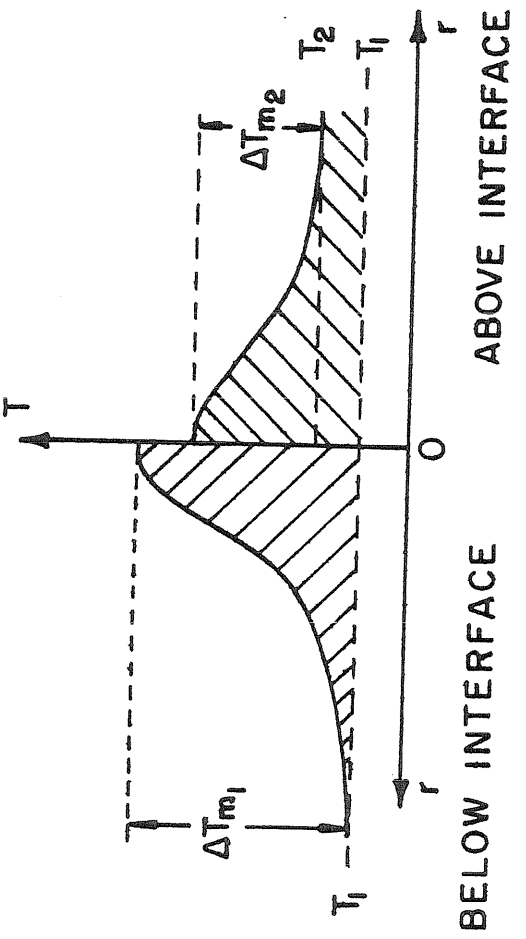

FIGURE 8.2 TEMPERATURE PROFILE ACROSS THE INTERFACE

$$\frac{F_2}{F_1} = 1 - g \frac{W_1}{F_1} \frac{(T_2 - T_1)}{T_0} = 1 - c_q \qquad (8.3)$$

The finite source plume model [equations (2.38) and (2.40)] can now be employed to estimate the upper level plume behavior with the new source given by (W_2, V_2, F_2). Note that this model implicity assumes that temperature profiles can instantaneously adjust as the plume crosses the interface. In reality, we expect a transition zone to occur, after which the upper stage plume profiles will again be self-preserving and of the form shown on the right hand side of Figure (8.2).

8.3 Plume Impingement

After the plume passes through the interface, it will proceed to rise, with diminished buoyancy, until it encounters the ceiling. Since the maximum velocity and temperature occur on the plume axis, the heat transfer to the stagnation point area will be large, as is shown by the data of Zukoski, Kubota, and Veldman (1975) for a bare ceiling in Figure (8.3). In order to calculate the heat transfer at the stagnation point and the subsequent ceiling jet flow, a knowledge of the behavior of impinging jets and plumes is required.

Recently a number of investigators have examined axisymmetric, turbulent impinging jets, including Tani and Komatsu (1964), Bradshaw and Love (1961), Poreh and Cermak (1959), Donaldson, Snedeker, and Margolis (1971), Bradbury (1972), Beltaos and Rajaratnam (1974), and Giralt, Chia, and Trass (1977). Their results indicate that for impingement surfaces sufficiently far removed from the jet nozzle for a free jet to have

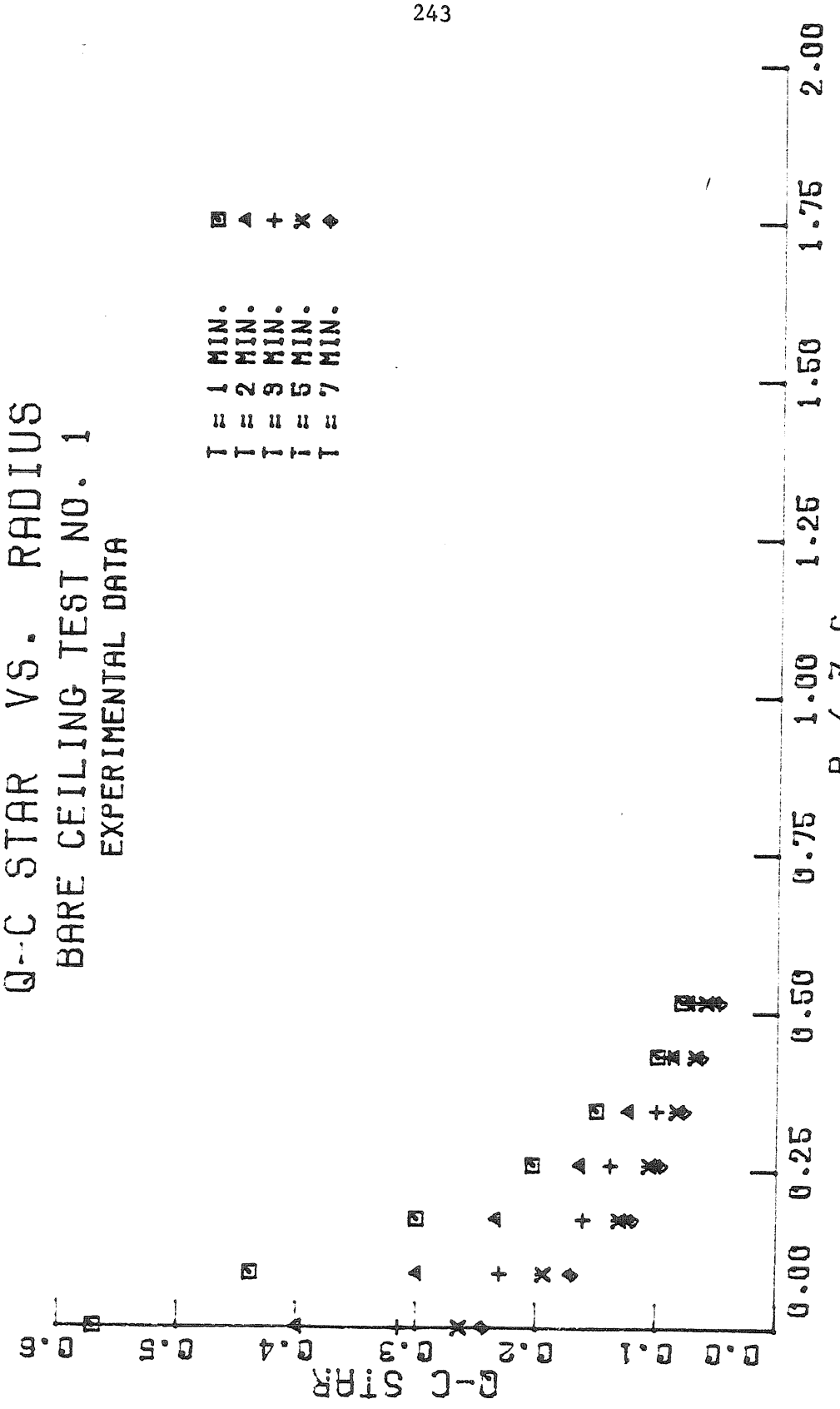

Figure (8.3) Heat Transfer to a Bare Ceiling

become fully developed ($z_c/d_o \geq 10$), the impinging jet behaves exactly like a free jet until it gets to within approximately 15% of the impingement surface (i.e. - $z/z_c \sim 0.85$). At that point it enters the impingement zone, characterized by an excess static pressure, in which the flow is turned from the axial into the radial direction. Along the impingement surface, this impingement zone extends radially outwards several jet radii from the stagnation point until the static pressure returns to ambient. Beyond this point, the flow along the impingement surface behaves as a radial wall jet.

We will use some of these results to develop our computational procedures. In particular, we will assume that the presence of the hot upper layer can be taken into account through its effect on the plume above the interface and we will use the mean upper layer temperature T_2 to characterize the transport properties. Note that the hotter this upper layer is, the more nearly jet-like the upper plume will be. Secondly, we will assume that impinging flows are dynamically similar so that we can scale them based on velocity and length scales in the equivalent free plume. Specifically, we will use b_c, the Gaussian radius of the equivalent free plume at the height of the ceiling (z_c) for the length scale. The impingement velocity scale w_{mt} is the impact velocity necessary to produce the stagnation point static pressure excess Δp_s. This velocity would occur in the equivalent free plume at a point, z_{th}, within roughly 10% of the impingement surface. This location defines an effective "termination height" for the equivalent free plume. One can thus visualize the actual impinging plume as being functionally equivalent to a free plume with constant entrainment properties, followed by an inviscid turning

region. Note that this inviscid region is of smaller extent than the impingement zone. If one denotes the distance from impingement by $\tilde{z}$, so that $\tilde{z} = z_c - z$, an average value for this termination height is

$$\tilde{z}_{th} = 0.77\ b_c \tag{8.4}$$

This value has been computed from the data of Giralt, Chia, and Trass (1977), Bradshaw and Love (1959), Bradbury (1972) for impinging jets and from Heskestad's (1980) impinging near-field plume data.

The radial extent of the impingement region can be defined arbitrarily as extending to the point, r_e, where the excess static pressure difference on the impingement surface has fallen to 5% of the stagnation point value. Based on this criterion, the mean value for r_e is,

$$r_e = 1.87\ b_c \tag{8.5}$$

based on the data of Giralt, Chia, and Trass (1977), Bradbury (1972), and Heskestad (1980).

8.4 Stagnation Point Heat Transfer

In their work on impinging axi-symmetric jets, Donaldson, Snedeker, and Margolis (1971) found that the stagnation point heat transfer for turbulent jets could be calculated in terms of the theoretical value for laminar flow corrected by a turbulence enhancement factor. You and Faeth (1979) assumed that a similar treatment was valid for turbulent plumes, and calculated the stagnation point heat transfer from a fire-plume to a bare ceiling (no upper layer of hot gas). A similar approach will be used here, taking the presence of the ceiling layer into account by using the interface jump conditions developed in Section (8.2).

For the case of constant density, laminar flow, Sibulkin (1952) found that the convective heat transfer at an axisymmetric stagnation point could be written as:

$$q_{lam} = \frac{0.762}{Pr^{0.6}} \sqrt{\nu \left(\frac{du_e}{dr}\right)_{r=0}} \rho c_p (T_{sp} - T_w) \quad (8.6)$$

The initial velocity gradient in (8.6) can be estimated from the measured pressure profiles of impinging jets and plumes, assuming that the flow is inviscid in this region:

$$\left(\frac{\partial u}{\partial r}\right)_{r=0} = \sqrt{-\frac{1}{\rho}\frac{\partial^2 p}{\partial r^2}} = \sqrt{-\tfrac{1}{2}\frac{\partial^2\left(\frac{\Delta p}{\Delta ps}\right)}{\partial\left(\frac{r}{b_c}\right)^2}}\ \frac{w_{mt}}{b_c} \quad (8.7a)$$

or

$$\left(\frac{\partial u}{\partial r}\right)_{r=0} = \lambda \frac{w_{mt}}{b_c} \qquad \lambda \equiv \sqrt{-\tfrac{1}{2}\frac{\partial^2\left(\frac{\Delta p}{\Delta ps}\right)}{\partial\left(\frac{r}{b_c}\right)^2}} \quad (8.7b)$$

Analysis of impinging jet pressure data of Donaldson and Snedeker (1971), and Giralt, Chia, and Trass (1977) yields a value for λ of 1.31. A similar analysis of Heskestad's (1980) data indicates that in the strongly-buoyant (non-Boussinesq), near field region plumes have a broader pressure profile, and hence a reduced value of $\lambda = 0.97$. However, Heskestad's impingement surfaces were within 3 effective source diameters of his fires and the flames themselves often impinged on these surfaces. Since we have assumed small, localized fires, we have chosen to use the jet data ($\lambda = 1.31$) as being more representative of the weakly buoyant plumes

considered here. In any case, since $q \propto \sqrt{\lambda}$, this difference in λ will only make a 14% difference in the heat transfer rate at the stagnation point.

Thus, in the absence of turbulence, the stagnation point heat transfer can be written in terms of the computed plume quantities as:

$$q_{lam} = \frac{0.762}{Pr^{0.6}} \rho_2 \; c_p \sqrt{\nu_2 \; \lambda \frac{w_{mt}}{b_c}} \quad (\kappa T_{mt} - T_w) \tag{8.8a}$$

or equivalently:

$$h_{c_{lam}} = \frac{0.762}{Pr^{0.6}} \rho_2 \; c_p \sqrt{\nu_2 \; \lambda \frac{w_{mt}}{b_c}} \tag{8.8b}$$

Where the transport properties have been evaluated at T_2 and the stagnation point gas temperature T_{sp} has been assumed proportional to $T_m(z_{th}) \equiv T_{mt}$. Comparing calculated values of T_{mt} with measured values of T_{sp} for the 1/2 scale room fires considered here and for the earlier bare ceiling and curtain wall tests of Zukoski, Kubota, and Veldman (1975), indicates that the mean value for κ is 1.02, with a standard deviation of 0.02.

Citing Gardon and Akfirat (1965), who showed that increasing the turbulence intensity levels of an impinging two dimensional jet significantly increased the stagnation point heat transfer, Donaldson, Snedeker, and Margolis (1971) proposed that the turbulence augmented heat transfer could be written as:

$$q = q_{lam} \; G \tag{8.9a}$$

or equivalently,

$$h_c = h_{c_{lam}} \; G \tag{8.9b}$$

where the enhancement function G depends on the state of the turbulence

in the jet. Following their suggestion, we assume G is primarily a function of the axial turbulence intensity $\tilde{w} = \left(\sqrt{\overline{w'^2}} / w_m\right)$.

A number of investigators have recently examined the role free stream turbulence plays in augmenting the heat transfer in the laminar boundary layer near the stagnation point of cylinders and spheres. Smith and Kuethe (1966) found that for cylinders in cross flow

$$G \sim 1 + c\ \tilde{w}\ \sqrt{Re_d} \tag{8.10}$$

where c is a constant, and explained this in terms of a semi-empirical eddy viscosity model. Galloway (1973) solved the transport equations numerically and found that the enhancement scaled with $(\tilde{w}\sqrt{Re}\ Pr^{1/6}/Pr_t)$, where Pr_t is the turbulent Prandtl number, which we set equal to unity. Lowry and Vachon (1975) found experimentally that the enhancement increased approximately linearly for small values of $\tilde{w}\sqrt{Re}$, but that the enhancement appeared to approach an asymptotic value for large $\tilde{w}\sqrt{Re}$. Chia, Giralt, and Trass (1977) used these results to fit their impinging jet mass transefer data, they found:

$$G = \begin{cases} 1.0 & \tilde{w}\ Re^{\frac{1}{2}} \leq 4 \\ 1.0 + 0.0156\ Pr^{1/6}\ (\tilde{w}\ Re^{\frac{1}{2}} - 4.0) & 4 \leq \tilde{w}\ Re^{\frac{1}{2}} \leq 34 \\ 1.0 + 0.468\ Pr^{1/6} & \tilde{w}\ Re^{\frac{1}{2}} \geq 34 \end{cases} \tag{8.11}$$

In order to apply this result to the problem at hand, we must estimate $\tilde{w}$ for buoyant plumes. George, Alpert, and Tamanini (1977) measured $\tilde{w}$ in a buoyant plume at 2 relatively modest values of (z_c/d_o). Their data have roughly the same growth rate as that of Donaldson, et al. (1971), although the plume values are roughly 20% larger than those for

the jet. Extrapolating the jet data to match the plume data, we obtain:

$$\tilde{w} = \begin{cases} 0.0935 \left(\frac{z}{d_o}\right)^{0.376} & 8 \leq \frac{z}{d_o} \leq 17.5 \\ 0.187 \left(\frac{z}{d_o}\right)^{0.133} & 17.5 \leq \frac{z}{d_o} \leq 40 \end{cases} \qquad (8.12)$$

Using (8.12) for $\tilde{w}$ in (8.11), with Re given by

$$Re = \frac{w_m(z_{th})\, d_{\frac{1}{2}}(z_{th})}{\nu_2} = \frac{1.665\, w_m(z_{th})\, b\,(z_{th})}{\nu_2} \qquad (8.13)$$

gives a reasonable fit to our data, as can be seen by comparing Figures (8.4) and (8.5). In Figure (8.4) the experimental stagnation point turbulence enhancement factor, defined as the ratio (hc_{exp}/hc_{lam}), has been plotted for 1/2 scale room fires, as well as for the bare ceiling and curtain wall fires of Zukoski, Kubota, and Veldman (1975). Figure (8.5) is a plot of the computed enhancement factor G, given by equation (8.11), for the same data. There is significant scatter in the stagnation point data, perhaps due to small motions of the plume. However, the overall average value of the ratio of the experimental enhancement factor to the theoretical value is 1.02 with a standard deviation of 0.18.

Thus it appears that we can calculate a reasonable estimate for the stagnation point heat transfer by first calculating the laminar flow value given by equation (8.8), and then correcting it by multiplying by the turbulence enchancement factor G, given by equation (8.11).

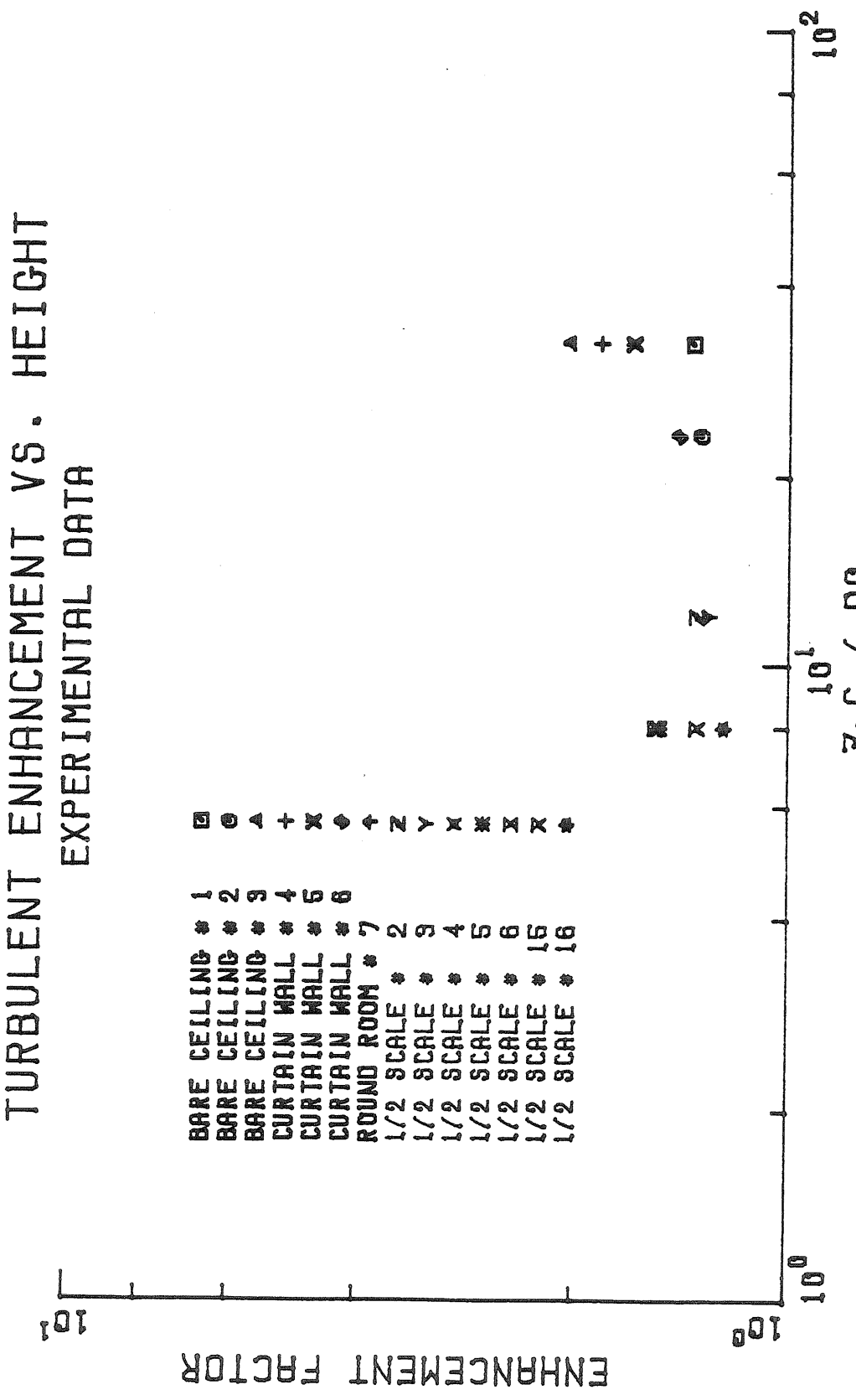

Figure (8.4) Turbulent Exhancement of Stagnation Point Heat Transfer (Experimental Values)

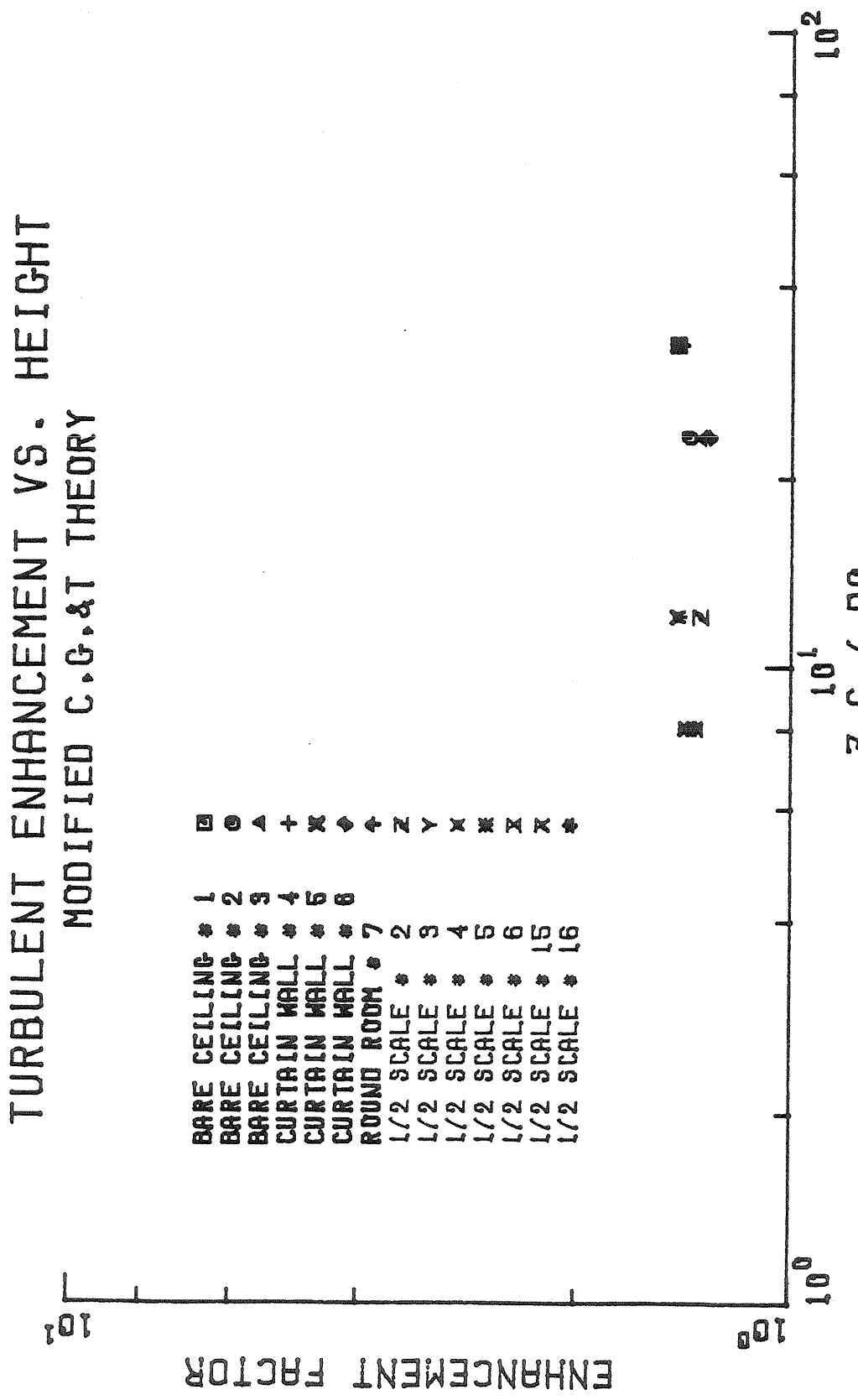

Figure (8.5) Turbulent Enhancement of Stagnation Point Heat Transfer
(Calculated Values Given by Equation (8.11))

In order to compare the heat transfer coefficient data from various experiments, it is useful to introduce a scaled, dimensionless heat transfer coefficient or Stanton number using the simple point source plume velocity as the velocity scale:

$$h_c' = \frac{h_c}{\rho_2 c_p \sqrt{g z_c}\ (Q^*_{z_c})^{1/3}} \tag{8.14}$$

This normalization, based on the dimensionless plume heat input parameter Q^*, defined by equation (2.55)

$$Q^*_{z_c} = \frac{Q_F}{\rho_o c_p T_o \sqrt{g z_c}\ z_c^2} \tag{2.55}$$

evaluated at the ceiling ($z = z_c$), will be used throughout the rest of this work. It has been found to correlate our data satisfactorily, which indicates that for the cases considered here, the plume's behavior is not radically altered by the presence of the hot upper layer. Tables (8.1) and (8.2) illustrate numerically the effect the ceiling layer temperature T_2 and the dimensionless interface height $\bar{z}_{int}$ have on the stagnation point heat transfer for a 14.8 kW fire in a 1.22m high room ($Q^*_{z_c} = 8.1 \times 10^{-3}$).

The results presented in Table (8.1) show that as the interface $\bar{z}_{int}$ is reduced, for a constant heat loss given by $(1-c_q) = 0.5$, the temperature of the upper layer increases rapidly. The buoyancy in the upper plume falls accordingly, resulting in a slower, thicker plume

at the ceiling [reduced $(w_{mt}/b_c)^{\frac{1}{2}}$]. On the other hand, the transport properties are calculated based on T_2, and the kinematic viscosity, given by an empirical fit to data tabulated by Schlichting (1968),

$$\nu_2 = \left(\frac{T_2}{T_{ref}}\right)^{1.7} \nu ref \qquad (8.15)$$

is particularly sensitive to changes in T_2. It is the increase in ν_2 that partially compensates for the decrease in (w_{mt}/b_c) and results in the rather mild decrease in the heat transfer coefficient h_c. Since h_c' is computed in terms of the mean upper layer density ρ_2, effects of T_2 are minimized and h_c' is remarkably constant except for the lowest interface height. Note that the increase in T_2 also causes the Reynolds number given by equation (8.13) to drop, and this in turn results in a decrease in the turbulence enhancement factor, G, from 1.44 to 1.33.

Table (8.2) shows that as more of the enthalpy delivered to the upper layer is lost [as measured by $(1-c_q)$], for a fixed interface height ($\bar{z}_{int} = 0.50$), the mean upper layer temperature T_2 falls significantly. As before, this increases the buoyancy in the plume, with a resulting rise in velocity and h_c'. Further, because we picked the wall temperature to be equal to T_2, the convective heat transfer rate goes to zero as the losses vanish ($c_q \rightarrow 1$).

TABLE (8.1) Effect of $\bar{z}_{int}$ on Stagnation Point Heat Transfer ($c_q = 0.50$)

$Q^*_{z_c} = 8.14 \times 10^{-3}$ $\quad z_c = 1.22m$ $\quad z_c/d_o = 8.00$

$T_o = 28.50$ C $\quad T_i = 36.38$ C $\quad$ Assume $T_{w_{sp}} = T_2$

$\bar{z}_{int}$	T_2 [C]	$(w_{mt}/b_c)^{\frac{1}{2}}$ $[s]^{\frac{1}{2}}$	T_{mt} [C]	$h_{c,lam}$ $\left[\frac{W}{m^2 K}\right]$	h_c $\left[\frac{W}{m^2 K}\right]$	q_c $\left[\frac{kW}{m^2}\right]$	$h'_c \times 100$
1.00	36.38	3.87	146.72	19.40	27.97	3.32	3.49
.75	73.15	3.62	129.19	17.82	25.70	1.65	3.59
.50	101.09	3.39	159.31	16.51	23.45	1.57	3.54
.25	189.27	3.33	251.14	15.70	20.90	1.51	3.90

TABLE (8.2) Effect of c_q on Stagnation Point Heat Transfer ($\bar{z}_{int} = 0.50$)

$Q^*_{z_c} = 8.14 \times 10^{-3}$ $\quad z_c = 1.22m$ $\quad z_c/d_o = 8.00$

$T_o = 28.50$ C $\quad T_i = 36.38$ C $\quad$ Assume $T_{w_{sp}} = T_2$

c_q	T_2 [C]	$(w_{mt}/b_c)^{\frac{1}{2}}$ $[s]^{\frac{1}{2}}$	T_{mt} [C]	$h_{c,lam}$ $\left[\frac{W}{m^2 K}\right]$	h_c $\left[\frac{W}{m^2 K}\right]$	q_c $\left[\frac{kW}{m^2}\right]$	$h'_c \times 100$
1.00	165.81	2.63	165.82	12.53	16.48	0.14	2.92
.75	133.45	3.06	163.64	14.74	20.16	0.78	3.31
.80	101.09	3.39	159.31	16.51	23.45	1.57	3.54
.25	68.74	3.65	153.55	18.02	25.99	2.43	3.58
.00	36.38	3.87	146.72	19.40	27.97	3.32	3.49

The two extreme cases of total heat loss from the upper layer (c_q=0) and no heat loss (c_q=1) are interesting to compare. The former case effectively represents a bare ceiling without an upper layer ($\bar{z}_{int}$ = 1), because the heat transfer losses have reduced the upper layer temperature to T_1 . In this case the plume retains all of its buoyancy. On the other hand for an adiabatic upper layer (c_q=1), the plume loses all of its buoyancy and behaves as a neutral jet above the interface.

8.5 Scaling the Impingement Region Heat Transfer

Although the details of the local heat transfer process in the impingement region may be expected to be quite complicated, one can find a relatively simple estimate of the total heat transfer to this area. Assuming the plume is fully developed before impinging on the ceiling, the impingement flow processes should be dynamically similar and should scale with parameters characterizing the plume before impingement. We have used this result to find the distribution of the heat transfer coefficient in this region. Chia, Giralt, and Trass (1977) presented detailed measurements of the mass transfer produced by an air jet impinging on a napthalene coated surface. A least squares polynominal fit of their data yields:

$$\frac{h_c}{h_{c_{sp}}} = 0.998 - 0.0938\left(\frac{r}{b_t}\right) - 0.250\left(\frac{r}{b_t}\right)^2 + 0.142\left(\frac{r}{b_t}\right)^3 - 0.0235\left(\frac{r}{b_t}\right)^4 \qquad (8.16)$$

where $h_{c_{sp}}$ is the stagnation point value of the heat transfer coefficient h_c , and b_t is the Gaussian plume radius at z_{th} . The total heat

transferred to this region of the ceiling is then

$$Q_{ir} = h_{c_{sp}} \Delta Tw_{sp} \int_0^{r_e} \frac{h_c}{h_{c_{sp}}} \left\{\frac{r}{b_t}\right\} \frac{\Delta Tw}{\Delta Tw_{sp}} \left\{\frac{r}{b_t}\right\} 2\pi \; r \; dr \qquad (8.17)$$

where ΔTw_{sp} is the stagnation point value of the temperature difference, ΔTw, between the gas and the ceiling. Conceptually, there are two limiting cases for Q_{ir}. First, if the temperature difference remains constant, the maximum heat loss is given by

$$Q_{ir_{max}} = 9.87 \; b_t^2 \; \Delta Tw_{sp} \; h_{c_{sp}} \qquad (8.18)$$

On the other hand, analysis of the insulated, bare ceiling data of Zukoski, Kubota, and Veldman (1975) indicates that early in the fire (1 minute after ignition), ΔTw falls approximately linearly with r. A least squares fit of this data yields:

$$\frac{\Delta Tw}{\Delta Tw_{sp}} = 0.978 - 0.145 \left(\frac{r}{b_t}\right) \qquad (8.19)$$

Using this result in (8.17) gives

$$Q_{ir_{min}} = 7.97 \; b_t^2 \; \Delta Tw_{sp} \; h_{c_{sp}} \qquad (8.20)$$

which estimates the loss to an insulated ceiling early in the fire. Of course, for a perfectly insulated ceiling, in the later stages of a fire, $Q_{ir_{min}}$ will decrease below the value given by (8.20) until the convective heat transfer rate just balances the net radiative losses and the internal conduction within the ceiling.

8.6 The Ceiling Jet

8.6.1 Introduction

At some distance away from the stagnation point, the character of the flow changes as the buoyant fluid flows radially outward to form a thin ceiling jet [Figure (8.1)]. If walls are present, the ceiling jet may be effectively channeled, at some larger distance, into a basically two-dimensional flow pattern. Since the radius of the stagnation region is of the order the plume radius, the stagnation region is usually small compared to the total area of the ceiling. Hence to compute the total heat transfer to the ceiling it is important to be able to estimate the heat transfer from the ceiling jet.

Alpert (1974) presented an integral model for the axisymmetric case. He treated the case of a bare ceiling (no upper layer), and assumed that the ceiling itself was either adiabatic or at the same temperature as the ambient gas in the room. In addition, he assumed that the normalized velocity and temperature difference profiles were proportional to each other in addition to being self-preserving. With these assumptions, he was then able to obtain a reduced similarity solution for the characteristic thickness and Richardson number of the ceiling jet, from which the physical variables of interest could be extracted.

In our 1/2 scale room fire tests, however, several of his assumptions were violated. First, since the room had 2:1 rectangular symmetry, the flow quickly became two-dimensional. Second, in a matter of seconds, the upper portion of the room was filled with hot gas so that the buoyancy

of the ceiling jet relative to the fluid outside it was greatly reduced. Finally since the walls were cooled, the ceiling temperature was significantly less than the ambient upper layer gas temperature T_2 . As a result, the temperature difference profile could differ significantly from the velocity profile. For example, far from the plume, we observed that much of the ceiling jet was colder than the upper layer temperature T_2 , so that the temperature difference $(T-T_2)$ was then negative, while the velocity was still positive.

To meet these observed requirements, we have adopted a more general approach, and have solved the integrated mass, momentum, and energy equations directly, in either cylindrical or cartesian coordinates. The velocity and temperature profiles can then vary independently, and the wall temperature can be arbitrarily specified.

In the following sub-sections, the key aspects of this calculation scheme will be described. We will first discuss the integrated equations of motion and the approximations that we have introduced regarding the flow. For generality, these equations will be written in terms of characteristic quantities, defined by profile integrals. As in the integral plume model, an entrainment assumption is required to close the system. Experimental data on non-buoyant and buoyant wall jets will be examined in order to estimate the entrainment coefficient. These data indicate that the relative buoyancy of the wall jet significantly affects the entrainment process so that the entrainment coefficient becomes a function of the wall-jet Richardson number. Finally we will discuss some simple assumptions which allow us to estimate the initial flow in the ceiling jet based on the flow in the upper part of the plume.

8.6.2 Integrated Equations of Motion

The ceiling jet can be thought of as a basically thin layer of fluid composed of two parts. The outer portion consists of an essentially inviscid, jet-like flow with assumed constant external pressure, while the inner portion is similar to a turbulent boundary layer. Assuming again that the Boussinesq approximation is valid, the equations of motion can be integrated across the ceiling jet to yield ordinary differential equations for the kinematic flux of mass, momentum, and enthalpy. In order to calculate the enthalpy loss from the layer to the wall the Reynolds analogy can be used to estimate the convective heat transfer.

As in the integral approach to the plume, one must make an entrainment assumption in order to relate the inflow of mass to the mean flow properties. However, unlike the case of the vertical plume, buoyancy and turbulent mixing tend to work against each other in a stably stratified shear flow such as the ceiling jet. Ellison and Turner (1959) found that in such situations the rate of entrainment appears to depend on a local Richardson number, which can be defined in terms of a characteristic kinematic buoyancy ∇, thickness h, and velocity U of the jet as:

$$Ri = \frac{h\nabla}{U^2} \tag{8.21}$$

Thus for buoyant wall jets we assume that the rate of entrainment is given by the product of the entrainment function and a characteristic velocity in the jet.

Because the flow starts out with axial symmetry, but often is turned by the presence of wall into a basically two-dimensional flow pattern,

it is convenient to write the equations of motion in a general form to handle either case. The index n is used for this purpose. Thus axisymmetric flows are represented by $n = 1$, and two dimensional flows are given by $n = 0$. Since the ceiling jet is thin, we assume that transverse gradients are large compared to gradients in the flow direction. Thus integrating the boundary layer form of the equations of motion across the ceiling jet, we obtain:

Conservation of Mass

$$\frac{1}{r^n} \frac{d}{dr} \int_0^\infty u\, r^n\, dz' = E\,(U - U_{ext}) \tag{8.22}$$

Conservation of Radial Momentum

$$\frac{1}{r^n} \frac{d}{dr} \int_0^\infty \rho u^2\, r^n\, dz' = -\tau_w - \int_0^\infty r^n \frac{\partial p}{\partial r}\, dz' - \frac{\partial P_{ext}}{\partial r} + U_{ext} E (U - U_{ext}) \tag{8.23}$$

Conservation of Energy

$$\frac{1}{r^n} \frac{d}{dr} \int_0^\infty \rho u\, c_p\, (T - T_2)\, r^n dz' = -q_c \tag{8.24}$$

In these equations z' is the local vertical distance measured from the ceiling, U is the characteristic velocity in the ceiling jet, and U_{ext} is a characteristic external velocity. The effective entrainment velocity, at which mass flows into the ceiling jet, is given by the entrainment function E times the net velocity $(U - U_{ext})$. In the radial momentum equation, the integral of $\frac{\partial p}{\partial r}$ gives the contribution of hydrostatic pressure acting on a differential volume element in the jet, while $\frac{\partial P_{ext}}{\partial r}$ gives the external pressure gradient. Note that the enthalpy is defined relative to that of the ambient upper layer gas at temperature T_2.

We will make two important simplifications in treating the ceiling jet. First, we assume that the pressure outside the ceiling jet is constant so that $\frac{\partial P_{ext}}{\partial r} = 0$. Second, we set $U_{ext} = 0$. In reality, because the plume and the ceiling jet continually entrain ambient fluid, there will always be some external flow to supply this mass, even in the case of a bare ceiling without side walls. In the case of a fire in a room, there will be an even larger external flow as fluid from the ceiling jet is recirculated. Brine flow visualization experiments indicated that the actual recirculating flow pattern was very complicated, being composed of a series of counterflowing layers [See Tangren, Sargent, Zukoski (1978)]. Since the details of this flow process are not well understood, we have been forced to ignore the external velocity.

As in integral boundary layer techniques, given a set of initial conditions, one can integrate equations (8.22) - (8.24) downstream and follow the growth of the ceiling jet. However, because we assumed the external pressure remains constant, this procedure can not take into account downstream boundary conditions which generate a pressure gradient. For the case of an infinite or bare ceiling, the external pressure will remain constant, and this calculation scheme should work well. However, the presence of walls perpendicular to the flow will cause a positive pressure gradient to form in the flow direction, and separation will occur as part of the flow turns and flows down the side walls. Our experimental data suggest that indeed a separated flow region exists, but that it is confined to the immediate vicinity of the sidewalls. Consequently, we have

simplified the model by ignoring the pressure gradient and treating the ceiling away from the walls as effectively infinite.

In addition, for buoyant ceiling jets, the initial flow will be supercritical, with densimetric Froude numbers as high as 6. In this case, an internal hydraulic jump may occur, depending on the downstream boundary conditions. Examination of the 1/2 scale room data, however, did not reveal any evidence of a hydraulic jump for the interior portion of the ceiling. As a result, we have not included provisions for such a jump in this model.

8.6.3 Formulation in Terms of Similar Profile Integrals

In order to use the equations of motion in integral form given by (8.22) - (8.24), we must make some assumptions about velocity and temperature difference profiles, and how these profiles change with downstream distance. Our primary assumption, based on experimental observations, is that the normalized profiles are similar and hence can be described in terms of functions of a similarity coordinate in the form (z'/ℓ), where ℓ is a length scale of the profile. However, we do not require that the profiles necessarily remain proportional to each other, because heat transfer may reduce the temperature difference to zero long before the velocity vanishes. This effect will be more pronounced in ceiling jets flowing through the hot upper layer of gas found in room fires, because the value of the initial ceiling jet temperature difference will be significantly reduced compared to the case when the upper layer is absent.

Given that velocity and temperature difference profiles are similar, it is convenient to define a characteristic velocity, thickness, buoyancy,

and integrated hydrostatic pressure force in terms of their integrals, as was done by Ellison and Turner (1959) and Alpert (1974). Thus we define:

$$Uh = \int_0^\infty u \, dz' \tag{8.25}$$

$$U^2h = \int_0^\infty u^2 \, dz' \tag{8.26}$$

$$Uh\nabla = \int_0^\infty g \, u \, (\frac{T-T_2}{T_2}) dz' \tag{8.27}$$

$$\hat{Sh}^2\nabla = \int_0^\infty g \, (\frac{T-T_2}{T_2}) \, z' \, dz' \tag{8.28}$$

The quantitites U, h, ∇ can be thought of as average over the profiles in the sense that they define an equivalent jet with a uniform or "top hat" profile which has the same kinematic mass, momentum, and enthalpy fluxes.

We can now substitute these relations into the equations of motion to obtain:

$$\frac{1}{r^n} \frac{d}{dr} (r^n \, U \, h) = E \, U \tag{8.29}$$

$$\frac{1}{r^n} \frac{d}{dr} (r^n \, U^2h) = -NU^2 - \frac{d}{dr} (\hat{Sh}^2\nabla) \tag{8.30}$$

$$\frac{1}{r^n} \frac{d}{dr} (r^n \, U\nabla h) = \frac{-q_c \, g}{\rho_2 c_p T_2} \tag{8.31}$$

where N is a friction factor given by

$$N = \frac{\tau_w}{\rho_2 U^2} = \frac{1}{2} (\frac{u_m}{U})^2 c_f \tag{8.32}$$

and where c_f is the conventional skin friction coefficient defined in terms of the velocity outside the inner layer, u_m. These equations can be put in dimensionless form by introducing the dimensionless variables:

$$\bar{r} = \frac{r}{z_c} \qquad \bar{h} = \frac{h}{z_c} \tag{8.33 a,b}$$

$$\bar{U} = \frac{U}{U_e} \tag{8.34}$$

$$\bar{\nabla} = \frac{\nabla}{\nabla_e} \tag{8.35}$$

where U_e and ∇_e are the initial values of the characteristic velocity and buoyancy respectively. The dimensionless set of equations is then:

$$\frac{1}{\bar{r}^n} \frac{d}{d\bar{r}} (\bar{r}^n \bar{U} \bar{h}) = E \bar{U} \tag{8.36}$$

$$\frac{1}{\bar{r}^n} \frac{d}{d\bar{r}} (\bar{r}^n \bar{U}^2 \bar{h}) = - N \bar{U}^2 - \gamma \frac{d}{d\bar{r}} (\hat{S} \bar{\nabla} \bar{h}^2) \tag{8.37}$$

$$\frac{1}{\bar{r}^n} \frac{d}{d\bar{r}} (\bar{r}^n \bar{U} \bar{h} \bar{\nabla}) = \frac{-N}{\sqrt{2}\, Pr^{2/3}} U \frac{(Tm - Tw)}{(Tm_e - T_2)} \sqrt{\sigma + 1} \tag{8.38}$$

where the parameter $\gamma = (\nabla_e z_c / U_e^2)$ is in the form of an initial Richardson number based on the room height, and where the Reynolds analogy has been used to replace q_c in (8.31). The $\sqrt{\sigma+1}$ arises from the use of Gaussian profiles in the plume.

Equations (8.36) - (8.38) represent the heart of our ceiling jet calculation scheme. In order to solve them, actual profiles must be specified in equations (8.25)-(8.28). In addition, we must be able to estimate the values of the entrainment function E, and the friction factor N. Finally, we must supply the initial conditions. These considerations will be discussed in the following sub-sections.

8.6.4 Choice of Velocity and Temperature Profiles

As in all integral models, the choice of profiles is limited only by the ingenuity and stamina of the person doing the calculations. Clearly, the more accurate the profiles are, the better the results will be. The great beauty of integral methods, however, is that one does not need to know the profiles exactly in order to get reasonable engineering estimates. Examination of equations (8.25 - 8.28) shows that for a given kinematic mass, momentum, and enthalpy flux, the characteristic variables U,h, and ∇ will all be constant, and that only $\hat{S}$ will change. Furthermore, the change is $\hat{S}$ will be small. For example, the values of $\hat{S}$ for uniform, exponential (σ=0.9), Gaussian (σ=0.9), and empirical (Poreh, et al. (1967)) profiles are respectively 0.50, 0.59, 0.49, and 0.49. To further illustrate this point, the author compared the numerical results using the empirical profile with those from the Gaussian profile and found there was indeed very little difference.

For this reason, and because simultaneous velocity and temperature profiles were not available, simple half-Gaussian distributions, with a maximum velocity u_m and a maximum temperature difference ΔT_m, will be used for convenience in evaluating the profile integrals (8.25) - (8.28).

These Gaussian profiles are indicated by the solid curves in Figure (8.6). However, since the velocity must obey the no-slip condition at the wall, the actual profile must look something like the broken line in Figure (8.6a).

The actual temperature profile is more complicated because the wall temperature is not uniquely specified. We can consider three typical cases

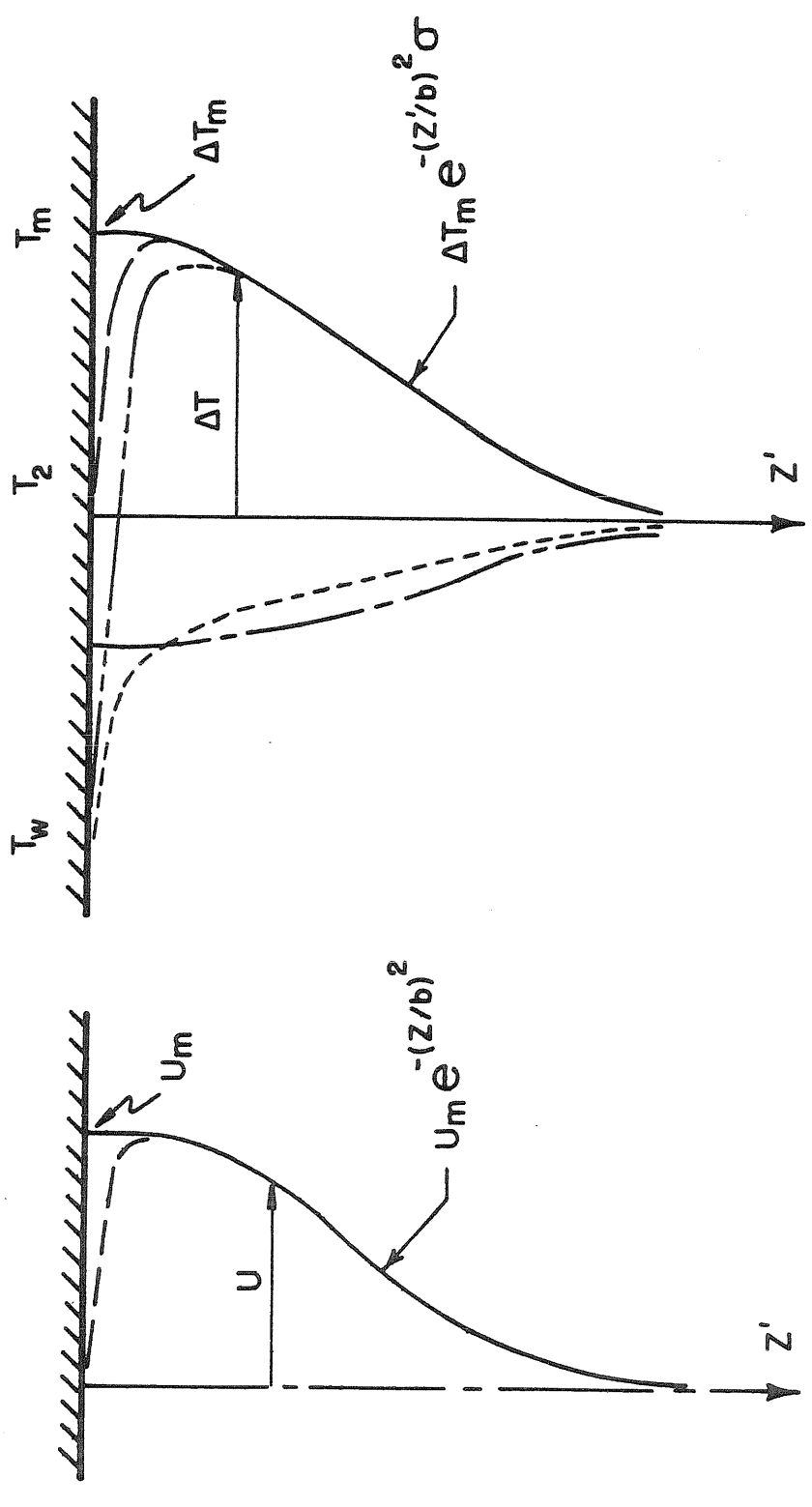

(b) TEMPERATURE DIFFERENCE $(T-T_2)$

(a) VELOCITY U

FIGURE 8.6 CEILING JET PROFILES

to illustrate this point. First, if the ceiling is adiabatic, the ceiling temperature will be equal to the maximum gas (Tw = Tm) and the half Gaussian profile will fit quite well. Second, if the ceiling temperature is equal to the upper layer gas temperature (Tw = T_2), the ceiling jet temperature difference will go to zero both at the wall and for large values of z', similar to the velocity profile. Finally, if the wall is colder than the upper layer gas (Tw<T_2), the temperature difference profile must fall to a negative value at the wall, as shown by the doubly broken curve. If the flow progresses far enough with this particular boundary condition, the enthalpy of the ceiling jet, relative to the upper layer gas, will be reduced to zero by convective heat transfer to the wall. Further heat transfer losses will produce a temperature deficit (ΔT_m<0). We will use the Gaussian profile, shown by the broken curve to the left of the z' axis for this case, even though the experimental curve, the dashed line, has a somewhat different shape.

8.6.5 Estimation of the Skin Friction

These half-Gaussian profiles represent a good approximation to the essentially inviscid outer flow. We know an inner layer, somewhat like a turbulent boundary layer, will develop which effectively couples the outer flow to the presence of the wall. Since this inner layer is thin, its presence will have little effect on the value of the profile integrals. However, the losses in momentum and enthalpy across the thin inner layer can be taken into account by specifying a skin friction coefficient c_f, and a convective heat transfer coefficient h_c.

The loss in momentum, given by the shear stress at wall, is:

$$\tau_w = \frac{c_f}{2} \rho u_m^2 \qquad (8.39)$$

where u_m is the maximum velocity at the outer edge of the inner layer.

Similarly, the convective heat transfer to the wall can be written:

$$q_c = h_c (Tm - Tw) \qquad (8.40)$$

where Tm is the corresponding maximum temperature at the edge of the inner layer and Tw is the temperature of the wall (ceiling). The turbulent transport of momentum and energy, across the inner layer are related, and we can use Reynold's analogy to estimate h_c in terms of c_f as:

$$h_c = \rho_2 u_m c_p \frac{(c_f/2)}{Pr^{2/3}} \qquad (8.41)$$

Thus, in this calculation scheme, all the effects that the solid boundary imposes on the flow are buried in the skin friction coefficient, c_f. Consequently, we must use reasonable values of c_f to obtain estimates of the heat transfer coefficients h_c. Depending on the

nature of the flow and the condition of the surface, c_f may be nearly constant, or it may vary with the Reynolds number of the inner layer. Therefore, the model has been constructed to handle either case.

If the Reynolds number is high enough and the surface is rough, c_f is known to be approximately constant, independent of the Reynolds number. In this case we can simply specify an appropriate value for c_f. Since most ceilings have appreciable surface roughness, this is a reasonable approach. Many of the calculations in the following chapter have been carried out for $c_f = 0.01 - 0.02$. Furthermore, measurements by Schwarz and Cosart (1961) and Nelson (1969) indicate that the skin friction may be nearly constant for turbulent two dimensional wall jets. Even if the skin friction of a surface does change, its variation is usually small. Specifying a constant value of c_f is then equivalent to approximating the function by its mean value.

Alternatively, empirical correlations may be employed to obtain the approximate variation of c_f with the inner layer Reynolds number $Re_m = (u_m \tilde{\delta}/\nu)$, where $\tilde{\delta}$ is the thickness of the inner layer. For example, Alpert (1974) used the results of Poreh, Tsuei, and Cermak (1967), who found their data on axisymmetric wall jets were correlated by:

$$c_f = 0.12\ Re_m^{-0.3}\ \left(\frac{r}{z_c}\right)^{-0.16} \qquad (8.42)$$

for inner layer Reynolds numbers in the range $2\text{-}10 \times 10^3$. Similarly, for the case of two dimensional ceiling jets, we can use the relation Launder and Rodi (1981) found most satisfactory in their recent comprehensive review of the experimental literature on two dimensional wall

jets. They found that for Re_m between 3×10^3 and 4×10^4:

$$c_f = 0.0315 \ Re_m^{-0.182} \tag{8.43}$$

At this point it should be noted that at least for laboratory scale fires, the relatively low velocities and high temperatures (and hence high viscosities) combine to produce rather samll values of Re_m, typically of the order of 400 ($Re_x \sim 2 \times 10^4$). Thus use of the above correlations may represent a rather crude approximation to c_f.

Finally, a complete model could, in principle, be constructed to calculate the details of the flow in the inner layer, from which the wall shear stress, and hence c_f, could be computed.

In this work, we have chosen to examine the first two approaches: specifying a constant value for c_f and using empirical correlations.

When using an empirical correlation for c_f, it is necessary to evaluate the inner layer Reynolds number. We assume the maximum velocity u_m occurs at the outer edge of the inner layer, and is equal to the value calculated for the assumed profile. From this viewpoint, the outer layer imposes the external velocity u_m on the inner layer. We can now estimate $\tilde{\delta}$ from an integral boundary layer analysis, as Alpert (1974) did in the axisymmetric case. For this purpose we assume a boundary layer velocity profile of the form:

$$\frac{u}{u_m} = \left(\frac{z'}{\tilde{\delta}}\right)^m \tag{8.44}$$

and evaluate the integral boundary layer equations:

$$\frac{1}{r^n}\ \frac{d}{dr}\left\{\int_0^{\tilde{\delta}} \rho u\, r^n\ dz'\right\} = \dot{m}'' \qquad (8.45)$$

$$\frac{1}{r^n}\ \frac{d}{dr}\left\{\int_0^{\tilde{\delta}} \rho u^2 r^n\ dz'\right\} = u_m\, \dot{m}'' - \tau_w \qquad (8.46)$$

where $\dot{m}''$ is the mass flow rate into the boundary layer from the outer portion of the ceiling jet. These relations can be combined with the expressions for the skin friction (8.42, 8.43) to yield a single equation for the boundary layer thickness:

$$\frac{1}{r^n}\ \frac{d}{dr}\ (r^n \tilde{\delta}) = A_n \frac{\tilde{\delta}}{u_m}\ \frac{du_m}{dr} + B_n c_f\ \left\{Re_m\ ,\ \bar{r}\right\} \qquad (8.47)$$

The value of the constants A_n , B_n depend on the profile chosen and the flow geometry (n = 0 two dimensional, n = 1 axisymmetric). We have chosen a value of $1/7$ for the profile exponent m in equation (8.44). The resulting values of A_n are $A_o = 65/7$, $A_1 = 7$, $B_n = 36/7$. Schwarz and Cosart (1961) found $m = 1/14$, so that for the two dimensional case, better values may be $A_o = 113/7$ $B_n = 60/7$.

In summary, if we opt for the constant c_f mode, we simply supply an appropriate value for the related friction factor N , and integrate equations (8.36) - (8.38). On the other hand, if we elect to use an empirical correlation for c_f , we must integrate equation (8.47) for $\tilde{\delta}$, in addition to addition to equations (8.36) - (8.38). At each step, we compute the inner layer Reynolds number. The skin friction is then found from either (8.42) or (8.43), depending on whether the flow is axisymmetric or two dimensional, respectively.

8.6.6 Entrainment in Non-buoyant Wall Jets

In modeling buoyant turbulent plumes and jets, we assumed the entrainment velocity of fluid entering the plume was directly proportional to a characteristic velocity in the plume (i.e. $-w_m$). However, the value of the entrainment coefficient differs for jets and plumes. It seems reasonable to suppose therefore that the value of the entrainment coefficient, α, for wall jets may be different from the value for plumes. An estimate of this value can be obtained by substituting experimental data on the growth rates of the velocity and length scales in wall jets into the continuity equation (8.22). Note that $\alpha u_m = EU$.

Let

$$\tilde{\delta}_{\frac{1}{2}} = \tilde{A}\, r^{\ell} \tag{8.48}$$

$$u_m = \tilde{B}\, r^{m} \tag{8.49}$$

where $u(\tilde{\delta}_{\frac{1}{2}}) = \frac{1}{2} u_m$. Substituting (8.48) and (8.49) into equation (8.22) yields, for half Gaussian profiles and $U_{ext} = 0$:

$$\alpha = \tilde{A}\tilde{C}\,(n + m + \ell)\, r^{(\ell-1)} \tag{8.50}$$

where

$$\tilde{C} = \tfrac{1}{2}\sqrt{\frac{\pi}{\ell n(2)}} = 1.064 \tag{8.51}$$

This expression shows that for a similarity solution to exist, the length scale must grow linearly with r (ℓ=1). Table (8.3) list several sets of data for both two dimensional (n = 0) and axisymmetric non-buoyant wall jets (n = 1).

TABLE (8.3) Non-buoyant Wall Jet Entrainment

Experiment	$Re_m x10^{-3}$	$\tilde{A}$	ℓ	m	n	$\alpha/r^{(\ell-1)}$
Schwarz & Cosart (1961)	4-11	.070	1.0	-0.552	0	0.0334
Nelson (1969)	5	.068	1.0	-0.555	0	0.0321
Launder & Rodi (1981)	3-14	.073	1.0	-0.500	0	0.0389
Mean Value		.070	1.0	-0.536	0	0.0348
Bakke (1957)	9	.104	0.94	-1.12	1	0.0906
Porch, Tsuei, & Cermak (1967)	2-10	.098	0.90	-1.10	1	0.0834
Witze & Dwyer (1977)	--	.095	1.01	-1.12	1	0.0896
Mean Value		.099	0.95	-1.11	1	0.0879

The entry labelled "Launder and Rodi" represents an average for several sets of experiments which they judged to have the best two dimensionality. It is interesting to note that although the two dimensional jet satisfies the similarity requirement $\ell = 1$, the axisymmetric jet exhibits an apparent small deviation. This may be a manifestation of the fact that the inner viscous region has different characteristics scales from the essentially inviscid outer region, and therefore a similarity solution is not strictly possible. It is also interesting to note the approximate factor of 2.5 difference in the entrainment coefficient caused by the change in the flow geometry. By comparison, the value of the entrainment coefficient for two dimensional plumes, 0.11 [Kotsovinos (1975)] is essentially identical to the value 0.1096 used here for axisymmetric plumes. This is not surprising since both

plumes exhibit relatively little lateral spreading.

We can now use the mean values computed in Table (8.3) to estimate the entrainment function in non-buoyant two dimensional and axisymmetric ceiling jets. Noting that $\alpha u_m = EU$ in the continuity equation, and that for Gaussian profiles $u_m = \sqrt{2}\ U$, we have $E = \sqrt{2}\ \alpha$, so that equation (8.50) becomes:

$$E_o = \sqrt{2}\ \tilde{\tilde{AC}}\ (n+m+\ell)\ r^{(\ell-1)} \tag{8.52}$$

where E_o denotes the entrainment function for the non-buoyant case (Ri = 0). Using the mean values from Table (8.3), we finally obtain:

$$E_o = 0.049 \quad \text{(two dimensional)} \tag{8.53a}$$

$$E_o = 0.124\ r^{-0.05} \quad \text{(axisymmetric)} \tag{8.53b}$$

8.6.7 Entrainment in Buoyant Wall Jets

The presence of buoyancy will further modify the entrainment function, E, since the buoyancy in the ceiling jet will tend to suppress the turbulent fluctuations which produce the entrainment. In their work on buoyant two dimensional surface and wall jets, Ellison and Turner (1957) found that the entrainment was strongly dependent on the overall jet Richardson number, $Ri = (h\nabla/U^2)$, which is a measure of the buoyancy relative to the turbulent shear stress, and noted that for large enough values of this Richardson number, the turbulent entrainment was virtually reduced to zero.

Studies by Wilkinson and Wood (1971), Koh (1971), Stefan (1972), and Chu and Vanvari (1976) have helped clarify the way in which buoyancy effectively controls the entrainment process in buoyant wall jets. Ceiling jets are typical of wall jets with a relatively large initial velocity and

small buoyancy, so that the initial jet Richardson number will be small compared to one (i.e. $U^2 >> h\nabla$), and the flow will be supercritical. In this regime the flow will be independent of the downstream boundary conditions and Wilkinson and Wood (1971) and Chu and Vanvari (1976) have shown that turbulent entrainment occurs and is qualitatively similar to entrainment in non-buoyant jets. If the conditions downstream are compatible with the supercritical solution, which in turn depends on the upstream conditions and the wall boundary conditions, the flow will remain supercritical throughout. On the other hand, if the downstream conditions are incompatible, the flow will undergo an internal hydraulic jump, referred to as a "density jump." In the region of the jump itself, there is some mixing due to the breaking of internal waves at the interface, but Stefan (1972) found that this is small. Downstream of the jump, the resulting sub-critical flow has been observed to have a sharp interface with no mixing across it.

In the work of Ellison and Turner (1957), it is not clear whether or not a density jump was present in their apparatus. Since they measured the total increase in the mass flux to determine the entrainment coefficient, the presence of such a jump would seriously effect their numerical results. Chu and Vanvari (1976) therefore conducted a set of several experiments in which they varied the initial velocity and density difference of a two-dimensional surface jet of fresh water flowing over a basically quiescent body of denser salt water. They carefully adjusted the inflow of salt water to insure that the density jump remained downstream of their test section. Their initial jet Reynolds numbers and Richardson numbers based

on the source velocity and thickness were in the range 1390 - 3630, and 0.007 - 0.023 respectively. These values compare favorably with those estimated for ceiling jets in the 1/2 scale room tests, where the initial jet Reynolds numbers and Richardson numbers have been estimated to be 5,000 - 7,000 and 0.017 - 0.027, respectively.

Chu and Vanvari (1976) noted that their surface jets behaved very much like non-buoyant walls for small jet Richardson numbers, while at larger Richardson numbers, the buoyancy tended to suppress the turbulent fluctuations. For example, their normalized mean velocity profiles were found to be similar and closely fitted by a Gaussian profile. From these profiles they computed the growth rate for the velocity half-width, $\frac{d\tilde{\delta}_{\frac{1}{2}}}{dx}$, which they noted had an initial value very close to the value 0.068 measured by Schwarz and Cosart (1961) in a neutral jet. In addition, the longitudinal maximum turbulent intensity $(u_m'/\bar{u}_m)$ was observed to compare favorably with the measurements of Guitton (1968) in a neutral jet, except near the edge of the jet $(z > \tilde{\delta}_{\frac{1}{2}})$. Chu and Vanvari (1976) attributed this to the suppression of convolutions of the interface due to buoyancy. More to the point here, they found the maximum turbulent intensity fell rapidly with increasing jet Richardson number as did the entrainment coefficient, α, determined from integrating the velocity profiles. As indicated by the growth rate data, the value of α for small Richardson numbers was close to that measured by Schwarz and Cosart (1961). Finally, Chu and Vanvari (1976) noted that a normalized entrainment coefficient, $\tilde{\alpha} = (\alpha/u_m')$, remained reasonably close to the value 0.18 observed in neutral jets, as the Richardson number was increased. Thus it appears that as buoyancy suppresses the turbulence (measured by $u_m'/\bar{u}_m$), the entrainment must fall proportionately.

The data of Chu and Vanvari (1976), taken at initial Reynolds and Richardson numbers approximately equal to those in our 1/2 scale fire tests, thus appear to give an accurate and consistent representation of the effects of buoyancy on entrainment in supercritical wall jets. We have therefore used their results as the basis for modeling the entrainment in buoyant ceiling jets, and have found that:

$$E = E_o \, e^{-\beta Ri} \tag{8.54}$$

closely approximates their results, where E_o is the value of the entrainment function for a neutral jet, β is approximately 5.1, and as before:

$$Ri = \frac{h\nabla}{U^2} \tag{8.21}$$

Although Chu and Vanvari (1976) investigated a two dimensional jet, equation (8.54) will be taken as the general expression for all ceiling jets, with E_o given by equations (8.53 a,b). In addition, we assume that for ceiling jets with slight negative buoyancy, the enhanced mixing generated by the flow instability can also be approximated by the now positive exponential term in (8.54).

With the specification of the entrainment function, given by (8.53a, b) and (8.54), the ceiling jet calculation scheme is now complete. For a given set of initial conditions, we can now calculate the subsequent evolution of the ceiling jet.

8.6.8 Entrance Conditions for an Axisymmetric Ceiling Jet

In order to initiate the ceiling jet calculations, some assumptions must be made as to the nature of the flow at the start of the ceiling jet. The source of the flow is the plume, which rises through the upper layer, impinges on the ceiling, and turns to flow outwards as an initially

radial wall jet. Referring to Figure (8.7a), let us suppose that the initial characteristic thickness of the ceiling jet, h_e, occurs at an initial radius r_e, given by equation (8.5), and that the initial maximum velocity and temperature differences in the profiles at this location are given by $u_{m,e}$ and $\Delta T_{m,e}$ respectively. We must now relate these quantities to the known solution for the finite source plume.

To do this we assume that the turning process is basically inviscid and adiabatic, so that the plume above the effective termination height, z_{th}, turns without losses or entrainment to form the ceiling jet. Then, when we apply the conservation of mass and energy along with Bernoulli's equation, we have three relations for the three variables $\{h_e, u_{me}, T_{me}\}$, or the equivalent set $\{h_e, U_e, \nabla_e\}$, which characterize the ceiling jet.

To simplify the problem, we can replace the actual plume and ceiling jet with the two equivalent flows shown in Figure (8.7b), each of which has a uniform or "top-hat" profile, chosen such that the total fluxes of mass, momentum, and enthalpy are the same as in the original flow. We can now use these equivalent flows to solve for the behavior of the effective mean flow.

Recalling that equations (8.25) - (8.27) define the equivalent uniform profile ceiling jet, we introduce characteristic quantities for the plume in the same spirit. Denoting these quantities by over-bars, we have:

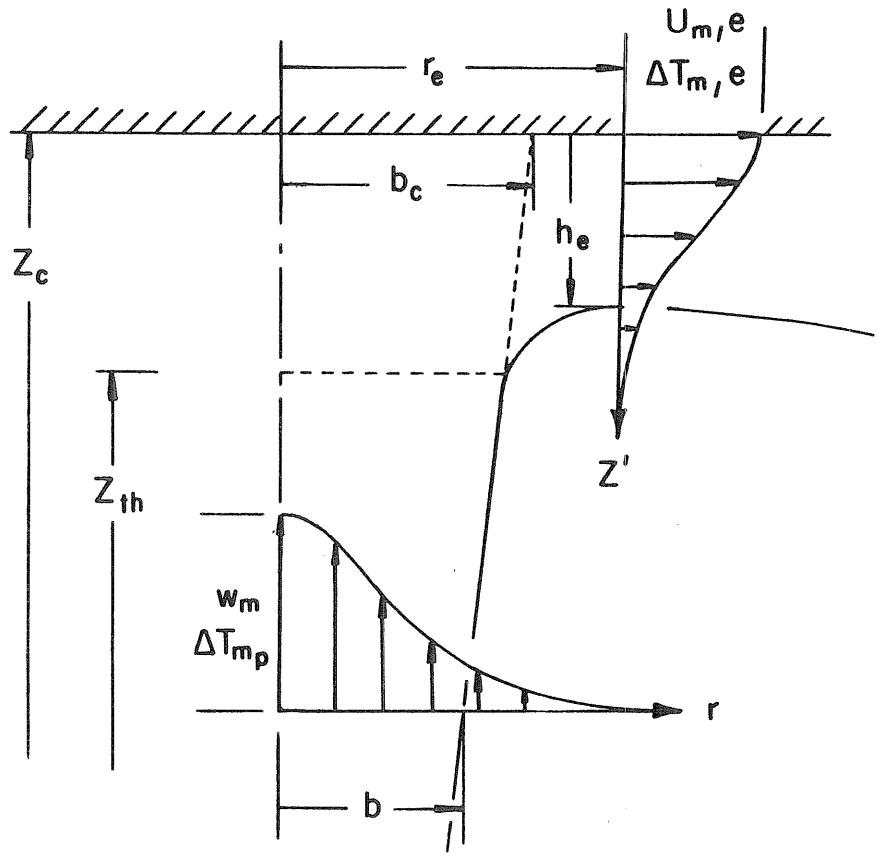

(A) GAUSSIAN PROFILE CASE

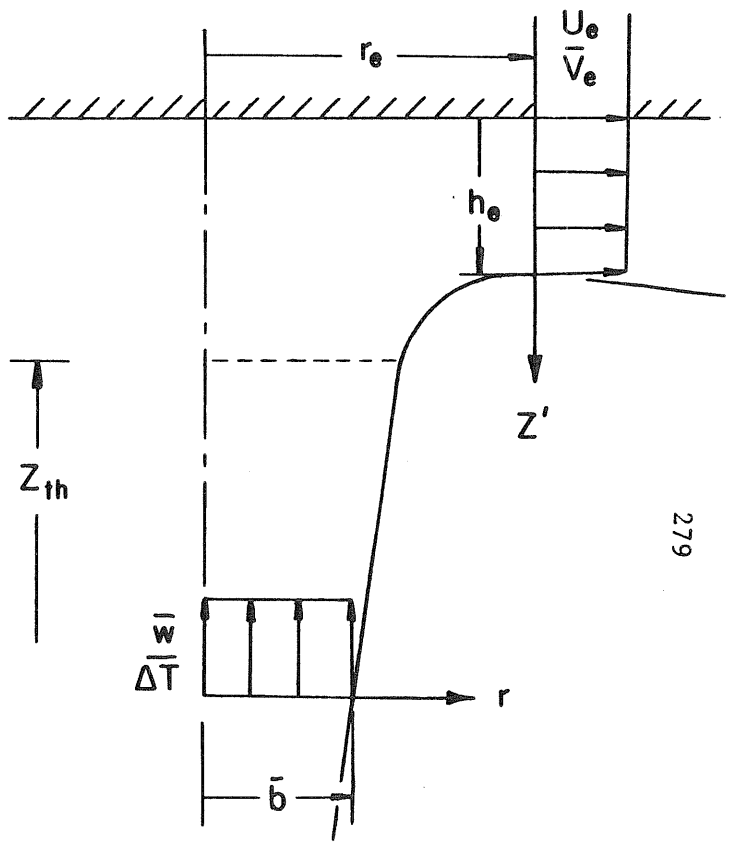

(B) EQUIVALENT TOP-HAT CASE

FIGURE 8.7 PLUME IMPINGEMENT

$$\overline{w}\,\overline{b}^2 = \int_0^\infty w\, dr^2 \tag{8.55}$$

$$\overline{w^2}\overline{b}^2 = \int_0^\infty w^2 dr^2 \tag{8.56}$$

$$\overline{w}\,\overline{\Delta T}_p\overline{b}^2 = \int_0^\infty w\Delta T_p\, dr^2 \tag{8.57}$$

We can now write the continuity equation, in terms of these mean or characteristic quantities, for the flow between the plume and the ceiling jet. Assuming that there is no entrainment in this idealized turning process we have:

$$\overline{w}_t\overline{b}_t^2 = 2r_e U_e h_e \tag{8.58}$$

where the quantities in the plume, and those in the jet, are evaluated at z_{th} and r_e, respectively.

Next, if we assume that the initial buoyancy is small ($Ri_e \ll 1$), Bernoulli's equation immediately yields:

$$\overline{w}_t = U_e \tag{8.59}$$

so that the effective mean velocity of the fluid does not change. This in turn implies that the magnitude of the integrated kinematic momentum flux remains constant as the flow turns. These results rest on the assumptions that the flow is inviscid and adiabatic, and that the pressure is constant outside of the plume and jet. If necessary we can empirically correct for the losses due to turbulence, and viscous effects, by reducing the exit velocity by a factor of ε_u, so that:

$$U_e = \varepsilon_u \overline{w}_t \tag{8.60}$$

The continuity equation then gives us the initial thickness:

$$h_e = \frac{\overline{b}_t^2}{\varepsilon_u 2 r_e} \tag{8.61}$$

For adiabatic flow, the conservation of enthalpy requires:

$$\overline{w}_t \, \overline{\Delta T}_{p_t} \, \overline{b}_t^2 = 2 r_e U_e h_e \, \frac{\nabla_e T_2}{g} \tag{8.62}$$

which we can correct in a similar fashion by multiplying by ε_T. With the help of the continuity equation we have:

$$\nabla_e = \varepsilon_T \left(g \frac{\overline{\Delta T}}{\overline{T}_2 p_t} \right) = \varepsilon_T \nabla_{p_t} \tag{8.63}$$

Throughout most of this work, we will approximate the actual mean velocity profiles in both the plume and the ceiling jet with Gaussian distributions. In this case, the conditions at the entrance to the ceiling jet can be expressed:

$$u_{m,e} = \varepsilon_u \frac{w_{m_t}}{\sqrt{2}} \qquad U_e = \varepsilon_u \frac{w_{m_t}}{2} \tag{8.64a,b}$$

$$\ell_e = \frac{1}{\varepsilon_u} \sqrt{\frac{2}{\pi}} \, \frac{b_t^2}{r_e} \qquad h_e = \frac{b_t^2}{\varepsilon_u r_e} \tag{8.65a,b}$$

$$\Delta Tm,e = \varepsilon_T \frac{\Delta Tmpt}{\sqrt{1+\sigma}} \qquad \nabla_e = \frac{\varepsilon_T}{1+\sigma} \left(g \frac{\Delta Tmpt}{T_2} \right) \tag{8.66a,b}$$

where ℓ_e is the Gaussian length scale in the ceiling jet at r_e. It is interesting to note that although Bernoulli's equation shows that the effective mean velocity is constant, the change in the geometry from axial flow to radial flow causes a decrease in the maximum velocity and temperature of the assumed Gaussian profiles. This reduction by a factor of approximately $\sqrt{2}$, is necessary to insure that the mean flow can satisfy Bernoulli's equation and the conservation of enthalpy.

At this point it should be noted that Alpert (1974) took a slightly different approach. Basically, in addition to using the conservation of

mass, he applied Bernoulli's equation along the stagnation streamline and assumed that both the plume and the ceiling jet had Gaussian profiles. With these assumptions be obtained:

$$u_{m,e} = w_{m_t} \tag{8.67}$$

As previously noted, this result will give a momentum flux in the ceiling jet that is a factor of $\sqrt{2}$ larger than in the plume. We can accommodate this behavior in the calculation scheme by setting $\varepsilon_u = \sqrt{2}$ in equations (8.64) and (8.65). However, although he did not attempt to treat the mean velocity behavior, Alpert (1974) did use the integrated form of the conservation of enthalpy. He neglected stagnation region losses so that $\varepsilon_T = 1$ in equation (8.66). Finally, it should be noted that many of the numerical case studies discussed in Section (8.7) were computed using an early version of the ceiling jet program based on Alpert's assumptions ($\varepsilon_u = \sqrt{2}$, $\varepsilon_T = 1$).

Other profiles, either theoretical or experimental, are possible candidates for the ceiling jet. For example, Kubota (1981) has pointed out that the Stokes stream-function can be used to show that for inviscid, adiabatic flow, the initial ceiling jet velocity and temperature distributions, resulting from a Gaussian plume, are actually exponential in nature. In this case we have:

$$u_m = \varepsilon_u w_{m_t} \qquad U_e = \varepsilon_u \frac{w_{m_t}}{2} \tag{8.68 a,b}$$

$$\ell_e = \frac{b_t^2}{\varepsilon_u 2 r_e} \qquad h_e = \frac{b_t^2}{\varepsilon_u r_e} \tag{8.69 a,b}$$

$$\Delta T_{m,e} = \varepsilon_T \Delta T_{m_{p_t}} \qquad \nabla_e = \varepsilon_T \left(g \frac{\Delta T_{m_{p_t}}}{T_2} \right) \tag{8.70 a,b}$$

In doing the actual calculations, the losses in momentum and enthalpy caused by turbulence and viscous effects can either be assumed or estimated from experimental data. For example, Poreh and Cermak (1959) presented data for a submerged jet which indicates ε_u may be as low as 0.73. Values for ε_T can be estimated using the results of Section (8.5) to calculate the total impingement region heat transfer, Q_{ir}. Calculations for typical 14.8 kw fires ($Q^*_{z_c} = 8.1 \times 10^{-3}$) shows that Q_{ir} at most represents only 7.6% of the enthalpy delivered by the plume. If this had been a bare ceiling case, the fractional loss would have been reduced to 5.9%. Thus we expect ε_T to be in the range 0.9 - 1.0 , while the variation in ε_u may be a good deal larger.

With the specification of the effective mean thickness, velocity, and temperature difference at the entrance to the ceiling jet, we now have a complete set of initial conditions, in terms of known quantities in the plume at z_{th} , with which to begin the calculation.

8.6.9 Entrance Conditions for a Two-dimensional Ceiling Jet

Since the plume itself is axially symmetric, the initial portion of the ceiling jet will be as well. However, the presence of side walls may begin to channel the flow into a basically two-dimensional flow pattern. We have observed this phenomenon in the 1/2 scale fire test room, shown in Figure (8.8), which had a ceiling height of 1.22m. Measured heat transfer coefficient data, taken near the centerline of the 1/2 scale room, agreed with the calculated axisymmetric solution until the presence of the side walls became important as $\bar{r}$ approached roughly 0.5. For larger distances, the data showed better agreement with a calculated two-dimensional solution than with the axisymmetric one.

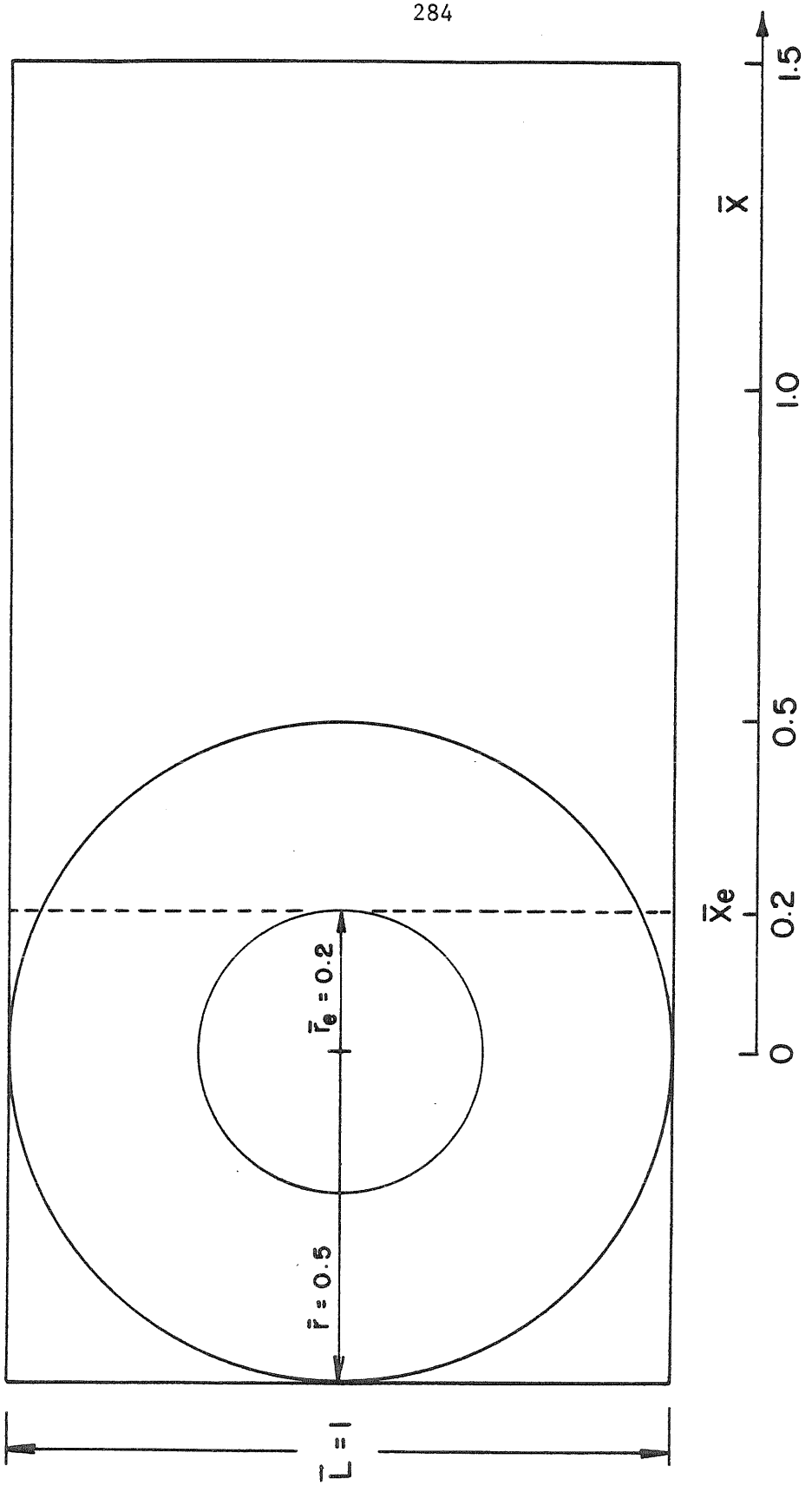

FIGURE 8.8 CEILING JETS FOR 1/2 SCALE FIRE ROOM ($Z_c = 1.22$ m)

Thus we must estimate the effective starting conditions for two-dimensional ceiling jets formed by the presence of the side walls.

The actual turning process occurs gradually over a finite distance, and may be complicated by secondary flows near the walls. However, we have chosen to approximate it in a very simple way. We first assume that buoyancy will tend to force the hotter gas which makes up the ceiling jet to remain near the ceiling throughout the turning process (thereby minimizing the possibility of secondary flows). Then we assume that some fraction, ξ, of the initially radial flow will be turned without losses into the x direction. Thus our two-dimensional calculation represents an effective asymptotic state, which the real ceiling jet flow should approach as the distance from the source becomes large compared to the distance separating the sidewalls of the room.

The actual value of the turning fraction ξ must be estimated, based on the room geometry, at the start of the calculation. For example, as shown in Figure (8.9), one might expect that for a long narrow room with the fire at one end (anti-symmetric case), most of the flow would be turned ($\xi \sim 1$). On the other hand, for a symmetrically placed fire, roughly half of the plume's output could be expected to go in each direction ($\xi \sim \frac{1}{2}$).

For a given turning fraction, ξ, we assume that the two-dimensional ceiling jet behaves as though produced by an effective two-dimensional source, located directly above the fire ($x=0$). This fictitious source supplies kinematic fluxes of mass, momentum, and enthalpy, whose values at the entrance to the jet are assumed to be a fraction ξ of the respective fluxes entering the axisymmetric ceiling jet. In addition, we

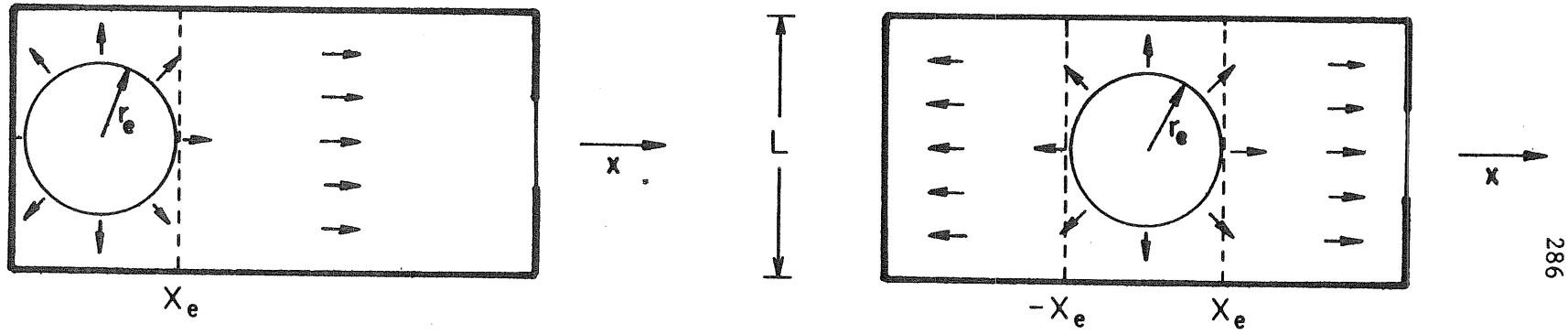

(A) ANTI-SYMMETRIC CASE

$\xi = 1$

(B) SYMMETRIC CASE

$\xi = 1/2$

FIGURE 8.9 AXISYMMETRIC AND TWO-DIMENSIONAL CEILING JETS

assume that the numerical values of x_e and r_e are identical.

If we denote the kinematic fluxes of mass , momentum, and enthalpy per unit width in the two-dimensional ceiling jet by $\tilde{m}$, $\tilde{M}$, and $\tilde{Q}$, respectively, and the respective total fluxes in the axisymmetric case by m, M, and Q , and if the width of the room is L , then at the entrance to the jet we have (dropping the subscript e):

$$\tilde{m}\, L = \tilde{U}\tilde{h}L = \xi\, m = \xi\, (2\pi r\ U\, h) \tag{8.71}$$

$$\tilde{M}\, L = \tilde{U}^2\tilde{h}L = \xi\, M = \xi(2\pi r\, U^2 h) \tag{8.72}$$

$$\tilde{Q}\, L = \tilde{U}\tilde{h}\tilde{\nabla}L = \xi\, Q = (2\pi r\, U\, h\nabla) \tag{8.73}$$

We can now write the two-dimensional starting values at $x_e = r_e$ as:

$$\tilde{U} = U \tag{8.74}$$

$$\tilde{\nabla} = \nabla \tag{8.75}$$

$$\tilde{h} = (\xi \frac{2\pi r_e}{L})\ h \tag{8.76}$$

Thus with expressions (8.74) - (8.76), we can estimate the effective starting conditions for the asymptotic two-dimensional ceiling jet formed by turning a fraction ξ of the initially axisymmetric flow into the x direction.

8.7 Numerical Results from Selected Ceiling Jet Case Studies

The ceiling jet calculation scheme developed in the preceding section contains a large number of parameters embodying the various assumptions underlying the model. In order to test the sensitivity of our calculation scheme to these parameters, a large number of numerical case studies were run in which the parameters were systematically varied. The results indicate that a few parameters effectively govern the behavior of the ceiling jet, and that they are the parameters one would intuitively expect to play key roles: the entrainment constant α , the friction

factor N , and the ceiling temperature T_w .

(8.7.1) Review of the Ceiling Jet Calculations

Before examining some selected numerical results, a brief review of the calculation scheme may be useful. For a given finite source fire, described by the kinematic fluxes of mass (W_o) , momentum (V_o) , and buoyancy (F_o) , and the mean value for the lower layer temperature T_1 , a computer program calculates the evolution of the plume up to the interface height z_{int} , using the relations developed in Section (2.4). Then, given the mean value for the hot upper layer temperature T_2 , the interface jump conditions of Section (8.2) are utilized to calculate new effect source conditions (W_2, V_2, F_2) for the plume program. This same finite source plume program then calculates the growth of the plume until it reaches the ceiling. There the stagnation point and overall impingement region heat transfer rates are calculated based on the results of Sections (8.4) and (8.5) respectively. The plume program also calculates the effective starting values for the ceiling jet variables (h_e, U_e, ∇_e), given turning efficiencies ε_u and ε_T introduced in Section (8.6.8). For a given ceiling temperature T_w , the ceiling jet program is then invoked to numerically integrate the three ordinary differential equations representing the integrated equations for the conservation of mass, momentum, and enthalpy. This set of equations (8.36 - 8.38) can be numerically integrated in either the axisymmetric or two-dimensional form. In the continuity equation (8.36), the entrainment function E is given as a function of the ceiling jet Richardson number by equation (8.54). There are two options for the friction factor N ; either N may be set to an arbitrary constant value by the user, or the program will calculate

the inner layer thickness $\tilde{\delta}$, given by equation (8.47), and use the result to estimate N from the inner layer Reynolds number Re_m according to equation (8.42) or (8.43) depending on the flow geometry.

The variables calculated by the ceiling jet program can be divided into two groups. First, the ceiling jet problem has been posed in terms of mean or characteristic quantities (h, U, ∇) which can be thought of as giving the bulk or average values for the ceiling jet's thickness, velocity, and buoyancy relative to the upper layer fluid beneath it. Second, for a given profile shape, one has the maximum values for the velocity u_m and temperature T_m, which are assumed to occur just outside the inner viscous layer. These maximum quantities then fix the transport rates across the inner layer, while the bulk quantities establish the overall flow characteristics.

In order to compare results between different experiments, it is useful to introduce dimensionless variables using the simple point source plume variables (given by equations (2.58) - (2.60)) to scale the physical variable. Thus, similar to the dimensionless heat transfer coefficient h_c' given by equation (8.14), we have

$$U^* = \frac{U}{\sqrt{g z_c}\,(Q^*_{z_c})^{1/3}} \tag{8.77}$$

$$T^* = \frac{T_m - T_2}{T_2 (Q^*_{z_c})^{2/3}} \tag{8.78}$$

$$q_c^* = \frac{q_c}{(Q/z_c^2)} = h_c' \frac{(T_m - T_w)}{T_2 (Q^*_{z_c})^{2/3}} \tag{8.79}$$

for the dimensionless mean velocity, maximum gas temperature difference, and convective heat transfer rate, respectively. Since $b \propto z$ for the

simple plume, all lengths are scaled by z_c, as was done in Section (8.6) for $\bar{h} = h/z_c$ and $\bar{r} = r/z_c$.

The majority of the numerical case studies were computed for typical conditions encountered in the ½ scale room fire tests. As our calculation scheme evolved, the sets of flow conditions and assumptions used in the calculation were revised several times. They are summarized for comparison in Table (8.4). The detailed effects of these changes are given by Sargent (1982 b).

Table (8.4) Typical ½ Scale Room Fire Conditions

(A) Source and Room Geometry

$Q = 14.8$ kW $\quad d_o = 0.152$ m $\quad z_c = 1.22$ m

$Q^*_{z_c} = 8.1 \times 10^{-3} \quad \bar{r} < 2.0$

(B) Original Conditions & Alpert's (1974) Assumptions

$\bar{z}_{int} = 0.50 \quad T_1 = 36.9°C \quad T = 116.5\ °C \quad c_q = 0.60$

$z_{th} = z_c - h_e \qquad r_e = 1.73\ b_e$

$\varepsilon_u = \sqrt{2} \qquad \varepsilon_T = 1 \qquad T_w = T_2$

$\alpha = 0.1096 \qquad \beta = 3.96 \qquad N$ variable

(C) Revised Conditions & Assumptions

$\bar{z}_{int} = 0.515 \quad T = 36.9\ °C \quad T = 121.5 \quad c_q = 0.664$

$$z_{th} = \begin{cases} z_c - h_e \\ z_c - 1.33\ b_c \end{cases} \qquad r_e = 1.73\ b_c \approx 1.59\ b_c$$

$\varepsilon_u = 1 \qquad \varepsilon_T = 1 \qquad T_w = T$ or $\bar{T}_w$, exp.

$$\alpha = \begin{cases} 0.0879 \text{ (Axi)} \\ 0.6348 \text{ (2D)} \end{cases} \qquad \beta = 5.10 \qquad N \text{ variable}$$

(D) Final Conditions & Assumptions

$\bar{z} = 0.539$ $T = 36.4°C$ $T = 122.9$ $cq = 0.740$

$z_{th} = z_c - 0.77\, b_c$ $r_e = 1.87\, b_c$

$\varepsilon_u = 1$ $\varepsilon_T = 1$ $T_w = T_2$ or $\bar{T}_w$, exp

$\alpha = \begin{cases} 0.0879 & \text{(Axi)} \\ 0.0348 & \text{(2D)} \end{cases}$ $\beta = 5.10$ N variable

Note that the final set (entry D in Table (8.4)) conforms to the values used in this chapter.

In order to demonstrate the sensitivity of the calculation scheme to the various parameters, we have plotted the behavior of certain key variables as functions of the downstream distance $\bar{r}$. Because this set of graphs is rather bulky, we will simply summarize the results here. The detailed results are given by Sargent (1982 b).

Basically, the most important consideration for predicting the heat transfer to the ceiling is the flow geometry. Simple dimensional arguments indicate that the heat transfer coefficient should scale as $1/r$ and $1/\sqrt{x}$ for axisymmetric and two-dimensional flows respectively. Our numerical results reflect this fundamental behavior.

For a given flow geometry, the parameter which effectively controls the overall growth of the ceiling jet is the entrainment function E, given by equation (8.45). In this equation, the important factor is E_o, the neutral jet (Ri = 0) entrainment coefficient. As expected, the larger the value of E_o, the faster the jet slows down and spreads out.

The coefficient β, which governs the exponential dependence of E on the Richardson number, is of secondary importance, provided β is greater than zero, because the entrainment function tends to be self-limiting (i.e. - the product $\beta \cdot Ri$ remains roughly constant).

With the basic flow pattern determined by the flow geometry and entrainment function, the final step in calculating the heat transfer to the ceiling involves specifying the conditions at the ceiling itself. This is done in two steps. First, the velocity boundary condition is effectively set by specifying a value for the friction factor N. Varying N produces large changes in the heat transfer coefficient h_c, and rate q_c. However, since N is small compared to one, these variations have relatively little impact on the mean ceiling jet flow. Second, the thermal boundary must be independently established by entering a value for the ceiling temperature T_w, which along with the heat transfer coefficient, then fixes the convective heat transfer rate to the ceiling. This thermal boundary condition can become especially important at large distances. If the ceiling is such that it is colder than the hot upper layer of gas $(T_w<T_2)$, the ceiling jet can become negatively buoyant, and hence unstable, at large distances. It is interesting to recall that the gas temperature data presented in Section (7.3.2) show that far from the fire the gas in the ceiling jet is in fact colder than bulk of the gas in the upper layer. This negatively buoyant gas can be seen flowing down the northwest corner of the room in Figures (7.15) - (7.18).

The numerical routines described in this chapter were coded by the author in VAX-11 FORTRAN for execution on a VAX-11/780 or similar machine supporting FORTRAN-77. These programs included both the finite source

plume and interface jump computation discussed in Section (8.2) and the ceiling jet calculation described in Section (8.6). The numerical features of these programs are briefly documented by Sargent (1982 a).

IX. CONVECTIVE HEAT TRANSFER DATA AND RESULTS

9.1 Introduction

A number of experiments were carried out in the ½ scale test room to investigate the effects of heat input, door geometry, and fire location on convective heat transfer. In order to simplify this presentation, we will examine a few cases in detail, and then discuss the variation of several pertinent dimensionless variables. In addition, we will also examine the previous results of Zukoski, Kubota, and Veldman (1975) for bare and curtain wall tests, and compare them to our present results.

Before proceeding with the discussion of the experimental results, it seems useful to review the semi-empirical calculation scheme used to predict the convective heat transfer to the ceiling. The heart of this scheme is the finite source plume rising through the interface and turning into the ceiling jet as it impinges on the ceiling. In order to start this Boussinesq calculation (described in Chapter II), we need the initial kinematic fluxes of mass, momentum, and buoyancy and the external ambient temperature. In both the bare ceiling and curtain wall test of Zukoski, Kubota, and Veldman (1975) and in the ½ scale room tests described here, the plumes emanated from pre-mixed burners. The mass flux is known from the flow rates of air and fuel. Given the fuel flow rate and the lower leating value for the fuel, the heat release can be immediately calculated, assuming that because the flame is pre-mixed, the flame radiation is negligbly small. Then given the heat release, equation (2.1) gives the initial kinematic buoyancy flux. Finally, the initial momentum flux was calculated by assuming that the fuel/air

mixture had a uniform velocity as it flowed across the burner's open area (i.e. - the area not blocked by the helical flame holder). Given the source conditions, one must also specify the mean ambient temperatures $\bar{T}_1$ and $\bar{T}_2$ encountered by the plume in the lower and upper layers respectively, and the height of the interface z_{int} between them. For each experiment, these values were determined from the vertical traverse temperature data described in Chapter VII. In addition, these experimental temperature plots also provided the reference temperature T_o, which was taken as the temperature of the gas at the floor near the fire. With the source and environmental conditions specified, the plume equations can be integrated to provide starting values for the ceiling jet calculation described in detail in Chapter VIII. Preliminary studies indicated that the assumption that the plume turns without losses ($\varepsilon_u = 1$, $\varepsilon_T = 1$) gave a reasonable fit to the data, and these values will be used here.

The remaining important parameters of the ceiling jet calculation are the flow geometry, the entrainment function E, the friction factor N, and the ceiling temperature T_w. At this point in time, our calculation scheme can not predict the actual transition from axisymmetric to largely two-dimensional flow. However, we can calculate the two asymptotic states of pure axisymmetric and pure two-dimensional flow. For those cases where this kind of flow transition may be expected, we do two calculations and present the two asymptotic estimates. The entrainment function, which depends on the ceiling jet Richardson number, has been described in Chapter VIII. We do not modify it here, except that the plume entrainment may be expected to change for fires located

in a corner, or near a wall. Again, preliminary studies showed that a constant friction factor seemed to give the best estimates of the dimensionless heat transfer coefficient h_c' compared with the data. Originally, we picked a constant friction factor for each experiment such that the initial ceiling jet value of h_c' matched the last impingement region h_c' estimate. This procedure gave a continuous h_c' curve. However, the stagnation point and ceiling jet heat transfer coefficients have a slightly different dependence on the Reynolds number, and therefore we have found it best to scale the friction factor with the initial ceiling jet Reynolds number. Finally, it is necessary to specify an approximate power law dependence for the ceiling temperature. As might be expected, merely specifying a mean ceiling temperature is adequate for computing the fluid mechanics and hence h_c' for the ceiling jet. However, in order to compute the convective heat transfer rate q_{conv} it is necessary to use a more accurate thermal boundary condition.

Three basic effects were studied in our ½ scale room tests. A standard door geometry was compared with a standard window geometry. Then for each case, the burner size and hence the heat input was varied. Finally, one set of tests was conducted with the fire located on the long axis of the room, a distance of ½ the room height z_c from the wall, while a second set was conducted with the fire located in the rear corner (0.15 z_c from each wall). In order to further extend the range of the dimensionless heat input parameter $Q^*_{z_c}$ and to examine the effects of the upper layer and of the ceiling jet flow geometry, we have also examined the data of Zukoski, Kubota, and Veldman (1975)

for axisymmetric bare ceiling (no upper layer) and curtain wall fires. Table (9.1) lists the basic characteristics of each of the experiments we will discuss.

In order to compare data between experiments, we will examine a set of dimensionless variables, which are scaled by representative quantities of a simple point source plume, and which are based on mean conditions in the upper layer. This approach would be expected to work very well for plumes impacting on an unconfined ceiling, many fire diameters from the source. On the other hand, when the plume rises through a hot upper layer before impinging on the ceiling, the upper plume will have reduced buoyancy and the characteristic dimensionless variables will become functions of the relative height of the interface (z_i/z_c) and of the fraction of heat lost from the upper layer given by $(1 - c_q)$. However, the behavior of the upper plume does not change radically as its buoyancy is varied from $c_q=1$ (neutral jet) to $c_q=0$ (fully buoyant plume). Thus our approach may be expected to work for ceilings with or without upper layers. As before, the dimensionless heat input parameter is given by;

$$Q^*_{z_c} = \frac{Q_F}{\rho_\infty \, c_p \, T_\infty \, \sqrt{g z_c} \, z_c^{\,2}} \qquad (2.55)$$

Using this parameter, plume velocities and temperature differences at the height of the ceiling can be expected to scale with $\sqrt{g z_c}\ (Q^*_{z_c})^{1/3}$ and $T_o (Q^*_{z_c})^{2/3}$ respectively. We can now introduce two dimensionless temperature differences which measure the buoyancy of the ceiling jet gas with respect to the lower and upper layers respectively:

$$T_1^* = \frac{T - \bar{T}_1}{T_0 (Q_{z_c}^*)^{2/3}} \qquad T_2^* = \frac{T - \bar{T}_2}{T_0 (Q_{z_c}^*)^{2/3}} \tag{9.1}$$

Similarly, we can form a Stanton number or dimensionless heat transfer coefficient based on the plume velocity scale:

$$h_c' = \frac{h_c}{\rho_2 c_{p_2} \sqrt{g \bar{z}_c} \; (Q_{z_c}^*)^{1/3}} \tag{8.14}$$

Finally, since the convective heat transfer rate is given as the product of the heat transfer coefficient and the gas-wall temperature difference, the dimensionless heat transfer rate is given by:

$$q_{conv}^* = h_c' \, \Delta T_{gw}^* = \frac{h_c \, (T_{mg} - T_w)}{\rho_2 c_{p_2} T_0 \sqrt{g z_c^2} \; Q_{z_c}^{2*}} \tag{9.2a}$$

$$q_{conv}^* = \frac{q_{conv}}{(\frac{\rho_2}{\rho_0}) \frac{Q_F}{z_c^2}} = \frac{q_{conv}}{(\frac{T_0}{T_2}) \frac{Q_F}{z_c^2}} \tag{9.2b}$$

For consistency, we will scale all local heat transfer rates by this same factor $[(T_0/T_2)\ (Q_F/ z_c^2)]$. Finally, we are also interested in the total or integrated heat transfer rates to or through the ceiling and walls. If we denote the total convective heat transfer rate by $Q_{T,\ conv}$, then

$$Q_{T,\ conv} = \int_0^r q_{conv} \, 2\pi r \, dr \tag{9.3}$$

and so

$$Q_{T,conv}^* = \int_0^{\bar{r}} q_{conv}^* \, 2\pi \bar{r} \, d\, \bar{r} \tag{9.4a}$$

or

$$Q_{T,conv}^* = \frac{Q_{T,\ conv}}{(\frac{T_0}{T_2}) Q_F} \tag{9.4b}$$

Table (9.1) Summary of Experimental Conditions

Experiment	Q_F[kw]	Fire Location	z_c[m]	$\bar{T}_1$[c]	z_i/z_c	$\bar{T}_2$[c]	$c_q^\dagger$	$Q^*_{z_c} \times 10^3$	Door Geometry
Bare Ceiling 1*	1.17		0.813	21.0			0.000	1.76	
Bare Ceiling 2*	1.17		0.584	19.3			0.000	4.13	
Curtain Wall 4*	1.17		0.813	21.0	0.631	34.9	0.357	1.76	
Curtain Wall 5*	1.53		0.813	22.0	0.639	39.9	0.397	2.36	
1/2 scale 15	14.87	CL	1.219	36.4	0.539	122.9	0.740	8.14	Door
1/2 scale 16	14.85	CL	1.219	68.3	0.488	154.9	0.590	8.13	Window
1/2 scale 7	3.67	SW	1.219	28.8	0.632	64.7	0.866	2.01	Door
1/2 scale 10	7.24	SW	1.219	30.4	0.605	89.9	0.881	3.96	Door
1/2 scale 13	14.33	SW	1.219	31.50	0.573	124.8	0.889	7.85	Door

Fire Locations: CL = on room center line SW = in southwest corner

Door Geometry: Door = standard door geometry 0.396 z_c x 0.183 z_c

Window = standard window geometry 0.396 z_c x 0.375 z_c

* Data of Zukoski, Kubota, & Veldman (1975)

† c_q calculated from equation (8.3) with constant plume entrainment (i.e. - without correcting far wall effects)

Note that for bare or unconfined ceilings, $T_2 = T_0$ and so the convective scaling parameters reduce simple expressions depending only on the heat release rate Q_F and the ceiling height.

9.2 Heat Transfer Data Reduction

During our half scale room tests, the primary heat transfer data were acquired after steady state conditions had been reached. This was necessary because although the temperature history of the wall and ceiling thermocouples were recorded on magnetic tape, the aspirated thermocouple probe could not be traversed fast enough to obtain the gas temperature history both as a function of time and position. Given steady state heat conduction through the wall as evidenced by approximately constant wall temperatures, the convective heat transfer rate at a given point could be easily computed from the heat conduction and net radiative rates.

$$q_{conv} = q_{cond} - q_{r,net} \tag{9.5}$$

where

$$q_{cond} = \frac{k_w}{\Delta_w} (T_w - T_{w_{out}}) \tag{9.6}$$

and

$$q_{r,net} = q_{r,incident} - q_{r,emitted} \tag{9.7}$$

In these expressions, we have neglected lateral conduction losses since the temperature gradients across the wall were always large compared to the lateral gradients, and preliminary calculations showed that this assumption introduced at worst a 3% error.

As shown by equation (9.5), the problem of calculating the convective heat transfer rate basically becomes one of estimating the radiant heat transfer rates given in equation (9.7). Actually the local emitted flux is readily computed as

$$q_{r,\text{emitted}} = \varepsilon \hat{\sigma} T_w^4 \tag{9.8}$$

where we have taken the emissivity ε to be one.

However, the incident flux is a good deal more complicated. In a real room fire, a sizable fraction of this incident flux would come from the flames themselves, in particular from the hot soot particles formed in the fuel rich portion of diffusion flames. However, in our experiments premixed burners were used with a lean air-fuel mixture, resulting in small pale blue flames. Zukoski, Kubota, and Veldman (1975) found that thermal radiation was negligible from such burners, and consequently we have simplified the estimation considerably by neglecting it. Furthermore, because entrainment of lower layer air into the plume greatly dilutes the concentration of CO_2 and water vapor delivered to the upper layer and simultaneously causes the plume temperatures to fall, thermal radiation from the large volume of hot upper layer gas to the walls will be neglected. Manual calculations for two different heat inputs showed that in fact radiation from the ceiling gas was on the average only 12-15% of the convective flux delivered to the ceiling and approximately 20% of the convective flux delivered to the west side wall. However, these manual calcualtions ignored absorption by the gas. Consequently, when absorption is taken into account, the radiant flux from the gas to the walls will probably be reduced to a small fraction of the convective flux. In these manual estimates, we were able to assume that the hot upper layer was reasonably well mixed and hence at a uniform temperature and composition. Unfortunately no similar simplifying assumption could be made about the plume itself, and so no estimates of its contribution to the radiant flux

were obtained. However, one may surmise that its impact of the ceiling heat transfer rates would be greatest near the stagnation point, and that it would tend to reduce the calculated convective heat transfer rate by adding to the incident flux there.

Thus, given the assumptions that thermal radiation from the upper layer gas and from the plume will be ignored, the incident radiant flux from the walls to an infinitesimal target area element becomes:

$$q_{r,inc} = \int_{A_i} \hat{\sigma} T_i^4 \frac{\cos\theta i \cos\theta t}{\pi r^2} dA_i \qquad (9.9)$$

Assuming that the temperature of each finite area element is constant this integral can be replaced by a sum containing the elemental temperatures and a geometrical view factor:

$$q_{r,inc} = \sum_{A_i} \hat{\sigma} T_i^4 F_i \qquad (9.10)$$

$$F_i = \frac{1}{\pi} \int_{A_i} \frac{\cos\theta_i \cos\theta_t}{r^2} dA_i \qquad (9.11)$$

The advantage of this approach is that the view factors need only be calculated once and then stored in a table for future reference. The incident flux for a given set of wall temperature data is then evaluated using equation (9.10). The room's 6 surfaces were first divided up by a grid into an integral number of one foot by one foot zones. A computer program was written which used bivariate interpolation to find an estimate for the node temperatures of each zone, based on the actual surface temperature data. A fourth power average temperature T_i was assigned to each zone based on its four node temperatures. Because the view factors had also been calculated based on integral distances, equation

(9.10) was evaluated at each node point on the surface. The results were then back interpolated to yield the incident radiation flux at each surface thermocouple locations. Next equations (9.5) - (9.7) were then evaluated in reverse order to find the local radiant, conductive, and convective heat transfer rates at each such location. A final manual step was then required to find the heat transfer coefficient. Estimates were made of the maximum gas temperature T_{mg} along the ceiling and west side wall, based on the traversing probe data. The heat transfer coefficient was then estimated as:

$$h_c = \frac{q_{conv}}{T_{mg} - T_w} \tag{9.12}$$

It should be noted that this procedure to calculate the local heat transfer rates differs in several respects from that used by Zukoski, Kubota, and Veldman (1975) for their bare (unconfined) ceiling and curtain wall tests. First, their experiments were all transient in nature, with their data taken in the first few minutes of the fire. Second, their ceiling was insulated so that after a long time the ceiling jet gas approach steady conditions which they designated T_{ad} for "adiabatic wall" conditions. Their heat transfer coefficient data are given by an expression like (9.12) except that T_{mg} is replaced by T_{ad}. Because heat transfer to the ceiling will reduce T_{mg} below T_{ad}, it must be kept in mind that their values for the heat transfer coefficient h_c will thus always be somewhat greater than our 1/2 scale room test values as of course will be their gas temperature data.

In addition, Zukoski, Kubota, and Veldman (1975) did not calculate the radiant heat transfer contributions to their transient energy balance. Early in their tests, the ceiling temperatures were approximately ambient, so that radiative effects would be a small fraction of the convective flux. However, for slightly later times as their ceilings became hot compared to the rest of the laboratory, they must have radiated energy away to other surfaces and hence the actual convective flux must be greater than that calculated by Zukoski, Kubota, and Veldman (1975). Consequently, their values of the heat transfer coefficient will also be lower than the actual values. Finally, when their "adiabatic wall" condition was reached, the convective flux would be equal to the net emitted radiant transfer. Even at modest times, however, these effects may become significant. As a worst case assume that the laboratory is filled with black objects at ambient temperature. Then at only 7 minutes after ignition, the net radiative flux would be on the average 40% of the convective flux for the first bare ceiling test. In reality, other objects in the laboratory would be heated by this radiation and the net radiative flux would fall to some smaller fraction of the convective flux. However, lacking the geometrical and temperature data for these other objects, it is impossible to estimate the actual radiant contribution.

9.3 Bare Ceiling Results

There are several reasons for re-examining the data of Zukoski, Kubota, and Veldman (1975) in light of the ceiling heat transfer calculation scheme described in the previous chapter. First, the apparatus had circular

symmetry so that the flow should remain axisymmetric throughout the entire range of measurement. Second, the ceiling thermocouples were spaced every 7 cm, compared to a typical 30 cm spacing in our 1/2 scale apparatus. This finer spacing allows us to compare our impingement region predictions to experimental data. Finally, by comparing their unconfined ceiling and curtain wall tests, we can check whether our calculations handle the presence of the hot upper layer correctly.

The simplest case to consider is that of a bare or unconfined ceiling. In this case the buoyant plume impinges directly on the ceiling and turns to form a radial ceiling jet which procedes outward until it flows up past the edge of the ceiling.

The average value of the dimensionless heat transfer coefficient h_c' for the first two bare ceiling tests is shown in Figure (9.1). The first test had a ceiling height to burner diameter ratio $z_c/d_o = 32$, compared to $z_c/d_o = 23$ in the second test. Shown on the same plot are the calculated values which are seen to fit the data quite well for both the impingement ($r/z_c \lesssim 0.25$) and the ceiling jet regions. In the ceiling jet calculations for these two experiments we have used constant values ($N_o = 0.0196$ and 0.0210, respectively) for the friction factor N. These values of N_o were chosen by matching the values of h_c' calculated in the impingement and wall jet regions at their boundary ($\bar{r} = \bar{r}_e$). The same data are replotted on a linear scale in Figure (9.2) to illustrate the rapid decrease in the heat transfer coefficient as a function of distance from the stagnation point. Note that the calculated value for the stagnation point heat transfer coefficient, which includes the turbulence enhancement function, fits the data

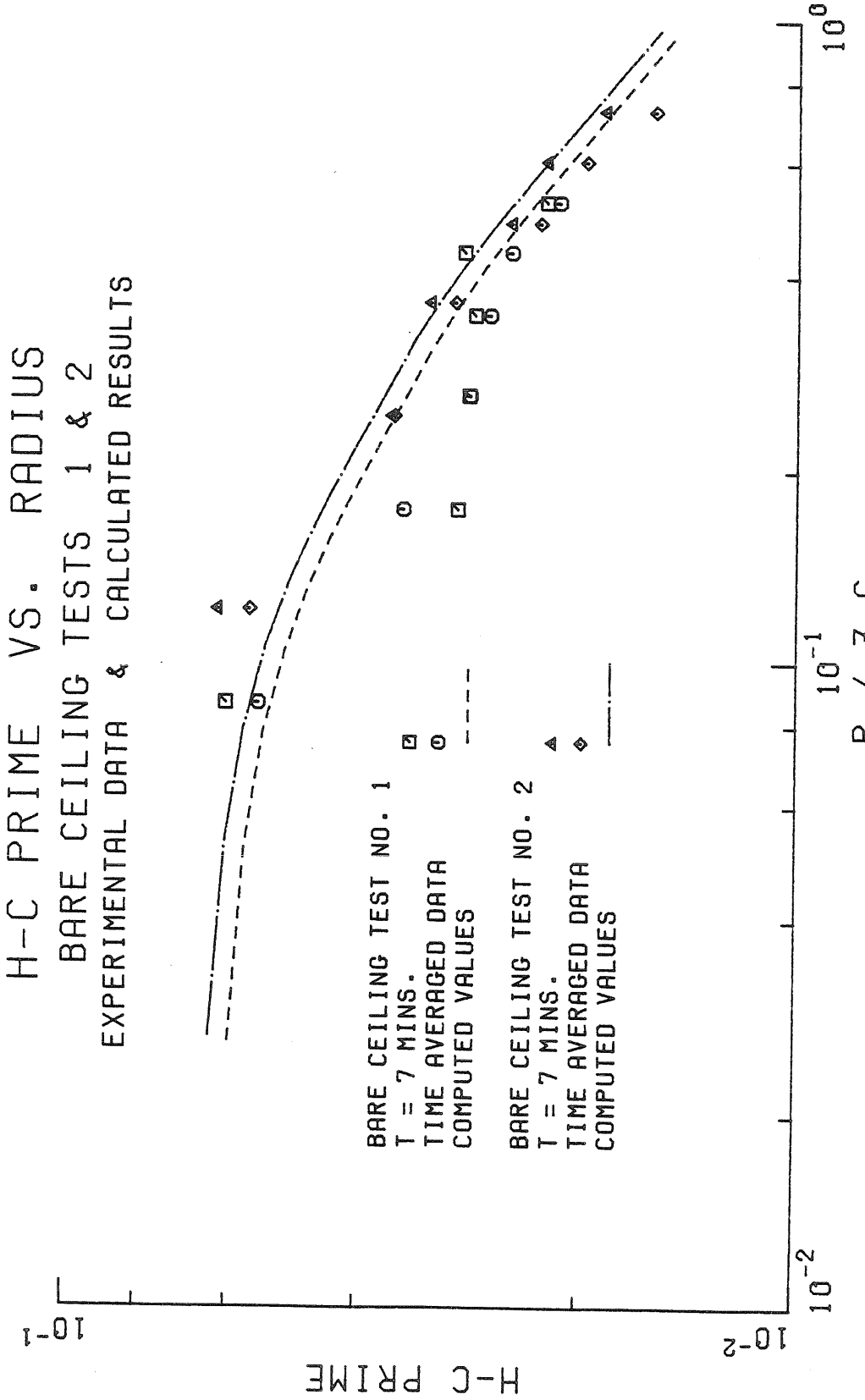

Figure (9.1) Dimensionless Heat Transfer Coefficient for 2 Bare Ceiling Experiments
[Data of Zukoski, et al. (1975)]

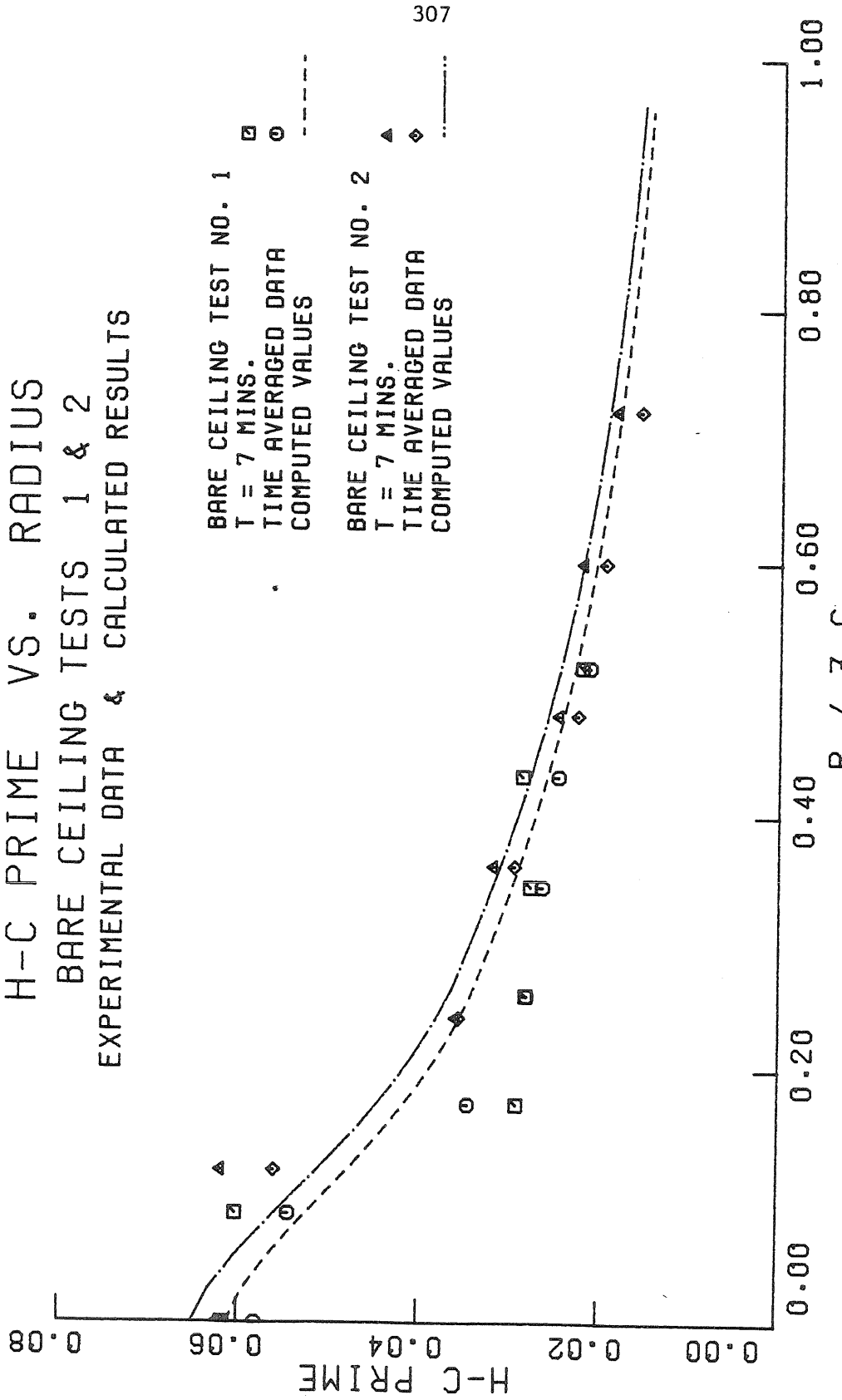

Figure (9.2) Dimensionless Heat Transfer Coefficient for 2 Bare Ceiling Experiments [Data of Zukoski, et al. (1975)]

well, as does the empirical fit for the impingement region.

Given the heat transfer coefficient, the next step in estimating the convective heat transfer rate is to calculate the temperature difference between the gas and the wall ΔT_{gw}. This implies that we must compute the local gas temperature, assuming we know the variation of the wall temperature. However, although we can get an approximate value for the gas temperature at the stagnation point from our plume computation, and can calculate the gas temperature directly for the ceiling jet regime, we do not have a way to estimate the gas temperature of the transitional flow in the impingement region. Therefore, we are forced to make some assumption about the variation of ΔT_{gw} in the impingement region. This is not as critical as it might seem at first glance. We would like to know the convective losses from the gas in the impingement region ε_T in order to estimate the initial temperature difference in the ceiling jet given by equation (8.63). However the rapid decrease in the heat transfer coefficient is the dominant factor and calculations have shown that ε_T is not very sensitive to the actual variation of ΔT_{gw}. Furthermore, as we shall see shortly, although the local convective rates are highest in the impingement region, they contribute a reasonably small fraction of the total heat transfer to the entire ceiling. Therefore, we will assume that the gas-wall temperature difference ΔT_{gw} either remains constant over the entire impingement region equal to its value at the stagnation point, or that it falls linearly as a function of (r/b_t) as described in Section (8.5) and given by equation (8.19). The actual ΔT_{gw} distribution in the impingement region varies greatly among the

experiments we examined and there was no clear trend to the data. The choice for ΔT_{gw} thus appears to be arbitrary and we are indeed fortunate that the calculation scheme as a whole is not sensitive to this parameter.

Thus given an estimate for the stagnation point gas temperature, and an assumed value for ΔT_{gw} in the impingement region, we can calculate the maximum gas temperature in the ceiling jet. These calculations for the first two bare ceiling tests, plotted in terms of the dimensionless temperature difference T_2^* , are displayed in Figure (9.3) along with the measured data points.

It is clear that the finite source plume calculation and the turning assumptions yield reasonable values for the ceiling jet temperatures near the start of the ceiling jet, but that the data fall off slightly faster than the predictions. The calculated values are approximately 3°C too high in the rest of the ceiling jet regime.

Finally, we make an approximate empirical power law fit of the experimentally measured variation of the ceiling surface temperature in the ceiling jet region for each experiment (which depends on details of the ceiling construction), and then we compute the convective flux to the ceiling with the results shown in Figures (9.4) and (9.5). Because of the transient nature of these experiments, the convective flux decreases with time as the ceiling heats up and approaches an approximately adiabatic condition. We have chosen to display the data taken at 5 times in Figures (9.4) and (9.5) to illustrate the importance of the wall temperature in fixing the convective flux. Consequently, in order to estimate this flux accurately

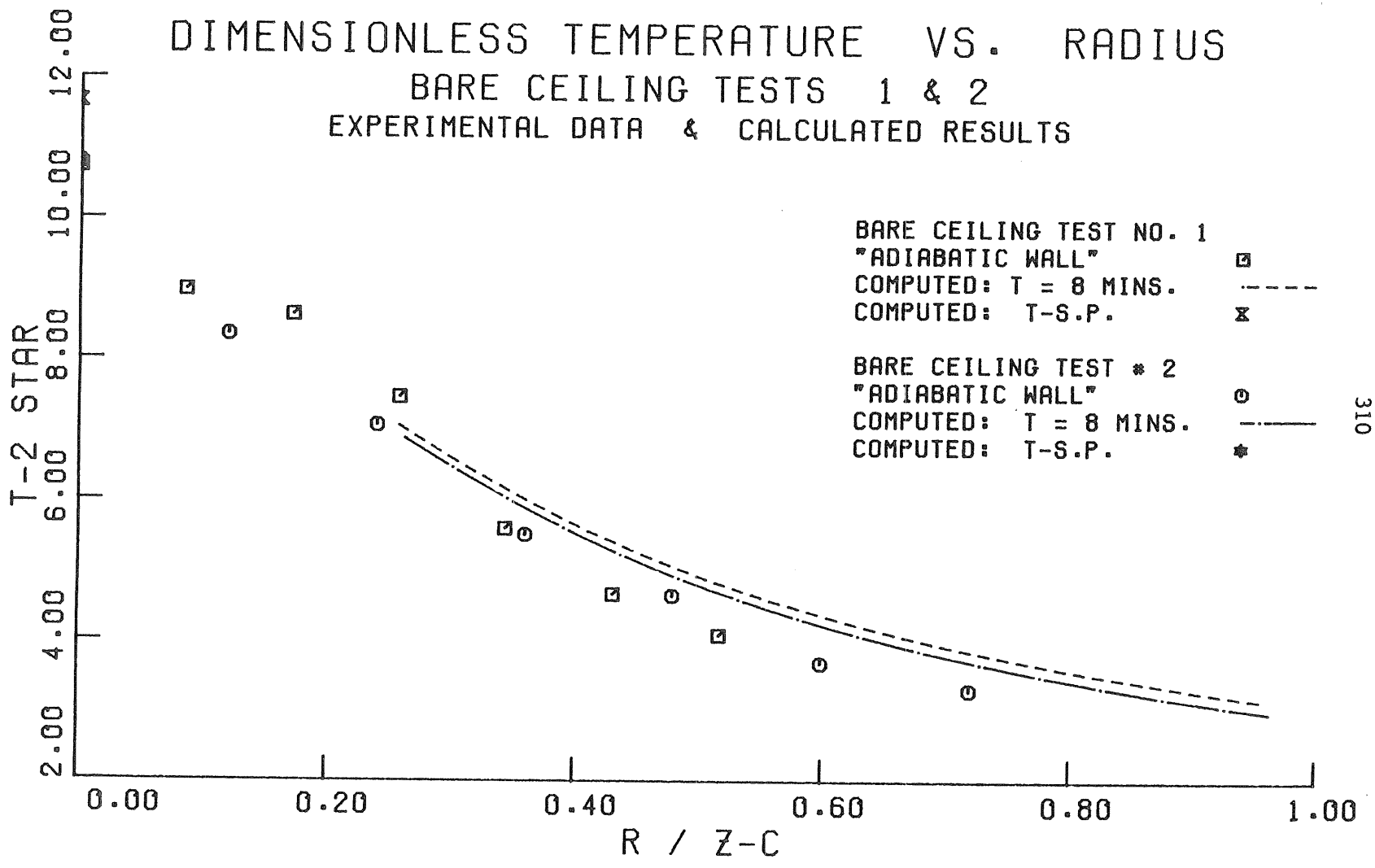

Figure (9.3) Dimensionless Gas Temperature Difference for 2 Bare Ceiling Experiments [Data of Zukoski, et al. (1975)]

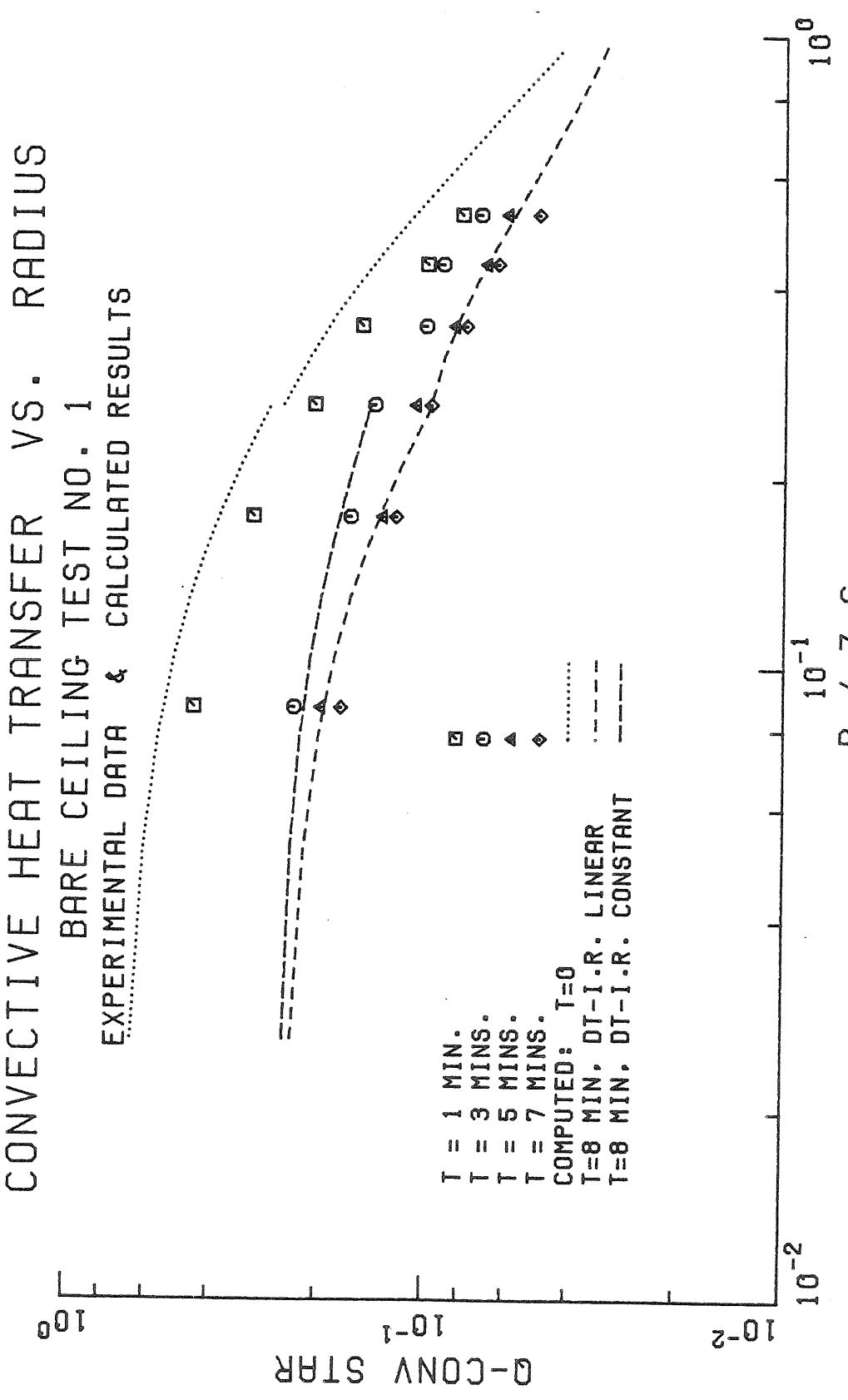

Figure (9.4) Dimensionless Convective Heat Transfer Rate, Bare Ceiling Test No. 1 [Data of Zukoski, et al. (1975)].

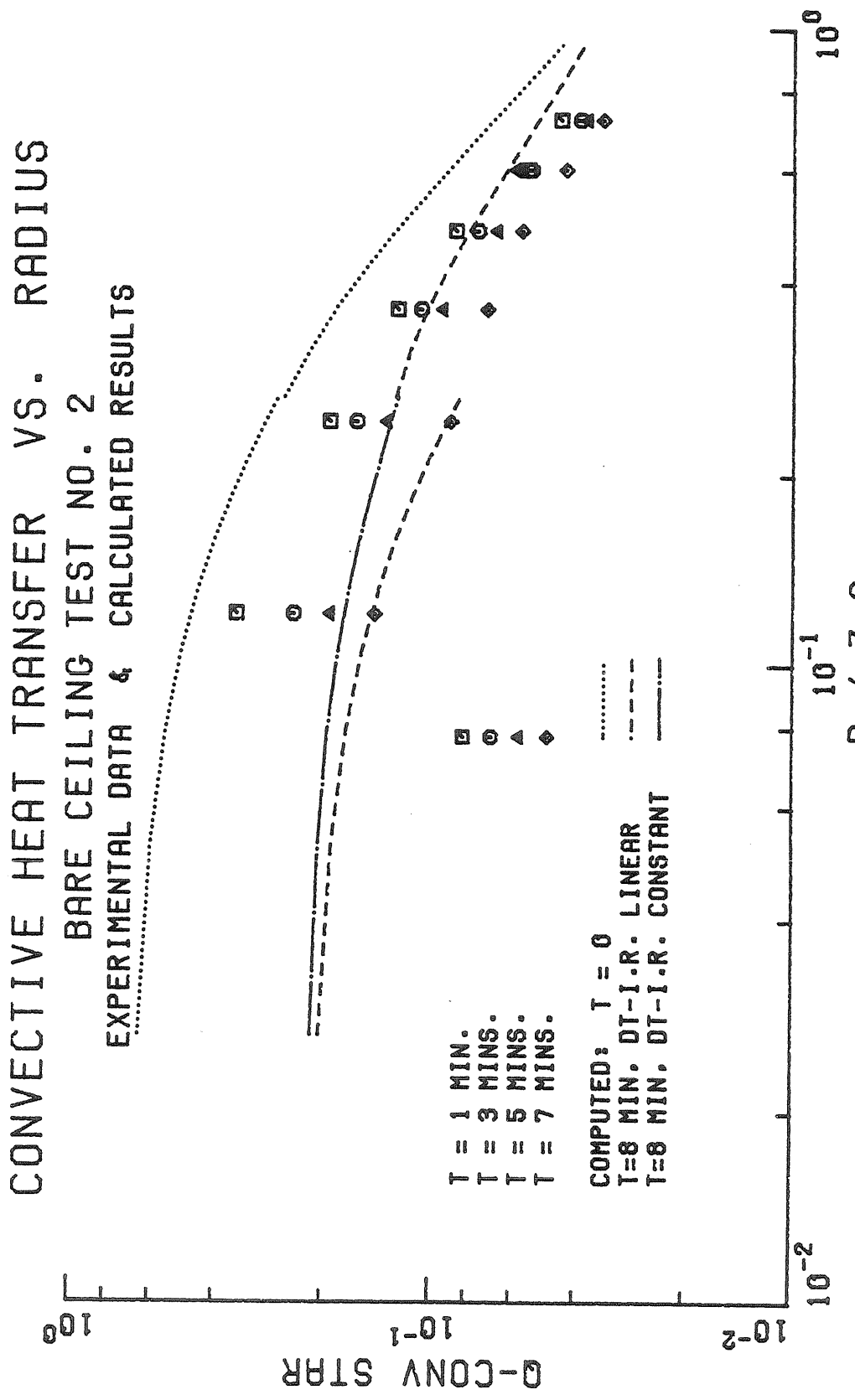

Figure (9.5) Dimensionless Convective Heat Transfer Rate, Bare Ceiling Test No. 2 [Data of Zukoski, et al. (1975)].

we must use different wall temperature distributions for different times. In these figures we have presented calculations for the two extreme cases of t = 0 and t = 8 minutes. Initially, the ceiling is assumed to be at a uniform temperature equal to the ambient gas temperature T_∞ . This cold wall condition produces the largest possible convective fluxes, and thus represents an upper bound for the data. On the other hand, after several minutes the convective heat transfer to the ceiling will produce a non-uniform, radial temperature distribution on the ceiling. To check this case, we fit a simple power law expression to the tabulated ceiling temperature data measured approximately 8 minutes after ignition. We therefore expect that the calculated values of q_{conv}^* should be close to the measured data points for t = 7 minutes, and indeed this is the case in Figure (9.4) for the first bare ceiling experiment. The agreement for the second bare ceiling test is not as good in part because the actual ceiling temperature data are not fit as well by a simple power law. This is typical of the general pattern: it is relatively easy to predict the heat transfer coefficient, but it is more difficult to compute the convective flux because in addition to the fluid mechanics, one must also get the thermal boundary conditions right. These figures also demonstrate that the assumed nature of the impingement region gas-wall temperature difference does not radically affect the local convective flux even in the impingement region itself. These data are replotted on a linear scale in Figures (9.6) and (9.7) which demonstrate that the stagnation point and impingement region calculations are reasonably accurate and

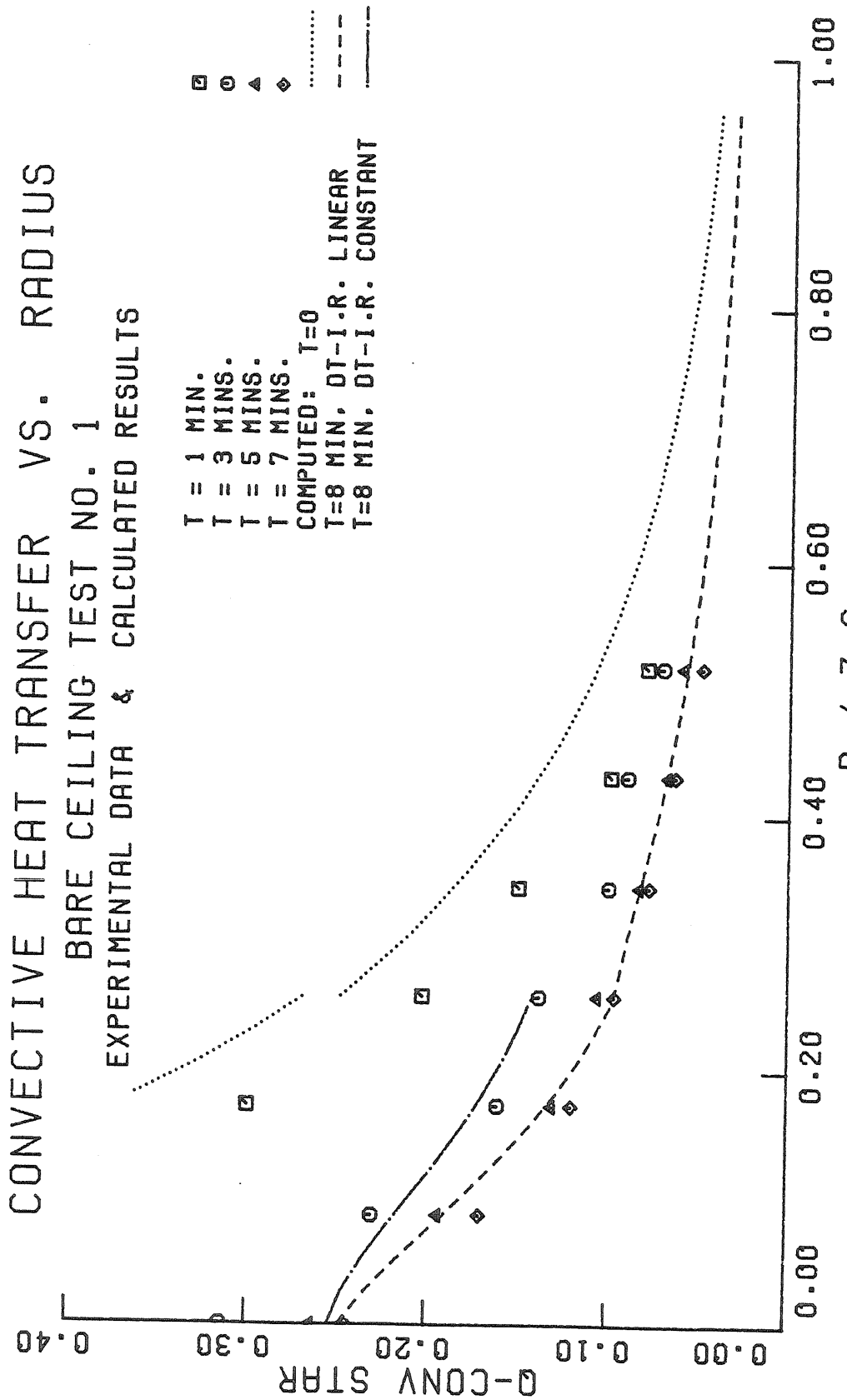

Figure (9.6) Dimensionless Convective Heat Transfer Rate, Bare Ceiling Test No. 1 [Data of Zukoski, et al. (1975)]

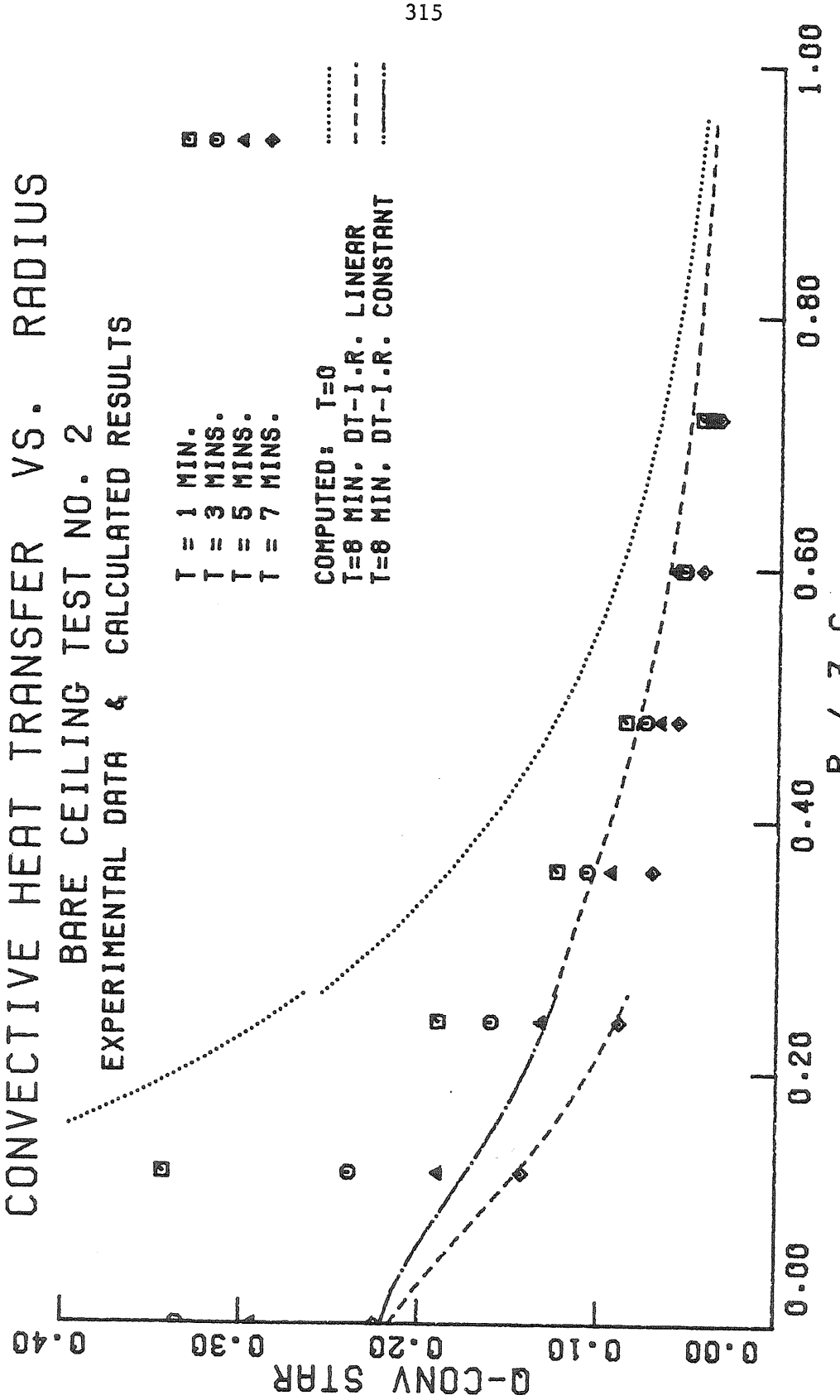

Figure (9.7) Dimensionless Convective Heat Transfer Rate, Bare Ceiling Test No. 2 [Data of Zukoski, et al. (1975)].

show the rapid decrease in convective flux as a function of distance from the stagnation point.

These plots can be deceiving though, if one is interested in the total convective flux to the ceiling. The integrated dimensionless convective flux, based on the computer calculations, is shown in Figure (9.8) as a function of the radius. This figure clearly demonstrates that although the local stagnation region fluxes are much larger than those in the ceiling jet, the quadratic growth of the area with radius is the dominant factor. Thus the total heat transfer in the stagnation region ($\bar{r} \leq 0.25$) is only 3% of the fire's heat release rate, compared to 17 - 20% over the ceiling to $\bar{r} = 1$. Consequently, the uncertainty in the impingement region approximations does not represent a major source of error in the total heat transfer calculation. Note that the divergence in the two curves is caused by the over estimate of q_{conv} for the second test case.

9.4 Curtain Wall Results

The next more complicated flow geometry to consider is that of an axially symmetric curtain wall extending down a certain distance from the ceiling. In this geometry, the fire plume quickly fills the upper layer with hot gas down to the edge of the curtain wall, and creates a well mixed upper layer with a sharp interface, with the excess fluid spilling out under the edge of the curtain wall.

The computer calculations and the time-averaged experimental values for the dimensionless heat transfer coefficient h_c' for curtain wall

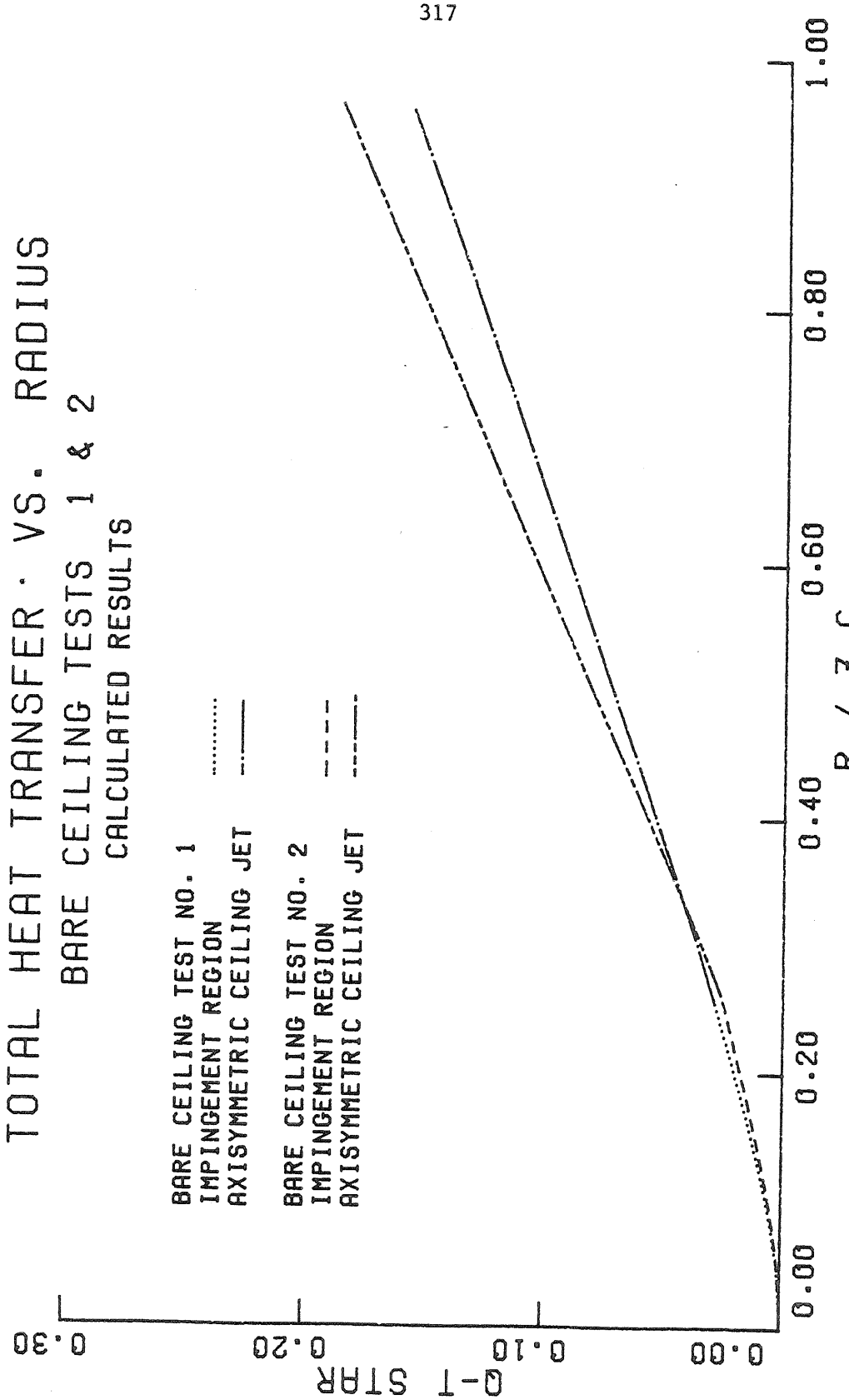

Figure (9.8) Calculated Dimensionless Total Convective Flux to the Ceiling for 2 Bare Ceiling Experiments.

tests number 4 and 5 of Zukoski, Kubota, and Veldman (1975) are shown in Figure (9.9). It appears that the calculation scheme again does a good job of predicting h_c' for both the impingement and ceiling jet regimes when an upper layer is present. The presence of the layer does affect h_c' though. A comparison of Figures (9.1) and (9.9) indicates that the curtain wall data have slightly lower h_c' values than the unconfined ceiling data, even though the Reynolds numbers are comparable. This decrease is a reflection of the reduction in the local mean density ρ_2, and of the decrease in the upper plume velocity scale w_{mt} and increase in its radial scale $b_{t.}$, with increasing upper layer temperature T_2. The dimensionless heat transfer coefficient h_c' is defined in terms of ρ_2 and so automatically takes density changes into account. However, h_c' is also normalized by the simple plume velocity scale $\sqrt{gz_c}(Q^*_{z_c})^{1/3}$, and thus can not recognize the reduction in the plume velocity caused by the loss of buoyancy above the interface. It is this deviation from the simple plume behavior as the upper layer becomes relatively hotter (measured by increasing values of c_q) which is responsible for the decrease in the values of h_c' which is not reflected in the quantity h_c.

The data and calculations are replotted linearly in Figures (9.10) and (9.11). A comparison of these plots reveals another of the effects that appears to be associated with the presence of a hot upper layer, namely the large increase in scatter of the stagnation point values seen in Figure (9.10).

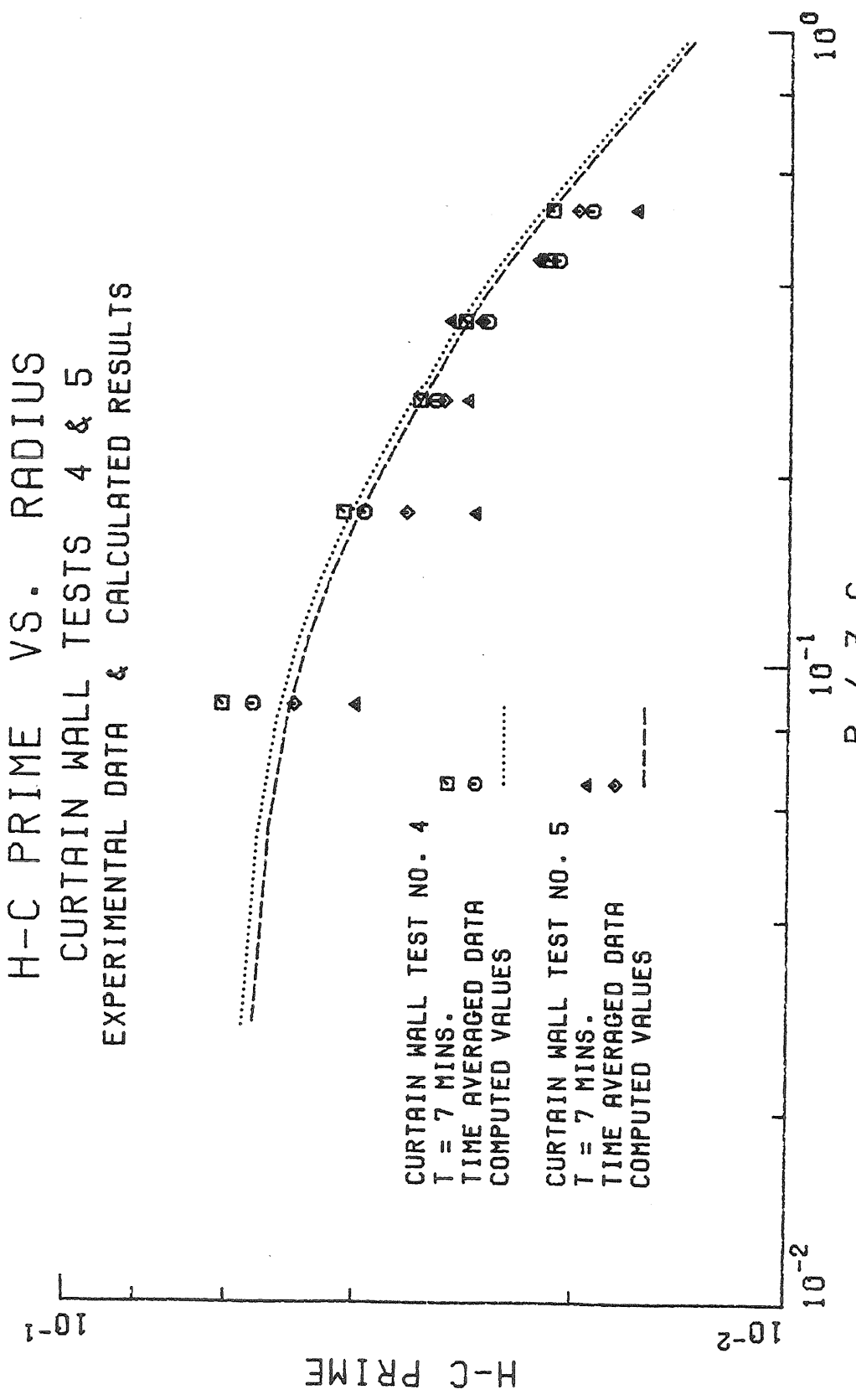

Figure (9.9) Dimensionless Heat Transfer Coefficient for 2 Curtain Wall Tests [Data of Zukoski, et al. (1975)]

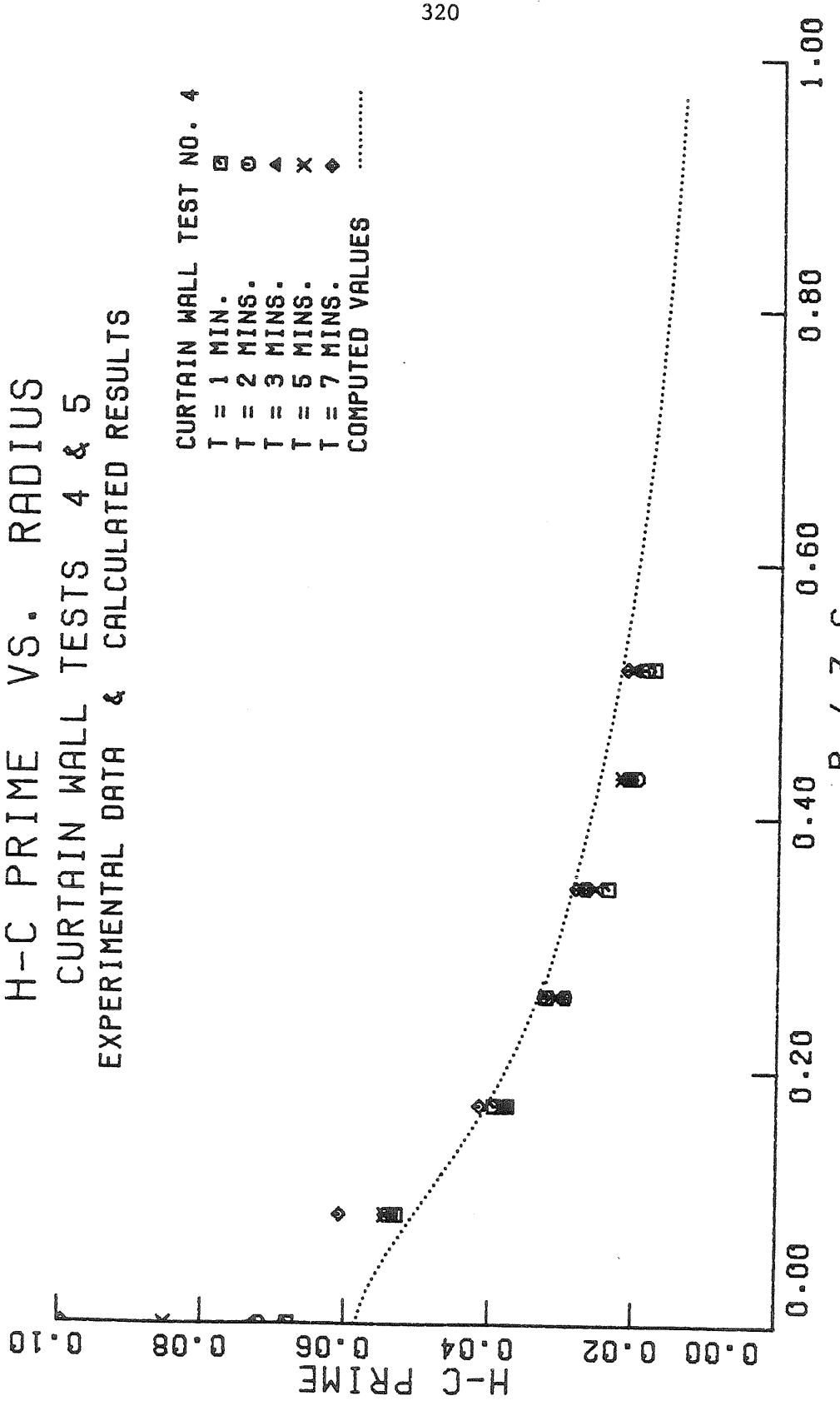

Figure (9.10) Dimensionless Heat Transfer Coefficient, Curtain Wall Test No. 4 [Data of Zukoski, et al. (1975)]

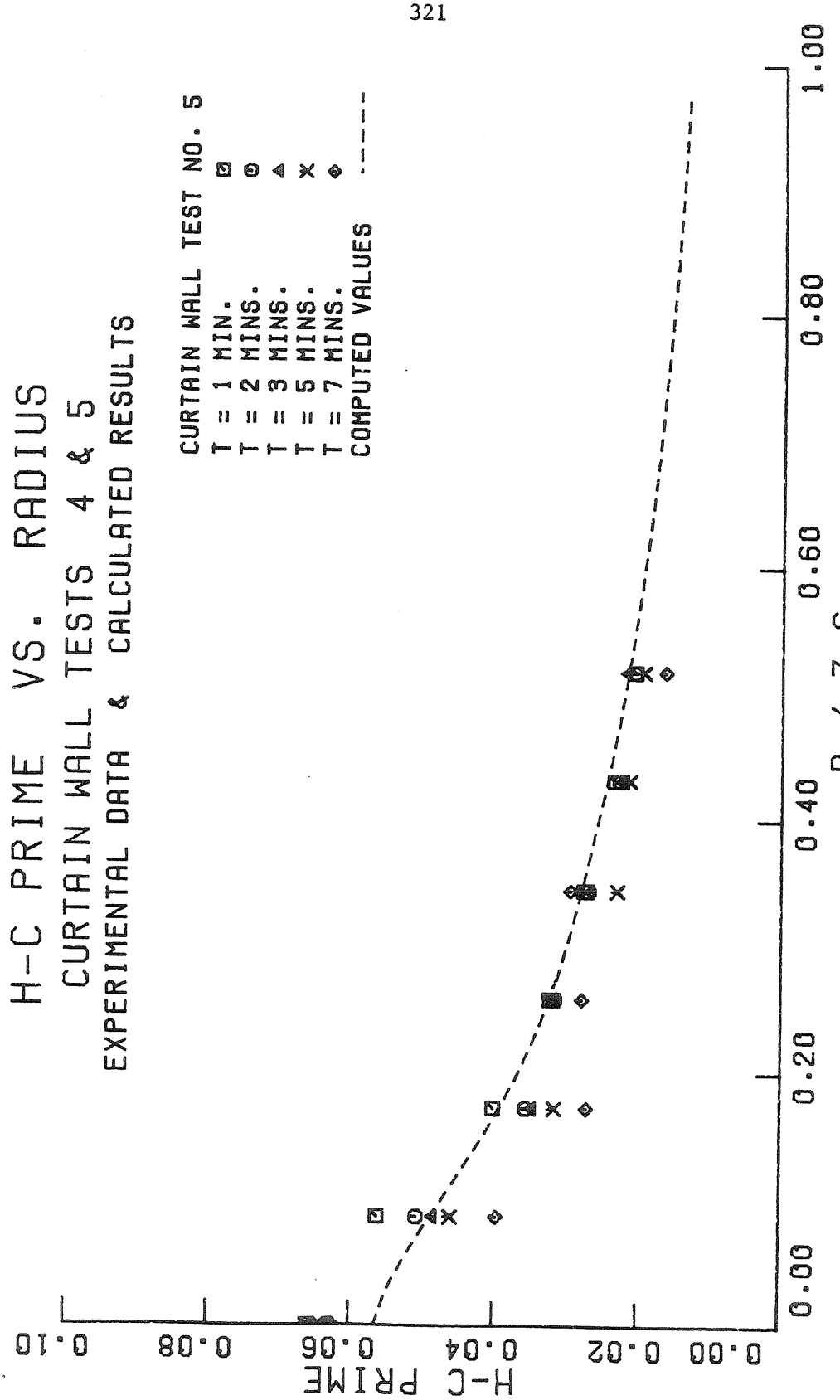

Figure (9.11) Dimensionless Heat Transfer Coefficient, Curtain Wall Test No. 5 [Data of Zukoski, et al. (1975)]

The measured and computed gas temperatures are presented in Figures (9.12) and (9.13). In Figure (9.12) we have plotted the dimensionless temperature difference with respect to the mean lower layer temperature T_1^*. Because the upper and lower layer temperatures are identical for an unconfined ceiling, this figure can be compared directly to Figure (9.3). Examined in this manner, the presence of the upper layer merely shifts the curve upwards slightly. However, if we compare the buoyancy of the ceiling jet, measured by T_2^* and plotted in Figure (9.13) for these curtain wall tests, to the bare ceiling data in Figure (9.3), we immediately see that the relative buoyancy of the ceiling jet is significantly reduced by the presence of a hot upper layer beneath it. Finally, upon comparing the data with the predicted values ($\kappa = 1.00$ curve), we note that the calculation scheme slightly underestimates the ceiling jet temperatures when an upper layer is present by approximately 3 - 5°C for gas temperatures in the range 60 - 70 °C. This effect, which also manifested itself at the stagnation point, appears to be a limitation of the Boussinesq plume calculation above the interface.

This upper plume calculation rests on several key assumptions for which we do not have any supporting data. In particular, we assumed that as the plume crosses the interface between the hot upper layer and the colder lower layer, the kinematic fluxes of mass, momentum, and enthalpy are conserved and that the plume instantly adjusts to the reduction in buoyancy it experiences on crossing the interface. These assumptions thus represent an idealized view of the actual flow process, which

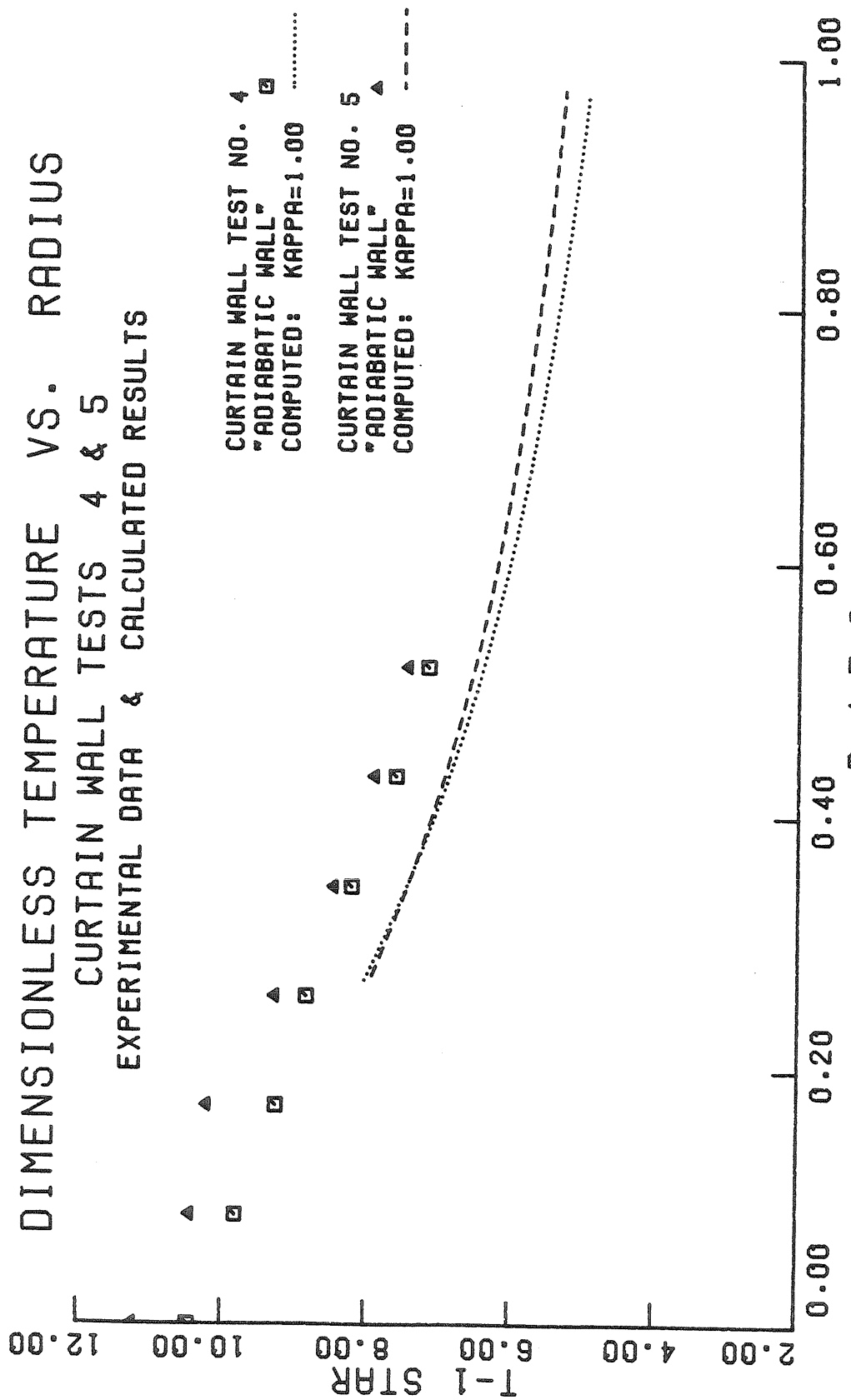

Figure (9.12) Dimensionless Gas Temperature Difference T_1^* for 2 Curtain Wall Tests [Data of Zukoski, et al. (1975)]

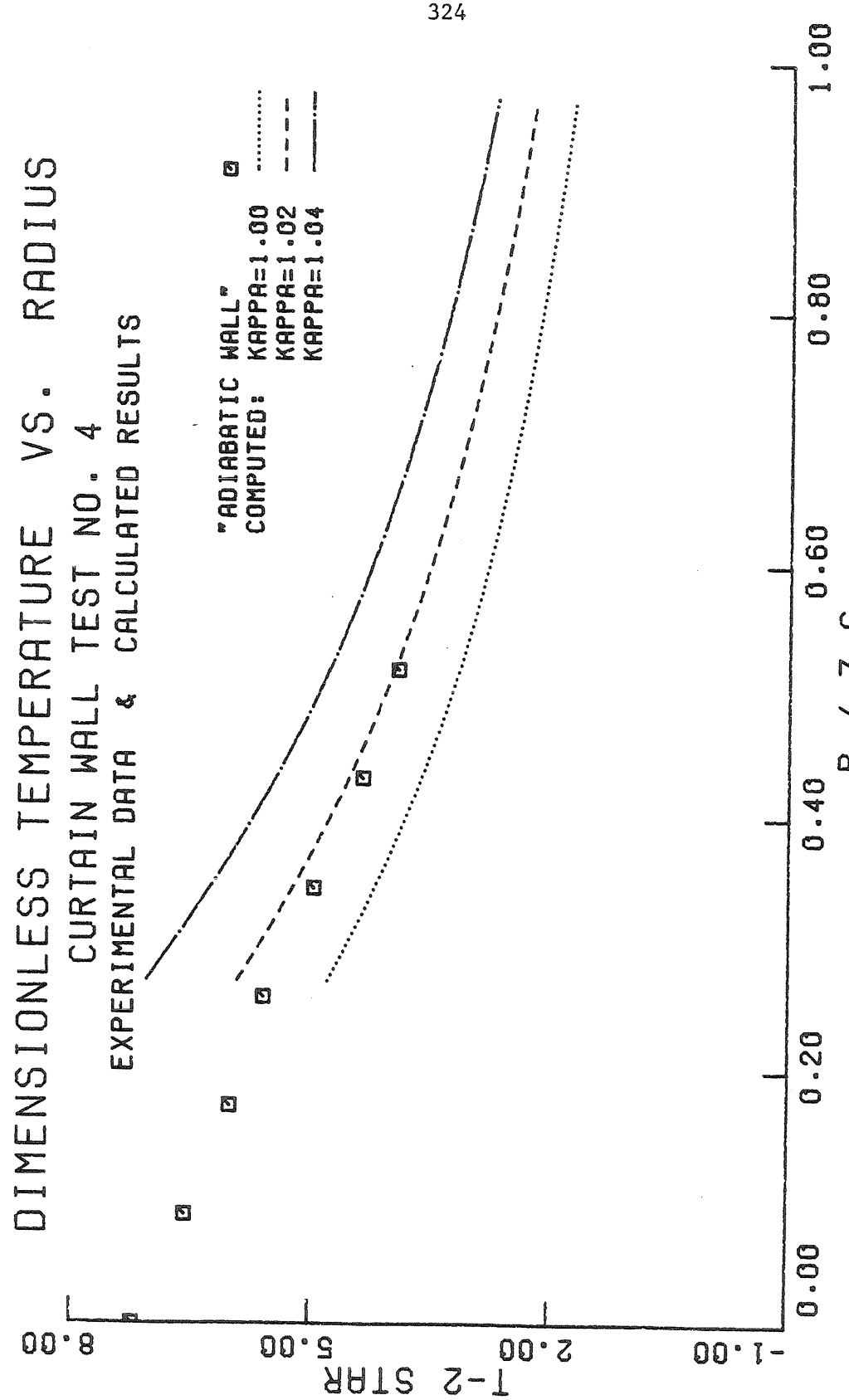

Figure (9.13A) Dimensionless Gas Temperature Difference T_2^*, Curtain Wall Test No. 4 [Data of Zukoski, et al. (1975)]

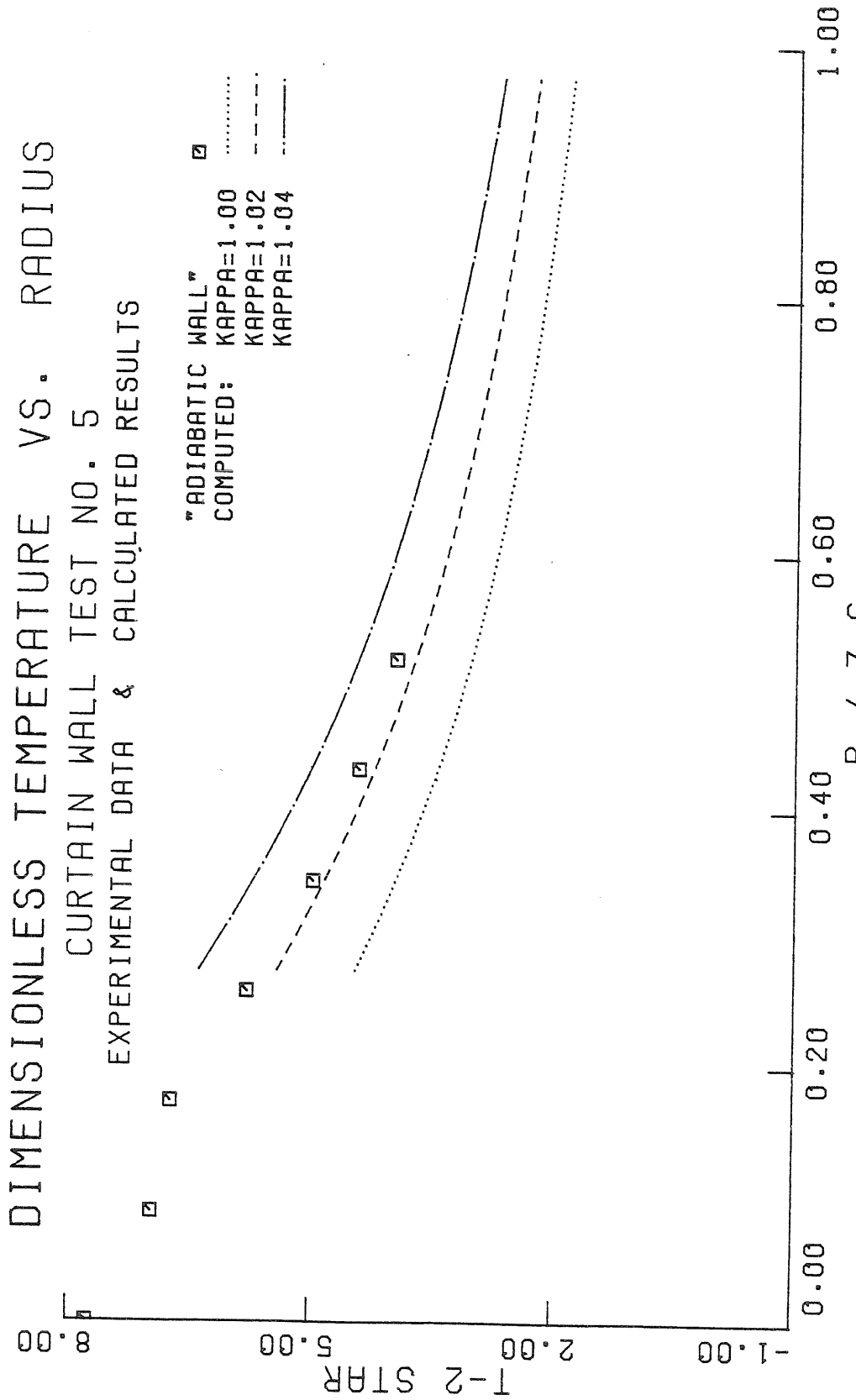

Figure (9.13B) Dimensionless Gas Temperature Difference T_2^*, Curtain Wall Test No. 5 [Data of Zukoski, et al. (1975)]

should yield reasonable results when we are far enough above the interface for the plume to again have attained a fully developed structure. However, the parameters in Table (9.2) indicate that in fact we are always in the near-field region of this part of the plume for all of the ceiling heights investigated. In this table, we have presented two measures of the plume's maturity both above and below the interface. First, there is the simple geometrical ratio of the height (z_i or Δz) to the effective source diameter (d_o, the burner diameter, or d_{eff}). We can see that in the 1/4 scale tests the interface or ceiling (for the unconfined ceiling tests) is located many source diameters above the fire and that we are indeed in the far field where our assumption of similarity is valid. The 1/2 scale tests, on the other hand, appear to be just barely in the far field regime. The second and possibly more sensitive measure is given by the ratio of the height to the magnitude of the virtual source z_{vs} (which is computed in terms of the actual finite source by equation (2.41)). This latter ratio takes into account the initial momentum of the forced plume relative to the buoyancy. Below the interface, the buoyancy is large compared to the initial momentum and the virtual source is small, so that z_i/z_{vs} is reasonably large. Above the interface, the plume's momentum is large compared to its reduced buoyancy and z_{vs} is large. This implies that above the interface we are in the near-field region of the plume, where its initial momentum may be important, and where our assumption of similarity is tenuous. Given this situation, it is indeed remarkable that our simple-minded plume

Table 9.2 Calculated Plume Conditions above the Interface

Experiment	Below the Interface*			Above the Interface	
	c_q	z_i/d_o	z_i/z_{vs}	$\Delta z/d_{eff}$ †	$\Delta z/z'_{vs}$
Bare Ceiling 1	0.0	32.00	20.88		
Bare Ceiling 2	0.0	23.00	15.05		
Curtain Wall 4	0.36	20.19	13.18	1.19	0.48
Curtain Wall 5	0.40	14.70	11.64	1.14	0.45
1/2 Scale 15	0.74	4.31	4.56	1.54	0.46
1/2 Scale 16	0.59	3.90	3.97	1.84	0.64
1/2 Scale 7	0.87	10.12	9.67	1.16	0.27
1/2 Scale 10	0.88	7.26	7.19	1.26	0.28
1/2 Scale 13	0.89	4.58	4.81	1.36	0.30

* For bare ceiling tests, let $z_i = z_c$.

† $d_{eff} = 2\ (1.731\ b_i)$ and $\Delta z = z_c - z_i$

calculation works as well as it does. Unfortunately we do not have enough detailed data on the plume's behavior in the upper layer to attempt to systematically refine our computation procedures at and above the interface. For example, we know that non-buoyant jets (which occur when $c_q = 1$) have a significantly smaller entrainment constant than fully buoyant plumes ($c_q = 0$). One might guess then that above the interface we should use an entrainment "constant" scaled by c_q. However, we have no velocity or entrainment data which we could use to either substantiate or deny this speculation. Consequently, we have chosen to retain the plume-interface computation with constant entrainment as described in Chapters II and VIII. This approach, as we have seen, seems to work well for the velocity and hence the heat transfer coefficient. To correct for the small temperature deficiency, we will multiply the calculated maximum plume temperature at the plume termination height T_{mt} by the small empirical constant $\kappa \sim 1.02$, which we introduced in Section (8.4) to calculate the stagnation point gas temperature $T_{sp} = \kappa T_{mt}$ We thus replace T_{mt} with κT_{mt} in the enthalpy equation (8.63), which determines the initial ceiling jet temperature. In Figures (9.13)A and (9.13)B, we have presented the effect of changing κ from 1.00 to 1.04. The temperature data appear to lie reasonably close to the $\kappa = 1.02$ curve, except for some scatter (as usual) at the stagnation point. It should be noted that these changes in κ have no perceptible effect on the distribution of the dimensionless heat transfer coefficient h_c'. We will therefore use $\kappa = 1.02$ for the rest of the computations unless explicitly

noted. Note that for a much deeper upper layer compared with either the effective plume radius at the interface or with the virtual source of the upper plume, we expect that the value of κ will approach unity.

Having calculated the heat transfer coefficient and the local maximum gas temperature, we can now find the convective heat transfer rate, given an expression for the ceiling temperature distribution. The results for various values of κ are presented, along with the measured data, in Figures (9.14) and (9.15) for curtain wall tests 4 and 5, respectively. These computations were performed with the assumptions that ΔT_{gw} was constant over the impingement region, and that the enthalpy losses could be neglected ($\varepsilon_T = 1$). In addition, we used the tabulated ceiling temperature data taken approximately 8 minutes after ignition as the basis of our empirical ceiling temperature fit. Consequently we expect the computations to approximate the data taken at t=7 minutes; and indeed they seem to over both the ceiling jet and impingement regions. Note that $\kappa = 1.02$ seems to be a reasonable value for both cases.

The effect that the upper layer has on the convective flux can be seen by comparing Figures (9.4) and (9.5) with Figures (9.14) and (9.15). It appears that the magnitude of q^*_{conv} is not strongly affected by the presence of the upper layer. However, as the radius increases, the curtain wall data do not fall as fast as the bare ceiling data because the ceiling jet entrains hot gas from the upper layer at T_2, rather than ambient air at T_∞ as it does in the unconfined ceiling geometry. Thus the ceiling jet temperature, and hence the convective flux remains higher for the curtain wall tests.

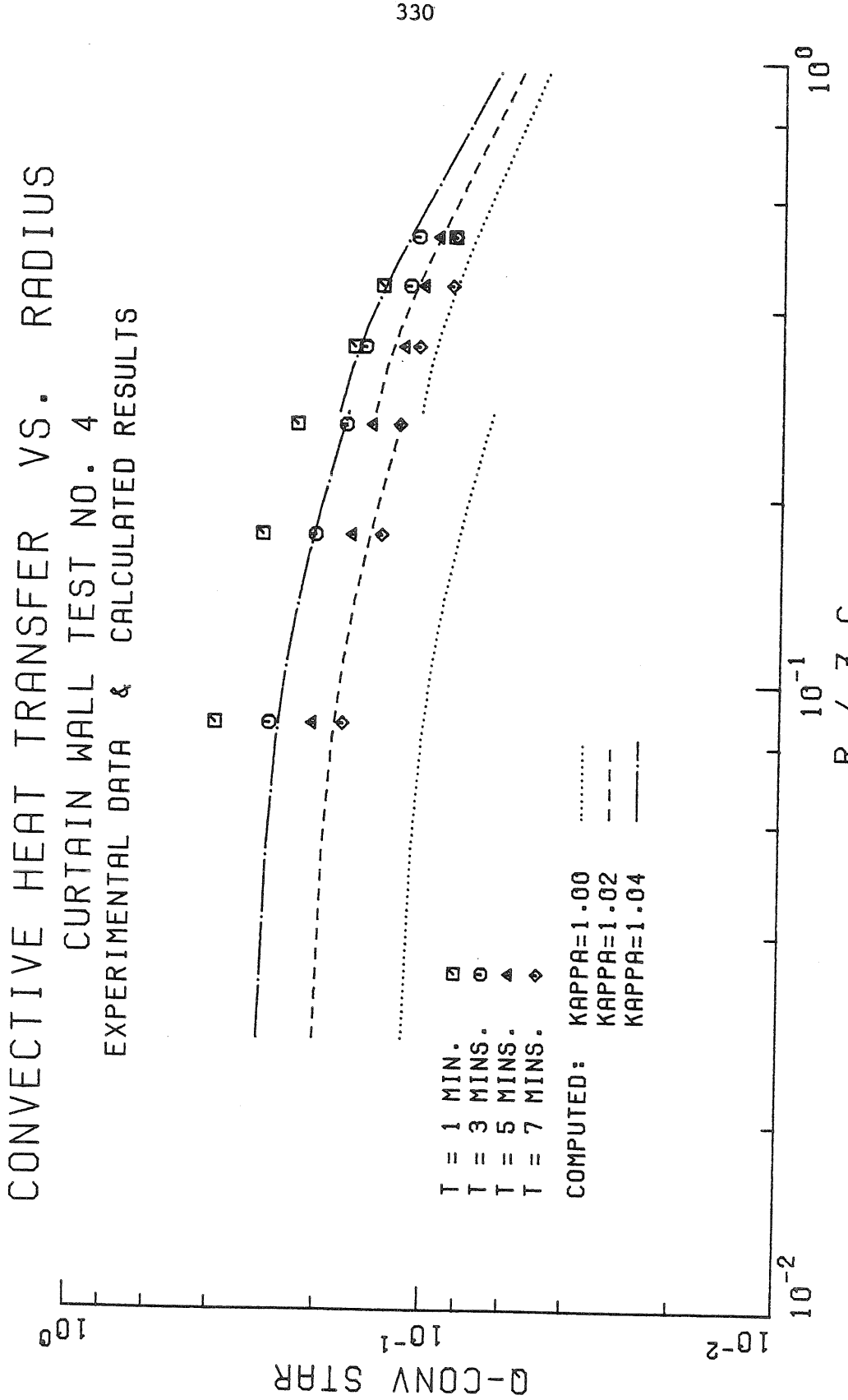

Figure (9.14) Dimensionless Convective Heat Transfer Rate, Curtain Wall Test No. 4 [Data of Zukoski, et al. (1975)]

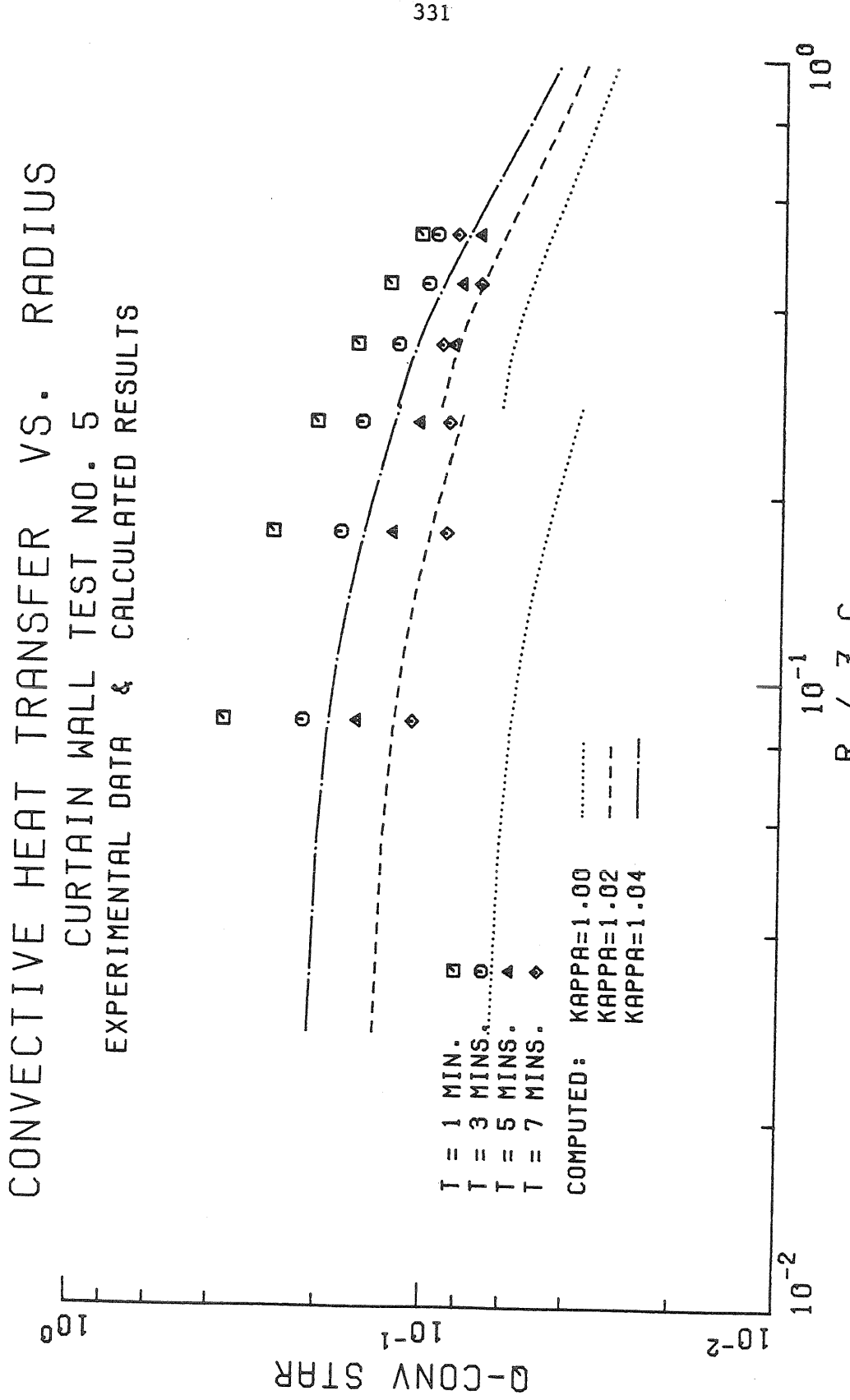

Figure (9.15) Dimensionless Convective Heat Transfer Rate, Curtain Wall Test No. 5 [Data of Zukoski, et al. (1975)]

Estimates of the integrated convective flux Q_T^* are presented in Figure (9.16). The values for curtain wall tests 4 and 5 are roughly comparable to the bare ceiling computations in Figure (9.8). The difference between the curves for tests 4 and 5 is caused by the larger values of q_{conv}^* observed in test number 4. In all cases, however, the stagnation or impingement region contributes a relatively small amount to the total convective heat flux delivered to the ceiling.

9.5 Typical 1/2 Scale Room Test Results

In this section we will present results of a typical experiment in our 1/2 scale apparatus. In the following section we will discuss the results of the three effects we investigated, namely the effects of door geometry, heat input, and fire location. In this section we will examine the results of 1/2 scale room experiment number 15. In this experiment, a 14.9 kW fire was produced by a 15.24 cm diameter, pre-mixed natural gas burner located on the major axis of the room at a dimensionless distance $\bar{r} = 1/2$ from the rear and side walls. The room had a standard door with a dimensionless height 0.81 and width 0.38.

The experimental heat transfer coefficient data are plotted in Figures (9.17) and (9.18). In Figure (9.17) the heat transfer coefficient data is displayed as a function of the dimensionless radial distance along the ceiling from the geometrical fire axis to the individual measurement location ($\bar{r} = r/z_c$). On the other hand, the same data are plotted versus the projected longitudinal distance along the room's major axis ($\bar{x} = x/z_c$; $\bar{x} = \bar{r} \cos \theta$) in Figure (9.18). As described in Section (8.6.9), the presence of the side walls can be expected to influence the initially

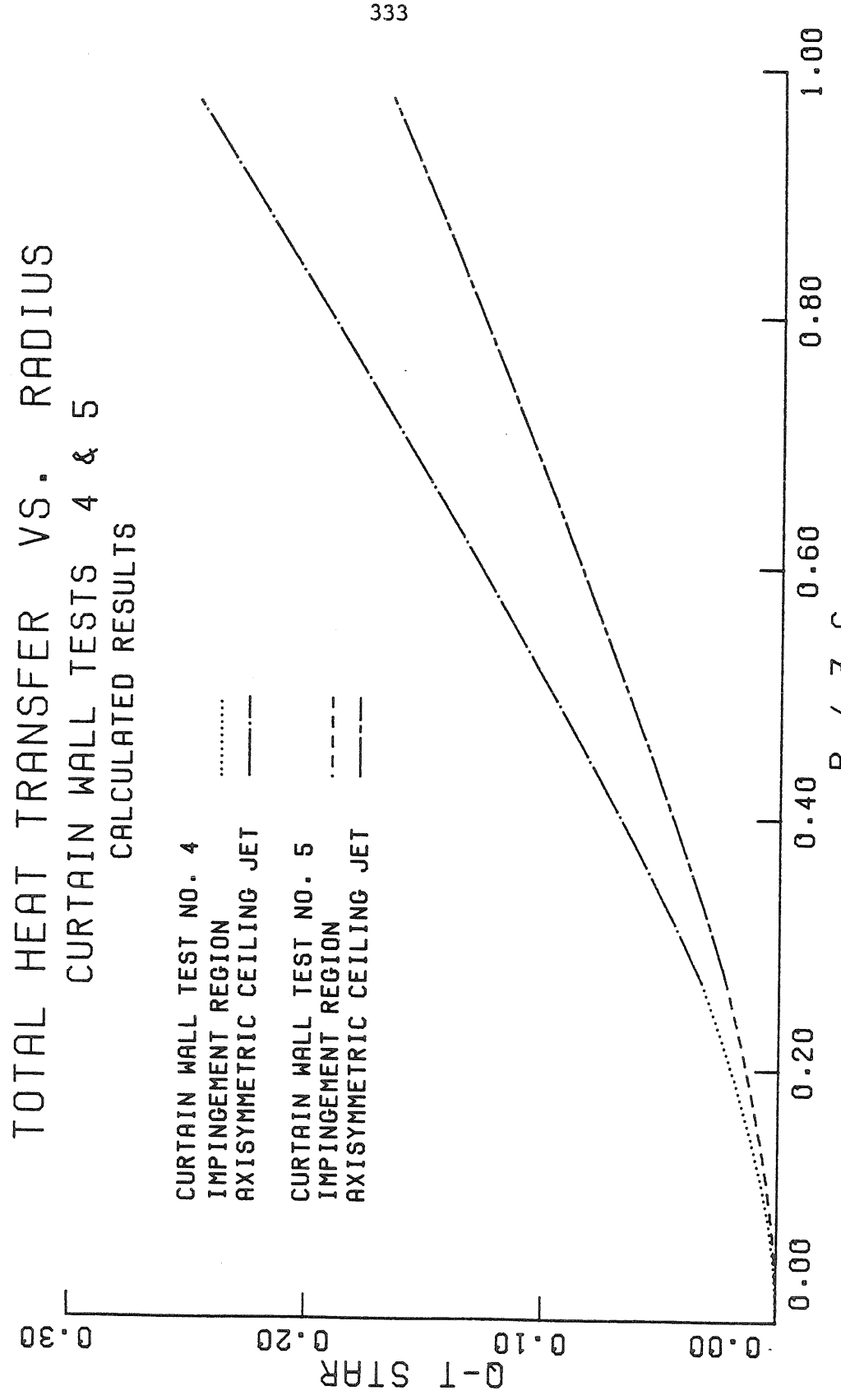

Figure (9.16) Calculated Dimensionless Total Convective Flux to the Ceiling for 2 Curtain Wall Tests

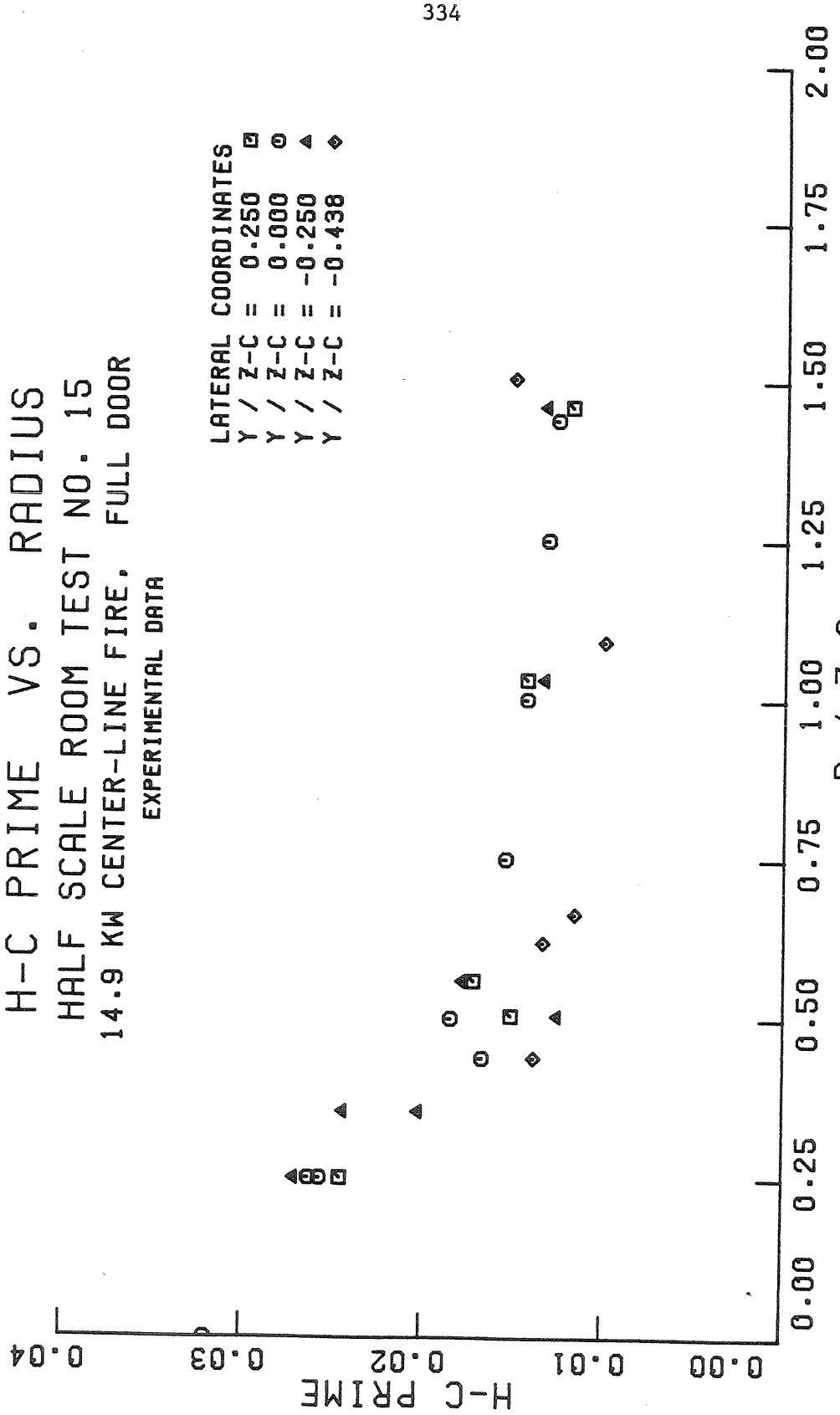

Figure (9.17) Dimensionless Heat Transfer Coefficient as a Function of Radial Distance, 1/2 Scale Room Test No. 15

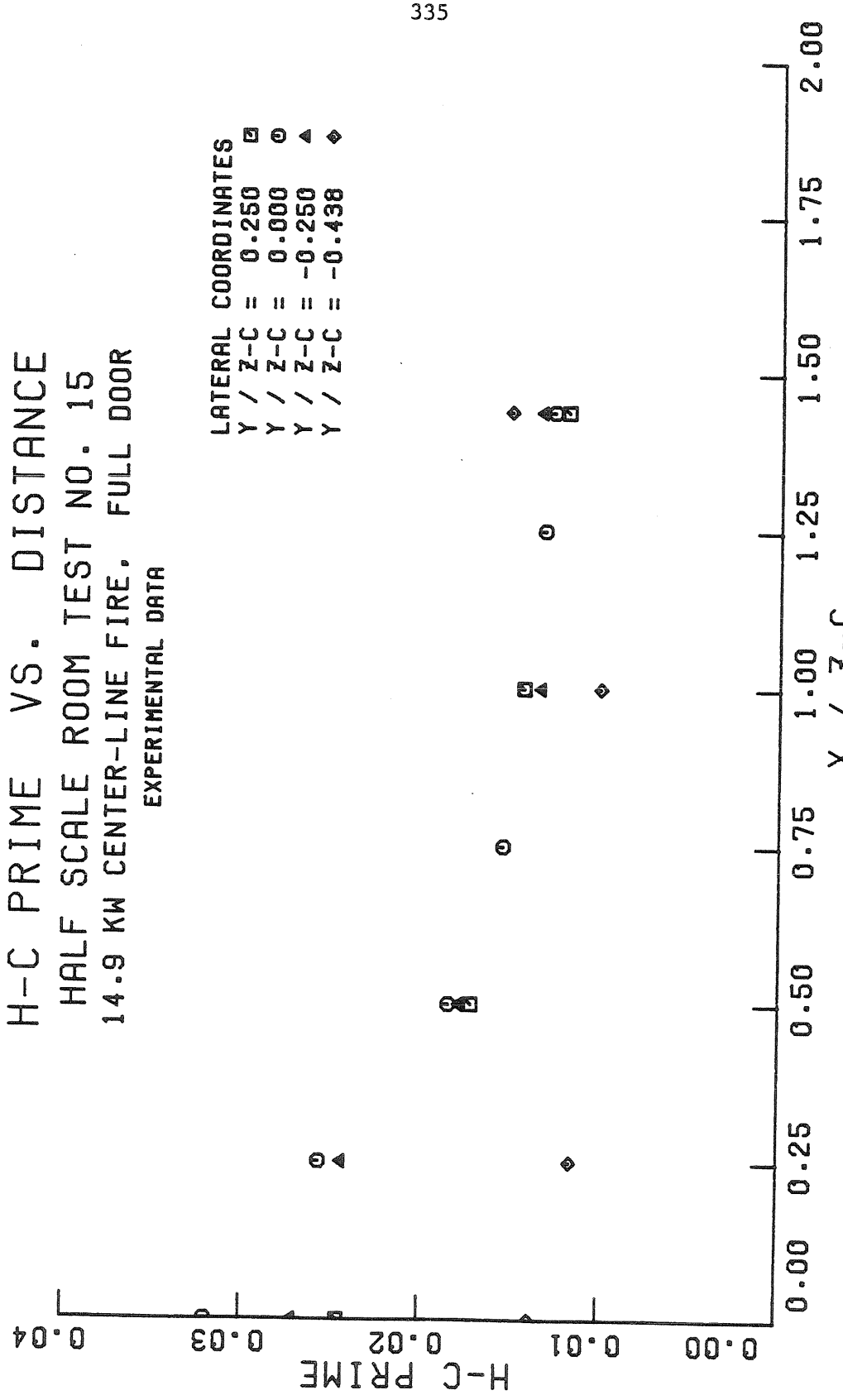

Figure (9.18) Dimensionless Heat Transfer Coefficient as a Function of Axial Distance, 1/2 Scale Room Test No. 15

radial ceiling jet flow at radii comparable to the distance to the nearest side wall, and to produce a more nearly two-dimensional flow pattern at larger distances. In this experiment, the distance from the fire axis to the south, east, and west sidewalls was 1/2 the room height. If one compares Figures (9.17) and (9.18), the data do appear to correlate better with $\bar{r}$ for $\bar{r} < 1/2$, corresponding to axisymmetric flow, and with $\bar{x}$ for $\bar{x} > 1/2$, corresponding to two-dimensional flow. The scatter of the data points on each of these figures for the largest distances is caused by close proximity ($\Delta\bar{x} = 0.63$) to the north end wall.

To study the effect of scale on the stagnation region, the 1/2 scale data are replotted in Figure (9.19) along with the 1/4 scale data from the first bare ceiling test and the fourth curtain wall tests. It is interesting to note the large decrease in the stagnation point heat transfer coefficient, by a factor of nearly 2, as the scale of the experiment increases. Table (9.3) lists the factors involved in calculating the stagnation point heat transfer coefficient and shows that the decrease in the dimensionless heat transfer coefficient h_c' at the stagnation point is largely due to the point source plume normalization. As the upper layer becomes relatively hotter, the plume becomes slower and broader by the time it reaches the ceiling, compared to the simple point source plume, as shown by the values in the second and third columns. Thus although the calculated laminar heat transfer coefficient decreases by only 16%, the dimensionless coefficient drops by 77%. The decrease in the turbulence-enhanced dimensionless coefficient is even

TABLE (9.3A) CALCULATED STAGNATION POINT HEAT TRANSFER COEFFICIENT DATA

Experiment	z_c [m]	$\frac{b_c}{z_c}$	$\frac{w_{m_t}}{\sqrt{g z_c}\,(Q^*_{z_c})^{1/3}}$	$\sqrt{\frac{w_{m_t}}{b_t}}\left[\frac{1}{s^{1/2}}\right]$	$h_{c,lam}$ [W/m^2-K]	$h_{c,lam}' \times 10^2$	$h_c' \times 10^2$
Bare Ceiling 1	0.813	0.138	3.94	3.65	17.50	4.25	6.13
Base Ceiling 2	0.584	0.140	3.92	4.50	21.58	4.67	6.52
Curtain Wall 4	0.813	0.145	3.57	3.41	16.13	4.10	5.87
Curtain Wall 5	0.813	0.147	3.53	3.53	16.63	3.93	5.66
1/2 Scale 15	1.219	0.169	2.89	3.35	15.11	2.40	3.32
1/2 Scale 16	1.219	0.163	3.04	3.47	15.58	2.67	3.64
1/2 Scale 7	1.219	0.144	3.27	3.04	14.10	3.06	4.42
1/2 Scale 10	1.219	0.130	3.54	3.70	17.15	3.18	4.56
1/2 Scale 13	1.219	0.135	3.43	3.99	18.25	2.95	4.07

TABLE (9.3B) CALCULATED STAGNATION POINT HEAT TRANSFER COEFFICIENT DATA

Experiment	z_c/d_o	z_i/d_o	c_q	$Q^*_{z_c} \times 10^3$	$\sqrt{\overline{w'^2}}/\bar{w}_m$	G	$Re \times 10^{-4}$
Bare Ceiling 1	32.00	—	0.000	1.76	0.292	1.442	1.31
Bare Ceiling 2	23.00	—	0.000	4.13	0.279	1.396	1.08
Curtain Wall 4	32.00	20.19	0.357	1.76	0.292	1.430	1.15
Curtain Wall 5	32.00	14.70	0.397	2.36	0.292	1.442	1.22
1/2 Scale 15	8.00	4.31	0.740	8.14	0.194	1.383	2.14
1/2 Scale 16	8.00	3.90	0.590	8.13	0.194	1.362	1.91
1/2 Scale 7	16.00	10.12	0.762*	2.01	0.254	1.442	1.71
1/2 Scale 10	12.00	7.26	0.680†	3.96	0.229	1.432	1.85
1/2 Scale 13	8.00	4.58	0.697†	7.85	0.196	1.379	2.00

*based on α_{plume} reduced by 10%.

†based on α_{plume} reduced by 20%.

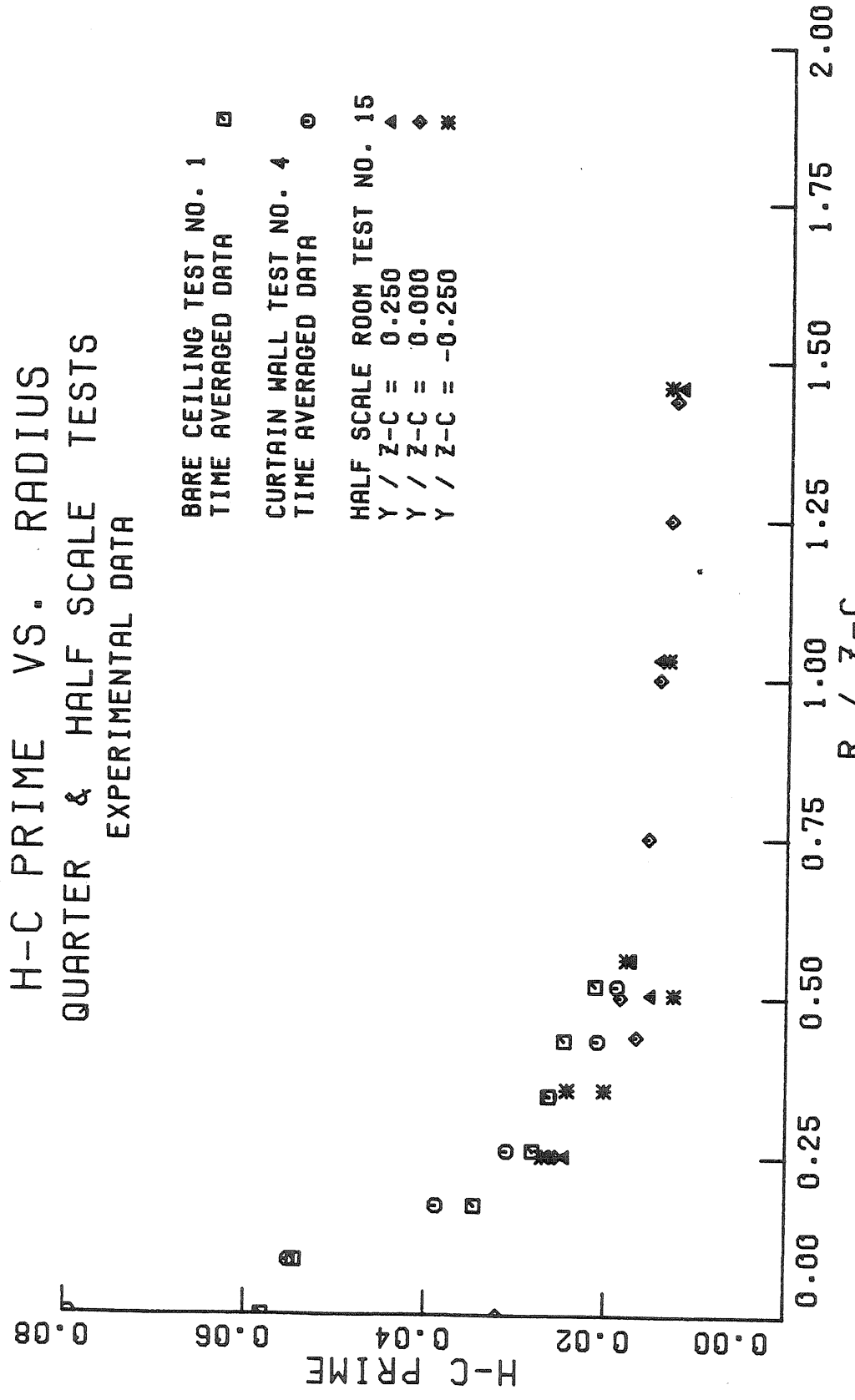

Figure (9.19) Effect of Scale on Dimensionless Heat Transfer Coefficient [1/4 Scale Data of Zukoski, et al. (1975)]

larger (85%), because the estimated plume turbulence intensity, and hence the turbulence enhancement function G, decrease with (z_c/d_o).

The ceiling can be conceptually divided into three regions: the stagnation point region, which we have just discussed, the impingement region, which is a transitional region with a falling pressure gradient, and finally the constant pressure, turbulent ceiling jet flow. Because of the difficulty in calculating this transitional flow in the impingement region, we adopted a simple empirical fit to the published data of Chia, Giralt, and Trass (1977) in order to estimate the heat transfer coefficient as a function of radius, given its value at the stagnation point. This approach worked reasonably well for the axisymmetric 1/4 scale data of Zukoski, Kubota, and Veldman (1975). However, the 1/2 scale data replotted in Figure (9.20), which is typical of our 1/2 scale results, have a flatter or less peaked distribution in this region. This may be due to an interaction of the door-jet of entering fresh air with the plume, which could cause the plume to be blown back or to wander. The effect of such a wandering motion would be to reduce the time-averaged stagnation point heat transfer coefficient and to increase the time-averaged value of nearby points. Similarly, if the plume were blown off the geometrical fire axis ($\bar{r} = 0$), the value of the heat transfer coefficient at $\bar{r} = 0$ would be smaller than expected, with larger than expected values at points closer to the actual stagnation point. Unfortunately, our gas temperature data do not have the spatial resolution to differentiate these effects or to precisely locate the actual stagnation point. Therefore, we are forced to assume that the plume rises vertically, with the stagnation point

located directly above the fire. Furthermore, as we shall discuss shortly, the Reynolds number dependence of the stagnation point and ceiling jet heat transfer coefficients is not identical, with the stagnation point heat transfer coefficient decreasing faster as the Reynolds number increases. Thus, as one increases the scale of the experiments, the impingement region heat transfer coefficient distribution must become progressively flatter, if, as we have assumed, the overall heat transfer coefficient curve is continuous.

Unfortunately, the thermocouple spacing in the ceiling was such that we could only measure one radial data point in this regime. Consequently we were unable to resolve the detailed shape of the heat transfer coefficient distribution in this region, although the trend is clear. Thus for lack of data we have been forced to retain the unperturbed, pure axsiymmetric relation given by Equation (8.16), and plotted for comparison in Figure (9.20). Although it would certainly be desirable to have a more accurate formulation for the impingement region heat transfer coefficient distribution, the heat transfered to the ceiling from this region is a small fraction of the total flux delivered to the ceiling. Consequently ε_T will be close to unity, and slight errors in the heat transfer coefficient distribution in this region will not seriously affect the subsequent ceiling jet computation.

We have assumed that as the flow leaves the impingement region, it is a fully developed turbulent, radial ceiling jet. In the calculation scheme for the ceiling jet, described in Section (8.6), the key parameter

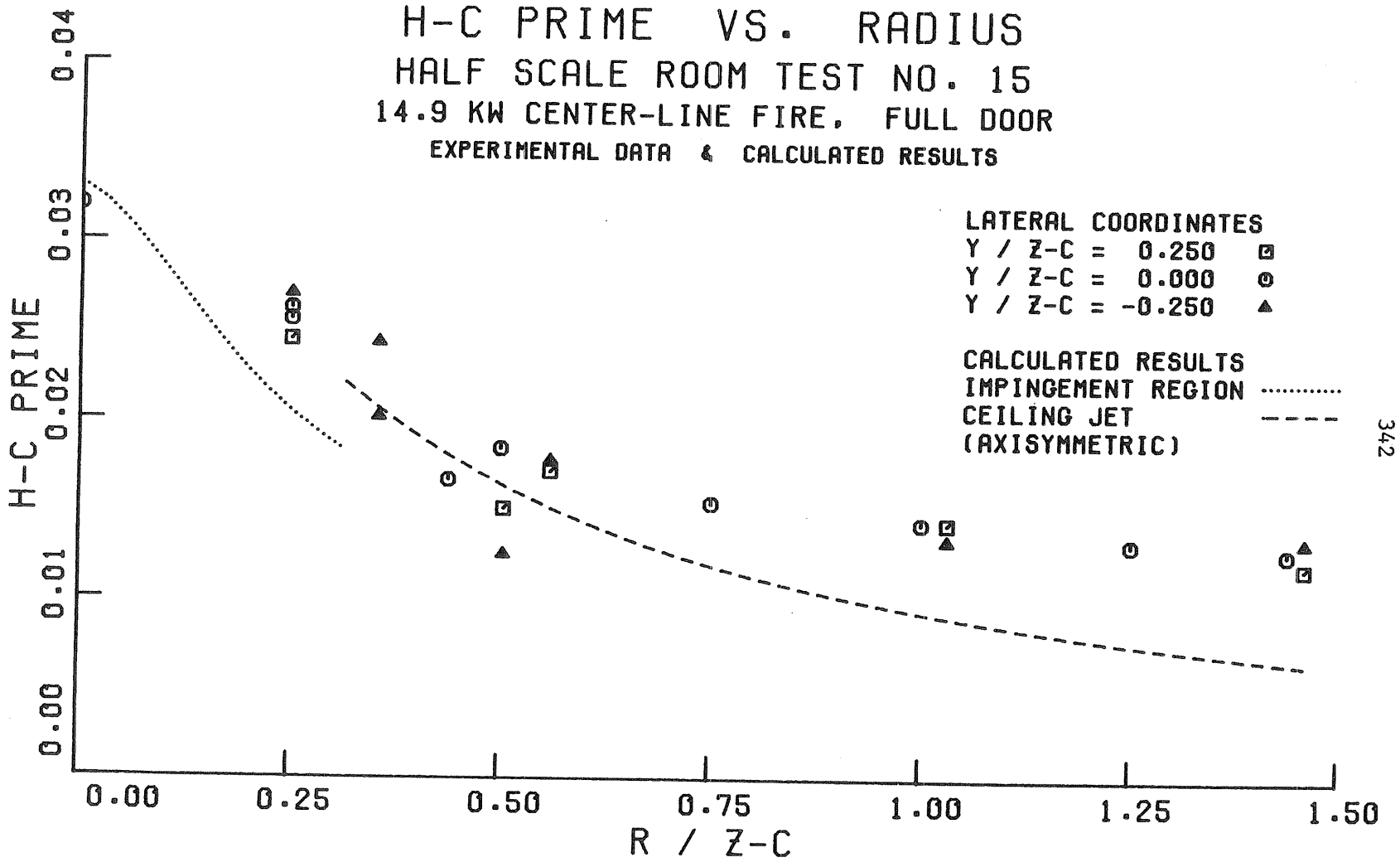

Figure (9.20) Dimensionless Heat Transfer Coefficients, Exp. 15 (Data and Impingement Region Calculations)

governing the behavior of the heat transfer coefficient, given the flow geometry and the entrainment function, is the friction factor N. There are two basic choices for this parameter: assume N is constant and pick a value N_o for it, or assume N varies as a function of the local inner layer Reynolds number Re_m and solve an ordinary differential equation to get the inner layer thickness $\tilde{\delta}$ with which to compute Re_m. Both options are presented in Figures (9.21) and (9.22), which compare the data with the variable N calculation results, and with the results for several values of the constant N_o, for axisymmetric and two-dimensional flow geometries.

The results plotted in Figure (9.21) for the variable skin friction option are typical in two important respects. First, in all the cases we have considered, they overestimate the heat transfer coefficient data. Second, these estimates always fall off faster with $\bar{r}$ than the data. These trends indicate that the constants in the empirical relation of Poreh, Tsuei, and Cermak (1967):

$$c_f = 0.12\ Re_m^{-0.3}\ \left(\frac{r}{z_c}\right)^{-0.16} \qquad (8.42)$$

may need revision for our range of inner layer Reynolds numbers, which are an order of magnitude smaller than the values in their experiments. In addition, Poreh, Tsuei, and Cermak only measured conditions for one nozzle to plate separation (z_c), so the value - 0.16 for the dependence on $\bar{r}$ is open to question. However, this approach does make sense for large scale tests with large Reynolds numbers.

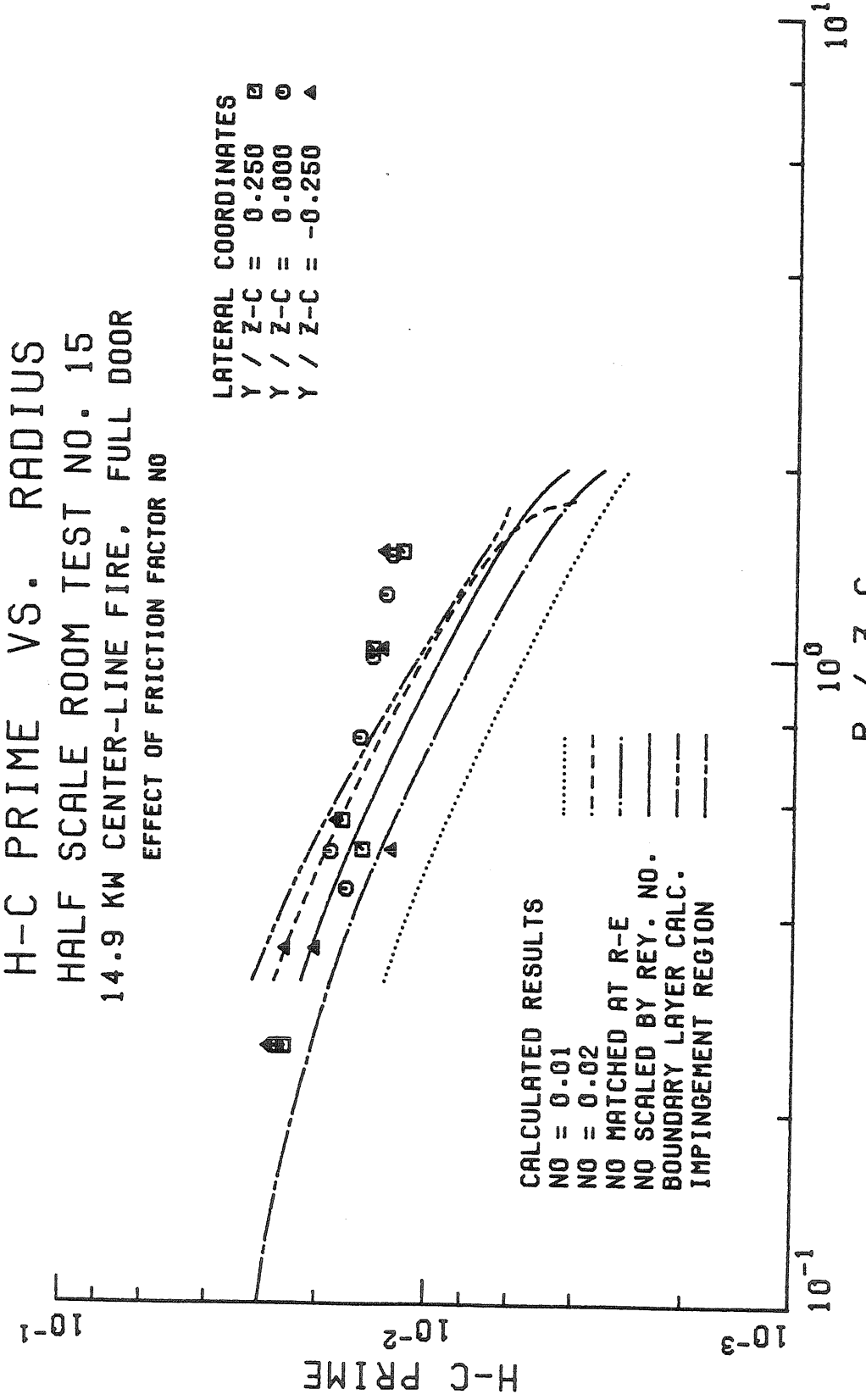

Figure (9.21) Dimensionless Heat Transfer Coefficients, Exp. 15. (Data and Axisymmetric Calculations).

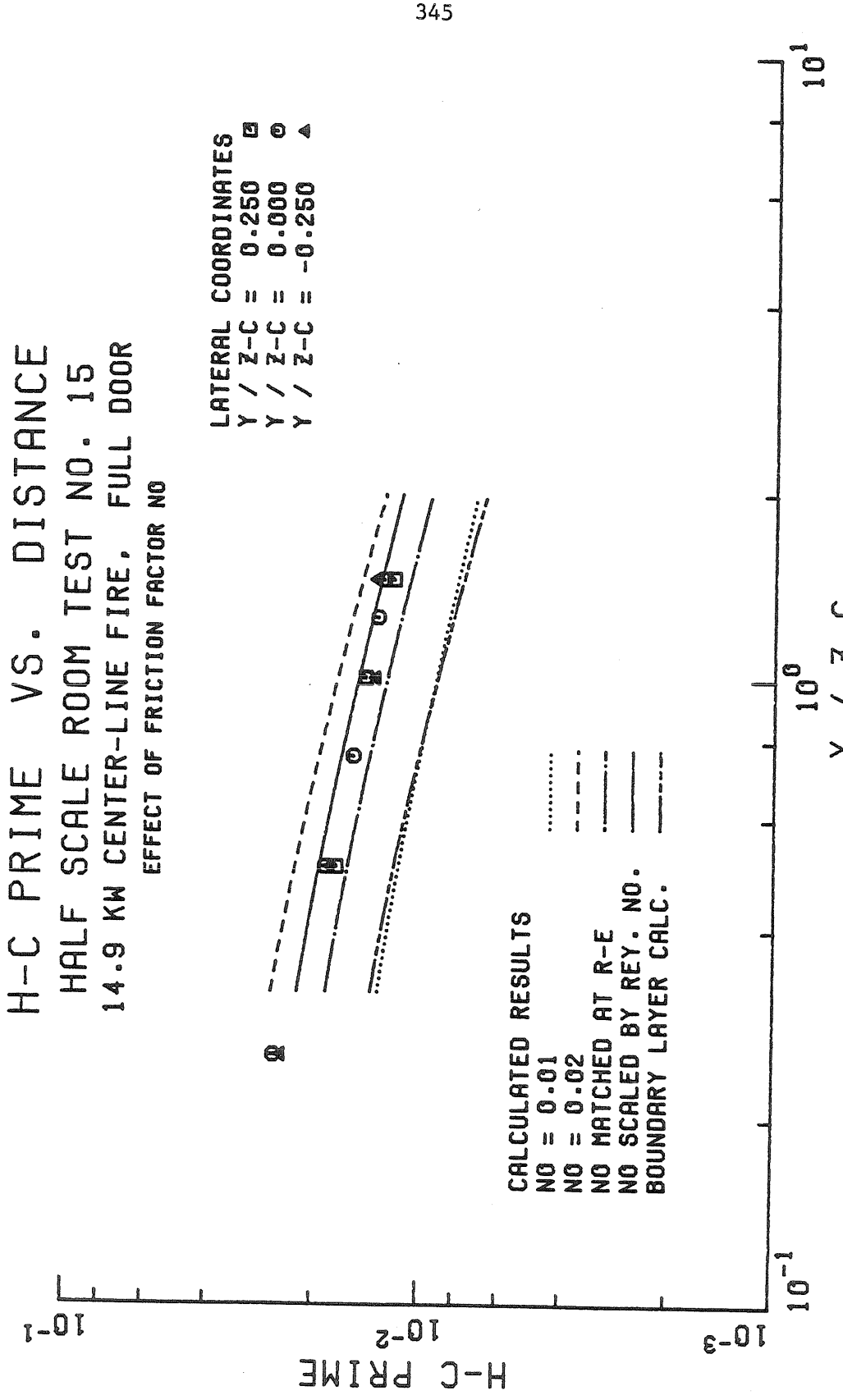

Figure (9.22) Dimensionless Heat Transfer Coefficients, Exp. 15. (Data and Two-Dimensional Calculations).

On the other hand, if one assumes that the friction factor remains constant, then one must specify a value N_o . Alpert (1974) suggested a value of $N_o = 0.01$ for $z_c = 3m$, but as shown by Figure (9.21), this value is too low. However, if we double N_o we slightly overestimate the data. An examination of the 1/4 scale data indicates that $N_o \sim 0.02$ is not an unreasonable first guess.

To avoid arbitrarily picking a value for the friction factor, one can choose N_o such that the heat transfer coefficient computed from the empirical impingement region relation (8.16) at the end of the impingement region just matches the ceiling jet calculation at that point $(\bar{r}_e)$. This scheme has the aesthetic advantage that it automatically produces a continuous h_c' distribution for all radii. However, despite the fact that it worked well for the 1/4 scale data, as we have seen, it suffers from two flaws. First, it is obviously only as good as the empirical relation for the impingement region, and as we have just seen, this relation appears to be influenced by the Reynolds number and by the room geometry. Second, there is a more fundamental difficulty in that one would expect the laminar, stagnation point heat transfer coefficient to scale differently with Reynolds number than the turbulent ceiling jet heat transfer coefficient. In fact, if we ignore turbulent enhancement for a moment, the stagnation point heat transfer coefficient scales like the plume velocity divided by the square root of a Reynolds number based on the local radius and velocity:

$$h_{c_{sp}} \propto \sqrt{\frac{\nu_2 \, w_{m_t}}{b_c}} \propto \frac{w_{m_t}}{\sqrt{\frac{w_{m_t} \, b_c}{\nu_2}}} \propto u_{m_e} \, Re_{r_e}^{-\frac{1}{2}} \qquad (9.13)$$

where we have used the facts that $r_e \propto b_c$ and $u_m(r_e) \propto w_{m_t}$. On the other hand, if we assume that the Reynolds number dependence of Poreh, Tsuei, and Cermak's (1967) relation for the friction factor is correct, then the heat transfer coefficient at the start of the ceiling jet ($r = r_e$) can be written:

$$h_c \, (r_e) \propto u_{m_e} \, Re_{r_e}^{-0.3} \qquad (9.14)$$

where we have used the fact that $\delta \propto r$ and thus $Re_m \propto Re_r$. Therefore, as the scale of the experiment, and hence the Reynolds number, increases the stagnation point heat transfer coefficient will decrease like $Re^{-0.2}$ compared to the initial ceiling jet heat transfer coefficient. This appears to be the case in Figure (9.21) where the "matched" friction factor option predicts ceiling jet heat transfer coefficients which are approximately 15-20% below most of the data, even though the stagnation point value was very close. In doubling the scale of the experiment, we changed the initial ceiling jet Reynolds number $Re_r = u_m r / \nu_2$ by a factor of approximately 2. Therefore, we would expect the "matched" ceiling jet friction factor to be low by a factor of $(2)^{0.2} = 15\%$, which indeed it is.

The Reynolds number dependence of the ceiling jet friction factor suggests a third option, which we believe to be preferable, for choosing a value for N_o. We have seen that for the 1/4 scale tests, which had initial ceiling jet Reynolds numbers in the range

$1.08 \times 10^4 \leq Re_r \leq 1.31 \times 10^4$, friction factors in the range $0.0196 \leq N_o \leq 0.0206$ fit the ceiling jet data very well. We can use the average values of these results to estimate the friction factor as a function of Reynolds number as:

$$N_o = 0.0201 \left(\frac{Re_r}{1.20 \times 10^4}\right)^{-0.3} = 0.336 \, (Re_r)^{-0.3} \qquad (9.15)$$

This empirical relation agrees with the 1/4 scale results to within 1%, and predicts a 20% increase in the friction factor for our 1/2 scale test compared to the "matched" calculation, as shown in Table (9.4), and the computation based on this friction factor lies right in the middle of the axisymmetric regime ($\bar{r}_e \leq \bar{r} \leq 0.5$) ceiling jet data in Figure (9.21).

The transition of the flow geometry from axisymmetric to two-dimensional is depicted in Figures (9.21) and (9.22). For small radii ($\bar{r} \leq 1/2$) the flow appears to be basically radial in nature and the h_c' data agree with the axisymmetric calculations shown in Figure (9.21). The data are bracketed by the calculations for $N_o = 0.014$ and $N_o = 0.020$. However, by $\bar{r} \sim 0.6$ the axisymmetric calculations begin falling much faster than the data. On the other hand, for moderate to large distances ($\bar{x} \geq 1/2$), the data agree reasonably well with the two-dimensional calculation shown in Figure (9.22). Again, the data are bracketed by $N_o = 0.014$ and $N_o = 0.020$, as they were for the axisymmetric case, with the best fit again given by the value of $N_o = 0.017$ based on the initial ceiling jet Reynolds number. Figure (9.22) also shows that the two-dimensional variable friction factor calculation significantly underestimates the heat transfer coefficient. However, because there is no explicit $\bar{x}$ dependence in the skin friction correlation of Launder and Rodi (1981) for two-dimensional

TABLE (9.4) FRICTION FACTOR DEPENDENCE ON REYNOLDS NUMBER

Experiment	$Re_r \times 10^4$	N_o ("matched")*	N_o (calculated)†
Bare Ceiling 1	1.31	0.0196	0.0196
Bare Ceiling 2	1.08	0.0210	0.0208
Curtain Wall 4	1.15	0.0206	0.0204
Curtain Wall 5	1.22	0.0201	0.0200
1/2 Scale 15	2.14	0.0140	0.0169
1/2 Scale 16	1.91		0.0175
1/2 Scale 7	1.71		0.0181
1/2 Scale 10	1.85		0.0177
1/2 Scale 13	2.00		0.0172

*N_o chosen to match h_c' at $\bar{r}_e$ with impingement region correlation (8.16).

†N_o calculated from Equation (9.15).

wall jets, given by equation (8.43):

$$c_f = 0.0315 \quad Re_m^{-0.182} \tag{8.43}$$

the friction factor remains practically constant $N \approx 0.01$. Again, the Reynolds number in our 1/2 scale test is an order of magnitude below those of Launder and Rodi (1981), so it is not surprising that this correlation underestimates the data. Finally, it may be noted that for this two-dimensional calculation we assume 1/2 the originally axisymmetric flow is turned into the x direction ($\xi = 1/2$).

This assumption regarding the fraction of the original flow which comprises the eventual two-dimensional ceiling jet flow represents an additional adjustable constant (ξ) in the two-dimensional computation. We have presented three values for this constant, which one might pick from symmetry considerations, in Figure (9.23). For these calculations we have chosen $N_o = 0.017$ based on the initial ceiling jet Reynolds number. The data are seen to lie very close to the $\xi = 1/2$ curve, which is typical of all our half scale experimental results. We will therefore use $\xi = 1/2$ to characterize the two-dimensional computation. However, it should be remembered that the value of this parameter depends on the room geometry, as discussed in Section (8.6.9).

Finally, it is interesting to compare the heat transfer coefficient data from the ceiling jet region of the three cases examined so far. There appears to be a trend toward smaller dimensionless ceiling jet heat transfer coefficients as the buoyancy of the ceiling jet decreases, or equivalently, as the relative losses from the upper layer decrease (measured by an increase in c_q). Upon comparing the h_c' data from the ceiling jet regime

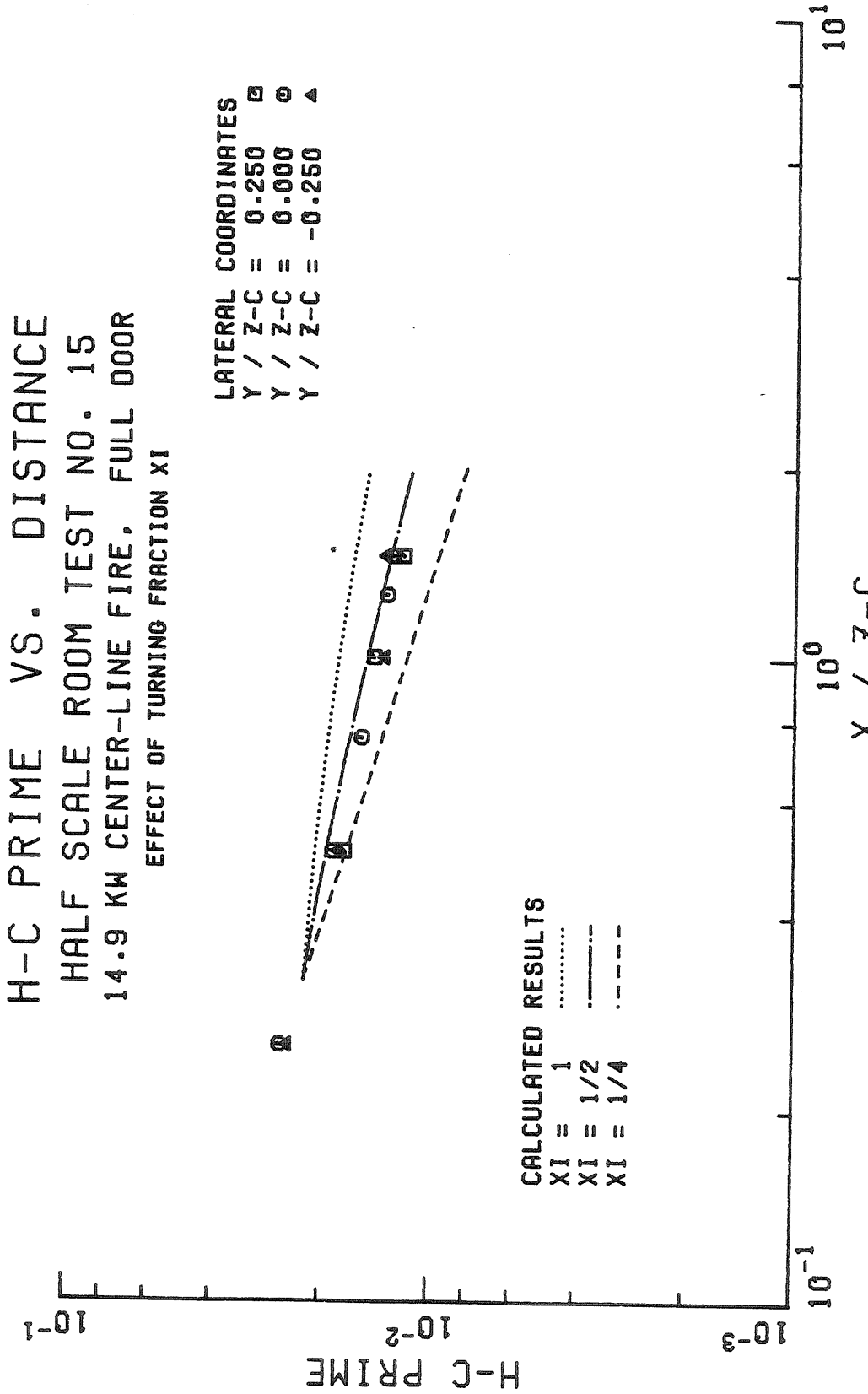

Figure (9.23) Dimensionless Heat Transfer Coefficient as a Function of Turning Fraction ξ.

($\bar{r} \gtrsim 0.25$) in Figures (9.1), (9.9), and (9.21), and replotted here in Figure (9.24), we see that the 1/2 scale test data (with $c_q = 0.74$) lie approximately 18% below the curtain wall data from test 5 ($c_q \sim 0.40$), which in turn fall roughly 9% below the unconfined ceiling data (c_q=0.00). This trend is not unreasonable because as c_q increases, the relative buoyancy of the upper layer plume and resulting ceiling jet decrease, resulting in smaller velocities and smaller heat transfer coefficients. As we saw with the stagnation point heat transfer coefficient, the simple point source plume scaling parameters do not take this decrease into account, and consequently the dimensionless heat transfer coefficients fall with increasing c_q.

The gas temperature data, presented in Figures (9.25) and (9.26) for the axisymmetric and two-dimensional cases respectively, show the same general trends as the heat transfer coefficient data. In particular, there appears to be less scatter for moderate distances ($\bar{r} \geq 1/2$) when the data are plotted versus $\bar{x}$ rather than versus $\bar{r}$, whereas the reverse is true for small distances ($\bar{r} < 1/2$). The agreement between the calculations and the data does not appear to be quite as good as it was for the heat transfer coefficient largely because the scatter of the data is more apparent on a linear plot. However, the computed temperatures with $\kappa = 1.02$ and $\varepsilon_T = 1$ again appear to lie in the middle of the data points for the axisymmetric portion of the ceiling jet ($\bar{r}_e \leq \bar{r} \leq 0.5$). Thus. for the axisymmetric portion of the ceiling jet, our calculation scheme seems to be able to predict the variation of both the heat transfer coefficient and the local maximum gas temperature. It may be noted that

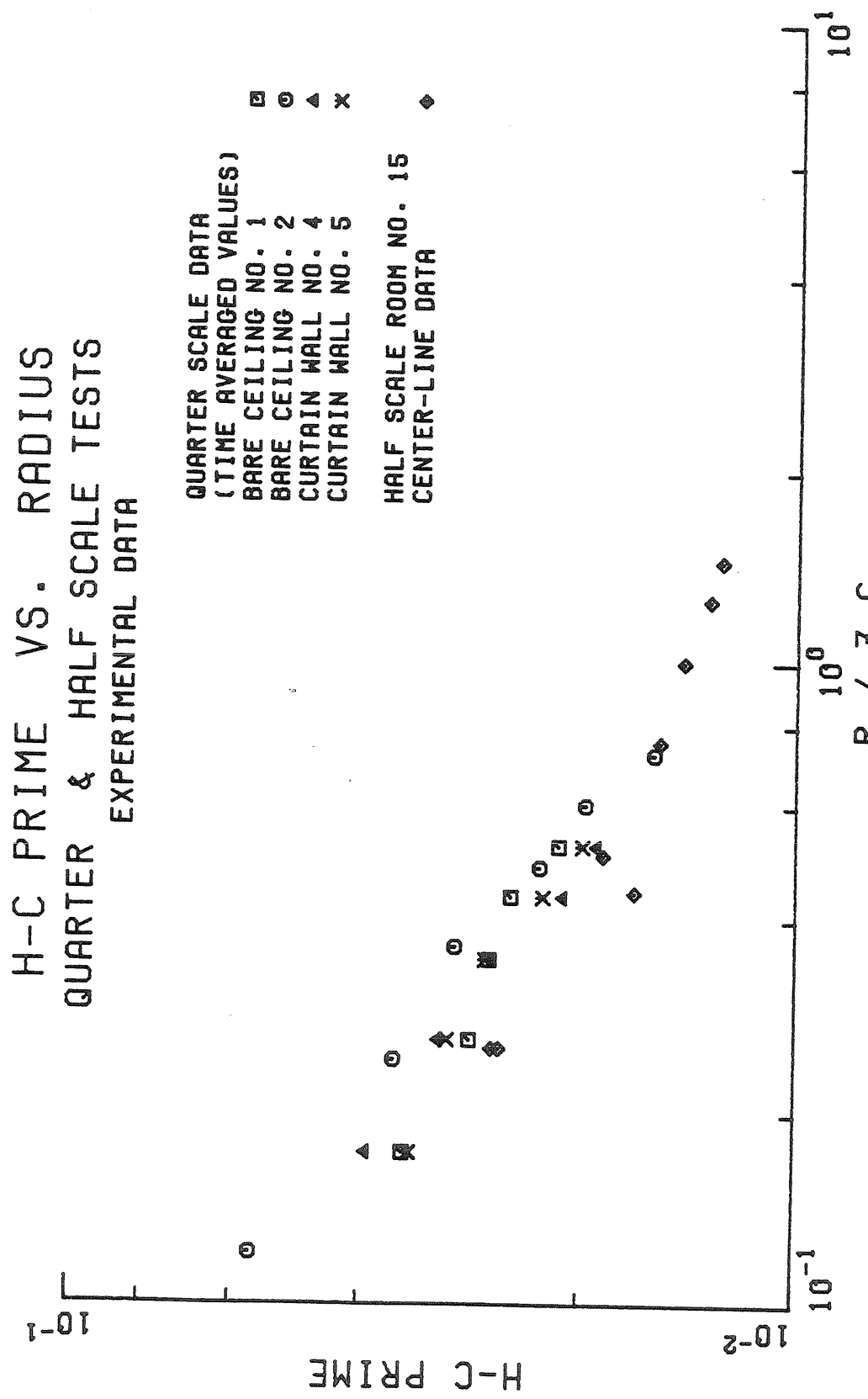

Figure (9.24) Effect of Scale on the Dimensionless Heat Transfer Coefficient in the Ceiling Jet.

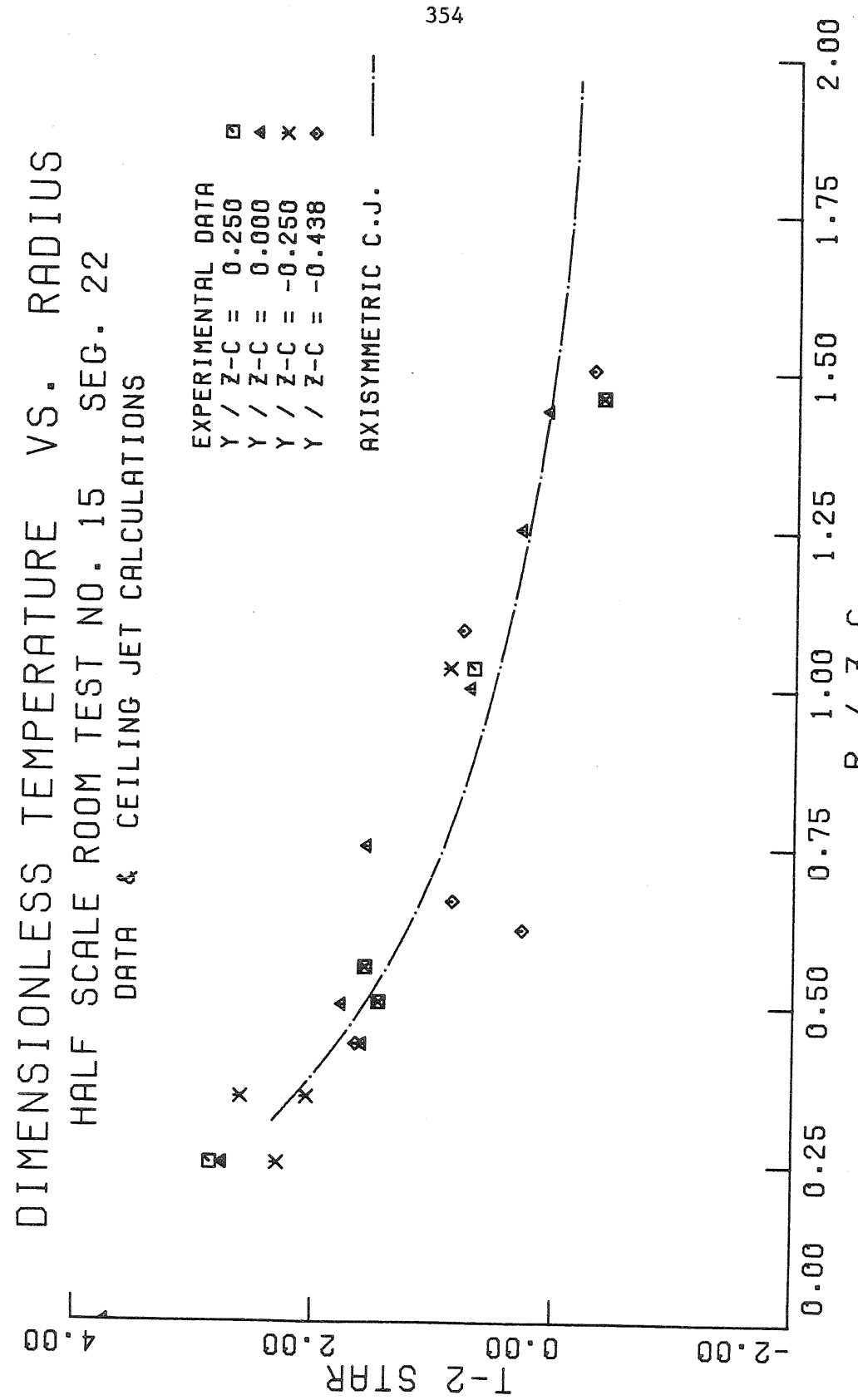

Figure (9.25) Dimensionless Gas Temperature Difference, Exp. 15. (Data and Axisymmetric Calculations).

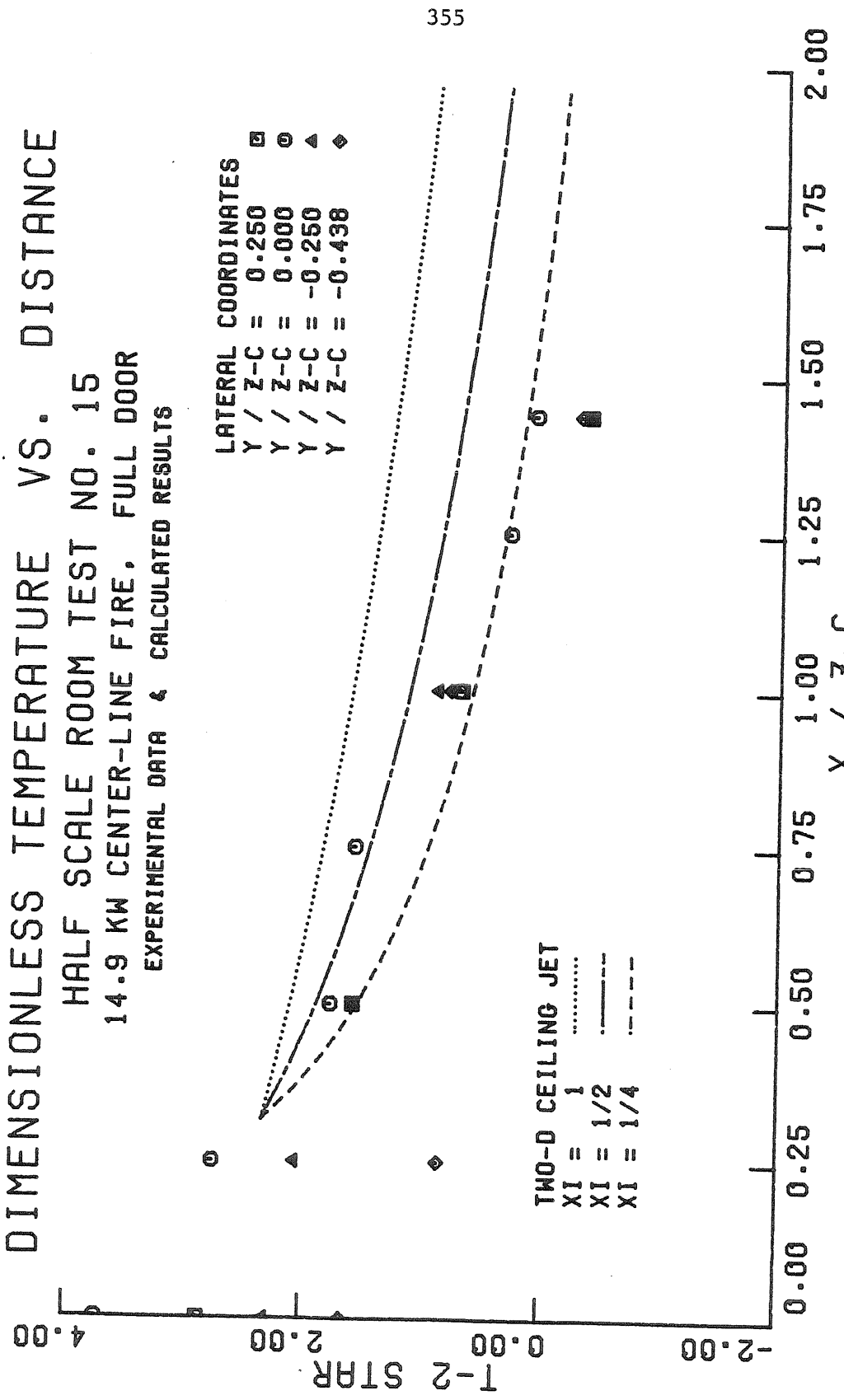

Figure (9.26) Dimensionless Gas Temperature Difference, Exp. 15 (Data and Two-Dimensional Calculations).

because the value of N_o based on the initial ceiling jet Reynolds number gave the best agreement with the heat transfer coefficient data, we will henceforth use this form of Reynolds number scaling for N_o.

On the other hand, the two-dimensional calculation with $K = 1.02$ seems to underestimate the convective losses, and consequently to overestimate the temperature, especially at large distances with the data bracketed by $\xi=1/4$ and $\xi=1/2$. This is not surprising because the two-dimensional computation is really an asymptotic calculation which assumes that the flow is purely two-dimensional and issues from a fictitious two-dimensional source at $\bar{x}_e = \bar{r}_e$. In reality the ceiling jet is in transition from a basically radial to a basically longitudinal flow pattern, with secondary flows created by the presence of the side walls. Because the axisymmetric ceiling jet experiences larger entrainment and convective losses than the two-dimensional ceiling jet, we expect that the two-dimensional calculation should overestimate the ceiling jet temperatures. Note that the last set of data points at $\bar{x} = 1.44$ should not be considered as part of the ceiling jet because of their very close proximity ($\Delta\bar{x} = 0.06$) to the north end wall. Note also that at large $\bar{x}$, the ceiling jet has lost most of its buoyancy ($T_2^* \to 0$).

It is also interesting to note that as the upper layer loses a smaller fraction of the input enthalpy (c_q increases from 0), the buoyancy of the upper layer falls, as shown by the decrease in T_2^* at the stagnation point. For example, for the bare ceiling tests ($c_q = 0$), $T_2^*(0)$ was between 10 and 11. In the curtain wall tests ($c_q \sim 0.4$), $T_2^*(0)$ had fallen to between 7 and 8, and for the 1/2 scale tests ($c_q \sim 0.7$) to less than 4. In the limit of no heat loss from the upper

layer ($c_q = 1$), the ceiling jet would be neutrally buoyant with T_2^* identically zero. On the other hand, $T_1^*(0)$, which measures the buoyancy (or temperature increase) of the gas with respect to the mean lower layer gas temperature, remains roughly constant at a value between approximately 10 and 11 for all three conditions. This indicates that the simple plume scaling does a good job of estimating the plume entrainment and heat addition, even though $Q^*_{z_c}$, $\bar{z}_i$, and c_q all change.

As before, with estimates of the heat transfer coefficient and gas temperature distributions available, and given an empirical expression for the ceiling temperature distribution, one can calculate the convective heat transfer rate at any point on the ceiling. These calculations are presented in Figures (9.27) and (9.28) for the axisymmetric and two-dimensional regimes. They were computed assuming the impingement region gas-wall temperature difference remains constant, the turning losses can be neglected ($\varepsilon_T = 1$), and that $N_O = 0.017$ based on the initial ceiling jet Reynolds number. Even though, as we have seen, the computed dimensionless heat transfer coefficients and gas temperatures were approximately equal to the mean value of the data points, the computed dimensionless heat transfer rate for $\kappa = 1.02$ is roughly 10% lower than the measured values. This discrepancy is caused by the empirical fit used to estimate the ceiling temperature distribution. It tended to overestimate the ceiling temperatures for small radii ($\bar{r} \leq 0.5$) although it worked well for the majority of the ceiling. This again is typical of the difficulty in calculating the local convective flux accurately because one must get the thermal, as well as the velocity boundary conditions right.

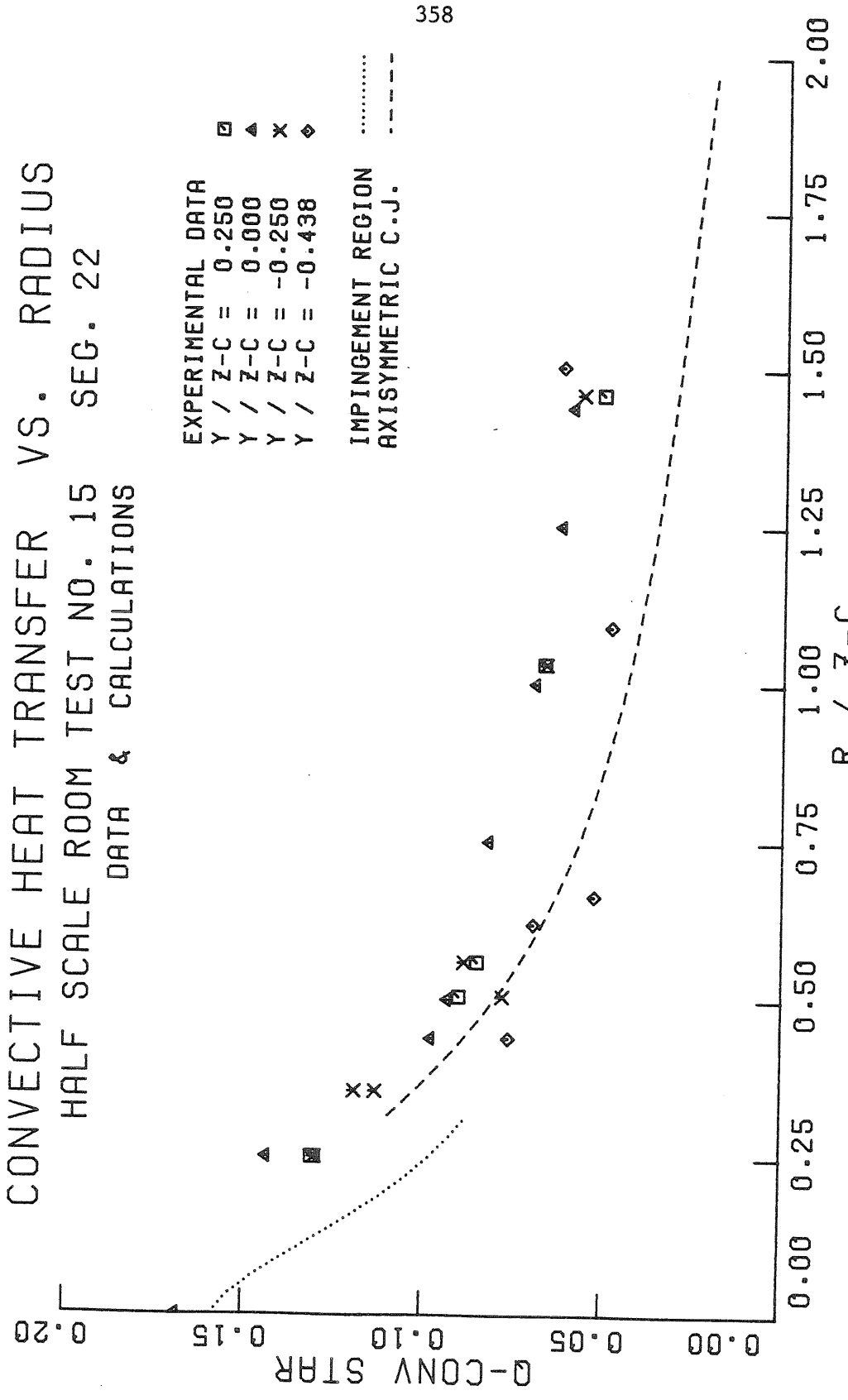

Figure (9.27) Dimensionless Convective Heat Transfer Rates, Exp. 15. (Data and Axisymmetric Calculations).

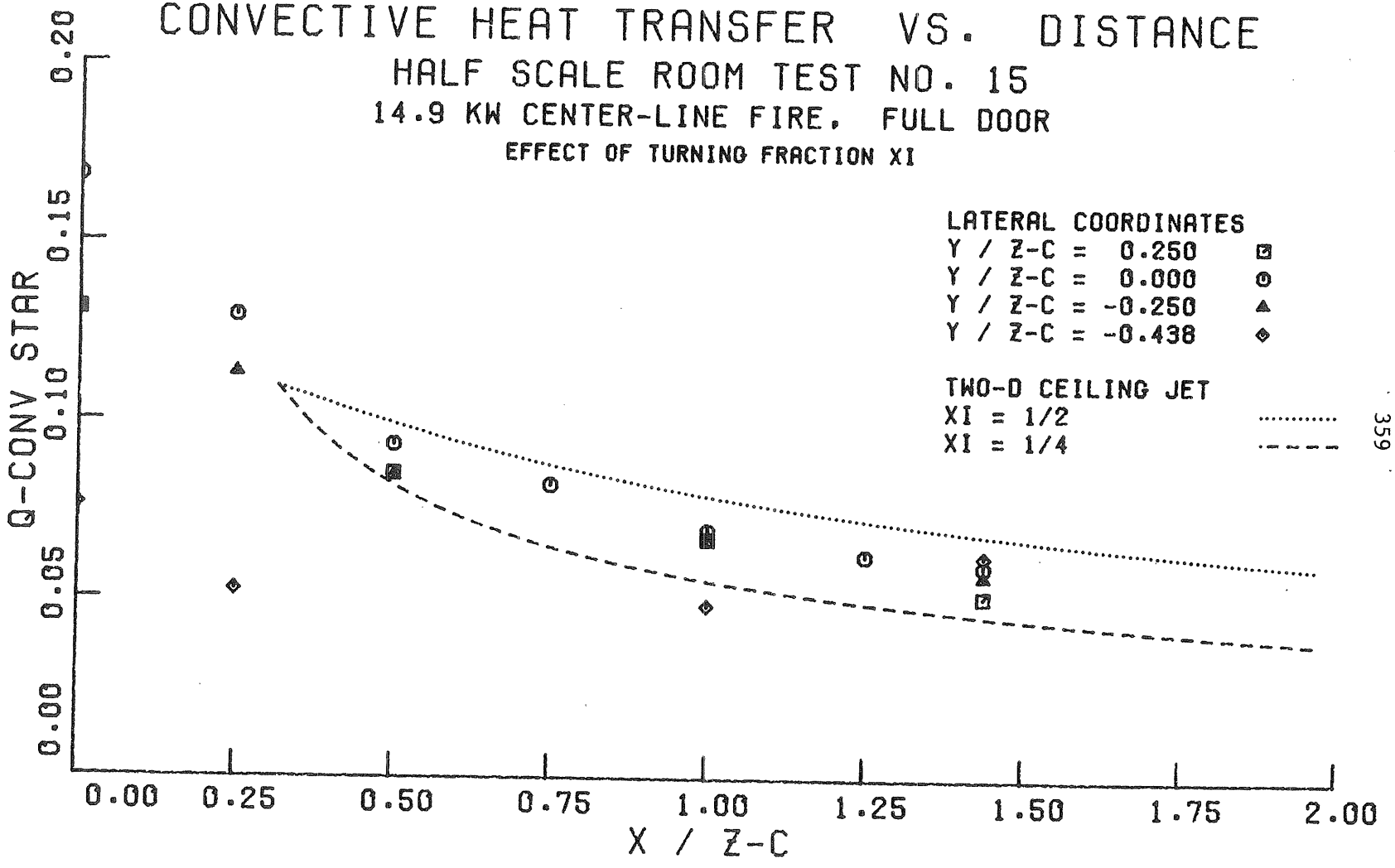

Figure (9.28) Dimensionless Convective Heat Transfer Rates, Exp. 15. (Data and Two-Dimensional Calculations.

In the two-dimensional regime, shown in Figure (9.28), the data are again bracketed by $\xi = 1/2$ and $\xi = 1/4$, as was the dimensionless temperature difference T_2^*.

It is interesting to note that the scaled dimensionless convective heat transfer rate q^*_{conv} does not change greatly between the three cases studied so far. For example, at the stagnation point its values range between approximately 0.20 and 0.25 for most of the unconfined and curtain wall tests, and between 0.17 and 0.20 for the 1/2 scale test. Again, this indicates that the simple plume scaling, corrected by the ratio (T_0/T_2) which partially takes into account the presence of the upper layer, seems to be reasonably accurate.

Finally, one can integrate the calculated convective rates to find the total convective heat transfer to the ceiling. In Figure (9.29) the calculated integrals are presented for both axisymmetric and two-dimensional flows. From these curves one can estimate the total ceiling heat transfer as follows. First, assuming axisymmetric flow for $\bar{r} \leq 0.5$ and two-dimensional flow for $0.5 \leq \bar{x} \leq 1.5$, the purely axisymmetric contribution can be read off the axisymmetric Q_T^* curve at $\bar{r} = 0.5$. Next, the purely two-dimensional contribution is given by the difference between the values of the two-dimensional Q_T^* curve at $\bar{x} = 0.5$ and $\bar{x} = 1.5$. Finally, the contribution of the corner areas, which lie between the square defined by $-0.5 \leq \bar{x} \leq 0.5$, $-0.5 \leq \bar{y} \leq 0.5$ and the inscribed circle of radius $\bar{r} = 0.5$, can be estimated as the fraction of the total heat transfer from the annulus $0.5 \leq \bar{r} \leq 0.707$ given by the fractional area of annulus covered by these corner areas. Thus from Figure (9.29) the purely axisymmetric contribution represents 6.1% of the fire's heat

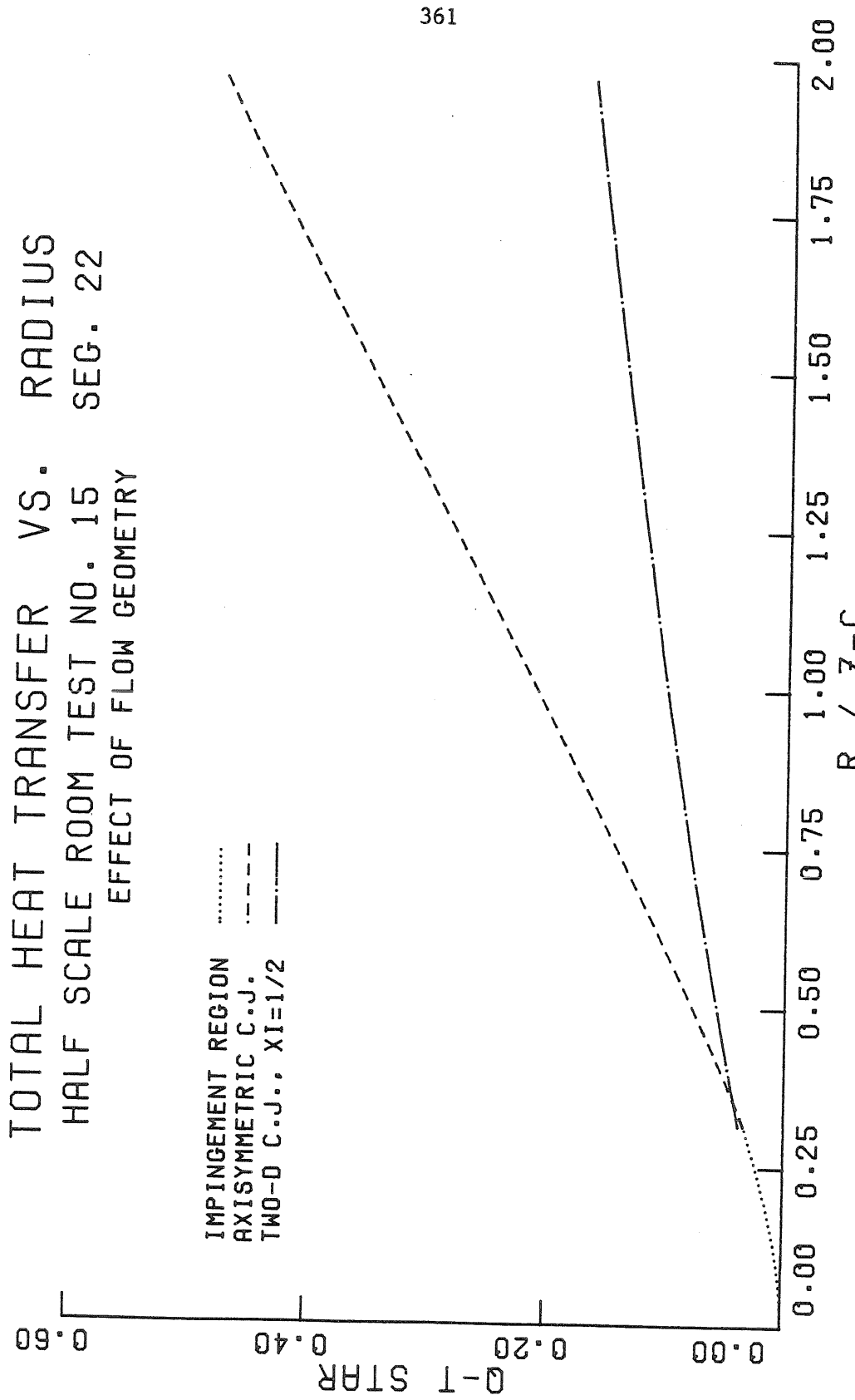

Figure (9.29) Dimensionless Total Convective Flux, Exp. 15. (Axisymmetric and Two-Dimensional Calculations).

release, with an additional 1.1% contributed by the corners. Finally, the two-dimensional contribution is 6.0%, bringing the total convective heat transfer to the ceiling to 13.2% of the fire's heat release. As we have seen, the calculated local convective heat transfer rates were as much as 10% lower than the measured data. Consequently, we can expect the integrated convective heat transfer to the ceiling to be closer to 14% of the heat release. We can check this by manually integrating the measured local convective heat transfer rates. However, because the measuring locations are distributed in a nonuniform pattern on the ceiling, we have approximated the integral as the product of the arithmetic average of the measured rates times the area of the ceiling. The experimental data thus indicate that between 12.5% and 13.4% of the heat release is delivered to the ceiling, depending, respectively, on whether one selects an equally spaced subset of the measuring locations, or uses all of them (which will emphasize the region near the stagnation point). Given the number of approximations involved, this seems to be rather good agreement. It is interesting to examine the integrated conduction through the ceiling for comparison. The experimentally measured rates indicate that between 9.8% and 10.3% of the heat release is conducted through the ceiling, again depending on whether a subset or the full set of measuring locations are used. These values in turn agree well with measured increase in enthalpy of the cooling air supplied to the back side of the ceiling which amounted to 9.8% of the heat release. This agreement indicates that our calculation procedures are internally consistent. It also indicates the integrated net radiative loss from the ceiling is roughly 3.1% of the heat release, or 23% of the total heat convected

to the ceiling.

Thus it appears that we have a reasonably complete picture of heat transfer processes to the ceiling. The next logical question to ask is, "What about the sidewalls?" We expect some portion of the ceiling jet flow to impinge on and flow down the sidewalls. In principle one could modify the ceiling jet calculation to take into account the change in the buoyancy term in the momentum equation and the change in the entrainment function. However, the initial conditions are complicated by the fact that for different points along the sidewall, the ceiling flow will have experienced different losses as it travels different distances to the sidewalls. Although it would thus be difficult to compute this sidewall flow, it is possible to compare the sidewall and ceiling data and establish some empirical relations. To this end we imagine cutting the room apart along the vertical wall seams like a paper box and folding the sides up so that they are in the same plane as the ceiling. In such a geometry one would expect the flow to be axisymmetric, starting on the ceiling and continuing radially outward along the folded up sidewall panels. We denote the effective radial distance by r' for such a geometry. However, in reality, the walls are not folded up and what we picture is a flow bifurcation process. In general, the initially radial ceiling jet flow will approach the sidewall at some oblique angle. The flow must then split, with some portion being reflected back along the ceiling to form the largely two-dimensional ceiling jet, while the remainder flows down the sidewall at some angle to the vertical. The distance traveled by this latter component along the ceiling and sidewall will be approximately given by r'. We therefore present the heat transfer

coefficient data for the west sidewall and for the ceiling in Figure (9.30), plotted versus $\bar{r}'$ and $\bar{r}$ respectively. From this figure we can see that the magnitude of the heat transfer coefficient is the same for both the ceiling and sidewall, although the radial extent of the latter flow is compressed because the upper layer only fills the upper half of the room. Therefore, the radial range of the data on the sidewall itself is limited to $\Delta\bar{r}' \sim 1/2$. Note that near the fire the minimum distance to the sidewall is $\bar{r}' = 1/2$ and the data points in this region ($r' \gtrsim 0.5$) have values comparable to the measured impingement region values on the ceiling, indicative of the flow separating from the ceiling as it approaches the sidewall and then impinging on the sidewall. Also note that for $r' \geq 1$, there is a bifurcation in the data. Most of the data lie below the ceiling data, with a few points above it. These latter points represent measuring locations on the sidewall just below the upper edge of the interface zone, where the gas temperature begins dropping rapidly. This reduces the gas-wall temperature difference, and because we divide by this difference to find h_c', the value of h_c' at these points may not be as accurate as the others. However, it is possible that the higher "turbulence" in this interfacial zone (as measured by the temperature fluctuations) may produce the larger heat transfer coefficients. Therefore, although it is difficult to calculate exactly, we can see that the sidewall convective heat transfer coefficient behaves roughly like the ceiling heat transfer coefficient, and that we could use the latter values in an approximate calculation without introducing a great error. If a slightly better estimate were needed, one could fit a simple empirical power law relation to the data above the interface:

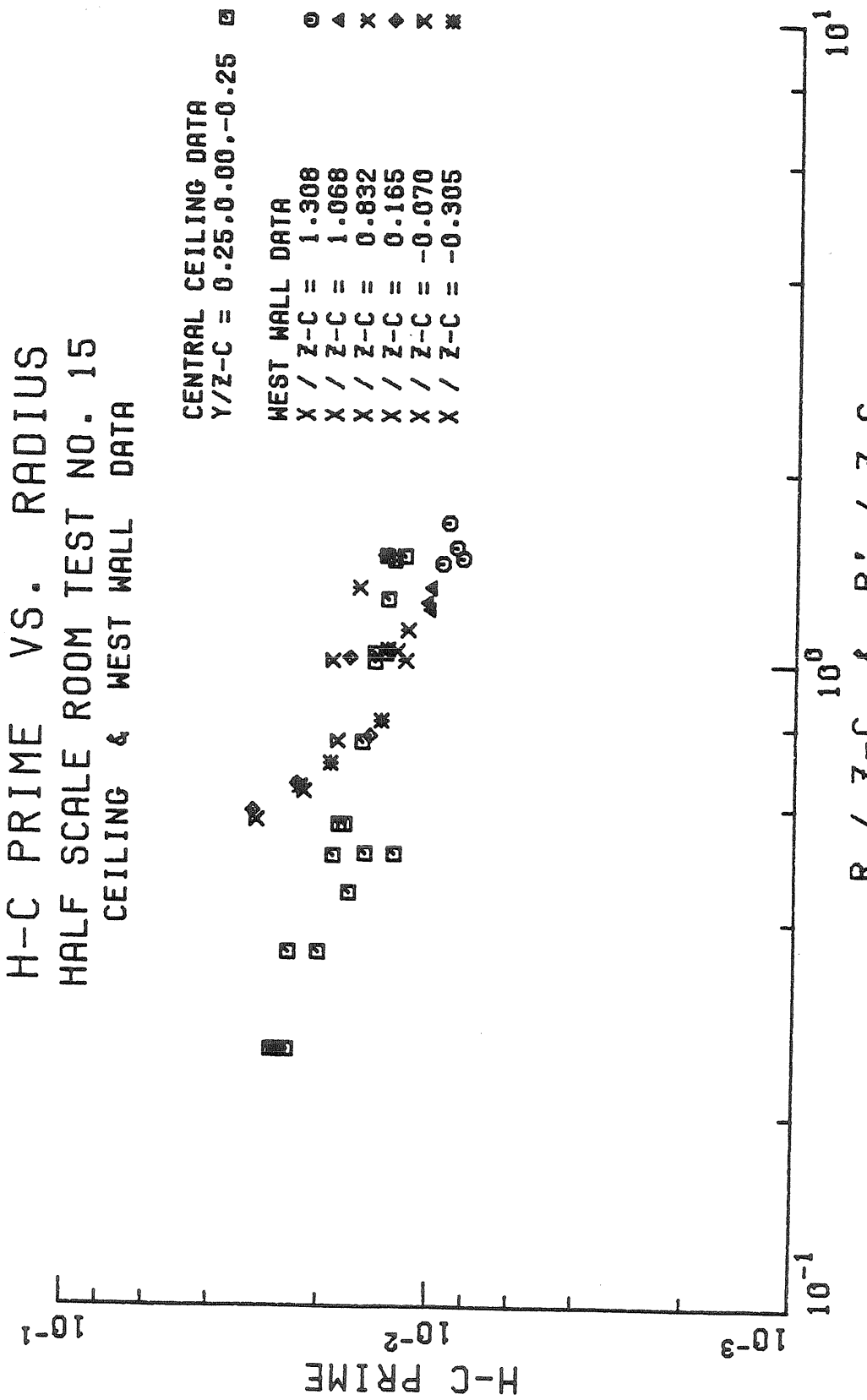

Figure (9.30) Dimensionless Heat Transfer Coefficient Data on the Ceiling and the West Wall, Exp. 15.

$$h_{c_{s.w.}}' = 1.37 \times 10^{-2} \, (\bar{r}')^{-1.20} \qquad (9.16)$$

This compares to a fit to the ceiling jet data for a similar range of $\bar{r} > 1/2$:

$$h_{c_{ceiling}}' = 1.43 \times 10^{-2} \, (\bar{r})^{-0.35} \qquad (9.17)$$

Similarly, Figure (9.31) shows a comparison of ceiling and sidewall gas temperatures measured relative to the mean upper layer temperature. Again, the sidewall data agree roughly with the ceiling data, and if one were to shift the west wall data by roughly $\Delta\bar{r}' = -0.17$, the sidewall data agree very well with the ceiling data within the scatter of the data. Thus with ways to estimate both the gas temperature and heat transfer coefficient, one could estimate the local convective heat transfer to the sidewall.

Finally, it may be noted that one might visualize a slightly different flow pattern on the sidewalls. After flowing radially across the ceiling, the ceiling jet might turn and flow straight down the sidewall, instead of at some angle to the vertical. We have compared data plotted according to this hypothesis to data plotted against $\bar{r}'$. There was no significant difference between the two sets of data and we have chosen the radial flow hypothesis ($\bar{r}'$) for convenience and because it seemed slightly more likely.

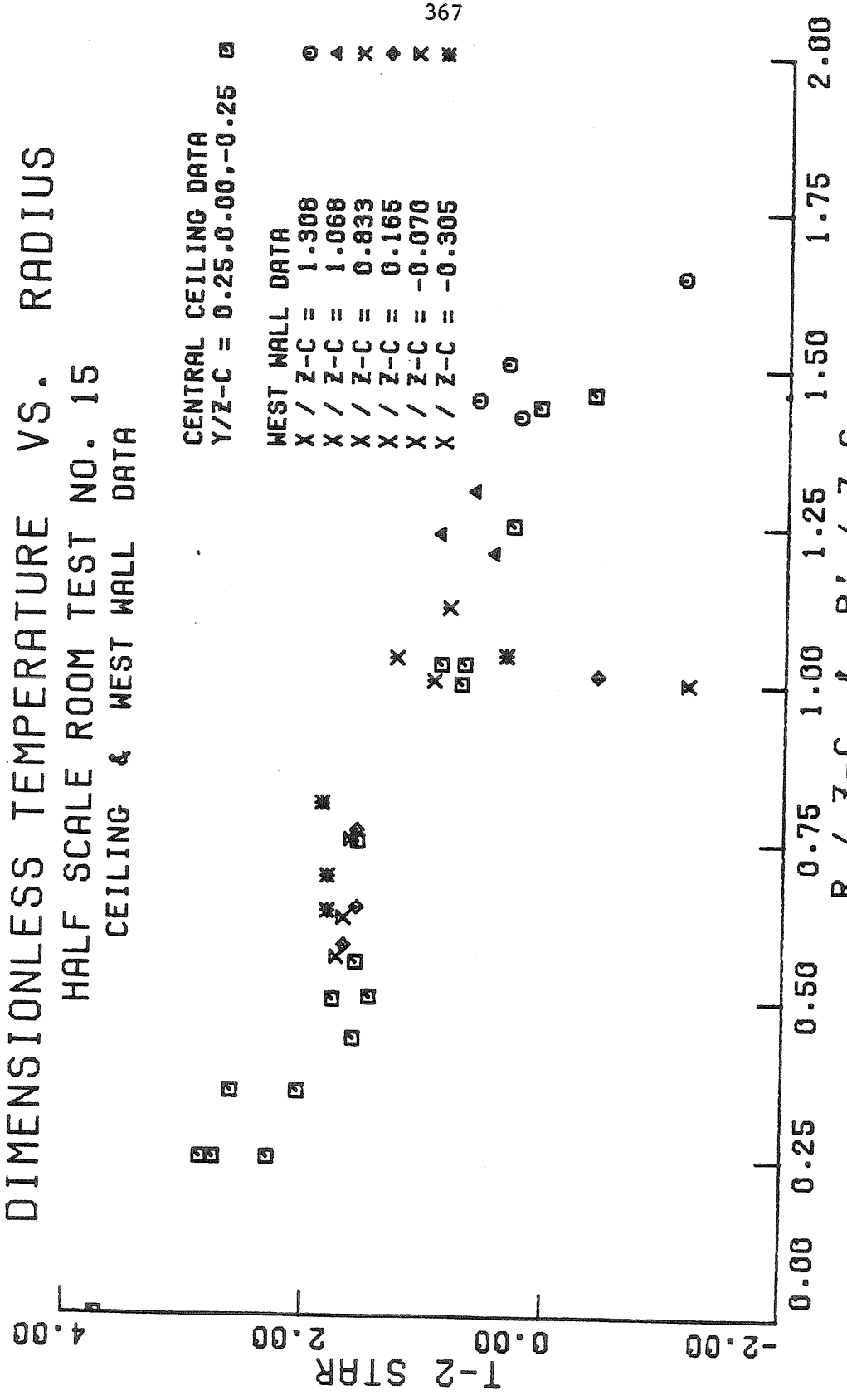

Figure (9.31) Dimensionless Gas Temperature Difference Data Near the Ceiling and the West Wall, Exp. 15.

9.6 Discussion of 1/2 Scale Results

In the previous section we examined both calculated and experimental values of several variables related to convective heat transfer for a typical 1/2 scale room fire. In this section we will investigate the effects observed in our 1/2 scale room tests produced by varying three basic parameters: the heat input, the door geometry, and the fire location. In order to keep this presentation to a manageable size, yet still cover the salient points, we have selected a subset of five parameters which effectively span the parameter space. The basic conditions for this subset, which includes experiments 7, 10, 13, 15, and 16, have already been given in Tables (9.1) along with additional information in Table (9.4). Briefly, experiments 7, 10, and 13, which all involved a corner fire in a room with a door, cover nearly a factor of 4 change in the dimensionless heat input parameter $Q^*_{z_c}$. On the other hand, experiments 15 and 16, which had identical strength fires located on the room's major axis, had the standard door and window geometries, respectively. Finally, by comparing experiment 15 with number 13, one can examine the effect of fire location.

In order to simplify the presentation and to keep this section to a reasonable length, we will compare the experimental data directly and not superimpose the results from the computation scheme. However, a complete set of figures comparing the data from each experiment with the calculated results may be found in the Appendix. The normalizing factors which we have chosen to make the physical quantities of interest dimensionless, and which were discussed in Section (9.1) are presented here in Table (9.5) for reference.

TABLE (9.5) NORMALIZATION FACTORS FOR DIMENSIONLESS VARIABLES

Dimension;		Velocity	Temperature	Heat Transfer Coefficient	Heat Transfer Rate
Definition:	$\frac{T_0}{T_2}$	$\sqrt{g\, z_c}\ (Q^*_{z_c})^{1/3}$	$T_o\ (Q^*_{z_c})^{2/3}$	$\rho_2\ c_p\ \sqrt{g\, z_c}\ (Q_{z_c})^{1/3}$	$\frac{T_0}{T_2}\ \frac{Q_F}{z_c^2}$
Units:		$\left[\frac{cm}{s}\right]$	$\left[K\right]$	$\left[\frac{W}{m^2K}\right]$	$\left[\frac{W}{m^2}\right]$
Experiment					
Bare Ceiling 1	1.000	34.10	4.22	411.4	1773
Bare Ceiling 2	1.000	38.07	7.40	461.9	3431
Curtain Wall 4	0.955	34.10	4.22	393.2	1693
Curtain Wall 5	0.943	37.29	5.15	423.3	2185
1/2 Scale 15	0.762	69.57	12.21	628.7	7639
1/2 Scale 16	0.784	69.55	13.57	583.7	7855
1/2 Scale 7	0.890	43.67	4.79	460.2	2206
1/2 Scale 10	0.830	54.73	7.53	539.0	4052
1/2 Scale 13	0.759	68.73	11.92	618.4	7340

The calculation procedure used to compute the axisymmetric and two-dimensional ceiling jet flows for these experiments was identical to the procedure just described for experiment 15. In particular, we found that a constant friction factor N_o, scaled by the initial ceiling jet Reynolds number and given in Table (9.4), yielded heat transfer coefficients that were very close to the experimental data. In addition, we have ignored turning losses in the impingement region ($\varepsilon_u = \varepsilon_T = 1$), and have again used $K = 1.02$ to obtain better estimates of the ceiling jet temperature distribution.

While the ceiling jet computation worked well without modification for all the experiments, it was necessary to adjust the plume entrainment constant in the plume calculation for those experiments in which the fire was located in the south west corner of the room (numbers 7, 10, 13). This is not unexpected. Tangren, Sargent, and Zukoski (1978) found, for example, that plumes placed directly in the corner of a room behaved as though they were 1/4 of a larger plume in a room four times as large. In our 1/2 scale facility the burner physically could not be positioned directly in the corner, and the center of the burner was located 18.4 cm from each sidewall. Consequently, we expect that the close proximity of the side walls should inhibit the plume entrainment process, thereby reducing the plume entrainment constant, although this reduction would not be as great as that observed by Tangren, et al. (1978). Furthermore, we expect that as the size of the fire increases, and hence distance between the edge of the plume and the sidewall decreases, this effect should become more pronounced. We therefore adjusted the plume entrainment constant downward in decrements of 10%

until the plume calculation (with $\kappa = 1.02$) produced reasonable agreement with the measured stagnation point ($\bar{r} = 0$) gas temperature, as it did without adjustment for the center line fires. Based on this criterion, we found that it was necessary to reduce the plume entrainment constant α by 10% for the smallest fire (number 7) and by 20% for the larger fires (numbers 10 and 13). The variable which is most sensitive to this parameter is the gas temperature. Typical results for experiment number 10 are shown in Figure (9.32) where we have taken the liberty of fairing in the curve over the impingement region (which we can not calculate). Clearly, by reducing α by 20% ($\alpha = 0.0877$) we obtain a significantly better fit to the temperature data, both at the stagnation point and thoughout the ceiling jet region, instead of using the standard value ($\alpha = 0.1096$).

9.6.1 Dimensionless Heat Transfer Coefficient

The dimensionless heat transfer coefficient h_c' remained remarkably constant as the three parameters at our disposal were varied.

Except for the points closest to the fire, the variation of $Q^*_{z_c}$ by a factor of 3.9 has almost no effect on the dimensionless heat transfer coefficient h_c', as shown in Figures (9.33). Similarly, the h_c' distributions on the sidewall for these experiments are virtually identical. In addition, the calculated axisymmetric ceiling jet values shown in Figure (9.34) are also almost indistinguishable with similar results for the two-dimensional case. This is not as surprising as it might seem because the plume velocity at fixed height scales as $(Q^*_{z_c})^{1/3}$, and thus increases by only 57%. Furthermore, as shown by Table (9.4), the calculated initial ceiling jet Reynolds number, which is also affected by the

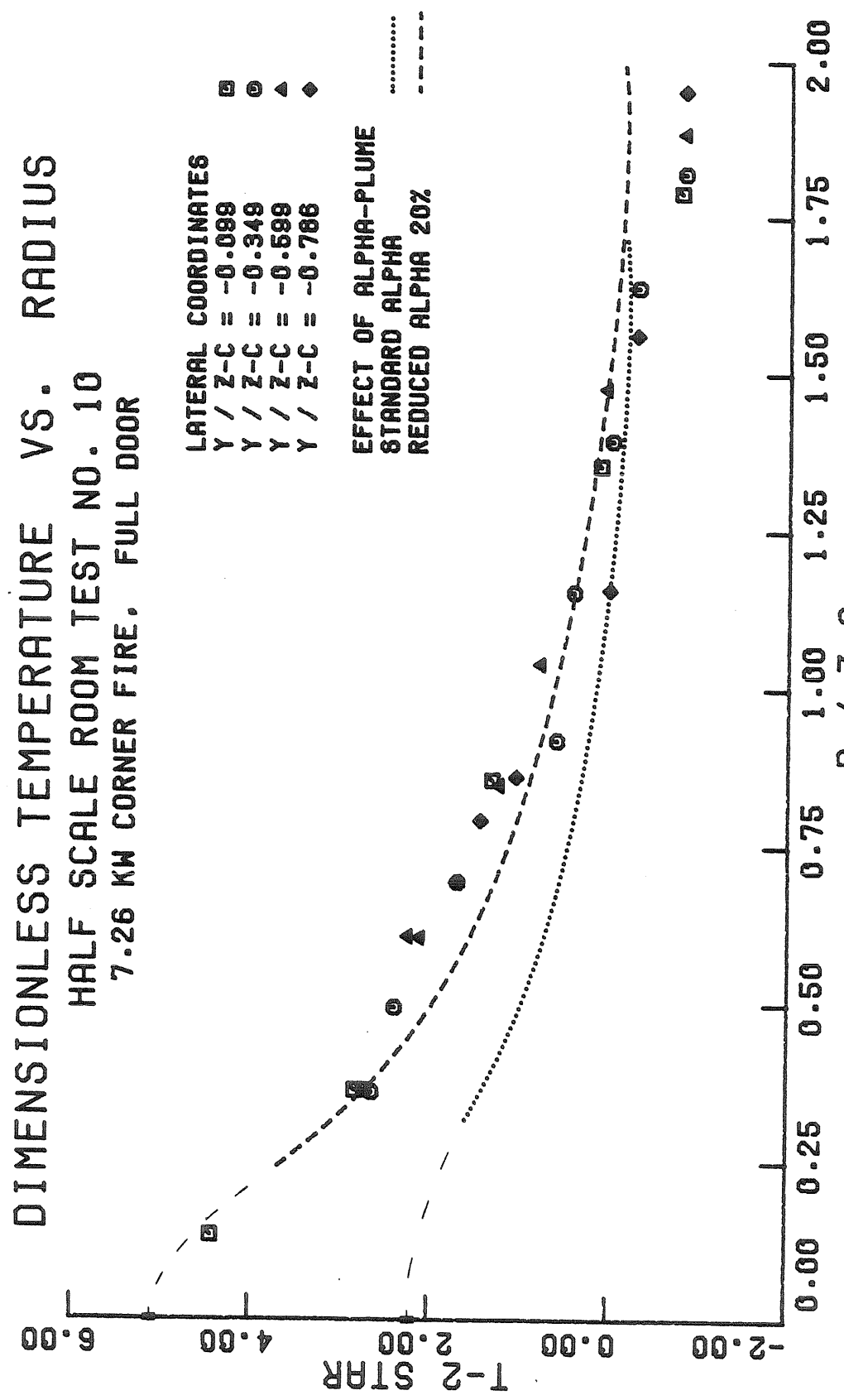

Figure (9.32) Dimensionless Gas Temperature Difference for a Corner Fire Test, Demonstrating the Reduction in Plume Entrainment.

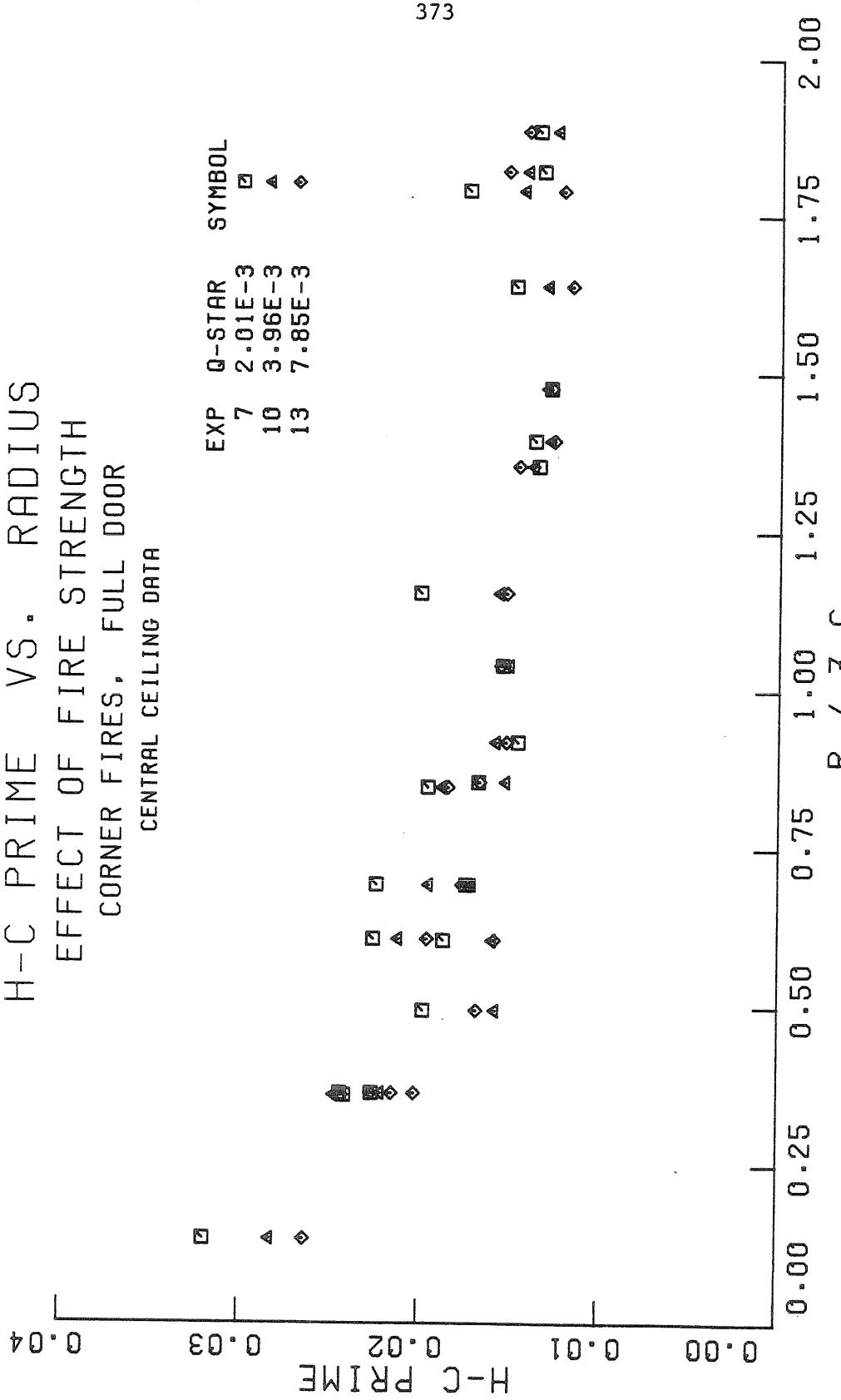

Figure (9.33) Effect of Q* on Dimensionless Heat Transfer Coefficient Data.

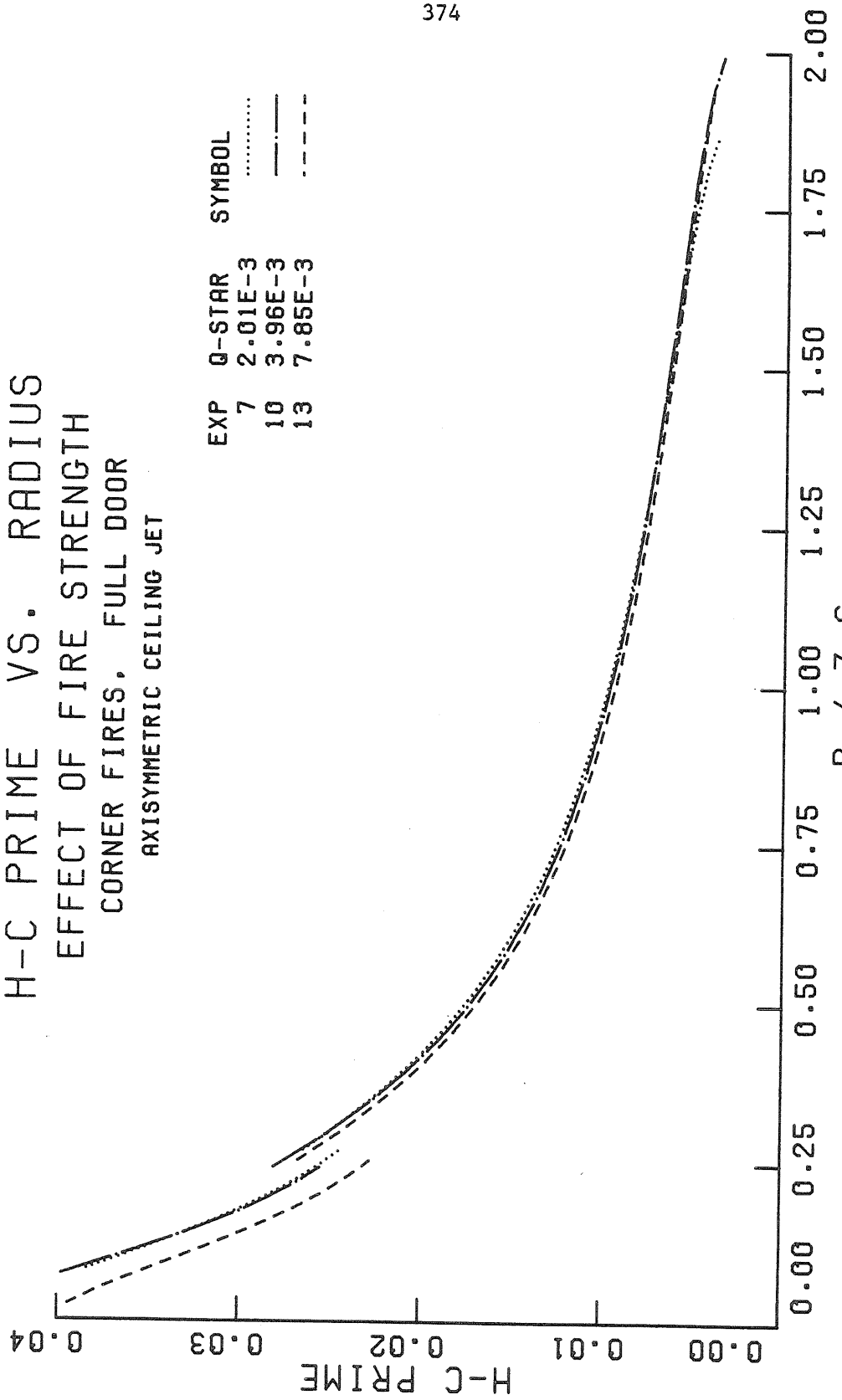

Figure (9.34) Effect of Q* on Axisymmetric Dimensionless Heat Transfer Coefficient Calculations.

upper layer temperature, increased by only 17% between experiments 7 and 13. So although the change is not as large as it might seem on first glance, our calculation procedures do accurately reflect the 34% increase in the actual heat transfer coefficient between these experiments (see Table (9.5)), and our choice of normalizing factors for the dimensionless heat transfer coefficient h_c' results in a curve which is independent of dimensionless heat input in the ceiling jet region. Near the fire, however, the dimensionless heat transfer coefficient does fall approximately 17% as $Q^*_{z_c}$ increases. One would expect this trend because (z_c/d_o) falls as the burner diameter d_o increases with larger fire size, and this results in smaller plume turbulence intensity and hence smaller heat transfer coefficients.

Similarly, Figure (9.35) demonstrates that the door geometry has only a slight effect on the dimensionless heat transfer coefficient distribution for the ceiling, with the case of the window (test 16) having approximately 8% greater h_c' values than the door (test 15). We believe that the large scatter of h_c' values at $\bar{r} = 0.25$ in the case of the window is caused by the deviation of the plume from the fire axis ($\bar{r} = 0$), which also explains the apparently low value of the stagnation point heat transfer coefficient. This trend toward larger dimensionless heat transfer coefficients for the window test is also seen in the west sidewall h_c' data. It is also clearly demonstrated in Figure (9.36) which shows the axisymmetric ceiling jet calculations for these two cases. The two-dimensional calculations are entirely analogous. It is interesting to note that the calculated actual heat transfer coefficients for these two tests are almost identical but that the normalizing factor for experiment

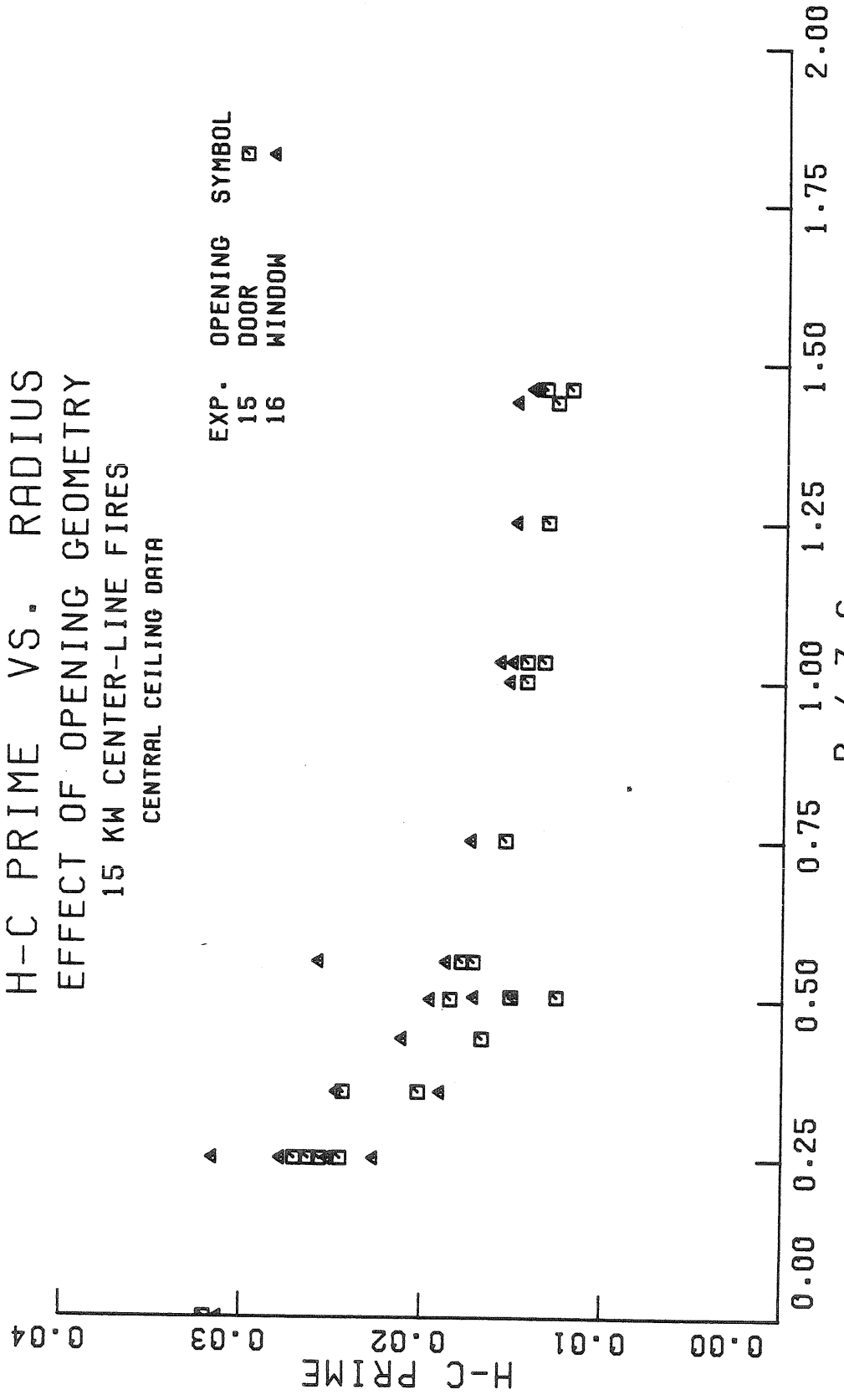

Figure (9.35) Effect of Opening Geometry on the Dimensionless Heat Transfer Coefficient Data.

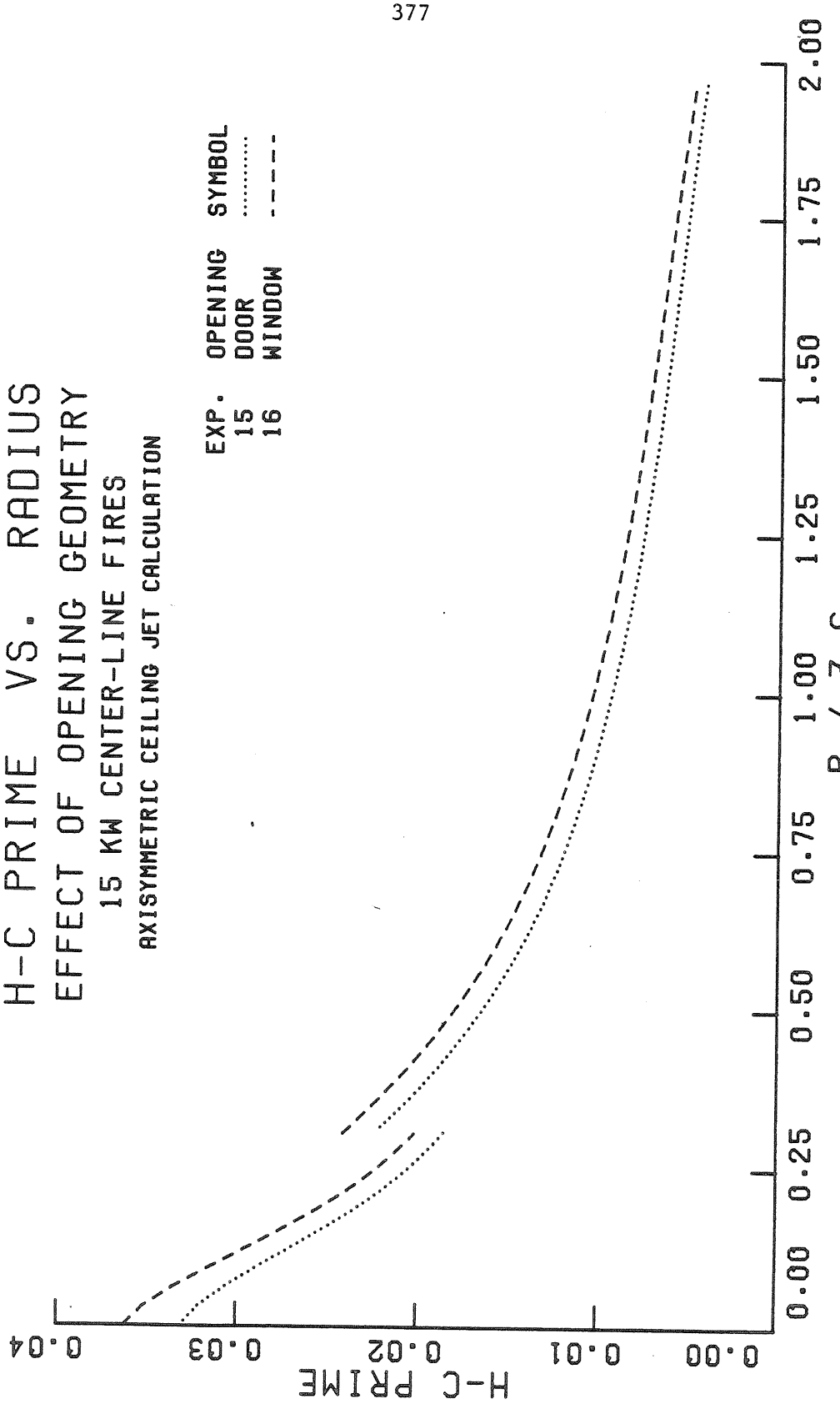

Figure (9.36) Effect of Opening Geometry on the Axisymmetric Dimensionless Heat Transfer Coefficient Calculation.

16 is 8% smaller than the value for experiment 15. This is a reflection of the difference in the buoyancy of the plume as it rises through the hot upper layer, and is not taken into account by the simple plume normalizing factors which assume constant buoyancy ($c_q = 0$).

The third and final experimental parameter at our disposal, the location of the fire, also has only a small effect on the dimensionless heat transfer coefficient distributions shown in Figure (9.37), with the data from the corner fire test having a smaller decrease with $\bar{r}$, typical of a two-dimensional flow. The computed values of h_c' from both the axisymmetric and two-dimensional ceiling jet calculations for these two experiments are reasonably close to each other over most of the ceiling jet region. The main difference in the calculations is the smaller initial ceiling jet radius $\bar{r}_e$ for the corner fire test number 13 because of the reduction in plume entrainment. Although the fire location does not alter the dimensionless ceiling heat transfer coefficient distribution significantly, it does affect the h_c' distribution on the west sidewall, which is one of the two sidewalls nearest the fire. This difference is depicted in Figure (9.38). Although the range of the h_c' values for these two experiments is comparable, when the fire is located in the southwest corner (test 13) the $\bar{r}'$ range is not as compressed as it is for a fire on the center line of the room (test 15), and looks more like the ceiling distribution. One would expect that for a plume rising in a corner, the flow pattern should be nearly symmetrical on the ceiling and sidewalls, provided the buoyancy of the wall jet is not too large. Indeed, as shown by Figure (9.39) this appears to be the case. Here the ceiling and sidewall h_c' data for the corner fire test have roughly the

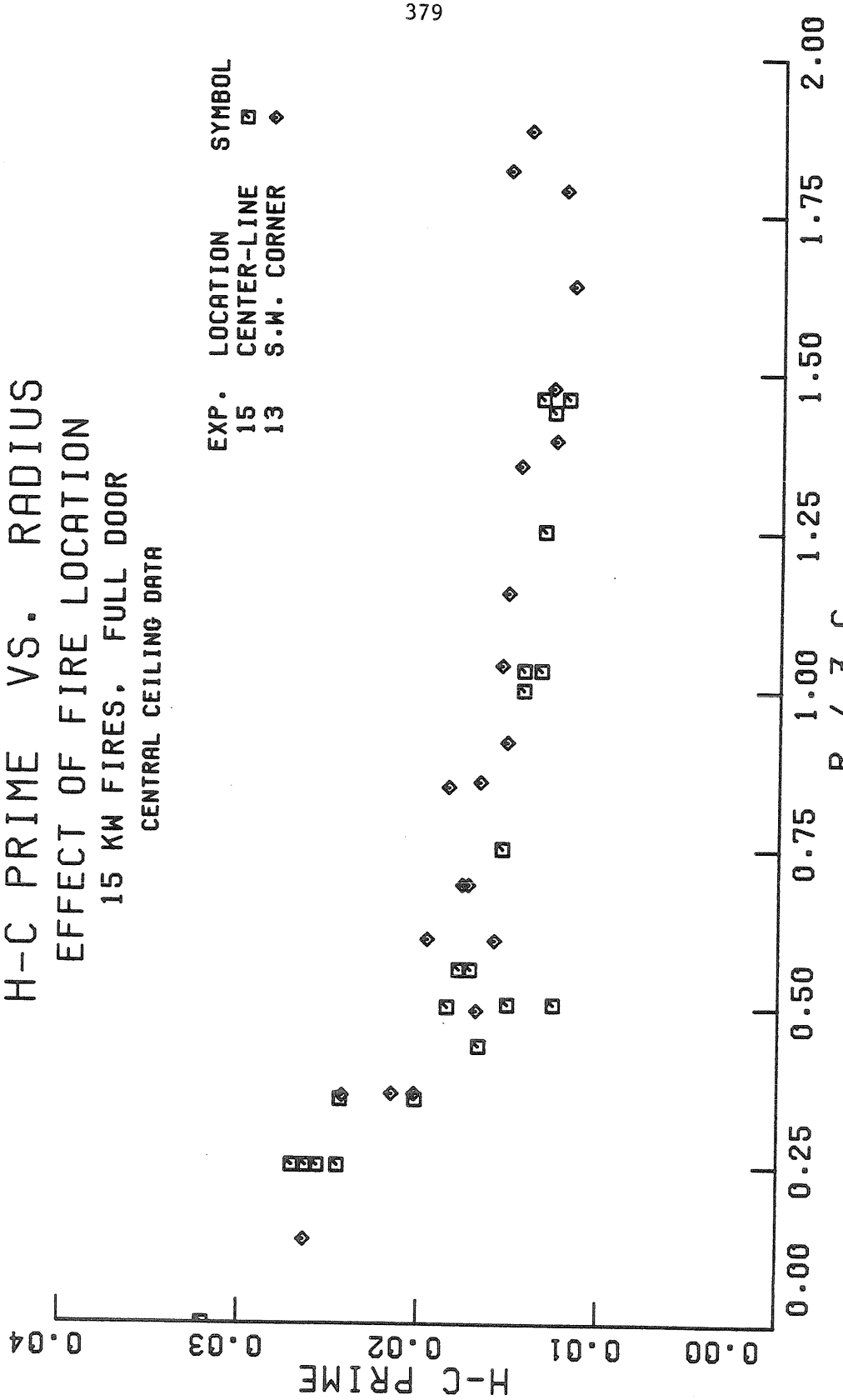

Figure (9.37) Effect of Fire Location on Dimensionless Ceiling Heat Transfer Coefficient Data.

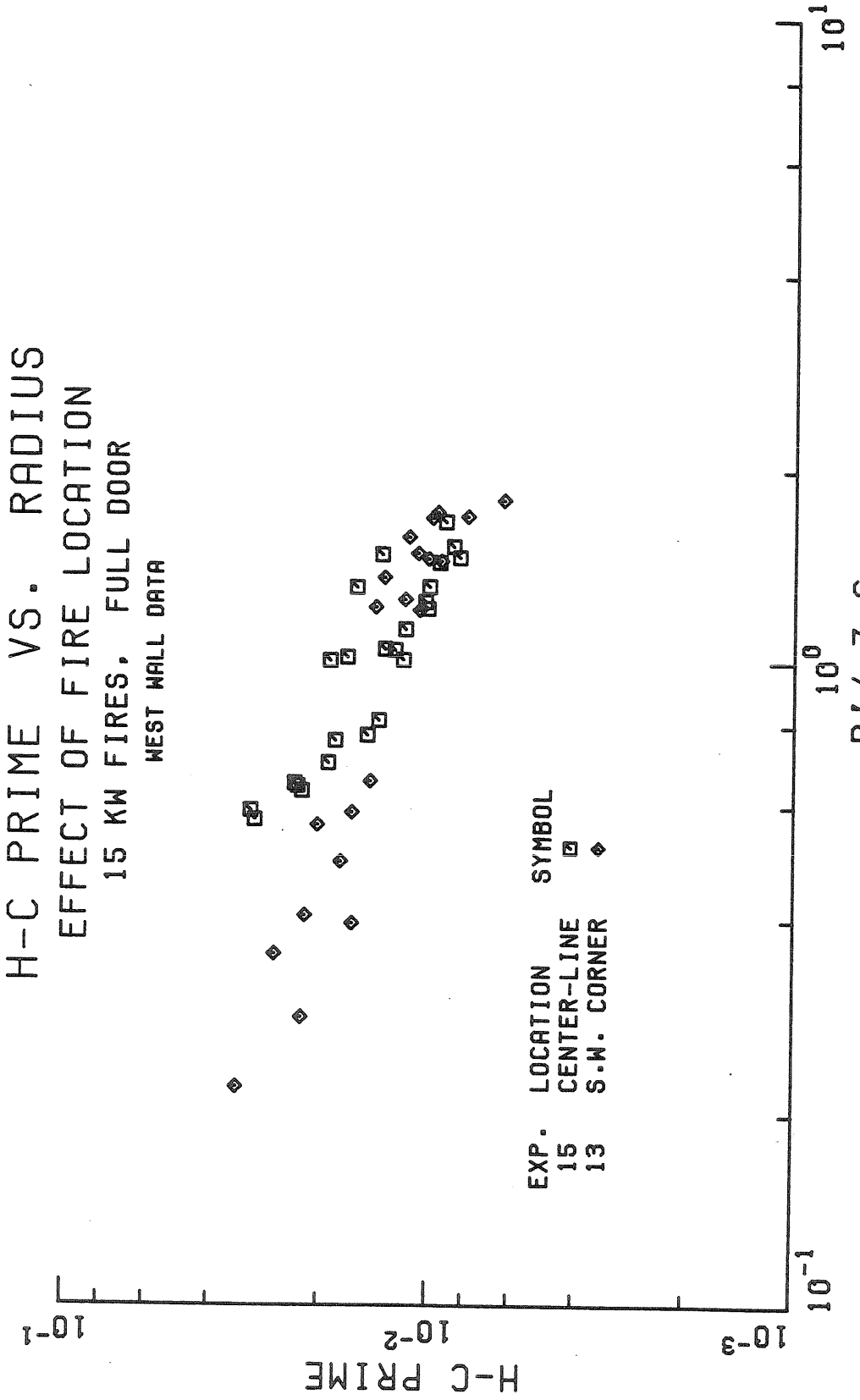

Figure (9.38) Effect of Fire Location on Dimensionless West Wall Heat Transfer Coefficient Data.

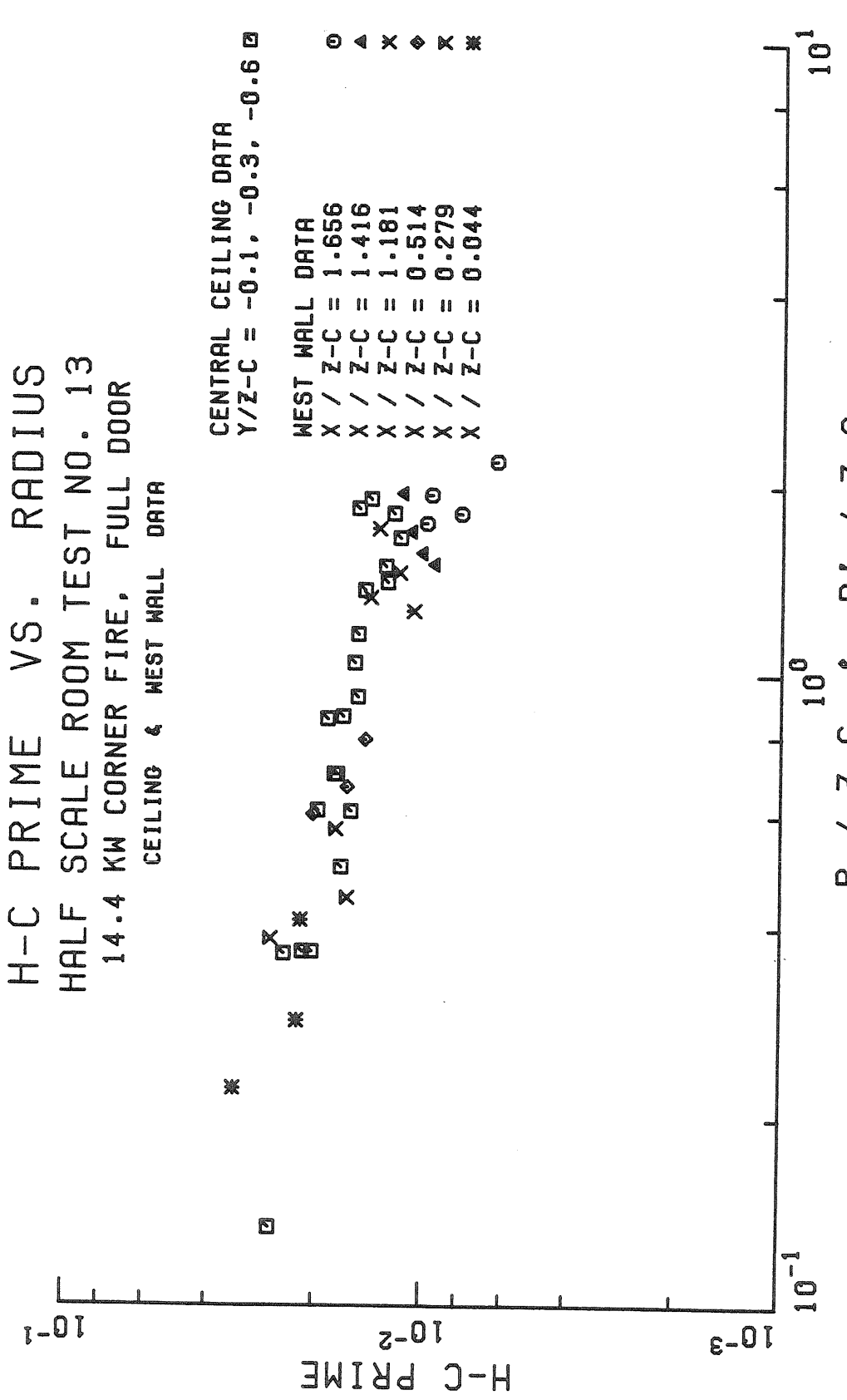

Figure (9.39) Dimensionless Ceiling and West Wall Heat Transfer Coefficient Data for a Corner Fire, Exp. 13.

same slope, with the ceiling distribution becoming slightly flatter as the flow pattern develops a more two-dimensional nature. For engineering calculations, one could approximate this corner fire data with the power law expressions:

$$h_{c_{s.w.}}' = 1.35 \times 10^{-2} \quad (\bar{r}')^{-0.59} \tag{9.18}$$

for the side walls, and

$$h'_{c_{ceiling}} = 1.55 \times 10^{-2} \quad (\bar{r})^{-0.27} \tag{9.19}$$

for the ceiling.

9.6.2 Dimensionless Ceiling Jet Temperature Difference

The buoyancy of the ceiling jet relative to the hot gas in the upper layer (at a mean temperature $\bar{T}_2$) is given by the dimensionless temperature difference T_2^*. Although one would expect the heat transfer coefficient to scale with the simple plume quantities, it is not clear that the local maximum gas temperature will do so as well, because changes in $\bar{T}_2$ and in the wall temperature directly affect it and these latter quantities do not necessarily scale like the plume. However, as we have seen the temperature difference between the upper and lower layers ($\bar{T}_2 - \bar{T}_1$) does correlate roughly with $T_o (Q_{z_c}^*)^{2/3}$, and for small dimensionless heat transfer coefficients ($h_c' << 1$) one would expect that the ceiling jet gas temperature would be more sensitive to the initial enthalpy delivered by the plume and to the temperature of the upper layer air which it entrains than to the actual ceiling surface temperature, at least for small to moderate distances. This approach appears to be verified in Figure (9.40), which shows that the variation in T_2^* as $Q_{z_c}^*$

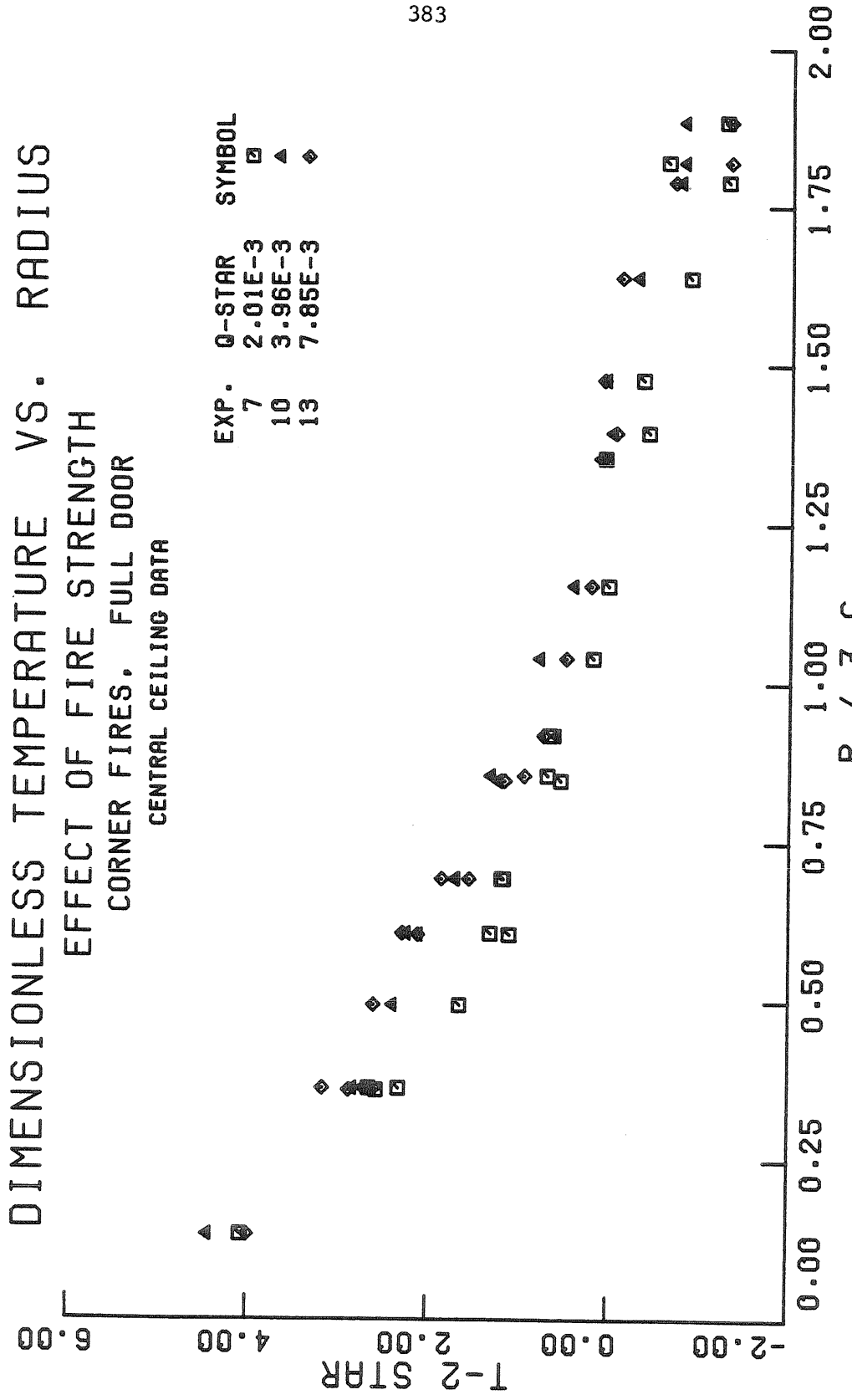

Figure (9.40) Effect of Q* on the Dimensionless Gas Temperature Difference Data.

changes by a factor of 3.9 is roughly the same as the inherent scatter in the data. Similarly, the calculated temperature curves for the axisymmetric ceiling jets shown in Figure (9.41) are all very close with no consistent trends apparent as $Q^*_{z_c}$ increases. It is also interesting to observe that the ceiling jet buoyancy (measured by T_2^*) drops to zero near $\bar{r} = 1.25$ in Figure (9.40) and the ceiling jet appears to become negatively buoyant near the far (north) end wall ($\bar{r} = 1.5$). Finally, the dimensionless gas temperature difference on the west side wall also appears to be invariant with this nearly four fold change in $Q^*_{z_c}$.

As we have seen in Chapter VII, changing the door geometry from a door to a window can result in significant increases in the temperatures of both the lower and upper layers measured by $\bar{T}_1$ and $\bar{T}_2$, respectively. Consequently, T_2^* for the window geometry is greater than for the door, even though $Q^*_{z_c}$ is constant. This effect is most pronounced near the stagnation point, as shown by the data in Figure (9.42). The calculated axisymmetric ceiling jet values of T_2^* for these two experiments, displayed in Figure (9.43), demonstrate this effect more clearly, with both curves approaching the common limit of no temperature difference ($T_2^* = 0$) as $\bar{r}$ increases. Again, the sidewall temperature data exhibit the same behavior as the ceiling T_2^* data, with the window test having larger T_2^* values than the door test.

Finally, the fire location does not seem to radically alter the T_2^* distribution, as shown in Figure (9.44) where we have replotted the data from experiments 13 and 15. Note that the corner fire data (experiment 13) are roughly 20% greater than the center-line fire data for small and

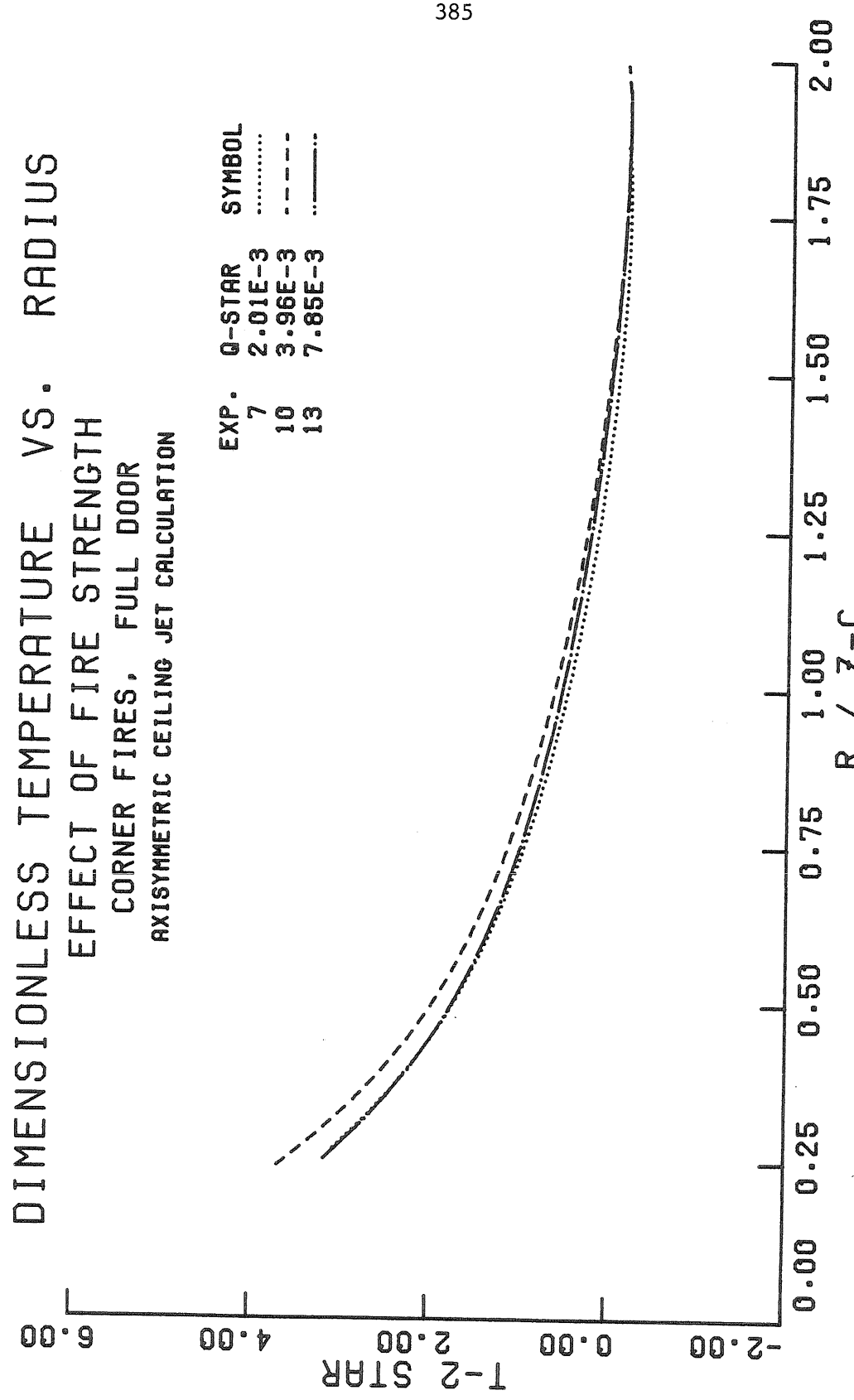

Figure (9.41) Effect of Q* on the Calculated Dimensionless Gas Temperature Difference.

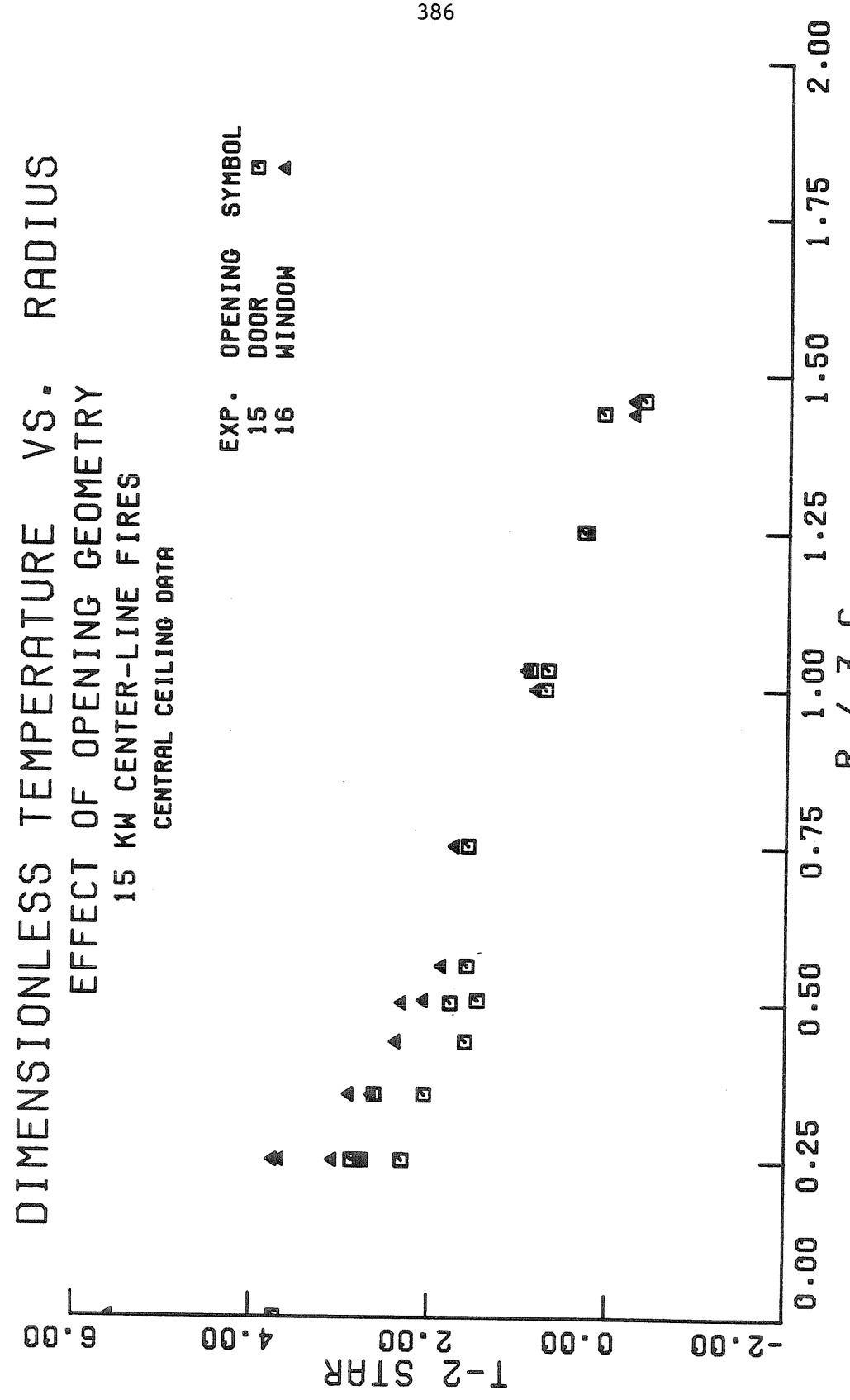

Figure (9.42) Effect of Opening Geometry on the Dimensionless Gas Temperature Difference Data.

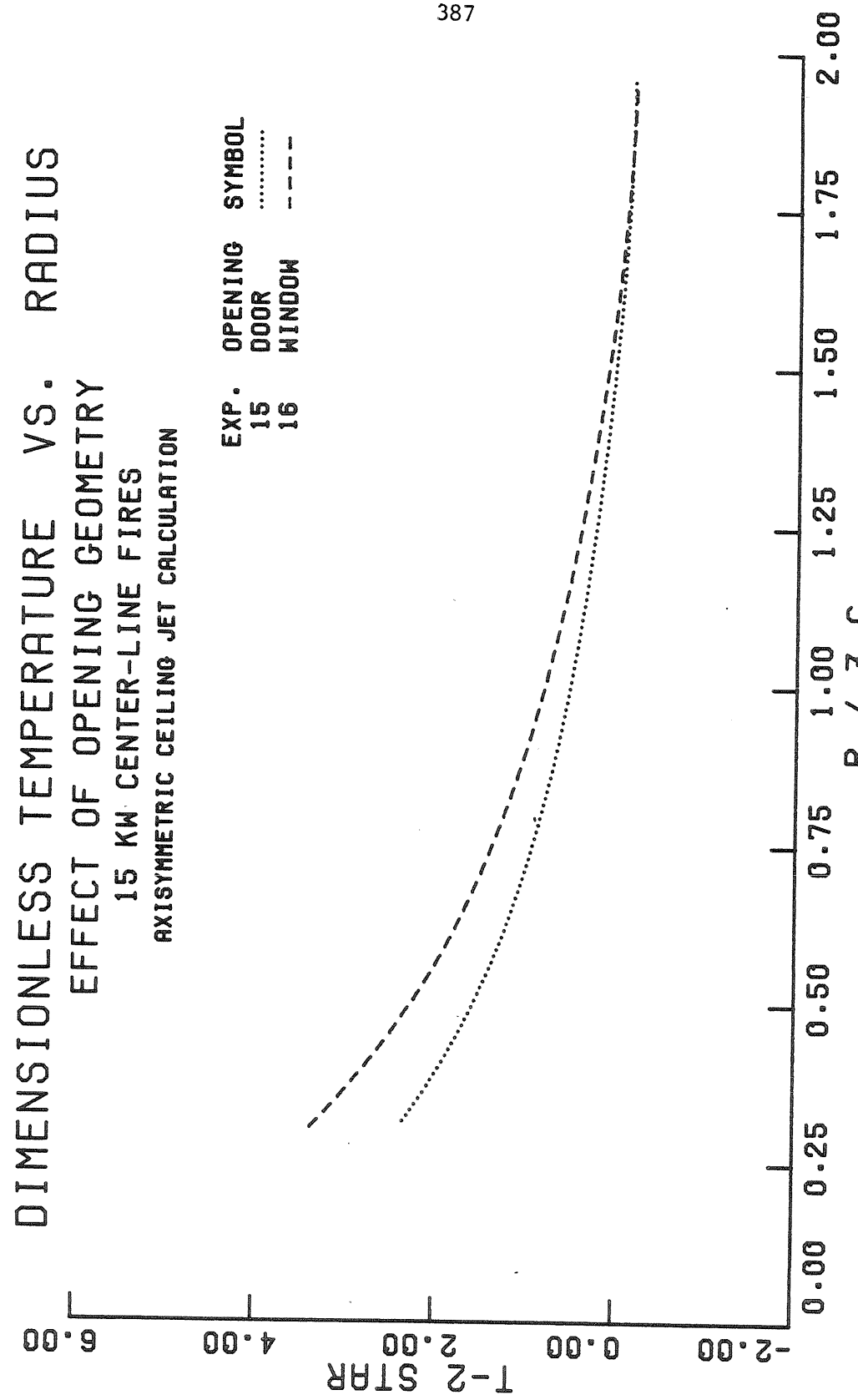

Figure (9.43) Effect of Opening Geometry on the Calculated Dimensionless Gas Temperature Difference.

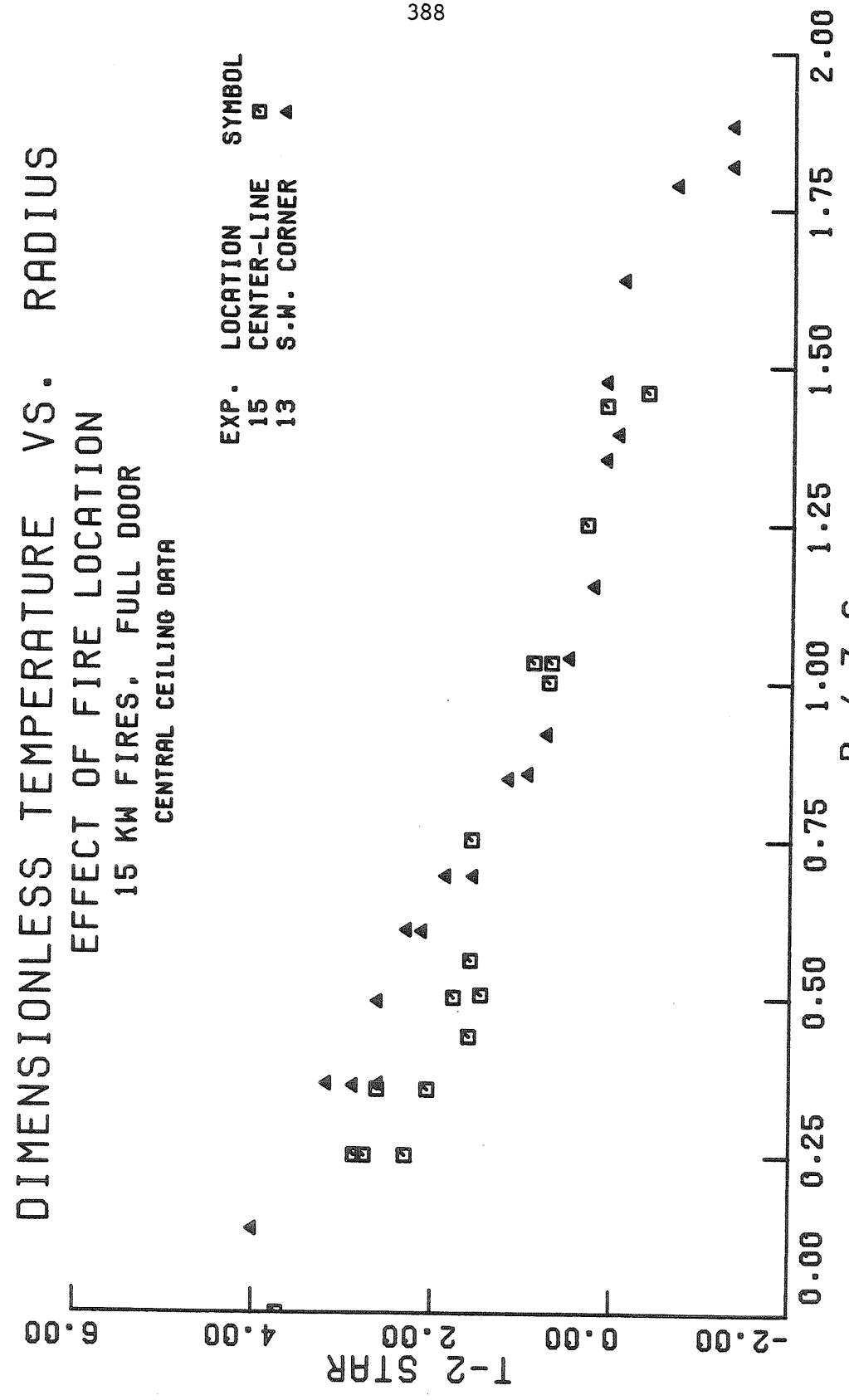

Figure (9.44) Effect of Fire Location on the Dimensionless Gas Temperature Difference Data.

moderate radii. This increase is partially due to the restriction of the plume's entrainment caused by the close proximity of the side walls. Based on measured gas temperatures near the stagnation point, we estimate that the plume entrainment coefficient is reduced approximately 20%. The axisymmetric calculations presented in Figure (9.45) show that this reduction in the plume's entrainment results in an initially hotter ceiling jet which starts at a smaller radius.

The sidewall temperature data, displayed in Figure (9.46), exhibit the same general features as the sidewall heat transfer coefficient data. Because of the symmetry when the fire is located in the corner, the side wall T_2^* data of experiment 13 are almost identical to the ceiling T_2^* data. On the other hand, when the fire is located on the major axis of the room, the gas must flow along the ceiling before impinging on the sidewall. It is interesting to note that this impingement process, which will be strongest along the back half of the west wall ($\frac{1}{2} \leq \bar{r}' \leq \frac{\sqrt{2}}{2}$), produces an almost uniform temperature in this region of the sidewall and is identical to the measured ceiling jet temperature at the same distance ($\bar{r}' \sim 0.6$). It is also interesting to note that the measured heat transfer coefficient at this location ($\bar{r}' \sim 0.6$) in Figure (9.30A) is very nearly equal to the value of the stagnation point heat transfer coefficient, even though the gas temperature has decreased significantly from its stagnation point value. On the other hand, when the fire is located in the corner, the plume impinges at a point ($\bar{r} = \bar{r}' = 0$), rather than along a line, and the west wall T_2^* data decline monotonically.

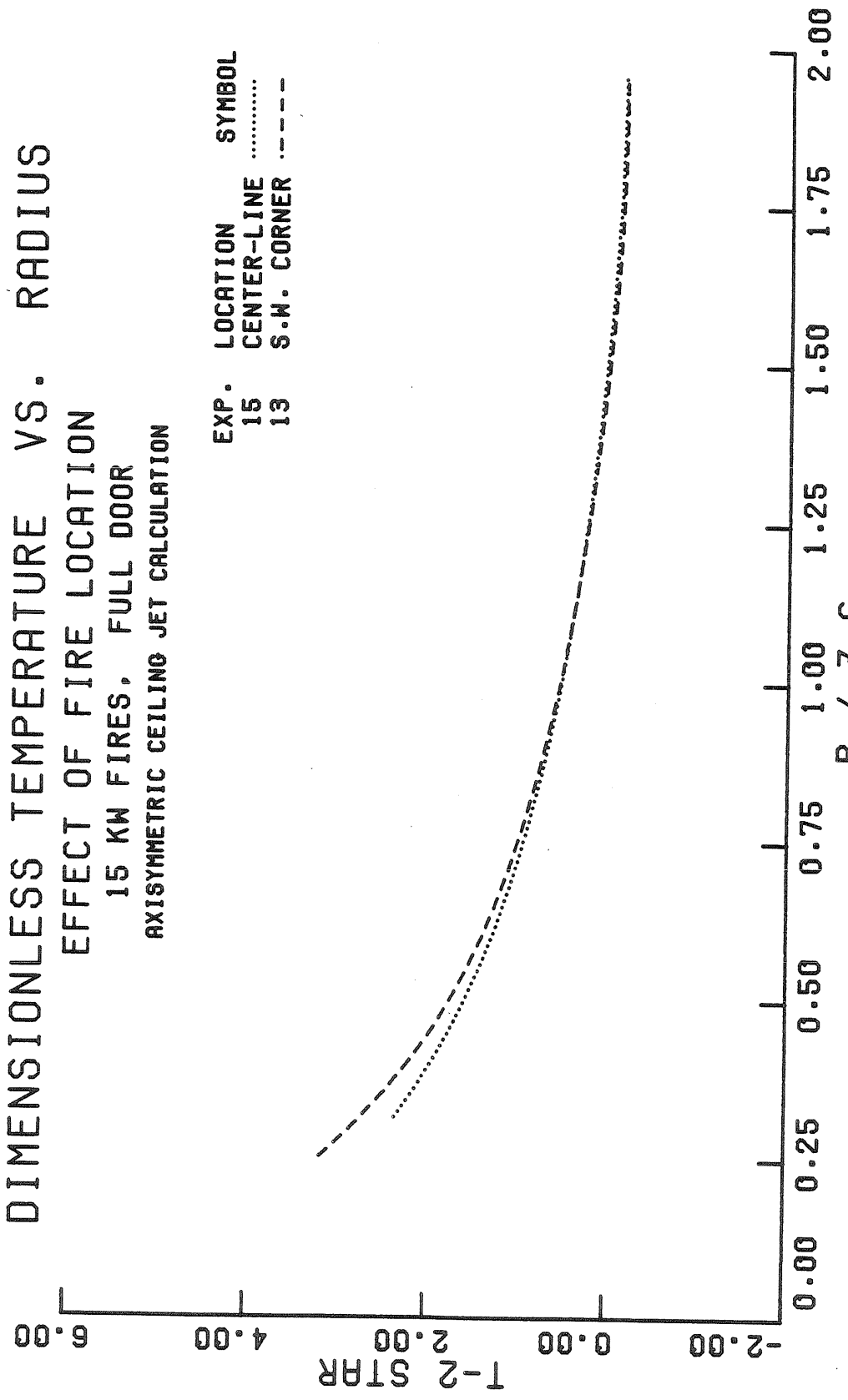

Figure (9.45) Effect of Fire Location on the Calculated Dimensionless Gas Temperature Difference.

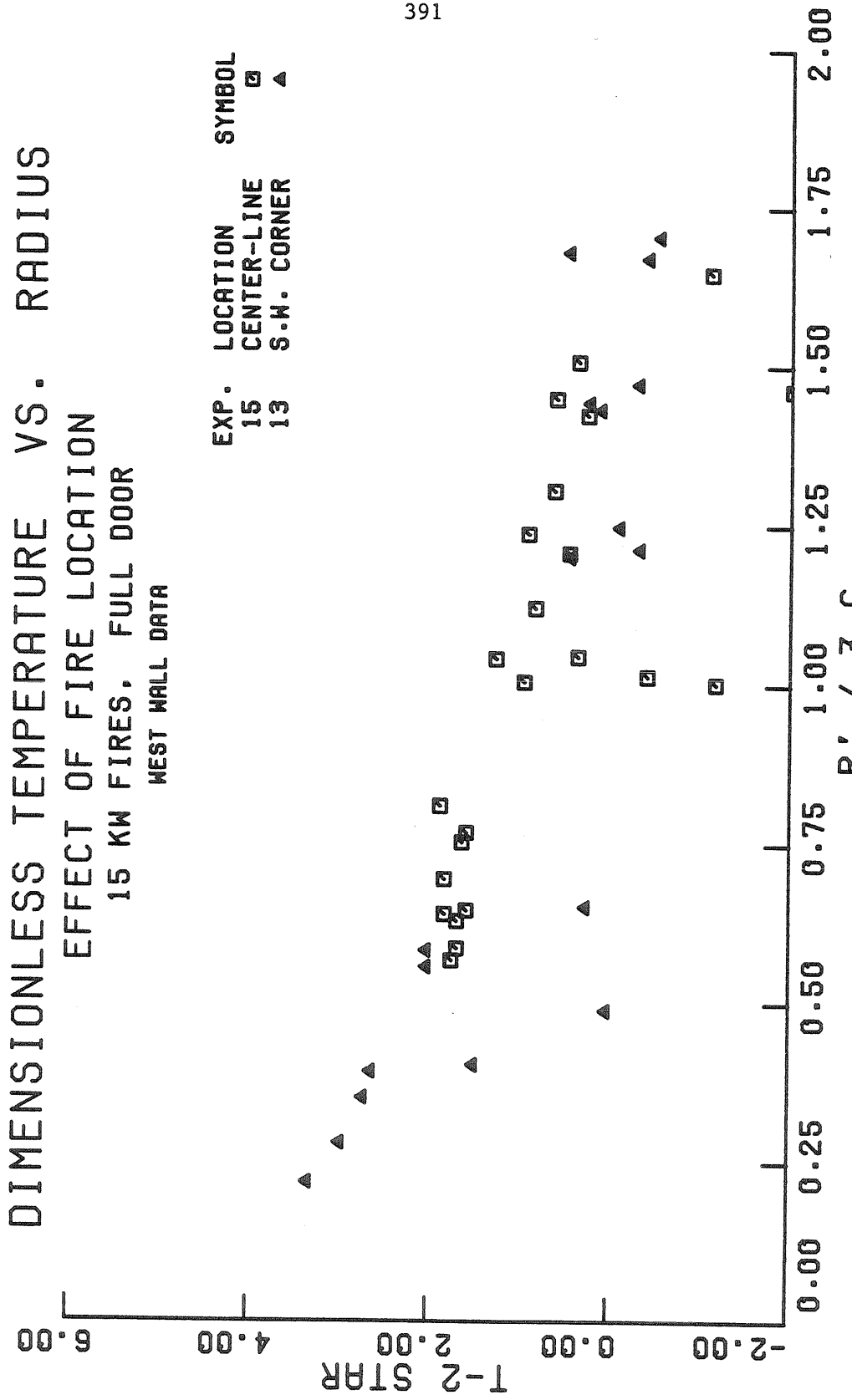

Figure (9.46) Effect of Fire Location on the Dimensionless West Wall Gas Temperature Difference Data.

9.6.3 Dimensionless Gas-Wall Temperature Difference

As previously described, the local convective heat transfer rate is given by the product of the heat transfer coefficient and the difference between maximum gas temperature and the ceiling temperature. We know how the heat transfer coefficient scales with $Q^*_{z_c}$. Can anything be said about the gas-wall temperature difference ΔT_{gw}?

We have seen that the gas temperature difference does scale like $T_o(Q^*_{z_c})^{2/3}$ for a given door or window geometry. On the other hand, the ceiling surface temperature T_w is determined by the intricate balance of the convective flux to the ceiling q^*_{conv}, the net radiant flux to the ceiling $q^*_{r,net}$, and the rate at which energy is conducted away from the surface q^*_{cond} ($q^*_{conv} = q^*_{cond} - q^*_{r,\,net}$). It is thus difficult to formulate a simple relationship for the behavior of T_w because $q_{r,net}$ depends on the distribution of surface temperatures throughout the room, and q_{cond} is determined by details of the ceiling construction and, in our case, by the forced cooling on the outer surface of the ceiling.

If we simply assume that q_{cond} and $q_{r,net}$ are both proportional to $(T_o/T_z)\ (Q_F/z_c^2)$, then q^*_{conv} will automatically be invariant with respect to changes in Q^*. These assumptions seem reasonable for steady-state equilibrium conditions, and appear to be roughly valid as shown by the q^*_{cond} data in Figure (9.53) and the $q^*_{r,net}$ data in Figure (9.56). Consequently, the gas wall temperature difference ΔT_{gw} will be proportional to $T_o(Q^*_{z_c})^{2/3}$.

An alternative way of looking at this is given by rewriting the dimensionless variables given in Section (9.1):

$$T_1^* = \frac{T_{mg} - \bar{T}_1}{T_o (Q_{z_c}^*)^{2/3}} \approx f_2(\bar{r};\ q_{conv}^*) \tag{9.1}$$

$$h_c' = \frac{h_c}{\rho^2 c_p \sqrt{g z_c}\ (Q_{z_c}^*)^{1/3}} \approx f_3(\bar{r};\ q_{conv}^*) \tag{8.14}$$

$$q_{conv}^* = h_c'\ \Delta T_{gw}^* = \frac{h_c\ (T_{mg} - T_w)}{\left(\frac{T_o}{T_2}\right) \frac{Q_F}{z_c^2}} \approx f_4\ (\bar{r};\ q_{conv}^*,\ T_w) \tag{9.2}$$

When the dimensionless heat transfer coefficient is small ($h_c' << 1$), the ceiling jet flow is not closely coupled to the boundary conditions on the ceiling itself. Thus for sufficiently small dimensionless convective rates q_{conv}^*, we expect that the dimensionless gas temperature difference T^* and the dimensionless heat transfer coefficient h_c' will be functions (given by f_2 and f_3, respectively) primarily of the dimensionless distance along the ceiling $\bar{r}$. To make the same assumption regarding the dimensionless convection heat transfer rate (i.e., that f_4 is primarily a function of $\bar{r}$), we must also require that either T_w can be ignored ($\Delta T_{gw} >> T_w$) or that $\Delta T_{gw} \propto T_o (Q^*)^{2/3}$. The former requirement may be reasonable early in the fire's history before the ceiling has been heated appreciably, while the latter is equivalent to the steady-state equilibrium assumption which we just discussed. Substitution of equations (9.1) and (8.14) into (9.2) then yields:

$$T_w - \bar{T}_1 = T_o\ (Q_{z_c}^*)^{2/3} \left[f_2 - \frac{f_4}{f_3} \right] \tag{9.20}$$

where, under the requirements just described, the term in brackets will

basically depend on the dimensionless radius. The dimensionless gas-wall temperature difference is given by:

$$\Delta T^*_{gw} = \frac{T_{mg} - T_{wall}}{T_o \, (Q^*_{z_c})^{2/3}} = \frac{f_4}{f_3} \tag{9.21}$$

which indicates that ΔT^*_{gw} is primarily a function of $\bar{r}$. For the $Q^*_{z_c}$ range investigated in these experiments, the experimental ΔT^*_{gw} data presented in Figure (9.47) confirm that equation (9.21) is valid, given the scatter of the data. However, although T^* and h_c' are relatively independent of door geometry, ΔT^*_{gw} is not, as shown by the data in Figure (9.48), where we have plotted both the experimental ΔT^*_{gw} data and the axisymmetric ceiling jet calculations. This discrepancy between the two experiments is caused by the wall temperature distribution which, for fixed Q^*, does not change as fast as the temperature does when the door geometry is changed.

The wall temperature distribution is also a function of the temperature, flow rate, and the direction of the flow of the air in the cooling jackets, which are mounted on the outside of the ceiling and sidewalls. The air enters the ceiling cooling jacket at the south end farthest from the door and flows north towards the door. This pattern results in the smallest wall temperatures being located near the end farthest from the door, and causes the double-valued nature of the ΔT^*_{gw} curves for centerline fires seen in Figure (9.48). For corner fires, the maximum gas temperatures and the minimum wall temperatures both occur near the southern end of the test room, with the result that ΔT^*_{gw} has a maximum in this region. For fires located on the center line of the room, the

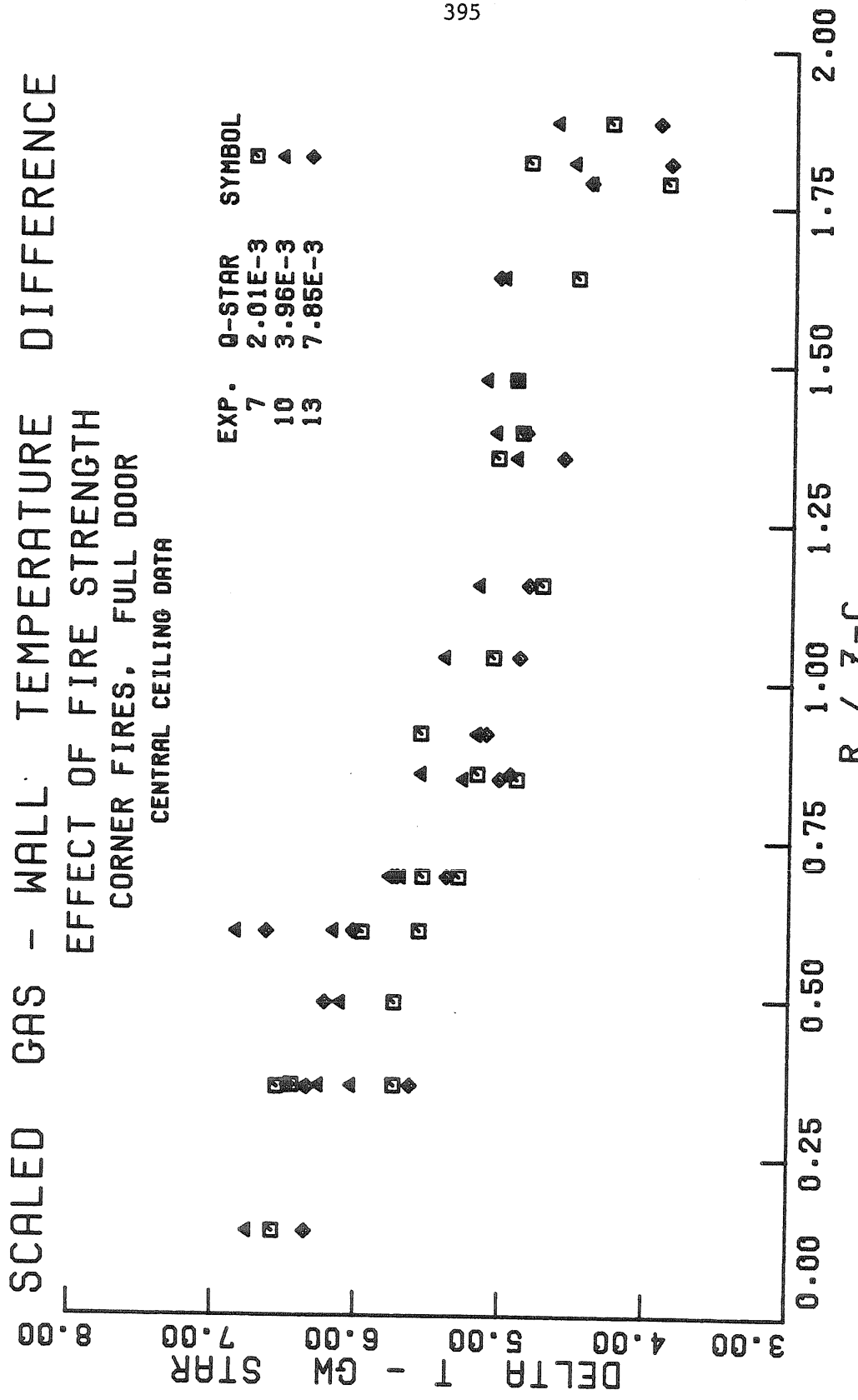

Figure (9.47) Effect of Q* on the Dimensionless Gas-Wall Temperature Difference.

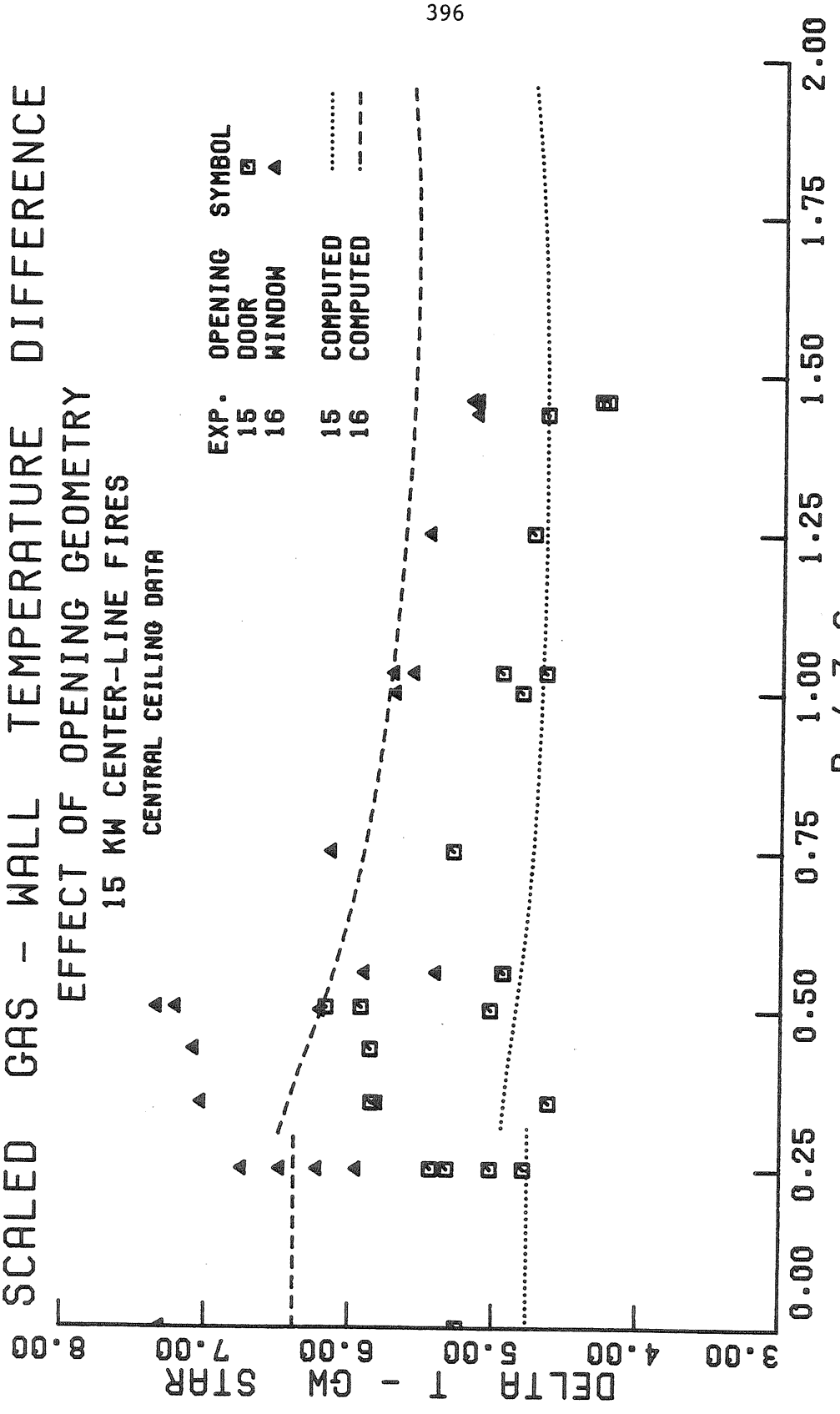

Figure (9.48) Effect of Opening Geometry on the Dimensionless Gas-Wall Temperature Difference (Data and Axisymmetric Calculations).

regions of maximum gas temperatures and maximum wall temperatures do not coincide, and ΔT^*_{gw} has a maximum value not at the stagnation point ($\bar{r} = 0$) but near the south end wall ($\bar{r} = 0.50$), behind the fire (as seen from the door).

To clarify this point, we have plotted both the measured ceiling surface temperatures and the empirical fit used by the ceiling jet calculations in Figure (9.49) for experiment 15. These surface temperatures are plotted relative to the mean upper layer gas temperature $\bar{T}_2$. They show that the ceiling is significantly colder than the gas and that the ceiling temperature behind the fire is less than it is in front of the fire at the same radial distance from the stagnation point.

Finally, it is interesting to note that the values of ΔT^*_{gw} are nearly twice as large as local gas temperature difference measured by T^*_2, indicating that despite the convective flux to it, the ceiling is considerably colder than the upper layer gas. In fact, ΔT^*_{gw} is roughly the mean of T^*_1 and T^*_2, which indicates that T_w is approximately midway between $\bar{T}_1$ and $\bar{T}_2$.

9.6.4 Dimensionless Convective Heat Transfer Rate

The dimensionless local convective heat transfer rate q^*_{conv} is the product of h_c', the dimensionless heat transfer coefficient and ΔT^*_{gw}, the dimensionless gas-wall temperature difference. Consequently, q^*_{conv} reflects some of the idiosyncrasies of its two component parts, which have already been discussed. For example, in Figure (9.50), which shows the effect of increasing the burner diameter d_o and hence the heat release, the tendency of the stagnation point heat transfer coefficient to fall approximately 17% with decreasing (z_c/d_o) manifests itself as a

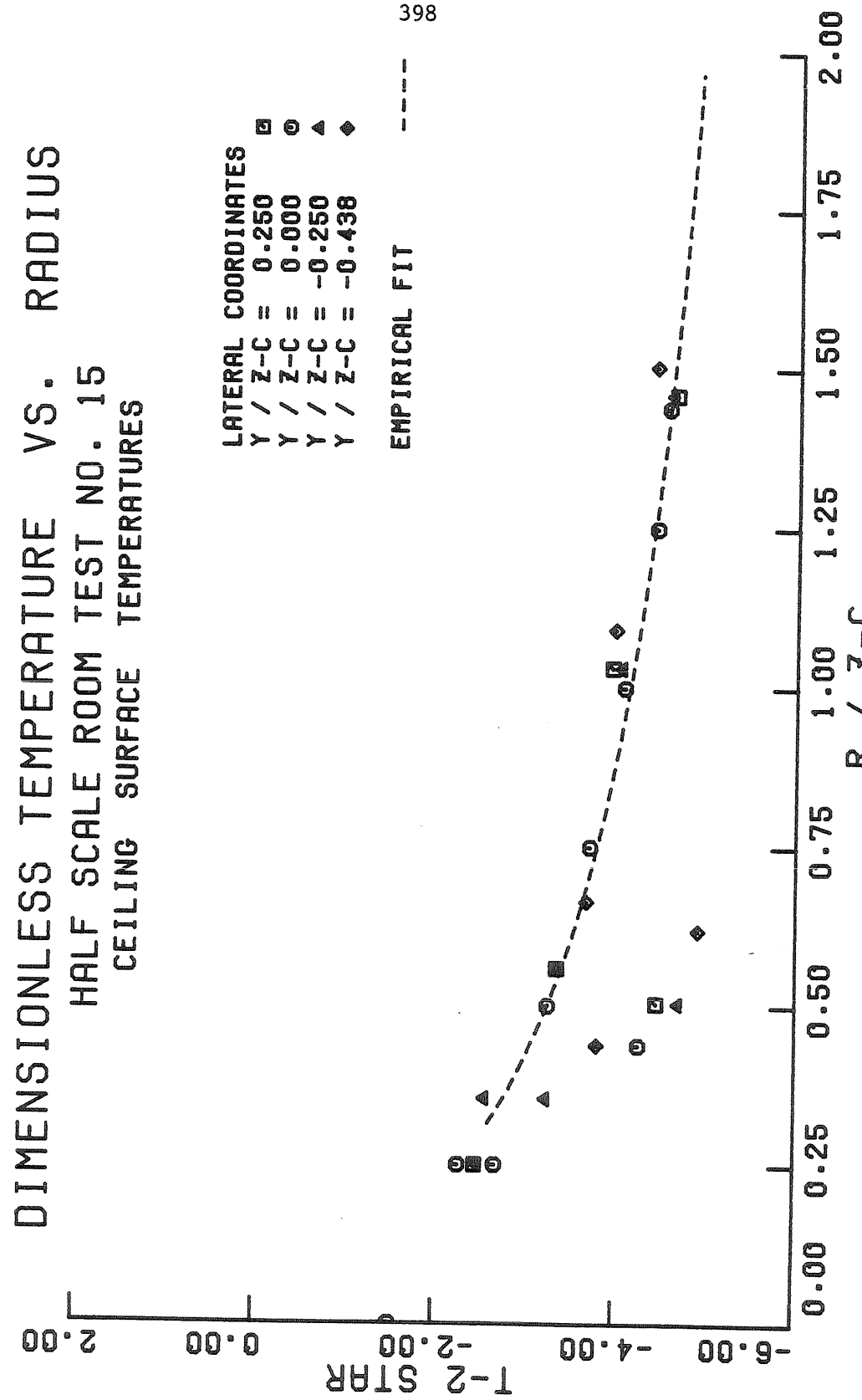

Figure (9.49) Dimensionless Ceiling Surface Temperature Difference Distribution.

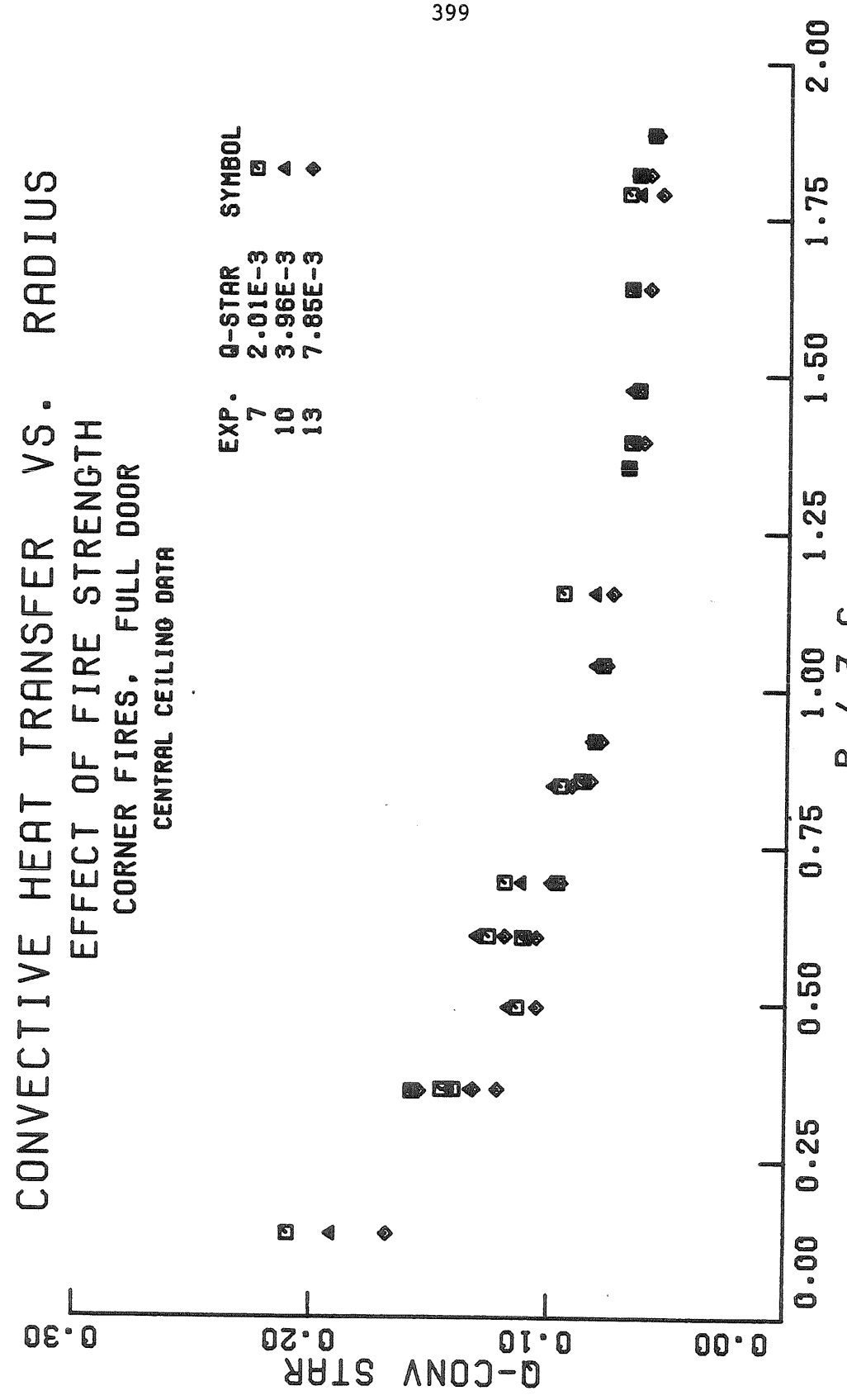

Figure (9.50) Effect of Q^* on the Dimensionless Convective Heat Transfer Rate.

family of q^*_{conv} curves which fall roughly 20% with increasing burner diameter. On the other hand, the heat transfer coefficient distribution is not strongly affected by the door geometry, while ΔT^*_{gw} is significantly greater for windows than it is for doors. As shown in Figure (9.51), where we have plotted both the data and axisymmetric calculations, this translates into a nearly 30% greater convective flux at the stagnation point for the window geometry. Finally, it is interesting to note that although both the heat transfer coefficient and the gas-wall temperature difference are functions of the fire location, Figure (9.52) shows that the convective flux is rather similar for corner and center-line fires with the corner fires having slightly larger q^*_{conv} values at small radii because of the reduction in the plume entrainment and consequent increase in the gas temperatures associated with these fires.

9.6.5 Dimensionless Conductive Heat Transfer Rate

The local conductive flux is given by the product of the measured temperature difference at a point in the ceiling or sidewalls $(T_w - T_{w_{out}})$ times the conductivity of the wall $(k_w = 0.245 \frac{W}{m\text{-}K})$ divided by the wall thickness $(\Delta_w = 1.27$ cm). It is made dimensionless by dividing by (T_o/T_2) (Q_F/z_c^2). Although we can make reasonable arguments regarding the gas temperature and heat transfer coefficient scaling for relatively small convective fluxes, it is difficult to advance similar schemes for the wall temperatures because they depend directly on this convective flux. In addition, they also directly depend on the details of the forced convection process which occurs in the cooling jackets. Nevertheless, we know that a large fraction of the convective flux will be conducted through the surface because we are cooling the back side of the ceiling

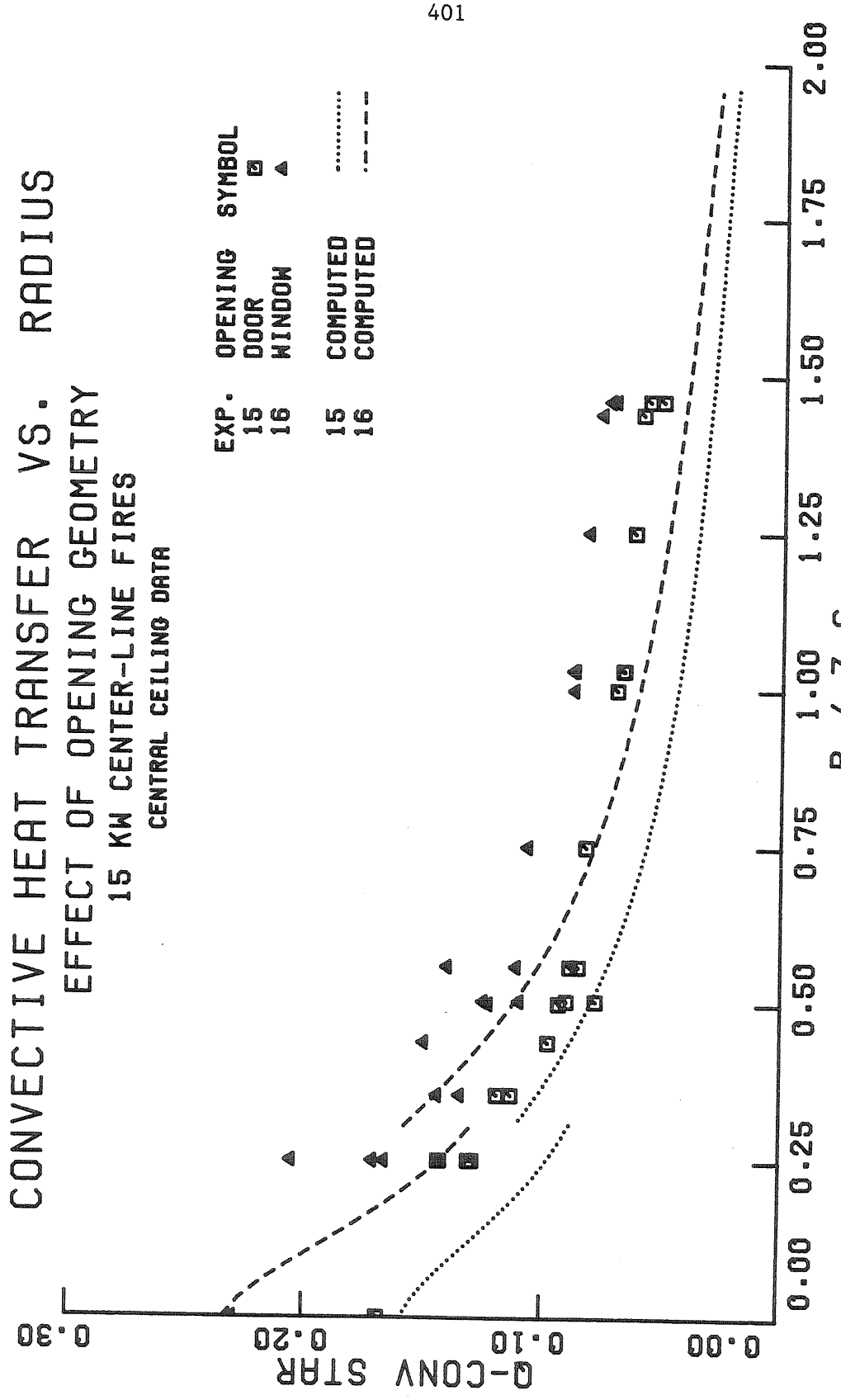

Figure (9.51) Effect of Opening Geometry on the Dimensionless Convective Heat Transfer Rate (Data and Axisymmetric Calculations).

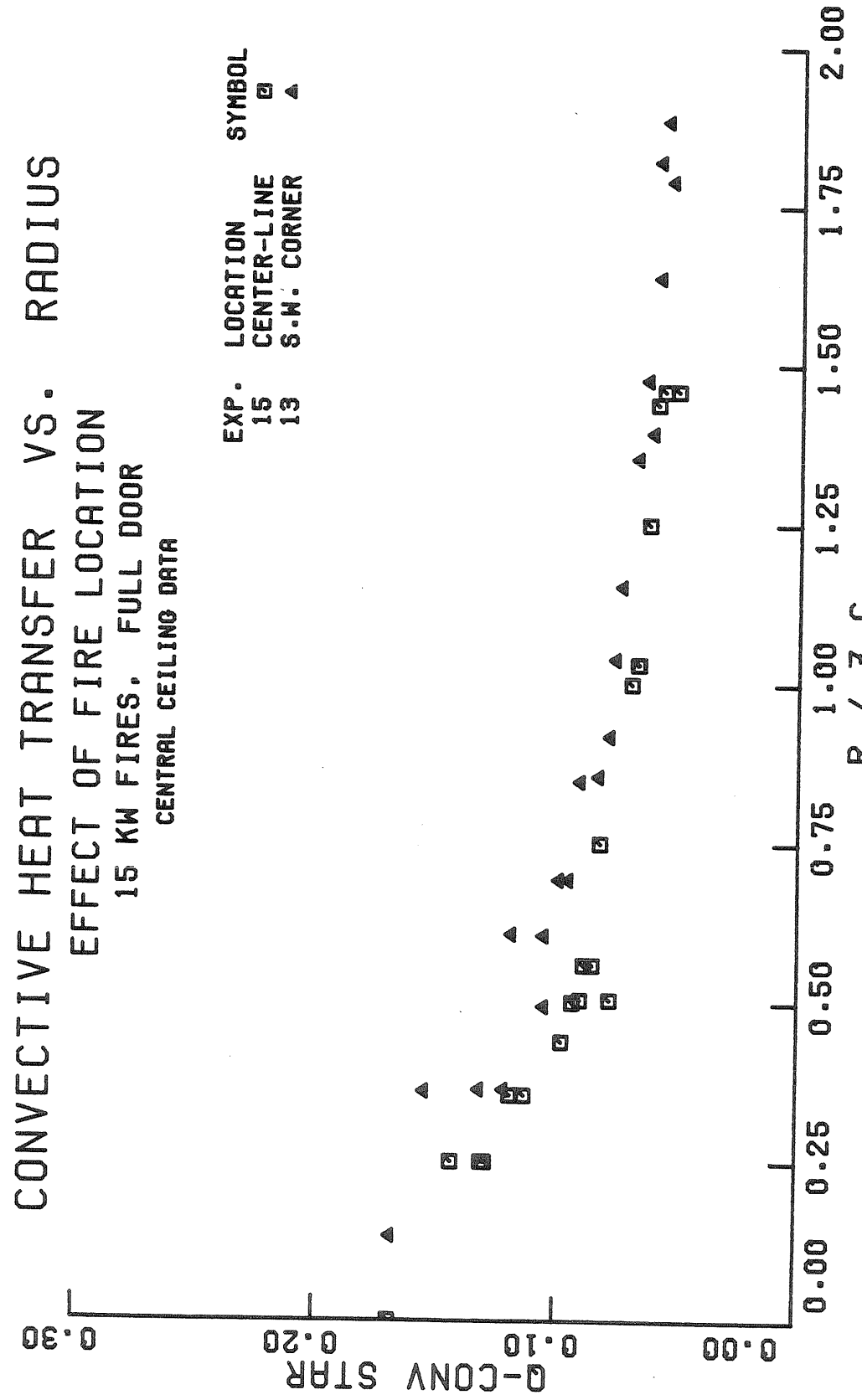

Figure (9.52) Effect of Fire Location on the Dimensionless Convective Heat Transfer Rate.

and side walls. Consequently, we expect that the dimensionless conductive flux will be proportional to the dimensionless convective flux. In Figure (9.53) this indeed appears to be the case with q^*_{cond} falling by roughly 14% as the burner diameter is doubled. Another factor complicating the wall temperature distribution is radiative transfer. As the convective flux to the ceiling increases and the surface temperature rises, the fraction of heat conducted through the surface drops as more of the incident convective flux is radiated away. This is why the q^*_{cond} curves in Figure (9.54), for the door and window geometries, appear closer together than do the corresponding q^*_{conv} curves. A similar effect explains why the corner fire in Figure (9.55) has greater q^*_{cond} values than does the center-line fire, while their q^*_{conv} curves are reasonably close. In this case, the ceiling near the corner "sees" the sidewalls in the sense that it receives a significant fraction of its incident radiant flux from them. When the fire is in the corner, these walls are almost as hot as the ceiling and the net radiative flux becomes small, which means a greater fraction of the convective flux will be conducted through the wall.

9.6.6 Dimensionless Radiative Heat Transfer

Because radiative heat transfer plays a significant role in our experiments, it seems reasonable to display the calculated net radiative flux for the three corner fires. Figure (9.56) shows that as $Q^*_{z_c}$ increases the dimensionless net radiative transfer does not change significantly. The fact that $q^*_{r,net}$ is negative indicates that the ceiling emits more radiant energy than it receives. These data are replotted in

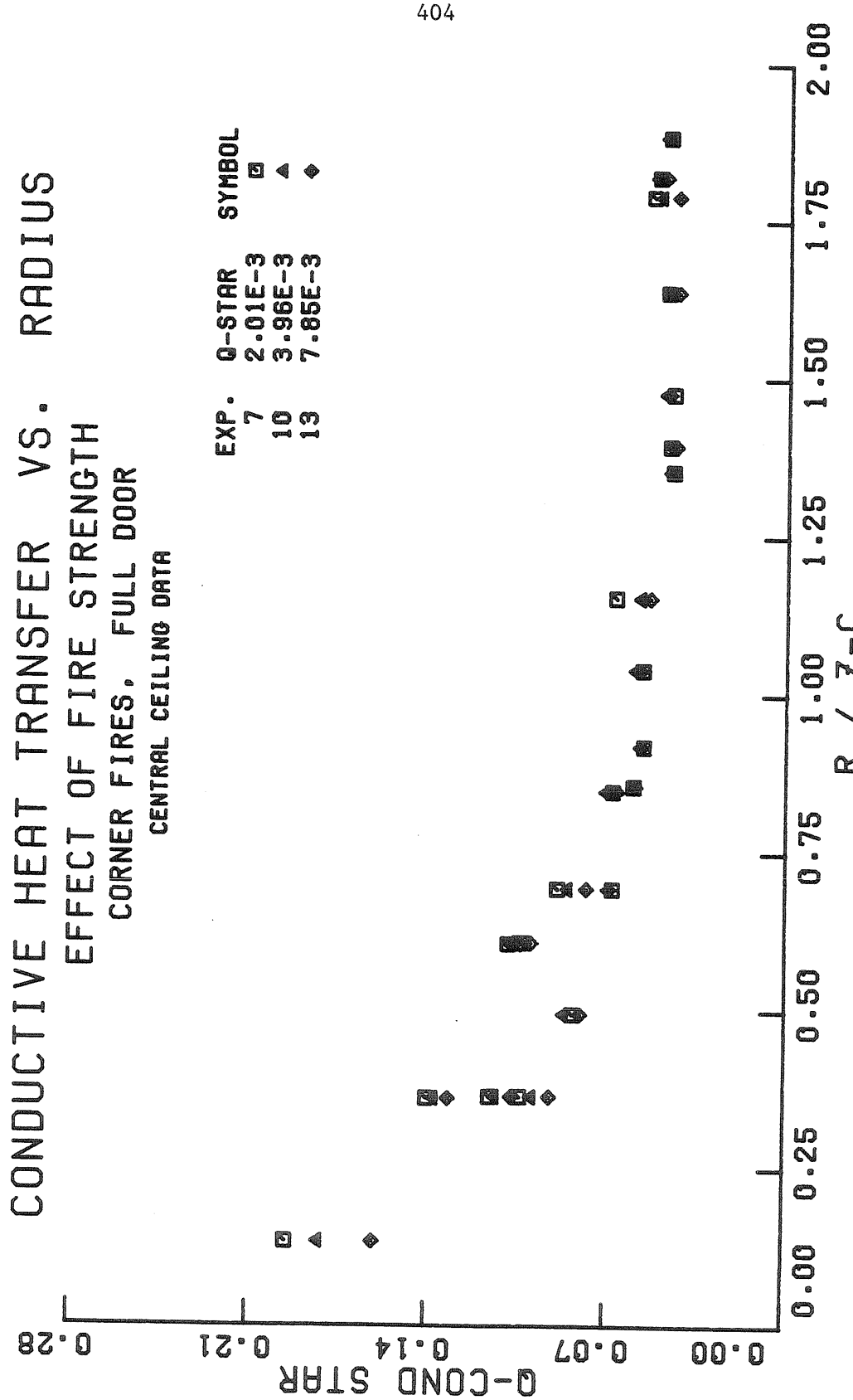

Figure (9.53) Effect of Q^* on the Dimensionless Conductive Heat Transfer Rate.

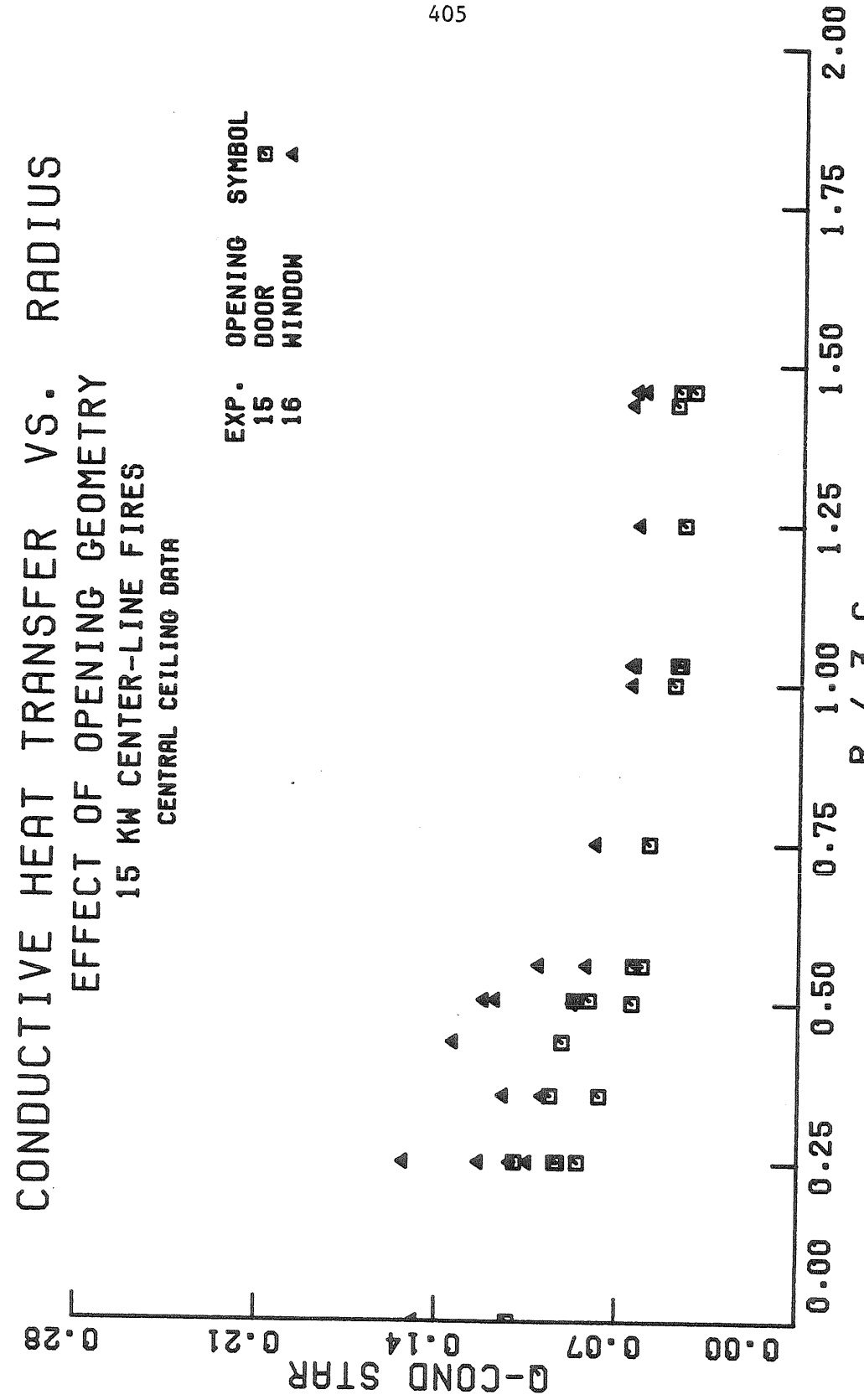

Figure (9.54) Effect of Opening Geometry on the Dimensionless Conductive Heat Transfer Rate.

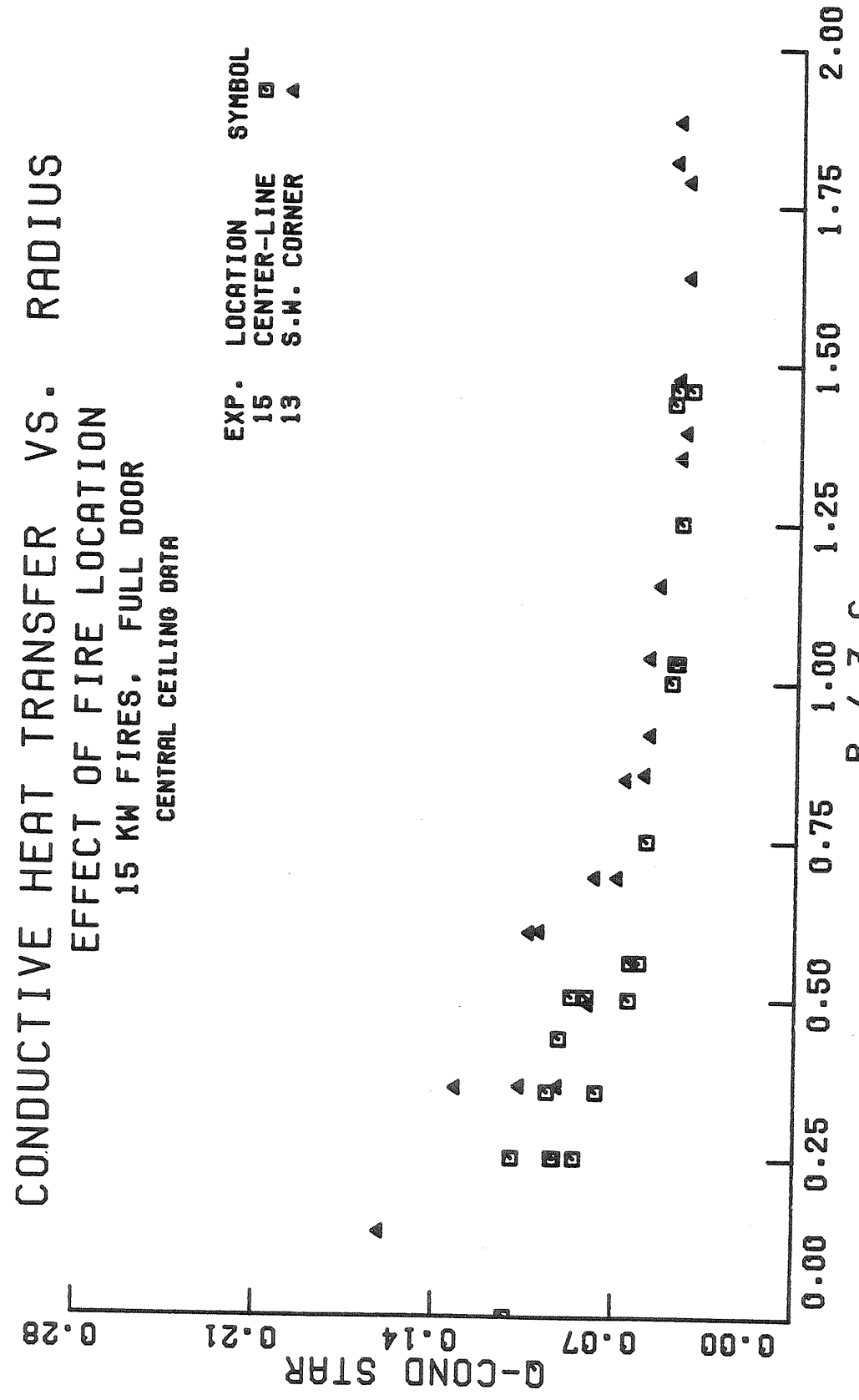

Figure (9.55) Effect of Fire Location on the Dimensionless Conductive Heat Transfer Rate.

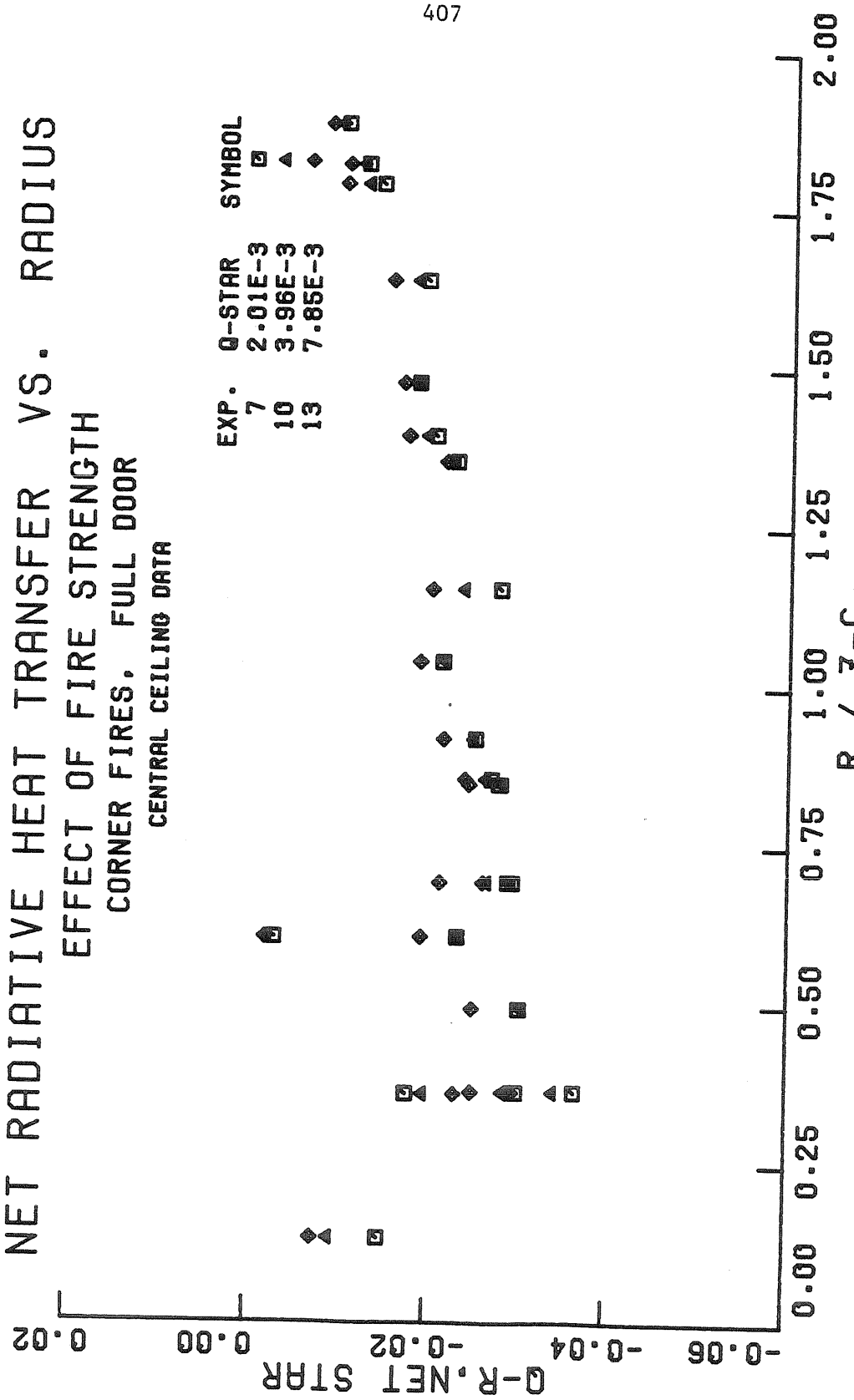

Figure (9.56) Effect of Q^* on the Dimensionless Net Radiative Heat Transfer Rate.

Figure (9.57) which demonstrates that for our geometry the ceiling loses approximately 30% of the incident convective flux to radiation over much of its surface. For constant $Q^*_{z_c}$, a room with a window will have larger temperatures than a similar room with a door. This results in the significantly more negative values of $q^*_{r,net}$ in Figure (9.58) for the window test. However, the gas temperature goes up faster than the wall temperature, resulting in larger convective rates and a relatively constant fraction ($q_{r,net}/q_{conv}$) shown in Figure (9.59). Finally, radiative heat transfer is significantly affected by the fire location, as already mentioned. These effects are documented in Figures (9.60) and (9.61). The key difference is that for corner fires, the area on the ceiling near the stagnation point receives large flux from the sidewalls. As a result, the net radiative flux goes to zero, compared to large, negative values for the center-line fires, where the ceiling basically sees the cold floor and the radiative loss can be greater than 33% of the convective flux. Finally, the radiative flux is also affected by the cooling air flow, which produces relatively cold ceiling temperatures near the south wall, behind the center-line fire. As a result the net radiative flux goes to zero in this region ($\bar{r} \sim 0.5$), and produces the characteristic double valued curves seen in the case of center-line fires.

9.6.8 Total Heat Transfer Rates

The local dimensionless convective and conductive heat transfer rates can be integrated to yield estimates for the total heat transfer rates to ceiling. As previously described, we approximate these integrals by averaging the local rates at the measuring locations and multiplying

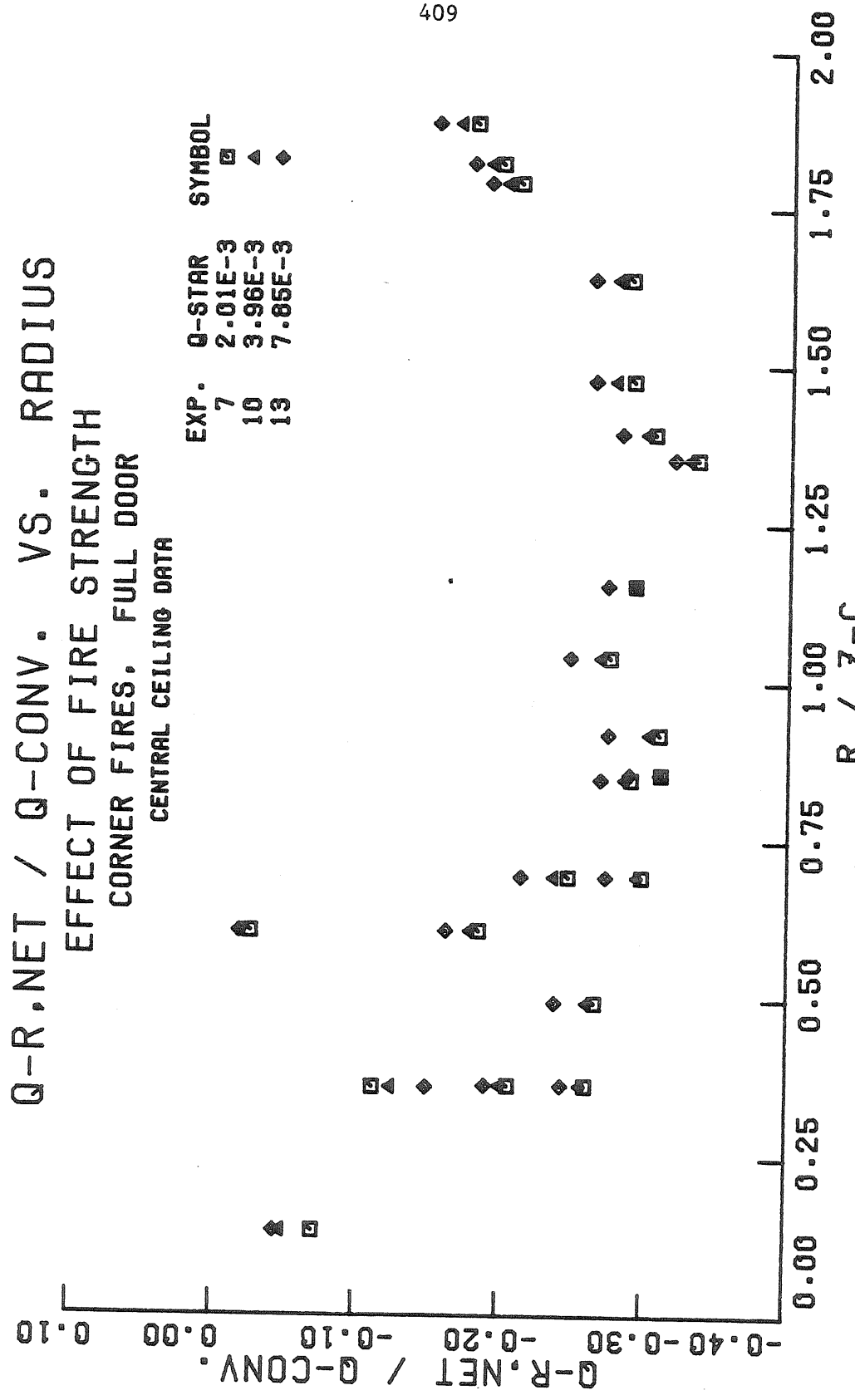

Figure (9.57) Effect of Q* on the Ratio of Net Radiative to Convective Heat Transfer Rates.

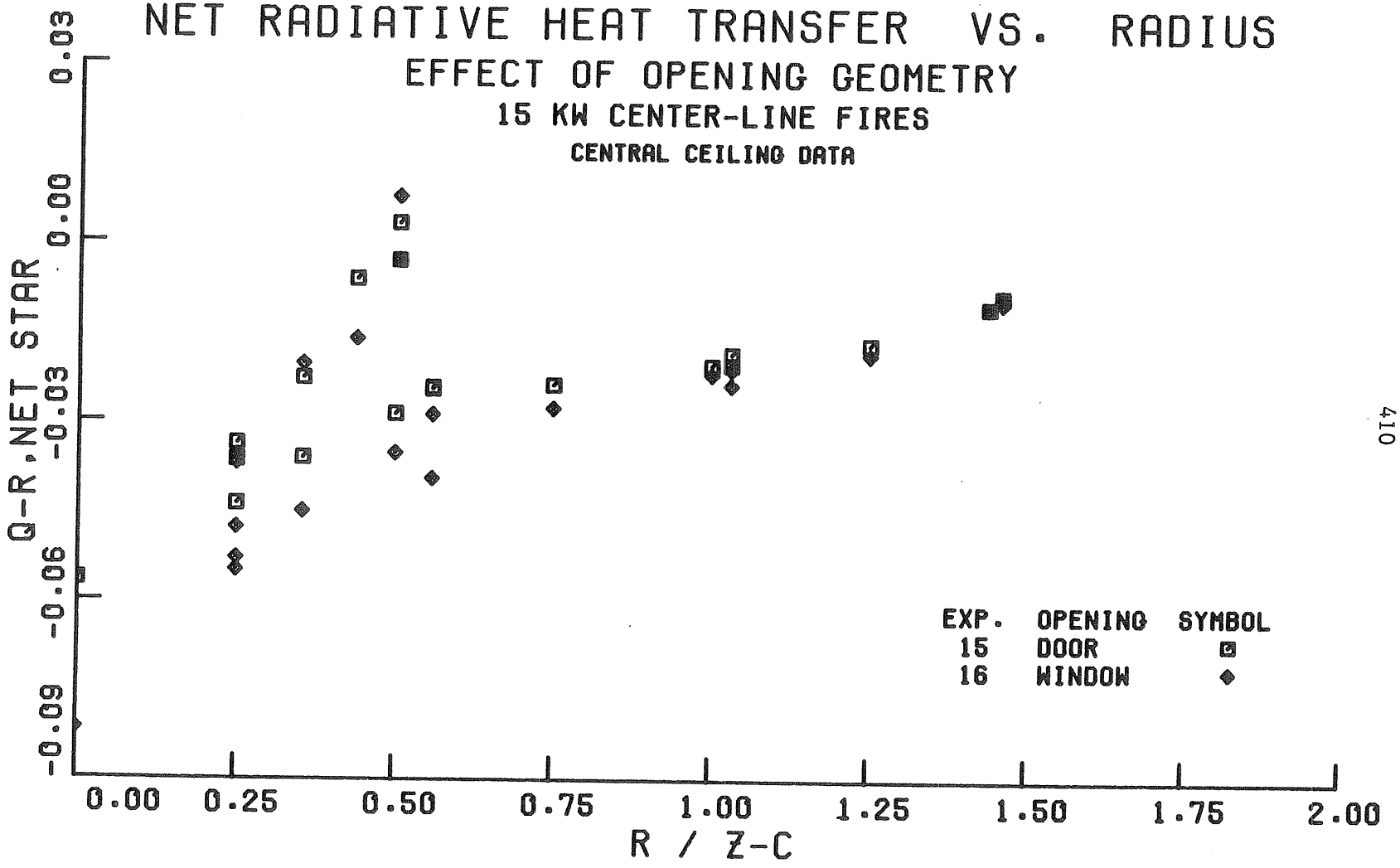

Figure (9.58) Effect of Opening Geometry on the Dimensionless Net Radiative Heat Transfer Rate.

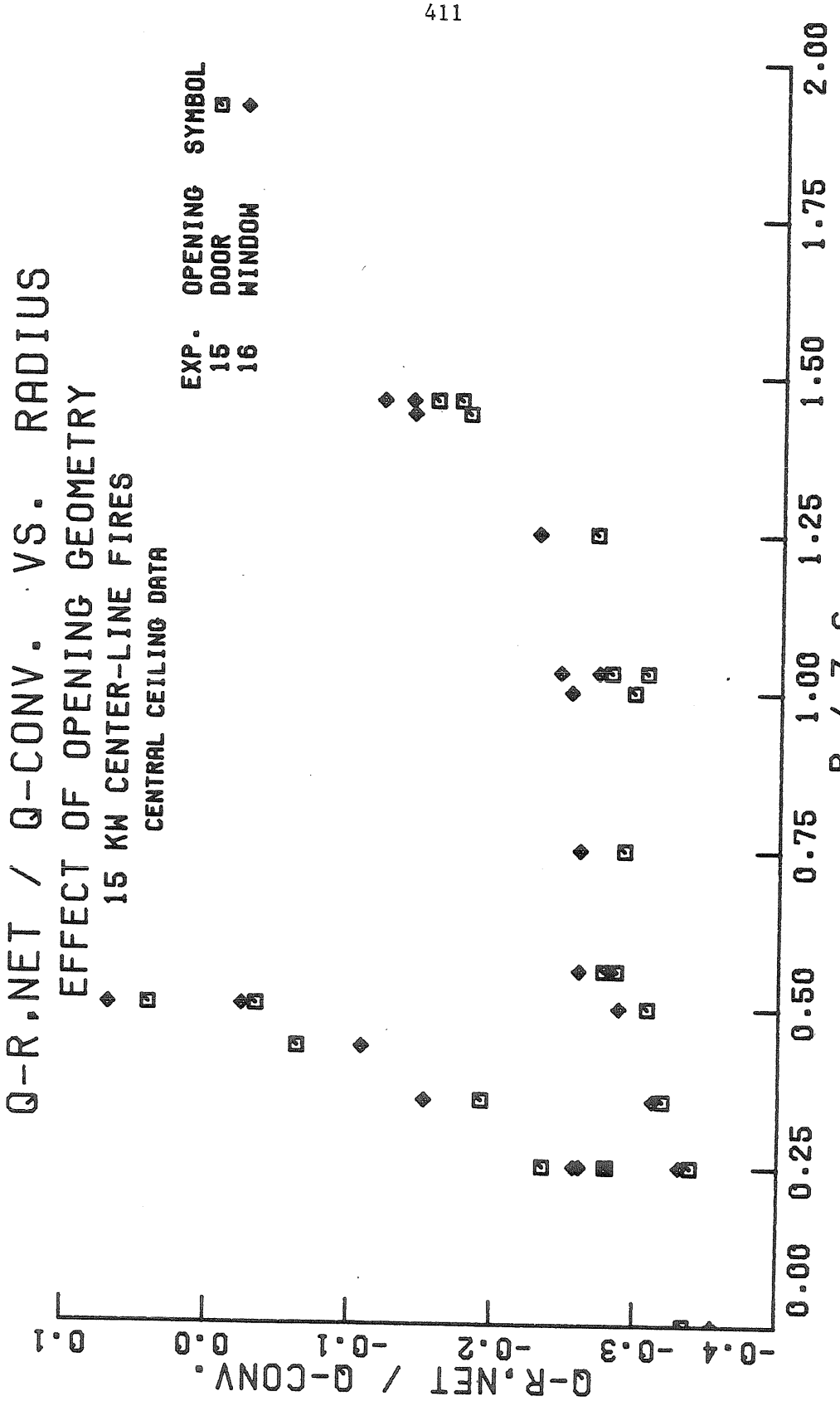

Figure (9.59) Effect of Opening Geometry on the Ratio of Net Radiative to Convective Heat Transfer Rates.

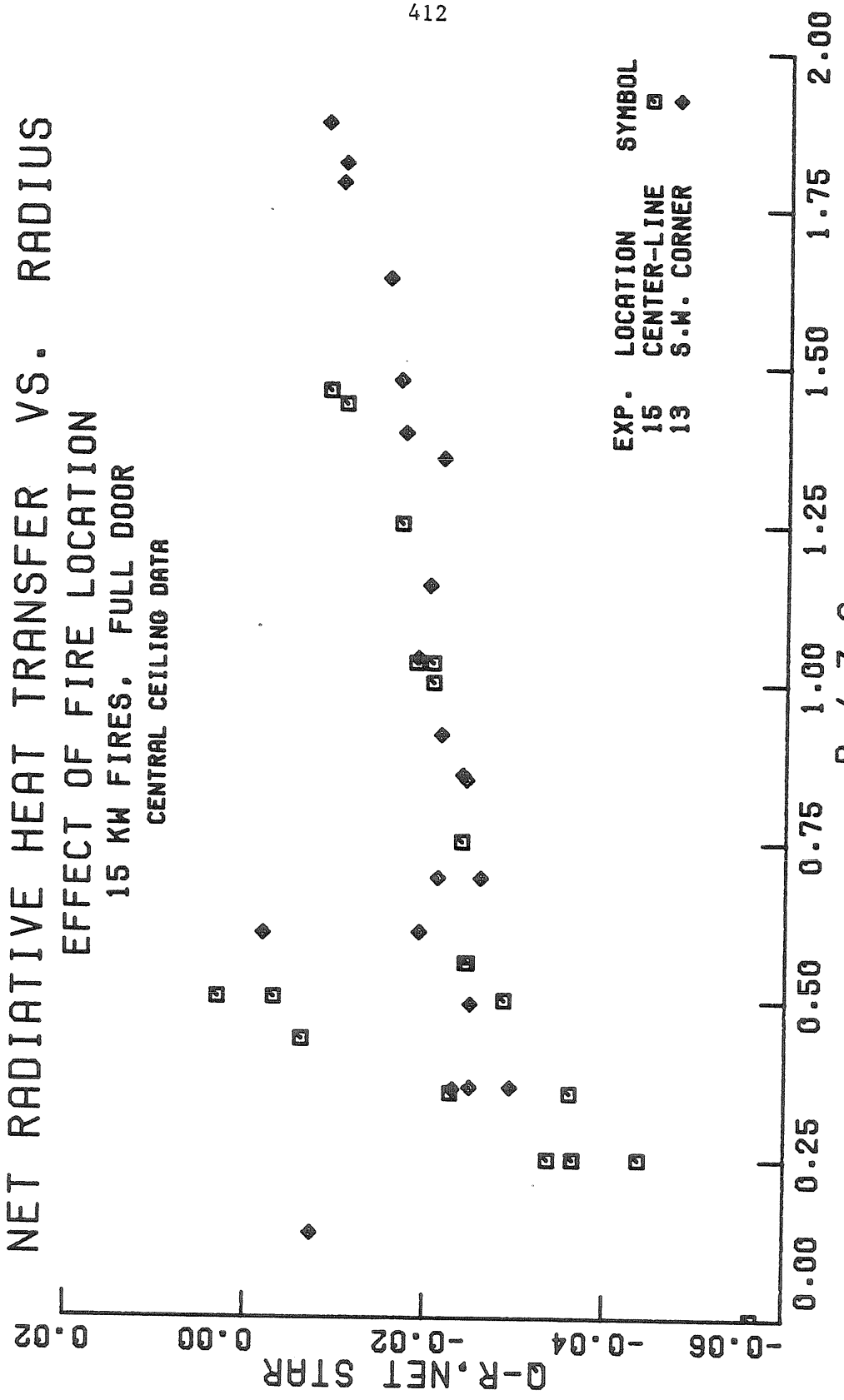

Figure (9.60) Effect of Fire Location on the Dimensionless Net Radiative Heat Transfer Rate.

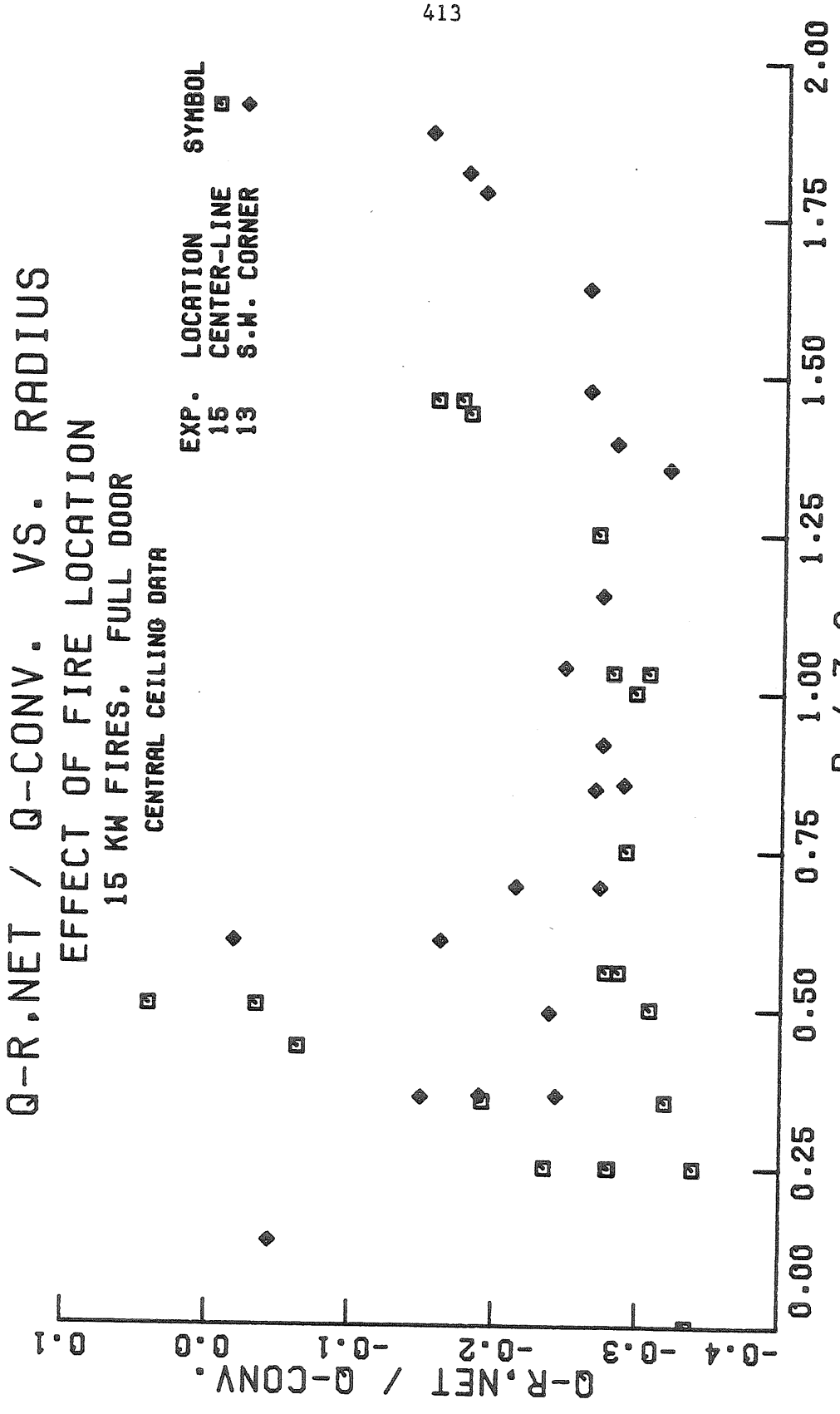

Figure (9.61) Effect of Fire Location on the Ratio of the Net Radiative to Convective Heat Transfer Rates.

by the ceiling area. The results, along with the enthalpy increase of the cooling jacket air flow, and the calculated values of Q_T^* for the ceiling are presented in Table 9.6 as dimensionless ratios of the integrated heat transfer rates normalized by the fire heat release times (T_o/T_2). This last factor arises in all the convective rate terms because ρ_2 rather than ρ_0 was used in the definition of h_c', and partially takes into account the presence of the hot upper layer. For example, the relative scatter among the data of the experiments examined is significantly smaller for Q_T^* than for the uncorrected ratio Q_T/Q_F.

Several trends can be inferred from the data in Table (9.6). First, as $Q_{z_c}^*$ increases, the relative convective and conductive loads on the ceiling decrease. This result is a reflection of the decrease in the local convective rates q_{conv}^* seen in Figure (9.50), with increasing fire size. Secondly, there is a marked increase in the convective and conductive loads on the ceiling when the opening is changed from a door to a window. This change in door geometry results in a large jump in ΔT_{gw}^* and hence in q_{conv}^*. Third, the fire location does not seem to significantly affect the total heat transfer to the ceiling. Finally, it is reassuring to note that the estimated total amount of heat conducted through the ceiling is reasonably close to the measured enthalpy increase of the air flowing through the cooling jacket on the back side of the ceiling. The agreement is best at low to moderate heat input rates. The cooling air enthalpy rise lags behind the conductive rate at large heat input rates and is probably symptomatic of insufficient insulation on the exterior of the cooling jacket.

TABLE (9.6) TOTAL HEAT TRANSFER RATES TO THE CEILING

Experiment		$Q^*_{z_c} \times 10^3$	T_0/T_2	$Q^*_{T,conv}$	$Q_{T,conv}$ (calculated)	$Q^*_{T,cond}$	Q^* cooling jacket
15	CL, Door	8.14	0.762	0.165 - 0.177	0.173	0.130 - 0.136	0.129
16	CL, Window	8.13	0.784	0.219 - 0.228	0.243	0.177 - 0.181	0.169
7	SW, Door	2.01	0.890	0.185 - 0.188	0.156	0.146 - 0.147	0.149
10	SW. Door	3.96	0.830	0.179 - 0.182	0.155	0.144 - 0.144	0.140
13	SW, Door	7.85	0.759	0.166 - 0.169	0.142	0.137 - 0.137	0.128

Where:

CL = fire located on room center line

SW = fire located in southwest corner of room

The lower value for Q_T^* represents the average over an equally spaced subset of measuring locations, while the upper value represents an average over all the measuring locations.

The entries in the fifth column are calculated by the ceiling jet computer program. For fires on the room center line, we assume the flow is purely axisymmetric within the circle $\bar{r} \leq \frac{1}{2}$ and purely two-dimensional (with $\xi = \frac{1}{2}$) in the half of the room farthest from the fire $\frac{1}{2} \leq \bar{x} \leq 1\frac{1}{2}$. On the other hand, we assume the flow is purely axisymmetric in the quadrant of the circle $\bar{r} \leq 1$ for fires located in the southwest corner, and two-dimensional in the front half of the room $1 \leq \bar{x} \leq 2$. For both fire locations we assume the heat transfer to the remaining areas of the ceiling is proportional to the axisymmetric flow heat transfer to the annulus defined by the minimum and maximum radii to these areas. The proportionality constant is taken to be the fraction of the area of this annulus covered by these remaining areas. Upon comparing the measured and calculated values of Q_T^* in Table (9.6) for fires on the center line, it is evident that our calculation scheme and the above assumptions work well. On the other hand, the calculations for the fires in the southwest corner are lower than the measured values. This discrepancy is due to the transition from axisymmetric to two-dimensional flow. We have assumed above that this occurs at the distance to the nearest major sidewalls which is $\bar{r} = 1$ for the corner-fire geometry. The q^*_{conv} data begin this transition sooner and consequently our Q_T^* estimates will be low.

One can make the same sort of estimates for the integrated conduction through the other five surfaces which comprise our 1/2 scale test room. The results are listed in Table (9.7), where $Q^*_{T,cond}$ is listed for each surface along with the total value for the room. The last column restates this total as a direct fraction of the fire heat release. It is interesting to note that as $Q^*_{z_c}$ increases, the relative amount of heat conducted

TABLE (9.7) TOTAL HEAT LOSS FROM ROOM

Experiment	$Q^*_{T,cond}$ Ceiling	East	West	South	North	Floor	Total	$\Sigma Q_T/Q_F$
15	0.136	0.087	0.089	0.054	0.033	0.010	0.408	0.311
16	0.181	0.144	0.139	0.083	0.060	0.009	0.616	0.483
7	0.147	0.075	0.099	0.041	0.028	0.011	0.400	0.356
10	0.144	0.076	0.097	0.048	0.029	0.013	0.407	0.338
13	0.137	0.081	0.105	0.058	0.028	0.014	0.423	0.321

through the ceiling actually decreases, while the losses through the sidewalls increase. In part this is due to the fact that the upper portion of the sidewalls see a hotter upper layer ($\bar{T}_2$ increases) which covers a larger fraction of them as $Q^*_{z_c}$ increases. Secondly, as the ceiling and upper sidewall temperatures increase, radiative transfer becomes relatively more important in heating the lower portions of the sidewalls and floor. If one replaces the door with a window, both the mean upper and lower layer temperatures will increase significantly, and consequently, so will the heat transfer loads on all the surfaces. Thus, for equal fire strengths, approximately 30% of the heat input will be lost through the walls for a room with a door, compared to 40% for an equivalent room with a window. Finally, a comparison of experiments 15 and 13, shows that fire location does not strongly affect the overall fraction of heat lost to the solid surfaces in the room. However, the local convective and conductive flux distributions do reflect the change in the fire location with the walls near the fire absorbing a greater fraction of the heat loss when the fire is located in the corner of the room.

9.7 Conclusions

The results presented in this chapter suggest that the dimensionless variables introduced in Section (9.1) provide a useful means of scaling the heat transfer data association with room fires, and that the calculation scheme formulated in Chapter VIII provides reasonable estimates for the heat transfer coefficient, the ceiling jet temperature, and the convective heat transfer rates, given the ceiling temperature distribution. It is not surprising that the agreement is best when the flow remains axisymmetric, as it should for the bare ceiling and curtain wall tests of

Zukoski, Kubota, and Veldman (1975). When the fire room has rectangular symmetry, as in our 1/2 scale test room, and when the plume's entrainment requirements are satisfied by a highly directional door-jet of inflowing fresh air, the agreement between calculated and measured values is not as good. We can partially compensate for the transition in flow geometry from axisymmetric to two dimensional, evidenced by the data, by making two computations for the two asymptotic states of purely radial and purely longitudinal flow. The effect of the plume interaction with the door-jet is more complicated, but could be taken into account by changing the empirical impingement region ($h_c'/h_{c\,sp}'$) distribution to produce a broader curve.

It is interesting to note that the dimensionless heat transfer coefficient as a function of dimensionless radius does not change greatly as a function of fire size, door geometry, or fire location, and that an empirical fit to the data might not be too bad for engineering calculations. Furthermore, the flow down the sidewalls behaves approximately as though the sidewalls were folded down continuations of the ceiling. One could thus use these results to obtain rough estimates of the convective heat transfer coefficient over the entire upper portion of the room.

On the other hand, the gas and wall temperature differences are intimately linked and are functions of the door geometry and, to a lesser degree, of the fire location in addition to their fundamental dependence on the heat release measured by $Q^*_{z_c}$. Furthermore, the wall temperatures are functions of the wall construction and, in our case, of the forced convection cooling which occurs on their outer surfaces. These interactions, along with the radiative transfer process, make it much more

difficult to estimate the temperature distributions, and hence the actual convective rates, in any simple way.

X. SUMMARY, DISCUSSION, AND CONCLUSIONS

10.1 Overview

We have studied the natural convection flows produced by a small fire in room with a single door or window opening, and have examined the heat transfer processes produced by these flows. Experimentally, we have examined these flow patterns both in a 1/4 scale hydraulic modeling facility, which offered good flow visualization and simulated very weak fires in rooms with adiabatic surfaces, and in a 1/2 scale fire test room in which we could measure the convective heat transfer to the ceiling and walls.

Most room fires start on a small scale with limited initial heat release. During this early phase, temperature, and hence density, differences will be modest within the room and we have used this fact in all of our calculations by employing the Boussinesq approximation, which treats the gas density as constant, except for density differences in the equations of motion. Using this approximation along with the far-field properties of turbulent buoyant plumes and hydraulic analysis of flow through an orifice, we have formulated a procedure to calculate the gross behavior of the gas in a room with a fire. In particular, given the room geometry, fire strength and other relevant parameters, we can estimate the mean temperature of the upper and lower layers and the height of the interface which separates them. In addition, we have combined a more detailed finite source, Boussinesq plume computation with an integral analysis of the turbulent ceiling jet formed by the impingement of the plume upon the ceiling to calculate the convective heat transfer to the ceiling as a function of distance from the impingement point.

The plume and ceiling jet calculation can be used in series with the simple room model computation to analyze or to predict several practical aspects of fire induced flow phenomena in rooms. For example, given the heat input and opening geometry, and an initial guess for the heat loss parameter c_q, one could use the simple room model to calculate initial values for the upper and lower layer temperatures and for the height of the interface between them. This information could then be input to the plume and ceiling jet computer programs to calculate the gas temperature and convective heat transfer rates along the ceiling. Finally, one could use the computed total integrated heat transfer rate to provide improved estimates of the gas temperature profile within the room and of the convective heat transfer rates to the ceiling and upper side walls.

These calculated results can be used to answer a number of practical questions. For example, one could use the computed ceiling jet gas temperature and local convective heat transfer rates to determine whether sprinklers or other fire detection sensors mounted in the ceiling of a new building would be triggered by a given strength fire. Similarly, if the ceiling contained materials which could char or melt, such as plastics or electrical insulation, these results could be employed to estimate the amount of damage that would be caused by a given fire. Finally, one could in principle combine these programs with other computer programs which would calculate the transient temperature behavior of the solid surfaces which make up the room for a given heat flux, and which would compute the radiant flux within the room. This computational procedure could

then be invoked to find both the ceiling temperature as a function of time and position, and the net radiant flux to the lower portion of the room. These factors are important in determining how fast the fire will spread and how hot the lower portion of the room will become. This latter factor obviously plays a vital role, along with the characteristics of the fuel load, in fixing the time required for the room to flash over.

Throughout this work we have found it useful to normalize our calculated results and experimental data with representative quantities based on the far field behavior of simple point source plumes, evaluated at the height of the ceiling z_c. Thus we choose z_c, $\sqrt{gz_c}(Q^*_{z_c})^{1/3}$, and $T_o(Q^*_{z_c})^{2/3}$ as the length, velocity, and temperature scales. This formulation is directly applicable to the case of a large room in which the height of the ceiling is large compared to the fire diameter, and in which the gas is at a uniform temperature. In almost all real rooms one or both of these conditions will not be met and the actual natural convection flows will be affected by finite source effects and by the presence of a hot upper layer of combustion products. However, in the early stages of the fire these effects will not be as important as the basic natural convection flow processes. For example, the dimensionless ceiling heat transfer coefficient h'_c has been found to be primarily a function of the dimensionless radius $\bar{r}$, and is only secondarily a function of the thickness and temperature of the upper layer. To be more specific, as the thickness or temperature of the upper layer increases, the upper portion of the plume will become relatively less buoyant and the velocity in the ceiling jet will

decrease. Because this effect is not taken into account by the normalization, the dimensionless heat transfer coefficient will decrease faster than the actual heat transfer coefficient as the temperature of the upper layer increases. In actual cases the depth and temperature of the upper layer will vary with room geometry and construction, and with the radiant flux distribution within the room. These factors are thus difficult to model in a simple manner, so that we are indeed lucky that our dimensionless variables form families of similar curves which are often only weakly affected by these factors.

Because we have examined a number of aspects of fire induced natural convection flow phenomena in this work, we will attempt to summarize the important results of the major theoretical and experimental topics separately in the following sections.

10.2 Plume Behavior

We have presented three related plume models which can accommodate progressively more complicated environmental conditions. All of these models rest on the same set of basic physical assumptions. First we assume that the density differences are small enough that the Boussinesq approximation is valid. Thus we rule out the flame or strong plume region. Second, we assume that the turbulence is fully developed so that velocity and temperature profiles will be similar at any height. Finally, all of these plume models are based on the entrainment hypothesis that the velocity of fluid entrained into the plume is directly proportional to the maximum velocity within the plume.

The simplest model, given by equations (2.52) - (2.54) or

alternatively (2.58) - (2.60), represents the solution for a plume generated from a source of buoyancy only which rises in a uniform environment. Thus it represents the far-field or asymptotic solution for a real plume emanating from a source mass and momentum in addition to buoyancy. This simple, power law relation has been used throughout this work to produce the normalizing factors in our dimensionless variables. In addition, we can improve the accuracy of this simple model by allowing the plume to start at a virtual source, whose depth is given by equation (2.41). With this correction which partially accommodates the effects of the source mass and momentum fluxes, the power law solution agrees with the finite source calculation within 1% above 3.5 virtual source height of the fire. This corrected point source plume model is used as the basis of our simple room model calculation.

The reduced set of ordinary differential equations (2.36) and (2.37) represent a second, more accurate model of a plume rising through a uniform environment. Because we integrate these ordinary differential equations which approximately describe a fully developed turbulent plume directly, this computation yields the exact solution, given by equations (2.38) and (2.39), for a finite source plume rising in a uniform environment. However, this solution rests on the Boussinesq approximation and the assumption that the proportionality factor in the entrainment hypothesis is in fact a constant. Thus although we refer to this as the finite source calculation, real sources may violate one or more of these fundamental assumptions. For example, this solution will not be strictly valid near flames or when the initial flow has very large

momentum and thus behaves as a jet.

We can apply this model to the case of a non-uniform environment if we can approximate this non-uniformity in the density of the external fluid by a sharp interface separating two uniform layers of fluid. In this case we can apply the interface jump conditions, with the change in the buoyancy flux given by equation (8.3), to find the effective starting conditions for the new, less buoyant finite source plume above the interface.

The basic validity of this model was confirmed in two independent ways. First, the heat loss parameter c_q calculated by the plume program agreed very well with estimates based on the total convective flux to ceiling and upper walls. Second, the measured ceiling zone CO_2 concentrations agreed very well with estimates based on this plume computation and measurements of the mean floor and interface zone CO_2 concentrations. Thus, at least for premixed fires, which have small flames and significant initial mass and momentum fluxes, this Boussinesq plume computation accurately models the finite source plume.

Finally, we can also integrate the three differential equations which describe a Boussinesq plume in a non-uniform environment, given by equations (2.29) - (2.31), directly. When this is done, using the three experimentally determined linear temperature profiles to specify the external temperature gradient, the calculated results evaluated at the ceiling agree very well with the calculations of the simpler uniform environment plus interface computation just described, provided that the height of the interface z_{int} is chosen as the upper boundary of the interface zone z^+. Because of this

agreement, we have chosen the simpler model to calculate the behavior of the upper plume in our ceiling jet computation.

10.3 Room Models

We have developed a simple calculation procedure, based on the far field behavior of a point source plume and hydraulic analysis of flow through an orifice, to model the steady state density distribution of the fluid within a room which contains a fire and which has a single door or window opening. Given the heat release of the fire, the room geometry, and estimates for the convective heat loss and for the turbulent mixing between the hot combustion products in the upper layer and the cooler gas beneath it, this computation scheme will calculate the height of the interface separating these two layers of fluid and their average temperature or density.

We have found that the basic form of the model described in Chapter III, which ignores heat loss from the upper layer and turbulent mixing between the two layers, worked well for the 1/4 scale brine flow simulations which involved large door-like openings. Because the fluid density differences were produced by salinity changes rather than by temperature differences, these experiments were exact simulations for the case of no heat loss from the upper layer. In addition, because the source strengths were very weak, there were no observable secondary flows, such as wall jets penetrating to or through the interface. The Richardson number at the doorway was also large indicating that the fluid was stably stratified and that little mixing should occur there. Thus the major assumptions on which

the model was based appear to be satisfied and the predictions agreed reasonably well with the measured density profiles. On the other hand, when the opening was a small window, the Richardson number dropped sharply and turbulent mixing was visually observed between the counterflowing streams at the opening. This mixing produced an increase in the floor layer density difference and prompted us to extend the basic model to include these effects.

A slightly generalized form of the room model, discussed in Chapter IV, was needed in order to accommodate some of the physical conditions encountered in our 1/2 scale room tests. These experiments involved actual room fires and, because the ceiling and walls were convectively cooled, the hot gas in the upper layer lost a significant fraction of its initial enthalpy to these cold surfaces. Secondly, because of the much larger initial buoyancy of the fluid, the dimensionless heat input parameter $Q^*_{z_c}$ was roughly two orders of magnitude larger than in the 1/4 scale brine tests. This resulted in a relatively much more vigorous plume which in turn produced significant secondary flows of hot gas penetrating down the side walls. For example, in the corners these secondary flows actually penetrated below the height of the interface and thus contributed to the thick interface zone seen in the 1/2 scale tests and may have contributed to the increase in the temperature of the lower layer. In addition, when the opening was a window, the Richardson number at the window fell and the counterflow mixing increased, just as in the 1/4 scale brine experiments. When these effects were modeled in this extended computation scheme by specifying the heat loss parameter

c_q, the fraction η of the plume mass flow rate which actually flows out under the soffit, and the fraction c_{fr} of the heat lost from the upper layer which is deposited in the lower layer by radiation and natural convection, the calculated temperature profiles agreed reasonably well with the measured average upper and lower layer temperatures. In particular, the average increase in enthalpy between the two layers, measured by $(\overline{T}_2 - \overline{T}_1)$, was very close to the calculated value, which shows that the model is consistent and that the point source plume emanating from a virtual source does a good job of simulating the actual finite source plume.

This room model also highlights the areas which need further research before this calculation scheme can be fully utilized. First, the fraction of heat lost by the upper layer $(1 - c_q)$ is difficult to estimate simply because the convective losses to the ceiling are affected by the transition from axisymmetric to two-dimensional flow in the ceiling jet and by the secondary flows down the walls. Secondly, these secondary flows appear to contaminate the floor layer gas with combustion products from the plume, thereby reducing η. In addition η is also a function of the Richardson number at the door or window opening Ri_c. As this number falls, the counterflow mixing increases and η drops still further. By further varying the opening geometry, one could generate enough data points to attempt an empirical correlation of η as a function of Ri_c. Third, if we knew the actual heat transfer through the floor, we could calculate c_{fr} with greater confidence. However, because c_{fr} ultimately depends on the radiant flux distribution within the room,

it is also difficult to estimate in any simple way. Finally, when the fire is located in close proximity to one or more of the side walls, entrainment into the plume will be impeded and the entrainment constant will fall. However, we do not have enough data to predict the functional form of this relationship between the distance separating the fire and the wall, and the entrainment constant.

10.4 Ceiling Jet Behavior

We have assembled a procedure to calculate the convective heat transfer to the interior region of the ceiling as a function of distance from the plume impingement point.

The uniform environment, finite source plume program is first invoked along with the interface jump conditions to calculate the plume's velocity, temperature, and width scales just below the ceiling. These quantities characterize the heat transfer processes at the stagnation point and in the impingement region, as well as providing estimates for the initial values of the ceiling jet variables.

The heat transfer at the stagnation point is given by the laminar flow expression for an axisymmetric stagnation point, in which the external velocity gradient is scaled by characteristic quantities from the upper plume. This expression is then corrected for turbulent enhancement by an empirical function of the plume Reynolds number and estimated turbulence intensity.

The impingement region, which extends from the stagnation point radially outwards to the start of the ceiling jet is a region of developing flow. Consequently, we cannot apply the integral analysis

here which we used for both the turbulent plume and the ceiling jet. In principle, one could compute the boundary layer flow in this region based on the external pressure graduent which is characterized by the velocity and width scales of the plume. However, the location of the greatest local heat transfer will be at the stagnation point, which we can calculate directly. In addition, the area covered by the impingement region is small compared to the total ceiling area for most practical rooms. Thus although the local heat transfer rates are large in the impingement region, this region is responsible for only a small fraction of the total convective heat loss to the ceiling. Furthermore only one of our ceiling data points lies within this region. Consequently we have not attempted to model in detail the flow in this region. Instead we have simply used an empirical correlation for the heat transfer coefficient, scaled by the value of the stagnation point heat transfer coefficient and the characteristic plume radius. This simple approach allows us to estimate the total convective loss from this region which we then use to calculate the initial enthalpy flowing into the ceiling jet.

The flow leaving the impingement region is a fully developed turbulent similarity flow, which we refer to as the ceiling jet. We have presented a calculation scheme to compute its evolution as a function of distance. Because this flow has attained similarity, we apply the standard integral analysis and integrate the three resulting ordinary differential equations numerically. The presence of side walls can channel the originally axisymmetric flow into a basically two dimensional flow pattern. Consequently, the program

includes the provision of integrating these equations for either of the two asymptotic states of purely axisymmetric or purely two-dimensional flow. Secondly, because the momentum and energy equations are integrated separately, the velocity and temperature scales of the ceiling jet can vary independently. This becomes important when the ceiling is colder than the upper layer gas, a condition which we would typically expect to find in the early stages of room fires. In this case, the temperature difference in the ceiling jet with respect to the upper layer temperature may be reduced to zero by convection losses to the ceiling long before the velocity scale in the ceiling jet decays.

The ceiling jet calculation scheme involves a number of adjustable parameters and computational options. Numerical studies have shown that of these, four groups of parameters are particularly important. First, as one would expect from dimensional analysis, the basic dependence of the heat transfer coefficient upon distance is fixed by the flow geometry. For a given flow geometry, the next most important parameter is the entrainment function E. Various studies have shown that for buoyant wall jets this function can be written as an entrainment constant times a negative exponential function of the wall jet Richardson number. As one would expect this entrainment constant fixes the growth rate of the ceiling jet, just as the plume entrainment constant controls the evolution of the plume. The exponential dependence on the Richardson number becomes important as the ceiling jet becomes relatively buoyant, because in this case, the buoyancy tends to suppress the turbulent mixing and hence the

entrainment. On the other hand, this term may also become large far from the source when convective losses to a cold ceiling produce a negatively buoyant, and hence unstable, ceiling jet. Finally, given the flow geometry and the entrainment function, which effectively control the flow outside the boundary layer, the transport processes across this layer are fixed by the friction factor N and the ceiling or wall temperature T_w. Because Reynolds' analogy was used in the energy equation, the friction factor N governs the transport of both momentum and energy across the boundary layer. Furthermore, because N is small ($N \sim 0.02$), the outer flow is not strongly affected by the actual value of N. Finally in order to compute the actual convective heat transfer rates, one must know the ceiling temperature as a function of distance.

The results of this ceiling jet calculation scheme agreed well with the 1/4 scale bare ceiling and curtain wall data of Zukoski, Kubota, and Veldman (1975). This agreement further confirms the accuracy of the finite source plume computation with the interface jump conditions, and indicates that the ceiling jet calculation works well when the flow geometry does not change.

In the 1/2 scale test room, on the other hand, the presence of the long side walls tended to channel the originally axisymmetric flow into a more two-dimensional pattern. As a result, for radii which are small compared to the distance to the nearest side walls, the heat transfer coefficient data are scattered about the calculated values for axisymmetric flow. Conversely, for radii which are large compared to this distance, the data appear to lie close to the values

computed for two-dimensional flow. These trends are most obvious with the heat transfer coefficient data. The temperature data appear to exhibit the same phenomenon, but the agreement with the two-dimensional calculations are worse because these calculations underestimate the heat lost at small radii where the flow is in fact axisymmetric. As a result, the calculation scheme will also overestimate the convective heat transfer rates for the two-dimensional computation. These trends are indicative of the general result that it is relatively easy to calculate the heat transfer coefficient while it is more difficult to compute the convective heat transfer rates themselves, because in the latter case one must also specify the thermal boundary conditions accurately.

The ceiling jet computation procedure thus provides a useful tool for estimating the heat transfer from the fire plume induced ceiling jet and may be used in its present form to study practical problems such as whether sprinklers will be triggered by a given strength fire. However a number of improvements would increase its utility. First, as we have just indicated, the rather ad hoc assumptions which we used to calculate the equivalent two-dimensional source might be adjusted to give a better estimate of the two-dimensional flow regime. Second, we noted that the heat transfer coefficient data behave roughly as though the side walls were merely folded down extensions of the ceiling. We could use this result to calculate the heat transfer along the sidewalls by rewriting the equations of motion to take into account the change in the gravity vector with respect to the flow direction. However, unless we had a circular room, we would need to repeat the side wall calculation

for a large number of rays along the ceiling because for a non-circular room, the initial conditions would be different along each ray. Third, if one is interested in the details of the impingement region heat transfer coefficient distribution, one could calculate the boundary layer in this region, given the external pressure gradient imposed by the impinging plume. Finally, there is the return flow problem. The ceiling jet calculation assumes that the ceiling zone gas beneath the ceiling jet is at rest when in fact this fluid must move towards the plume to satisfy the entrainment requirements of the plume and ceiling jet. Unfortunately we do not have flow visualization data to reveal the details of this flow process, and so we have been forced to ignore it in our computations.

10.5 Experimental Results

The experimental investigations reported in this work were carried out in two quite different facilities. The early work was done in an approximately 1/4 scale facility in which denser brine was injected into a room model filled with water. The later experiments were conducted in a 1/2 scale fire test room in which a pre-mixed flow of air and natural gas was burned at floor level.

The 1/4 scale brine flow simulations provided a good experimental model of very small room fires. Because the density differences in these tests were generated by the addition of brine, which was only slightly denser (~ 5%) than the ambient water, the effective source strengths in these tests were very small ($Q^*_{z_c} \sim 10^{-6}$). Consequently the upper layer residence times were large, indicating that the fluid in the upper layer was rather quiescent. Flow

visualization confirmed this fact for the fluid near the interface, even though there were flows observed near the ceiling. Furthermore, because the density differences arose from salinity rather than temperature differences, there were no heat transfer effects. Thus the upper layer fluid could not lose its buoyancy except by mixing with the lower layer fluid ($c_q = 1$). As a result, the density was nearly constant throughout the upper layer and no ceiling jet was detectable in the density profiles. Similarly, the density in the floor layer was also constant. Thus the 1/4 scale facility provided a useful way of studying the primary flow phenomena of very small fires in rooms with adiabatic surfaces. Furthermore, because this work was done in a clear-walled tank, it was easy to visually observe the flow patterns throughout the room, in addition to measuring the density profiles. The chief disadvantage of this facility is that the plumes were not strong enough to generate the secondary flows seen in the 1/2 scale room fire tests.

The 1/2 scale room fire experiments complemented the earlier 1/4 scale brine flow simulations by providing a realistic test of moderately small room fires in which heat transfer processes play significant roles. These tests simulated the early stages of a fire in a room, when the solid surfaces are cold compared to temperatures in the plume, and the gas in the upper layer loses a significant fraction of its initial enthalpy to these surfaces. In addition because we used relatively small diameter premixed burners, these experiments model fires which are of limited extent and which have small flames. Again, one might expect to encounter these conditions very

early in the history of a typical room fire.

In the 1/2 scale facility the outer surfaces of the ceiling and walls were cooled by forced convection. Consequently, convective heat losses from the hot combustion products in the upper layer were large even under steady state conditions. For example, when the opening was a doorway roughly 26% of the heat input to the upper layer was lost to these relatively cold surfaces. In the first few minutes of the fire we expect these losses to be even higher because the time scale for the the gas to reach quasi-steady state conditions is much shorter than for the solid surfaces. In other words, shortly after ignition the gas will have attained its steady state temperature while the solid surfaces are still near ambient temperature. Thus we expect convective heat transfer to play a significant role in the early stages of real room fires and throughout the course of our 1/2 scale experiments.

Several of these heat transfer effects are apparent from the temperature profile data presented in Chapter VII. First, near the fire there is an obvious ceiling jet made up of gas from the plume which is hotter than the majority of the upper layer fluid. As this ceiling jet flows outwards along the ceiling it continually loses enthalpy and its temperature excess is continually eroded until at very large distances it has developed a temperature deficit. In addition, as this ceiling jet fluid impinges upon and flows down the upper portion of the side walls, it will lose still more enthalpy. Thus by the time this fluid is returned to the ceiling zone it will be significantly cooler than it was when it left the plume. This temperature change manifests itself as the non-zero

temperature gradient visible in the temperature profiles measured in the interior of the room. On the other hand the CO_2 concentration profiles through the upper layer are nearly constant, indicating that the temperature change is indeed largely due to heat transfer effects. In addition, the floor zone gas also experiences a non-zero temperature gradient. In this case, radiation from the hot upper surfaces heats the lower surfaces to temperatures above the floor zone temperature. As a result natural convection flows will be created which will tend to lift the hotter gas to the interface.

In addition to heat transfer effects the stronger plumes in these 1/2 scale experiments give rise to secondary flow patterns which we did not consider in our room model. In particular, the vigorous ceiling jet flow impinges on the side walls and flows down them. This flow is particularly strong in the corners and temperature measurements there indicate that this hot gas consistently penetrates below the height of the interface in the interior of the room. This secondary flow in the upper layer appears to be responsible, along with the rising natural convection flows in the lower layer, for thickening the interface zone and consequently reducing the mean temperature gradient there.

Unfortunately, although this 1/2 scale facility was ideal for measuring the convective heat transfer from the gas to the solid surfaces, these same surfaces made it impossible to do flow visualization studies except in the immediate vicinity of the doorway. Consequently our knowledge of these secondary flow

patterns must be inferred from the measured temperature data, and so our understanding of these flows is incomplete.

The results which we have just discussed were observed in all of our 1/2 scale experiments. We also observed some additional effects as we changed the door geometry, fire location, and fire size.

The most significant factor affecting the temperature distribution within the room for a given fire strength is the opening geometry. The same result also holds for the 1/4 scale brine experiments. In particular, blocking the lower portion of the doorway to form a window causes the interface within the room to fall. In addition the high shear between the counter-flowing streams in the vicinity of the window causes turbulent mixing to occur. As a result, the entering jet of fresh air becomes contaminated with hot combustion products and the floor layer temperature and CO_2 concentration rise appreciably above ambient levels. Then, because the floor zone gas is preheated before being entrained into the plume, the upper layer temperature also rises.

After the opening geometry, the next most important factor affecting the temperature response of the room for a fixed heat input is the fire location. In both the 1/4 scale and 1/2 scale facilities we observed that the plume entrainment was reduced as the source was moved close to one or more of the side walls. This resulted in hotter plumes with smaller mass flow rates.

Finally, there is the obvious factor of fire strength; the greater the heat release, the larger the temperature difference

between the gas in the floor and ceiling layers. However, despite changes in factors such as the net radiant flux distribution and the heat loss from the upper layer, which are ignored in our simple plume normalization, this normalization does a reasonably good job in predicting the temperature difference between these layers. Thus, at least for the 1/2 scale experiments which we have conducted, this temperature difference $(T_2 - T_1)$ is given approximately by $9.5\ T_o(Q^*_{z_c})^{2/3}$.

10.6 Suggestions for Further Experiments

The experimental facilities described in this work represent very useful tools for studying the natural convection flow phenomena produced by a small fire in a room. Further series of experiments in both the 1/4 scale brine facility and the 1/2 scale test room would help clarify some of the features of these flows.

The data from the 1/2 scale test room span a $Q^*_{z_c}$ range of $2\text{-}8 \times 10^{-3}$, so that $Q^*_{z_c}$ changes by a factor of 4. However, the velocity scale, which varies as $(Q^*_{z_c})^{1/3}$, is only altered by a factor of 1.6. Thus it would be useful to extend the range of $Q^*_{z_c}$. This would be easy to accomplish. On one hand, we never used the full diameter of the burner. The largest heat input tests were conducted with a 15.2 cm diameter opening. If we maintain the same fuel-air ratio and burner exit velocity, but use the full 20.3 cm burner diameter we can increase the heat input by a factor of 2.1. On the other hand, our calculations indicated that the fuel-air ratio was lean. If we were able to richen the mixture to the stoichiometric value, we could generate a further 35% increase in the heat release. Combining these two effects,

we potentially could change $Q^*_{z_c}$ by a factor of 11.5. This would result in a variation of the velocity scale, which is used to normalize the heat transfer coefficient data, by a factor of nearly 2.3. This represents an increase of 42% over the present variation and would add significant credence to our finding that the distribution of the dimensionless ceiling jet heat transfer coefficient is independent of $Q^*_{z_c}$.

In the final series of experiments studying the direct effects of the heat input it would be very interesting to replace the pre-mixed burner with a series of small diffusion flame burners, such as the ones used by Zukoski, Kubota, and Cetegen (1980). Using a diffusion flame as the heat source would certainly provide a more realistic simulation of a fire in a room, and, provided the flame heights were small compared to the height of the interface, would be a good further test of our computational procedures. However, it is well known that diffusion flames lose a significant fraction of their heat release to radiation and so we would no longer be able to ignore this effect, as we did for our pre-mixed fires.

All of the 1/2 scale tests were conducted with the same width door and with the same soffit height. Therefore the height of the interface, which depends primarily on the soffit height and width of the door did not change greatly among the experiments which involved open doorways. It would therefore be very interesting to conduct a series of experiments in which this basic doorway geometry would be radically altered.

The first tests in this series should be experiments in

which the north wall is completely removed. In such a case, the upper layer would consist simply of the ceiling jet and there would be no return flow. The plume would entrain strictly floor zone air. In addition the ceiling jet exit conditions would be uniform across the width of the room and we might expect to find a more nearly two-dimensional flow pattern. Then, by varying the fire location, we might be able to obtain a better understanding of the flow turning process in which the side walls channel the originally axisymmetric ceiling jet into a two-dimensional flow pattern.

Ideally the next set of experiments in this series could be conducted with a series of panels to progressively block the opening at the north end of the room. In the course of this set of experiments the soffit, which would span the entire room, would be lowered from 100% of the room height to some small value, say 10% of the room height. By thus changing the height of the soffit, we would cause the height of the interface to vary between the two possible extreme cases of the interface very near the ceiling and of the interface very near the floor. In addition, because the soffit would span the full width of the room, the exit conditions would be uniform across the room. It would be interesting to see what effect this would have on the ceiling jet behavior and on the secondary flow phenomena which we have detected.

The final set of experiments in this series should involve progressively narrowing the door for a fixed soffit height. This geometry should produce the secondary flow phenomena of hot gas flowing down the corners of the room and, in the case of the

north wall, possibly interacting with the incident stream of fresh air. In addition, by narrowing the door we will also cause the height of the interface to drop. We could then cross-check the results of these experiments with those of the second set which involved full width soffits to see the effects of these secondary flows for a given interface height. In addition, the Richardson number at the doorway should fall as the width of the doorway is reduced, and we could use these data to help correlate the mixing at the door as a function of Richardson number.

We have listed a series of experiments which would radically alter the doorway geometry. Given the time and patience, it would also be useful to design a set of experiments to systematically alter the window geometry. By measuring the additional mixing that occurs when a window is present, we might be able to formulate an empirical correlation for the counterflow mixing as a function of the Richardson number, and possibly parameterized by geometric factors such as the aspect ratio of the window.

10.7 Suggested Technical Improvements

The 1/2 scale fire test room is a very useful facility for studying the natural convection flows and associated heat transfer processes in room fires. However, a few minor improvements in the hardware, the experimental protocol and data processing software could significantly improve its performance.

There is currently room for 45 more thermocouples on the thermocouple stepping switch. In addition, 36 thermocouples are connected in duplicate. We could use this reserve capacity to add at least seven pairs of thermocouples to the ceiling so that we

would have a symmetric pattern of measuring locations. In addition it would be very useful to add an additional 15 pairs of thermocouples along the lower portion of the side walls so that we could study the natural convection flow in this region. Finally, it would be very helpful to add ten pairs of thermocouples to the floor and ten individual thermocouples to the outer surface of the floor beneath the existing inner surface floor thermocouples, so that we would have a symmetric pattern of measuring locations over the entire floor at which we could measure not only the floor temperature, but also the heat conduction rate through the floor. These improvements would significantly reduce the uncertainty in our radiant heat transfer calculations and would provide more data points to help understand the ceiling jet's transition from axi-symmetric to two-dimensional flow.

After the 1/2 scale experiments described in this report were concluded, the outer surfaces of the cooling jackets were thoroughly insulated. We could therefore conduct a further series of experiments in which we vary the airflow to the cooling jacket to study the effect of heat loss for a given interface height. We could also extend this concept by installing a heat exchanger in front of the fan which supplies this air. In this manner we could vary the heat loss parameter c_q from a value near unity (no heat loss) to a value approaching zero (total heat loss).

Even without these major physical improvements, the existing facility is still quite useful and experience gained from the

experiments described here will allow us to improve our data acquisition and processing procedures. In particular, in future experiments we should segregate those traverses through the gas inside the room in which we wish to measure temperature from those to measure the CO_2 content. These latter traverses should be duplicates of the temperature traverses. In this manner, we will not have to sacrifice one probe's temperature data because of the low aspiration rate imposed by the CO_2 analyzer. With a full set of probe temperature data we could construct more accurate contour plots, and from these we could estimate where the maximum plume temperature occured as a function of height. This would allow us to measure distances along the ceiling from the actual stagnation point rather than from the geometrical fire axis. In the event that the plume were blown off this axis by the incident door jet, this approach would tend to reduce the scatter of our heat transfer coefficient data in the impingement region. A second advantage of segregating the temperature and composition traverses is that calibration gases could be run through the CO_2 analyzer while the temperature traverses were in progress. This procedure would significantly reduce the uncertainty in the CO_2 concentration measurements caused by drift in the analyzer, and would help clarify what fraction of the floor zone temperature increase is caused by heat transfer and how much is due to mixing with the hot combustion products from above. We could further refine this estimate by choosing a reference site at which to monitor the ambient laboratory air temperature and

CO_2 concentration throughout the course of the experiments.

We should also modify the probe data acquisition program to record the minimum and maximum temperatures experienced by the door and aspirated probe thermocouples. This information would complement the existing mean and standard deviation data by showing whether the distribution of temperatures was highly skewed, as we expect it would be near the edges of the interface zone.

10.8 Conclusions

We set out to investigate the flow patterns and convective heat transfer produced by a small fire in a room with a single door or window opening. In this investigation, we used both experimental and computational tools to study the flow phenomenon.

As a starting point, we carried out a careful series of experiments in both quarter and half scale facilities. The results of these tests revealed the basic flow patterns which are established by a fire in a room, under a variety of conditions. The tests in the half scale test room also provided us with a detailed data base which we used to find the convective and radiant heat transfer to the surfaces of the room.

The results from the quarter scale hydraulic simulations revealed the basic flow patterns, as functions of the fire strength, fire location, and room opening geometry. Because the magnitude of the dimensionless heat input parameter was limited by the initial density difference between the brine and the fresh water, these tests simulated very

small fires. As a result, they represented a good test of our Boussinesq room model calculation. In addition, because the density was primarily a function of the salinity, these experiments modeled the case of a room with adiabatic surfaces. These tests showed that for a given fire strength, the size of the opening had a profound effect on the conditions within the room. Not only did the interface height fall as expected because of the reduced counter-flow through the opening, but the increased shear greatly increased the mixing between the two streams. This produced significant contamination of the lower layer fluid with hot combustion products from above.

On the other hand, in the half scale test facility actual fires were used and the outer surfaces of the walls were convectively cooled. In these tests, the dimensionless heat input parameter was significantly greater than in the quarter scale tests, and heat transfer effects were important.

Because of the increased dimensionless heat release, the fire plume was significantly stronger. As the plume impinged on the ceiling, it spilled out to form an initially radial ceiling jet. When this jet reached the side walls, it had sufficient momentum to penetrate all the way down to the interface. In addition, because convective heat transfer to the relatively cold ceiling and walls reduced the temperature of the fluid in this jet, and because of the mixing set up by the secondary flows, there was a clearly discernable non-zero temperature gradient within the hot upper layer. Finally, radiant heat transfer from the ceiling and upper walls heated the floor and lower walls, and

generated natural convection currents in the lower layer. These currents were partially responsible for heating the lower layer fluid, and, together with the secondary flows in the upper layer, resulted in greater mixing at the interface, indicated by a diffuse interface zone.

These two series of tests allowed us to simulate a range of fire strengths and heat loss conditions. By comparing our half scale data to our earlier quarter scale results, we were able to determine the roles played by the secondary flows and heat transfer processes described above. These latter effects can be expected to be significant in real fire situations.

In addition to our experimental program, we also developed two computation procedures to estimate some of the major flow phenomena in the room.

Guided by our experimental results, we generalized the simple room model of Zukoski (1975) to include a number of features observed during our experiments. In particular, we unified the treatment of the plume and incorporated Kubota's (1977) virtual source calculation to accomodate finite source effects. These can become important in laboratory models of fire plumes, which may have significant initial fluxes of mass and momentum in addition to buoyancy. We also adopted a lumped parameter approach to empirically estimate the mixing which occurs across the interface as a result of the combined action of secondary flows down the side walls, and of the shear between the counter-flowing streams at the doorway. In a similar spirit, we have also included parameters which

model the total heat transfer losses from the upper layer due to convection, and the heat added to the lower layer fluid by natural convection. A comparison of these calculations and our quarter scale results indicated that this simple approach worked well in predicting the height of the interface and the density of the ceiling zone fluid, when mixing and heat transfer effects were absent. Further comparisons between our half scale data and the computed results, based on empirical estimates of the mixing and heat transfer parameters, showed that the model was internally consistent, and that the calculated interface height and temperature difference across the interface agreed very well with our data.

We also developed a two part integral-model computation procedure to calculate the evolution of the buoyant, turbulent plume which rises above the fire, and of the turbulent ceiling jet which is produced by the impingement of the plume upon the ceiling.

The finite source plume calculation assumes that the external temperature is constant in both the upper and lower layers, and that the decrease in buoyancy experienced by the plume as it crosses the interface between these layers is given by the interface jump conditions suggested by Kubota(1977). Given the approximations inherent in this formulation, our data agree remarkably well with the calculated results.

After reviewing the literature, and in particular the earlier work of Alpert(1974), we developed a computational procedure to estimate the convective heat transfer produced by the impingement of the buoyant plume upon the ceiling and the subsequent buoyant ceiling jet flow which

results from it. This work is a generalization of Alpert's approach because we have assumed that the plume will very quickly fill the upper portion of the room with a hot upper layer and that the ceiling jet will entrain this hot upper layer fluid. Alpert(1974), on the other hand, treated the bare ceiling case in which the ceiling jet entrains cold, ambient air. As a result, our ceiling jets can be relatively much less buoyant than those he considered. In addition, our computation is formulated for either axisymmetric or two-dimensional flow, whereas his only treated the axisymmetric case. This extension is necessary because the presence of the sidewalls, in addition to trapping the hot gas which comprises the upper layer, will also channel the initially axisymmetric ceiling jet flow into a basically two-dimensional flow pattern for certain room-fire geometries. We also integrate the momentum and energy equations separately because early in the fire's history when the ceiling is still relatively cold, the temperature difference in the ceiling jet can be reduced to zero while there is still a non-zero momentum flux. Examination of our gas temperature data indicate that this in fact happens in our half scale test facility.

Finally, we have used the results of published turbulent jet and plume impingement studies to estimate the turbulence enhanced stagnation point heat transfer, and the approximate distribution of the heat transfer coefficient over the impingement region. We have also used these results to reformulate the initial conditions of the ceiling jet in terms of characteristic quantities in the upper plume in a consistent manner. Although the data is somewhat scattered, the agreement with the

computed results is quite reasonable. The computed heat transfer coefficients in particular are very close to the measured data. These data show that at small radii, the flow is axisymmetric, whereas at larger distances the data approach the predicted two-dimensional values asymptotically.

These results can be applied to address several practical problems. For example, by using some judicious estimates for the mixing and heat transfer parameters in the simple two layer room model, we can make reasonably accurate predictions of the height of the interface and the temperature of the upper and lower layers as functions of the heat input and opening geometry. These factors have an obvious bearing on the chances for survival for someone in the room. Secondly, our ceiling heat transfer calculation allows us to estimate the convective heat transfer across the entire ceiling. This information has a direct bearing on how quickly the ceiling can be expected to heat up, and on how much damage it may sustain. In addition, these results can be used to study how sensitive sensor systems must be to react to a given strength fire in a given time.

Furthermore, the specification of the convective heat transfer to the ceiling and upper walls, and the consequent temperature increase of these surfaces, is a necessary first step in calculating if and when the room will reach the "flash over" state.

Finally, the success of these simple, semi-empirical models gives us hope that this same approach may be employed to model the flow of

smoke and fire spread in large, multi-room structures. The advantage of this approach is that it should be easy to adapt the calculation to the complicated and varied geometries encountered in real buildings. The procedures which we have developed to calculate the flow patterns and heat transfer processes in the room with the fire effectively establish the source conditions for such a multiple room calculation.

REFERENCES

Alpert, R. L. (1974), "Turbulent Ceiling Jet Induced by Large-scale Fire", Tech. Report # 22357-2, Factory Mutual Research Corporation.

Baines, W. D. and Turner, J. S. (1969), "Turbulent Buoyant Convection from a Source in a Confined Region", J. Fluid Mech. ,Vol. 37, pp. 51-80.

Bakke, P. (1957), "An Experimental Investigation of a Wall Jet", J. Fluid Mech. , Vol. 2, p. 467.

Batchelor, G. K. (1954), "Heat Convection and Buoyancy Effects in Fluids", Quarterly J. Roy. Meteor. Soc. , Vol. 80, pp. 339-358.

Becker, H. A. and Yamazaki, S. (1978), "Entrainment, Momentum Flux, and Temperature in Vertical Free Turbulent Diffusion Flames", Combustion and Flame , Vol. 33, pp.123-149.

Beltaos, S. and Rajaratnam, J. (1974), "Impinging Circular Turbulent Jets", J. Hydr. Div., ASCE , Vol. 100, HY10, pp. 1313-1328.

Bradbury, L. J. S. (1972), "The Impact of an Axisymmetric Jet onto a Normal Ground", Aeronautical Quarterly , Vol. 23, p. 141.

Bradshaw, P. and Love, E. M. (1961) "The Normal Impingement of a Circular Air Jet over a Flat Surface", R & M # 3205, Aero Research Council, England.

Cannon, J. B. and Zukoski, E. E. (1976), "Turbulent Mixing in Vertical Shafts under Conditions Applicable to Fires in High Rise Buildings", California Institute of Technology, Technical Report # 1, NSF Grant # 31892X.

Chia, C. J., Giralt, F., and Trass, O. (1977), "Mass Transfer in Axisymmetric Turbulent Impinging Jet", Ind. Eng. Chem., Fundam. , Vol. 16, p. 28.

Chu, V. H. and Vanvari, M. (1976), "Experimental Study of Turbulent Stratified Shearing Flow", J. Hydr. Div., ASCE , Vol. 102, HY6, pp. 691-706.

Corrsin, S. and Uberoi, M. S. (1950), "Further Experiments on the Flow and Heat Transfer in a Heated Turbulent Air Jet", NACA TN 1865.

Donaldson, C. DuP. and Snedeker, R. S. (1971), "A Study of Free Jet Impingement. Part 1 -- Mean Properties of Free and Impinging Jets", J.

Fluid Mech. , Vol. 45, p. 281.

Donaldson, C. DuP., Snedeker, R. S., and Margolis, D. P. (1971), "A Study of Free Jet Impingement. Part 2 -- Free Jet Turbulent Structure and Impingement Heat Transfer", J. Fluid Mech. , Vol. 45, p. 477.

Eckert, E. R. G. and Jackson, T. W. (1950), "Analysis of Turbulent Free-convection Boundary Layer on a Flat Plate", NACA TN 2207.

Ellison, T. H. and Turner, J. S. (1959), "Turbulent Entrainment in Stratified Flows", J. Fluid Mech. , Vol. 6, p. 423.

Emmons, H. W. (1973), "Natural Convection Flow Through an Opening", Harvard Univ., Div. of Engr. and Appl. Sci., Technical Report No. 1, NSF Grant GI 30957.

Galloway, T. R. (1973), "Enhancement of Stagnation Flow Heat and Mass Transfer through Interactions of Free Stream Turbulence", AIChE J. , Vol. 19, p. 608.

Gardon, R. and Akfirat, J. C. (1965), "The Role of Turbulence in Determining the Heat Transfer Characteristics of Impinging Jets", Int. J. Heat Mass Transfer , Vol. 8, p. 1261.

George, W. K. Jr., Alpert, R. L., and Tamanini, F. (1977), "Turbulence Measurements in an Axisymmetric Buoyant Plume", Int. J. Heat Mass Transfer , Vol. 20, pp. 1145-1154.

Giralt, F., Chia, C. J., and Trass, O. (1977), "Characterization of the Impingement Region in an Axisymmetric Turbulent Jet", Ind. Eng. Chem., Fundam. , Vol. 16, p. 21.

Glauret, M. B. (1956), "The Wall Jet", J. Fluid Mech. , Vol. 1, p. 625.

Guitton, D. E. (1968), "Correlation of Hot Wire Data for High Intensity Turbulence, Longitudinal Cooling, and Probe Interference", Rep. No. 68-6, Dept. of Mech. Eng., McGill University.

Heskestad, G. (1980), "Peak Gas Velocity and Flame Heights of Buoyancy Controlled Turbulent Diffusion Flames", Eighteenth Intl. Symp. on Combustion, University of Waterloo, p. 951.

Heskestad, G. (1980), "Pressure Profiles Generated by Fire Plumes Impacting on Horizontal Ceilings", Factory Mutual Research Corp., FMRC J. I. OFOE1.RU RC80-T-54.

Kawagoe, K. (1958), "Fire Behavior in Rooms", Bldg. Res. Inst., Tokyo, Japan, Report No. 27.

Koh, R. C. (1971), "Two-Dimensional Surface Warm Jets", J. Hydr. Div., ASCE , Vol. 97, HY6, pp. 819-836.

Kotsovinos, N. E. (1975), "A Study of the Entrainment and Turbulence in a Plane Buoyant Jet", Calif. Inst. Tech., W. M. Keck Lab of Hydr. and Water Res., Report No. KH-R-32.

Kubota, T. (1977), "Turbulent Buoyant Plume in Stratified Medium", Calif. Inst. Tech., Jet Prop. Center.

Kubota, T. (1981), private communication.

Launder, B. E. and Rodi, W. (1981), "The Turbulent Wall Jet", Prog. Aero. Sci. , Vol. 19, pp. 81-128.

Lowery, G. W. and Vachon, R. I. (1975), "The Effect of Turbulence on Heat Transfer from Heated Cylinders", Int. J. Heat Mass Transfer , Vol. 18, p. 1229.

List, E. J. and Imberger, J. (1973), "Turbulent Entrainment in Buoyant Jets and Plumes", J. Hydr. Div., ASCE , Vol. 99, HY9, pp. 1461-1474.

McCaffery, B. J. and Quintiere, J. G. (1976), "Buoyancy Driven Countercurrent Flows Generated by a Fire Source", Turbulent Buoyant Convection 1976 Intl. Seminar, Intl. Center for Heat and Mass Transfer, Dubrovnik, Yugoslavia, Aug. 30 - Sept. 4, 1976.

Morton, B. R. (1959a), "The Ascent of Turbulent Forced Plumes in a Calm Atmosphere", Int. J. Air Pollution , Vol. 1, p. 184.

Morton, B. R. (1959b), "Forced Plumes", J. Fluid Mech. , Vol. 5, pp. 151-163.

Morton, B. R. (1971) "The Choice of Conservation Equations for Plume Models", J. Geophys. Res. , Vol. 76, pp. 7409-7416.

Morton, B. R., Taylor, G. I., and Turner, J. S. (1956), "Turbulent Gravitational Convection from Maintained and Instantaneous Sources", Proc. Roy. Soc. A , Vol. 234, pp. 1-23.

Nelson, J. L. (1969), "An Experimental Investigation of the Turbulent and Mean Flow Properties of a Plane Two-Dimensional Turbulent Wall Jet", University of Tenn., Ph.D. Thesis, Chem. Engr.

Owen, W. W. (1965), "Density of Aqueous Sodium Chloride Solutions -- Tables and Graphs", Tech. Mem. 65-11, W. M. Keck Lab. of Hydr. and Water Res., Calif. Inst. of Tech.

Poreh, M. and Cermak, J. E. (1959), "Flow Characteristics of a Circular Submerged Jet Impinging Normally on a Smooth Boundary", Proc. 6th Midwest Conf. on Fluid Mech.

Poreh, M., Tsuei, Y. G., and Cermak, J. E. (1967), "Investigation of a Turbulent Radial Wall Jet", J. Applied Mech. , Vol. ,pp. 457-463.

Prahl, J. and Emmons, H. W. (1975), "Fire Induced Flow through an Opening", Combustion and Flame , Vol. 25, pp. 369-385.

Priestley, C. H. B. and Ball, F. K. (1955), "Continuous Convection from an Isolated Source of Heat", Quart. J. Roy. Meteor. Soc. , Vol. 81, pp. 144-157.

Ricou, F. P. and Spalding, D. B. (1961), "Measurements of Entrainment by Axisymmetric Turbulent Jets", J. Fluid Mech. , Vol. 11, pp. 21-32.

Rockett, J. A. (1975), "Fire Induced Gas Flow in an Enclosure", Combust. Sci. and Tech. , Vol. 12, pp. 165-175.

Rouse, H., Yih, C. S., and Humphreys, H. W. (1952), "Gravitational Convection from a Boundary Source", Tellus , Vol. 4, p. 201.

Sargent, W. S. (1982a), "A User's Guide for Three Computer Programs which Calculate Conditions within a Room with a Fire", Calif. Inst. Tech., Jet Propulsion Center.

Sargent, W. S. (1982b), "Numerical Studies of the Wall Jet Formed by the Impingement of a Fire Plume upon the Ceiling in a Room with a Fire", Calif. Inst. Tech., Jet Propulsion Center.

Schlichting, H. (1968), Boundary Layer Theory , 6th Ed., McGraw-Hill, New York, p. 257.

Schmidt, W. (1941), "Turbulente Ausbreitung eines Stromeserhitzer Luft", ZAMM , Vol. 21, pp. 265-278, 351-363.

Schwarz, W. H. and Cosart, W. P. (1961), "The Two-dimensional Turbulent Wall-Jet", J. Fluid Mech. , Vol. 10, pp. 481-495.

Sene, K. and Zukoski, E. E. (1980), private communication.

Sibulkin, M. (1952), "Heat Transfer Near the Forward Stagnation Point of a Body of Revolution", J. Aero. Sci. , Vol. 19, p. 570.

Smith, M. C. and Kuethe, A. M. (1966), "Effects of Turbulence on Laminar Skin Friction and Heat Transfer", Phys. Fluids , Vol. 9, pp. 2337-2344.

Snedeker, R. S. and Donaldson, C. DuP. (1964), "Experiments on Free and Impinging Underexpanded Jets from a Convergent Nozzle", Report No. 63, Aero. Res. Assoc. Princeton.

Stefan, H. (1972), "Dilution of Buoyant Two-Dimensional Surface Discharges", J. Hydr. Div., ASCE , Vol. 98, HY1, pp. 71-86.

Tangren, E. N., Sargent, W. S., and Zukoski, E. E. (1978), "Hydraulic and Numerical Modeling of Room Fires", NSF Grant # ENV 76-06660 and NBS Center for Fire Res. Grant # 5-9004, Calif. Inst. Tech.

Tani, I. and Komatsu, Y. (1964), "Impingement of a Round Jet on a Flat Surface", Proc. 11th Intl. Congr. Appl. Mech. , Munich, pp. 672-676.

Taylor, G. I. (1945), "Dynamics of a Mass of Hot Gas Rising in Air", U. S. Atomic Energy Comm., MDDC 919. LADC 276.

Tennekes, H. and Lumley, J. L. (1972) A First Course in Turbulence , The MIT Press, Cambridge, pp. 104-113, 127-144.

Turner, J. S. (1973), Buoyancy Effects in Fluids , Cambridge Univ. Press, Cambridge, pp. 165-207.

Wilkinson, D. L. and Wood, I. R. (1971), "A Rapidly Varied Flow Phenomenon in a Two Layer Flow", J. Fluid Mech. , Vol. 47, pp. 241-256.

Witze, P.O. and Dwyer, H. A. (1977), "Impinging Axisymmetric Turbulent Flows: The Wall Jet, The Radial Jet, and Opposing Free Jets", Symp. on Turb. Shear Flows , Vol. 1, April 18-20, 1977.

Wright, S. J. (1977), "Effects of Ambient Crossflows and Density Stratification on the Characteristic Behavior of Round Turbulent Buoyant Jets", Report No. KH-R-36, W. M. Keck Lab. of Hydr. and Water Res., Calif. Inst. Tech.

Wygnanski, I. and Fiedler, H. (1969), "Some Measurements in the Self-Preserving Jet", J. Fluid Mech. , Vol. 38, pp. 577-612.

Yokoi, S. (1960), "Study on the Prevention of Fire Spread Caused by Hot Upward Current", Report No. 34, Building Res. Inst., Tokyo, Japan.

You, H. Z. and Faeth, G. M. (1979), "Ceiling Heat Transfer during Fire Plume and Fire Impingement", Fire and Materials , Vol. 3, p. 140.

Zukoski, E. E. (1975), "Convective Flows Associated with Room Fires", Semiannual Prog. Report, NSF Grant GI 31892XI, Cali. Inst. Tech., June 1975.

Zukoski, E. E. (1977), "A Brief Review of Calculation Schemes for Fire Induced Flows through Openings", Calif. Inst. Tech., Jet Propulsion Center, Sept. 1977.

Zukoski, E. E. (1978), "Development of a Stratified Ceiling Layer in the Early Stages of a Closed Room Fire", Fire and Materials , Vol. 2, pp. 54-62.

Zukoski, E. E. and Kubota, T. (1978), "A Computer Model for Fluid Dynamic Aspects of a Transient Fire in a Two Room Structure", NBS Center for Fire Res. Grant No. 5-9004, Calif. Inst. Tech., June 1978.

Zukoski, E. E. and Kubota, T. (1980), "Two-layer Modeling of Smoke Movement in Building Fires", Fire and Materials , Vol. 4, pp. 17-27.

Zukoski, E. E. and Kubota, T., and Cetegen, B. (1980), "Entrainment in Fire Plumes", Fire Safety Journal , Vol. 3, pp. 107-121.

Zukoski, E. E., Kubota, T, and Veldman, C. C. (1975), "An Experimental Investigation of the Heat Transfer from a Buoyant Gas Plume to a Hortizontal Ceiling. Part I: Unobstructed Ceiling. Part II: Effects of Ceiling Layer", Tech. Report No. 1, NBS Grant No. 5-9004, Calif. Inst. Tech., Oct. 1975.

Appendix A

EXPERIMENTAL DATA AND CALCULATIONS

In Chapter IX we examined one case (experiment 15) in some detail, and then presented a comparison of results from several other experiments in order to study the effects of varying the strength of the fire, the type of the opening to the external environment (door or window), and the location of the fire. However, in order to simplify the figures, we did not present a comparision between the experimentally measured data from each of these other typical experiments and the corresponding calculated results. Therefore we have collected here a complete set of figures for experiments 7, 10, 13, and 16. Each figure contains the axisymmetric and two-dimensional ceiling jet calculations in addition to the measured data. The variables plotted include the dimensionless heat transfer coefficient, the dimensionless gas temperature measured 2.5 cm below the ceiling, the dimensionless temperature difference between the gas and the ceiling above it, the dimensionless local convective heat transfer rate, and the dimensionless total heat transfer rate to the ceiling.

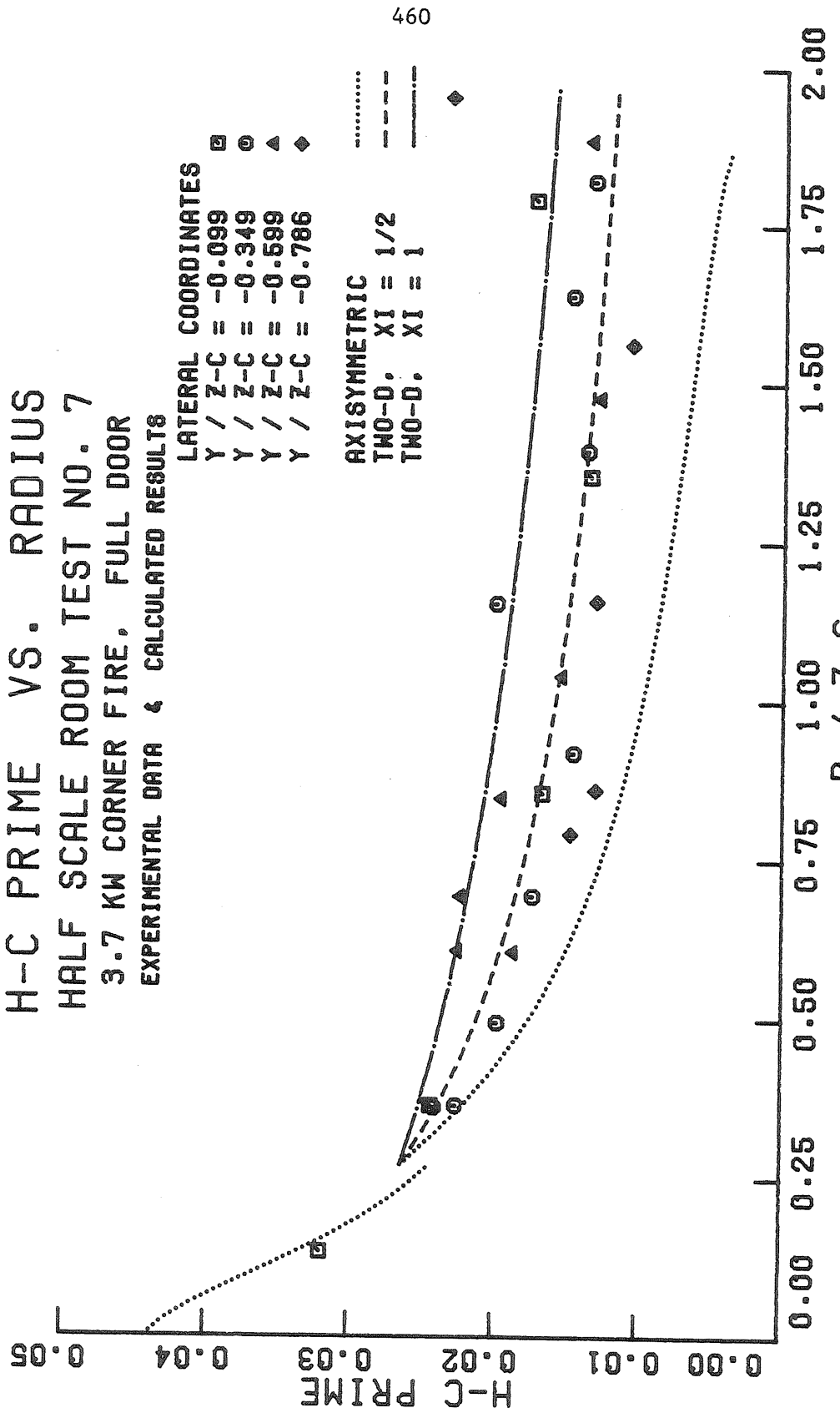

Figure (A.1) Dimensionless Heat Transfer Coefficients, Exp. 7 (Experimental Data and Calculated Results).

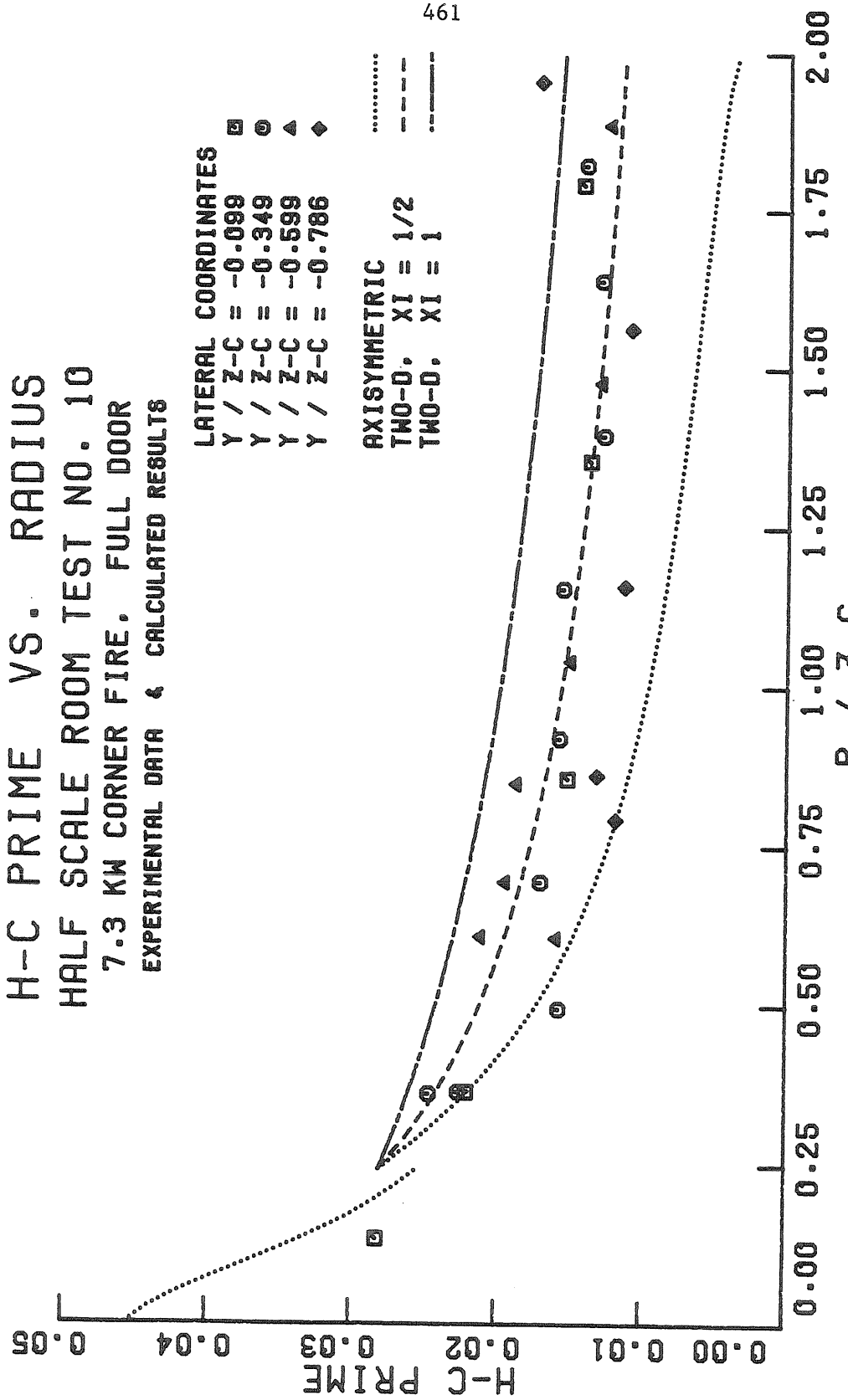

Figure (A.2) Dimensionless Heat Transfer Coefficients, Exp. 10 (Experimental Data and Calculated Results).

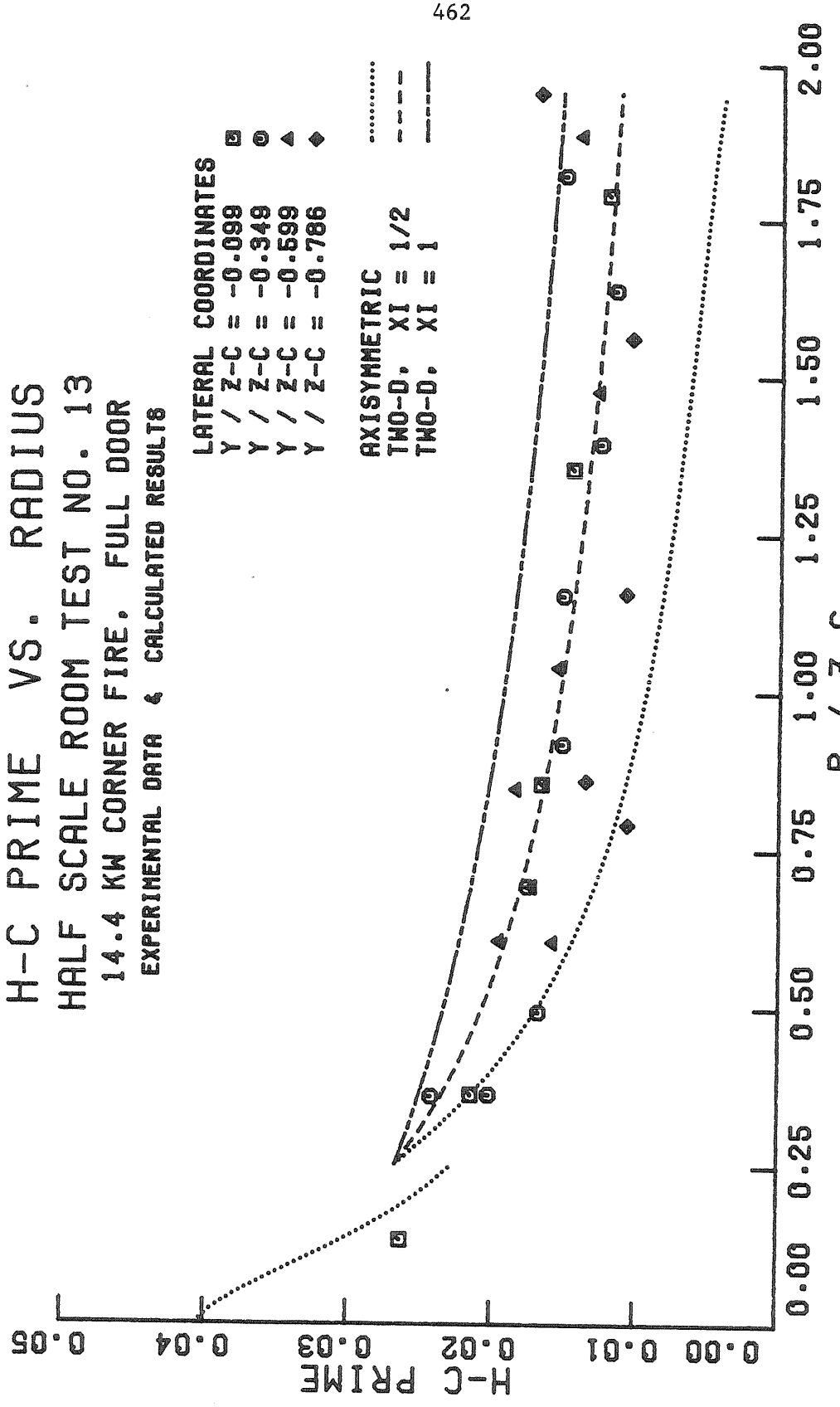

Figure (A.3) Dimensionless Heat Transfer Coefficients, Exp. 13 (Experimental Data and Calculated Results).

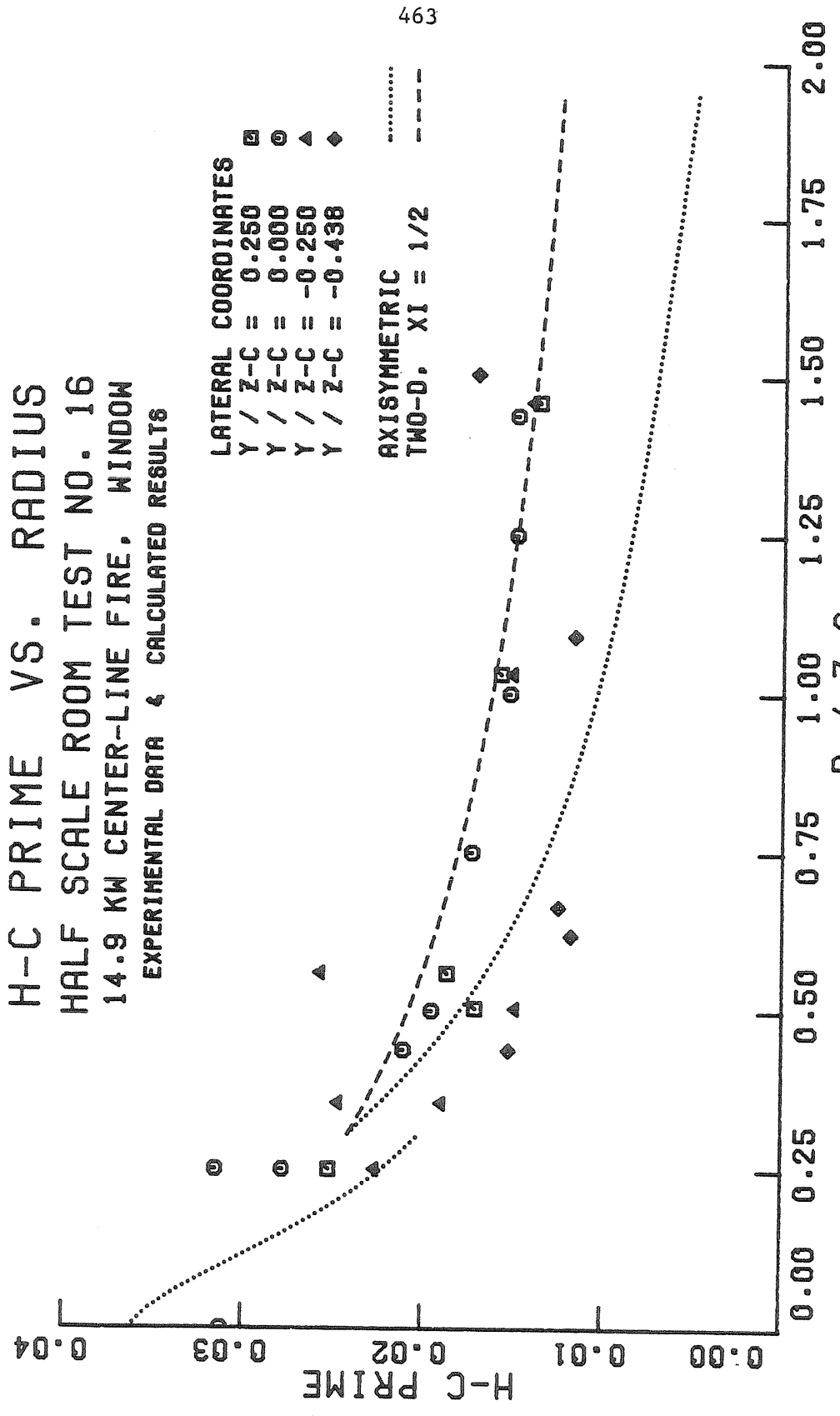

Figure (A.4) Dimensionless Heat Transfer Coefficient, Exp. 16 (Experimental Data and Calculated Results).

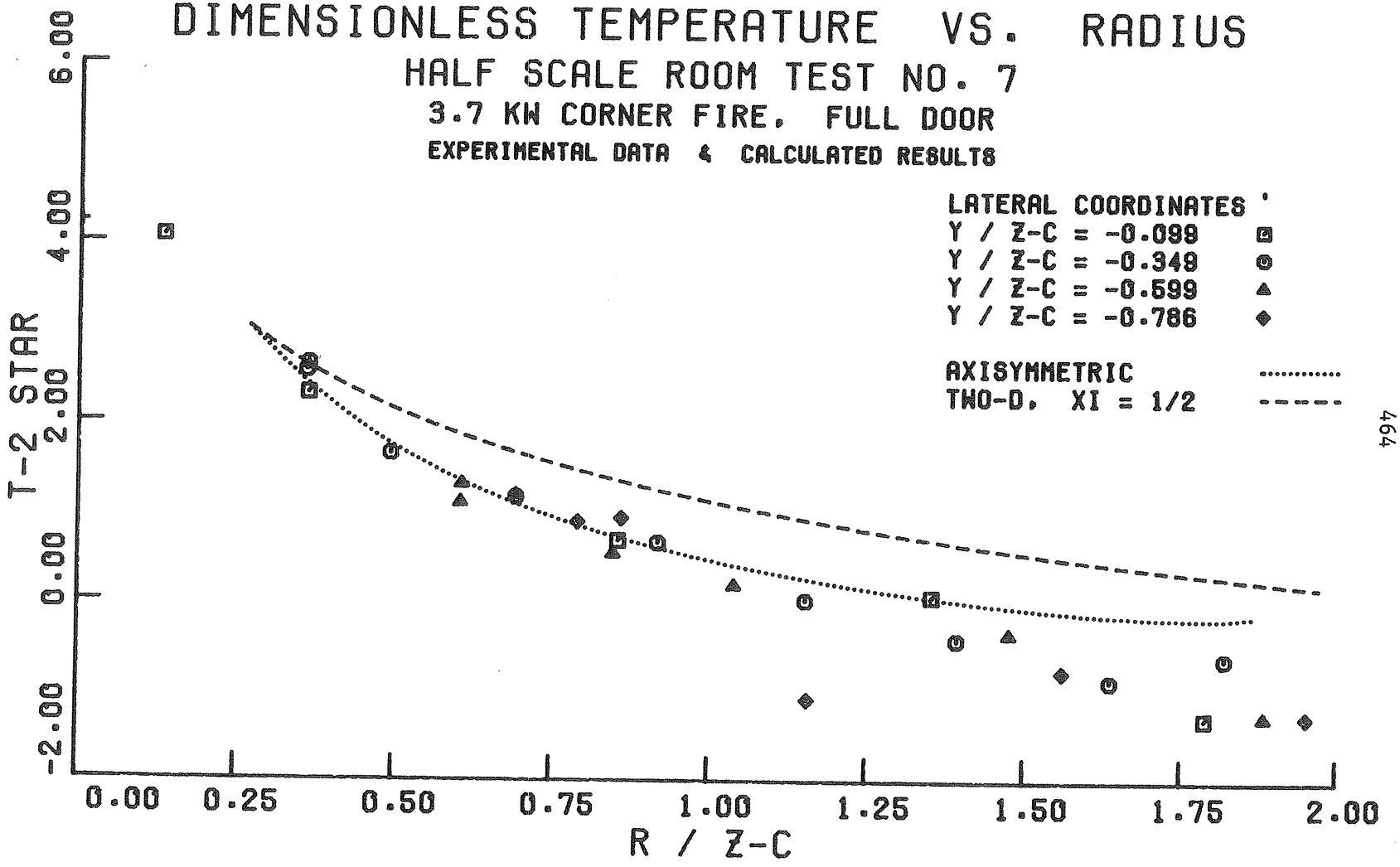

Figure (A.5) Dimensionless Gas Temperature Difference, Exp. 7 (Experimental Data and Calculated Results).

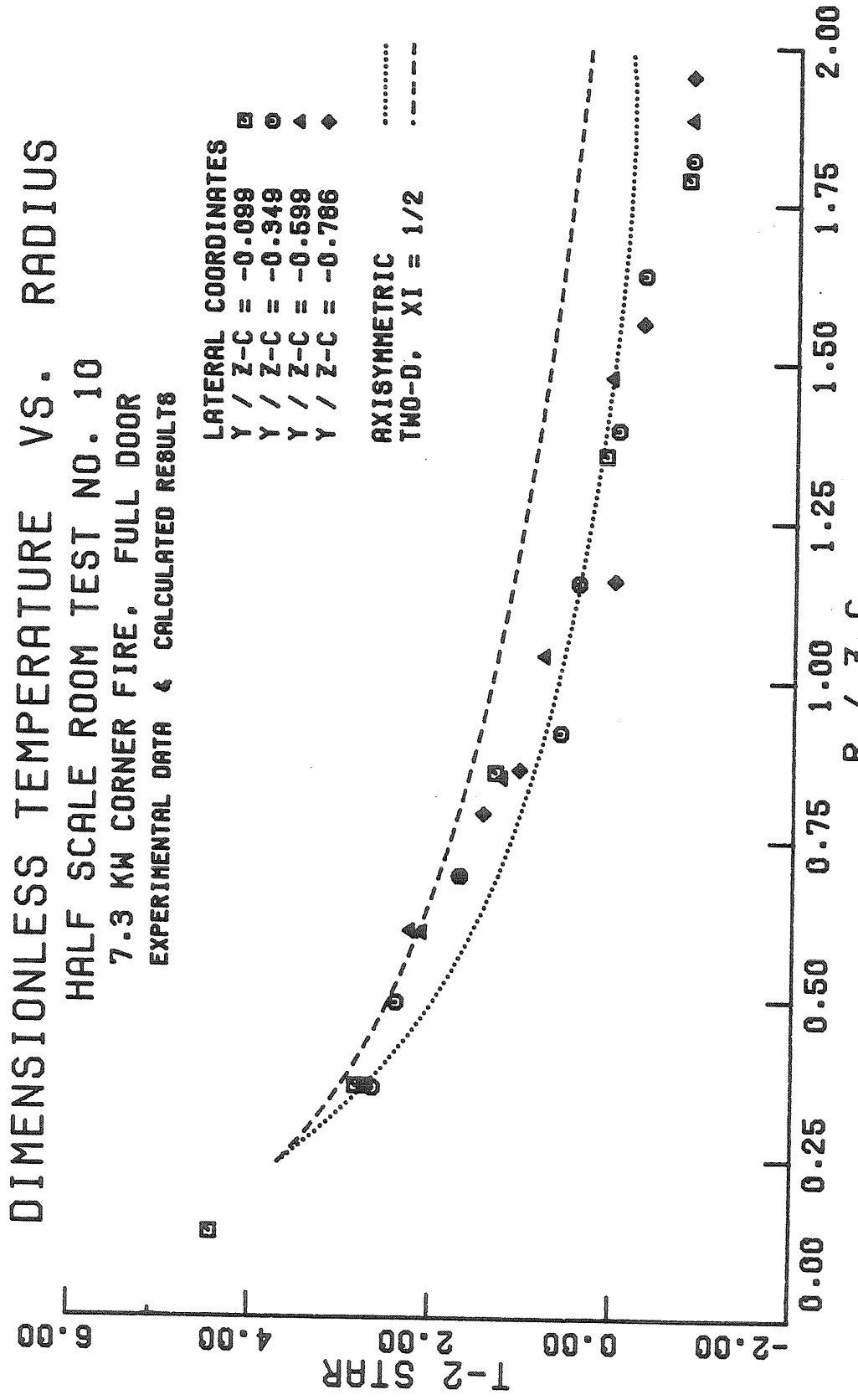

Figure (A.6) Dimensionless Gas Temperature Difference, Exp. 10 (Experimental Data and Calculated Results).

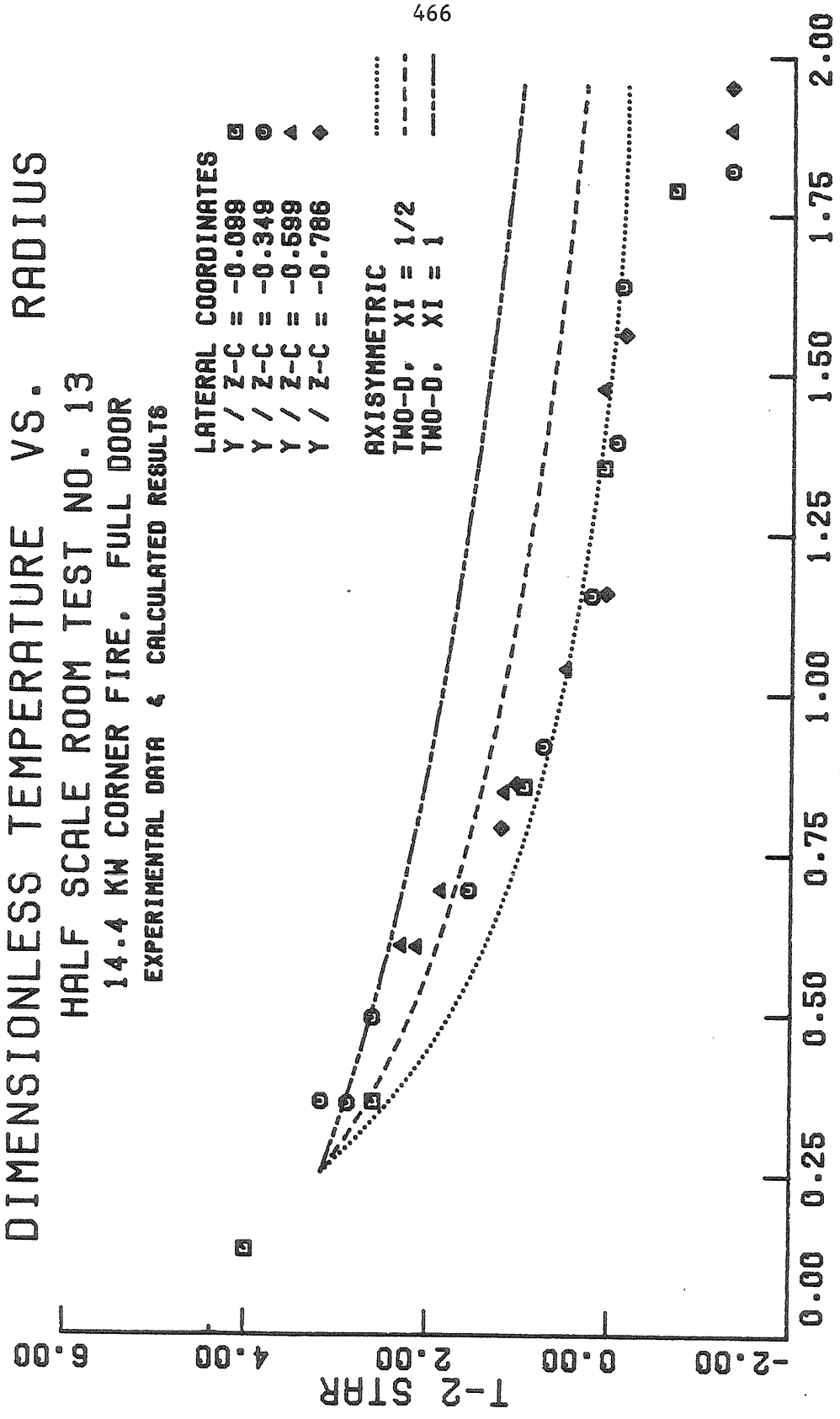

Figure (A.7) Dimensionless Gas Temperature Difference, Exp. 13 (Experimental Data and Calculated Results).

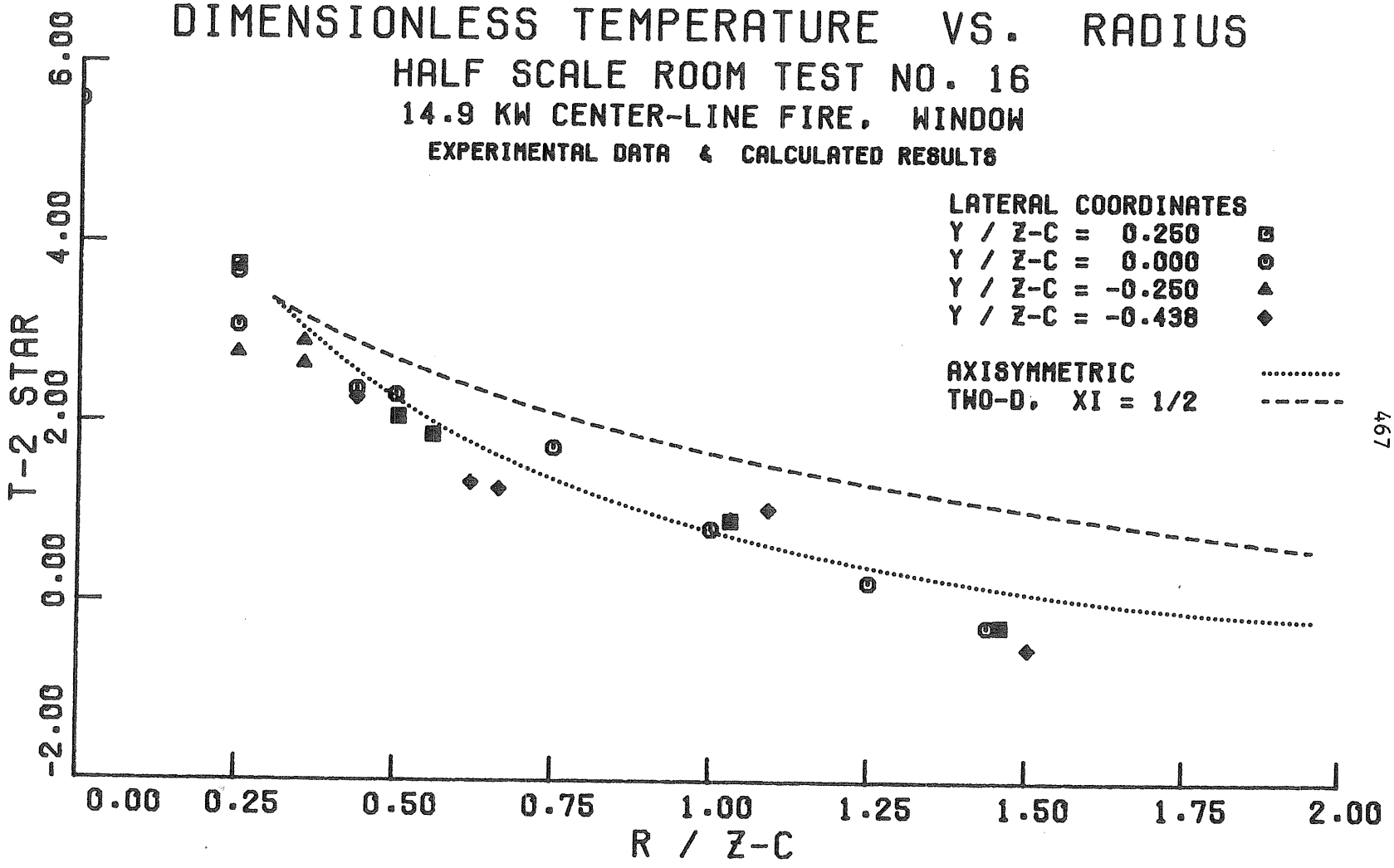

Figure (A.8) Dimensionless Gas Temperature Difference, Exp. 16 (Experimental Data and Calculated Results).

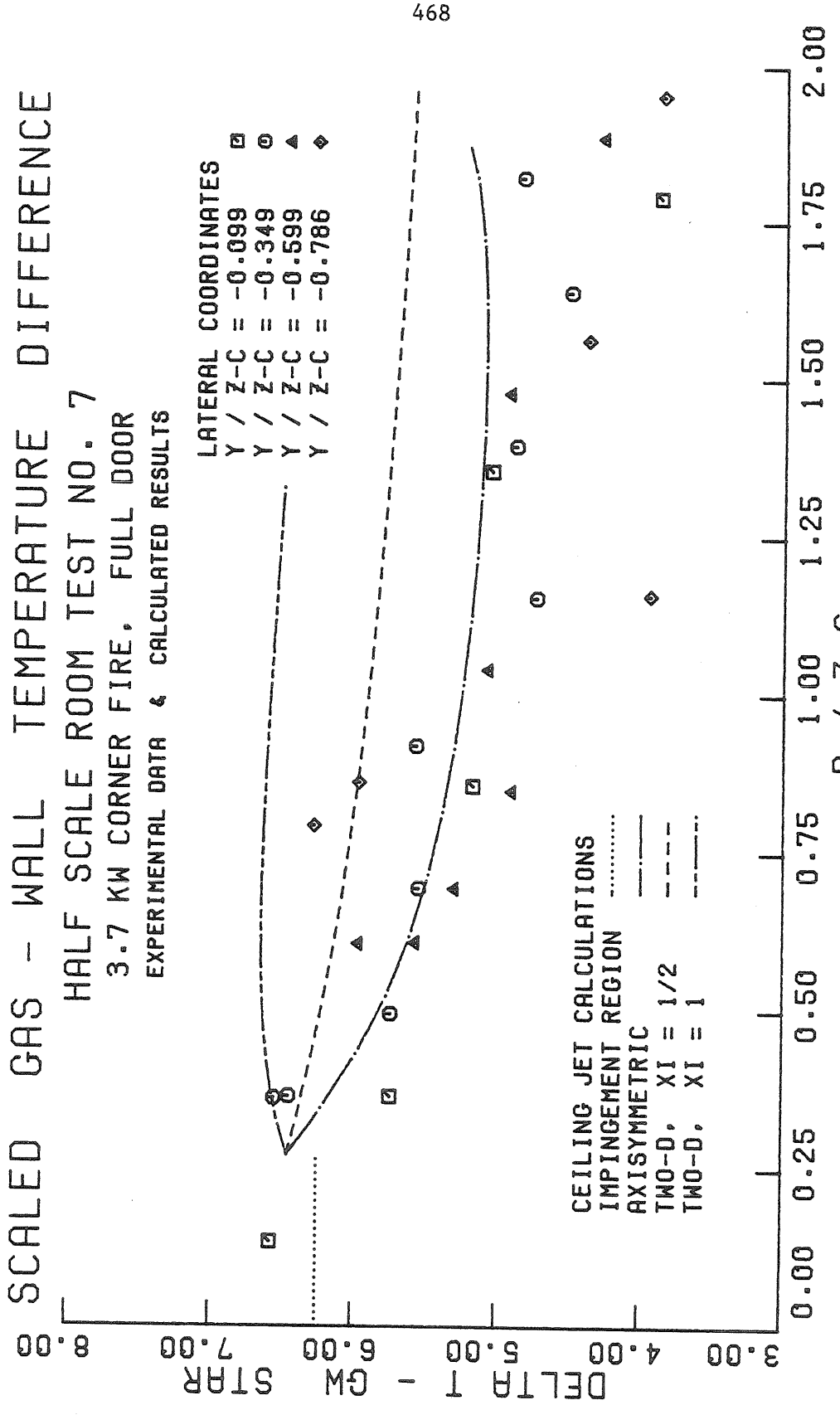

Figure (A.9) Dimensionless Gas-Wall Temperature Difference, Exp. 7 (Experimental Data and Calculated Results).

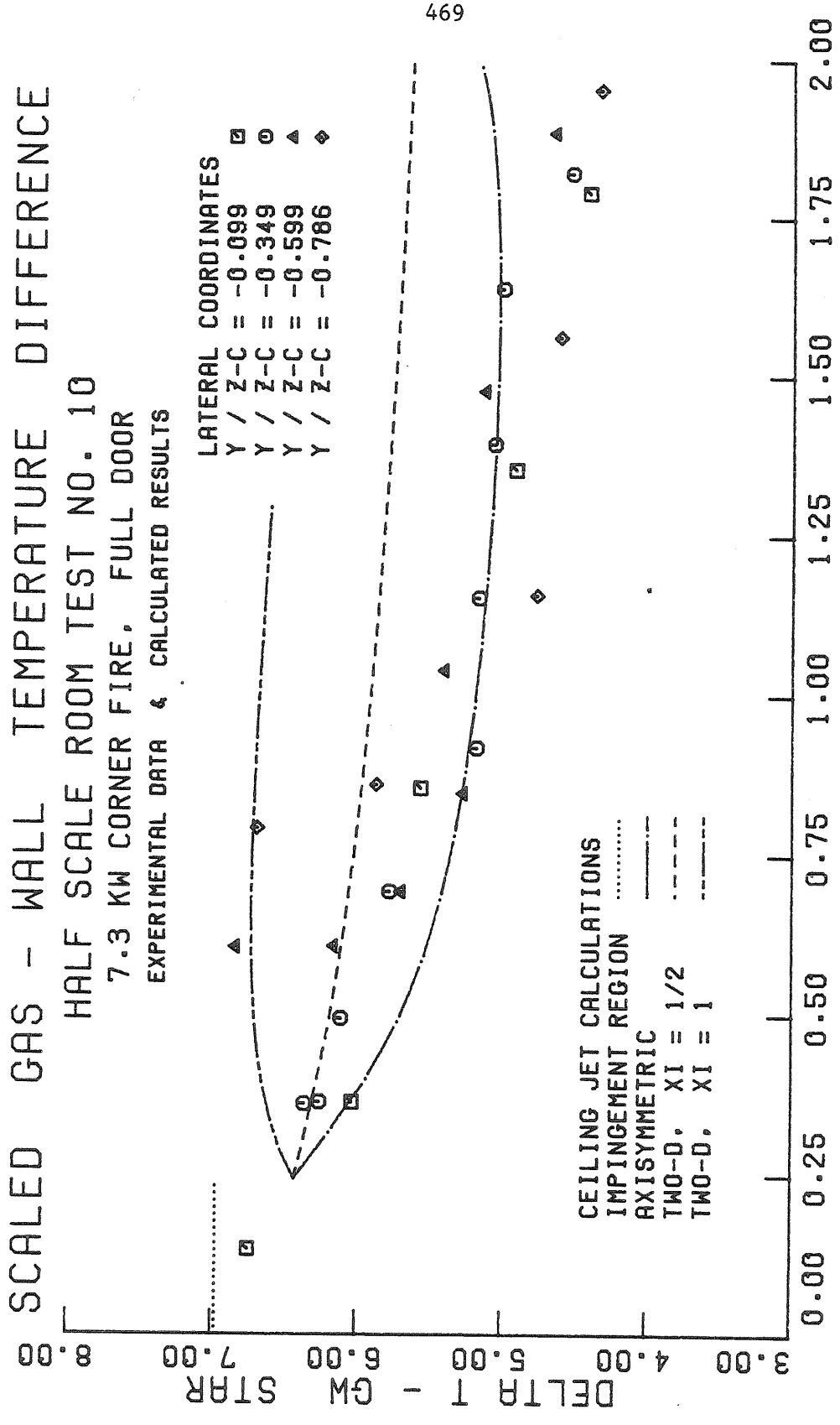

Figure (A.10) Dimensionless Gas-Wall Temperature Difference, Exp. 10 (Experimental Data and Calculated Results).

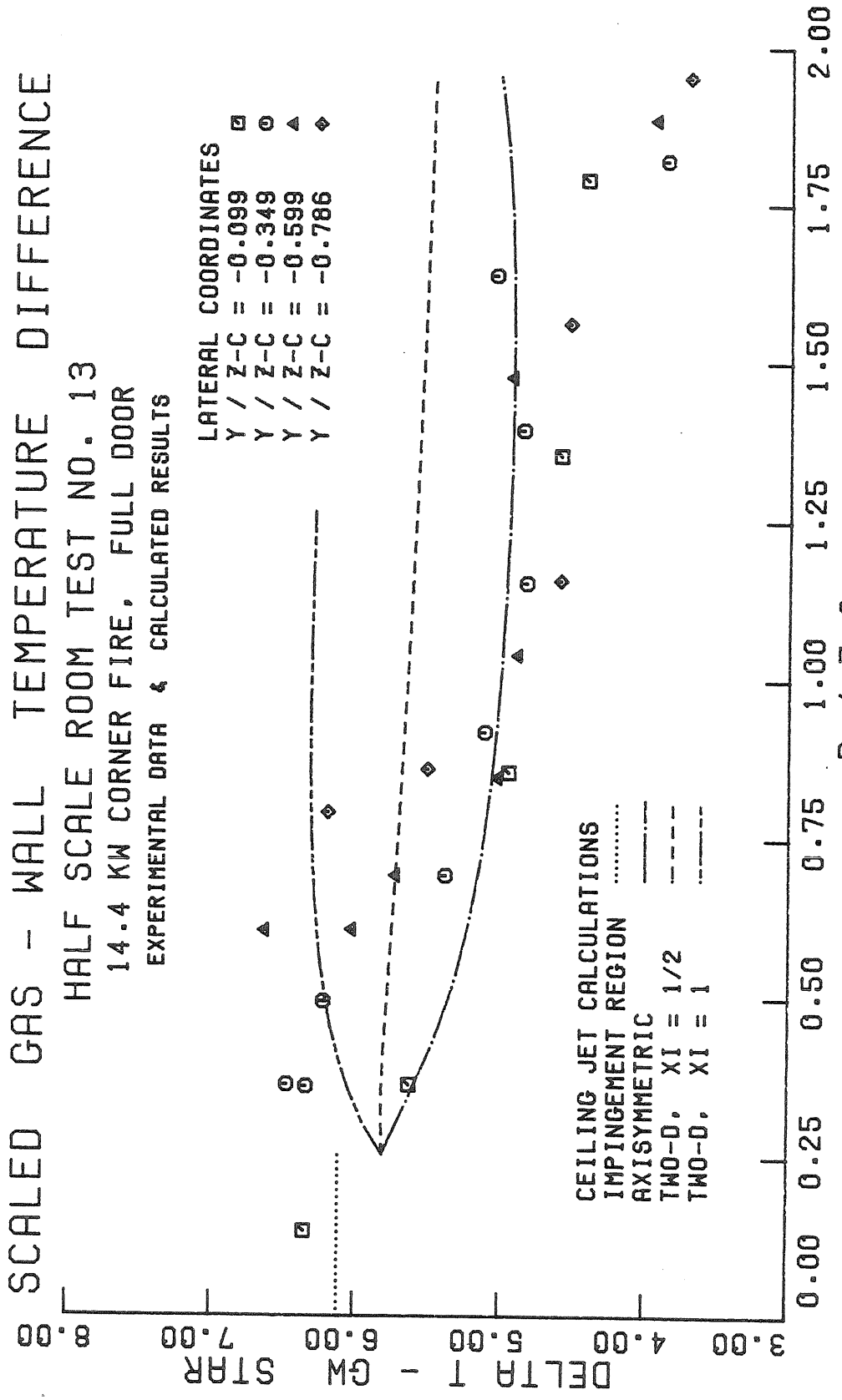

Figure (A.11) Dimensionless Gas-Wall Temperature Difference, Exp. 13 (Experimental Data and Calculated Results).

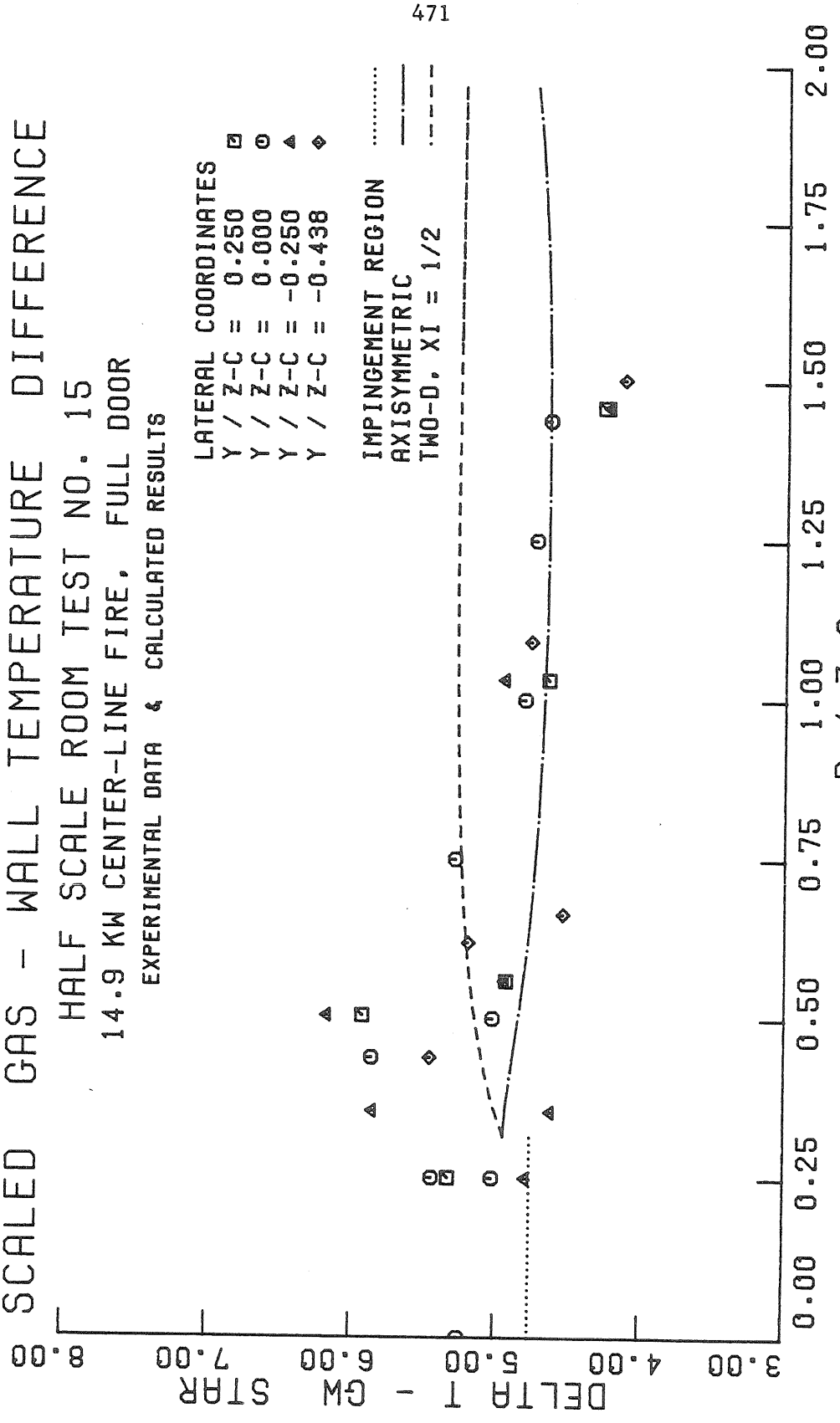

Figure (A.12) Dimensionless Gas-Wall Temperature Difference, Exp. 15 (Experimental Data and Calculated Results).

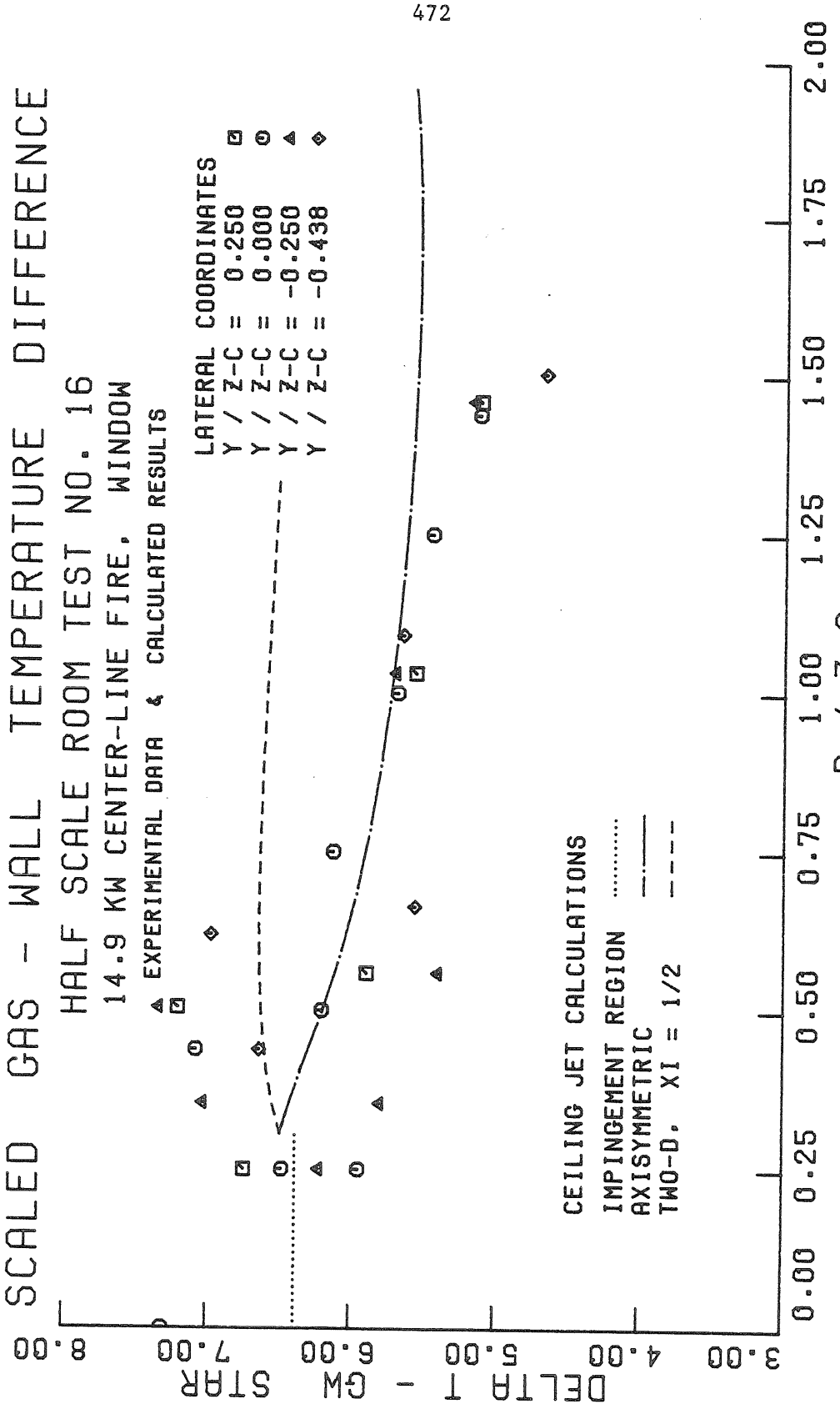

Figure (A.13) Dimensionless Gas-Wall Temperature Difference, Exp. 16 (Experimental Data and Calculated Results).

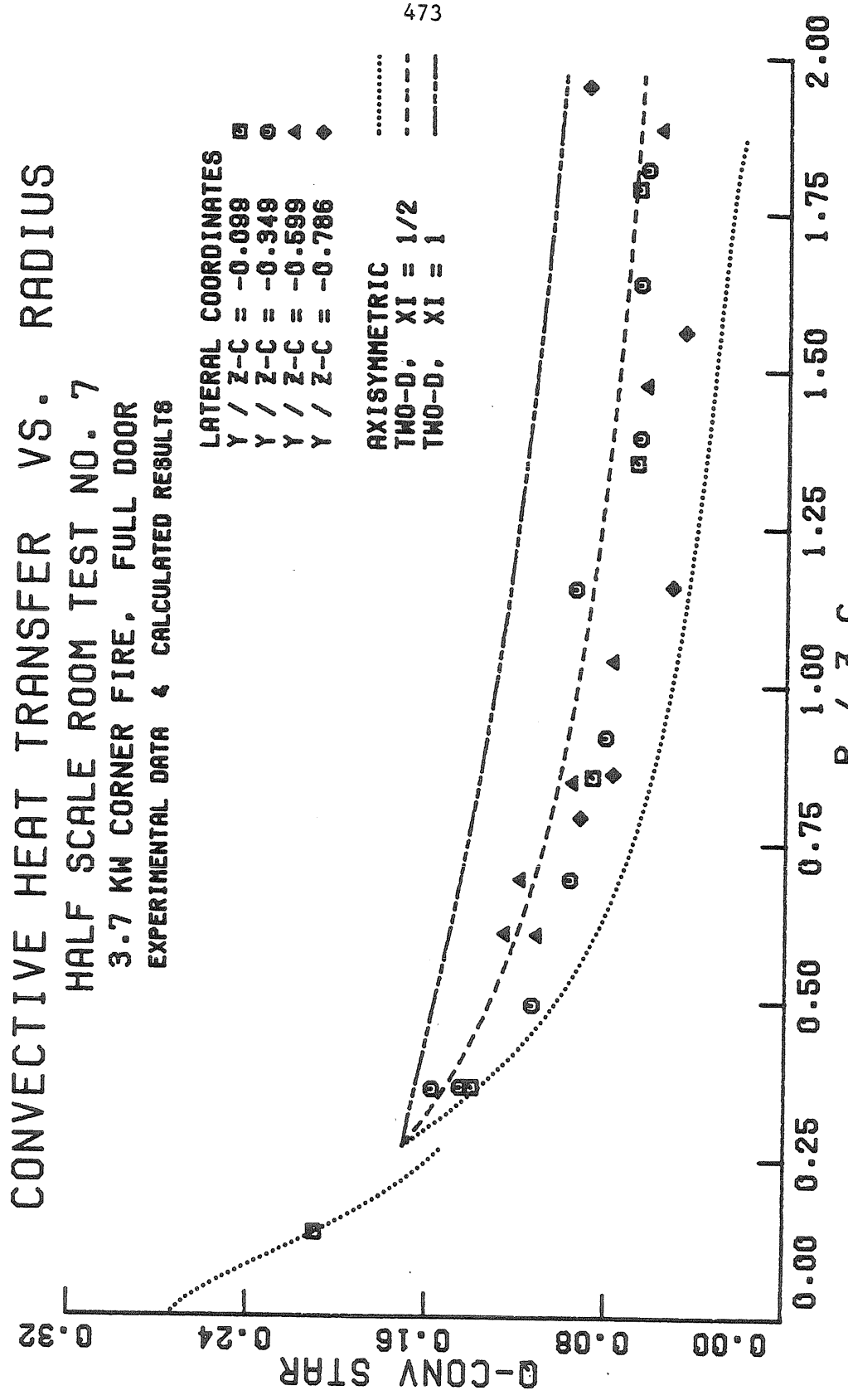

Figure (A.14) Dimensionless Convective Heat Transfer Rate, Exp. 7 (Experimental Data and Calculated Results).

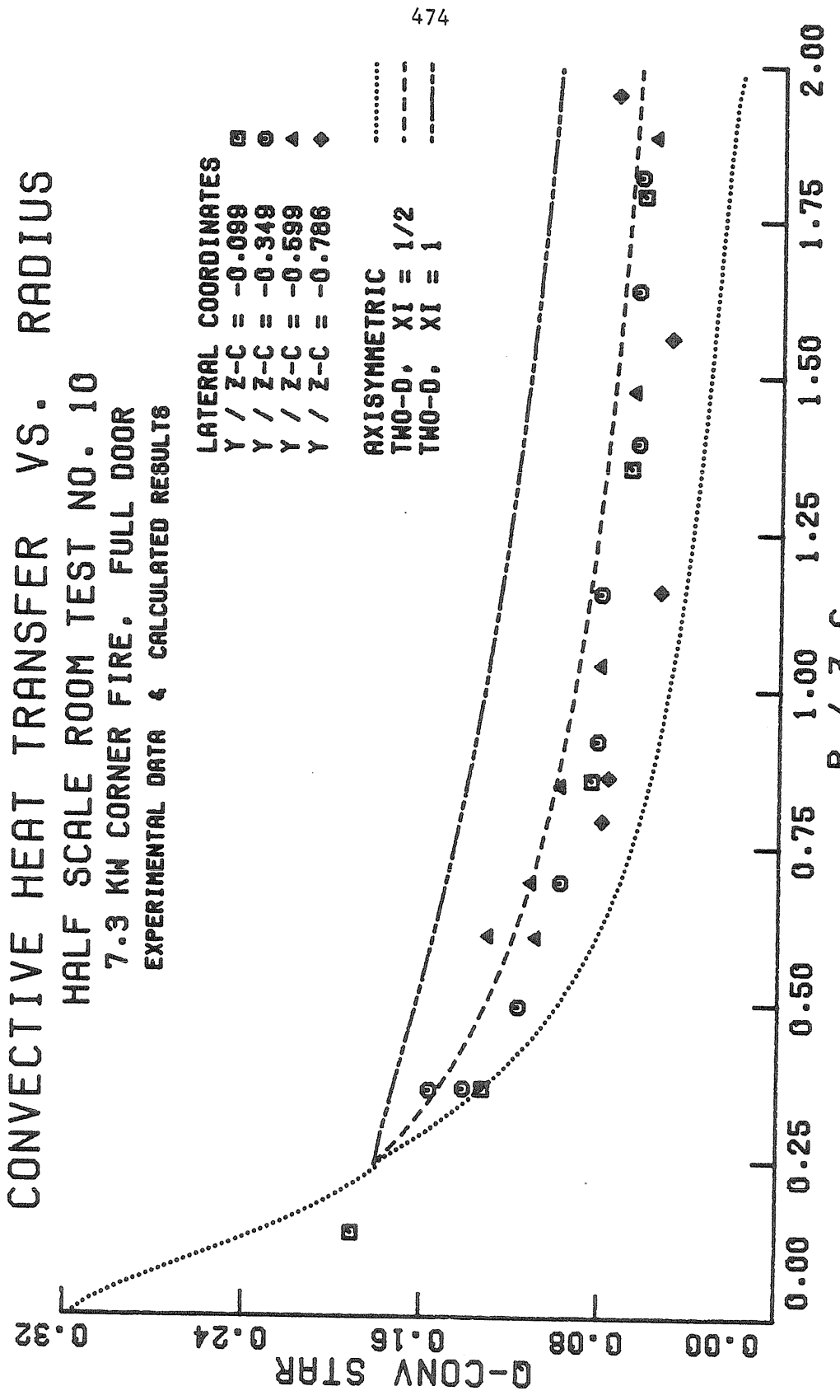

Figure (A.15) Dimensionless Convective Heat Transfer Rate, Exp. 10 (Experimental Data and Calculated Results).

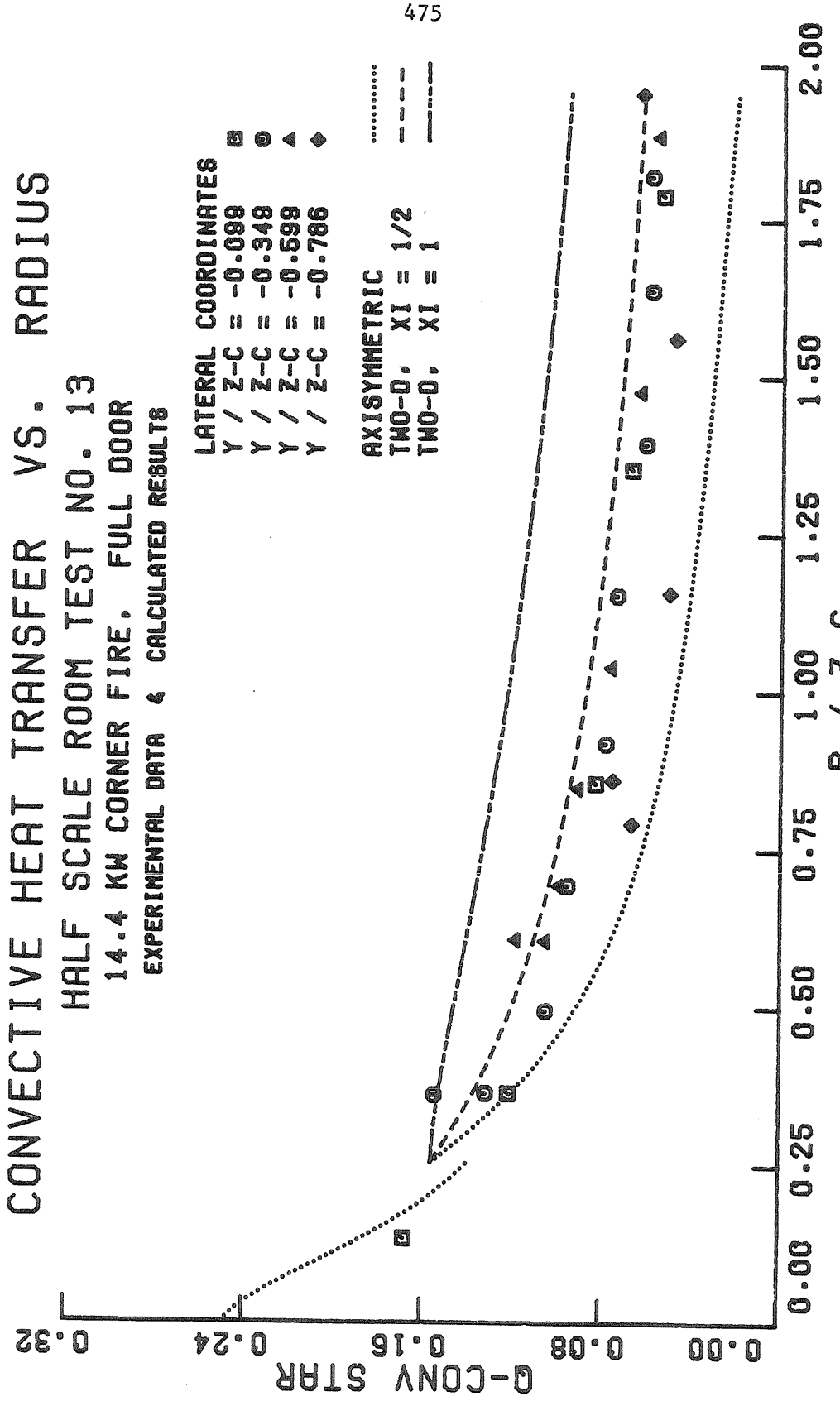

Figure (A.16) Dimensionless Convective Heat Transfer Rate, Exp. 13 (Experimental Data and Calculated Result).

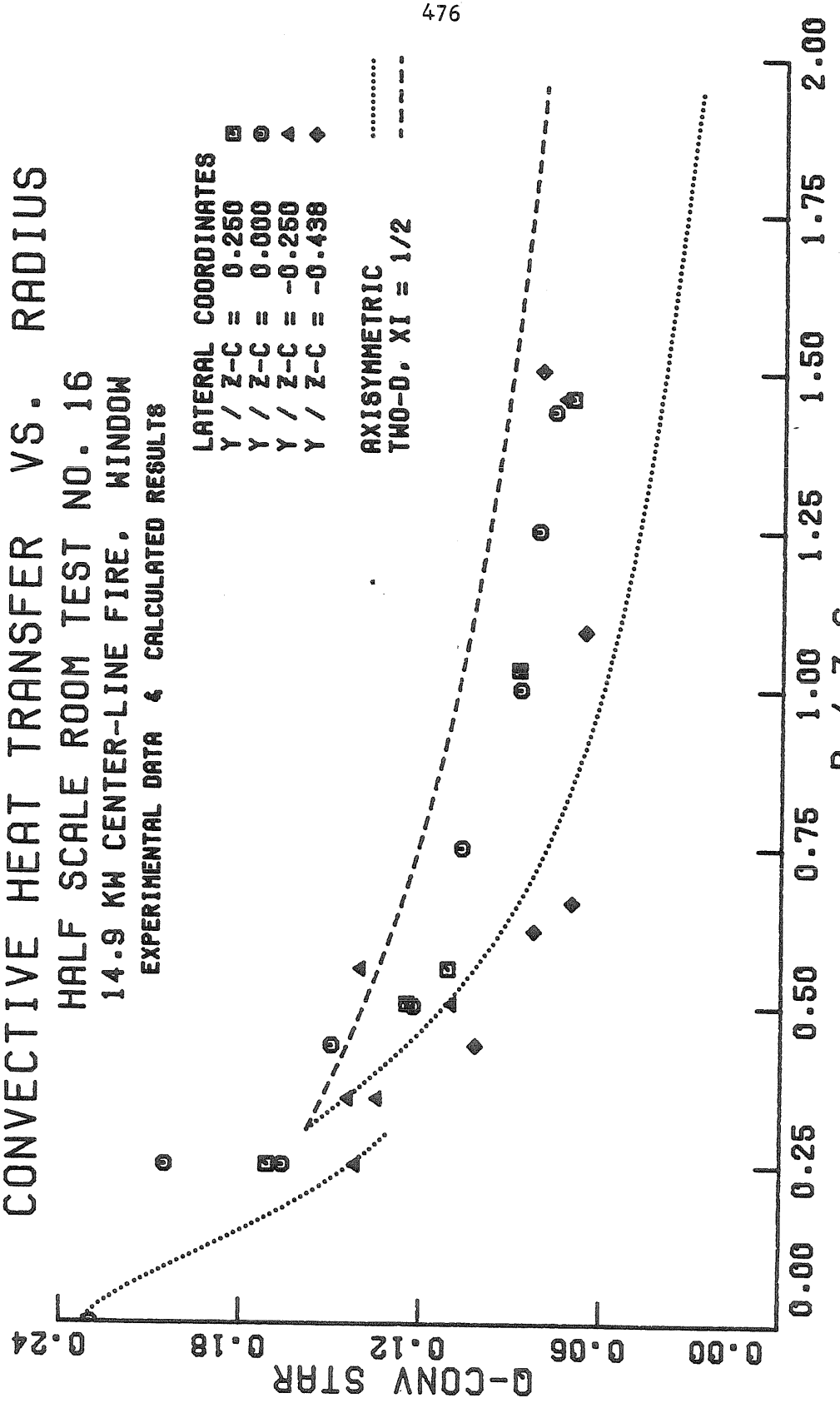

Figure (A.17) Dimensionless Convective Heat Transfer Rate, Exp. 16 (Experimental Data and Calculated Results).

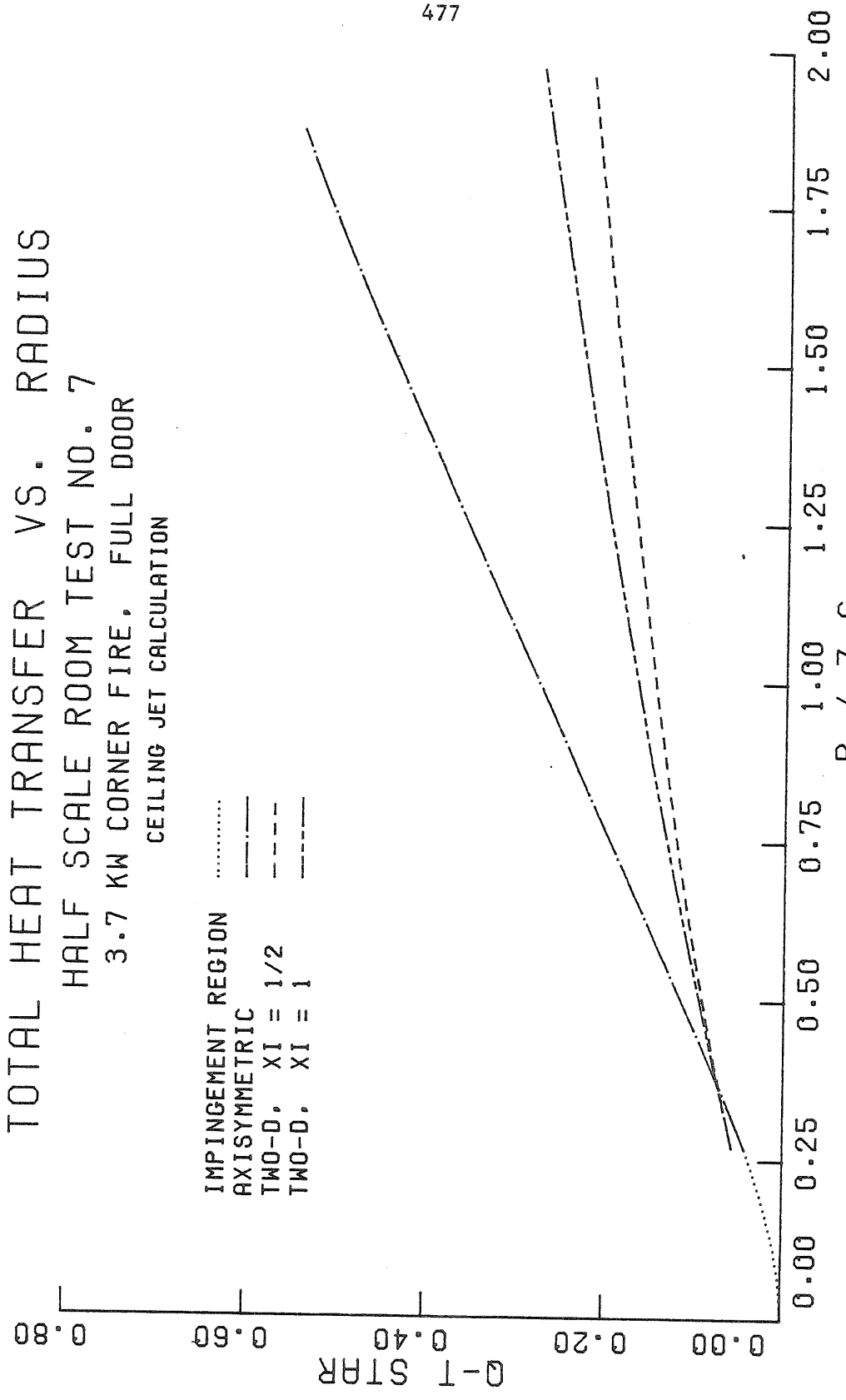

Figure (A.18) Dimensionless Total Convective Flux to the Ceiling, Exp. 7 (Axisymmetric and Two-dimensional Calculations).

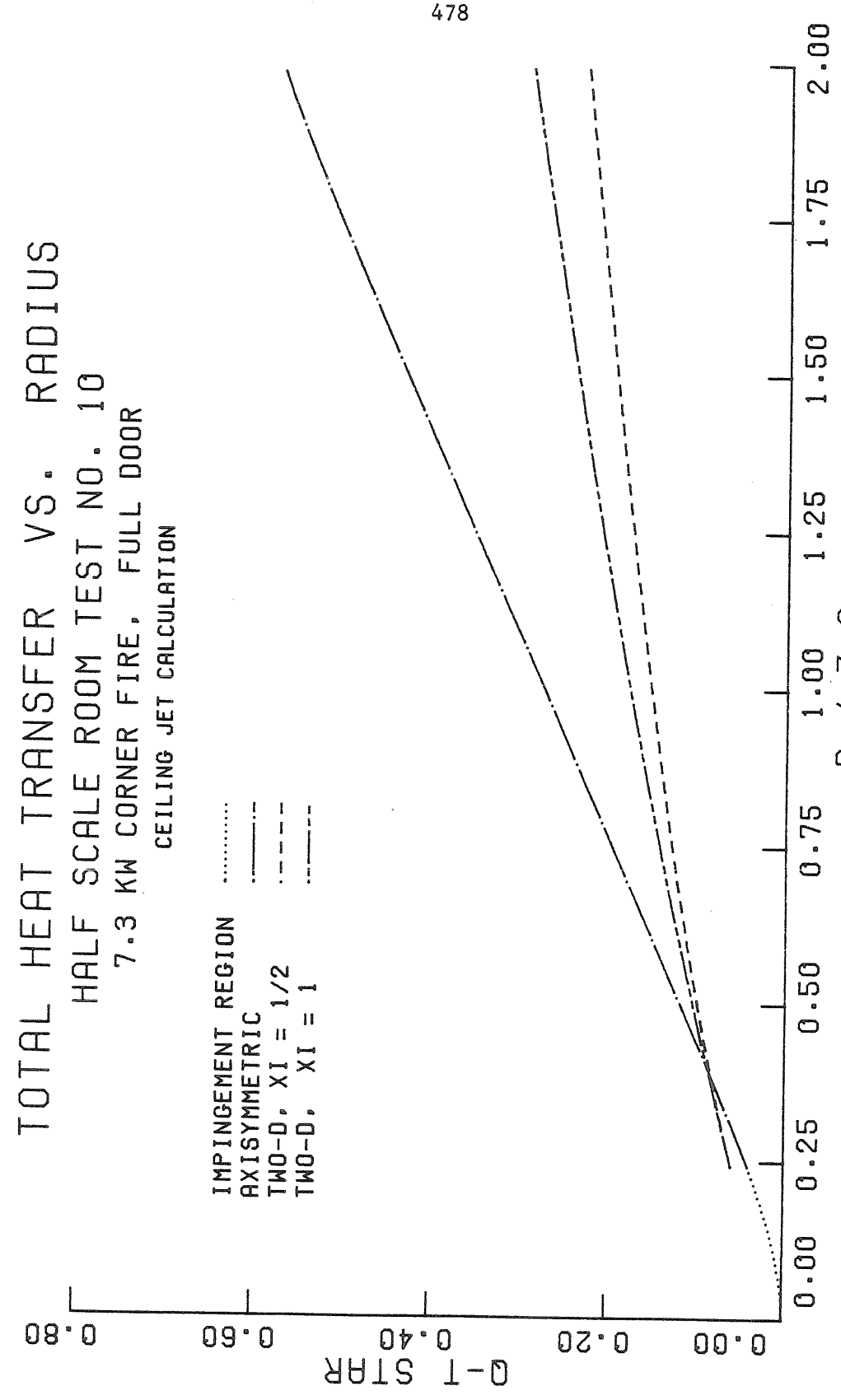

Figure (A.19) Dimensionless Total Convective Flux to the Ceiling, Exp. 10 (Axisymmetric and Two-dimensional Calculations).

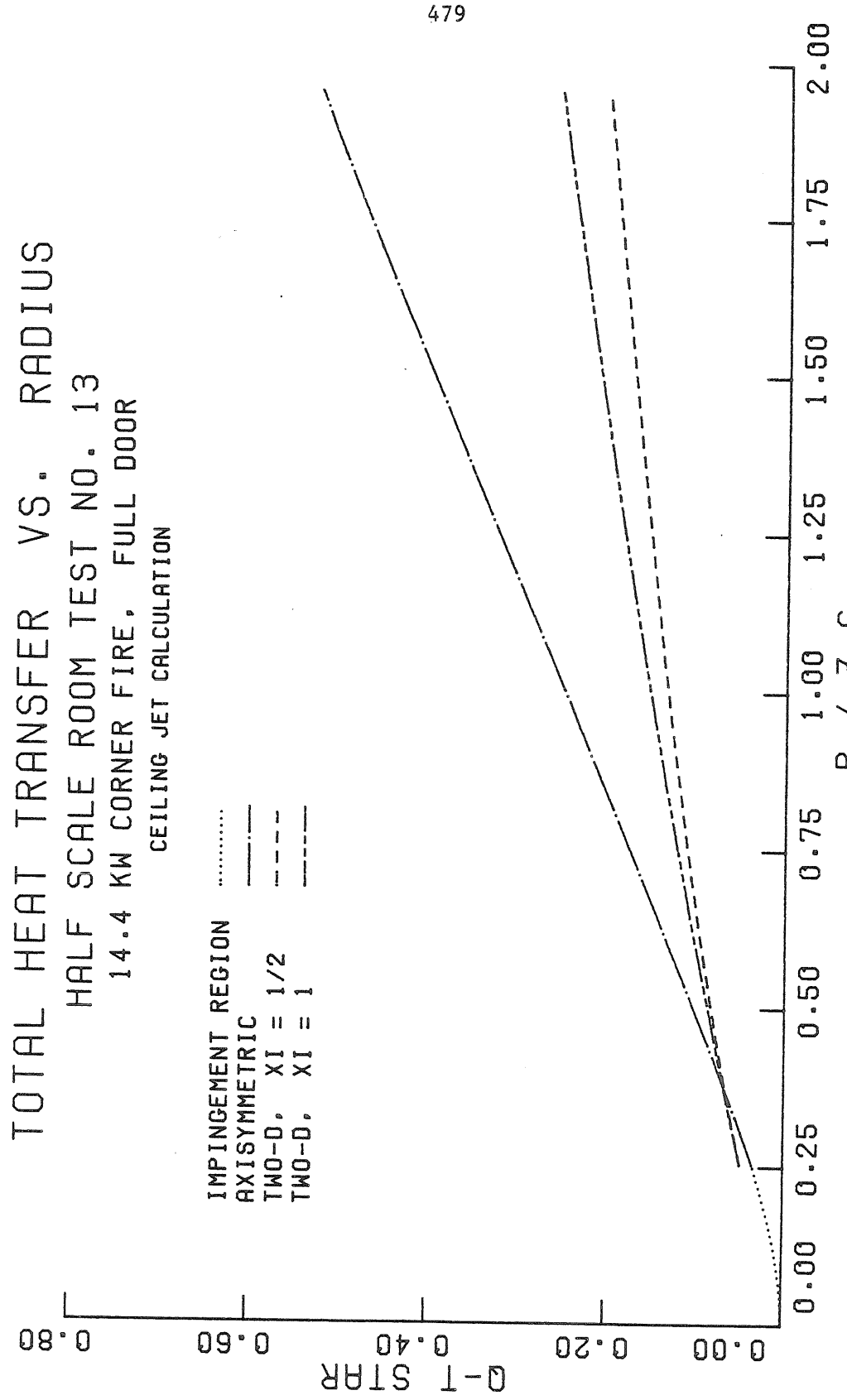

Figure (A.20) Dimensionless Total Convective Flux to the Ceiling, Exp. 13 (Axisymmetric and Two-dimensional Calculations).

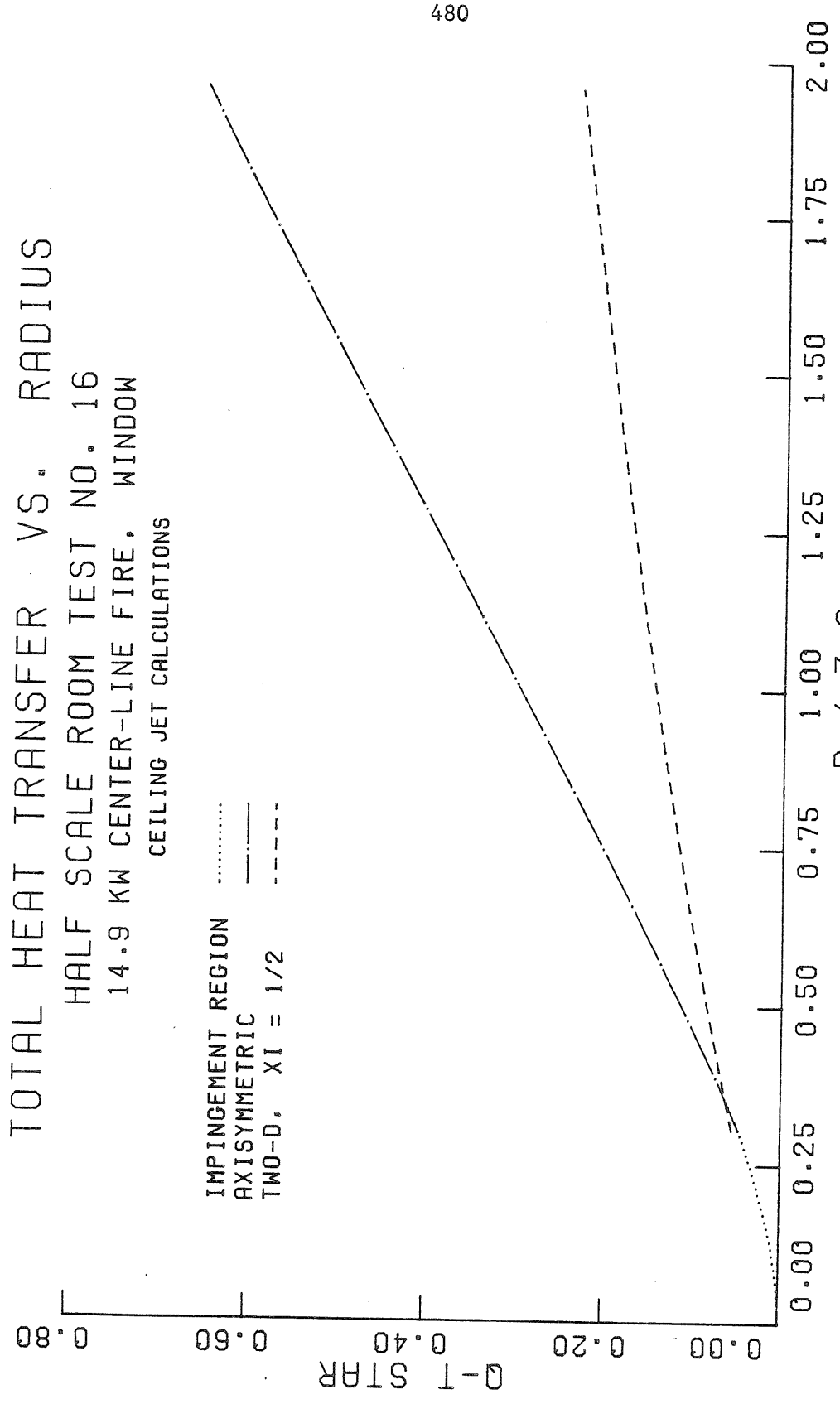

Figure (A.21) Dimensionless Total Convective Flux to the Ceiling, Exp. 15 (Axisymmetric and Two-dimensional Calculations).